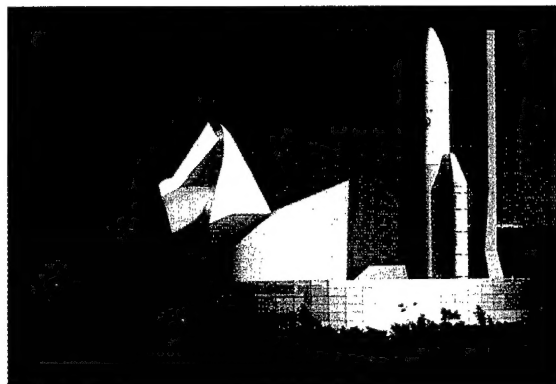
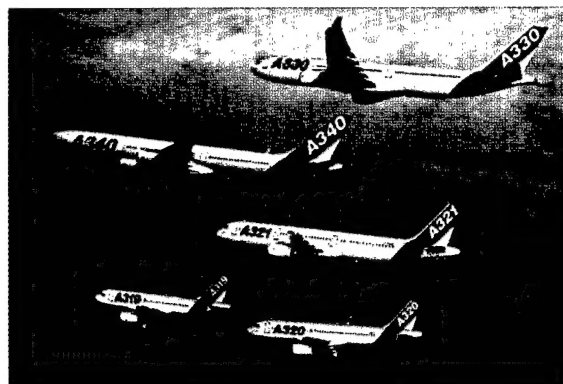
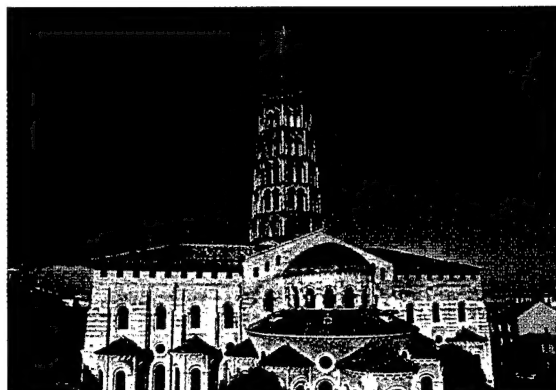
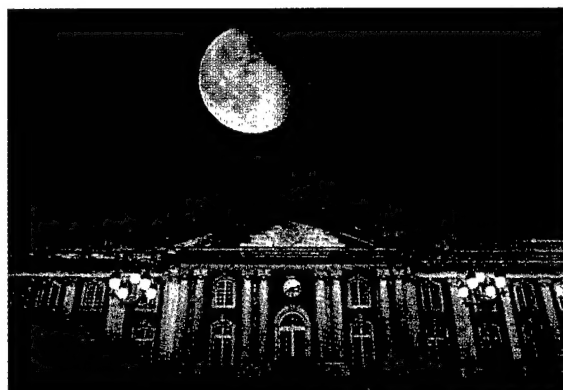


ICTASF 99

18th International Congress on Instrumentation in Aerospace Simulation Facilities



TOULOUSE, France
June 14-17, 1999

ONERA



DISTRIBUTION STATEMENT A
Approved for Public Release
Distribution Unlimited



REPORT DOCUMENTATION PAGE

Form Approved OMB No. 0704-0188

Public reporting burden for this collection of information is estimated to average 1 hour per response, including the time for reviewing instructions, searching existing data sources, gathering and maintaining the data needed, and completing and reviewing the collection of information. Send comments regarding this burden estimate or any other aspect of this collection of information, including suggestions for reducing this burden to Washington Headquarters Services, Directorate for Information Operations and Reports, 1215 Jefferson Davis Highway, Suite 1204, Arlington, VA 22202-4302, and to the Office of Management and Budget, Paperwork Reduction Project (0704-0188), Washington, DC 20503.

1. AGENCY USE ONLY (Leave blank)		2. REPORT DATE 18 June 1999		3. REPORT TYPE AND DATES COVERED Conference Proceedings	
4. TITLE AND SUBTITLE 18th International Congress on Instrumentation in Aerospace Simulation Facilities (ICIASF)				5. FUNDING NUMBERS F61775-99-WF050	
6. AUTHOR(S) Conference Committee					
7. PERFORMING ORGANIZATION NAME(S) AND ADDRESS(ES) Onera/DMAE B.P. 4025; 2, Avenue Edouard Belin Toulouse 31055 France				8. PERFORMING ORGANIZATION REPORT NUMBER N/A	
9. SPONSORING/MONITORING AGENCY NAME(S) AND ADDRESS(ES) EOARD PSC 802 BOX 14 FPO 09499-0200				10. SPONSORING/MONITORING AGENCY REPORT NUMBER CSP 99-5050	
11. SUPPLEMENTARY NOTES					
12a. DISTRIBUTION/AVAILABILITY STATEMENT Approved for public release; distribution is unlimited.				12b. DISTRIBUTION CODE A	
13. ABSTRACT (Maximum 200 words) The Final Proceedings for 18th International Congress on Instrumentation in Aerospace Simulation Facilities (ICIASF), 14 June 1999 - 18 June 1999 This is an interdisciplinary conference. Topics include New and improved mechanical, electrical, and optical measurement devices; Measurement in high temperature and cryogenic environments; Instrument research in subsonic, supersonic, hypersonic, and real gas flows; Analog and digital acquisition and analysis techniques; Propulsion systems and turbomachinery - In flight sensors; New testing techniques and test environments - Space applications; Future instrumentation and simulation requirements - Flow field diagnostics.					
14. SUBJECT TERMS EOARD, Instrumentation, Simulation, Test & Evaluation, Measurement Techniques, Data Acquisition				15. NUMBER OF PAGES Too many to count	
				16. PRICE CODE N/A	
17. SECURITY CLASSIFICATION OF REPORT UNCLASSIFIED	18. SECURITY CLASSIFICATION OF THIS PAGE UNCLASSIFIED	19. SECURITY CLASSIFICATION OF ABSTRACT UNCLASSIFIED	20. LIMITATION OF ABSTRACT UL		

NSN 7540-01-280-5500

Standard Form 298 (Rev. 2-89)
Prescribed by ANSI Std. Z39-18
298-102

19990707 013

ICIASF 99

18th International Congress on
Instrumentation in Aerospace
Simulation Facilities

RECORD

ONERA-Centre de Toulouse
2 Avenue Edouard Belin
31055 Toulouse Cedex 4
France
June 14-17, 1999

ONERA



Foreword

The eighteenth International Congress on Instrumentation in Aerospace Simulation Facilities, hosted by the ONERA Toulouse center in June 1999, continues a series of congresses devoted to research on aerospace instrumentation. Since 1964, the previous meetings have provided, every two years, an important forum for scientists and engineers. Many papers were at the origin of new ideas and techniques, now confirmed and used in current measurement systems. All these papers are widely accessible and referenced in the scientific community. It is hoped that the papers included in this record will continue this tradition.

The rapid evolution in the world economy and techniques has challenged the international aerospace simulation community to perform a more efficient experimental research. Due to the complexity of the aerospace problems, the experimental approach is essential and has to be performed in parallel to theoretical and numerical methods.

From this point of view, the 18th ICIASF congress illustrates the development of more and more efficient mapping techniques used for surface or flow field measurements. Today flight and wind tunnel tests particularly related to unsteady flows, constitute a challenging domain for the future instrumentation researches.

It is a great pleasure for us to welcome all the participants of the 18th ICIASF in Toulouse. This congress was organised in co-operation with SUPAERO, the famous Aerospace Engineering School, located in the same scientific complex. Teaching activities and training through research are the keys to success.

We first thank all the authors for their vital contributions, the organisation committee, the panel members, the Best Paper Award committee, and all the people implied in this congress for their participation.

For their sponsorship, the following companies deserve special thanks:

- Institute of Electrical and Electronic Engineers (IEEE) first sponsor in 1964.
- European Office of Aerospace Research & Development (EOARD)
- Délégation Générale à l'Armement
- Conseil Régional Midi-Pyrénées
- Mairie de Toulouse
- Companies presenting instrumentation systems

Acknowledgements are extended to the management and the personnel of ONERA who, in many important ways, supported the preparation of the congress.

André MIGNOSI
Chairman 18th ICIASF



Instrumentation in Aerospace Simulation Facilities Panel

General Chairman :

André Mignosi ONERA France

Chairman : **Mr. Pieter H. Fuykschot**

NLR
Netherlands

Dr. Keisuke Asai
NAL
Japan

Mr. Rodney K. Bogue
NASA Ames-Dryden
USA

Dr. K.A. Bütelfish
DLR
Germany

Mr. A. Collier
AEDC
USA

Mr. David G. Coulton
Aircraft Research Association
England

Mr. Gary A. Dale
AF Wright Laboratory
USA

Mr. Peter W. Fuller
Royal Armament Research
& Development Estab.
England

Dr. Ernest Hanff
National Research
Council of Canada
Canada

Mr. Fred H. Heltsley
Sverdrup Technology/AEDC
USA

Mr. André Mignosi
ONERA
France

Dr. F.K. Owen
NPS
USA

Mr. Daniel M. Parobek
AF Wright Laboratory
USA

Dr. Hans. J. Pfeifer
French German Research Institute (ISL)
France

Mr. P. Roberts
NASA
USA

Pr. Arnan Seginer
SNI
Israel

Dr. Mark Wernet
NASA Lewis
USA

BEST PAPER COMMITTEE

Dr. Mark Wernet : President

Mr. Fred H. Heltsley

Mr. Daniel M. Parobek

Dr. Hans. J. Pfeifer

Pr. Arnan Seginer

LOCAL ORGANIZING COMMITTEE

Alain Carrère
SUPAERO

Christiane Bourdiol
ONERA

Brigitte Giacomini
ONERA

André Mignosi
ONERA

Pierre Millan
ONERA

Roger Payrau
ONERA

Marie-Josèphe Payry
ONERA

Philippe Plantade
ONERA

Table of Contents

SESSION 1: PARTICLE IMAGE VELOCIMETRY

Chairman : Dr. K.A. Bütetisch, DLR, Germany

- Quantitative Flow Field Measurements in a Catapult Facility Using Particle Image Velocimetry** 1.1
L. Dieterle, K. Ehrenfried, R. Stuff, G. Schneider : DLR, Göttingen, Germany
P. Coton, J.C. Monnier, J.F. Lozier : ONERA - Lille, France
- Fuzzy Logic Enhanced Digital PIV Processing Software** 2.1
M.P. Wernet : National Aeronautics and Space Administration, USA
- Particle Image Velocimetry to quantify 3D-Flow Properties of Gas Turbine Forced Mixers** 3.1
W. Scheuerpflug, N. Lawin : BMW Rolls-Royce GmbH, Germany

SESSION 2: AERO-ENGINES

Chairman : Mr. F.H. Heltsley, A.E.D.C., U.S.A.

- An Integrated Approach to the Application of High Bandwidth Optical Pyrometry to Turbine Blade Surface Temperature Mapping** 4.1
J. Douglas, C.A. Smith, S.J.R. Taylor : RODATA Ltd., England
- Special Probes for Measurements of Flow Parameters in a Gas-Turbine Engine** 5.1
Z.M. Romicki, S. Zurkowski : Institute of Aviation, Poland
- Phosphor Thermography for High Temperature Gas Turbine Applications** 6.1
J.P. Feist, A.L. Heyes, K.L. Choy, B. Su : Imperial College Of Science Technology and Medicine, England
- LIF Imaging of Species and Temperature in Technical Combustion at Elevated Pressures** 7.1
U.E. Meier, D.Wolff-Gassmann, J. Heinze, M. Frodermann : DLR, Germany
I. Magnusson, G. Josefsson : AB Volvo, Sweden
- Laser Anemometer Measurements in a Centrifugal Compressor** 8.1
N. Saddour, A. Carrere : SUPAERO, France

SESSION 3: DOPPLER VELOCIMETRY

Chairman : Dr. H.J. Pfeifer, I.S.L., France

- Doppler Global Velocimetry : accuracy tests in a wind tunnel** 9.1
C. Lempereur, P. Barricau, J.M. Mathé, A. Mignosi : ONERA-Toulouse, France
- Experimental Investigations on Vortex Breakdown over Delta Wings with Doppler Global Velocimetry** 10.1
M. Förstermann, K.A. Bütetisch : DLR, Germany
- Flow Velocity Visualization Using Doppler Picture Interference Velocimetry** 11.1
F. Seiler, A. George, F. Leopold, J. Srulijes, G. Smeets : ISL, France

Chairman : Mr. A. Collier, A.E.D.C., U.S.A.

- Measurement Technology of the Impact of Alumina Liquid Particles on a Hot Surface** 12.1
C. Escure, M. Vardelle, A. Grimaud, P. Fauchais : University of Limoges, France
- 3-Component-Doppler-Laser-2-Focus : a New Kind of Three Component Velocimeter** 13.1
I. Roehle, G. Karpinsky, R. Schodl : DLR, Germany
- Application of 3 Component Laser-Doppler Velocimetry in Transonic Flow Over a Delta Wing** 14.1
T.J. Möller, A. Wiedemann, K.A. Bütetisch : DLR, Germany, F. Micheli : ONERA, France, D. Scholz : INTA, Spain, K. Sjors : FFA, Sweden

SESSION 4: SENSITIVE PAINT TECHNIQUES I

Chairman : Mr. Gary A. Dale, AF Wright Laboratory, U.S.A.

- Status of Pressure-Sensitive Paint Technology at NAL** 15.1
K. Asai : NAL, Japan

Comparison of Luminescent Paints Measurement Systems

M. Guille, J.P. Sullivan : Purdue University, USA
J. Holmes : DERA, England

16.1

The Recent Methods for Surface Pressure and Skin Friction Measurements on the Models

A. Bykov, V. Kulesh, A. Orlov, V. Pesetsky : Central Aero-Hydrodynamics Institute, Russia

17.1

Pressure and Temperature Measurements with a Dual-Luminophor Coating

B.F. Carroll : University of Florida, USA
J.P. Hubner : AeroChem Corporation, USA
K.S. Schanze, J. Bedlek : University of Florida, USA
M.J. Morris : Bradley University, USA

18.1

Vortical Flow Field Investigation Using a Two-Component Pressure Sensitive Paint at Low Speed

M.C. Mérienne, F. Bouvier : ONERA/DAFE - Chatillon, France

19.1

SESSION 6: FLIGHT INSTRUMENTATION

Chairman : Mr. D.G. Coulton, A.R.A., England

LDA System for In-Flight Local Velocity Measurements on Airplane Wings

S. Becker, F. Durst, H. Lienhart : LSTM, Germany

25.1

Development and Applications of a Rapid Flight Test Prototyping System for Unmanned Air Vehicles

E. Hallberg, J. Komlosy, T. Rivers, M. Watson, D. Meeks, J. Lentz, I. Kaminer, O. Yakimenko : Naval Postgraduate School, USA

26.1

An Optical Technique for Detecting Fatigue Cracks in Aerospace Structures

D. Banaszak, G.A. Dale : AFRL, USA
A.N. Watkins, J.D. Jordan : ISS Incorp, USA

27.1

Investigations on a Dynamic Forebody Flow Control System

E.S. Hanff : IAR, Canada
R. Lee, R.J. Kind : Carleton University, Canada

28.1

New ONERA Set-Ups for the Characterization of the Resistance of Materials to Liquid and Solid Impacts

A.A. Déom, M. Lemistre, D.L. Balageas : ONERA, France

29.1

Incompressible Aerodynamics of a Planetary Entry Capsule

Ö. Karatekin, R. Voets, J.M. Charbonnier, F.Y. Wang : VKI, Belgium

30.1

SESSION 7: WIND TUNNEL MEASUREMENT TECHNIQUES

Chairman : Pr. Arnan Seginer, S.N.I., Israel

Implementing Pressure Sensitive Paint in the AFRL Subsonic Aerodynamic Research Laboratory

G. A. Dale, H. Baust : AFRL, USA
G.A. Clinehens : WPAFB, USA

20.1

Pressure-Sensitive Paint Measurements in a Large Scale Commercial Engine Test Stand

J. D. Jordan, A.N. Watkins, J. Davis, W. L. Weaver : ISS Inc., G. A. Dale, K. Navarra : AFRL, J. Urban, W. Devold, R. Strange : Pratt & Whitney, USA

21.1

Pressure Sensitive Paint Measurements on a Wing Model in a Low-Speed Wind Tunnel

C. Klein, R.H. Engler, S.D. Fonov, O. Trinks : DLR, Germany

22.1

Application of the Direct PSP-Lifetime Method on Pyren-Based Paint as a Completion of the Existing DLR PSP System

O. Trinks, R.H. Engler, C. Klein, S.D. Fonov : DLR, Germany

23.1

Pressure Sensitive Paint for Oscillating Pressure Fields Measurements

S.D. Fonov, R.H. Engler, C. Klein : DLR, Germany
S.V. Mihailov, V.E. Mosharov, V.N. Radchenko : TsAGI, Russia
E. Schairer : NASA, USA

24.1

A New Generation Traversing Rig with Minimum Disturbances for a Closed Test Section of Subsonic Wind Tunnels

T.Seung : Darmstadt University of Technology, Germany

31.1

Half-Model-Balances for Cologne-Cryogenic-Wind-Tunnel Development and Test Results

K. Hufnagel : Darmstadt University of Technology, Germany
R. Rebstock, J. Zhai : DLR, Germany

32.1

A New Approach to Measuring Model Deflection 33.1
R.K. Van Der Draai, R. Van Shinkel, A. Telesca :
N.L.R., Netherlands

Feasibility of Airfoil Tests with a Small High Subsonic Cryogenic Wind Tunnel 34.1
Y. Yamaguchi, M. Kashitani, K. Kaibara, T. Saito :
National Defense Academy, Japan

Determination of Residual Wall Interferences for Measurements on the TWIG Model - Comparison of Different Methods and Analysis 35.1
H. Holst, M. Jacobs : DLR, Germany
J-P. Archambaud, A. Mignosi : ONERA-Toulouse, France

SESSION 8: TEST TECHNIQUES

Chairman : Mr. P. Fuykschot, N.L.R.,
Netherlands

Electronically Scanned Pressure Measurement Scanner for Cryogenic Wind Tunnel Applications 36.1
Q.A. Shams, A.J. Zuckerwar: NASA, USA

Using of Oscillatory Conning Experimental Rig for Separation of Rotary and Unsteady Aerodynamic Derivatives 37.1
A. Khrabrov, K. Kolinko, O. Miatov, J. Vinogradov,
A. Zhuk : Central Aerodynamics Institute (TsAGI),
Russia

Determining the Transfer Function for Unsteady Pressure Measurements Using a Method of Characteristics Solution 38.1
D.D. McBride, J.F. Henfling : Sandia National
Laboratories, USA
E.L. Clark : Consultant

A Re-Evaluation of a Pulsed Laser Technique for Measuring Surface Heat Transfer Co-Efficients 39.1
W.E. Carscallen, W.O. Turnbull : National Research
Council, Canada

Performance Studies of the Constant Voltage Anemometer in a Mach 2.3 Boundary Layer 40.1
G. Comte-Bellot, : Ecole Centrale Lyon, France
G. Sarma : Tao Systems Inc., USA
T. Faure : LEMFI, France
J-P. Dussauge, P. Dupont, J-F. Debiève : IRPHE,
France

SESSION 9: HIGH SPEED FLOW DIAGNOSTICS

Chairman : Dr. M. Wernet, NASA Lewis, U.S.A.

Non-Intrusive Diagnostics for the AEDC Impulse Facility : Applications and Results 41.1
W.D. Williams, M.S. Smith, F.L. Heltsley, C.W.
Brasier, P.M. Sherrouse, W.M. Ruyten, L.L. Price,
E.J. Felderman, K.M. Stephens : AEDC Group., USA

A Comparative Study of Planar Mie and Rayleigh Scattering for Supersonic Flowfield Diagnostics 42.1
U. Brummund : DLR, Germany
B. Mesnier : University of Orléans, France

Multiple Point Dynamic Gas Density Measurements Using Molecular Rayleigh Scattering 43.1
R. Seasholtz : NASA, USA
J. Panda : Modern Technologies Corp., USA

Author's Index

ARCHAMBAUD J-P.	35.1	GEORGE A.	11.1	MIGNOSI André	9.1-35.1
ASAI Keisuke	15.1	GRIMAUD A.	12.1	MIHAÏLOV S.V.	24.1
		GUILLE Marianne	16.1	MÖLLER Thorsten	14.1
BALAGEAS Daniel	29.1			MONNIER J.C.	1.1
BANASZAK David	27.1	HALLBERG E.	26.1	MORRIS Martin	18.1
BARRICAU Philippe	9.1	HANFF Ernest	28.1	MOSHAROV V.E.	24.1
BAUST Henry	20.1	HEINZE J.	7.1		
BECKER Stefan	25.1	HELTSLEY Fred	41.1	NAVARRA K.	21.1
BEDLEK Joanne	18.1	HENFLING John	38.1		
BOUVIER F.	19.1	HEYES Andy	6.1	ORLOV A.	17.1
BRASIER C.	41.1	HOLMES Jim	16.1		
BRUMMUND Uwe	42.1	HOLST Hartmut	35.1	PANDA Jayanta	43.1
BÜTEFISCH K.A.	10.1-14.1	HUBNER James	18.1	PESETSKY Vladimir	17.1
BYKOV Anatolii	17.1	HUFNAGEL Klaus	32.1	PRICE L.	41.1
CARRERE Alain	8.1	JACOBS Markus	35.1	RADCHENKO V.N.	24.1
CARROLL Bruce	18.1	JORDAN Jeffrey	21.1-27.1	REBSTOCK Rüdiger	32.1
CARSCALLEN Bill	39.1	JOSEFSSON G.	7.1	RIVERS T.	26.1
CHARBONNIER J-M.	30.1			ROEHLE Ingo	13.1
CHOY K.L.	6.1	KAIBARA Kenji	34.1	ROMICKI Zbigniew	5.1
CLARK Edward	38.1	KAMINER Isaac	26.1	RUYTEN W.	41.1
CLINEHENS Gary	20.1	KARATEKIN Özgür	30.1		
COMTE-BELLOT G.	40.1	KARPINSKY G.	13.1	SADDOUR N.	8.1
COTON Patricia	1.1	KASHITANI Masashi	34.1	SAITO Teruo	34.1
		KHRABROV A.	37.1	SARMA Garimella	40.1
DALE Gary	20.1-21.1-27.1	KIND R.J.	28.1	SCHAIRER E.	24.1
DAVIS John	21.1	KLEIN Christian	22.1-23.1-24.1	SCHANZE Kirk	18.1
DEBIEVE J-F.	40.1	KOLINKO K.	37.1	SCHEUERPFLUG W.	3.1
DEOM Alain	29.1	KOMLOSY J.	26.1	SCHNEIDER G.	1.1
DEVOID Wayne	21.1	KULESH V.	17.1	SCHODL R.	13.1
DIETERLE Lutz	1.1			SCHOLZ D.	14.1
DOUGLAS J.	4.1	LAWIN N.	3.1	SEASHOLTZ Richard	43.1
DUPONT Pierre	40.1	LEE Richard	28.1	SEILER Friedrich	11.1
DURST F.	25.1	LEMISTRE Michel	29.1	SEUNG Tähun	31.1
DUSSAUGE J-P.	40.1	LEMPEREUR C.	9.1	SHAMS Qamar	36.1
		LENTZ J.	26.1	SHERROUSE P.	41.1
EHRENFRIED K.	1.1	LEOPOLD F.	11.1	SJÖRS K.	14.1
ENGLER R.H.	22.1-23.1-24.1	LIENHART H.	25.1	SMEETS G.	11.1
ESQUIRE Cyril	12.1	LOZIER J.F.	1.1	SMITH Cheryl	4.1
				SMITH M.	41.1
FAUCHAIS P.	12.1	MAGNUSSON I.	7.1	SRULIJES J.	11.1
FAURE Thierry	40.1	MATHE Jean-Michel	9.1	STEPHENS K.	41.1
FEIST J.P.	6.1	McBRIDE Donald	38.1	STRANGE Richard	21.1
FELDERMAN E.	41.1	MEEKS D.	26.1	STUFF R.	1.1
FONOV S.D.	22.1-23.1-24.1	MEIER Ulrich	7.1	SU B.	6.1
FÖRSTERMANN M.	10.1	MERIENNE M-C.	19.1	SULLIVAN John	16.1
FRODERMANN M.	7.1	MESNIER Bérangère	42.1		
		MIATOV O.	37.1	TAYLOR Simon	4.1
		MICHELI Francis	14.1		

TELESCA A.	33.1	VINOGRADOV J.	37.1	WOLFF-GASSMANN D.	7.1
TRINKS O.	22.1-23.1	VOETS R.	30.1	YAKIMENKO Oleg	26.1
TURNBULL Wayne	39.1			YAMAGUCHI Yutaka	34.1
		WANG F.Y.	30.1		
URBAN Justin	21.1	WATKINS Neal	21.1-27.1	ZHAI Junnai	32.1
		WATSON M.	26.1	ZHUK A.	37.1
VAN DER DRAAI R.	33.1	WEAVER William	21.1	ZUCKERWAR Allan	36.1
VAN SCHINKEL R.P.M.	33.1	WERNET Mark	2.1	ZURKOWSKI Stanislaw	5.1
VARDELLE M.	12.1	WIEDEMANN A.	14.1		
		WILLIAMS William	41.1		

SESSION : 1

PARTICLE IMAGE VELOCIMETRY

QUANTITATIVE FLOW FIELD MEASUREMENTS IN A CATAPULT FACILITY USING PARTICLE IMAGE VELOCIMETRY

L. Dieterle, K. Ehrenfried*, R. Stuff, G. Schneider^a - P. Coton, J.C. Monnier, J.F. Lozier^b

^a DLR, Institut für Strömungsmechanik
Bunsenstr. 10, D-37073 Göttingen, Germany
e-mail: lutz.dieterle@dlr.de

^b ONERA, Institut de Mécanique des Fluides de Lille (IMFL)
5, Bvd Paul Painlevé, F-59045 Lille Cedex, France

In order to investigate the long term behaviour of the wake vortex flow behind an aircraft, quantitative whole-field measurements have been carried out in a free flight analysis laboratory using the PIV (Particle Image Velocimetry) technique. Instantaneous velocity fields were measured in successive planes crosswise to the flight path of a free flying air-liner model, so that the evolution, interaction and decay of vortices originating from the wing, flap and slat tips can be described. The optical measurement system consisting of two aerosol generators for seeding, a pulsed laser system for illumination, two CCD cameras for image recording and trigger electronics for synchronisation had to be adapted to the particular test conditions of a catapult facility, where a long-lasting, unsteady "single event" initiated by the model's launch is subject of the experimental study. The paper focuses on the technical aspects of interfacing a catapult facility and a digital PIV system.

INTRODUCTION

Wind tunnel versus catapult facility

The size of the observation area around a model put into the test section of a wind tunnel is limited by the dimensions of the test section itself and is, as a rule, of the same order of magnitude as the model's characteristic length, e.g. the wingspan of an aircraft. If the flow to be investigated is far away from the model, the wind tunnel as an experimental tool for flow simulations becomes inappropriate; either the model must be scaled down considerably and consequently, for the sake of Reynolds similarity, the wind speed multiplied or the model has to be brought to a

much larger wind tunnel. In both cases the wind tunnel costs would become prohibitively large.

In aeronautic research catapult facilities constitute a convenient alternative or supplement to wind tunnels in order to overcome the shortcomings mentioned above. As the measurement of flow quantities in a free flight analysis laboratory takes place in a ground-based reference frame instead of the model's, the spatial distance between the model and a certain place of its wake flow transposes to terms of time elapsed after the initiating event, i.e. the model's launch. If the lateral and vertical expansion or movement of the interesting flow does not exceed the dimensions of the laboratory's observation area and if the ambient conditions inside the laboratory do not change over the period between the model's launch and the measurement, no practical limit is set in the investigation of long-lasting flow phenomena.

For this reason, catapult facilities are an indispensable tool for experimental studies of an aircraft's wake flow, the physical understanding of which becomes increasingly the subject of commercial interest. The aircraft trailing vortices give cause for a safety distance between air-liners landing and consequently limit the passenger throughput of an airport. As the persistence and strength of these vortices depend on the aircraft's weight, wide-bodied airliners call for big safety distances. If the decay of their wake vortices can not be accelerated, the advantage of a higher passenger capacity would be partly lost.

Of course, from the experimentalist's point of view a free flight analysis laboratory involves some practical disadvantages. A catapult works discontinuously, only a few launches per day can be performed creating single, unsteady events, during which all conditions for a successful

* present address: TU Berlin, Hermann-Föttinger-Institut, Straße des 17. Juni 135, 10623 Berlin, Germany

measurement have to be met; whereas – in the case of a static model – a wind tunnel provides a continuous flow, steady on average. The latter facilitates considerably the adjustment, operation and optimisation of measurement systems. This can be done on-line while the flow experiment runs. In contrast to that, the measurement in a free flight analysis laboratory must be synchronised with the model's launch. System optimisation progresses step by step, that means launch by launch, so that normally a few launches or even a few days respectively are gone before the first successful measurement is done.

Particle image velocimetry (PIV)

Since PIV became a mature technology for flow field investigations in industrial research, see for instance Kompenhans *et al.* [1], it has been increasingly challenged by more complicate applications. As far as static models in wind tunnels are concerned, the experiment does not need to be synchronised with the measuring instrument. But if a dynamic system is the subject of examination, the situation changes. Recently, the continuous but alternating and, with regard to the measurement system, asynchronous wake flow of a helicopter's rotor blade was first interfaced with a PIV system in order to investigate defined planes in the rotor blade's frame of reference, see Raffel *et al.* [2].

Within the framework of the European research programme WAVENC (Wake Vortex evolution and wake vortex ENCounter, Brite/EuRam project BE97-4112) PIV has been first applied to a discontinuous experiment, i.e. the wake flow of a free flying air-liner model in the catapult facility of ONERA, Lille. The goal was to provide an experimental database for the far-wake evolution of the trailing vortices. The data base will be used to validate CFD calculations. First results of the PIV measurements as well as a comparison with smoke visualization tests have already been presented by Coton *et al.* [3]. A general description of the PIV experiments will be given by Dieterle *et al.* [4]. The present paper focuses on the technical aspects of interfacing the ONERA's catapult facility and the digital PIV system. Flow field studies in the near-wake of an airliner's half model applying the PIV technique as well took place in the LLF (Large Low-speed wind tunnel Facility) of the DNW (German Dutch wind tunnel), the results of which are compared with the catapult's ones by Dieterle *et al.* [5].

EXPERIMENTAL SET-UP

ONERA/DCSD Flight Analysis Laboratory

The tests have been carried out in the Flight Analysis Laboratory of the Department for System Control and Flight Dynamics of ONERA. In this facility non-motorised

free flying scaled models are propelled by means of a pneumatic catapult via a trolley. Once launched, the model flies freely without any wall or mounting interference in a 30 m long, 9 m wide and 10 m high observation area, Figure 1. Afterwards the model is recovered in a volume of plastic foam.

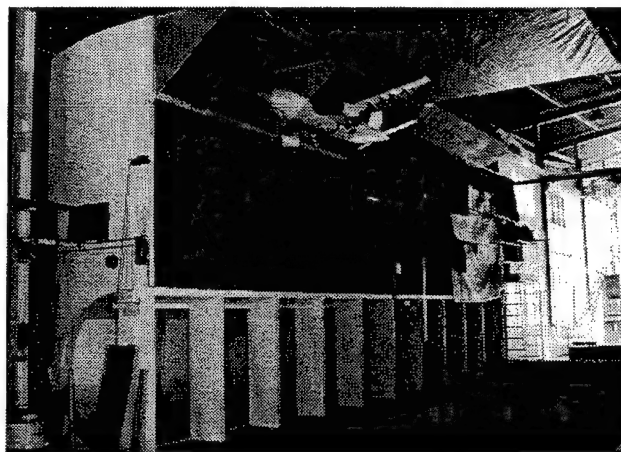


Fig. 1: Photograph of a scaled model flying in the laboratory

The basic in-board equipment of these models is composed of some accelerometers and gyrometers, a PCM (Pulse Code Modulation) encoder (30 channels, 12 bit words, scanning frequency = 520 Hz per channel) and static memories for data storage. The in-board information are supplemented by ground-based measurements: the initial velocity of the flight, the Euler angles and position of the centre of gravity of the model at well-known moments of the flight.

The trajectory and the different flight parameters (linear and angular accelerations, linear and angular velocities, ...) are then obtained through a coherence study between the data from the in-board equipment and the information from the ground. The global aerodynamic efforts are determined from these parameters and the model inertial characteristics which have been previously measured.

In the case of wake characterisation the flights to be realised are steady glides. That means that the aerodynamic forces balance the model weight. The observations of the wake vortices, generated by the scaled model, are carried out in a ground-fixed frame and the flow field can be observed from zero up to a hundred spans behind the model.

Model

A 1/22 scale model of a well-known European airliner (full span width 2.04 m) without any nacelle representation was employed and set in a high-lift configuration with

inner and outer flap angles equal to 0° and 15° respectively, Figure 2. The aimed lift level was 1.2 and the flight velocity was 23 m/s.

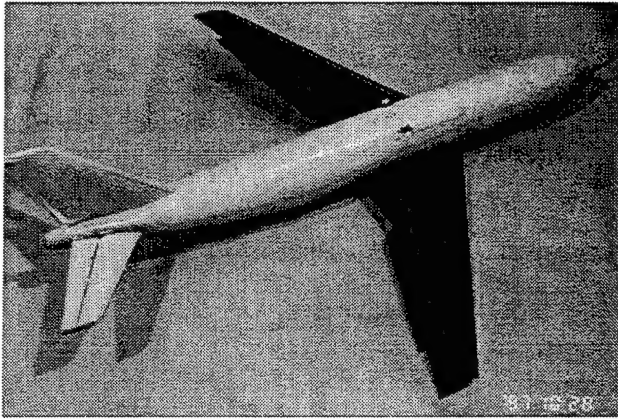


Fig. 2: Photograph of the model used for this study

Measurement technique

Despite photographic PIV being superior to a digital system as far as resolution and sensitivity of the recording medium is concerned, digital particle image velocimetry (DPIV) has been almost exclusively employed for flow field diagnostics in big wind tunnels for a few years now. Apart from rather secondary technical reasons, e.g. the directional non-ambiguity of particle motion if progressive scan cameras are used, DPIV saves time and, —due to the high running costs of large flow simulation facilities— consequently, money. Digital PIV makes possible an on-line check of the particle images and a quick quality assessment of the velocity data after storing and processing the images digitally, whereas in the case of photo-

graphic PIV the recorded film has to be taken out of the camera and developed manually before digitalizing the negative with a scanner for a digital evaluation or even evaluating the negative optically. All these evaluation methods are described by Raffel *et al.* [6].

The DPIV system introduced to ONERA's Flight Analysis Laboratory consists of the following components: two aerosol generators for air seeding, a laser light source and light sheet optics for particle illumination, two CCD cameras and a double set of lenses for particle imaging and recording, trigger electronics for synchronisation as well as computer hard- and software for system operation, image acquisition and evaluation, Figure 3. All these components are described in the following subsections.

Seeding

The observation area was seeded with olive oil droplets, about $1\ \mu\text{m}$ in diameter, produced by two identical aerosol generators, Figure 4. Pressurised air enters a closed, cylindrical container via two separate air inlets. The first is connected to four pipes equipped with so-called *Laskin* nozzles and submerged in olive oil. The Laskin nozzles create bubbles containing small oil droplets, see Echols and Young [7]. The bubbles rise to the liquid surface and release the particles. The bigger ones are detained by a circular impactor plate, the smaller ones pass the gap between the plate and the inner wall of the container and leave the latter through an outlet in its top. The amount of particles and the aerosol concentration can be reduced by disconnecting single nozzle pipes and, respectively, opening the valve of the second air inlet.

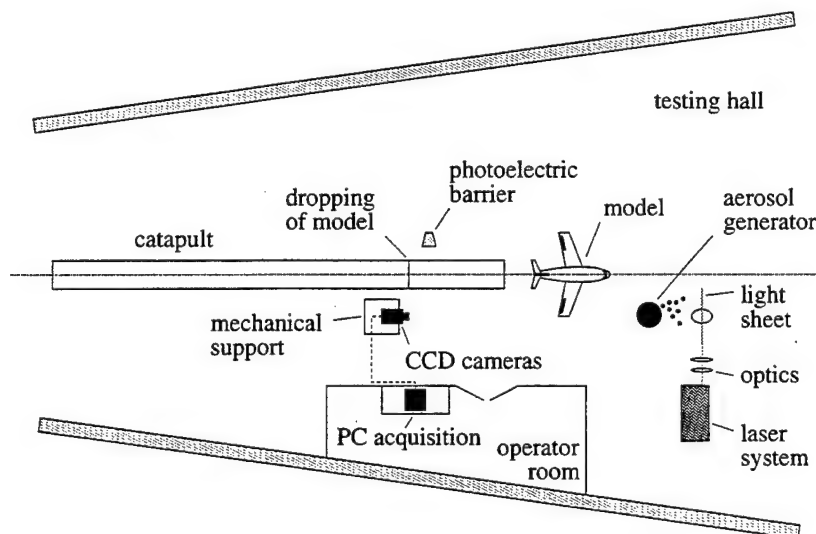


Fig. 3: Experimental set-up

The two aerosol generators were connected to a remote-controlled compressed air distributor. They were placed on the laboratory's floor between the dropping section of the catapult and the light sheet.

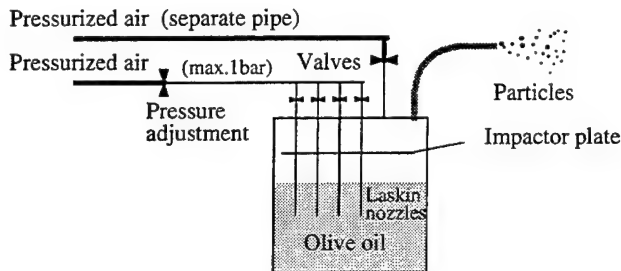


Fig. 4: Schematic view of the aerosol generator

Prior to a launch the observation area was seeded for a quarter of an hour. After that it took about 5 minutes until the circulating air came to rest. Over this period of time the model's launch had to be counted down to make sure that the flow field being investigated was not altered by convection currents.

Particle illumination

A Q-switched and frequency-doubled Nd:YAG laser system was utilised for particle illumination. It consists of two independent oscillators generating infra-red radiation (1064 nm). The two beams are combined by a dichroic mirror which makes use of their different wavelength: One beam is frequency-doubled before combination, the other one after that. The laser system creates double pulses with separation times in the range of 10^{-6} s to 10^{-2} s. A single light pulse has the following specifications:

wavelength: 532 nm
energy: 350 mJ
repetition rate: 10 Hz

The laser is water-cooled and draws a lot of power. Its flashlamps and Q-switches were triggered externally. The cavity gain needed to be resistant to a unique asynchronous trigger signal as described in a following subsection.

A set of cylindrical and spherical lenses formed the laser beam to a light sheet, which illuminated a vertical plane crosswise to the flight path of the model, Figure 3. The distance between the light sheet plane and the photo-electric barrier within the dropping section of the catapult was 7.95 m.

Particle imaging and recording

For image recording two identical progressive scan CCD cameras were used. Their fields of view covered neighbouring areas of the object plane so that a double-sized part of the flow field could be observed without loss of resolution. The cameras have so-called *full frame interline transfer* sensors allowing them to take two full frames in quick succession; a dead time of about 1 μ s separates the exposures of the first and the second frame. The specifications of the CCD sensor are:

number of pixels: 1280 x 1024
pixel size: $6.7 \times 6.7 \mu\text{m}^2$
dynamic range: 12 bit
frame rate: < 4 Hz

High sensitivity is achieved by Peltier-cooling the CCD sensor down to -15°C . Image data are transferred to a PCI interface board via optical fibre. Image recording was controlled by external triggering. The cameras mounted to a mechanical support were placed below and – for safety reasons – behind the dropping section of the catapult resulting in a fixed working distance of more than 8 m. They looked on the model's starboard side in the flight direction, Figure 3.

Tab. 1: Imaging data

focal length	observation area	magnification
100 mm	$72 \times 57 \text{ cm}^2$	$12 \cdot 10^{-3}$
180 mm	$40 \times 32 \text{ cm}^2$	$22 \cdot 10^{-3}$
300 mm	$23 \times 18 \text{ cm}^2$	$37 \cdot 10^{-3}$

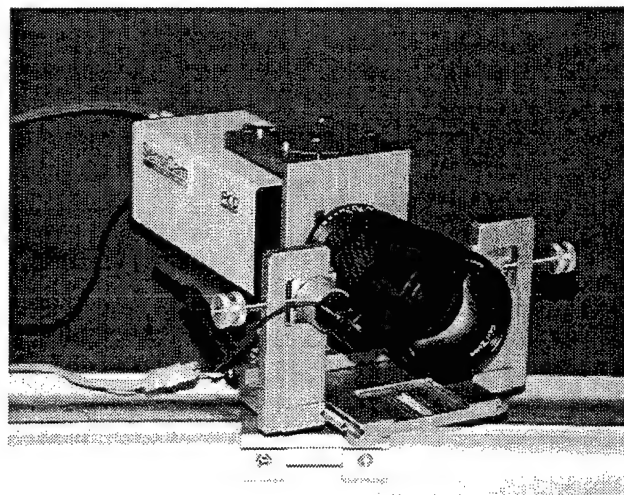


Fig. 5: Motor-driven focus adjustment of a 180 mm lens

A double set of three lenses each imaged the tracer particles by their scattered light at different magnifications but with a constant $f_{\#}$ 2.8. A 100 mm lens was employed for an overall view on the flow field including the model's wing when crossing the light sheet. The standard lens had a focal length of 180 mm, and small flow structures were resolved by a 300 mm lens, Table 1. A small remote-controlled DC-driven motor focussed the respective lens via a toothed belt, Figure 5.

Synchronisation and system operation

The most demanding task was to interface the measurement system with the flight experiment in order to be able to study the wake flow in defined planes behind the model. Three independent technical processes had to be synchronised:

- *Particle illumination* with the pulsed laser is stringently limited to its 10 Hz repetition rate in order to keep the thermal conditions inside the oscillators stable. After switching on the laser, the oscillators need a warming-up time of half an hour before meeting the conditions for a successful PIV measurement, that is to say, maximum pulse energy, pulse-to-pulse energy stability and beam pointing stability as well as an optimum beam profile. Consequently, the laser must be triggered continuously prior to a measurement.
- *Image recording* should not be started before the model is launched because the total amount of image data being read out in real time by the PCI board is limited by the PC's RAM. The camera's frame rate is variable up to a maximum of 4 Hz.

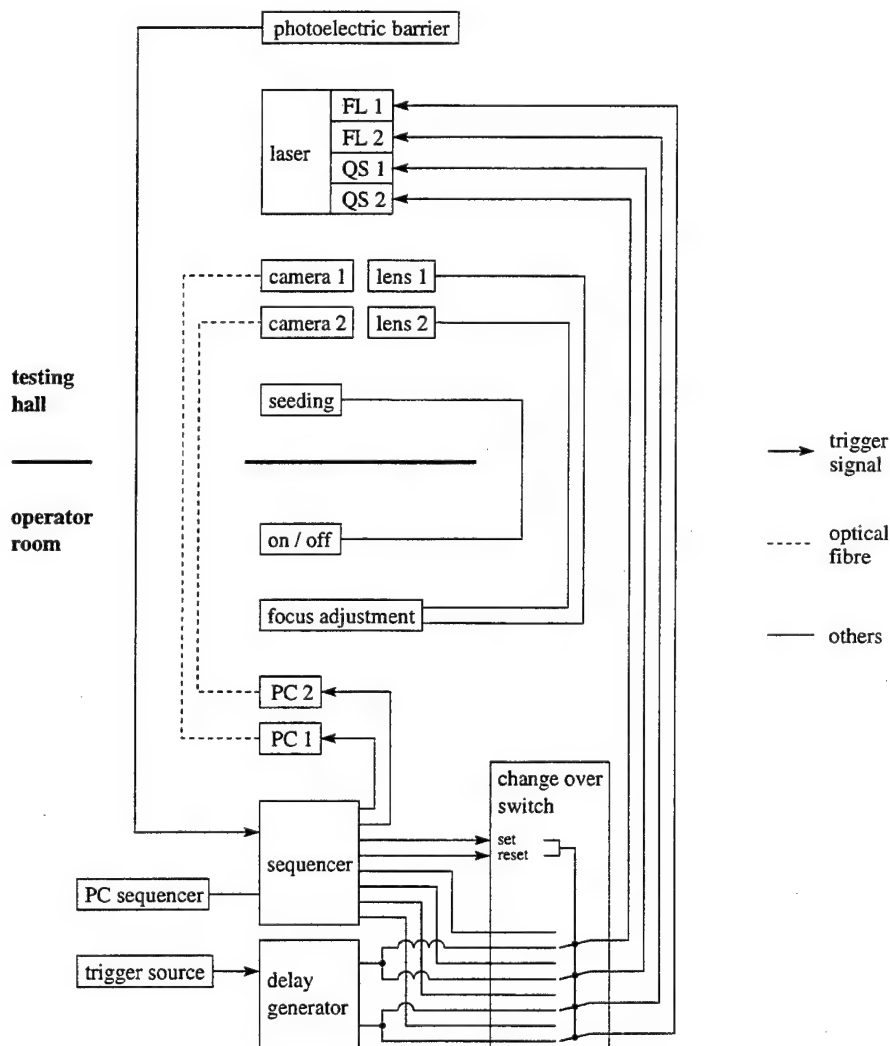


Fig. 6: PIV operation scheme

- Regarding the trigger time of the laser, the *model's launch* is a random and asynchronous single event initiating a long-lasting (≈ 10 s) and unsteady course of flow during which the conditions for a high-quality PIV measurement are altering. As the trailing vortices are drifting and decaying gradually during the measurement series, the place as well as the magnitude of the maximum velocity changes in time. This fact has to be taken into account when designing the PIV system operation.

Consequently, the measurement system and the flight experiment can not be synchronised without (i) changing at least once, i.e. on the model's launch, the trigger time of the laser and (ii) increasing the separation time between the two consecutive light pulses during the measurement series in order to take advantage of the full dynamic range of particle image displacement. Therefore the PIV system was operated as follows, Figure 6.

A delay generator activated by an external 10 Hz trigger source creates a repetitive sequence of two TTL trigger signals. The first one triggers the two flashlamps (FL 1 and FL 2), the second one triggers the two Q-switches (QS 1 and QS 2), so that the laser system stabilised thermally fires continuously with its maximum cavity gain. The launching model passes a photoelectric barrier which activates a PC-controlled, programmable sequencer being in a state ready to release a single, extended sequence of TTL trigger signals via eight channels. The first signal – via the sequencer's third channel from the top in Figure 6 – flicks an electronic change over switch ('set'), so that the sequencer is substituted for the delay generator as the laser's trigger source. A series of trigger cycles is then released via six channels connected to the PCI boards of the cameras' image acquisition PCs (PC 1 and PC 2) as well as to the laser's flashlamps and its Q-switches. Image recording starts and the laser is now firing in a defined phase with regard to the model's launch. After the trigger cycles are executed completely, which is synonymous with the measurement's ending, a final signal – via the sequencer's fourth channel from the top in Figure 6 – will change the laser's trigger lines back to the delay generator ('reset'). Laser triggering will continue and keep the oscillators stable and ready for the next measurement.

The signal 'set' flicks the change over switch within the interval $0 < t \leq 100$ ms between two successive signals of a delay generator's trigger line, Figure 7. This corresponds to a frequency of $1/t > 10$ Hz with regard to the last trigger signal sent to the laser by the delay generator. In order to avoid the laser system being damaged by a single repetition exceeding considerably 10 Hz even for $t \rightarrow 0$, the first sequencer's trigger signal is sent to the laser

system 100 ms after flicking the change over switch. Consequently, the interval between two successive signals of a flashlamp's trigger line, the first coming from the delay generator and the second created by the sequencer, is $100 \text{ ms} < \tau \leq 200 \text{ ms}$. It is crucially important, that this single asynchronous trigger corresponding to a repetition rate between 5 Hz and 10 Hz does not diminish momentarily the laser's cavity gain as already mentioned above. Otherwise the first two or three double light pulses would not provide enough energy for a successful particle imaging. The same trigger procedure is performed at the end of the measurement. In order to avoid once more the laser's repetition rate being exceeded, the sequencer resets the change over switch 100 ms after releasing the last trigger signal addressed to the laser.

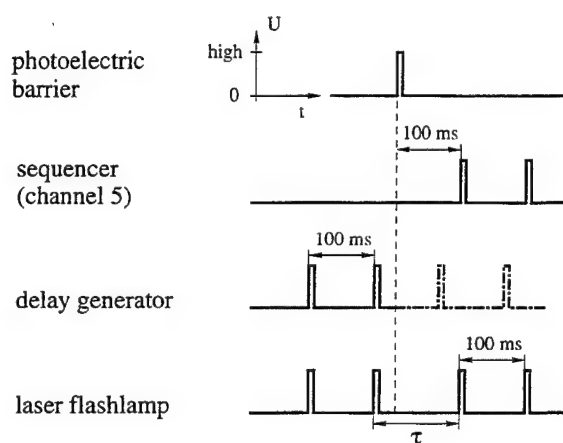


Fig. 7: Timing diagram of laser triggering with $100 \text{ ms} < \tau \leq 200 \text{ ms}$, U: voltage, t: time

As the CCD cameras' frame rate is limited to 4 Hz, they can take use of every third laser pulse only. Therefore, the Q-switches are triggered on every third triggering of the flashlamps, resulting in a repetition rate and frame rate respectively of 3.3 Hz. The cameras take their first image pair 300 ms after the model's launch. At this time, the model is just going to cross the light sheet, Figure 8. The second shot is made 600 ms after the launch and with the model being 2.7 wingspans beyond the light sheet. Regarding the model's reference frame all following planes of the wake flow being recorded are separated from one another by about 3.5 wingspans.

The cameras are triggered via different channels of the sequencer, so that in principle they can start image recording at different times (Of course, the interval is restricted to multiples of 300 ms.). But this option was not used for the measurements described here because the capacity of the PCs' RAM was not fully exploited for real-time image recording.

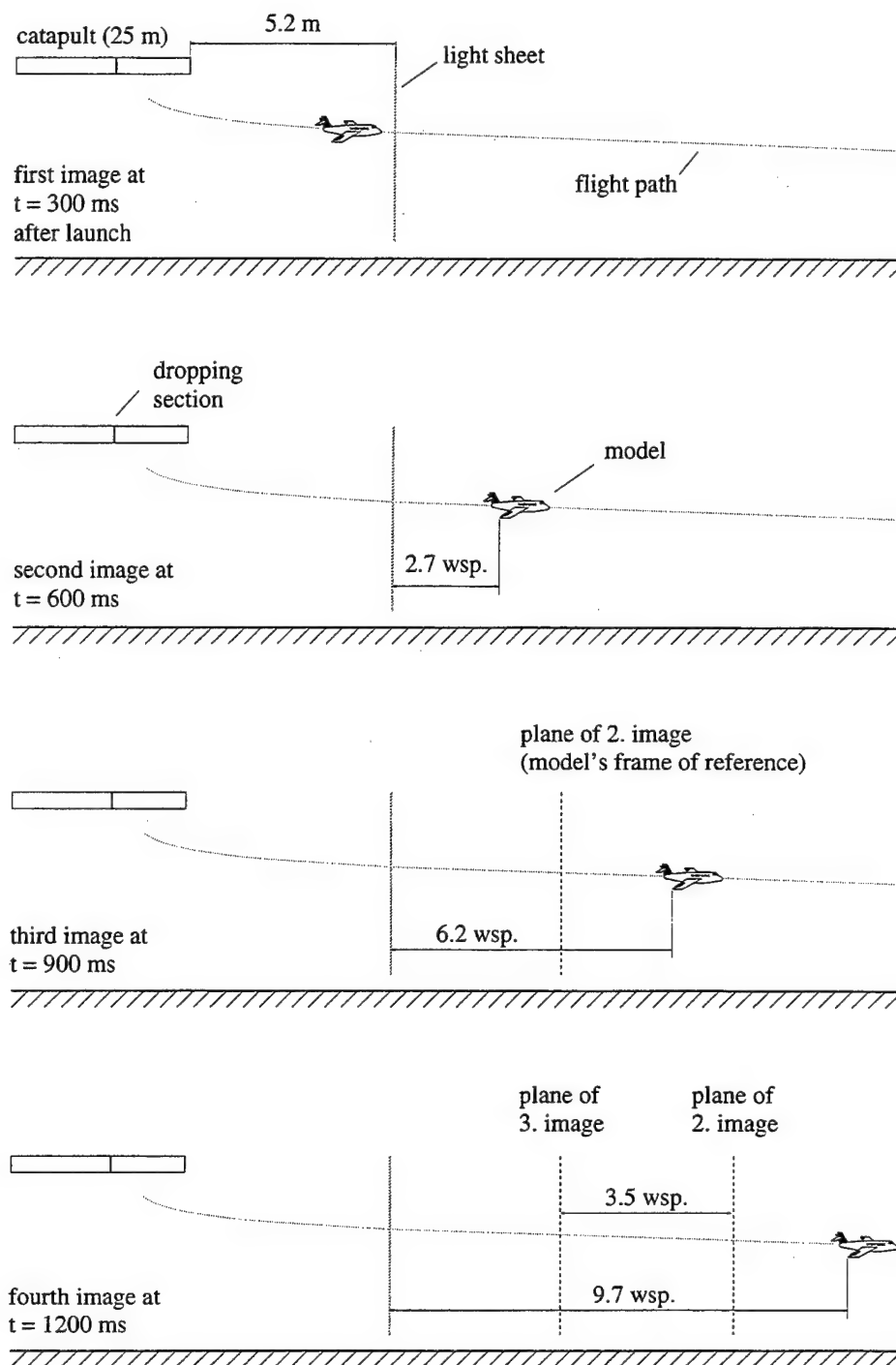


Fig. 8: Planes of measurement at different times of image recording (wsp. = wingspans)

Theoretically, the complete wake up to about 120 wing spans behind the model could be recorded during a single run, but in all cases the subject of interest, i.e. the trailing vortex, disappeared at sometime from the cameras' field of view.

If the separation time between the two consecutive light pulses is constant during the measurement series, the maximum particle image displacement would gradually decrease and be rather too small for the last image pair of a series due to the vortex' motion and decay, as already mentioned above. Consequently, the dynamic range of the

velocity measured as well as the accuracy of the derived flow quantities, like vorticity, would become smaller and worse respectively. For this reason the sequencer's trigger cycles contain a dynamic adaptation of the separation time to the experiment. Prior to a measurement series the initial value of the separation time, its absolute increment and the number of image pairs, after which the increment will be added at any one time, have to be fed into the sequencer. In this way the maximum particle image displacement can be kept nearly constant and optimum for all image pairs of a single run.

Image acquisition and evaluation

Between 15 and 30 image pairs per camera were taken during a measurement series. One double frame comprised about 5.2 Mbytes image data. Depending on the lens' focal length, the initial value of the separation time was set to 175 μ s or 350 μ s. After every second double image the separation time went up with an increment between 30 μ s and 80 μ s.

The image pairs were evaluated by means of digital cross-correlation, see Raffel *et al.* [6]. Calculation of particle image displacement took place in windows of 32 x 32 pixels. Neighbouring windows overlapped by 50 % resulting in a total number of almost 5000 displacement vectors per double image.

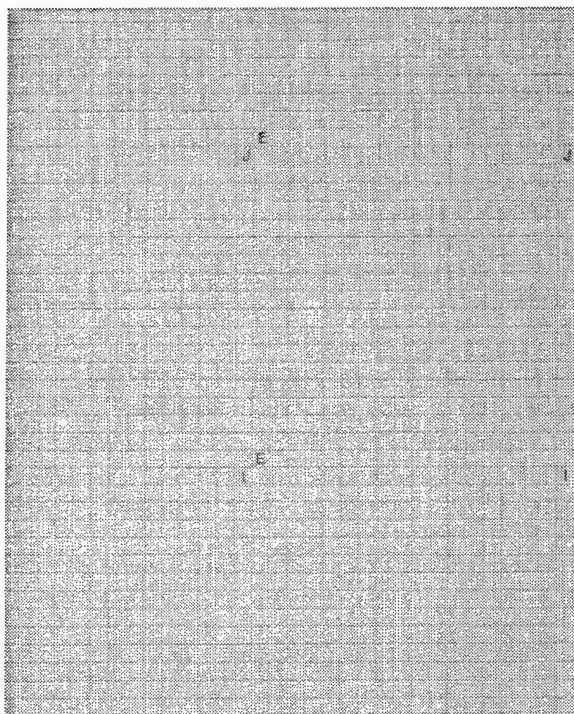


Fig. 9: Calibration grid taken with one camera and a 180 mm lens, distance between two grid points \approx 10 mm

Displacement data were converted into velocity data according to

$$v = \frac{s}{\Delta t \cdot M}, \quad (1)$$

where v is the velocity, s the calculated image displacement within the respective window, Δt the separation time between the two consecutive light pulses and M the magnification of the imaging system, see Table 1. M was determined by means of a calibration grid placed and recorded in the light sheet plane prior to a measurement series, Figure 9. From the well-known position of the calibration grid in the ground-fixed frame, the exact position of the cameras with regard to the object plane could be derived.

RESULTS

Figure 10 shows the first frame of an image pair taken with one camera 2.7 s after the model's launch or 26.9 wingspans behind its wing tip. The picture looks quite different from those taken at the very beginning of a measurement series, such as Figure 11. Except the black centre representing the core region of the anti-clockwise rotating trailing vortex behind the model's starboard wing the picture reveals a homogeneous seeding in the object plane.



Fig. 10: First frame of the ninth image pair of a measurement series taken with the same camera at the same position as in Figure 9

The lower brightness in the picture's right half is apparently caused by an incomplete illumination of the object plane and can be observed for all images of this series, see Figure 11. The most conspicuous feature of Figure 10 is the exceptional high radial gradient of particle image density close to the core region of the vortex. The inner part of the core region seems to be completely blank.



Fig. 11: First frame of the second image pair of the same measurement series as in Figure 9, but taken with the other camera at a different position, see Figure 13

Seeding appears quite inhomogeneous in the case of Figure 11 depicting the first frame of a previous image pair of the same measurement series. The image pair was taken 0.6 s after the model's launch or 2.7 wingspans behind its wing tip, see also Figure 8. Strands of particles originating from the seeding generation prior to the measurement are visible around the vortex being in development. They are going to mingle so that particle image density becomes more and more uniform as already happened inside the vortex. Finally, the inhomogeneity of seeding vanishes completely apart from the vortex core, see once more Figure 10.

The core region being somewhat lacking in particles is much bigger in the case of Figure 10 causing a considerable amount of spurious vectors in the corresponding velocity plot, Figure 12. Nevertheless, the velocity field inside the vortex core could be resolved. The vector plot confirms the anti-clockwise rotation of the trailing vortex

and gives quantitative information about its structure. The maximum valid particle image displacement is about 10 pixels and does not change considerably during this measurement series due to the dynamic adaptation of the separation time Δt between the two consecutive light pulses.

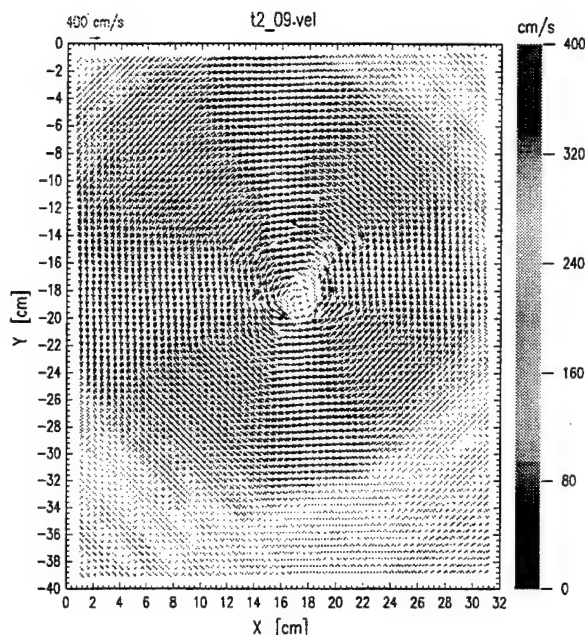


Fig. 12: Local distribution of velocity calculated from the image pair, the first frame of which is shown in Figure 10

For the same measurement series the motion and evolution of the trailing vortex in the range between 2.7 and 40.7 wingspans behind the model are depicted chronologically in Figure 13 by means of instantaneous vorticity fields. A detailed interpretation of the PIV results is given by Coton *et al.* [3].

CONCLUSIONS

A digital PIV system has been successfully interfaced with a catapult facility, where a discontinuous and unsteady flow experiment takes place. The repetitive measurement system was synchronised with the launch of an aircraft model, so that its wake flow could be studied in defined planes with regard to the free flying model. The full dynamic range of the velocity measured could be exploited by a dynamic adaptation of the separation time between the two consecutive light pulses during the measurement series. The local distribution of instantaneous velocity and vorticity of the trailing vortices were measured in a ground-based reference frame yielding the chronology of vortex formation, evolution and decay in the range between 3 and nearly 100 wingspans behind the model.

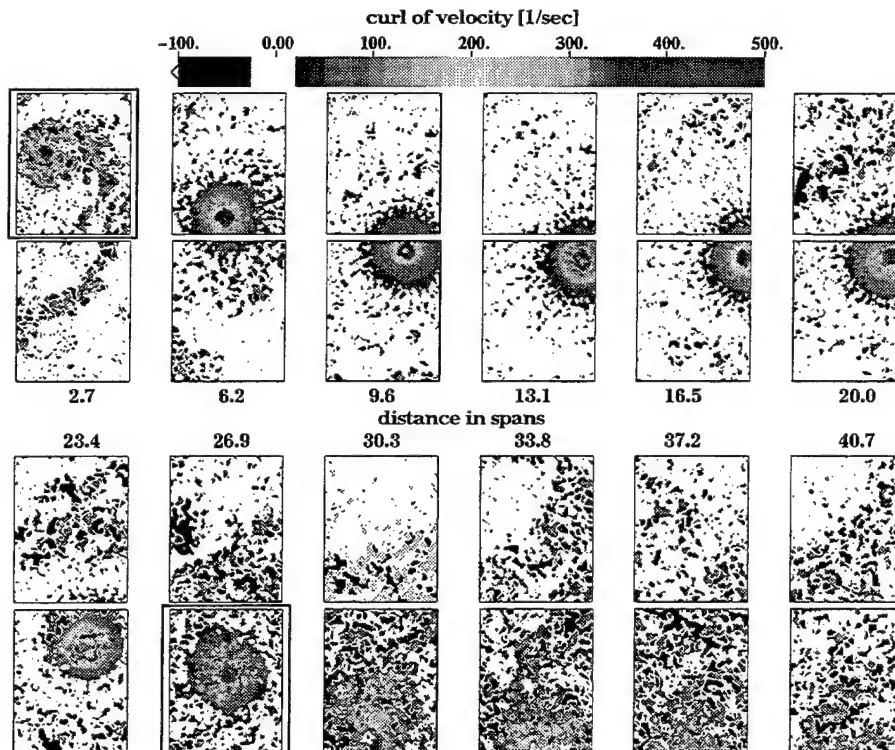


Fig: 13: Chronology of vorticity fields in terms of wingspans behind the model measured with two cameras. The two vorticity fields framed are derived from image pairs the respective first frames of which are shown in the Figures 10 and 11

ACKNOWLEDGEMENTS

Special thanks to C. Kähler (DLR) and G. Croisier (ONERA), who assisted the PIV measurements.

REFERENCES

1. Kompenhans J., Raffel M., Dieterle L., Dewhirst T., Vollmers H., Ehrenfried K., Willert C., Pengel K., Kähler C., Schröder A., Ronneberger O.: *Particle image velocimetry in aerodynamics: technology and applications in wind tunnels*; Proceedings of VSJ-SPIE98, paper no. KL306, December 6-9, 1998, Yokohama (Japan)
2. Raffel M., Willert C., Kompenhans J., Ehrenfried K., Lehmann G., Pengel K.: *Feasibility and capabilities of particle image velocimetry (PIV) for large scale model rotor testing*; Heli Japan 98, paper no. T3-1, April 21-23, 1998, Gifu (Japan)
3. Coton P., Monnier J.-C., Stuff R., Dieterle L., Schneider G.: *Characterisation of the wake far field from high lift configurations of the Airbus A 300 by PIV measurements in the ONERA/ Lille Flight Analysis Laboratory*; AAAF-DGLR Symp. on Large Aircraft Operational Challenge: Wake Vortices – Aerodynamics and Noise Effects, January 21-22, 1999, St. Louis (France) submitted to the *Journal of Aerospace Science and Technology*, Elsevier
4. Dieterle L., Stuff R., Schneider G., Kompenhans J., Coton P., Monnier J.-C.: *Experimental investigation of aircraft trailing vortices in a catapult facility using PIV*; submitted to the 8th Int. Conf. on Laser Anemometry – Advances and Applications, EALA, September 6-9, 1999, Rome (Italy)
5. Dieterle L., Stuff R., Vollmers H., Coton P.: *Wake vortex studies in the ONERA catapult facility and in the DNW wind tunnels*; submitted to the 1st ONERA-DLR Aerospace Symp., June 21-24, 1999, Paris (France)
6. Raffel M., Willert C., Kompenhans J.: *Particle image velocimetry – a practical guide*; Springer Verlag, 1998, Berlin (Germany)
7. Echols W.H., Young J.A.: *Studies of portable air-operated aerosol generators*; NLR (Naval Research Laboratory) Report 5929, 1963, Washington (USA)

FUZZY LOGIC ENHANCED DIGITAL PIV PROCESSING SOFTWARE

Mark P. Wernet

National Aeronautics and Space Administration
Glenn Research Center
Cleveland, OH

ABSTRACT

Digital Particle Image Velocimetry (DPIV) is an instantaneous, planar velocity measurement technique that is ideally suited for studying transient flow phenomena in high speed turbomachinery. DPIV is being actively used at the NASA Glenn Research Center to study both stable and unstable operating conditions in a high speed centrifugal compressor. Commercial PIV systems are readily available which provide near real time feedback of the PIV image data quality. These commercial systems are well designed to facilitate the expedient acquisition of PIV image data. However, as with any general purpose system, these commercial PIV systems do not meet all of the data processing needs required for PIV image data reduction in our compressor research program. An in-house PIV PROCessing (PIVPROC) code has been developed for reducing PIV data. The PIVPROC software incorporates fuzzy logic data validation for maximum information recovery from PIV image data. PIVPROC enables combined cross-correlation/particle tracking wherein the highest possible spatial resolution velocity measurements are obtained.

INTRODUCTION

Digital PIV provides near real-time flow field measurements through the use of refined data processing techniques combined with continuous increases in computational power and advances in CCD sensor technology. Digital PIV is a planar measurement technique that utilizes a pulsed laser light sheet to illuminate a flow field seeded with tracer particles small enough to accurately follow the flow. The positions of the particles are recorded on a digital CCD camera at each instant the light sheet is pulsed. In high-speed flows, pulsed Q-switched lasers are required to provide sufficient light energy ($\sim 100\text{mJ/pulse}$) in a short time interval ($< 10\text{ nsec}$) to record an unblurred image of the particles entrained in the flow. The data processing consists of determining either the average displacement of the particles over a small interrogation region in the image or the individual particle displacements between pulses of the light sheet. Knowledge of the time interval between light sheet pulses then permits computation of the flow velocity. Different data processing schemes are employed depending on the number of exposures per frame and the seed particle concentration. While each technique has some inherent benefits, the appropriate choice depends on

the characteristics of the flow and recorded image constraints.

DPIV is being actively used at the NASA Glenn Research Center to study both stable and unstable operating points in the diffuser of a high speed centrifugal compressor. A commercial PIV system is used to provide near real time feedback of the acquired PIV image data quality, which facilitates the expedient acquisition of PIV image data. However, these commercial PIV systems do not meet all of the data processing needs required for PIV image data reduction in our compressor research program. Therefore, an in-house PIV PROCessing (PIVPROC) code has been developed for reducing PIV data. The PIVPROC software incorporates fuzzy logic data validation for maximum information recovery from PIV image data. PIVPROC enables combined cross-correlation/particle tracking wherein the highest possible spatial resolution velocity measurements are obtained. The PIVPROC software also supports batch processing of the large volumes of PIV data collected in the compressor research program.

The PIVPROC software has been used to reduce the data obtained from the successful application of digital PIV in a centrifugal compressor. Measurements have been obtained in the diffuser section of a 431 mm diameter 4:1 pressure ratio centrifugal compressor facility at GRC. Measurements were obtained from 6 to 95% span with the impeller running at the design speed of 21,789 rpm and 4.54 kg/s mass flow. Previous measurements using LDV could not get closer than 50% span to the hub surface in the small height passages (17 mm) in the diffuser. For a more detailed description of the PIV system used for image acquisition in the centrifugal compressor facility see reference 1. A discussion of the unstable operating point data obtained in the centrifugal compressor can be found in reference 2. A once-per-rev signal is used to synchronize the DPIV image capture with the impeller circumferential position. The PIVPROC software is being used to reduce the over 60 gigabytes of PIV image data obtained from the compressor facility. The PIV data are being used to construct phase-stepped, time-averaged velocity vector maps of the compressor flow. The improved data quality obtained via the fuzzy logic based data validation in the PIVPROC software will be presented. Also, particle tracking results will be shown which utilize the cross-correlation processed velocity vector maps as a guide in

the fuzzy logic based particle tracking.

PROCESSING PIV IMAGE DATA

Particle Image Velocimetry (PIV) is a technique for measuring the in-plane two-component velocity field of a flow seeded with tracer particles small enough to accurately follow the flow. A pulsed laser light sheet is used to illuminate the particles entrained in the flow, as shown in figure 1. The light scattered by the particles is collected normal to the plane of the light sheet and is imaged onto a photographic plate or a CCD camera, where the positions of the particles are recorded at each instant the light sheet is pulsed. Basically, there are three types of data reduction techniques used in PIV: auto-correlation, cross-correlation and particle tracking. The choice of a processing technique depends primarily on the available equipment used to record the particle image data and the seed particle concentration.

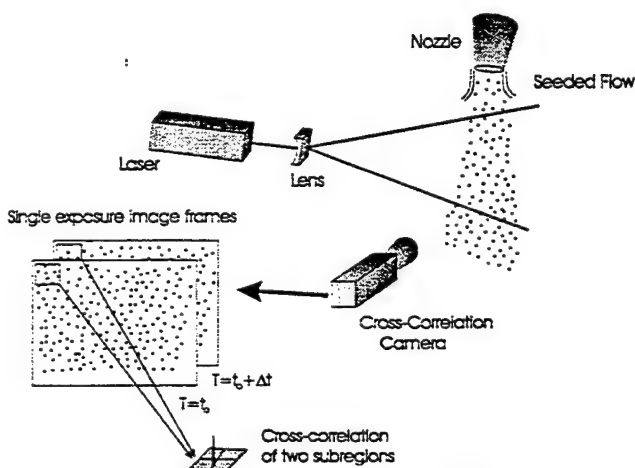


Figure 1 showing the main elements of a PIV system.

Correlation based processing techniques produce spatially averaged velocity estimates. The recorded image frame is divided into small subregions, each containing particle images. By processing the image over a regular grid of small subregions, a velocity vector map is generated. The optimum number of particles per interrogation region for PIV is nominally 10 image pairs[3].

In the auto-correlation technique a single image frame is exposed multiple times (≥ 2) and processed over a regular grid of small subregions. For a multiple exposure image, the average displacement of the recorded particle image pairs is determined by computing the auto-correlation of the subregion.

The 2-D auto-correlation is a symmetric function having a characteristic dc peak at the origin of the correlation plane and two satellite peaks, oriented symmetrically about the dc peak. Figure 2 shows a sample input double exposure subregion and the resulting auto-correlation plane output. The dc peak originates from the correlation of all of the

particle images in the subregion, hence the size of the dc peak is related to both the total number and size of the particles in the subregion[3]. The satellite peaks originate from the average displacement of the particle image pairs between exposures. In order for the displacement peaks to be discernable from the dc peak, the particle displacements must be greater than the average particle diameters across the subregion. This requirement places a dynamic range limitation on the auto-correlation technique. A second shortcoming is in the symmetry of the auto-correlation function. The existence of two diametrically opposed displacement peaks about the dc peak yields a 180 degree directional ambiguity in the velocity vector direction. The directional ambiguity can be eliminated by imposing a dc offset on the particle image records, whereby the particle images are mechanically shifted between laser pulse firings[4]. Image shifting introduces extra complexity in the experimental setup and also additional errors due to optical path differences resulting from the image shift.

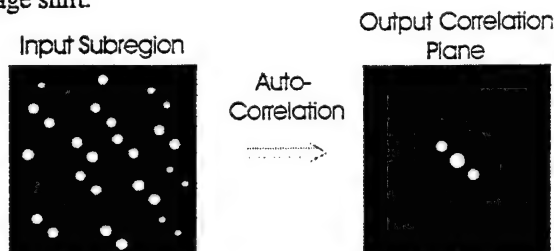


Figure 2: Double exposure input subregion and the corresponding output auto-correlation plane. Note the central dc peak and the symmetry of the auto-correlation function.

The second spatially averaged PIV data reduction technique, cross-correlation processing, is superior to the auto-correlation technique; however, this technique places more difficult demands on the recording system. In cross-correlation PIV, two single exposure image frames must be recorded. The standard convention is to use a cross-correlation camera which utilizes the "frame-straddling" technique first demonstrated on nozzle flows[5]. The cross-correlation operation is similar to auto-correlation where again the image frames are divided into small subregions. However, now a subregion from image #1 (recorded at the first laser pulse) is cross-correlated with a subregion from image #2 (recorded at the second laser pulse) as shown in figure 1. The resulting output on the correlation plane is a single peaked function, where the peak represents the average displacement of the particles across the subregion between the two laser pulses. Figure 3 shows a pair of input single exposure subregions and the resulting cross-correlation output plane. The direction of the displacement is determined unambiguously because the images from exposures 1 and 2 are recorded separately. Since there is no self-correlation peak, even zero particle displacements can be measured, hence, the cross-correlation technique provides a higher dynamic range

measurement capability than the auto-correlation technique.

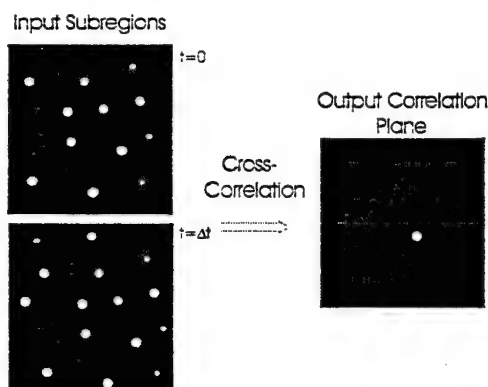


Figure 3: Two single exposure input subregions and the corresponding output cross-correlation plane. The location of the single bright correlation peak from the origin is the average displacement across the subregion.

In contrast to the spatially averaged correlation techniques discussed above, Particle Tracking Velocimetry (PTV) techniques attempt to identify the displacement of individual particles[5]. Typically, particle tracking techniques require lower seed particle concentrations than are used for correlation based processing. The lower seed particle images yield randomly distributed velocity vector maps with lower accuracy and fewer vectors than correlation processed vector maps.

Both single and double exposure imagery can be used in particle tracking algorithms. Single exposure data are again preferred since knowledge of the particle time history adds direction information, which aids in the tracking process. Most particle tracking techniques require more than two single exposure image frames in order to perform efficiently. For high speed flows, obtaining more than two single exposure image frames is difficult; therefore, multi-frame (>2) tracking techniques are not readily applicable to high speed flows. Correlation techniques succeed by extracting the average displacement of a group of particles in a subregion. In order for tracking techniques to succeed with only two single exposure image frames, information from the surrounding displacements must be used in the tracking operation. There are two approaches for extracting the individual particle displacements based on the surrounding particle displacements: fuzzy logic and neural networks. Fuzzy logic techniques utilize a rule base (flow continuity) for allowed particle displacements[6-7]. Particle pairs close together must move in similar directions and must have similar displacements. Neural Net approaches to data extraction rely on training the nets to identify patterns[8-9]. The nets must be trained on flows similar to those that they will be used to process. Determining the number of layers and training sets required for neural nets is a nebulous problem.

Alternatively, combining correlation and particle tracking

techniques has been proposed to create a PIV data processing system which can cover a wide range of flow seeding conditions and offers the potential for "super-resolution" PIV measurements[10]. As mentioned above, particle tracking by itself is typically not capable of successfully tracking particles at the high seed particle densities normally used for auto- or cross-correlation analysis. Conversely, correlation techniques must use large subregion sizes, with a concomitant reduction in spatial resolution, in order to perform adequately in the low seed particle density regimes where particle tracking techniques are normally applied. In the combined technique, correlation analysis is used first to obtain a benchmark velocity vector map, which then serves as a guide for the particle tracking operation. Hence, highly seeded flow field images can be processed with small correlation subregion sizes, and then the spatial resolution of the measurements improved by following with particle tracking. For moderately seeded flow field images, the correlation subregion size is increased so that a good velocity vector map is obtained, and then this is followed by particle tracking in order to obtain high spatial resolution measurements. For low-seed particle concentration cases, the standard particle tracking technique can be used alone. Low seed particle concentrations are where the average distance between particle pairs is larger than the average particle displacements between exposures. The first demonstration of the combined correlation/particle tracking technique was performed on a supersonic nozzle flow[7]. A high seed density flow was processed to obtain over 2300 individual velocity vectors in a 300 mm^2 area.

Using the combined correlation processing/particle tracking technique determines the individual particle displacements for even high seed particle concentration flows, yielding the highest spatial resolution velocity measurements possible. A super-resolution correlation-based technique has been described, which claims spatial resolution on the order of the particle size[11]. This claim does not appear appropriate, since the limiting spatial resolution is physically bounded by the particle displacement between exposures. Hence, the combined correlation processing/particle tracking approach yields the ultimate spatial resolution velocity measurements for seeded flow fields.

FUZZY LOGIC PROCESSOR APPLIED TO PTV

The control of complex processes has been aided by the development of fuzzy control systems. Fuzzy control systems have been used to control traffic flow, appliances, and even subways for optimal energy efficiency and passenger comfort. Fuzzy logic employs a tolerance for imprecision to achieve system control. An exact model for the system inputs and outputs is not required. Fuzzy inference control utilizes membership functions and a rule base developed by the user to process information. The

physical mechanisms underlying the process are irrelevant to the controller. The process of identifying and tracking particles in a flow is a good candidate for fuzzy control since the procedure is not clear cut, but involves some gray area decisions. Fuzzy logic principles have been used to track particles directly in low seed particle concentration flows, to validate correlation peaks in correlation processing, and to perform particle tracking in the combined correlation processing/particle tracking approach for high seed particle concentration flows.

In the discussion that follows, the use of fuzzy logic to track particles in a low seed particle concentration case will be described. The extension of the approach for correlation peak validation and for combined correlation processing/particle tracking is straightforward. In the fuzzy logic particle tracking technique, local particle displacement information is used to identify candidate particle tracks. The fuzzy inference processor is used to determine the most probable particle trajectories based on common sense rules that an observer would use to identify particle tracks.

The experiment is set up such that two single exposure image frames are acquired. The particle centroids on frame #1 are used as starting points for possible particle displacements. The user specifies a search region radius, R_s , typically 10-20 pixels, to search for frame #2 particles. Each frame #2 particle within a radius R_s from the initial particle centroid is a candidate displacement vector. All possible displacements of the initial particle to the second particle locations within the search region are recorded and stored as lists of candidate displacement vectors for each initial particle. Hence, for high data density areas, many initial particles may be competing for the same second exposure particle centroids. At this stage in the processing, the vector field is very convoluted and noisy. The fuzzy inference processor operates on these lists of candidate displacement vectors to determine the most likely displacement vector for each initial particle centroid location.

The list of vectors for each initial particle is compared to all other initial particle displacement vector lists to determine if there is any commonality. If two separate initial particles do claim the same second exposure particle, then all possible vector pairings between the candidate lists for each of these initial particles are compared. The main assumption is that if two initial particles are close enough to interact (claim the same second particle) then the pair of vectors that look the most similar (in direction and magnitude) must be the correct pair of displacement vectors for the two separate initial particles. This assumption also holds for tertiary and higher interactions.

There are four inputs to the fuzzy PTV processor for each

vector pair: distance between the vector midpoints in pixels (Sep); average vector magnitude (Mag); difference in vector magnitudes (MagDif); and the sum of the squares of the differences of the x- and y-components of the two velocity vectors (Delta). The first (Sep) and third (MagDif) measures, when combined, act as a velocity gradient measure. The last measure operates in the opposite manner to the dot product. This measure is small when the vectors are similar in magnitude and direction and large when they are different. Each input measure is assigned to a fuzzy set, where the degree of membership for each element in the set varies between 0 and 1. Standard 25-50% overlapping triangular input membership functions are used[6]. The degrees of membership for each input are processed through a rule base of "IF...THEN" blocks. The rule base defines an output fuzzy set. For a given vector pair, up to 16 rules may fire depending on the number of unique combinations of membership values. In lieu of the more common centroiding technique, the fuzzy PTV processor output is computed via the singleton technique with a weighted average, which is computationally simpler.

For example, given two pairs of vectors formed from two initial points competing for the same second particle as shown in table 1 and in figure 4:

	X_i	Y_i	\bar{V} [pixels]	θ°
V_1	100	100	8.5	45
V_2	100	100	11	30
V_3	105	100	6	81
V_4	105	100	7.1	51

Table 1: Sample data for an interacting pair of vectors.

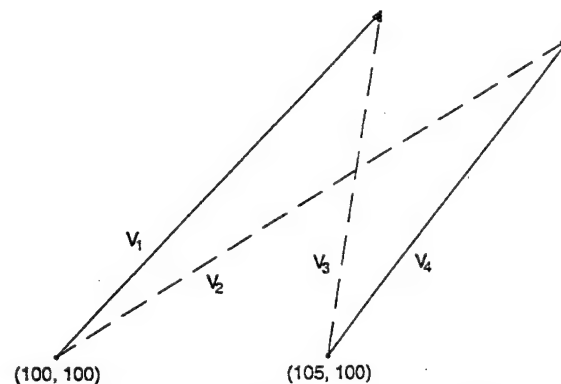


Figure 4: Two pairs of interacting vectors with separate initial points. Dashed line indicates incorrect vectors, solid line denotes correct vectors.

From the data in table 1 we find the following combinations, and their respective input measures to the membership functions:

	Sep	Mag	MagDif	Delta	Confidence
V ₁ V ₃	2.5	7.3	2.5	25	0.24
V ₁ V ₄	4.3	7.8	1.4	2.5	0.67
V ₂ V ₃	1.7	8.5	5	71.6	0.11
V ₂ V ₄	2.6	9.0	3.9	24.4	0.24

Table 2: Fuzzy processor input measures and outputs for sample vector pair combinations

Looking at the first case, V₁V₃ has the fuzzy set memberships: Sep { $\mu_{small}=0.875$, $\mu_{Med}=0$, $\mu_{Large}=0$ }; Mag { $\mu_{small}=0.276$, $\mu_{Med}=0.724$, $\mu_{Large}=0$ }; MagDif { $\mu_{small}=0.504$, $\mu_{Med}=0$, $\mu_{Large}=0$ }; Delta { $\mu_{small}=0$, $\mu_{Med}=0$, $\mu_{Large}=1$ }. With these fuzzy sets the following rules are fired:

IF(Sep=Small AND Mag=Small AND MagDif=Small AND Delta=Large) THEN

Conf_Out₁=Med

$\mu_{out_2} = \text{MIN}(\mu_{Sep}=\text{Small}, \mu_{Mag}=\text{Small}, \mu_{MagDif}=\text{Small}, \mu_{Delta}=\text{Large})$

END IF

IF(Sep=Small AND Mag=Med AND MagDif=Small AND Delta=Large) THEN

Conf_Out₂=Low

$\mu_{out_2} = \text{MIN}(\mu_{Sep}=\text{Small}, \mu_{Mag}=\text{Med}, \mu_{MagDif}=\text{Small}, \mu_{Delta}=\text{Large})$

END IF

The fuzzy "AND" of the memberships in rule #1 gives

$\mu_{out_1}=0.276$ and rule #2 gives $\mu_{out_2}=0.504$. Using Conf_Out values of LOW=0.1 and MED=0.5, the corresponding fuzzy processor output for this vector pair is computed as:

$$\text{Confidence} = \frac{\sum_{i=1}^{N_R} \text{Conf_Out}_i \cdot \mu_{out_i}}{\sum_{i=1}^{N_R} \mu_{out_i}} \quad (1)$$

$$\text{Confidence} = \frac{0.5 \cdot 0.276 + 0.1 \cdot 0.504}{0.276 + 0.504} = 0.24 \quad (2)$$

where N_R is the number of fired rules. The fuzzy processor output confidence level in each vector pair is shown in table 2. For the vector pairs listed, the V₁V₄ pair has the highest confidence level of all the combinations. In the actual implementation of the fuzzy processor, pairings V₁V₃ and V₂V₄ are not permitted since in both of these cases independent initial particles are competing for the same second exposure particle, hence these pairings will not produce a valid pair of vectors. Initially, all of the vectors are assigned a confidence level of 0. The

computed confidence level for the vector pair is compared against the current confidence level for each vector in the pair, and the maximum confidence value is stored for each vector. When all of the interacting vector pairs have been analyzed, the list of candidate vectors for each initial point will have confidence levels relative to one another. The vector in the list with the highest confidence level is assumed to be the most probable vector for the current initial point and is moved to the top of the list.

FUZZY LOGIC PEAK DETECTION

The correlation processing technique requires identification of the correlation peak on the correlation plane corresponding to the average displacement of particles across the subregion. Noise on the images and particle dropout contribute to spurious peaks on the correlation plane, leading to misidentification of the true correlation peak. The subsequent velocity vector maps contain spurious vectors where the displacement peaks have been improperly identified. Typically these spurious vectors are replaced by a weighted average of the neighboring vectors, thereby decreasing the independence of the measurements. In the PIVPROC program, fuzzy logic techniques are used to determine the true correlation displacement peak even when it is not the maximum peak on the correlation plane, hence maximizing the information recovery from the correlation operation and minimizing the number of spurious velocity vectors. Correlation peaks can be correctly identified in both high and low seed density cases. The correlation velocity vector map can then be used as a guide for the particle tracking operation. Fuzzy logic techniques are used to identify the correct particle image pairings between exposures to determine particle displacements, and thus velocity. The advantage of this technique is the improved spatial resolution that is available from the particle tracking operation. Particle tracking alone may not be possible in the high seed density images typically required for achieving good results from the correlation technique. This two staged approach offers a velocimetric technique capable of measuring particle velocities with high spatial resolution over a broad range of seeding densities.

The particle tracking fuzzy inference engine has been used in the PIVPROC program to detect the correct auto- and cross-correlation plane displacement peaks. Ideally, when the image data are of high quality and high seed density the highest amplitude peak on the correlation plane represents the average displacement of particles across the subregion being processed. An example of a high signal to noise case was shown in figure 3. However, particle out-of-plane motion, velocity gradients, image noise, and low particle concentration are all contributing sources for a noise peak to be misidentified as the average particle displacement across the subregion. In these cases the peak corresponding to the average motion of the particles across the subregion between exposures is not the highest

amplitude peak, and possibly not even the second highest amplitude peak on the correlation plane. Figure 4 shows a pair of noisy input subregions and the resulting correlation plane output. Vectors have been drawn on the correlation plane indicating the possible displacement vectors that could be derived from this correlation result. The correct average particle displacement for the subregions is the same as the case shown in figure 3, down and to the right. However, as is observed on the correlation plane, the brightest peak is not the one corresponding to the average displacement across the subregion. The brightest peak is up and to the right, yielding an incorrect estimate of the local flow velocity.

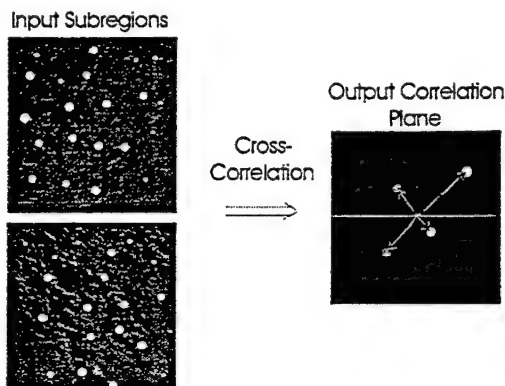


Figure 4: Noisy input subregions result in spurious peaks on the correlation plane. The brightest peak is not always the correct displacement peak.

In the actual PIV processing, each correlation plane is scanned for the 5 highest amplitude peaks, which are then stored. After all subregions in the image have been processed, the fuzzy inference operation is applied. The five highest amplitude peaks detected on each subregion correlation plane are treated as candidate velocity vectors for that subregion. The fuzzy logic processor uses flow continuity to determine the appropriate correlation peak. The stored correlation peaks from each subregion are compared on a pairwise basis to the surrounding 4 subregion results. The displacement peaks resulting in velocity vectors with the most similar qualities are given the highest confidence weighting. The highest confidence weighting velocity vector for each processed subregion is taken as the correct correlation displacement peak. Hence, the fuzzy inference technique is very similar to the weighted average replacement technique, except that the surrounding velocity vectors are used to identify the correct displacement peak from the correlation information, instead of merely replacing the spurious vector.

A comparison of actual flow field image data processed with and without the fuzzy peak detection is shown in figure 5. The main flow direction is down and to the right. The vectors with hollow heads represent displacements that were correctly identified by both processing

techniques. The original spurious vectors are shown with open line vector heads. The vectors with solid filled heads represent displacements that were initially incorrectly identified, but have been subsequently correctly identified by the fuzzy processor.

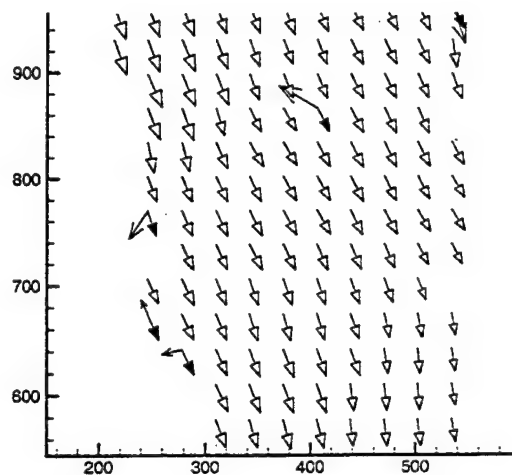


Figure 5: A vector field containing spurious vectors, which have been correctly identified using the fuzzy processor.

CORRELATION PROCESSING COMBINED WITH FUZZY LOGIC PARTICLE TRACKING

The availability of a high quality velocity vector map obtained from the cross-correlation operation offers the opportunity to perform particle tracking on length scales smaller than the correlation subregion size. Instead of using the nearest neighbor and flow continuity approach to track particles, the correlation velocity vector map can be used as a guide for the particle tracking. Using the same two single exposure image frames from the computed cross-correlation step, the first exposure image is scanned for particle centroids. All second exposure particles located within a user specified search region around each first exposure particle are detected and stored. Next, the fuzzy inference engine is employed to determine which detected particle pairings are correct. The first exposure particles and their associated list of candidate second exposure particles are now individually examined. The four nearest neighboring velocity vectors from the cross-correlation vector map to the initial particle location are found and used to compute a spatially weighted mean velocity vector, called a "benchmark vector". The benchmark vector is then used in a pairwise fuzzy comparison with all of the candidate vectors in the list for this initial particle. The candidate vector most similar to the benchmark vector, is assigned the highest confidence weighting. Benchmark vectors are computed for all remaining initial particle locations and used to identify the most probable velocity vector for each initial particle. Proceeding in this manner the correct particle pairs for all of the initial exposure particles are determined. In

practice, the particle pair operation has a success rate of approximately 30%. In some good quality PIV imagery, pair rates higher than 50% are not uncommon.

PROGRAM INTERFACE & PROCESSING

All of the data processing routines used in PIVPROC are written in FORTRAN. The user interface is created and serviced using Microsoft Windows Application Programming Interface (API) function calls. PIVPROC starts out by creating a full screen window with a white client area (workspace). Across the top of the page is the main task bar. All of the data processing, analysis and display features of the program are accessed via the main task bar. Dialog boxes are used to change the image settings and to set the correlation processing parameters. The image settings dialog box enables the user to select the gain of the image and threshold level. The images can also be left/right reversed and flipped vertically. These features are convenient if the image acquisition camera is mounted in a non-standard manner relative to the flow field of interest, or for viewing the illuminated plane through a mirror. The correlation settings dialog box is shown in figure 6. Here the user can set the subregion size, spacing between subregions and subregion image shifting.

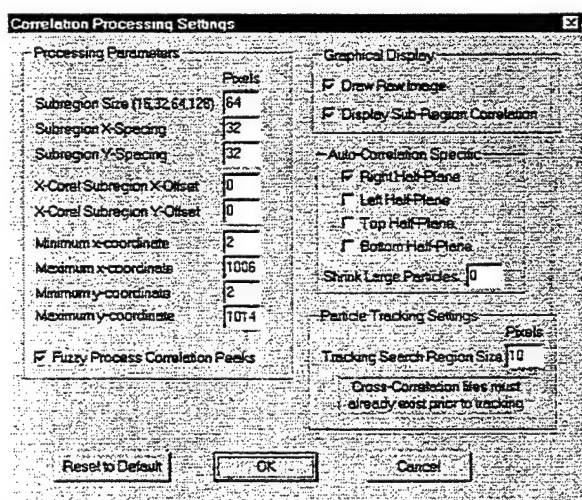


Figure 6: Correlation processing dialog box.

The maximum displacement on the correlation plane is limited by the subregion size. To avoid aliasing in the correlation plane, the displacement search region must be restricted to $\frac{1}{4}$ of the subregion size[3]. The easiest method for dealing with large displacements is to increase the correlation subregion size. However, this results in substantially increased processing times due to the larger subregions.

The best approach for processing single exposure PIV imagery that have a fairly constant displacement across the entire image is to use subregion shifting in the data processing procedure[12]. In cross-correlation processing, the second correlation subregion can be spatially shifted

with respect to the first subregion by an amount equal to the mean flow displacement between exposures, which keeps the correlation peak at the center of the correlation plane and minimizes any distortion effects caused by the windowing of the FFT based correlation operation. Image shifting has another very important benefit; shifting the second subregion window by the mean flow velocity significantly increases the probability that the particles that were in the first image frame subregion will be in the second image frame subregion. If the number of particles entering and leaving the subregions are reduced, then the false correlation rate is also reduced. Employing subregion shifting also enables the use of smaller interrogation regions (yielding faster processing times), provided the smaller subregions still contain a sufficient number of particles to provide a correlation result. Hence, particle seed concentration determines if the image shifting combined with smaller correlation subregions is a possible processing strategy for a given data set.

In the correlation processing modes, the user can select between Point Processing, Line Processing, Region of Interest or Entire Image. The portion of the raw image loaded into memory that is currently being processed via a correlation operation is displayed at the side of the image. In addition to the image subregion, the output correlation operation on the subregion is plotted, see figure 7. The x and y-displacements of the correlation peak, corresponding to the average particle displacement on the subregion are displayed on the client area below the correlation output.

The Point Processing mode is intended to be a diagnostic mode to determine the optimal image and correlation settings for processing the image. Moving the mouse around on the image space updates the pointer position display just above the image. Each time the left mouse button is clicked, a correlation operation is performed at that location on the image. The image subregion being processed is displayed along with the correlation output plane. A sample of the client area after a Point operation has been performed is shown in figure 7. Note the correlation subregion and output correlation plane to the right of the image. The bright spot on the correlation output plane corresponds to the average particle displacement across the subregion. A peak centered in the correlation plane corresponds to zero velocity across the subregion.

The data shown in these figures is from the application of PIV to the diffuser region of a high speed centrifugal compressor. The nominal flow velocity is 350 m/s and the impeller tip speed is 490 m/s. The time between laser pulses is 1.8 μ s. The imaged field of view is approximately 45x45 mm. The light sheet propagates up through the diffuser passage. The diffuser vanes are not readily observed in the figures.

The Line Processing mode is intended to be a diagnostic

tool for looking at flow profiles in the particle image data. Click the left mouse button at two locations on the image and a series of correlations are performed along the line connecting the two mouse click locations, as shown in figure 8. More than one line of correlations can be computed. The image subregion being processed is displayed along with the correlation output plane.

Region of Interest processing mode enables the user to select only a portion of the image to be processed. The Entire Image processing mode processes the entire image. In both of these modes the current subregion being processed and the corresponding correlation output plane are displayed on the screen in real time. A sample of the Region of Interest processing mode output is shown in figure 9, where over 300 valid vectors were found. Spurious vectors are obtained outside the region of the light sheet.

The Particle Tracking operation can only be performed after a correlation velocity vector map is obtained. Using the correlation vector map obtained from figure 9, a particle tracking operation was performed. The resulting particle tracking velocity vector map is shown in figure 10, where over 3400 velocity vectors have been tracked. The particle tracking result has a much higher spatial resolution than the spatially averaged correlation result.

In addition to the correlation and particle tracking operations, the PIVPROC program can be used to edit the velocity vector maps or interpolate the randomly sampled particle tracking data over a uniform grid. The vector maps displayed on the screen can be sent to a printer to generate a hardcopy. In the manual vector removal mode, the velocity vector data are displayed on the screen, and the current location of the mouse pointer is displayed just above the vector plot. Position the mouse pointer over the tail of the velocity vector to be removed. Click the left mouse button and the vector is deleted, both from the screen and from memory.

CONCLUSIONS

A description of the main processing features of a PIV data reduction software package has been presented. The principles of fuzzy logic are used to maximize the information recovery from PIV image data and also to facilitate combined correlation processing/particle tracking. The combined correlation/particle tracking technique yields the highest spatial resolution velocity measurements possible from the PIV image data. A description of the PIVPROC user interface was given, along with examples of the dialog boxes used to set the processing parameters. Examples of using the PIVPROC software to process PIV image data from a high speed centrifugal compressor have been presented. Particle tracking results were shown to have much higher spatial resolution than the correlation results.

REFERENCES

- [1] Wernet, M. P., "Digital PIV Measurements in the Diffuser of a High Speed Centrifugal Compressor", AIAA-98-2777, *Advanced Measurement and Ground Testing Technology Conference*, Albuquerque, NM, June 15-18, 1998.
- [2] Wernet, M. P. and Bright, M. M., "Dissection of Surge in a High Speed Centrifugal Compressor Using Digital PIV", AIAA-99-0270, 37th AIAA Aerospace Sciences Meeting, Reno, NV, January 11-14, 1999.
- [3] Adrian, R. J., "Multi-Point Optical Measurements of Simultaneous Vectors in Unsteady Flow -A Review", *Int. J. of Heat and Fluid Flow*, Vol. 7, pp 127-145, 1986.
- [4] Landreth, C. C., Adrian, R. J., Yao, C. S., "Double Pulsed Particle Image Velocimeter with Directional Resolution for Complex Flows", *Experiments in Fluids*, Vol. 6, pp119-128, 1988.
- [5] Wernet, M. P., "Particle Displacement Tracking Applied to Air Flows", *Fourth International Conference on Laser Anemometry*, Cleveland, OH, pp 327-335, August 5-9, 1991.
- [6] Wernet, M. P. "Fuzzy Logic Particle Tracking Velocimetry", *Proceedings of the SPIE conference on Optical Diagnostics in Fluid and Thermal Flow*, San Diego, California, July 11-16, 1993.
- [7] Wernet, M. P., "Fuzzy Inference Enhanced Information Recovery From Digital PIV Using Cross-Correlation Combined with Particle Tracking", *Proceedings of the SPIE conference on Optical Diagnostics in Fluid and Thermal Flow*, San Diego, California, July 9-14, 1995.
- [8] Cenedese, A., Paglialunga, A., Romano, G. P., Terlizzi, M., "Neural Net for Trajectories Recognition in a Flow", *Sixth International Symposium on Applications of Laser Techniques to Fluid Mechanics*, Lisbon, Portugal, July 20-23, pp27.1, 1992.
- [9] Grant, I., "Particle Imaging Velocimetry: a Review", *Proc. Instn Mech Engrs*, Vol. 211, Part C, pp 55-76, 1997.
- [10] Keane, R. D., Adrian, R. J. and Zhang, Y., "Super-Resolution Particle Imaging Velocimetry", *Meas. Sci. Technol.*, Vol. 6, pp754-768, 1995.
- [11] Hart, D. P., "Sparse Array Image Correlation", *Proc. of the 8th International Symposium on Applications of Laser Techniques to Fluid Mechanics*, Lisbon, Portugal, 1998.
- [12] Westerweel, J., "Fundamentals of Digital Particle Image Velocimetry", *Meas. Sci. Technol.*, Vol. 8, pp 1379-1392, 1997.

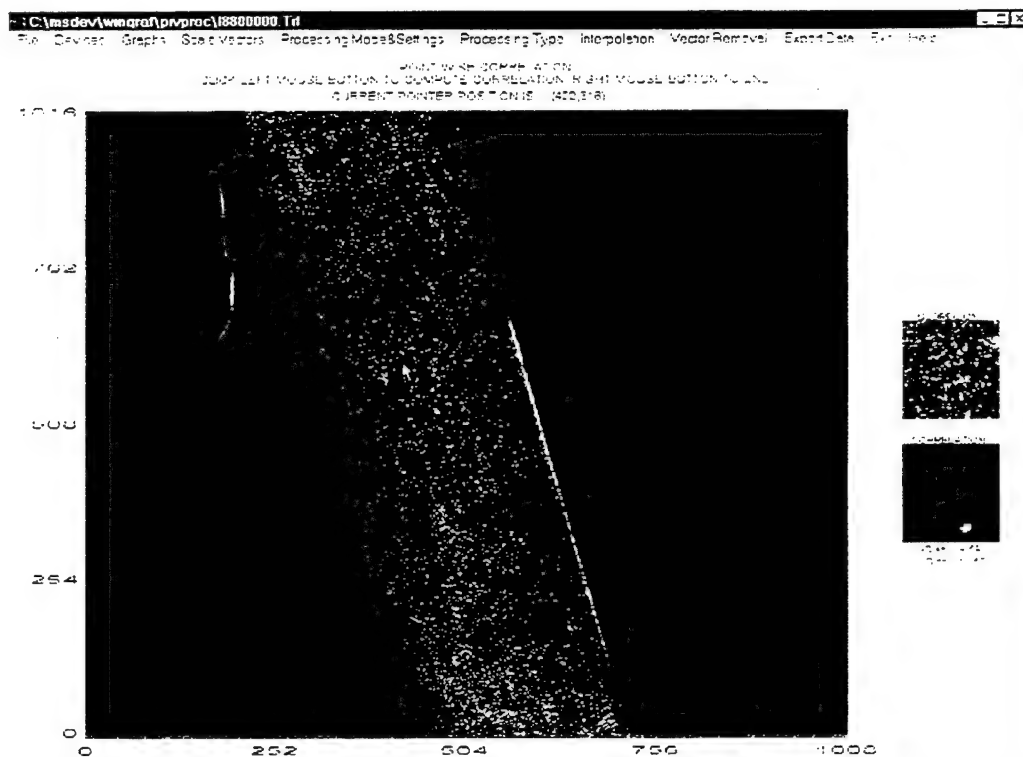


Figure 7: Point Processing mode showing the raw image file. The correlation subregion and correlation output plane are shown to the right of the image. The image data shown are from measurements obtained in the diffuser of a high speed centrifugal compressor. The impeller is observed to the left of the light sheet.

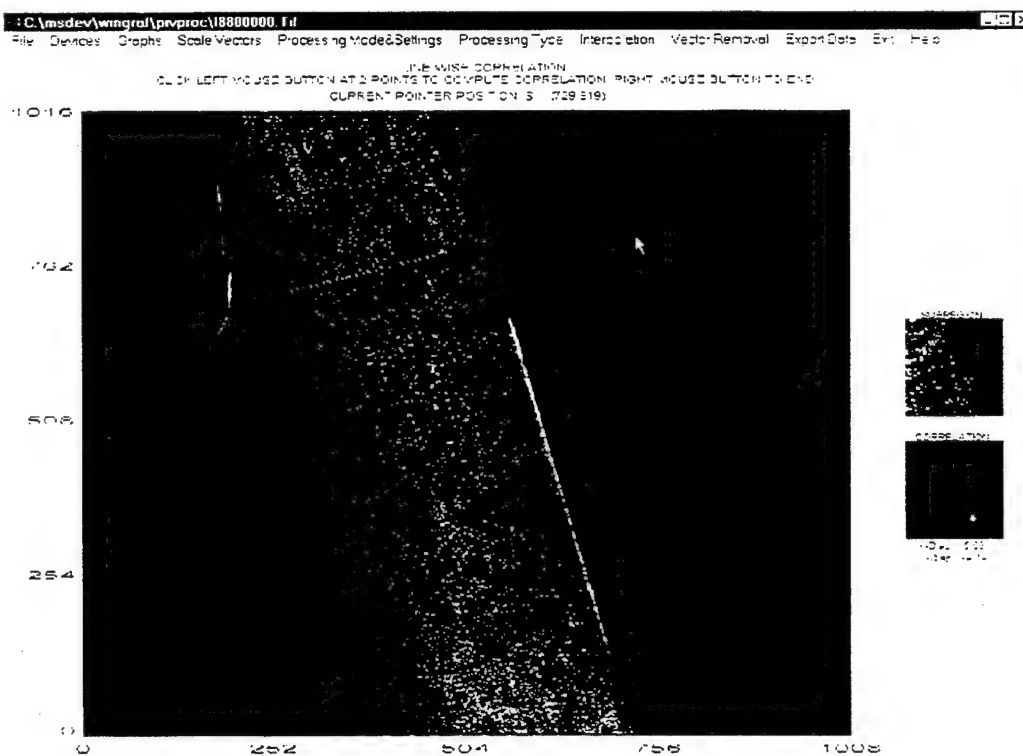


Figure 8: Line Processing mode showing the line of computed velocity vectors overlaid on the raw image file.

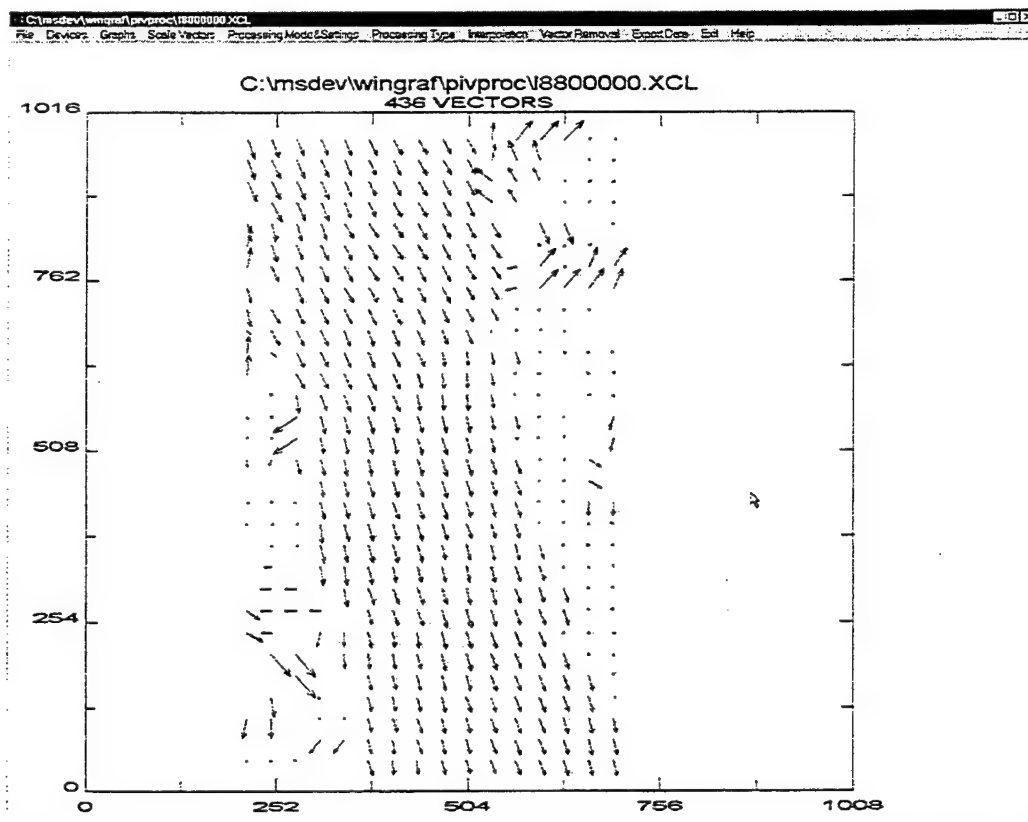


Figure 9: Region of Interest correlation processing result. Approximately 300 good vectors have been detected. Spurious vectors occur outside of the light sheet.

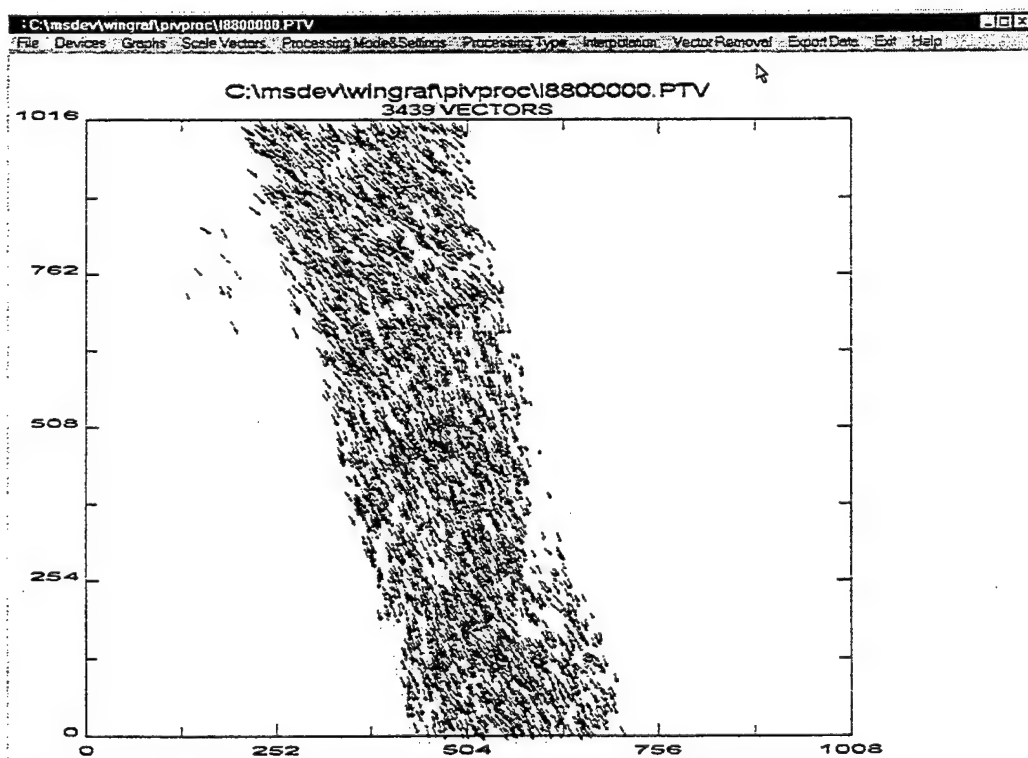


Figure 10: Particle tracking result using correlation processing vector map from figure 9 above. Over 3400 vectors have been detected.

Particle Image Velocimetry to quantify 3D-Flow Properties of Gas Turbine Forced Mixers

W.Scheuerpflug, N.Lawin
BMW Rolls-Royce AeroEngines GmbH
Eschenweg 11
D-15827 Dahlewitz
Germany

ABSTRACT

Forced Mixers are typically used in turbofan engines with low and medium bypass ratio to increase the cruise performance and to reduce the jet mixing noise [1]. Most of the design criteria are still based on empirical considerations using qualitative visualisation methods such as smoke injections, or in case of water simulations with dye injection, chemical color reaction and the like. The judgement about the quality of different mixers is therefore based on visual impressions only. Since the flow fields in an engine are highly turbulent, it is nearly impossible to get a representative image of the flow with qualitative measurements. Quantification and subsequent averaging to obtain the steady state flow distribution is a necessity. The techniques used are large scale 2-D-PIV to examine the axial, radial and circumferential velocity distribution at specific sections. A conductive method was used to determine the global mixing properties at the beginning and at the end of the mixing section and to deliver an empirical mixing coefficient.

INTRODUCTION

The following results were achieved in a water analogy application representing the turbulent conditions of realistic applications under momentum similarity and used particle image velocimetry (PIV) both in its 2-dimensional standard application of PIV as well as in a new 3-dimensional demonstration.

The tests were made in a perspex water analogy rig. The model consists of interchangeable mixers, the jet pipe and the bullet. Also some special supporting structure and OGV's were modelled. The water channel is a continuously driven closed circuit with a flow rate of 100 kg/s. The ratio fan flow velocity to core flow velocity was chosen to be 1.3 for the simulation of take-off and 1.04 for cruise.

PARTICLE IMAGE VELOCIMETRY

Up to now quantitative experiments used single point measurements with hot wire or laser doppler anemometry. Mixing structures e.g. need a 3-D volume to be recorded. These techniques require a long and expensive time on the test bed. Particle Image Velocimetry (PIV) is a continuously improving measurement technique to determine flow fields. It has evolved out of the laboratory into more complex fluid

environments. In contrast to standard flow visualisation it delivers quantitative data, most notably the instantaneous 2-D-velocity distribution. The development of PIV to deliver the 3-D-velocity distribution and more subtle flow property data is ongoing. To get the flow properties of the complicated flow structures behind a forced mixer the flow section was recorded in the following manner: The light sheet was introduced in the axial plane at specific angles as shown in figure 1.

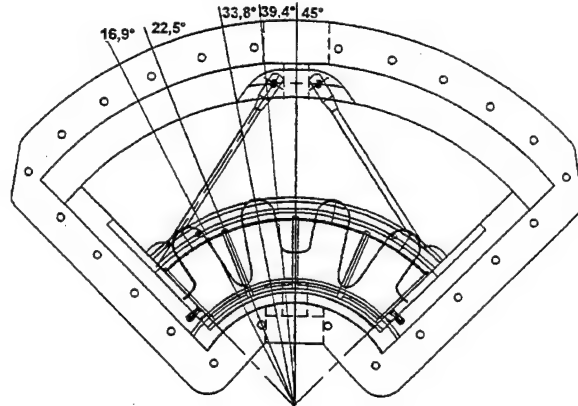


Figure 1: Circumferential Measurement Sections

Thus the radial and axial components can be acquired using a modulated laser light sheet. The camera acquires images of tracers during each laser pulse. The tracers are assumed to follow the flow without delay. Hence the velocity and direction of the flow can be determined from the displacement of the tracers and the time between the two pulses. This will show the instantaneous flow patterns. The mixing properties depend largely on 2nd. order functions such as vorticity. To resolve small structures this requires a very high spatial resolution. Given a limited number of camera pixels, the 2-D-capture of a flow is reduced to a relatively small field of view, typically of 40 x 40 mm. For a large flow field such as in mixers it is required to put together a large number of test sections (fig.2). This gives both a high spatial resolution, i.e. eddies and other flow phenomena can be determined, and the full overview of the mixing structures.

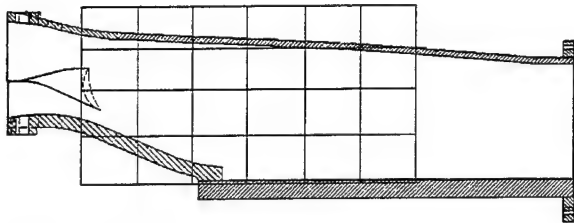


Figure 2: Axial Composition of Large Scale PIV

Since PIV will give instantaneous velocity fields in the first place, an averaging of the results to determine the steady state conditions is necessary. For the tests mentioned 4 x 6 sets of areas of interest or more depending on the complexity of the flow with 162 x 178 vectors each were composed into one flow field. The local averaging consisted of 20 images to obtain a quasi-steady flow field.

By sweeping the PIV system through the sector the whole axial and radial velocity distribution could be acquired.

GENERAL OBJECTIVES

A set of mixers with different lobe configurations was designed and tested. For this report the results of mixer 1 acting as a benchmark are being compared against mixer 4. Mixer 1 and 4 are shown in figure 4. As an example the axial flow distribution of both mixers is shown in figure 5 at cruise.

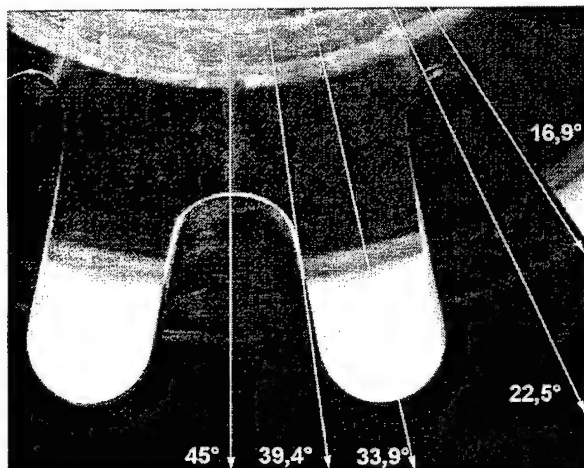


Figure 4a: Mixer 1

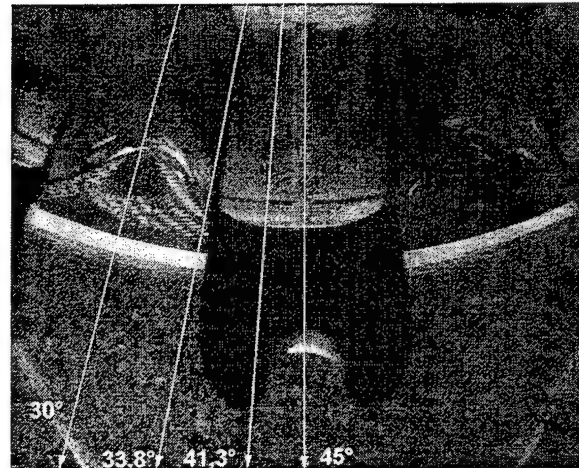


Figure 4b: Mixer 4

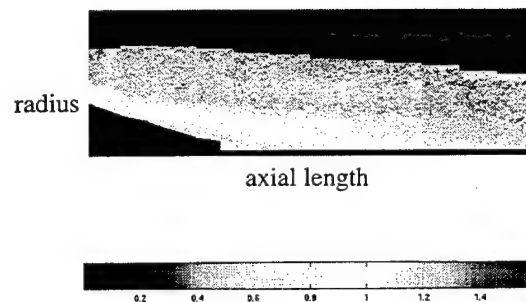


Figure 5a: Mixer 1 during Cruise at 45°
Height 1 Height 2

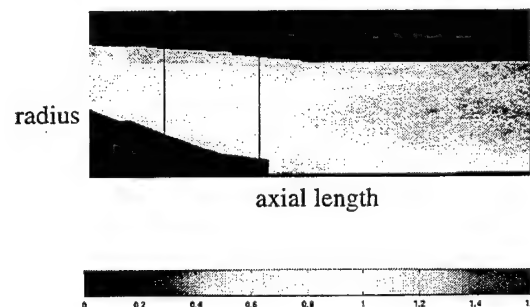


Figure 5b: Mixer 4 during Cruise at 45°

The different flow patterns can easily be identified and compared.

AXIAL AND RADIAL FLOW DISTRIBUTION

At first the PIV planes were measured such that axial and radial velocities could be determined. As an example the different flow distributions at the circumferential sections of mixer 1 at 23° and 45° during take-off are shown in figure 6 and figure 7. Since plotting the individual vectors is not helpful for the visual impression, the axial respectively the radial content was converted into color to illustrate the flow properties in a manner easier to identify for the human eye.

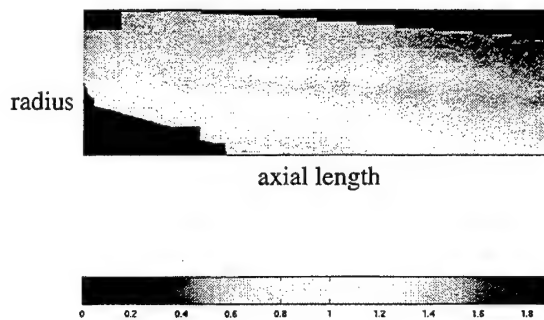


Figure 6a: Axial Velocity Distribution during Cruise at 23°

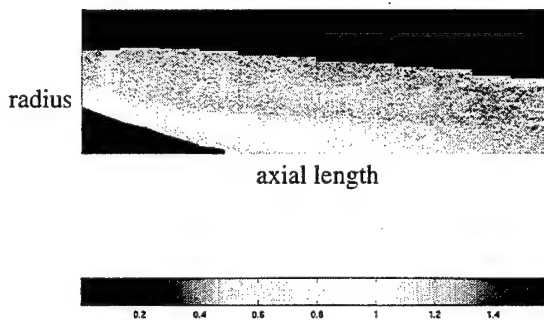


Figure 6b: Axial Velocity Distribution during Cruise at 45°

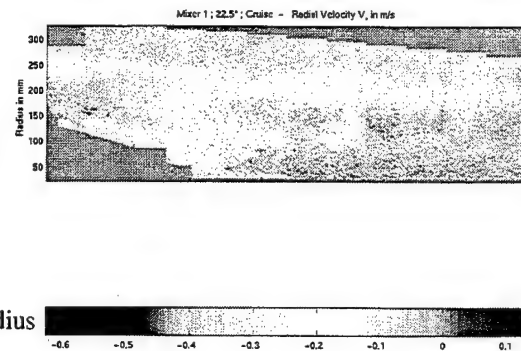


Figure 7a: Radial Velocity Distribution during Cruise at 23°

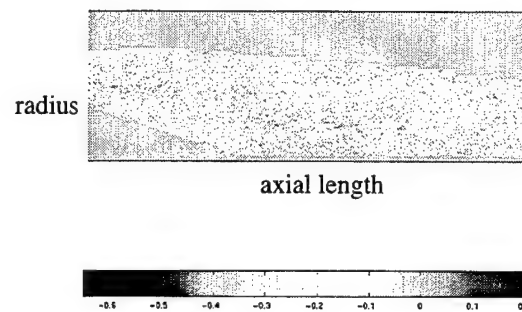


Figure 7b: Radial Velocity Distribution during Cruise at 45°

CIRCUMFERENTIAL FLOW DISTRIBUTION

At dedicated axial positions the light sheet was positioned horizontally and the camera looked upstream through a windows. This way the circumferential flow distribution could be obtained. It required a carefully matched thickness of the light sheet and a drastically reduced number of particles in the flow to prevent "fogging" and speckle noise in the respective plane.

These recording were carried out with adjusted laser pulse separation to quantify the circumferential velocities (fig. 8) at several heights. All of the above mentioned tests on several sets of mixers were carried out at cruise and take-off conditions shown here of mixer 4.

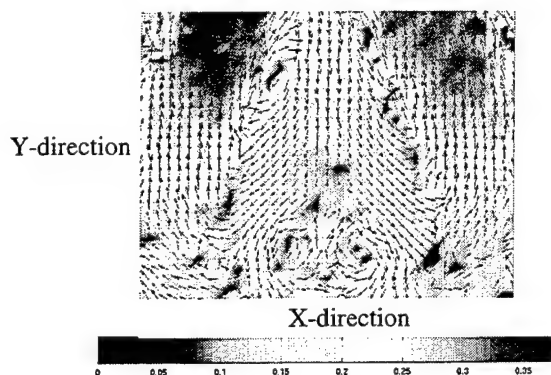


Figure 8: Circumferential Velocity Distribution of Mixer 4 during Cruise at height=1

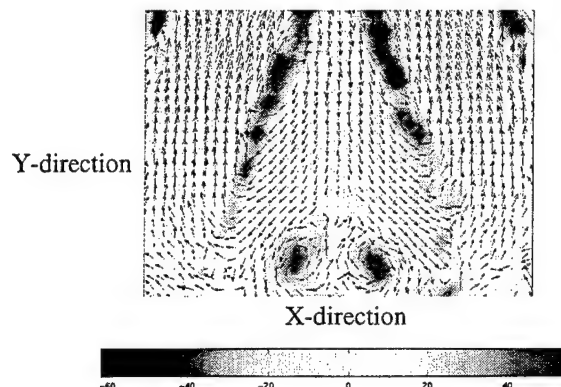


Figure 10: Circumferential Vorticity Distribution of Mixer 4 at height=1

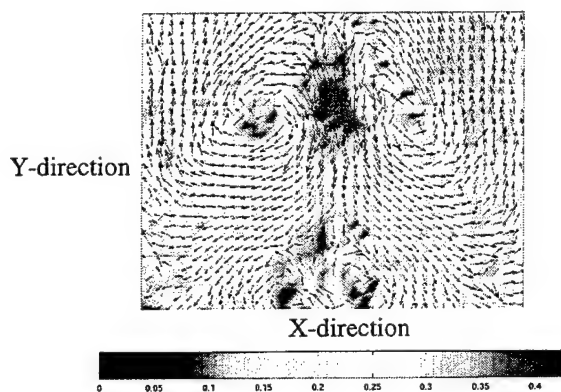


Figure 9: Circumferential Velocity Distribution of Mixer 4 at height=2

DERIVED FLOW PROPERTIES

The mixing properties of flows are largely dependant on small scale eddies and vortices. Therefore the local gradients of velocities can contribute to the understanding of the flow structures and its implications on mixing. The vorticity distribution shows very distinctive structures (fig. 10, fig.11). For the calculation of vorticity the formula of [2] was used.

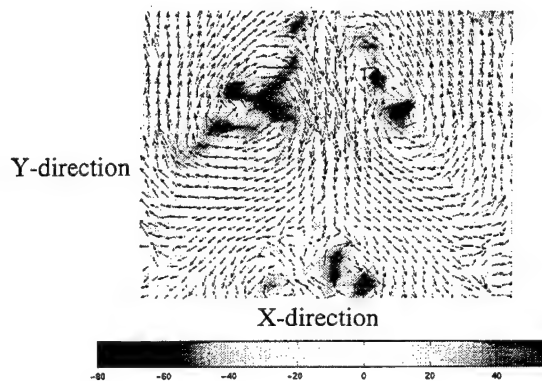


Figure 11: Circumferential Vorticity Distribution of Mixer 4 at height=2

These quantitative visualisations show clearly the different mixing conditions with increasing distance from the mixer.

COMPARISON WITH CFD

The measurements were accompanied with CFD calculations for various mixer designs. As an example mixer 4 was both calculated and measured. The axial flow distributions are shown in figure 12. They show a fairly good agreement between calculation and measurement for water corrected flow. Further comparisons are currently under investigations.

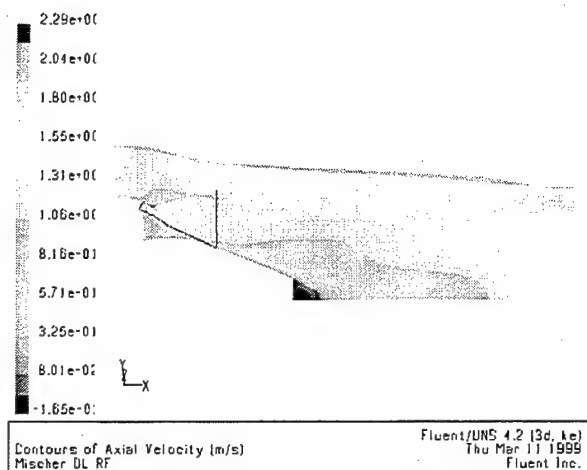


Figure 12a: CFD Result for Axial Flow of Mixer 4 during Cruise

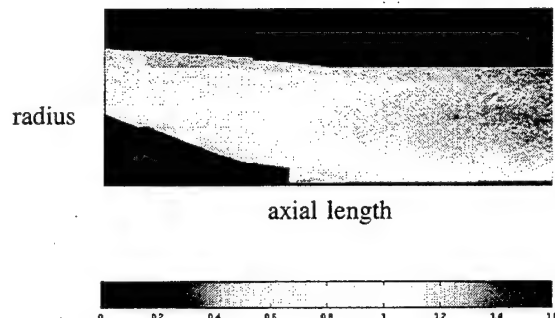


Figure 12b: PIV Result for Axial Flow of Mixer 4 during Cruise

CONDUCTIVE MEASUREMENT METHOD

PIV results give quantitative data at the sections required, but they cannot deliver global informations such as mixing rates or efficiencies. To accomplish this a conductive method was developed using the idea to measure the resistance of suitable flow sections at the inlet and the outlet separately. The resistance is dependant on the conductivity of the water properties which can be doped by salt injection at one inlet (i.e. the outer passage). The excitation was done with a AC voltage supply at 15 kHz frequency to avoid polarisation effects. The voltage is measure across the outer passage and the current is determined, too. Thus the voltage drop across the inner passage can be determined as well (figure 13). In the exit plane a central electrode was placed at a position which was calculated assuming separated flows, i.e. constant area.

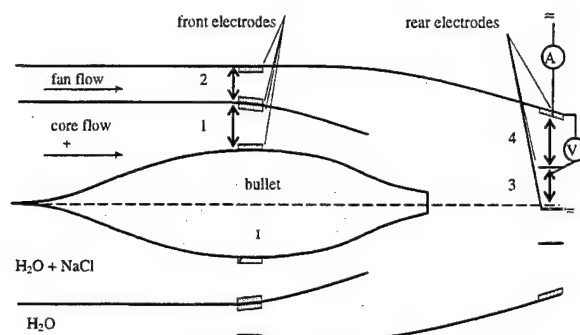


Figure 13: Principle of the Conductivity Method

The measurement at each plane must be done separately from the measurement in the other plane to avoid crosstalk or electric crossflows. (In principle they could be done simultaneously using 2 different excitation frequencies and according filtering equipment which was unavailable for the time of the test).

For the determination of the mixing efficiency the ratio of the relevant voltages γ before run and during run were determined for each position.

$$\gamma_x = \gamma_0 / \gamma \quad (1)$$

The mixing efficiency V was determined as

$$V = 1 - \frac{\gamma_3 - \gamma_4}{\gamma_1 - \gamma_2} \quad (2)$$

Thus the following results were obtained:

Mixer Efficiency [%]	Cruise	Take-off
Mixer 1	21,5	15
Mixer 4	53,5	49

CONCLUSIONS

With PIV quantitative flow fields in all 3 directions can be obtained. The time for testing is much shorter than other quantitative techniques. The mixing properties can be determined using velocities and their 2nd. order functions. The flows of different mixers can be easily and objectively identified and compared with each other.

ACKNOWLEDGEMENT

This project was supported by the "Bundesministerium für Forschung und Technologie" under contract number 20T9606. The help from colleagues and partners especially with respect to mechanical design, CFD calculations and support is acknowledged.

LITERATURE

/1/ Ch.Mundt, M.Wegner: Improvement of forced mixing in turbofan engines with respect to both noise and performance, 7th.European Propulsion Forum "Aspects of engine/airframe integration", Pau, March 1999

/2/ M.Raffel, C.Willert, J.Kompenhans: Particle Image Velocimetry, Springer-Verlag 1998

SESSION : 2

AERO-ENGINES

AN INTEGRATED APPROACH TO THE APPLICATION OF HIGH BANDWIDTH OPTICAL PYROMETRY TO TURBINE BLADE SURFACE TEMPERATURE MAPPING

J Douglas, C A Smith, S J R Taylor

Rotadata Ltd. Derby, U.K.

ABSTRACT

As gas turbine manufacturers strive for improved efficiency the turbine operating temperatures increase which can only be met by improvements in blade and coating materials together with advances in cooling and coating technologies. The ultimate, and possibly the only, environment capable of testing modern blade systems is in a working engine and it is from this environment that instrumentation a range of instrumentation technologies must acquire valid blade performance data. A critical blade parameter is the surface temperature distribution and this paper will review the various technologies currently applied to blade surface temperature distribution measurement. Optical Pyrometry, is discussed in more detail and the definition of an integrated high bandwidth detection and data collection system developed.

The system developed collects turbine and stores radiance measurements at the rate of 1 million per second and this paper explores the benefits that can accrue from this approach in areas such as noise reduction and blade scanning techniques.

The output from such a system is a data file representing a 'thermal image' of all the blade surfaces viewed by the pyrometer. The conversion of the 'thermal image' into a temperature image is discussed and the role of complimentary measurement methods in refining the temperature image is reviewed.

The integration of measurement techniques limits the ability of suppliers to deliver an 'Off-The-Shelf' measurement capability. In the light of this the limitations of the system outlined in the paper are discussed and the need for collaborative effort between the system supplier and the users technical departments emphasised.

INTRODUCTION

As the performance and efficiency of modern gas turbines improve the environment in which instrumentation has to survive and provide viable measurements becomes increasingly hostile. Turbine blades are possibly the components most at risk as gas temperatures and pressures are increased and knowledge of surface

temperature and temperature distribution is vital if blade integrity is to be assured.

High temperature, high pressure, static rigs can be used to test blade characteristics but they are of limited value as the engine environment cannot be simulated outside an engine. This means blade temperature and temperature distribution information has to be acquired from the operating engine if confidence in the blade design and manufacturing processes is to be assured. Established and emerging methods to acquire temperature measurements from rotating blades are briefly examined with reference to the increased environmental conditions.

BLADE TEMPERATURE MEASUREMENT METHODS

Temperature Sensitive Paint

The main means of acquiring blade temperature distribution information has been, and still is, temperature sensitive paints. These have been under continuous development in parallel with the gas turbine and provide a blade surface temperature map at a single operating condition.

The principle advantages of this method are that it can be applied to all areas of the blade and there is a huge background of experience in both application and interpretation. However, the method has limitations some of which are:

- It is a "one shot" method. The engine is taken to the condition at which measurements are required, stabilised for a short period then the paints have to be read.
- The paint acts as a thermal insulator influencing the blade temperature it is supposed to measure.
- Limited temperature resolution - only discrete temperature change points can be recognised.
- Interpretation is dependent on operator and blade condition - the colour change is a gradient and an assessment of the change point is made. The colour value and definition are variable due to actual engine condition etc.
- Paint may be lost during running giving reduced coverage.
- New blade designs and coatings are producing surface temperatures significantly higher than the paints can survive.

Thermal Melts

The blades are coated with an alloy which undergoes a change of phase at a specific temperature. Like thermal paint the resulting temperature contour is only indicative

of the maximum temperature experienced. Because it is a metallic coating it has little influence on the blade temperature but only one measurement temperature is available per coating.

Thermocouples

Thermocouples are regularly used for blade temperature measurement but their ability to measure local, surface temperature is limited by their physical size and installation method. Normally they are bonded into grooves machined in the blade surface with the connections strapped to the disc and along the shaft to slip-rings or radio telemetry signal transfer systems.

In addition to the high cost of installing thermocouples some other concerns are:

- Uncertainty over the exact junction position on the surface and within the blade wall.
- Coverage is limited to one or two measurements per blade and a few blades per rotor.
- The cost of the installation and readout is high. (Slip-rings, radio telemetry.)
- The lead up to the junction can act as a conductor of heat into, or out of the junction depending on local temperature gradients.
- The presence of the slot and its 'filling' changes the local aerodynamics and heat transfer characteristics.

Laser Induced Fluorescence

Some ceramic materials fluoresce when excited by laser radiation. A short pulse of radiation causes the material to produce a pulse of fluorescence whose amplitude and decay rate are a function of temperature.

As the decay rate is independent of surface and optical system cleanliness this is the parameter measured. Apart from the complexity and size of a possible probe to apply the technique to surface temperature distribution measurement the fluorescence signal amplitude and decay time vary inversely with temperature making signal collection and processing increasingly difficult as the temperature rises.

Optical Pyrometry - Engine Control

Optical Pyrometry has been developed and applied to gas turbines for over thirty years and the fundamental theory behind the measurement, and the problems associated with its application to turbine blades are well reported.

The most successful application to date has been to engine control. Here pyrometers continually monitor the mean radiance temperature at a single radial position. The pyrometer output is correlated with engine operating parameters and predicted blade metal temperature during the engine production tests. The engine control system uses the output to avoid blade over temperature conditions.

Optical Pyrometry - Engine Health Monitoring

Improvements in signal processing permit the extension of this relative measurement approach to detecting changes in individual blades that may indicate to the engine management system a potential blade failure. This role is exploited in ground based turbine operation and may extend to flight use in the not too distant future.

Optical Pyrometry - Blade Development

The signal received by an optical pyrometer is the sum of the radiation from all the sources in the optical path modified by any attenuating material between the blade and the lens. Selection of operating wavelength can minimise the attenuation effects and signal processing can reduce the effect of any transients due to flame and hot particles passing through the optical path.

What is left is the best measurement of the radiation leaving the blade surface. This consists of blade emission plus any radiation from the blade environment reflected off the blade. The magnitude of these reflections is dependent on which stage rotor and which blade surface is being measured.

The measurement priority is usually the highly loaded first stage rotor blade. Its pressure, (upstream), surface is in direct radiation exchange with the combustor so the pyrometer signal will contain a significant combustor contribution varying with location on the blade. Methods employed to identify the combustor contribution include:

- Multi-spectral pyrometers to analyse the spectral distortion in the measured radiation to identify the contribution from the hotter combustor.
- Blade mounted thermocouples to provide a spot metal temperature from which to calculate the error due to reflected radiation. As the reflection characteristics vary over the blade surface this correction is only ideally applicable to the surface local to the thermocouple though it can be used to correct identical locations on other blades.

Applying the correction to all the blade data will reduce the error significantly and improves the accuracy of blade to blade comparisons.

While the combustor creates the biggest error all measurements are influenced by the presence of surfaces at temperatures the same as, or close to, the one being measured.

Thermal Barrier Coatings

These are applied to the blade as a thermal insulator to reduce the heat transfer into the blade from its environment.

Flame sprayed ceramic coatings generally reduce the blade emissivity and increase its reflectivity. The pyrometer measures the coating surface temperature and metal temperatures must be deduced from the measured value.

Vacuum deposited coatings are semi-transparent in the spectral range most used to measure surface temperatures meaning the pyrometer indicates a temperature between

the coating outer surface and the blade metal surface. Exactly what temperature is indicated is a function of coating thickness, optical properties, condition and temperature gradient.

The transmission is a function wavelength so selecting wavelength can bias the measurement towards either the blade or coating surface. With the engine running the coating becomes increasingly contaminated and the optical properties change as a function of running condition, time, and location on the blade.

The coatings can be doped by applying laser induced fluorescence measurement but the effects reviewed above can affect the viability of the technique as the signal will be generated in the bulk of the coating dependent on transmission etc and the higher temperature will reduce the available signal.

THE ROTADATA APPROACH

Introduction

The higher surface temperatures now being realised raise doubts over the viability of paints in the future and of the alternatives optical pyrometry is, in our view, the most likely one to offer a "Thermal Paint" performance on the accessible blade areas. This can be done by collecting a 'thermal image' of the turbine and processing it to give a corrected 'temperature image'.

To do this a viable system must be able to:

- Access the blade surfaces with minimum intrusion into the turbine.
- Collect sufficient data to adequately define blade radiance distribution.
- Perform the above functions in the minimum time.
- Carry out pre-defined data processing.
- Provide scope for user specific processing to give acceptable temperature distribution information.
- Offer a range of data display options.

Engine Access

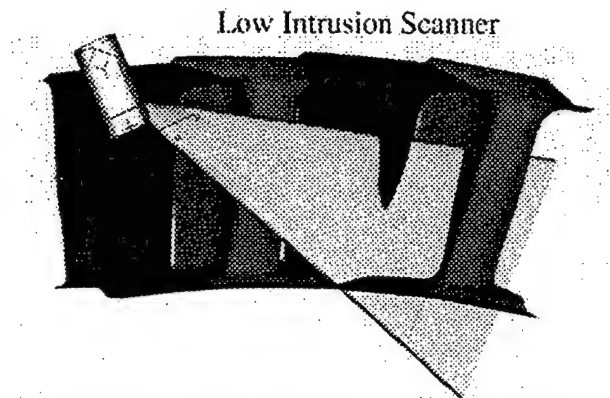
Current scanning pyrometer systems collect circumferential profile data at a series of pre-determined radial positions and combine them to generate a 2D map as required. If signal averaging or minimum picking is required then sufficient data must be collected at each radial position to support the level of processing needed. This increases the time spent at each station and is in conflict with blade vibration and probe life restrictions.

Access itself into the turbine, however, is usually available through existing apertures such as boroscope holes, not requiring the inclusion of the pyrometers at the casing design phase.

To reduce the time spent in the turbine gas stream the scanning process has been re-defined as a non-stop traverse into and then out of the turbine with continuous data collection.

Where full insertion is not feasible a low insertion system has been developed. A probe is inserted into the turbine,

approximately 12mm typical depth, and a mirror scanner moves the pyrometer target area up / down the blades.



Equivalent Scanning speed > 20 mm / second possible

Figure 1 Low Intrusion Scanner.

Detector System

From consideration of temperature range, spatial resolution, optical and detector efficiency a target diameter of 2 mm is used.

Blades travelling at 500 metres per second take 4 microseconds to travel 2mm. Recording a step between blades with an error less than 5%, (5°C approx.) requires a rise time of approximately 1 microsecond. This equates to a system bandwidth of DC to 330Khz.

For operation with a traversed periscope scanner the pyrometer is a rigid, probe which fits in the periscope. It employs an objective lens, a glare stop and a field stop to define the target geometry and working distance.

A lens based relay system transfers the collected radiation from the field stop to the detector via a rigid tube. The overall probe length is adjusted by changing the length of the rigid tube. The detector and processing electronics are integrated into the probe and a single multi-way cable is used for power services and data transfer.

In the low insertion version the optics and electronics are integrated into the probe / scanner. As the optical path only contains lenses and mirrors the spectral band used can be varied by changing lens material and detectors. Multi-spectral capability can be included with only minor changes in probe length.

A 12 bit A/D converter digitises the detector output at 1 million samples per second within the probe. The resulting 12 MHz data stream is passed from the engine to the ground station via a single multi-way cable.

Data Synchronisation

A prerequisite for any post processing is accurate synchronisation between the rotor and probe positions and the collected data. Engine 'speed' probes provide the former and motor / encoder pulses the latter.

Data Collection

The 12 megabit per second data stream is fed from engine to the ground station via the multi-way cable. A digital receiver converts the 12 bit serial data into parallel format

as the 12 high bits in a 16 bit word. The 4 low bits are used to record the synchronisation pulsed from the rotor and, if required, motor encoder pulses from the scanning system. In this way a single binary file is created containing a continuous record of the pyrometer signal and the necessary timing pulses with 1 microsecond resolution.

The data is generated at 2 Mbytes per second and a typical measurement cycle lasting 15 seconds will generate two 15 Mbyte files, one on the "In" stroke and the other on the "out" one. The data is stored directly in RAM and transferred to two hard drives for storage and backup immediately on completion of a measurement cycle.

Data Processing

The potential users of the system are in competition with each other and have their own methods and strategies for analysing pyrometer data. The 'common ground' between users is the data acquisition and immediate data processing to 'clean up' the data and generate the 'thermal image' with the best possible data.

Processing strategies and methods applied to the thermal image are possibly commercially sensitive so the system is configured to make the thermal image file available for either further processing with the users algorithms etc. in the system or transfer to the users system for 'In-house' analysis.

System Integration and Control

To maximise the benefits of the elements described above they have to be fully integrated to give minimum traverse times and keep the exposure of the probe and the engine to any hazards to a minimum.

The system developed and described below combines accurate pyrometer control and high-speed acquisition processes to enable non-stop traversing with continuous data collection.

Although designed to be fully automatic, manual over ride is possible. The use of intelligent motor control modules gives a greater degree of accuracy, higher speed of traverse, wider flexibility in velocity profiling and feedback control features such as damping.

Collected data positional integrity is by the integration of the pyrometer position data, provided by the encoder pulses, with the temperature data.

Additional safety features included are monitoring of the pyrometer cell temperature, purge air test routines and automatic emergency retract controlled by the intelligent motor drives, thus providing additional safety in case of computer failure.

Data Processing

In addition to the control of the probe and the control and management of the data acquisition process, the system also includes post-processing facilities for the manipulation and display of the acquired data.

The basic functions provided are:

- Speed variation Effects
- Noise removal
 - Minimum Picking
 - Averaging
 - Customer Specific Processing
 - Linearisation

Engine Speed Effects

Although the engine may be 'stable' when sampling at more than 3000 points per revolution minor speed changes can be recognised.

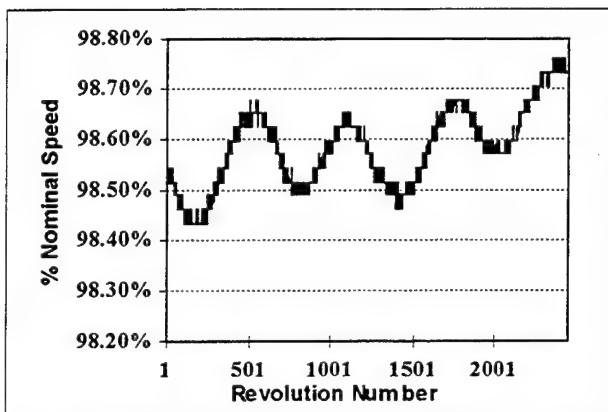


Figure 2 Speed Variation during an 8 second Traverse.

The measurements shown in figure 2 were extracted from a pyrometer file from a 'stable' engine. Note the number of revolutions from which data was recorded.

In this case the increase in speed would have displaced the measurement location by one sixth of a blade.

This effect is corrected by tabulating the number of samples taken per revolution using the recorded speed probe data. It is then re-sampled to generate a new file with an equal number of points per revolution. Re-sampling uses linear interpolation between adjacent points and with several thousand measurements per revolution little data degradation occurs.

Minimum Picking/Averaging

Once the data has been arranged according to position, combinations of techniques to remove flame noise and enhance the signal to noise ratio may be selected to suit the requirements of each data set. The high sampling rate employed at the acquisition stage allows greater scope for the application of the noise reduction methods to the data.

Customer Specific Processing

The steps outlined above are the common ground between users. Further processing can be incorporated in the system or the files can be transferred to the customer for processing. CD file transfer capability is available.

Linearisation

The final standard processing stage is to convert the radiance data to actual temperature by making use of

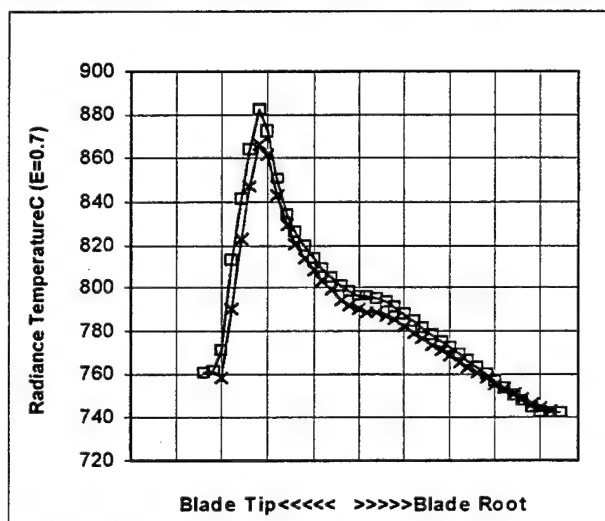
calibration information and the user input value for the emissivity.

A 1 million point per second digital lineariser is available if required to linearise the data prior to storage.

Data Display

The first level display is a 2D image with the data plotted in polar format with the signal level as brightness / colour, i.e. a thermal image. Displaying the file, corrected for speed variation only, will show any noise or flame effect and the level of averaging or minimum picking etc. can be adjusted to provide an acceptable image. This image can then be converted into a temperature image if required or subjected to further processing. The actual processing applied depends on the user requirements.

It is not possible to show the 2D colour image formats in this paper and examples of other standard display options



are shown below.

Figure 3 Average Radial Profiles.

The two curves in figure 3 are from the In and Out strokes of a measurement cycle lasting 16 seconds. The lower one is the In stroke. They are diverging with time due to the periscope mirror heating up due to a cooling / purge air failure. The total scan time of 16 seconds resulted in a 16 Mbyte file for each direction.

Figure 4 shows data from a single circumferential profile round the turbine covering all blades while figure 5 shows a section of the profile in greater detail. Note that the individual blades are clearly visible as are the differences between them.

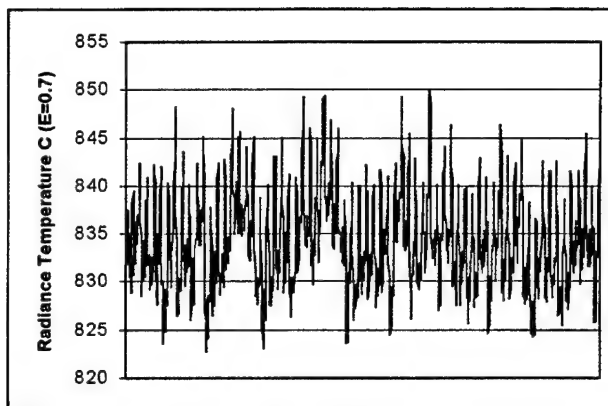


Figure 4 A Single Circumferential Profile – 3700 data points, 67 blades.

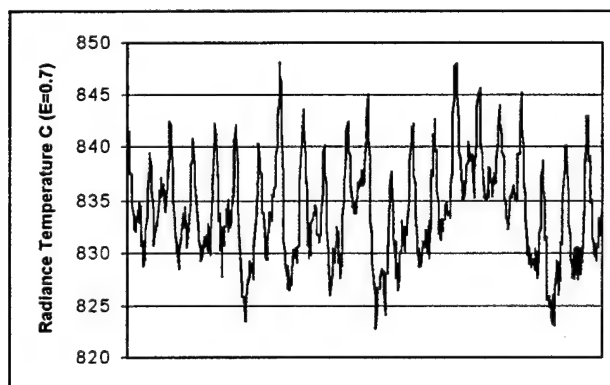


Figure 5 The first 1200 points from Figure 4.

Figure 6 below shows a surface plot of a section of rotor showing the inner 25mm of two blade passages. The vertical scale is from 735°C to 805°C (Emissivity 0.7) with lines at 10°C intervals.

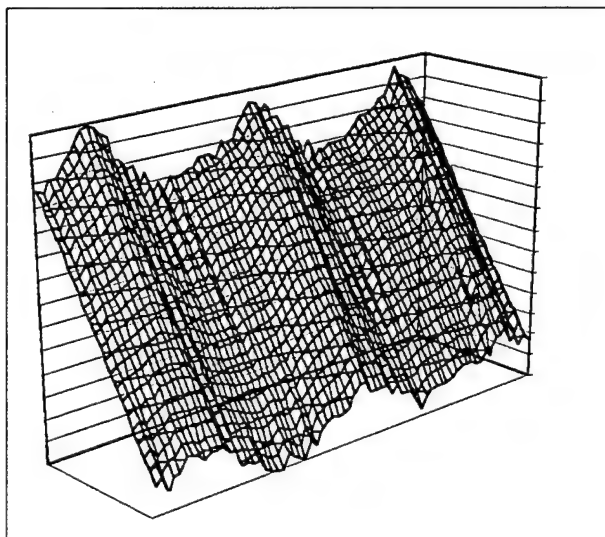


Figure 6 Surface Plot of Rotor Section.

Conclusions

Turbine blade temperature measurement / visualisation with optical pyrometry offers a way forward as surface temperatures move steadily upwards.

The very serious problem of access to modern high performance turbines is addressed by the fast, continuous traverse approach and the low intrusion scanned mirror system.

The system introduced in this paper has been designed to give users a flexible tool with which to concentrate on the issues surrounding the data analysis and conversion into temperature.

The optical design is adaptable to different spectral working ranges and detectors and multi-spectral operation if required.

The core data processing methods to remove engine effects are available as standard and the subsequent processing can be configured to meet the users needs.

SPECIAL PROBES FOR MEASUREMENTS OF FLOW PARAMETERS IN A GAS-TURBINE ENGINE

Zbigniew M. Romicki, Stanisław Zurkowski
Institute of Aviation, Warsaw, Poland

ABSTRACT

Three special probes have been designed for measurements of flow parameters, particularly in a combustion chamber of a gas turbine engine.

The first arrangement has been designed for measurements of static pressure in a flow with high value of streamline curvature. The probe consists of two flat round plates (*Saïre* plates) fixed parallel very near to each other to the stem of the probe. Pressures are measured in the centre of the inner side of each plate and averaged inside the stem.

The design of the second probe (compound probe) has been governed by the purpose in doing simultaneous measurements of total pressure and total temperature, exactly at the same point of a flow. The probe is based on the direction non-sensitive *Pitot* probe, but with the sheathed thermocouple placed inside the pressure pipe. The same probe was used to collect samples for analysis of an exhaust gas composition.

The design of the third probe has been based on the idea to measure air total pressure and static pressure in the inlet of combustion chamber vaporizer without disturbing its normal operation. The probe is based on a typical fuel injector for the annular vaporizing combustion chamber. The fuel injector has been equipped with two additional pressure pipes arranged to enable measurements of total pressure and static pressure on the outer side of the fuel outlet.

NOTATION

- K_p - dynamic pressure correction caused by dynamic pressure variation
 K_α - dynamic pressure correction caused by angle of attack variation
 N_p - static pressure correction caused by dynamic pressure variation
 N_α - static pressure correction caused by angle of attack variation
 p [Pa] - static pressure
 p_0 [Pa] - total (or stagnation) pressure
 q [Pa] - dynamic pressure (or head)
 α [°] - pitch angle
 β [°] - yaw angle

Subscripts

- A - air
F - fuel
r - real (reference) value
ind - value indicated by a probe
 α - pitch angle
 β - yaw angle

INTRODUCTION

R&D activity in the area of aero-engines consists mainly in test verification of calculations done on the stage of technical design. The ability to make such calculations is different for different components of a jet engine. For any combustion chamber it is necessary to make calculations for 3D, two-phase, turbulent reacting flow with heat exchange [1]. Only a few most advanced manufacturers created proper, highly specialised codes for this purpose by themselves. Others use codes available on the market and more or less adapt them to make the job.

Lack in computation abilities drive people to develop combustion chambers mostly by "cut-and-try" method: a series of changes which effect on combustion chamber operation must be determined every time by experimental methods. This methodology of progress requires constant development of research abilities.

Properly organised gasdynamics research of a combustion chamber should clarify following critical problems [1-4]:

1. The ignition performance of a chamber.
2. The range of stable operation (stability loop).
3. Is the expected flow field created in a combustion chamber during its operation?
4. Aerodynamic losses during isothermal and "hot" operation of a chamber.
5. Distribution of the temperature in the efflux gases discharging into the turbine.
6. Chemical composition of the efflux gases.
7. Noise generated from the combustion chamber during its "hot" operation.
8. Overall efficiency of a combustion chamber.

In order to give answer to all above questions it is necessary to make many measurements of velocity, temperature and concentration of reacting medium in the combustion chamber. Optical methods, although rapidly

developed during previous 30 years, did not oust probes from industrial laboratories where aero-engines combustion chambers are tested. The most important are following reasons [5]:

1. Very difficult optical access to the inside of the combustion chamber;
2. Very complicated instrumentation for optical research and its high cost;
3. Necessity to engage very skilled staff to conduct optical research;
4. Probes and accompanying them equipment and procedures are mostly standardised [6].

By these reasons, when the Institute of Aviation started R&D program of combustion chamber for a Polish jet engine K-15 at the beginning of eighties, it was decided to employ probes. However, it was realised at the very early stage that probes described in available literature, e.g. [7,8], would not be sufficient enough to complete our test plan [9,10] in time and within the budget. To move forward with our R&D program it was necessary to design new probes which closely met our requirements. Some probes designed that time in the Institute of Aviation proved their usefulness, have been patented [11-13] and are still used [14].

PROBES DESIGN

Probes presented in this paper have been made to measure parameters of air and hot, reacting gaseous medium in a flow with highly curved streamlines. Hence it was strongly required to create designs that ensure probes insensitivity to flow angle variations in a broad range and survive in a high temperature environment.

Dual-plate probe

The probe has been designed to measure stream static pressure away from walls of a channel. It was intended to use the probe first of all for studying dump diffuser. Our design, presented on the Fig. 1, has been created as an assembly of separate two static pressure probes, so called *Saire* plates [8].

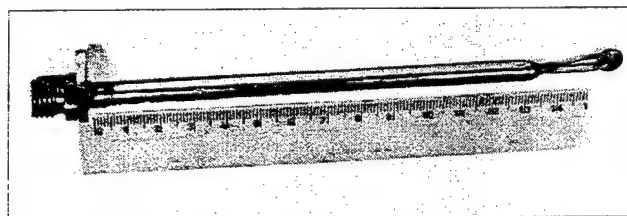


Fig. 1. Dual-plate probe.

The device consists of two parallel plates diameter 8 mm, spaced 1 mm from each other. It was necessary to keep the probe size small to avoid streamline distortion, performance deterioration of the component under test caused by blockage and problems with a space for mountings (and holes) on an engine body, arranged to access the flow. Static pressure is measured on the inner side of each plate, in its centre, and averaged inside of the probe. In the plane of plates, the probe is completely insensitive to the flow direction.

Test injector

The probe has been designed to determine the air-fuel ratio (or equivalence ratio) in a vaporizer of a combustion chamber during normal running, but without disturbing its operation. The test injector has been developed from the main fuel injector used in the Polish K-15 jet engine (Fig. 2), by implanting two additional pipes, each one with connector, for measurement of total and static pressure of the air flowing by the injector outlet (Fig. 3, 4).

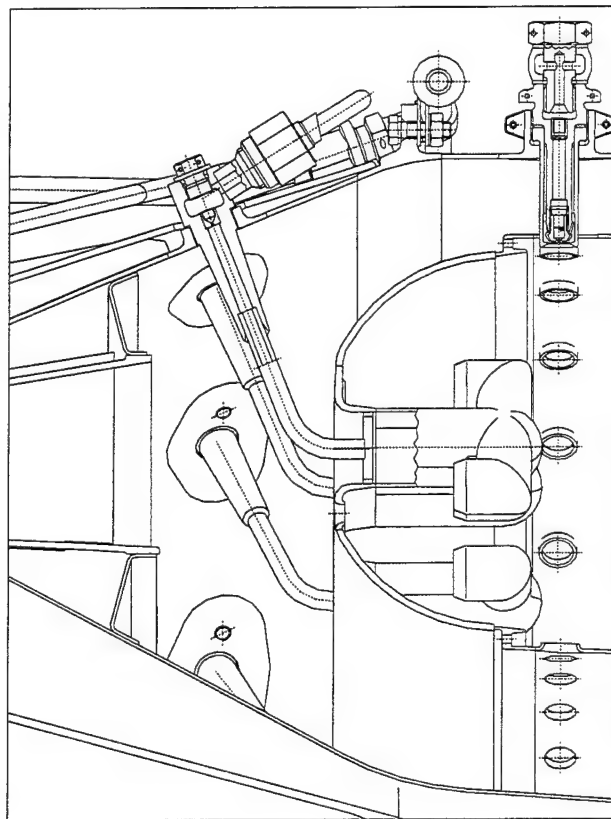


Fig. 2. Head of the flame tube with main fuel injectors - annular vaporizing combustion chamber of a Polish jet engine K-15.

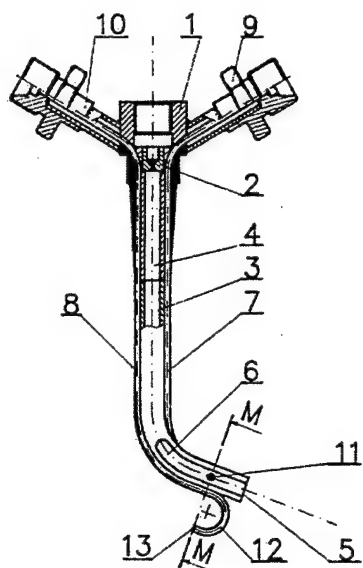


Fig. 3. Test injector [11]. 1 - Body; 2 - Fuel nozzle; 3 - Fuel outlet pipe; 4 - Fuel channel; 5 - Injector outlet; 6 - Flat cut; 7 - Static pressure pipe; 8 - Total pressure pipe; 9 - Static pressure connector; 10 - Total pressure connector; 11 - Static pressure pipe inlet; 12 - Half-loop at the total pressure pipe; 13 - Total pressure pipe inlet.

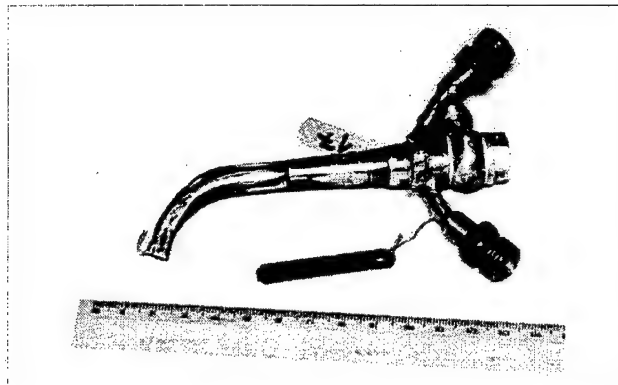


Fig. 4. Test injector.

Taking the full advantage of the design requires additional simultaneous measurement of fuel flow through the injector. The design of this test injector has been patented [11].

Compound probe.

The probe has been designed for simultaneous measurements of temperature and total pressure exactly at the same point of the flow. The basic idea of the probe is to assembly sheathed thermocouple into the total pressure pipe as it is presented in Fig. 5. The design of this probe has been patented [12].

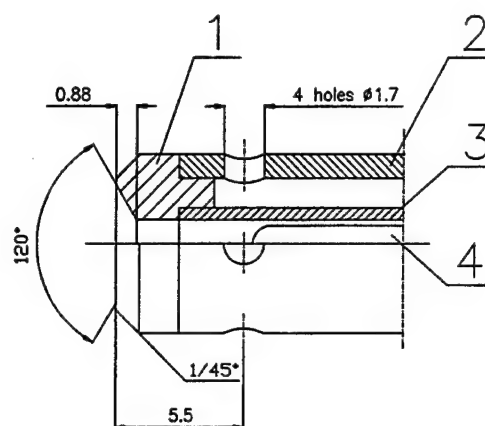


Fig. 5. Compound probe. 1 - Inlet tip; 2 - Body; 3 - Total pressure pipe; 4 - Sheathed thermocouple.

Minor modifications in laboratory pneumatic transmission lines added sample collecting for gas analysis to the probe applications.

To ensure proper operation of the probe its after end with cable and pipe connector (Fig. 6) must be protected from the high temperature environment.

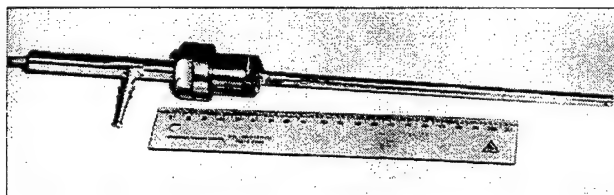


Fig. 6. Compound probe.

For this reason, to acquire the flow field parameters in the exit of a test combustion chamber, it was necessary to install the probe in a special traversing holder with an arm formed like a big, empty turbine vane (Fig. 7). For additional protection of cables and pipes ducted in the arm, during "hot" tests an air taken from before the combustion chamber rig was supplied into the vain to pass throughout it from billow to the top.

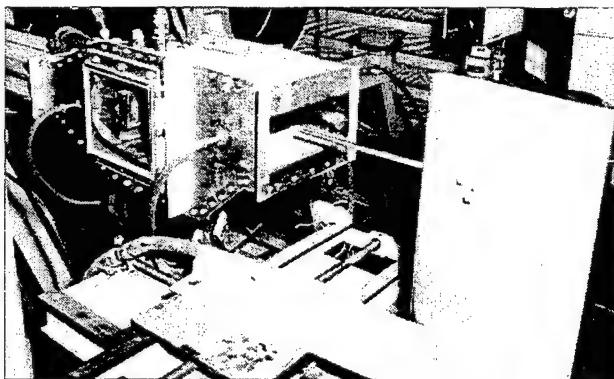


Fig. 7. Compound probe in cooled holder.

EXPERIMENTAL SET-UP AND PROCEDURE

Instrumentation

The Low Turbulence Wind Tunnel is the basic installation for probe calibration in the Institute of Aviation [15]. The tunnel is of the open circuit type with closed, rectangular test section. Basic data of the tunnel:

• dimensions of the test section	0.5 x 0.65 m
• length of the test section	1.5 m
• contraction of the nozzle	12.25
• power of electric AC motor	64 kW
• max. velocity in the test section	90 m/s
• additional DC motor for small velocities	2 kW
• max. velocity on additional motor	37 m/s.
• intensity of turbulence [16]: up to 40m/s	0.02%
for the max. velocity	0.08 %

This tunnel was built first of all for determination of two dimensional aerodynamic characteristics of laminar airfoils and for calibration of pressure probes. The tunnel enables reliable measurements in full incompressible range of flow velocities with very good distribution of velocity field across and along the test section. The additional advantage of the tunnel is its ability to control and set a static pressure gradient along full length of the test section.

The basic equipment for calibration of pressure probes are micromanometers of Betz type (accuracy 0.1 mm H₂O) and of Ascania type (accuracy 0.01 mm H₂O) as well as reference, certified Pitot tubes. This equipment and above-mentioned tunnel properties assure the ability of proper calibration of probes.

Very good characteristics of this installation enabled to complete many basic research programs on generation and decay of turbulence and boundary layer.

In our tests we used as a reference probe the Pitot tube Ø10 No 18589 with valid calibration certificate; pressures were measured with micromanometer of the Betz type manufactured by the Swiss company E. Schildknecht ing. Sia type 612c. Pitch and yaw angles of attack of calibrated probes were measured by vernier bevel protractor with accuracy 0°05'.

Scheme of the measuring system for calibration of the dual-plate probe is presented on Fig. 8, arrangement for calibration of the test injector is presented on Fig. 9 and Fig. 10 while scheme of measuring system for calibration of the compound probe is presented on Fig. 11.

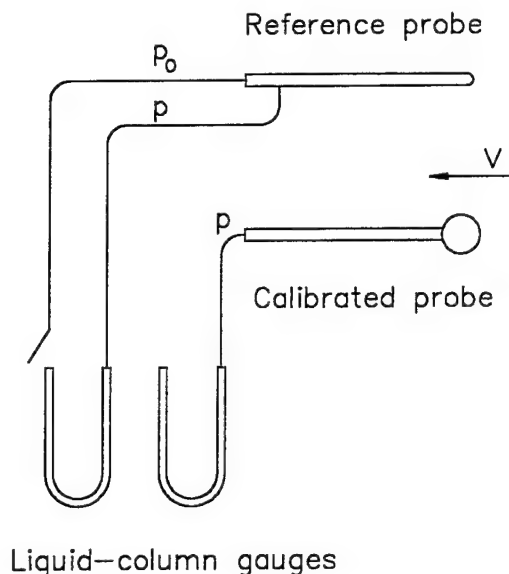


Fig. 8. Scheme of the measuring system for calibration of the dual-plate probe.

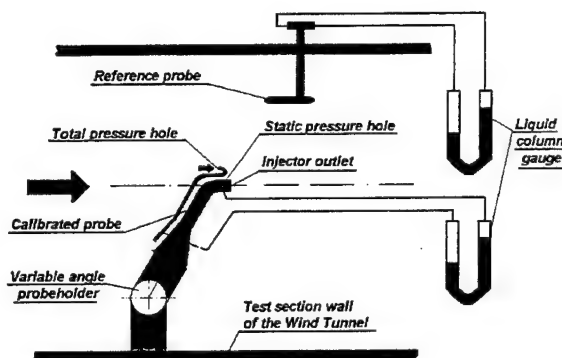


Fig. 9. Scheme of the measuring system for calibration of the test injector.

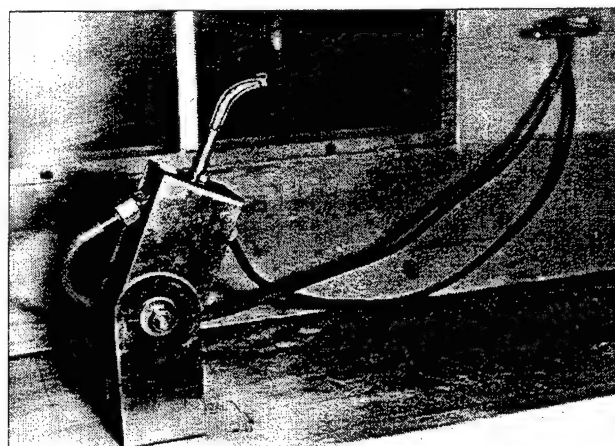


Fig. 10. Test injector in the Low Turbulence Tunnel during calibration tests. Reference Pitot probe is visible in the right upper corner of the photo.

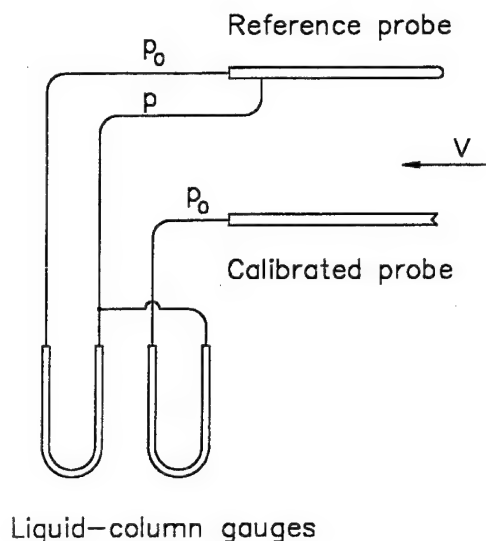


Fig. 11. Scheme of the measuring system for calibration of the compound probe.

Test conditions

Variation of probe pressure error with dynamic pressure q_r for all probes was studied in the range $1.6 \div 76.4$ mm H₂O ($15.7 \div 749.2$ Pa).

Variation of dual-plate probe pressure error and compound probe pressure error with an angle of attack were studied for dynamic pressure $q_r = 57.3$ mm H₂O (561.9 Pa); for the test injector variation of pressure error with an angle of attack was studied for dynamic pressure $q_r = 57.4$ mm H₂O (562.9 Pa).

Procedure of data analysis

Any manometer or pressure transducer connected with a pressure probe placed in a flow indicates a value of pressure somewhat different than the real one - a pressure error occurs. The estimation of measurement uncertainty requires beforehand, among others, to figure out for every probe this pressure error, usually in the form of two calibration curves: variation of pressure correction with dynamic pressure and variation of pressure correction with an angle of attack.

Dual-plate probe

For the dual-plate probe it is necessary to employ static pressure corrections. The static pressure correction N_p is defined as:

$$N_p = \frac{P_r}{P_{ind, \alpha=0}}$$

and corresponding calibration curve is a function of dynamic pressure in form:

$$N_p = f(p_o - p)_r$$

The static pressure correction N_α is defined as:

$$N_\alpha = \frac{P_{ind, \alpha}}{P_{ind, \alpha=0}}$$

and corresponding calibration curve is a function of an angle of attack α in form:

$$N_\alpha = f(\alpha)$$

The scheme of metering of the angle of attack for this probe is presented on Fig. 12.

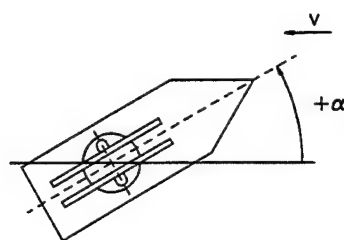


Fig. 12. Scheme of metering of the angle of attack α during the dual-plate probe calibration.

The knowledge of probe calibration data in the form of above-mentioned corrections N_p and N_α enables calculation of the real static pressure in the flow on the basis of measured (indicated) static pressure:

$$P_r = \frac{N_p}{N_\alpha} P_{ind, \alpha}$$

Compound probe

For the compound probe it is necessary to employ dynamic pressure corrections. The dynamic pressure correction K_p is defined as:

$$K_p = \frac{(p_o - p)_{ind, \alpha=0}}{(p_o - p)_r}$$

and corresponding calibration curve is a function of dynamic pressure in form:

$$K_p = f(p_o - p)_r$$

The dynamic pressure correction K_α is defined as:

$$K_\alpha = \frac{(p_o - p)_{ind,\alpha}}{(p_o - p)_{ind,\alpha=0}}$$

and corresponding calibration curve is a function of an angle of attack in form:

$$K_\alpha = f(\alpha)$$

For ideally axial symmetric probe, its K_α calibration curve should not depend on a plane of α variation. In reality, because of unavoidable manufacturing errors, a probe has derivations from designed shape and K_α calibration curves obtained in two perpendicular planes differ. Thus, the complete set of calibration plots should include two curves representing variation of pressure correction with pitch and yaw angles of attack. The scheme of metering of angles of attack α and β for this probe is presented on Fig. 13. However, if a probe is well manufactured these two curves would differ inconsiderably.

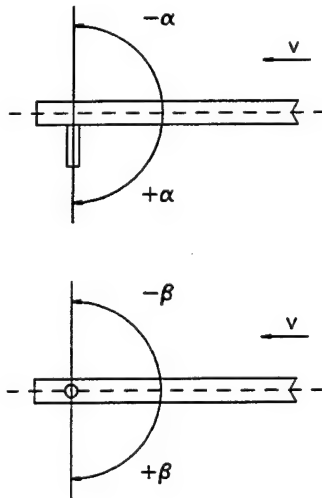


Fig. 13. Scheme of metering of angles of attack α and β during the compound probe calibration.

The knowledge of probe calibration data in the form of above-mentioned corrections K_p and K_α enables calculation of the real dynamic pressure in the flow on the basis of measured (indicated) dynamic pressure:

$$(p_o - p)_r = \frac{(p_o - p)_{ind,\alpha}}{K_p K_\alpha}$$

Test injector

For the test injector it is necessary to employ both static and dynamic pressure corrections. In a set of calibration curves required, the static pressure correction N_p is needed, defined and presented as for the dual-plate probe. Moreover, the set of calibration curves for this probe includes dynamic pressure correction K_p and dynamic pressure correction K_α , both exactly as described previously for the compound probe. However, this time, because of the asymmetrical shape of the test injector, curves representing variation of pressure correction with pitch and yaw angles of attack should considerably differ from each other. The scheme of metering of angles of attack α and β for this probe is presented on Fig. 14.

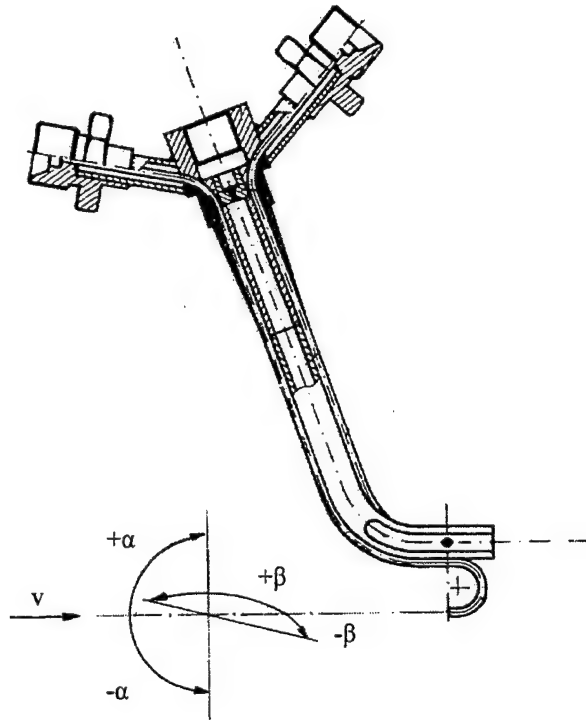


Fig. 14. Scheme of metering of angles of attack α and β during the test injector calibration.

EXPERIMENTAL RESULTS AND DISCUSSION

Dual-plate probe

Calibration curves of this probe are presented on Fig. 15 and Fig. 16.

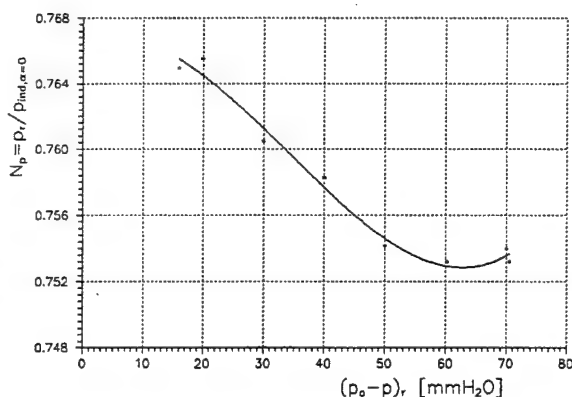


Fig. 15. Dual-plate probe calibration curve: variation of pressure error with dynamic pressure.

From the plot of variation of static pressure error with dynamic pressure (Fig. 15) outcomes that:

- the value of the static pressure indicated by the probe will be always higher than the real static pressure in a flow;
- with an increase of the flow speed (an increase of the real dynamic pressure) the difference between the indicated static pressure and the real static pressure diminishes and for a certain value of dynamic pressure this difference can be conceded to be constant, namely for $q_r \geq 55 \text{ mm H}_2\text{O}$ (539.4 Pa) it is recommended to employ correction $N_p = 0.7535$.

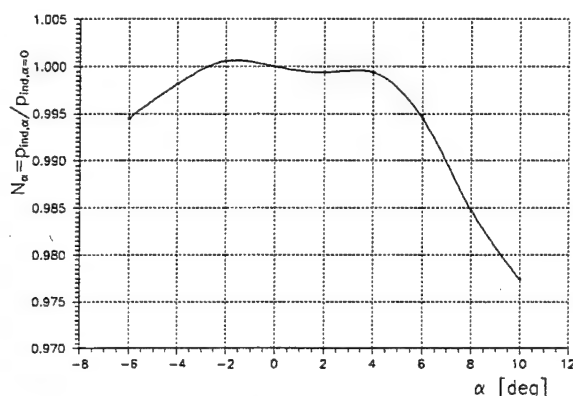


Fig. 16. Dual-plate probe calibration curve: variation of pressure error with angle of attack

From the plot of variation of static pressure error with an angle of attack (Fig. 16) outcomes that in the certain range of angles the difference between the indicated static pressure and the real static pressure is negligible small as to be safely disregarded, namely for α between $-4^\circ \div 2^\circ$ it is recommended to employ correction $N_\alpha = 1$.

Test injector

Calibration curves of this probe are presented on Fig. 17 ÷ 19.

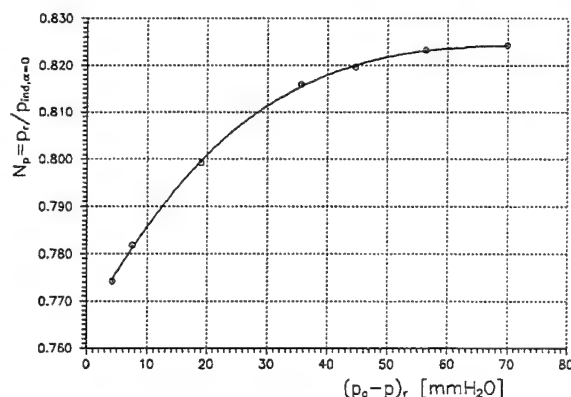


Fig. 17. Test injector calibration curve: variation of static pressure error with dynamic pressure.

From the plot of variation of static pressure error with dynamic pressure (Fig. 17) outcomes that:

- the value of the static pressure indicated by the probe will be always higher than the real static pressure in a flow;
- with an increase of the static pressure in the flow the difference between the indicated static pressure and the real static pressure diminishes and for a certain value of the static pressure this difference can be conceded to be constant, namely for $q_r \geq 65 \text{ mm H}_2\text{O}$ (637.4 Pa) it is recommended to employ correction $N_p = 0.824$.

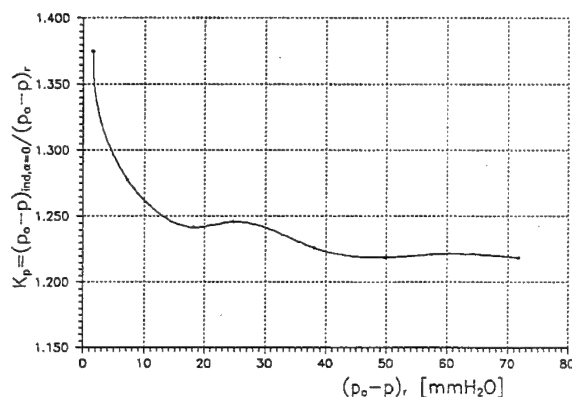


Fig. 18. Test injector calibration curve: variation of dynamic pressure error with dynamic pressure.

From the plot of variation of dynamic pressure error with dynamic pressure (Fig. 18) outcomes that:

- the value of the dynamic pressure indicated by the probe will be always higher than the real dynamic pressure in a flow;
- with an increase of the flow speed (an increase of the real dynamic pressure) the difference between the indicated dynamic pressure and the real dynamic pressure diminishes and for a certain value of dynamic pressure this difference can be conceded to be constant,

namely for $q_r \geq 40 \text{ mm H}_2\text{O}$ (392.3 Pa) it is recommended to employ correction $K_p = 1.245$.

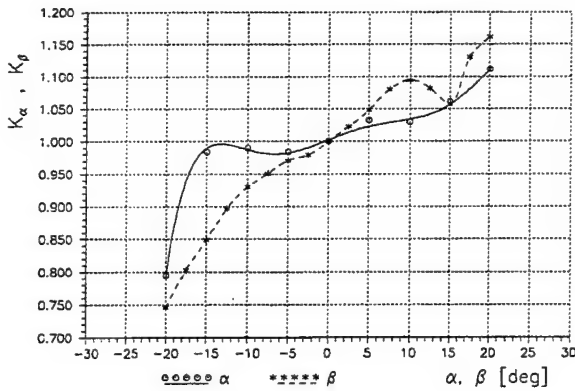


Fig. 19. Test injector calibration curve: variation of dynamic pressure error with angles of attack.

From the plot of variation of dynamic pressure error with an angle of attack (Fig. 19) outcomes that:

- both curves representing variation of pressure correction with pitch and yaw angles of attack are asymmetrical with regard to its neutral (zero degrees adjustment) position;
- generally the calibration curve depicting variation of pressure correction with pitch considerable differs from the calibration curve depicting variation of pressure correction with yaw, however, in the certain range of angles of attack, namely between $-2^\circ \div 2^\circ$, differences between K_α and K_β curves are negligibly small as to be safely disregarded.

Compound probe

Calibration curves of this probe are presented on Fig. 20 and Fig. 21.

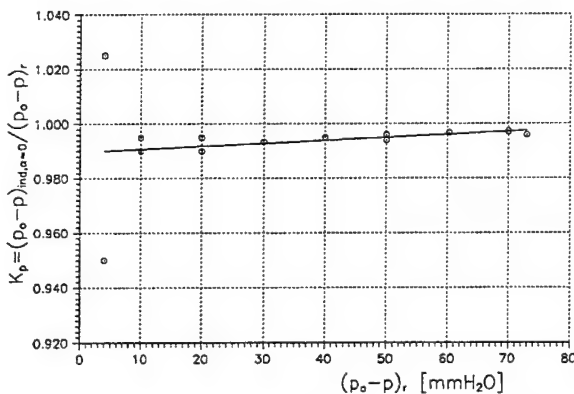


Fig. 20. Compound probe calibration curve: variation of dynamic pressure error with dynamic pressure.

From the plot of variation of dynamic pressure error with dynamic pressure (Fig. 20) outcomes that:

- the value of the dynamic pressure indicated by the probe will be always slightly higher than the real dynamic pressure in a flow;
- with an increase of the flow speed (an increase of the real dynamic pressure) the difference between the indicated dynamic pressure and the real dynamic pressure diminishes asymptotically to zero.

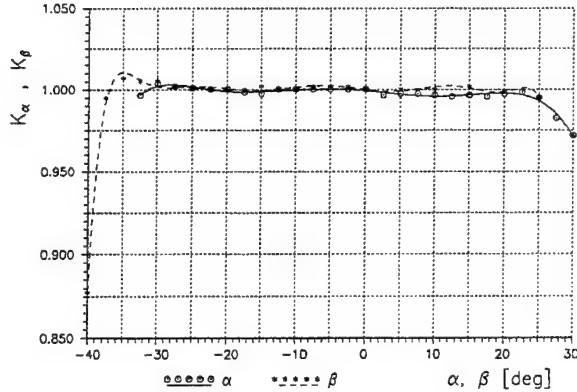


Fig. 21. Compound probe calibration curve: variation of dynamic pressure error with angles of attack.

From the plot of variation of static pressure error with both pitch and yaw angle of attack (Fig. 21) outcomes that in the broad range of angles the difference between the indicated dynamic pressure and the real dynamic pressure is negligibly small as to be safely disregarded, namely for α and β between $-32^\circ \div 22^\circ$ it is recommended to employ corrections $N_\alpha = 1$, $N_\beta = 1$.

UNCERTAINTY ASSESSMENT

Post-test evaluation of uncertainty of probes calibration revealed the following values of resulting accuracy:

- dual-plate static pressure correction N_p was determined with the relative error from 0.99% to 0.23%;
- dual plate static pressure correction K_α was determined with the relative error 0.25%;
- test injector static pressure correction N_p for dynamic pressures above 18 mm H₂O (176.5 Pa) was determined with the relative error from 1% to 0.24%.
- test injector dynamic pressure correction K_p for dynamic pressures above 18 mm H₂O (176.5 Pa) was determined with the relative error from 1% to 0.25%;
- test injector dynamic pressure corrections K_α , K_β were determined with relative error from 0.35% to 0.27%;
- compound probe dynamic pressure correction K_p for dynamic pressures above 20 mm H₂O (196.1 Pa) was determined with the relative error from 1% to 0.27%;
- compound probe dynamic pressure corrections K_α , K_β were determined with relative error 0.35%.

CONCLUSIONS

The dual-plate probe demonstrated its usefulness, as calibration tests proved that for this probe a curve representing variation of pressure error with angle of attack has evident insensitive range.

Tests also proved usefulness of the test injector: curves of variation of both static and dynamic pressure errors with the dynamic pressure have evident insensitive range, moreover, curves of variation of dynamic pressure error with angles of attack have small but sufficient insensitive range.

Calibration tests of the compound probe revealed its superb properties; pressure corrections for this probe may be safely disregarded in a wide range of dynamic pressures and angles of attack.

ACKNOWLEDGEMENTS

This work was partly supported by the Grant No. PB 0358/S6/94/06 from the State Committee for Scientific Research, Poland.

REFERENCES

- [1] Lefebvre A. H.: „Gas Turbine Combustion”. McGraw-Hill. New York 1983.
- [2] Solochin E. L.: „Ispytanja aviacionnykh vozdušno-reaktivnykh dvigatelej” („Testing of Aero Jet Engines” - in Russian). Mashinostroenie. Moskva 1975.
- [3] Tunakov A. P.: „Metody optimizacii pri dovodkie i proektirovanii gazoturbinnnykh dvigatelej” („Methods of Optimisation During Development and Design of Gas-Turbine Engines” - in Russian). Mashinostroenie. Moskva 1979.
- [4] Zuyev V. S., Skubachevskii L. S.: „Combustion Chambers for Jet Propulsion Engines”. Pergamon Press. New York 1964.
- [5] Durao D. F. G., Whitelaw J. H., Witze P. O. (editors): „Instrumentation for Combustion and Flow in Engines”. Kluwer Academic Publishers. Dordrecht 1989.
- [6] Saravanamuttoo H. I. H. (editor): „Recommended Practices for Measurement of Gas Path Pressures and Temperatures for Performance Assessment of Aircraft Turbine Engines and Components”. AGARD-AR-245. 1990.
- [7] Fuhs A. E., Kingery M. (editors): „Instrumentation for Airbreathing Propulsion”. Progress in Astronautics and Aeronautics, vol. 34. MIT. 1974.
- [8] Petunin A. H.: „Mietody i tehnika izmierienii parametrov gazovogo potoka” („Methods and Technology of Measurements of Flow Parameters” - in Russian). Mashinostroenie. Moskva 1972.
- [9] Lapucha R., Woloszczuk L., Zurkowski S.: „Program of the Type 150 Combustion Chamber Tests with the No 2 Prototype” (in Polish). Institute of Aviation Report K 15.5.12. Warsaw 1985.
- [10] Zurkowski S.: „Program of the Type 150 Combustion Chamber Tests with the No 4 Prototype” (in Polish). Institute of Aviation Report K 15.5.15. Warsaw 1986.
- [11] Lapucha R., Swidzinski P., Zurkowski S.: „Research Injector”. Polish Patent Office No 164037, 1994.
- [12] Rzeszutek L., Lichota A., Racz R.: „Research Probe”. Polish Patent Office No 279456, 1992.
- [13] Zurkowski S.: „Probe” Polish Patent Office No 162997, 1993.
- [14] Zurkowski S. at al.: „New Generation of Combustion Chambers” (in Polish). Part I, II. Institute of Aviation Report. Warsaw 1996.
- [15] Romicki M.: „Research of Thermoanemometric Probes for Measurements of Flow Direction” (in Polish). Institute of Aviation Report 28/TA/70. Warsaw 1970.
- [16] Romicki M.: „Analysis of Abilities to Decrease of Turbulence Intensity in an Aerodynamic Tunnel” (in Polish). XI National Conference of Fluid Mechanics. Military University of Technology No 2277/94. Warsaw 1994.

PHOSPHOR THERMOMETRY FOR HIGH TEMPERATURE GAS TURBINE APPLICATIONS

J P Feist, A L Heyes
Department of Mechanical Engineering

K L Choy, B Su
Department of Materials

Imperial College of Science, Technology and Medicine
London

ABSTRACT

In the paper developments and some preliminary experiments concerning the application of thermographic phosphors for surface temperature and heat flux measurements in gas turbine combustion chambers are presented. When illuminated with UV light (typically from a pulsed laser) these material exhibits phosphorescence, which is temperature dependent by virtue of variations in the relative intensity of distinct emission lines or of variations in the time constant of the exponential emission decay which occurs once excitation has ceased. Both modes of sensitivity have been investigated with a range of phosphors including are YAG:Tb, YAG:Dy and $Y_2O_3:Eu$. Of these YAG:Dy has been shown to be best suited to measurements in combustion chambers. It is sensitive to temperatures in the range 300 to 1500K, emits light in the blue green region of the spectrum where blackbody radiation is relatively weak and exhibits both modes of sensitivity.

In addition a number of techniques for laying down phosphor coatings on metal substrates are reviewed and an experimental investigation of two techniques is presented. Firstly, the use of chemical binders similar to those used in thermal paints and, secondly, a new cost effective coating technique referred to as Electrostatic assisted Combustion Chemical Vapour Deposition (EACVD) which has been developed in the Materials Department at Imperial College. The latter allows thin layers of phosphors to be laid down without the need for a chemical binder and with close control of coating composition and thickness. To demonstrate the technique a 2 μ m thick layer of $Y_2O_3:Eu$ has been laid down on a nimonic substrate and a performance comparison made with a similar coating laid down using the alternative chemical binder technique. The EACVD coating has been shown to be more robust than those laid down with chemical binders whilst the coating shows similar temperature sensitivity.

INTRODUCTION

In order to achieve improvements in efficiency, successive generations of gas turbines have seen a steady increase in turbine entry temperature. In future engines the trend is set to continue with additional constraints due to more stringent requirements in terms of component lifetime and compliance with safety and environmental regulations^{2,4,14}. These temperature increases have been made possible by the use of advanced cooling schemes and ceramic thermal barrier coatings on combustor walls and turbine blades so that the engines can operate with turbine entry temperatures which are higher than the underlying superalloys can survive. The design of appropriate cooling schemes and the development of predictive design codes both require accurate measurements of temperature and heat transfer on combustor and turbine surfaces. In this paper we will describe developments and some preliminary experiments with a technique involving the use of thermographic phosphors for surface temperature measurements in harsh high temperature environments. In addition we will introduce a new cost effective coating technology called 'Electrostatic Assisted Chemical Vapour Deposition' (EACVD)^{8,9} which can be used to lay down high quality robust phosphor layers on Ni-alloys.

In combustors and high-pressure turbines the application of conventional pyrometry is problematic due to stray light (from flames for example) and reflections and also due to changes in the surface emissivity. Thermocouples may not survive the rigours of this environment, are intrusive and are not suitable for use on rotating components. However, these problems can be overcome by utilising the temperature sensitive luminescent properties of thermographic phosphors. Thermographic phosphors typically consist of a ceramic host matrix doped with a rare earth ion and examples are YAG:Tb, YAG:Dy and $Y_2O_3:Eu$. To make temperature measurements a thin layer of phosphor is deposited on the surface under investigation. When illuminated with UV light (typically from a pulsed laser) the material exhibits phosphorescence, which is temperature dependent by virtue of variations in the relative intensity

of distinct emission lines or of variations in the time constant of the exponential emission decay which occurs once excitation has ceased. The former mode is exhibited by YAG:Dy and lends itself to the measurement of surface temperature distributions by the use of a CCD camera to record the emission intensity distribution at two specific wavelengths. The relative intensities of corresponding points in the two images can then be compared to obtain an intensity ratio which can be used to calculate temperature using calibration data in what is referred to as the 'intensity ratio method'. The latter mode, which is exhibited by all the phosphors mentioned, is independent of absolute intensity values and enables measurements to be made with high background noise. It requires characterisation of the exponential decay which is typically around 100 μ s. This can be achieved using a photomultiplier and hence this mode is best suited to point temperature measurement in what is called the 'decay lifetime method'. The phosphor emission lines are well defined and can be distinguished from other background sources. Since some of these phosphors are ceramics they can also resist high temperatures before they start to melt (YAG:Tb ~2100°C) and, therefore, are well suited for use in combustion chambers.

PHOSPHOR PHYSICS

Thermographic phosphors for high temperature applications consist of a ceramic host material doped with rare-earth ions (Lanthanides) at concentrations typically between 1% and 10%. These ions produce well defined electronic states located in the band gap of the ceramic host. Excitation of the phosphor by a light source such as a laser generates electrons in these energy states. Depopulation of this excited state may occur by both radiative and non-radiative means. The radiative process causes the luminescence effects, which are observed for temperature measurement, but these compete with a phonon quenching process (electron interaction with the thermal vibrations of the host) which is non-radiative. The latter becomes particularly strong at high temperatures and it is this which influences the emission properties like intensity and decay time and leads to temperature sensitivity.

The exponential decay in phosphorescence which occurs when illumination of the phosphors ceases can usually be characterised by the decay time constant τ of a single exponential function of the form:

$$I(T) = I_0 e^{\left(-\frac{t}{\tau(T)}\right)} \quad (1)$$

where I is the measured intensity of the luminescence and I_0 the intensity at time $t=0$. Sometimes a multi-exponential decay function must be applied when a single exponential approach is found to be inaccurate. Decay times of the phosphors employed in combustion research

are typically in the range of 1ms downwards. The lifetime decay method has previously been applied to rotating elements such as turbine blades and examples of previous work include Bird et al.⁴, Allison et. al.² and Tobin et al.¹⁸. Other applications of the lifetime decay method include the work of Allison & Cates et al.³ who made temperature measurements below 100° C.

In the intensity ratio method the relative intensities of two distinct emission lines, at equilibrium, under constant illumination is the temperature sensitive measurement^{13,17}. Relative intensities reflect the relative electron population between the energy states which can be described using the Boltzmann equation

$$n_1 = n_2 e^{\left(-\frac{\Delta E}{k_B T}\right)} \quad (2)$$

which has been shown to be valid and is discussed in a later section. Here n_2 and n_1 are the electron populations of the lower and upper level respectively. ΔE the energy gap between them, T the temperature in Kelvin and k_B the Boltzmann constant. Successful use of the intensity ratio measurements was demonstrated by Goss¹³, Bizzak & Chyu^{5,10}, Ervin¹² et al and Turley et al¹⁹. The method has been shown to be applicable for temperature measurements on curved surfaces¹² with the possibility of measuring two-dimensional temperature distributions and of the measurement of heat flux^{5,10}. This method has also been used to measure the temperature of a reacting surface¹³.

An in-depth review of the physics of the process can be found in the publications of Hüfner¹⁶, Blasse¹⁵ and Wybourne²⁰.

COATING TECHNIQUES

An essential component to the successful application of the thermographic phosphor thermometry technique in gas turbines is the fabrication of a reliable phosphor coating on the surface under investigation capable of withstanding a hostile combustion environment. Several methods have been investigated for the fabrication of phosphor films. Chemical binders can be used to prepare phosphor paints⁴ and produce good quality films for use in development testing (not in-service) at temperature up to around 1100°C.

Other techniques, such as chemical vapour deposition¹⁵ pulsed laser ablation¹⁵ and physical vapour deposition (PVD) (e.g., RF-sputtering and electron-beam deposition¹) are known to produce more robust films but require complicated and expensive equipment and a controlled atmosphere for their application. Moreover, the PVD methods are line-of-sight processes, which are not easily scaled up for films on large components of complicated shape such as combustion chambers.

There is a new patented cost-effective coating technique called electrostatic assisted chemical vapour deposition (EACVD) recently developed by Choy et al., which can be used in the application of thermo-luminescence phosphor films. This novel technology has been shown to be capable of depositing a wide range of oxide films in a cost-effective manner. The process involves spraying atomised precursor droplets across an electric field where the droplets undergo combustion and chemical reaction in the vapour phase near the vicinity of the heated substrate. This produces a stable solid film with excellent adhesion onto the substrate in a single production run. The process is capable of producing thin or thick strongly adherent films with well-controlled stoichiometry, crystallinity and texture. EACVD has already been applied to the deposition of simple oxides (e.g., Al_2O_3 , SiO_2 , SnO_2), multi-component oxides (e.g., $\text{La}(\text{Sr})\text{MnO}_3$, BaTiO_3 , PbTiO_3 , $\text{Pb}(\text{Ti,Zr})\text{O}_3$) and doped oxides (e.g., $\text{Y}_2\text{O}_3\text{-ZrO}_2$, $\text{SnO}_2\text{-In}_2\text{O}_3$) as well as polymer films (e.g., polyvinylidene fluoride) for a wide range of applications.

In work carried out to date the authors have primarily used the paint technique with paints prepared using proprietary chemical binders similar to those used in the production of thermal paint. However, a feasibility study has also been carried out using the new EACVD method.

EXPERIMENTS

The experiments described below include calibration of a range of phosphors, including those most appropriate for applications in gas turbines and a preliminary investigation of an EACVD prepared coating as compared to a similar coating produced using a 'phosphor paint'. In all cases the paint was produced by mixing commercially available phosphor powder (Phosphor Technology) of particle sizes between $1\mu\text{m}$ and $10\mu\text{m}$ into a high temperature binder. The resulting slurry was sprayed onto a Ni-alloy substrate and oven cured for several hours at temperatures up to 1000°C . Finished coupons with different phosphor paints were also provided by Rolls Royce for comparative testing. The thickness of the coatings were between $14\mu\text{m}$ and $50\mu\text{m}$.

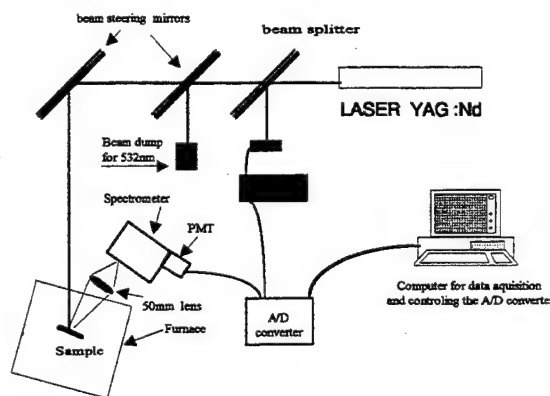


Figure 1: Experimental arrangement

The EACVD coating was fabricated using Yttrium 2-ethylhexanoate (98%, Aldrich) and Europium acetate hydrate (99.9%, Aldrich) as precursor materials. These were dissolved in ethanol (99.7%, BDH) and the molar concentration of the precursor solution was 0.05 M. The Eu-doping level was 3 to 6 mol.%. The substrates were Ni-based alloys. The apparatus used for EACVD processing was described in reference⁹. The deposition temperature varied from 300°C to 550°C , and the deposition time was varied from 20 to 60 min to obtain a range of film thickness and establish the thickness required to give a reasonable signal-to-noise ratio for luminescence property measurement. Post-deposition annealing was also performed in a tube furnace at a temperature within the range 1000°C to 1200°C to increase the crystallinity of as-deposited films. The cross-section examination showed that the film thickness was about 2 to $5\mu\text{m}$.

The lifetime decay characteristics of the excited phosphor coating was determined using the set-up shown in figure 1. A pulsed YAG:Nd laser (Spectra Physics; Model 201) was used to excite the sample, which was housed in a furnace capable of reaching temperatures of 1200°C and specially modified to provide optical access to the samples. The laser was operated at 266nm or 355nm (with Q-switch), a repetition rate of approximately 16 Hz and with output energy of about 60 mJ or 100mJ per pulse respectively. As shown in Fig. 1, an external beam dump was incorporated to avoid accidental irradiation of the sample by the 532 nm emission line of the laser, present due to leakage from the harmonic crystal assembly. The beam was steered through a synthetic fused silica window of diameter 25mm into the furnace and the subsequent luminescence was observed through a second similar window by a standard 50mm camera lens, which focused an image of the sample on to the entrance slit of a crossed Czerny-Turner spectrometer (Jarrell-Ash MonoSpec 18). The systems optical performance was limited by the diameter of the observation window with an estimated reduction in the effective f-number from 3.8 to 12. A photomultiplier was placed at the exit slit of the spectrometer (spectral width 1.5nm) and used to measure the decay lifetime. An analogue to digital converter (PICO; ADC-200; 50MHz; 8-bit resolution) transferred data simultaneously from the PMT and the power meter to a personal computer. An exponential decay was fitted using custom written software to either a single shot or to the average of a series of pulses. The power meter data was used to monitor irradiation of the sample during testing and for triggering purposes. To detect the spectra for different phosphor coatings the PMT was replaced with a linear CCD array (Alton LS2000) which was linked to a grabber card housed in the computer.

Using the above apparatus the temperature sensitive emission characteristics of a range of phosphors were studied and the results compared. Commonly used phosphors such as $\text{Y}_2\text{O}_3\text{:Eu}$, YAG:Tb and YAG:Dy were

chosen for lifetime decay measurements whilst the intensity ratio technique was carried out on YAG:Dy only. $\text{Y}_2\text{O}_3\text{:Eu}$ coatings were produced with both the EACVD and paint techniques and the results compared. In all other cases the coatings were prepared using the paint technique.

RESULTS AND DISCUSSION

Characterisation of EACVD coatings:

Figure 2 shows the x-ray diffraction (XRD) patterns of 3 mol% Eu-doped Y_2O_3 films deposited on a Ni-alloy at different temperatures. Cubic phase Y_2O_3 films could be formed at a temperature of 550°C (upper diffraction pattern). Annealing the film at higher temperatures (1000°C to 1200°C) increases the crystallinity, but the crystal size remains more or less the same as that of the as-deposited film estimated using Scherrer's formula.

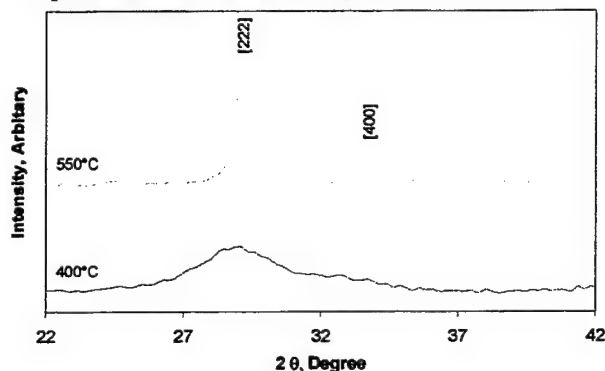


Figure 2: X-ray (XRD) diffraction pattern of the EACVD $\text{Y}_2\text{O}_3\text{:Eu}$ coating for different annealing temperatures.

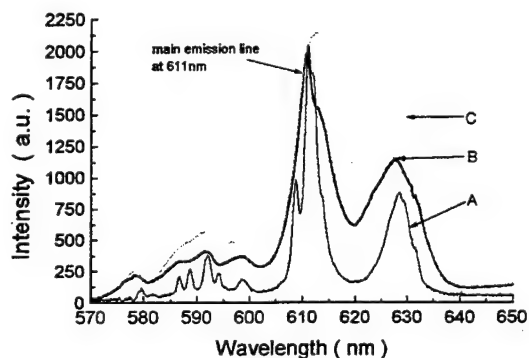


Figure 3: The optical spectra of EACVD $\text{Y}_2\text{O}_3\text{:Eu}$ films. A: deposited 400°C, annealed 1000°C, B: deposited 550°C, no annealing, C: deposited 400°C, no annealing.

Figure 3 presents the optical spectra of $\text{Y}_2\text{O}_3\text{:Eu}$ films deposited and annealed at different temperatures. The emission lines become sharper with the increase in deposition and annealing temperatures. An additional line shift can also be noticed for particular wavelengths such as 592 nm, 598 nm, 611 nm and 628 nm. This is

due to the crystallisation process of the Y_2O_3 film from an amorphous state, which influences the crystal field splitting of the energy levels of the Europium. Similar spectra were reported for Ytria-Eu-doped Zirconia and pure $\text{Y}_2\text{O}_3\text{:Eu}$ powders. The emission lines presented in Fig.3 belong to electronic transitions from the $^5\text{D}_0$ state down to the $^7\text{F}_{2,1,0}$ states of the europium¹¹. For the lifetime decay measurements, only well crystallised $\text{Y}_2\text{O}_3\text{:Eu}$ films were used.

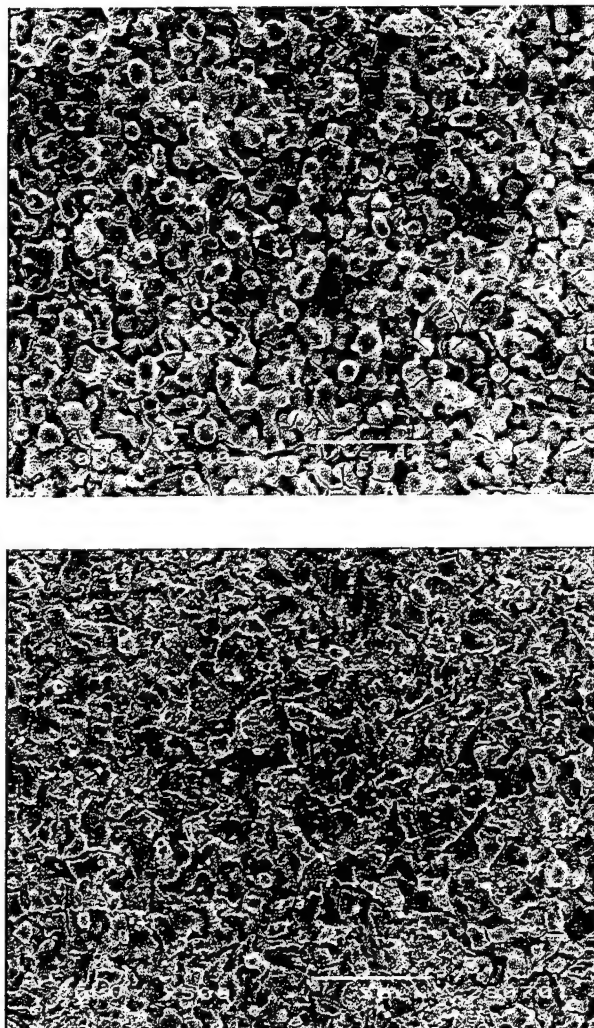


Figure 4: Scanning electron micrographs of the EACVD $\text{Y}_2\text{O}_3\text{:Eu}$

Figure 4 shows the surface morphology of the $\text{Y}_2\text{O}_3\text{:Eu}$ films deposited via EACVD process. It can be seen that the as-deposited film (shown in the upper image) is porous with some microcracks. The film adhered firmly to the substrate before heat-treatment and, after heat treatment at 1000°C, it remained firmly adhered whilst the surface became smoother but with pores and microcracks still present (lower image). Such pores and microcracks are desirable for high temperature applications. The presence of the pores will lower the thermal conductivity of the film and the microcracks allow some degree of stress-strain tolerance in the film at

elevated temperatures and thus prevent spallation. These features hence augur well for the production of thermographic phosphor films for use at high temperatures using EACVD.

The EACVD film proved to be suitable for use at temperatures exceeding 1100°C with no spallation or degradation apparent. However, the painted layer showed cracks and eventually flaked off when operated at a similar temperature.

Lifetime decay results:

Figure 5 shows the lifetime decay versus a temperature range going from 100°C to 1000°C of the main emission line of $\text{Y}_2\text{O}_3:\text{Eu}$ (611nm) for the EACVD sample and a painted coupon. In both cases each measurement point corresponds to the average of the time constants derived from 10 individual laser pulses. The standard error bars shown correspond to the standard deviation of this mean. From the figure it can be seen that for both samples the indicated dynamic range is between 500°C and 750°C.

However, for temperatures below 600°C the EACVD sample shows a consistently lower time constant than the painted sample. This difference in the τ values may be caused by different dopant levels since while the dopant level of the EACVD sample was known to be 6% the phosphor dopant level in the painted sample was unknown. Furthermore, experiments with EACVD coatings with different dopant levels have shown variations consistent with those seen in the figure. During the experiment it was noted that the intensity levels for the painted sample were about 2 to 3 times higher than those for the EACVD sample. This thought to be due to the thickness of the painted coating, which was around 20 μm compared to the thickness of the EACVD coating which was 2-3 μm , although variations in the dopant level may also effect intensity. Nevertheless, it is anticipated that the efficiency of the EACVD sample can be improved by further optimisation of the coating process. The contribution by blackbody radiation at elevated temperatures is very high at 611nm and makes it difficult to observe the phosphorescence so that the stable decay time beyond a temperature of 800°C could be caused by a diminishing signal-to-noise ratio and the limited resolution of the A/D converter. Dynamic response of this phosphor at temperatures above 800°C has previously been recorded¹⁸.

The lifetime decay investigations of YAG:Tb at 543nm and YAG:Dy at 455nm and 493nm are shown in figures 6 and 7 respectively. The dynamic range of both of these phosphors is greater than that for $\text{Y}_2\text{O}_3:\text{Eu}$ and in the case of YAG:Dy extends to temperatures in excess of 1200°C (which was the maximum temperature that could be obtained with the furnace used in the current investigation). Once again the

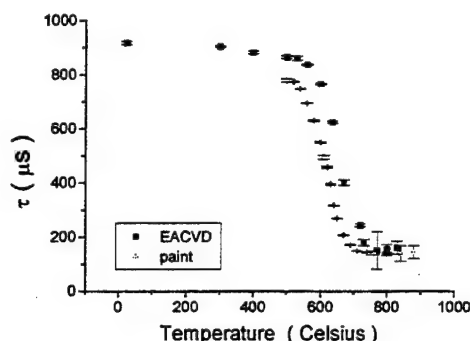


Figure 5: Comparison of EACVD and a painted sample for $\text{Y}_2\text{O}_3:\text{Eu}$.

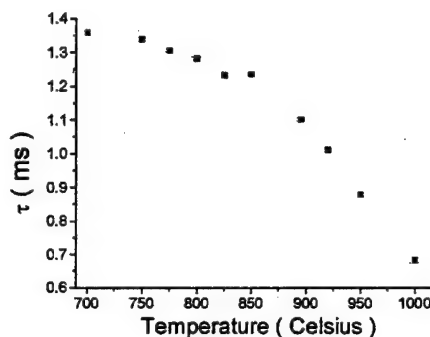


Figure 6: YAG:Tb calibration curve.

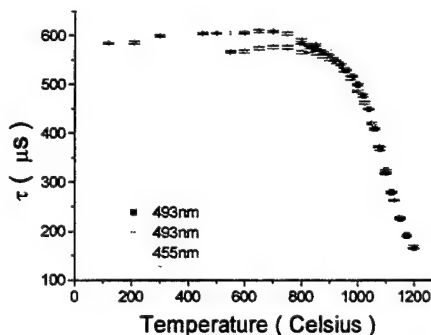


Figure 7: YAG:Dy lifetime decay for two emission lines at 455nm and 493nm.

error bars shown on these figures correspond to the standard deviation of 10 emission decay lifetime values. In every case the standard deviation is seen to be very small demonstrating the excellent repeatability of the results. At around 1100°C the YAG:Dy curve reaches a maximum gradient of approximately -2.2 $\mu\text{s}/^\circ\text{C}$. At this value the standard error in the measured time constant implies a temperature uncertainty of $\pm 0.5^\circ\text{C}$ although it should be recognised that this represents the region of the distribution where errors are smallest. The emission lines for YAG:Dy and YAG:Tb are in the blue-green part of the spectrum and at these wavelengths blackbody

radiation is weaker than at the red end ie the emission wavelength of $Y_2O_3:Eu$. This gives a better signal to noise and, hence, these phosphors are better suited for applications in combustion chambers. YAG:Tb shows the wider dynamic range which also extends to lower temperatures but the steep gradient of the YAG:Dy response implies greater accuracy and here the dynamic range extends to beyond $1200^{\circ}C$.

Intensity ratio method:

For the intensity ratio method the experimental arrangement was changed, as described previously, to utilise a linear CCD array detector rather than the photomultiplier. Spectra were obtained by integrating the response of the phosphor (YAG:Dy) over approximately 0.5s corresponding to seven laser pulses. Figure 8 shows the spectrum of the phosphor scaled using the 493nm emission line as a reference. From the figure, the increase with temperature of the relative intensity of the 455nm line with respect to 493nm line can clearly be seen. The intensities of the 493nm and the 455nm line were calculated by integration of the lines over a region of width approximately 1nm. An Arrhenius plot (figure 9) presents the ratio versus the temperature and confirms an underlying Boltzmann distribution. Thus the slope determines the energy gap and from the data ΔE was calculated to be $1490cm^{-1}$ in units of the wave number. ΔE is calculated from the difference in wavelength between the emission lines. From 455nm ($21978cm^{-1}$) and 493nm ($20325cm^{-1}$) it follows an energy gap of about $\Delta E=1653cm^{-1}$. The difference might be explained with additional line splitting since the model assumed only two electronic states. Figure 9 shows a linear response in the emission intensity ratio in accordance with the Boltzmann equation for temperatures from $600^{\circ}C$ to $1200^{\circ}C$. Below $600^{\circ}C$ the response of the phosphor departs from that described by the simple Boltzmann relation. However, by calibration, temperatures can be measured down to at least room temperature. Based on the linear region of the response function the error in temperature measurements made using the intensity ratio technique are estimated to be around 5%.

From the results obtained with YAG:Dy it can be seen how this phosphor could be used to obtain surface temperature distributions. Two CCD cameras can be used to record images of the coated surface where each camera views the surface through a band pass filter one centred on the 455nm line and the other centred on the 493nm line. In this way intensities from corresponding pixels in the two recorded images can be used to form the emission intensity ratio and hence obtain the temperature. This principal has been demonstrated by Goss¹³ who measured a one-dimensional temperature distribution on a reacting surface.

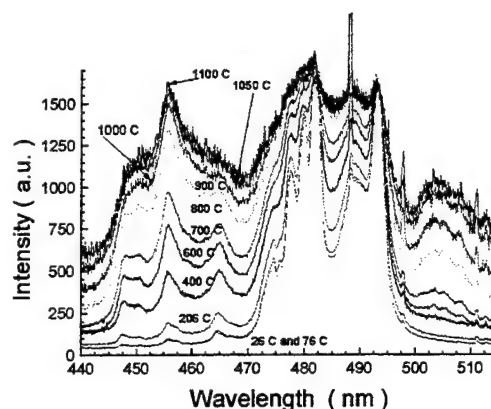


Figure 8: Scaled spectrum of YAG:Dy illustrating the increasing emission lines around 455nm.

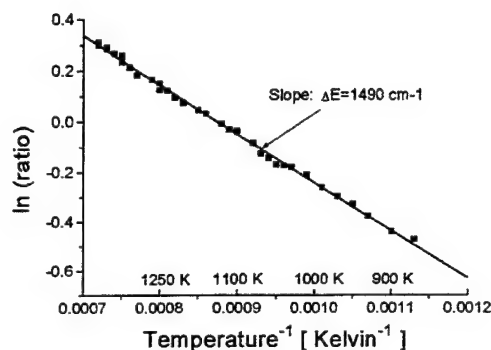


Figure 9: Arrhenius plot of the ratios vs. temperature.

From the results presented it is possible to comment on the relative merits of the phosphors considered for application in surface temperature measurements in gas-turbine combustors and for this application YAG:Dy has a number of advantageous characteristics. With this phosphor both the lifetime decay and intensity ratio techniques can be applied. The former to give high accuracy point measurements and the latter to give surface temperature distributions. With lifetime method the dynamic range is limited to temperatures above $800^{\circ}C$ (with the upper limit undefined) but this is compensated by the ratio method which has a dynamic range extending to room temperature. The emission from this phosphor is in the blue-green region of the spectrum and here the contribution from blackbody radiation is at a minimum relative to the other phosphors considered. All these characteristics make YAG:Dy the preferred phosphor for combustor application and future developments of the technique by the authors will concentrate on this phosphor.

The EACVD coating technique has also been shown to be effective for production of robust phosphor coatings suitable for use in combustors and work to produce YAG:Dy coatings with this technique is planned.

CONCLUDING REMARKS

The thermo-luminescence properties of selected phosphors ($Y_2O_3:Eu$; $YAG:Dy$; $YAG:Tb$) were studied using laser irradiation over a temperature range from 300 to 1500K. Two different coating techniques EACVD and chemical binders (paint) have been employed.

EACVD produced robust coatings and has great potential for the application of thermographic phosphor to surfaces exposed to high temperatures. Additionally the observation of line shifts make it possible to detect progress of the crystallisation processes inside these coatings and might provide another diagnostic tool for characterising ceramic films.

Temperature measurements were carried out using both the lifetime decay and intensity ratio method. Both methods proved to be suitable for high temperature measurements. However, $YAG:Tb$ and particularly $YAG:Dy$ are preferred for application in a combustion chamber. Here, the emitting lines show better signal-to-background ratios and the dynamic range reaches higher temperatures than for $Y_2O_3:Eu$.

Two approaches will be taken in the future. First the fabrication of adherent EACVD phosphor films and the production of phosphorescence and temperature sensitive thermal barrier coatings⁸. Secondly the application of selected phosphors to measure temperature, temperature distributions and heat transfer in a gas turbine combustor rig.

ACKNOWLEDGEMENT

The authors wish to thank the EPSRC for the financial support and Colin Bird, Rolls-Royce, for the phosphor samples.

REFERENCES

- Alaruri, S., McFarland, D., Brewington, A., Thomas, M., Sallee, N., *Optics and Lasers in Engineering*, 22, 17 (1995).
- Allison, S.W., Beshears, D.L., Cates, M.R., Noel, B.W., Turley, W.D., *Mechanical Engineering*, January, (1997).
- Allison S.W., Cates M.R., Noel B.W., Gillies G.T., *IEEE Trans. Instrum. Measurem.*, Vol.37, No.4, p.637, (1988).
- Bird, C., Mutton, J.E., Shepherd, R., Smith, M.D.W., Watson, H.M.L., Internal Report, Rolls-Royce plc, Derby.
- Bizzak, D.J., Chyuk, M.K., *Int.J. Heat Mass Transfer*, 38, No.2, 267-274, (1995).
- Blasse, G., 'Chemistry and Physics of R-activated Phosphors', *Handbook on the Physics and Chemistry of Rare-Earths*, edited by Gschneidner, K.A., Jr., , Eyring, L., North Holland Publishing Company, (1979).
- Choy, K.L., Feist JP, Heyes, AL, *British Patent Application No.:* 9823749.8
- Choy, K. L., and Bai, W., *British Patent*. 9525505.5 (1995).
- Choy, K. L., *Materials World*, 6, 144 (1998).
- Chyu, M.K., Bizzak, D.J., *Transactions of the ASME*, Vol.116, 264, Febr. (1994).
- Dexbert-Ghys, J., Faucher, M., Caro, P., *J. Solid State Chem.*, 54, 179-192 (1984).
- Ervin, J., Murawski, C., Macarthur, C., Chyu, M., Bizzak, D., *Experimental Thermal and Fluid Science*, 11, 387-394, (1995).
- Goss, L.P., Smith, A.A., Post, M.E., *Rev.Sci.Instrum.* 60 (12), pp.3702-3706, (1989).
- Gupta, AK, *Energy Convers. Mgmt. Vol.* 38, No.10-13, pp.1311-1318, (1997).
- Hirata, G. A., McKittrick, J., AvalosBorja, M., Siqueiros, J. M., and Devlin, D., *Appl. Phy. Sci.*, 114, 509 (1997).
- Hüfner, S., 'Optical Spectra of Transparent Rare Earth Compounds', Academic Press, (1978).
- Kusama, H., Sovers, O.J., Yoshioka, T., *Japanese Journal of Applied Physics*, Vol.15, No. 12, pp.2349-3258, December, (1976).
- Tobin, K.W.Jr., Beshears, D.L., Turley, W.D., Lewis, W.III, Noel, B.W., *Fibre Optic and Laser Sensors*, Vol. 1585, IX(1991), p.23.
- Turley, W.D., Borella, H.M., Noel, B.W., Beasley, A., Sartory, W.K., Cates, M.R., *Los Alamos Report*, LA-11408-MS, UC-000, January, (1989).
- Wybourne, B.G., 'Spectroscopic Properties of Rare Earths', J.Wiley Sons, Inc., (1965).

LIF IMAGING OF SPECIES AND TEMPERATURE IN TECHNICAL COMBUSTION AT ELEVATED PRESSURES

U.E. Meier, D. Wolff-Gaßmann
Institute of Combustion Technology
J. Heinze, M. Frodermann
Institute of Propulsion Technology
DLR - German Aerospace Center

I. Magnusson, G. Josefsson
AB VOLVO, Göteborg, Sweden

ABSTRACT

Planar laser-induced fluorescence (PLIF) has been used to measure time-resolved spatial distributions of temperature, fuel and OH in an SI engine, modified for optical access, and a jet engine combustion chamber segment. For temperature measurements, a two-line PLIF scheme was used: Two different rotational lines of the OH radical, which served as indicator molecule, were excited successively using nanosecond pulses from two laser systems operating on different wavelengths. The resulting fluorescence intensity is proportional to the population of the initial rotational state; the ratio of the two fluorescence signals is therefore proportional to the ratio of the populations, which in turn depends on the temperature. The fluorescence signal resulting from excitation by one of the two lasers is proportional to the OH density and provides thus information on flame structure. If the laser is tuned away from an OH resonance, fluorescence resulting from kerosene can be observed. The measurements presented here provide information on flame structure, heat release and mixing properties, which can serve as design aids, as well as for CFD code validation purposes.

INTRODUCTION

Design and development of advanced combustion chambers for gas turbines – both for power generation and aircraft propulsion –, as well as automotive engines relies to an increasing extent on experimental data on flowfield properties obtained in suitable test rigs. These data comprise mainly velocity fields, temperature and constituent distributions. The measurements may serve as validation basis for CFD modeling and as empirical support for combustor design.

In recent years, the increasing need for experimental data from combustion chambers under realistic conditions has

driven the development of laser-based diagnostic techniques applicable under the adverse conditions usually prevailing in practical combustion, like high pressure, particle load, high luminosity, or limited optical access. Laser-induced fluorescence (LIF) spectroscopy has proven its potential for the measurement of even minor constituent concentrations or temperature. Its capability of providing instantaneous planar measurements of constituent concentrations makes it particularly attractive for application in test rigs with high operating costs. Our efforts aim at the design of a transportable, robust and versatile LIF apparatus capable of performing measurements of different observables under the specific boundary conditions imposed by test rig operation.

In this paper, we present results of LIF studies in an SI engine cylinder, as well as in an aeroengine combustor test rig. We used a two-channel planar LIF setup, which allows alternatively simultaneous detection of two constituents or planar temperature measurements.

For temperature measurements, the OH radical is used as indicator species. The two lasers are tuned to different absorption lines of the molecule; the intensity ratio of the two resulting fluorescence signals is basically a function of temperature, apart from additional spectroscopic secondary effects that can be accounted for. This relationship is used to obtain an instantaneous temperature information. The accessible temperature range is limited typically to values above 1500 to 1700 K; at lower temperatures, the OH concentration generally drops below the signal limit for sufficient signal-to-noise ratio.

This technique has been applied in an SI piston engine modified for optical access, provided by AB VOLVO, Göteborg/Sweden. The compression was reduced, resulting in peak pressures up to 14 bar. The engine was operated on iso-octane; this fuel reduces potential interference problems resulting from simultaneous excitation of large hydrocarbons, which usually absorb

strongly in the ultraviolet.

Similar experiments were performed in a jet engine combustion chamber segment at 6 bar, designed by BMW-Rolls Royce, and operated at the Institute of Propulsion Technology at DLR Cologne. In contrast to the piston engine, this engine was running on realistic fuel, i.e., kerosene. This raises the issue of perturbation of the OH detection by fluorescence from the fuel. It was found that this was indeed an effect that prevented temperature measurements in the immediate vicinity of the injectors, where a high abundance of fuel - both as liquid or dense vapor - is found. By subtracting the kerosene signal after proper normalization of the two detection channels, the image from the second camera could be converted to relative OH densities. In this manner, the effect of design features on flame structure, like mixing properties of secondary air, could be investigated; also, the dependence of the flame structure and fuel distribution on operating parameters, like intake air temperature, AFR or fuel staging, could be studied.

SPECTROSCOPIC BASICS

This section summarizes briefly the fundamental spectroscopic principles on which LIF thermometry is based. Detailed discussions of the spectroscopic framework in general and of LIF-based thermometry can be found in the literature [1-4].

The LIF signal intensity $I_{\beta}^{(1)}$ from an electronically excited state 1 after linear excitation from ground state level i is given by

$$I_{\beta}^{(1)} = \alpha^{(1)} \cdot N_i \cdot B_{i1} \cdot I_L^{(1)} \cdot g^{(1)} \cdot \eta^{(1)} \quad (1)$$

$\alpha^{(1)}$ summarizes all factors related to detector sensitivity, transmission of the detection optics, and probe volume; N_i is the ground state population; B_{i1} is the Einstein coefficient for absorption $i \rightarrow 1$. $g^{(1)}(v_L^{(1)}, v_a^{(1)})$ describes the spectral overlap between laser lineshape $v_L^{(1)}$ of the laser with intensity $I_L^{(1)}$ and molecular absorption line profile $v_a^{(1)}$. Finally, $\eta^{(1)} = A^{(1)} / (A^{(1)} + Q^{(1)})$ is the fluorescence quantum yield. In the case of a simple two-level system, $A^{(1)}$ is the Einstein coefficient for spontaneous emission from the excited level, and $Q^{(1)}$ is the collisional deactivation rate. Since, in general, rotational and (depending on excitation scheme) vibrational relaxation can not be ignored, $A^{(1)}$ and $Q^{(1)}$ are rather "population-weighted" sums of the emission and relaxation coefficients from all emitting states. (A more detailed description can be found in Ref. 1). Accordingly, for state 2 (excited from ground state level j):

$$I_{\beta}^{(2)} = \alpha^{(2)} \cdot N_j \cdot B_{j2} \cdot I_L^{(2)} \cdot g^{(2)} \cdot \eta^{(2)} \quad (2)$$

The ratio of the ground state populations N_i and N_j is, according to Boltzmann statistics,

$$\frac{N_i}{N_j} = \frac{2J_i + 1}{2J_j + 1} \cdot e^{-\frac{(E_i - E_j)}{kT}} \quad (3)$$

$(2J+1)$ and E are the degeneracy and energy, respectively, of a ground state with rotational quantum number J ; T is the temperature of the system.

Combining these three equations yields the desired relationship between the temperature and the ratio of the fluorescence signals following excitation from two different rotational levels of the electronic ground state:

$$e^{-\frac{(E_i - E_j)}{kT}} = \frac{I_{\beta}^{(1)}}{I_L^{(1)}} \cdot \frac{I_L^{(2)}}{I_{\beta}^{(2)}} \cdot \frac{\alpha^{(2)}}{\alpha^{(1)}} \cdot \frac{B_{j2}}{B_{i1}} \cdot \frac{g^{(2)}}{g^{(1)}} \cdot \frac{\eta^{(2)}}{\eta^{(1)}} \cdot \frac{2J_j + 1}{2J_i + 1} \quad (4)$$

The factors containing experimental quantities ($\alpha^{(2)} g^{(2)} / \alpha^{(1)} g^{(1)}$) can be determined by recording the same fluorescence signal with both detection systems.

These relations hold for non-saturated excitation of isolated spectral lines. In a practical combustion system at high pressure, most available lines with sufficient signal-to-noise (S/N) ratio are in general not isolated, because of pressure-broadening of the spectrum. In addition, signal intensities drop rapidly with increasing pressure, due to collisional broadening and non-radiative collisional deactivation. Therefore, a straight-forward evaluation of a two-line measurement according to Eq. (4) is frequently not possible. Instead, we use calculated "calibration curves" for the temperature as a function of the intensity ratio of two spectral "structures" (i.e., in general superpositions of two or more lines). These curves are generated using a spectral simulation program [5], which calculates excitation spectra with regard to pressure broadening coefficients (which may be line-dependent), laser lineshape, and temperature as parameters. Repetitive runs for different input temperatures yield curves like the ones in Fig. 1, which show temperature as a function of the fluorescence intensity following excitation of two different pairs of spectral structures. The choice of the excitation lines depends on the available S/N ratio in the individual experiment, as well as the expected temperature range. In general, lines with a large energy spacing of the initial rotational states lead to a good accuracy of a

measurement at high temperatures; however, such line pairs suffer frequently from a poor S/N ratio. Therefore, the line pair selection is always a compromise between desired temperature sensitivity and available S/N ratio. The line pairs shown in Fig. 1 were used for the aeroengine combustor; for the piston engine, a line pair with larger ground state energy spacing could be used.

The fact that the calibration curves in Fig. 1 are non-linear means that there is no unique figure for the accuracy of a two-line temperature measurement. Instead, the accuracy depends on line selection and temperature itself. The propagation of an error in the measured intensity ratio into a temperature uncertainty can be calculated from the derivative of the curves in Fig. 1. A typical uncertainty in the intensity ratio resulting from S/N limitations is 10% for the measurements described here. For the pair of spectral structures $Q_1(1) / Q_1(11)$ of the (1-0) vibrational band of the A-X transition of OH, which has the lower energy spacing, the resulting temperature error is 5.9% or 105K at 1800K, 6.7% or 135K at 2000K, and 7.5% or 164K at 2200K. For the line pair $Q_1(1) / Q_1(13)$ with the higher energy spacing, the corresponding errors at the same temperatures are lower: 4.2% or 75K at 1800K, 4.8% or 95 K at 2000K and 5.3% or 117K at 2200K. This advantage, however, is usually set off by the poorer S/N ratio on the $Q_1(13)$ line. The line pair $Q_1(1) / Q_1(11)$ had to be used for the aeroengine combustor segment measurements, in order to obtain an acceptable S/N ratio at 6 bar. The generally higher temperatures in the piston engine, associated with higher OH-concentrations, allowed use of a line pair comparable with $Q_1(1) / Q_1(13)$.

EXPERIMENTAL ARRANGEMENT

Optical Section

The experimental setup for the aeroengine test rig is shown in Fig. 2. A temperature measurement requires two light pulses with wavelengths according to absorption lines of the OH radical, and with a temporal delay shorter than the time scale for the fastest process that can alter the structure of the flame. Tunable UV light pulses were generated by two frequency-doubled Nd:YAG lasers, each of which pumping a frequency-doubled dye laser. The UV pulses had a duration of 5 to 10 ns, with a relative delay of ≈ 500 ns. Typical pulse energies were 5 to 10 mJ per pulse at a bandwidth of about 0.5 cm^{-1} ; the resulting spectral power density at the measurement point was sufficiently low to avoid saturation at the pressure of 6 bar in the aeroengine test rigs and about 10 bar in the piston engine, respectively; this is an indispensable prerequisite for a temperature measurement. For the piston engine measurements, the laser pulses were synchronized with the engine speed by means of a trigger circuit controlled by an

angle encoder on the crank shaft. In the case of the jet engine combustion chambers, the lasers were running at a fixed frequency of 10 Hz. The data acquisition rate, however, was limited by the camera system which allowed recording of about three sets of images per second. Depending on the system under investigation (see below), the lasers were tuned to suitable absorption lines in the 282 to 286 nm range.

The two beams were combined by mirror M and formed into a light sheet of typically 60 mm width and 200 to 300 μm thickness inside the combustion chamber. Although the laser beams were not exactly collinear, the displacement at the measurement location was smaller than the thickness of the sheets itself. The resulting fluorescence was divided by a 50% beam splitter and directed onto two image-intensified CCD cameras (ICCD's), equipped with f/2 UV lenses and interference filter which transmit in a spectral range of about 30 nm around 315 nm. The image intensifier gate of each camera was synchronized with one of the lasers; therefore each camera records fluorescence resulting from excitation of one of the two rotational lines only.

The LIF images have to be normalized with respect to the non-uniform intensity distribution across the light sheets. Strictly, this has to be done on a pulse-by-pulse basis. In the case of the aeroengine combustor test rigs, a small fraction of the combined light sheets was split off the beams before entering the pressure vessel and directed into a cuvette filled with a highly diluted dye solution. The resulting fluorescence was recorded by two additional cameras at right angles. Each of the camera gates was timed to pick up fluorescence excited from one of the two lasers only.

If the pulse-by-pulse power fluctuations and long-term drifts across the light sheet are small, the experimental effort can be reduced drastically by measuring the power distribution not in real-time, but before and/or after the actual measurement in the test volume directly. This procedure was applied in the case of the VOLVO engine. For this purpose, a very small amount of acetone was introduced into the cylinder while the engine was stopped. The acetone evaporates quickly and fills the cylinder homogeneously with sufficiently dense vapor to produce a strong LIF signal following excitation with 284 nm. This procedure makes the two cameras that record the power density distribution in the case of the aeroengine test rig measurements obsolete, since the light sheet profile is measured with the same two cameras that record the LIF signal. In addition, the complexity of the data evaluation is reduced significantly, because it is not necessary to perform a superposition of the sheet LIF and OH LIF images before the actual correction of the LIF image with

respect to the power distribution. This simplification, however, is achieved at the expense of accuracy, because the LIF image is normalized not with the correct laser sheet intensity distribution, but with an average profile that deviates from the real shape to some degree. We measured a standard deviation from the average profile of 5% for single pulses. The propagation of the resulting error in the LIF intensity ratio with respect to temperature has been discussed earlier. It should be emphasized that only the fluctuation in the distribution of the laser power across the light sheet has to be considered, not the variation of the total pulse energy, because the latter was recorded with a fast photodiode for both lasers, and both LIF signals were normalized with respect to the pulse energy.

Measurement Objects

Piston engine

The piston engine test rig comprised an AVL 528 single cylinder engine with 85 mm bore and 92 mm stroke with optical access, equipped with a VOLVO 4-stroke DOHC series production cylinder head. The engine was operated on iso-octane and pre-heated intake air. The laser light sheet passed the cylinder in a plane parallel to the piston surface with variable distance through a quartz liner. Fluorescence was collected at right angles through a quartz window in the piston.

Aeroengine test rig

A detailed description of the test rig can be found in Ref. [6]. In brief, the test section consisted of a rectangular axially staged combustor segment with two main and three pilot fuel injectors. Pilot and main burners are staggered in circumferential direction. The fuel was kerosene. Optical access for the laser light sheets was provided by quartz panels in the inner and outer liner walls, respectively. The fluorescence was collected through large side windows, which could be inserted at different positions to cover almost the entire cross-section of the combustor with approximate dimensions of 250 mm axially by 150 mm radially. The rig was operated at 6 bar, and series of measurements were performed for several sets of operating conditions, where air and fuel mass flow, air preheat temperature and main/pilot fuel split ratio were varied, as well as the position of the measurement plane.

DATA REDUCTION

According to the complex experimental procedure and the large amount of data obtained for each measurement, the data reduction process is very involved. In a first step, the images of all four cameras are normalized with respect to the image intensifier gain settings and the non-uniformity

of the sensitivity distribution of the pixel and image intensifier area. Next, any luminosity recorded by the LIF cameras (with the lasers turned off) caused by OH emission or soot radiation, has to be subtracted from the LIF images. Since these emissions can not be recorded simultaneously, they can be considered only on an average basis. Since the contribution of these emissions is in the range of only a few percent even in the worst cases, the systematical error induced by subtraction of an average background is small.

In the next step, the fluorescence image had to be normalized with respect to the intensity distribution across the laser sheet. For this, the image from each sheet profile recorder camera had to be aligned to match the field of view of the associated LIF camera. This was achieved using geometrical image transformation routines. From the adjusted intensity distribution images, a vector was extracted by which the LIF images were divided in the direction perpendicular to the propagation direction.

The temperature information is derived from the ratio of the OH fluorescence intensities in both images at each location. Before the ratio of the LIF intensities was calculated, the pairs of LIF images have to be superimposed very precisely in order to relate signals originating from identical locations in the flame. It is usually not possible to achieve a perfect superposition by mechanical alignment alone. Therefore, image processing techniques were invoked for the "fine tuning" of the image areas. In addition, the sensitivities of the two detection channels need to be scaled with respect to each other prior to calculation of the intensity ratios. The relative sensitivities are not only determined by the adjustable intensifier gain, but are also affected by the overall transmission of the camera lens / interference filter system, as well as the slightly angle-dependent dividing ratio of the beam splitter. The relative sensitivity of the two detection systems could be determined by temporarily synchronizing both cameras with the same laser and recording identical LIF signals, either from OH or from fuel vapor.

From the LIF signal ratios, temperature images could be obtained according to the procedures outlined before. However, it is necessary to exclude regions from the temperature images where a reliable measurement can not be obtained due to one of two possible reasons: Either the signal-to-noise ratio in at least one of the images is too low because of very small local OH densities, or the OH LIF signals are affected by interfering fuel fluorescence. The latter situation prevailed usually in the vicinity of the fuel injectors in the aeroengine combustor experiments, where kerosene concentrations were high. It was found that kerosene both absorbs and fluoresces continuously in a

wide wavelength range; therefore it was not possible to discriminate spectrally between OH and fuel fluorescence, neither on the excitation nor the detection side. This problem was not encountered in the case of the VOLVO engine operated on iso-octane, which did not noticeably absorb and/or fluoresce in the spectral range covered by the OH spectrum.

Strictly, subtraction of the signal fraction due to fuel fluorescence would have to be performed on a pulse-by-pulse basis. This would require at least an additional camera equipped with suitable filters, just for the purpose of recording the kerosene fluorescence separately. In order to avoid this enormous additional experimental expenditure, we identified regions where interference from fuel fluorescence may potentially occur *at any time* separately by tuning one laser off an OH resonance and recording the remaining signal on a time-averaged basis. Regions where the average LIF signal from fuel exceeded 1% of the highest OH LIF signals in a typical image were discarded. As will be shown in the discussion of the results, this procedure leads to exclusion of large areas near the fuel injectors in the case of the aeroengine combustor measurements, because it assumes a worst case situation: A point may be disregarded although most of the time there is no fuel interference, but a high LIF signal from fuel occurs only sporadically.

RESULTS AND DISCUSSION

For each of the two test objects described here, large sets of measurements for different operating parameters and measurement positions were performed. Since this paper focuses mainly on diagnostic aspects, only one example for each engine is presented, which allows discussion of the main features of the experiments.

Single-Cylinder Engine

The S/N ratio in the VOLVO engine was relatively good, mainly because of the high temperatures in the burnt gas which lead to high OH concentration levels. In addition, no interference of the OH fluorescence signal by fuel or intermediate combustion products was observed. This allowed the choice of two excitation lines ($P_1(1)$ and $R_1(14)$ of the (1-0) vibrational transition of the A-X system of OH) starting from rotational energy levels with a large energy spacing of 3800 cm^{-1} . This resulted in a somewhat better temperature accuracy of the measurements in this engine, compared to the jet engine combustor segment: 130 degrees statistical error at 2200K. Fig. 3 shows several examples of time-resolved temperature images recorded in a plane 7 mm above TDC for different crank angles. The engine was running at 1200 rpm in skip-fired mode. The ignition, which could be

controlled independently, was at 330° . The sketch at the right bottom shows schematically the field of view. The images were taken at three different crank angles; each column shows three individual instantaneous temperature distributions for crank angles of 342° (the smallest crank angle for which OH could be detected at all), 348° , and 354° , respectively. In the black areas, no OH signal was found, and consequently no temperature measurement was possible. The images illustrate clearly the progression of the flame front through the cylinder, away from the spark plug, with increasing crank angle. An interesting result was that the temperature distributions in the burnt gas region were relatively homogeneous. Average temperatures were calculated for small regions (about $3 \times 3\text{ mm}$) in a homogeneous burnt gas region for each individual image; these values were then averaged over 30 cycles to obtain an "average temperature" for a given crank angle, although it should be mentioned that, particularly for small crank angles, the flame structure was so different from cycle to cycle that the averaging region was usually at different locations in the measurement plane for different images. A noticeable increase of the average temperature was observed with increasing crank angle: 2330K at 342° , 2450K at 348° and 2740K at 354° .

Jet Engine combustion chamber segment

As a representative example for a large set of operating conditions and measurement locations, we discuss results of measurement of fuel- OH-, and temperature distributions, respectively, in a plane passing through the centerline of a pilot burner, which means that is located in the center between the two main burners. The combustion chamber was operated at 1.1 kg/s air at 820K preheat temperature, and 67.9 kg/h total fuel mass flow with a pilot/main split ratio of 20/80.

Fuel Mapping

As mentioned before, the OH fluorescence signal was affected by a contribution from vaporized or liquid kerosene at least in regions near the burners. This prevented temperature measurements in these areas, because the two-line technique requires OH signals free from interference. Since the two laser systems were both needed for excitation of OH, it was not possible to record LIF from kerosene simultaneously, in order to subtract the signal contribution resulting from fuel from the OH part on a single-pulse basis. However, it was possible to obtain an average kerosene LIF distribution by tuning one of the two lasers away from an OH resonance line. This allowed simultaneous recording of OH and fuel LIF distributions. Fig. 4b shows averaged kerosene LIF distributions in front of a pilot burner. Two lobes resulting from a central intersection of the spray cone can be seen. Since the

measurement plane is in the middle between two main burners, there is no fuel LIF signal from the main injectors. In measurement planes through the centerline of the main burners, the kerosene signal was much stronger, and distributed over a larger area than in the case of the pilot burners, because the mass flow through the main burner was much higher.

It was not attempted to convert the kerosene LIF signal into quantitative concentrations; this would be an extremely tedious task, requiring a lot of information on the dependence of the fuel fluorescence on laser power, temperature, pressure etc. Instead, the signal was used for the identification of regions where the fuel interference prevented evaluation of the OH signals in terms of temperature. For this purpose, all locations were discarded where the average fuel LIF signal exceeded 1% of the maximum signal on the weaker of the two OH signals.

OH Imaging: Flame Structure

Average OH images, calculated from 40 single-pulse exposures, are shown in Fig. 4a. To obtain such distributions, the LIF signal from an OH excitation line with a small temperature-dependence of the lower state thermal distribution was evaluated, in order to minimize the effect of the temperature-dependent thermal population fraction. A remaining uncertainty in the quantification of the OH LIF signals results from the extent of fluorescence quenching, due to non-radiative collisional deactivation. Because this process depends in a very complex way on the thermochemical state of the bath gas, i.e., temperature and chemical composition, this effect is extremely difficult to quantify for a large chemical reaction system [7,8]. However, in a temperature/equivalence ratio regime where detectable quantities of OH exist, the error due to these effects can be estimated to be smaller than a factor of two.

Figure 4a shows areas of high OH concentrations, i.e. large heat release, in front of the pilot burner, as well as in a region somewhat downstream from the main burners. An interesting feature is the attachment of the flame to the upper wall of the combustor. Single-pulse images show the same behavior, with small pulse-to-pulse fluctuations. Another interesting observation is the mixing characteristics of dilution air, which is added through outer and inner mixing ports in the primary region. A dark "channel" of cold air penetrating deeply into the combustion zone from below can be clearly seen. As a result of mixing of the reacting gases with this cold air, the temperature decreases, which manifests itself by lower OH densities downstream from the dilution air port.

The average OH distributions provide information about the homogeneity of the combustion across the burner, as

well as regions where heat release occurs close to the combustor wall and leads to increasing thermal strain on the structure.

Temperature Imaging

Fig. 5a shows a distribution of the *average* temperature across a plane through the pilot burner. Qualitatively, it shows the same features as the OH distribution, with the difference that gradients are less pronounced. This is understandable because small fluctuations of the temperature result in large changes of the OH equilibrium concentrations; in addition, fluctuations in the equivalence ratio result in varying OH concentrations without necessarily affecting the temperature. The highest average temperatures of about 1800 to 2000 K occur in a region in the secondary zone, not behind the pilot burner. The time-resolved peak temperatures obtained from single-pulse measurements are substantially higher: Around 2200 to 2300K.

There are two large "blank" areas which did not allow a meaningful temperature measurement; the first one is at the end of the primary zone near the inner wall of the combustor. In this region, the temperature was constantly below the measurement limit. The second region is a conical-shaped area downstream from the pilot burner. The corresponding region in a measurement plane through the main burners is even more pronounced; it had to be discarded because of an unacceptably high contribution from fuel fluorescence.

Remarks on Temperature Statistics

Performing statistics on planar temperature measurements using OH as indicator involves an issue specific for this technique: The question of completeness of the measurement samples.

This issue is related to the fact that using OH as indicator molecule, it is technically not possible to probe the full probability distribution of temperatures. Because OH concentrations drop rapidly with decreasing temperature (by approximately a factor of 2 each 100 degrees Kelvin, given stoichiometric equilibrium), the limited sensitivity and dynamic range of typical ICCD cameras restricts the accessible temperature range to values above 1500K. These limits depend to some extent on line selection, equivalence ratio and overall detection sensitivity. The question arises how to deal with measurements that do not produce a meaningful temperature measurement on every laser pulse at a given location, because due to a high degree of turbulence, the temperature is frequently below the lower measurement limit. The maximum of information that can be extracted at these points is the

calculation of an average temperature discarding all events that can not be evaluated, while at the same time recording the number of such events. The result is an average temperature that is systematically biased towards higher temperatures, and a variance that is lower than it would be if the complete distribution could have been probed, together with the percentage of events for which the temperature is below the lower measurement limit. This type of information is represented by Fig. 5b: It shows the local fraction of measurements in percent that could be used for a temperature measurements. Again, the structure of this image resembles closely the average OH distribution, because a high average OH density results in a large number of single-pulse measurements that can be used for the calculation of temperatures. The high percentage of usable events near the outer wall of the combustor in the secondary zone means that the average temperature calculated here is very close to the "true" average temperature, i.e., the above-mentioned bias towards higher temperatures is small. Conversely, in regions with a small percentage of usable measurements, like in the zone behind the secondary air mixing port at the inner wall in the primary zone, the actual temperature has to be lower than the one calculated from OH measurements.

CONCLUSIONS

It has been demonstrated that laser-induced fluorescence of the OH radical can be used for the visualization of flame structures and for the measurement of time-resolved temperature distributions in relatively adverse environments, characterized by elevated pressure, complex chemical composition (in the case of the aeroengine combustor) or unsteady operation (in the case of the piston engine). Limitations for temperature measurements exist in regions where the temperature is too low, or if the OH fluorescence signal contains an additive contribution from fuel interference. If only a fraction of all measurements can be used for temperature measurements because of S/N limitations, the temperature will be biased towards higher values.

In addition, with the experimental setup used for OH thermometry, i.e., two independent lasers for excitation and two camera systems for fluorescence detection, it is alternatively possible to measure time-resolved correlated distributions of fuel and OH, respectively.

ACKNOWLEDGEMENT

The authors gratefully acknowledge the stimulating discussions with Dr. M. Ziegler, BMW-Rolls Royce.

REFERENCES

- [1] Eckbreth A.C., "Laser Diagnostics for Combustion Temperature and Species" second edition; Gordon and Breach Publishers, Combustion Science and Technology Book Series, 1996
- [2] Kohse-Höinghaus K., "Laser Techniques for the Quantitative Detection of Reactive Intermediates in Combustion Systems" Progress in Energy and Combustion Science 20 (1994) 203
- [3] Kohse-Höinghaus, K., Meier U.E., "Quantitative Two-Dimensional Single Pulse Measurements of Temperature and Species Concentrations Using LIF" Third International Symposium on Special Topics in Chemical Propulsion: Non-Intrusive Combustion Diagnostics, May 10-14, 1993; Scheveningen, The Netherlands in: Non-Intrusive Combustion Diagnostics (K.K. Kuo, T.P. Parr Eds.); Begell House Inc., New York/Wallingford pp. 53-64 (1994)
- [4] Seitzman J.M., Hanson R.K., "Two-Line Planar Fluorescence for Temporally Resolved Temperature Imaging in a Reacting Supersonic Flow over a Body"; Appl. Phys. B57 (1993) 385
- [5] Atakan B., Heinze J, Meier U., "OH Laser-Induced Fluorescence at High Pressures: Spectroscopic and Two-Dimensional Measurements Exciting the A-X (1,0) Transition"; Appl. Phys. B 64 (1997), 585
- [6] Hassa C., Carl M., Frodermann, M., Behrendt T., Heinze J., Röhlé I., Brehm N., Schilling Th., Doerr Th. "Experimental Investigation of an Axially Staged Combustor Sector with Optical Diagnostics at Realistic Operating Conditions"; Paper 18, AVT Symposium on Gas Turbine Engine Combustion, Emissions and Alternative Fuels, Lisbon, 12-16 October 1998
- [7] Meier U., Kienle R., Plath I., Kohse-Höinghaus K., "Two-Dimensional LIF Approaches for the Accurate Determination of Radical Concentrations and Temperature in Combustion"; Ber. Bunsenges. Phys. Chem. 96 (1992), 1401
- [8] Jörg A., Meier U., Kienle R., Kohse-Höinghaus K., "State-Specific Rotational Energy Transfer in OH ($A^2\Sigma^+$, $v'=0$) by some Combustion-Relevant Collision Partners"; Appl. Phys. B55 (1992), 305

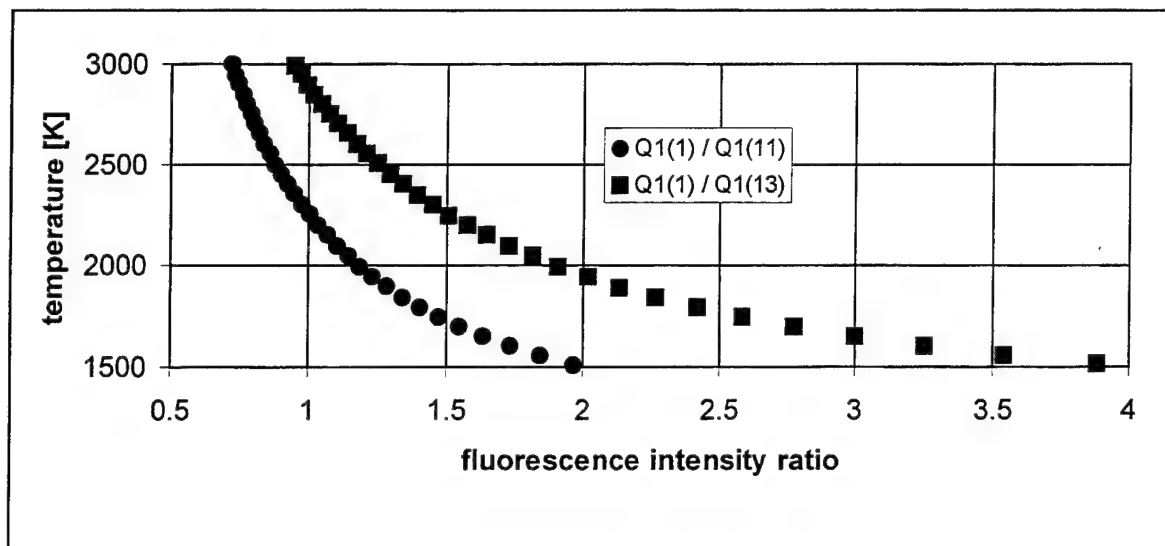


Fig.1 : Calibration curves for temperatures as function of the measured OH spectral structure intensity ratio for $p=6$ bar and 0.43 cm^{-1} laser linewidth

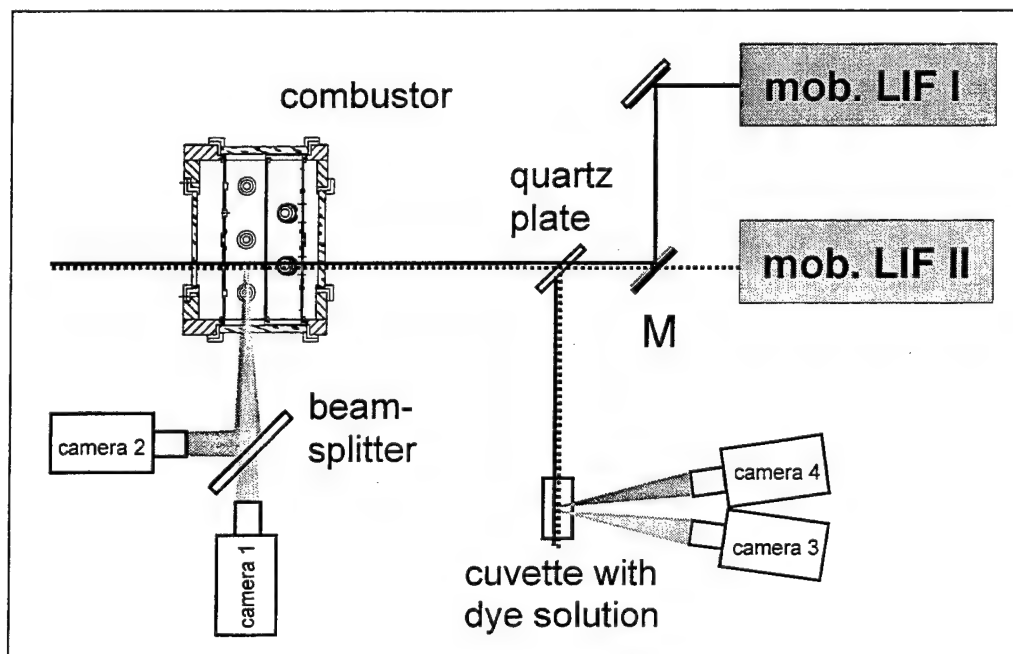


Fig. 2: Experimental arrangement for the aeroengine rig measurements. M: Combining mirror

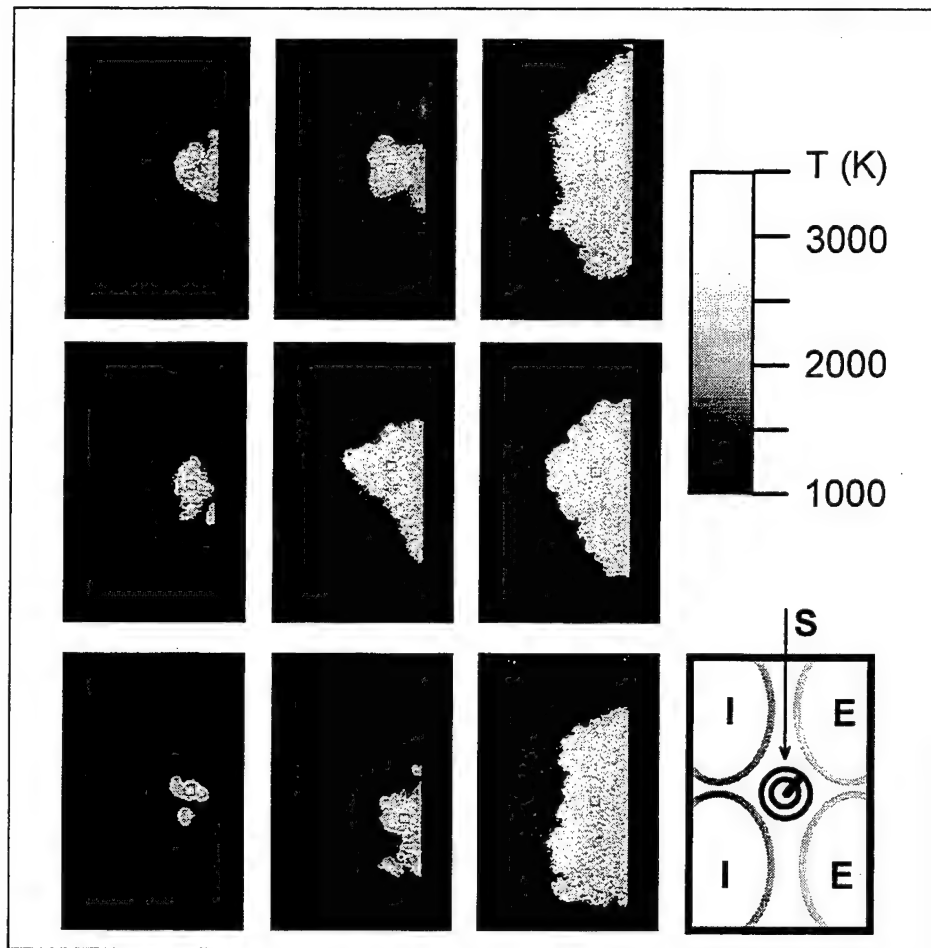


Fig. 3: Temperature imaging in a piston engine. Bottom right: field of view; S: spark plug, I: intake valves, E: exhaust valves. Images were taken at crank angles 342° , 348° , and 354° (from left to right)

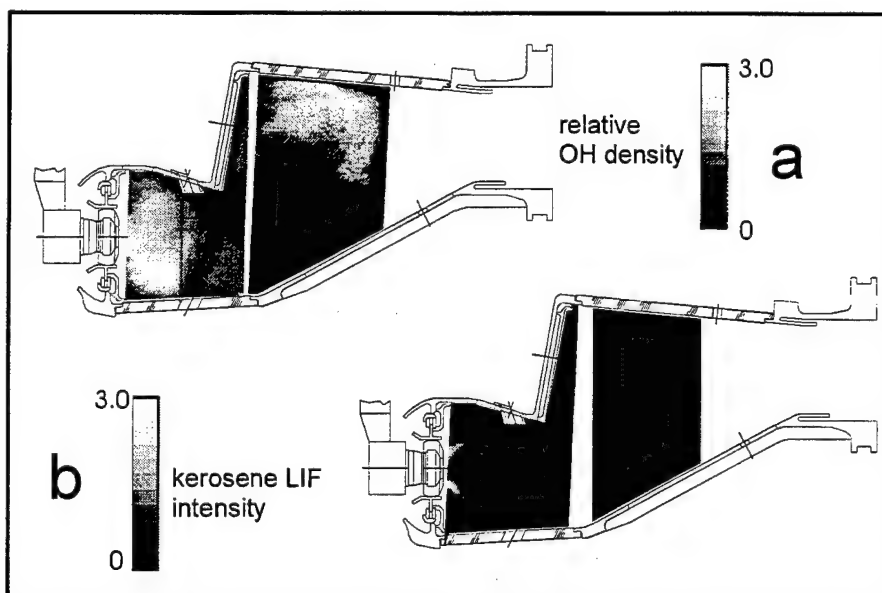


Fig. 4: OH density (a) and kerosene LIF (b) distribution in a plane through a pilot burner of the BMW-RR combustion chamber segment

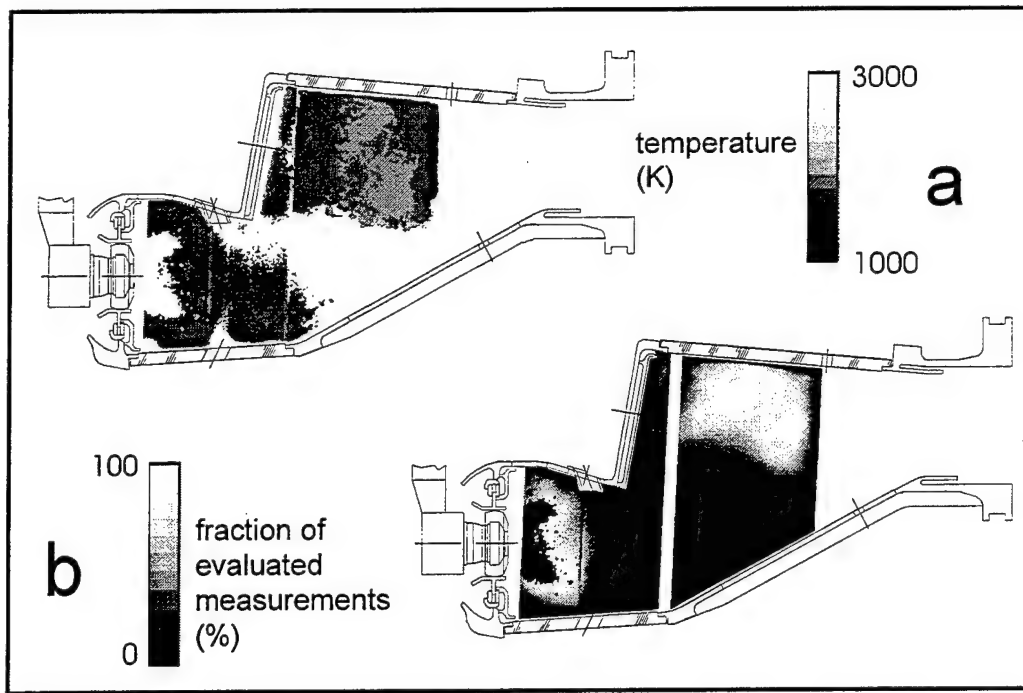


Fig. 5: Average temperature distribution (a) and fraction of usable measurements (b) in a plane through a pilot burner of the BMW-RR combustion chamber segment

Laser Anemometer Measurements in a Centrifugal Compressor

N. SADDOUR *and A. CARRERE †

Abstract

The measurement of the flowfield in vaneless and vaned diffuser of high speed centrifugal compressor is reported in this paper. The flow measurement was carried out using a laser two focus velocimeter. The blade to blade distributions of absolute velocity and angle are compared with numerical distributions. The numerical results was obtained by using three-dimensional Navier-Stokes solver. The calculations are conducted on isolated impeller in steady approach.

Introduction

In the design process of high performance compressors, the use of numerical solvers intensifies due to the drop of the cost of calculations. For better understanding of their behavior, comparaison with experimental results is necessary [5, 10, 11, 12].

The objective of this investigation is to obtain a set of data necessary for the validation of 3D Navier Stokes solvers and better comprehension of the flow field in a centrifugal compressor of a representative machine.

Test rig and experimental facility

The measurements are carried out in a centrifugal compresseur composed of a transonic backswept impeller coupled with a vaned diffuser. The rotor has a splitter for every full blade passage and fixed hub. The compressor has a shroud inserted window providing optical access to the vaneless diffuser, semi-vaneless space and a part of the vaned diffuser. The compressor was designed to produce stage pressure ratio around 4.0 and a mass flow around 2.0 kg/s. The impeller isentropic efficiency is then over 90 %.

*Phd Student at the ENSAE

†Professor at the ENSAE

The impeller is driven by a 400 kw variable speed direct current electric motor (Fig 1). It is coupled to the electric motor through a speed reducer with adapted reduction ratio. The speed is controled by a computer which monitor the electric motor and the lubrication pump. The precision of the rotation speed of the impeller is about 1 rpm. As the operating point of the compressor is given by corrected value of speed, the real speed must be corrected by the inlet temperature. The precision obtained for the reduced iso-speed depends then on the fluctuation of the inlet temperature and the precision of its measurement.

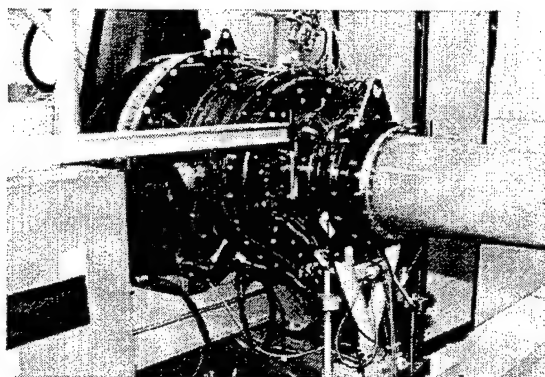


Figure 1: Test rig

The measurement of the mass flow is given by a precalibrated air intake. The mass flow is deduced from the measurement of differential pressure (difference of the total and static pressure) on a given section of the air intake. The desired pressure ratio is reached by means of butterfly valve installed in the principal discharge duct. A surge bleed valve is placed on a secondary duct. This valve is activated to increase instantaneously the outlet area and avoid the destruction of the compressor by maintained surge. This valve is also automatically opened when the electric motor is suddenly stopped by a power cut or any other failure (bearing overheat , insufficient pressure provided by the lubrication pump, ...).

42 pressure probes give the statique pressures dis-

tribution in the compressor. Temperature probes give the temperature in the compressor and the bearing for overheat detection .

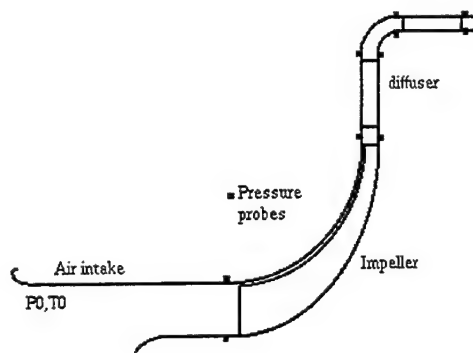


Figure 2: Pressure probes locations

Laser Two Focus measurement technique

Laser velocimeters enable non-intrusive measurements of the flow field. Unlike the probe measurement methods, the laser velocimetry measurements is independent of the properties of the fluid and environmental conditions such as temperature, pressure and density. Calibration is not necessary as laser velocimetry is an absolute method. The volume in which the measurements are made is very small and is limited only by optical means so that measurements can be made even in boundary layers and at place that cannot be reached by probes [1, 2, 3].

The laser velocimeters commonly used are the Laser Doppler Velocimeter (LDV) and the Laser Two-Focus (L2F). Both operate by detecting scattered light from small particles as they pass through the measuring volume. The L2F has the advantage over the LDV [4, 5] in that the shorter and narrower probe volume allows measurements to be made closer to walls with a given particle size .

In this investigation, due the narrowness of the fluid passage, a Laser Two Focus velocimeter was used to obtain flow field velocity measurements. The L2F operates by detecting scattered light from particles as they pass through two focal volumes formed by two highly focused laser beams. The velocity is derived from the time of flight of particles

moving from one beam to the other and the beam separation.

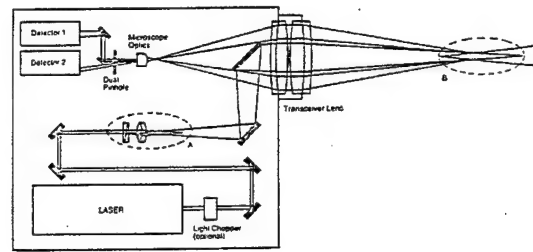


Figure 3: L2F optics

The optical system (Fig 3) include a prism which divides the incoming laser beam into two beams. One emerges undeviated while the other beam deviates at a small angle with respect of the optical axis. The splitting plane of the beamsplitter prism is in the front focal plane of a lens which focuses the beams down to two small focal volumes. These focal volumes are relayed via two deflection mirrors and the transceiver lens into the real probe volume at some distance of the optical head. Part of the backscattered light due to the passage of a particle through the focal volumes is collected by the transceiver lens and focused into the double pinhole. Only light from the focal volumes passes through these apertures. The detected light is converted by two sensible photomultiplier tubes into electrical pulses.

When the particle passes through the first focal volume a signal pulse derived from the scattered light is generated which starts a clock in the signal processor. When the particle passes the second focal volume it causes a second pulse which stops the clock. The time of light is the time interval between the start and stop pulse of the same particle (Fig 5).

The measurement direction is a plane which contains the two focal volumes. As the diameter of these volumes is small compared to their distance apart the L2F has a highly directional measuring volume. Only particles with very small traverse angles contribute to the L2F data. To obtain the direction of the flow, it is necessary to rotate the spots to get information for more than one flow direction. This is done by rotating the off axis beam around the beam which lies on the optical axis (Fig 4).

Incorrect time of flight measurements occur when a particle passes the first focal point generating a start pulse for timing and another particle at some random time later passes the second focal volume

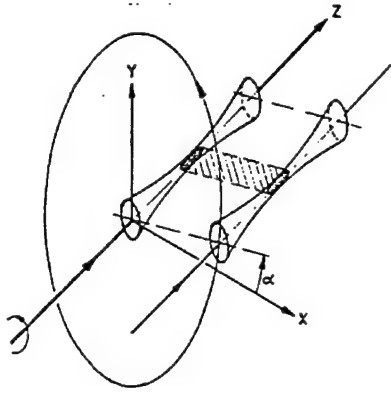


Figure 4: Rotation of the measurement direction

and stops the timing clock. Such a measurement of the transit time is spurious (Fig 6). For that reason, a significant number of time interval measurements have to be made such that correlated time interval measurements are reinforced while erroneous measurements are averaged as background noise.

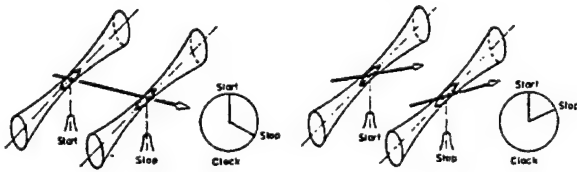


Figure 5: correlated pulses

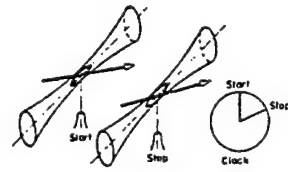


Figure 6: uncorrelated pulses

Statistic treatments of angle and time of flight histograms allow the determination of the velocity modulus, angle and turbulent rates [6]. Generally, 2D distribution (Fig 7) is needed to calculate the mean values. The formula for evaluating the mean values is :

$$\bar{F}(x) = \frac{\sum_{i=1}^m \sum_{j=1}^n F(\alpha_i, t_j) \frac{N_{ij} - N_{Ri}}{s/t_j}}{\sum_{i=1}^m \sum_{j=1}^n \frac{N_{ij} - N_{Ri}}{s/t_j}}$$

s: separation distance ; N_{ij} : measured 2D frequency distributions; N_{Ri} : basic level of measured frequency distribution generated by the uncorrelated time measurements.

To minimize the necessary number of measurement events, the 2D distribution is replaced by the marginals distributions (Fig 8 , Fig 9). The formula becomes:

$$\bar{F}(x) = \sum_{i=1}^m \sum_{j=1}^n F(\alpha_i, t_j) P_t(t_j, x) P_\alpha(\alpha_i, x)$$

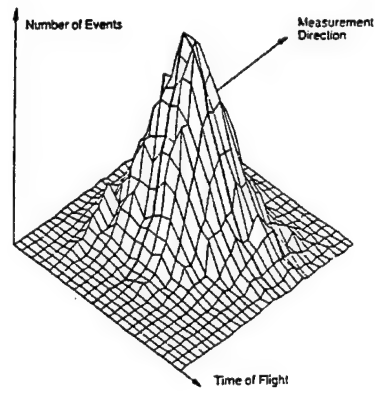


Figure 7: 2D distribution

$$P_t(t_j, x) = \frac{N_{tj} - N_{tR}}{s/t} / \sum_{j=1}^n \frac{N_{tj} - N_{tR}}{s/t}$$

$$P_\alpha(\alpha_i, x) = (N_{\alpha i} - N_{\alpha R}) / \sum_{i=1}^m (N_{\alpha i} - N_{\alpha R})$$

The comparison between the mean velocity values calculated with the two different methods shows that the relative error of the velocity components is less than 1% and of the turbulence intensities less than 5% for turbulence intensities less than 20%.

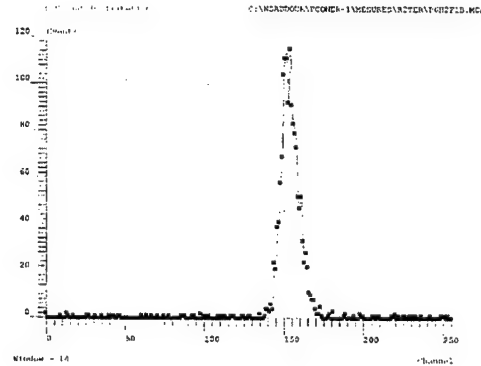


Figure 8: Time flow histogram

The measurements are synchronized to the blade crossing to obtain data for various relative locations of the impeller in front of the diffuser. The measurements are carried out in three sections: mean radius of the vaneless diffuser, vaned diffuser leading edge radius and the throat of the vaned diffuser. The main radius section contains 10 measurements locations for several relative depths. The others sections contains 9 measurements locations. The positions of the measurement locations require an adjustment taking into account the thermal expansion of the compressor.

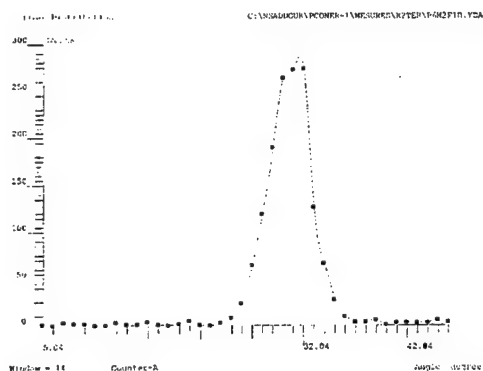


Figure 9: Angle histogram

Test results

In the mean radius section, the measurements show strong influence of the blade wake characterized by high absolute speed and low absolute angle (absolute angle is equal to zero for circumferential direction). This influence is reduced in the proximity of the diffuser walls and in the vaned diffuser leading edge radius section. Outside the wake, The absolute angle increase from suction side to pressure side, the absolute velocity decrease slightly which correspond to lower relative velocity near the suction side. However the flow does not show a jet-wake structure.

In order to compare the experimental results to calculation results, "Rampant" (Fluent Inc) solver is used. The solver models fluid by solving the three-dimensional Navier Stokes equations. In this code turbulence is modeled using "two-equation" turbulence models ($k-\epsilon$ model) [7, 8]. The spatial discretization is based on the finite-volume method applied to preconditioned governing equations [9]. Integration in time is handled with a multi-stage Runge-Kutta scheme with multigrid convergence acceleration. The code is unstructured solver that can handle both tetrahedral and hexahedral grid elements.

Two meshes was used in this comparison:

- tetrahedral mesh: obtained by solution-adaptive refinements on near wall cells of an initial mesh.
- hexahedral mesh: require more effort to generate the initial mesh. The adaption is not available for hexahedral meshes.

The simulations are conducted on isolated impeller in steady approach.

The table (Table 1) presents one dimensional comparison. The values are differences between experimental and numerical results in percent.

	tetrahedral mesh	hexahedral mesh
G	-0.4	1.5
P_i	-1.7	-0.8
P_s	0.9	0.2
T_i	-0.4	-0.7
μ_{is}	0.3	1.8

Table 1: Mono-dimensionnal results

The comparison of the evolutions of the absolute velocity and angle (Fig 10 -12) shows that blade to blade gradients are well rendered by the calculations outside the wake. The wake height is better rendered by the simulation conducted in the hexahedral mesh. This is due to the better resolution of the near wall region. The extension of the wake is underestimated by both simulations.

The steady nature of the calculation and the absence of the diffuser do not permit to obtain a different numerical evolutions of velocity and angle at different measurement locations in the absolute frame reference. For that reason, the positions selected for the comparison have a reduced pitch of 0.4, 0.5 and 0.6.

Conclusion

The L2F measurements and the numerical studies carried out in a high speed centrifugal compressor lead to some conclusions:

- Strong influence of the wake along the vaneless diffuser even in the vaned leading edge section is observed.
- Jet-wake structure is not present in blade to blade evolutions.
- Blade to blade gradients are well rendered by calculations but the extension of the wake is underestimated.
- Steady calculations in isolated impeller are insufficient to predict the influence of the vaned diffuser on the impeller flow.

References

- [1] C. FRADIN. *Detailed measurements of the flow field in vaneless and vaned diffusers of*

centrifugal compressors . Journal de l'ONERA
1992-147, 1992.

- [2] M. ISHIDA, Y. SENOO, H. UEKI . *Secondary flow due the tip clearance at exit of centrifugal impeller* . Journal of Turbomachinery, 1990.
- [3] G. BOIS, A. VUILLARMET, J.M. DUCHEMIN, K.D. PAPAILLOU. *Experimental flow analysis in a stage of centrifugal machinery* . AGARD-CP-282, 1980.
- [4] G.J. SKOCH, P.S. PRAHST, M.P. WERNET, J.R. WOOD, A.J. STRAZISAR. *Laser anemometer measurements of the flow field in a 4:1 pressure ratio centrifugal impeller* . NASA 107541, 1997.
- [5] L.M. LAROSILIERE, G.J. SKOCH, P.S. PRAHST. *Aerodynamic synthesis of a centrifugal impeller using CFD and measurements* . NASA 107515, 1997.
- [6] R. SCHOLD. *Laser Two Focus Velocimetry* . AGARD-CP399, 1986.
- [7] L. CAMBIER, CH. VUILLEZ . *Mise en oeuvre de modèles de turbulence pour les calcul d'écoulements compressibles en turbomachines*. Journal de l'ONERA 1990-192, 1990.
- [8] BUDUGUR LAKSHMINARAYANA. *FLUID DYNAMICS AND HEAT TRANSFER OF TURBOMACHINERY*. John Wiley & Sons, 1996.
- [9] JONATHAN M. WEISS , WAYNE A. SMITH . *Preconditioning Applied to Variable and Constant Density Flows*. AIAA Journal Vol. 33 No. 11, 1995.
- [10] C. HAH , H. KRAIN . *Secondary flows and vortex motion in a high-efficiency backswept impeller at design and off-design conditions* . Journal of Turbomachinery, 1990.
- [11] H. KRAIN , W. HOFFMANN . *Centrifugal impeller geometry and its influence on secondary flow* . AGARD Secondary Flows in Turbomachines, 1990.
- [12] M. D. HATTAWAY, R. M. CHRISS, J. R. WOOD, A. J. STRAZISAR. *Experimental and Computational investigation of the NASA low-speed centrifugal compressor flow field* . Journal of Turbomachinery, 1993.

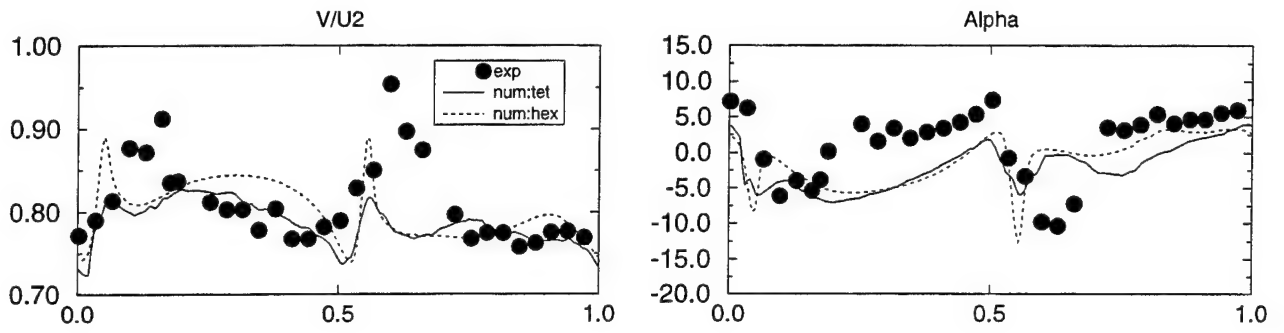


Figure 10: Midspan evolution, reduced pitch 0.4

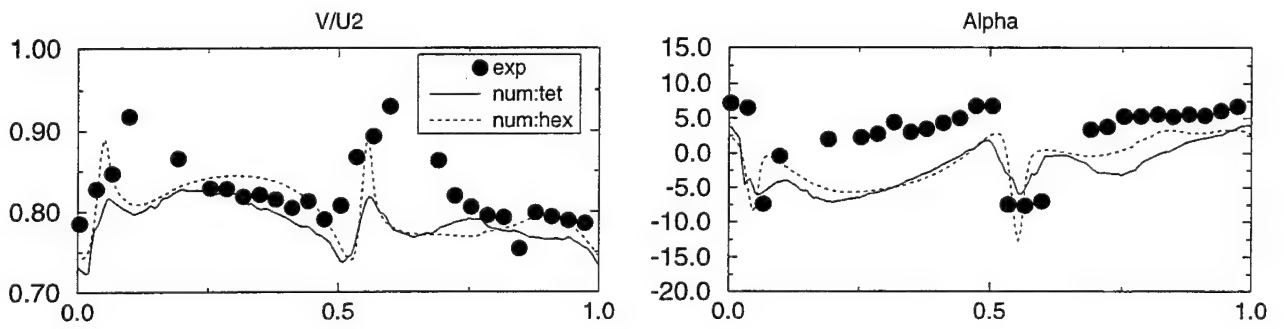


Figure 11: Midspan evolution, reduced pitch 0.5

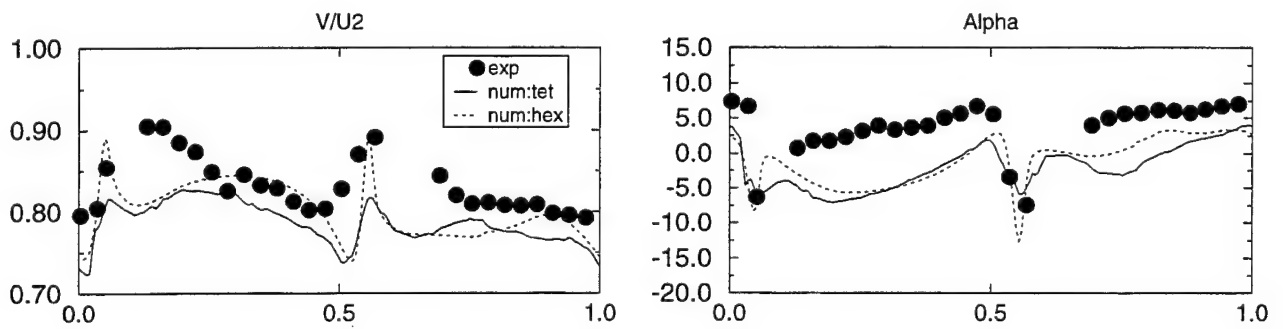


Figure 12: Midspan evolution, reduced pitch 0.6

SESSION : 3

DOPPLER VELOCIMETRY

DOPPLER GLOBAL VELOCIMETRY : ACCURACY TESTS IN A WIND TUNNEL

Christine LEMPEREUR , Philippe BARRICAU, Jean-Michel MATHE, André MIGNOSI

ONERA / DMAE / TME

Centre de Toulouse, 2, Avenue Edouard Belin
31055 TOULOUSE CEDEX France

ABSTRACT

A one-component Doppler Global Velocimeter has been designed and tested in an empty wind tunnel generating a perfectly calibrated flow. Most of the technical choices involving light sheet generation, optical components, cameras, iodine cell, are described and argued, as well as geometrical calibration and processing steps. A specific device has been developed, but not yet described, to relax constraints on the stabilization of laser frequency and iodine cell temperature. Velocity maps obtained by this D.G.V. system are compared to the known Mach number. These promising results show the interest of following such a procedure to qualify and optimize a prototype.

CONTEXT

Doppler Global Velocimetry has been developed this last decade as a new class of laser-based technique, obtaining simultaneous measurement of velocities over an entire viewing plane. This performance is of growing interest to aerodynamicists as it drastically reduces wind tunnel tests duration: a point measurement such as classical LDA requires many hours to map an entire flow field. Long lasting experiments are expensive and imply difficulties in maintaining the flow stationarity. With the D.G.V technique, 2D velocity maps can be achieved in real time up to a rate of a few tens of Hz if necessary.

Many papers from US research centers related to NASA[4][5][6], and University laboratories [8][9] have shown the progress of DGV technique since the first use of an iodine cell as a frequency dependent optical filter in 1990 [1]. Various applications have been undertaken in the USA, implementing continuous or pulsed lasers [7], even in large facilities [2][4]. But improvements can still be made as regards accuracy and ease of use. Developments remain scarce in Europe and often limited to laboratory prototypes. DLR in Germany is probably the more experienced laboratory; a 3C system, available in an industrial form, is dedicated to the study of confined stationary flows [3].

Another well-known technique, PIV, is able to offer planar measurements too. It is being more and more often used in industrial contexts, but its main drawback lies in its poor viewing area as seeding particles must be spatially

resolved. Moreover, its processing algorithms are time-consuming and require a certain understanding of flow characteristics. Nevertheless, the method is well adapted to restore 2C instantaneous velocity fields with a quite good accuracy. Depending on the application, either PIV or D.G.V can be recommended as the best method. They may even be considered as two complementary ways to investigate a flow field.

As regards large facilities, a real need is expressed by ONERA for planar velocity measurement. A project, called BADGE¹, was recently undertaken in DMAE, in order to develop a 3C DGV system to investigate stationary flows. The first stage consists in designing a 1C prototype with a continuous laser, and making it accurate and easy to use. Testing a 1C system requires to generate a calibrated velocity field. Instead of using a rotating disc[4], which is a convenient way to know the direction and modulus of velocity at each point in a plane, experiments have been conducted in an empty transonic wind tunnel, generating a perfectly calibrated flow. Thus, seeding, light scattering and geometrical issues are similar to those met in the final aerodynamic applications and can be tackled in the very first tests.

This paper first recalls the basic principle of D.G.V. Most of the technical choices made to design this prototype are described. Error sources due to camera system, optics and geometrical configuration are then analyzed. The processing procedures and some results of these experiments in a wind tunnel are finally reported.

MEASUREMENT PRINCIPLE

$$\Delta f = \frac{1}{\lambda_0} \vec{V} \cdot (\vec{R} - \vec{E}) \quad \text{Equation 1}$$

This simple equation completely defines the measurement principle: the Doppler frequency shift Δf of the light scattered by a seeding particle can be connected to its velocity vector \vec{V} and to the geometrical conditions of emission and collection of light, where \vec{E} and \vec{R} are unit vectors (Figure 1). The dot product shows that only one component of velocity can be measured for a given pair of

¹ Banc Anémométrique Doppler Global pour les Ecoulements

\vec{E} and \vec{R} vectors. As these directions are potentially different at each point of the object plane, the measured component of \vec{V} may not be the same all over the field of view. This phenomenon can be more or less sensitive according to the arrangement of light sheet generator and receiving optics. For instance, the light sheet can be made parallel instead of divergent, and viewing angles perpendicular to it, so as to reduce the variation in \vec{E} and \vec{R} . But in any case, these parameters have to be taken into account, because their effect on the final accuracy is far from negligible.

Planar velocity measurement started being attractive for industrial purposes when measurement of Doppler shift was transformed into light intensity measurement, thanks to an iodine cell. This element has many absorption lines in the visible spectrum. If the laser is sharply tuned and frequency-stabilized in one of these bands, any Doppler shift will be seen as a change in light intensity through the cell. The transmission ratio $\tau = I_{out}/I_{in}$ can be plotted versus frequency (Figure 2). For each measurement point in the plane, the global process to obtain velocity consists in three major steps :

1. measuring light intensity on both sides of the cell.
2. obtaining the Doppler shift corresponding to this transmission ratio
3. determining \vec{E} and \vec{R} vectors at that point.

The first stage is mainly dependent on optical components and cameras, and will be analyzed in the corresponding paragraphs.

The second step is often crucial because :

- * the temperature of the « cold finger » of the iodine cell has a strong influence on the slope and location of the absorption profile, if the cell is saturated (Figure 2).
- * the laser frequency, even with all the stabilization devices, needs a few tens of minutes to get stable and is still subject to low frequency drifts and adjustments.

In BADGE, a specific device has been designed and tested as a prototype during these tests. It gives real time information on the relationship between τ and Δv . For this reason, frequency stabilization as well as iodine temperature regulation become less demanding and experiments can be conducted more quickly and easily. Accuracy is improved too. This device, which is now being patented, cannot be described here but will be the key item of a next paper.

Finally, geometrical considerations must not be forgotten ; forward or backward scattering observation generates high perspective effects which must be taken into account. This point will be developed in the « calibration steps » paragraph.

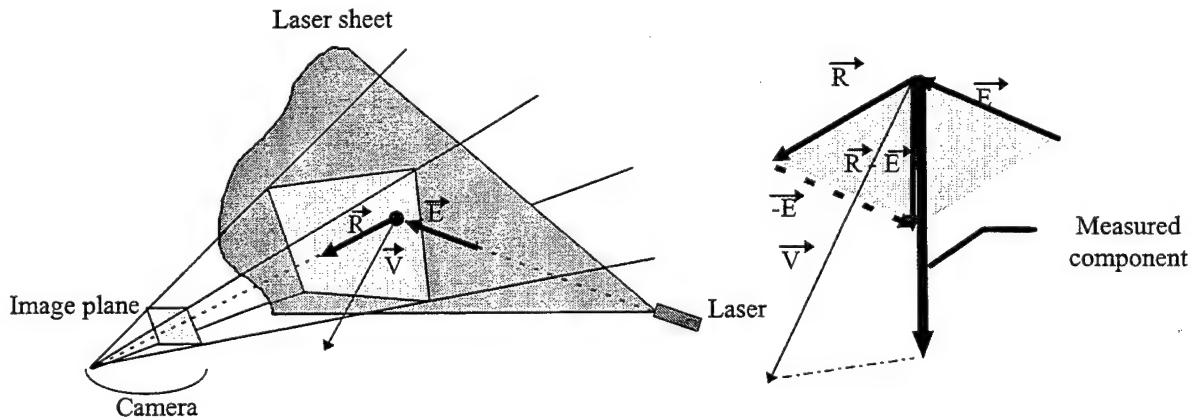


Figure 1 : Measurement geometry for one velocity component

$T_{cell}=70^{\circ}\text{C}$

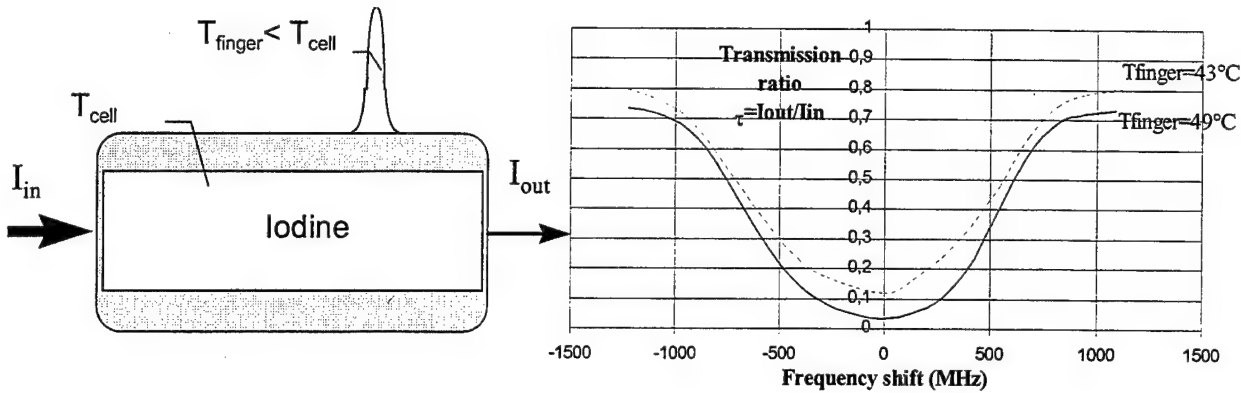
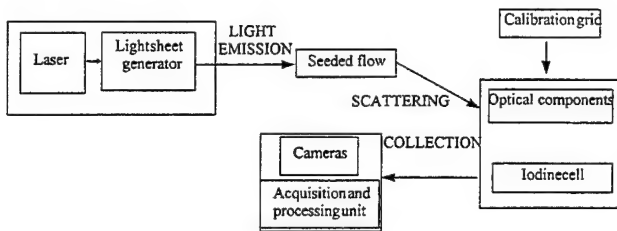


Figure 2 : Transmission ratio through the iodine cell versus frequency

TECHNICAL CHARACTERISTICS OF THE COMPONENTS



LASER SOURCE

The laser oscillator is a « Spectra-Physics Argon 2060/65 BeamLok » model. This continuous wave laser is configured with a monochromatic rear mirror to impose a wavelength of 514.5 nm. An intracavity Fabry-Perot etalon ensures a single frequency emission with a full width at half maximum not greater than 2 MHz. Specific devices known as BeamLok and J-Lok permit to keep respectively a stable laser beam position and the smallest frequency jitter in the range of 10 Hz to 500 Hz, with a maximum output power of 2 W. The frequency of the oscillating wave is controlled by the solid etalon temperature. The polarization state of the emitted light is kept linear by Brewster windows.

LIGHT SHEET GENERATOR

Two different systems can be used to light the flow seeded with particles. The first one is made of several cylindrical and spherical lenses to spread the laser beam in one direction (Ox for example). The optical arrangement of the illuminating device implemented in the wind tunnel is represented in Figure 3. The fan angle α can be adjusted.

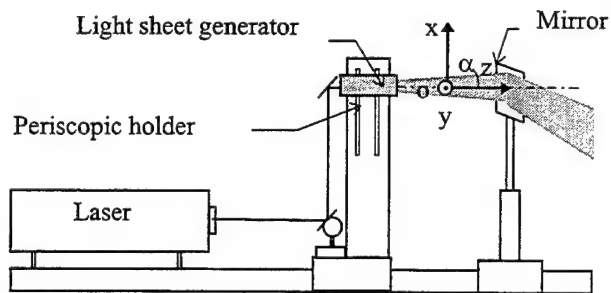


Figure 3 : Light sheet generator at T2 wind tunnel.

The radiance distribution according to the two perpendicular directions respectively noted Ox and Oy, remains gaussian. One of the main drawbacks is the high intensity dynamics on the resulting images both in x and z directions, which complicates the adjustments and may reduce in turn the application range. Moreover, this device may induce high spatial frequencies due to components of insufficient optical quality. In the case of continuous measurements, these problems can be avoided by using a rotating polygon with reflective facets providing the scan of the incident laser beam.

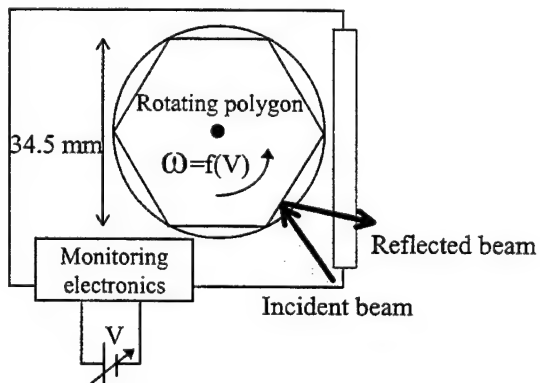


Figure 4 : Rotating polygon generating a sweeping beam

However, as the optical path of the laser beam is modulated during the rotation of the polygon, a frequency shift is generated on the reflected beam. Given a motionless particle, the phase velocity shift V_{ps} induced on the optical wave by the rotating mirror is estimated here, assuming the incident laser beam is parallel to Oy axis, and at an angle $\theta_0 = 45^\circ$ to the facet.

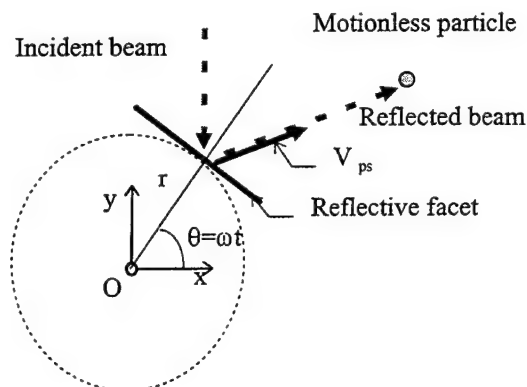


Figure 5 : Phase velocity shift generated by the rotating polygon

$$V_{ps} = 4\pi Nr \left[1 / \sqrt{2} - \cos(\theta) \right] \text{ with}$$

$\theta = \omega t = 2\pi Nt$, N : rotation speed (revs/s)

ω : pulsation, t : time

r : radius of the circle tangential to the centre of the reflective facet

θ : angle between the normal to the facet and Ox axis.

The rotation speed ω of the polygon can be estimated from the frequency of the current generated by a photo diode illuminated by the reflected beam. It ranges from 40 to 150 revs per second.

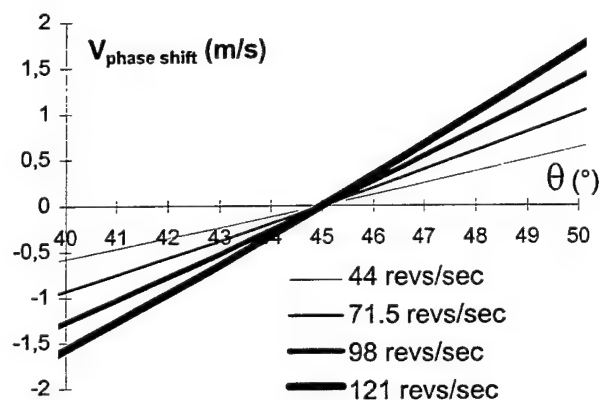


Figure 6 : Evolution of V_{ps} versus θ and rotation speed

A systematic error, which is far from negligible, is generated in the whole measurement plane, depending on the local direction of \vec{E} . It could be taken into account by associating this calculation to a specific calibration

procedure. But it would be better to reduce it by keeping reflection angles as small as possible, which is achieved with a high number of facets, and limiting rotation speed. The latter constraint may not be compatible with short integration times.

In brief, this phenomenon must be evaluated when generating a light sheet with a sweeping beam.

RECEIVING OPTICS

The optical arrangement of the receiving optics is described on the following graph. The front lens is an interchangeable camera objective. A second lens is introduced to move back the image and form it on the two CCD sensors, with the help of a beamsplitter cube. A green additive dichroic filter limits the unwanted incoming light emitted by the environment.

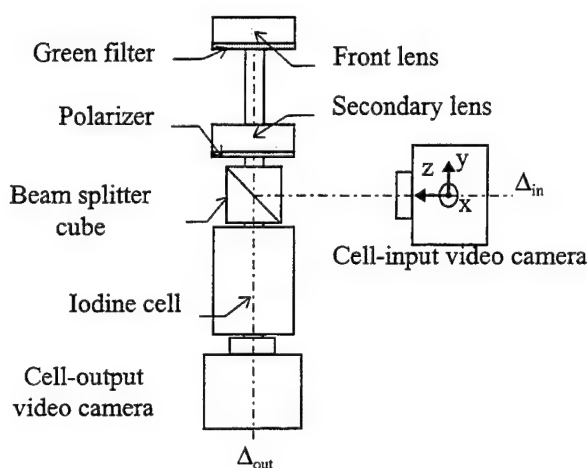


Figure 7 : Optical arrangement of the receiving optics.

The *cell-output camera* is adjusted and clamped on the optical axis Δ_{out} . To ensure overlapping of the two views, the *cell-input camera* is mounted on a set of translation stages and on a goniometer which respectively enables adjustments along Ox, Oy, Oz axis, and around the optical axis Δ_{in} . The two other rotation adjustments are not necessary thanks to an important depth of field.

As shown in Figure 2, the iodine cell is a glass cylinder of 30 mm in diameter and 60 mm long, equipped with a cold finger on which crystals always remain. The cell body contains iodine vapour, maintained at a temperature T_{cell} at least 10°C higher than that of the finger T_{finger} . In this configuration, the number of iodine molecules, and consequently the transmission through the cell, mainly depends on the temperature of the finger as reported in many papers [4]. This temperature can be adjusted to modify sensitivity in the $\tau(\Delta\nu)$ function; Figure 2 also shows the influence on the absorption profile, of a few degrees change in T_{finger} .

EFFECTS DUE TO THE POLARIZATION OF SCATTERED LIGHT

CAMERA ISSUES

The transmission ratio τ depends on the transmission and reflection coefficients of the beamsplitter cube. As they fluctuate with the polarization state of the incident wave, a polarizer must be introduced in front of the beamsplitter, to maintain these features during the flat field correction and the measurement sequences. Indeed, the polarization state of the light scattered by the particles injected in the flow, may be modified according to their size and complex refraction index. The seeding particles are oil droplets of about 0.5 micron diameter. According to the theory of Mie, the ellipses described by the extremity of the scattered electric field, depending on three receiving directions \vec{e}_r , have been computed for these particles to show the influence of φ on the polarisation state of the scattered light, for the following parameters : $\lambda=514.5\text{nm}$ $\phi_{\text{particle}}=0.5\mu\text{m}$ $n=1.47+0.1i$ $r=0.5\text{m}$.

The smaller the particles, the better the polarization of the scattered light is maintained.

However, the polarizer induces intensity losses and is able to extinguish the incoming light if its polarisation state is linear and crossed with the orientation of the plane of the preferred transmission given by this component.

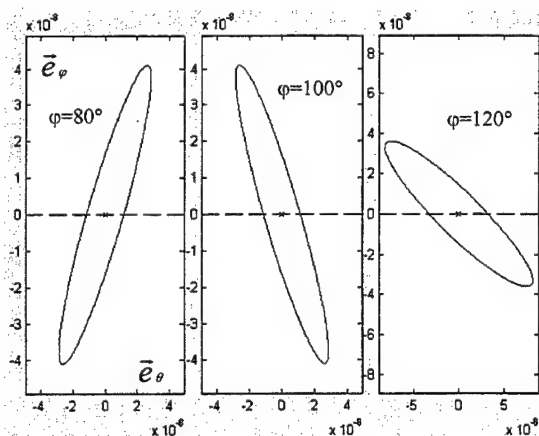
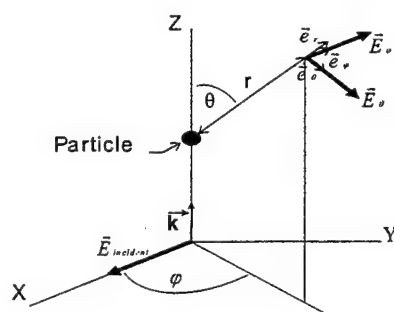


Figure 8 : Polarization state of light scattered by a particle ($\theta=150^\circ$)

The transmission ratio τ results from the division of light intensities measured on either side of the cell, from corresponding pixels. The cameras performance in terms of responsivity is of the utmost importance. After some preliminary tests mentioned below, 12-bit digital cameras (SMD-1M15) were chosen : the resolution is 1024^2 , the frame rate is 15 Hz and 2x2 binning mode is available.

As regards digitization, if only digital truncation (± 1 ADU for Analog to Digital converter Unit) is considered at first, the ensuing errors on transmission ratio ($\Delta\tau$), frequency shift (Δf) and velocity (ΔV) are calculated here, given the following assumptions :

- $\tau'=2.10^{-3}\text{MHz}^{-1}$ is the slope of the iodine line at $\tau=0.25$
- the geometrical arrangement is the one of Figure 14.

Camera	τ	I_{out}	I_{in}	$\Delta\tau$	Δf	ΔV
		ADU			MHz	m/s
8-bit	0.25	50	200	± 0.006	± 3	± 5
12-bit	0.25	800	3200	± 0.0004	± 0.19	± 0.3

The inadequacy of 8-bit cameras can thus be illustrated : the sole truncation may generate an error of $\pm 5\text{m/s}$.

In fact, all camera system parameters such as read noise, full well capacity, gain, linearity must be studied. Noise has different physical origins and levels, according to the incoming illumination. These parameters can be measured using the photon transfer technique [10]. A classical curve is represented in Figure 9. Under dark conditions (area 1), the CCD output amplifier and external processing electronics are responsible for the so-called « read noise ». This parameter (rms value= σ_R), independent of the illumination level, is used in the calculation of the « signal-to-noise ratio » : the SNR, expressed in dB, is equal to $20\log(S_{\text{ADUmax}}/\sigma_R)$.

This figure, which only represents the best possible performance of the camera, is not sufficient to characterize noise on the global measurement range. As the camera is not devoted to work in the dark, noise sources must be thoroughly analyzed as illumination increases. Photon shot noise then becomes predominant (area 2) ; its standard deviation is proportional to the square root of the input signal. At rather high levels, pixel response non uniformity becomes sensitive (area 3) ; the rms value of noise is proportional to the input signal. Close to the maximum output (area 4), noise may decrease due to a spilling-over of charges when full-well capacity is reached : this phenomenon should not occur if the camera system is calibrated so that maximum output is obtained just before the onset of full-well.

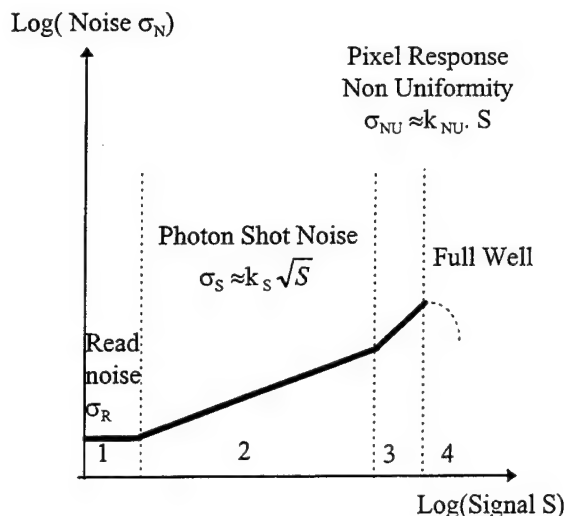


Figure 9 : Typical photon transfer curve

In order to measure the performance of our camera, specific experiments have been conducted with an integrating sphere, generating a flat illumination field.

1. Shot noise can be measured using the photon transfer technique. Data collection process and ensuing calculations are described in [10]. They are based on the difference of two consecutive images of the same uniform and constant scene, the integration time being equal to 1/15s. The maximum variance of photon shot noise is equal to $\sigma_{Smax}^2 = 56$. The standard deviation of readout noise is equal to $\sigma_R = 1.5$, so the SNR is about 70 dB. The gain of the camera system is the number of electrons converted per ADU ; it is the inverse of the slope of the following graph (Figure 10).

$$G = S_{ADU \max} / (\sigma_{Smax}^2 - \sigma_R^2) = 75 \text{ e-/ADU}$$

The full-well capacity, expressed in electrons, is the product of the gain by the maximum output :

$$FW = G \cdot S_{ADU \max} \approx 300 \text{ 000 electrons.}$$

This parameter is of great interest when choosing the camera.

2. Pixel response non-uniformity cannot be measured by the same process, because it is cancelled by the subtraction between images. However, it can be done during this experiment, by time averaging images so as to decrease statistical noise sources, for a set of flat-field illumination levels. Each pixel has its own sensitivity and saturation level, related to non uniformity in geometry, materials, etc... involved in the fabrication of the CCD. A matrix of offsets and gains is generated to correct these relative non-uniformities according to the lighting level.
3. Linearity is an important feature too, as regards DGV measurement : the camera response in ADU must be proportional to the input illumination. The calibration

conducted by the camera manufacturer shows that linearity is qualitatively achieved on the whole range, but slight deviations from a best-fit straight line may occur, that are not evaluated. The experiment to be carried out in this purpose is difficult to settle as regards metrology but will soon be undertaken. So, up to now, non linearity is supposed to be negligible but will be evaluated later on.

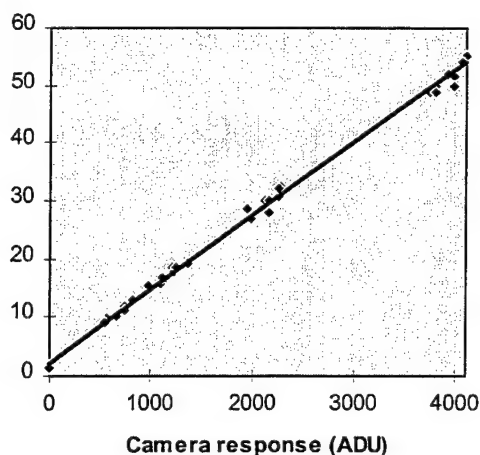


Figure 10 : Measured variance (σ_S^2) of photon shot noise versus camera response

Assuming pixel non uniformities are corrected, it is interesting to see the influence on velocity of the statistical source of noise due to the camera system, which is photon shot noise. The calculations are based on the same assumptions as previously, but will be completed on the whole rising edge of the absorption line of the iodine cell. I_{in} is supposed constant and equal to 85% of full range. I_{out} varies from 0 to I_{in} , generating a transmission ratio ranging from 0 to 1. The global error on τ can be deduced from the photon shot noise on I_{in} and I_{out} . Combining it with τ' , the derivative of τ according to frequency, plotted versus τ (Figure 11), one obtains the ensuing error on Doppler shift, and consequently on velocity, for several viewing angles θ .

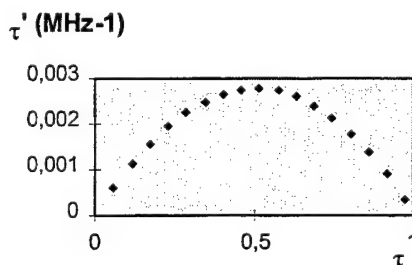


Figure 11 : Measured slope $\Delta\tau/\Delta f$ versus τ

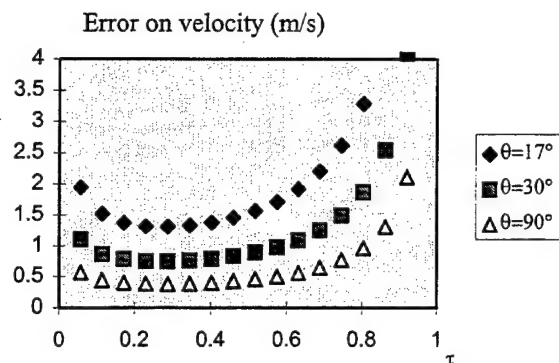


Figure 12 : Estimated error on velocity due to photon shot noise.

This curve confirms that it is better to use the linear part of the iodine line, where the slope is maximum. For high intensities on both cameras, the decrease in slope combined with the increase in photon shot noise, may generate important errors on velocity. Even when light is collected at 90° , (which makes the dot product $\vec{V} \cdot \vec{R}$ maximum), the minimum error on velocity is 0.5m/s. This geometrical configuration is not in favor of scattered light intensity ; in our experiments, the viewing angle θ is close to 17° , which generates a minimum error of 1.5m/s. These figures are valid for a single image shot ; if the scene is stationary, time averaging on several consecutive images decreases the contribution of this noise source.

EXPERIMENTAL SETUP

WIND TUNNEL CHARACTERISTICS

T2 wind tunnel is a closed-circuit, induction-driven facility capable of runs between 30 and 120 s. It is transonic, pressurized, and cryogenic. The two latter characteristics will not be of interest here. The test section ($L=1,32\text{m} \times W=0,39\text{m} \times H=0,37\text{m}$) is equipped with two large rectangular side windows, made of specific BK7 optical glass. For these DGV tests, a uniform flow in an empty test section had to be achieved. Top and bottom adaptive walls can be positioned to minimize wall interference effects. Here, their shape is a straight line diverging with an angle of 0.12° to compensate the boundary layer growth. In this case, the test section Mach number is almost constant in module and direction in all the measurement volume. The uncertainty on the Mach number is about ± 0.002 , and on the deviation angle less than 0.1° .

The operation mode was limited to ambient temperature and stagnation pressure between 1 and 2 bars. The downstream throat is used to accurately fix test section Mach numbers greater than 0.6. For lower Mach

numbers, stability and repeatability are not ensured, but the Mach number value can be recorded during the run. When the flow is stabilized, oil droplets are injected in the return leg of the circuit at constant mass flow and the intensity of scattered light progressively reaches equilibrium. After the measurement phase, seeding is switched off and the density of oil particles decreases to zero. Then, the run is stopped by closing the air injection valve. This operating technique reduces contamination of the glass windows by the seeding.

The evolution versus time of the particle density can be modeled and compared to intensity measurements (Figure 13). The time of a circuit cycle is about 1s ; at each turn, the illumination increases with a step corresponding to the additional seeding to the main flow. The time to reach the steady condition of illumination is about 20s. The calculated illumination at equilibrium is seven times higher than this of the first step. These considerations help in the timing and in the regulation of seeding during the experiments.

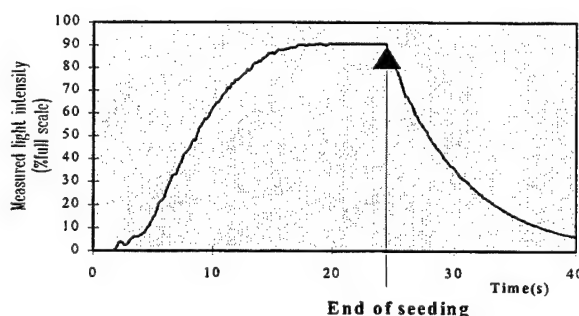


Figure 13 : Time evolution of mean scattered light in the test section.

GEOMETRICAL ARRANGEMENT

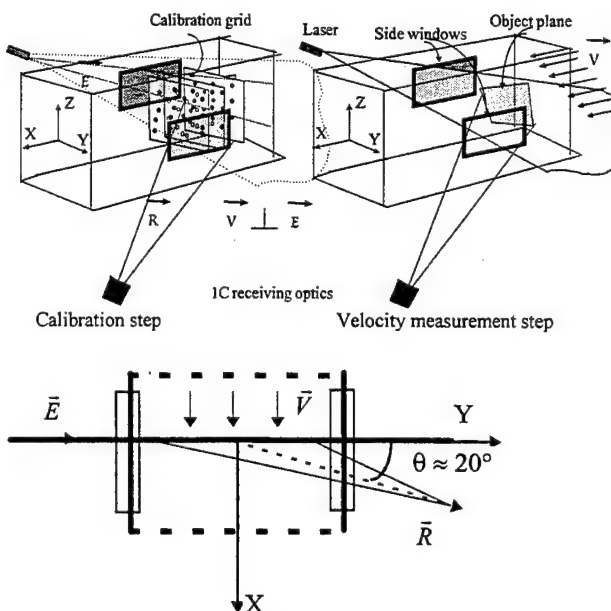


Figure 14 : Experimental 2D 1C setup

The laser beam is expanded into a vertical plane, entering from the left side window, and perpendicular to the velocity field. The light sheet is observed in forward scattering at a mean angle θ of 20° . Under these conditions, the dot product $\vec{V} \cdot \vec{E}$ is equal to 0, and the only component of \vec{R} on X direction remains : the formula to calculate velocity thus becomes

$$V = \lambda_0 \Delta f / R_x \quad \text{Equation 2}$$

CALIBRATION STEPS

Prior to the test campaign, a calibration grid, made of black dots on a white background, is brought into alignment with the measurement plane, ie the laser sheet. In this position, the grid is first used to superimpose the images of both cameras (a). When this stage is achieved, image to object mapping (b) can be derived. In a second phase, this plate is shifted forward and backward along X axis in order to complete an accurate measurement of vector \vec{R} at each image point (c).

a) The blob centers are detected and plotted in real time for both cameras, on the same graph. Image to object identification is automatic and statistics on the differences in image coordinates between the two views are calculated, so that the translation and rotation stages can be adjusted to optimize the overlapping of images. An average remaining shift of 0.2 pixel on both u and v image coordinates is easily achieved. This mechanical process is still manual but will be automated soon, as the system can calculate the necessary adjustments on the camera position and send orders to motorized stages.

b) The coordinates systems are illustrated on Figure 15, which represents the real image of the grid (below) and a reconstructed « image » in the laser sheet plane (upper left). Image-to-object mapping from (u,v) to (YZ) plane is modeled as a perspective projection. Given a large set of (u,v) versus (Y,Z) correspondences, Lij coefficients of the 3x3 ((L)) matrix can be calculated.

$$(su, sv, s)^t = ((L))(Y, Z, 1)^t \quad \text{Equation 3}$$

Geometrical aberrations are taken into account by adding a specific model, where extra coefficients must be identified.

The upper left image in Figure 15 is obtained from a matrix of equally spaced points in the object plane (Y_i, Z_i) which is projected on the image plane via ((L)) matrix. The intensity level of this calculated « object-image » is the result of an interpolation, either bilinear with a weighted average of the four adjacent pixels, or bicubic if the sixteen nearest pixels are concerned.

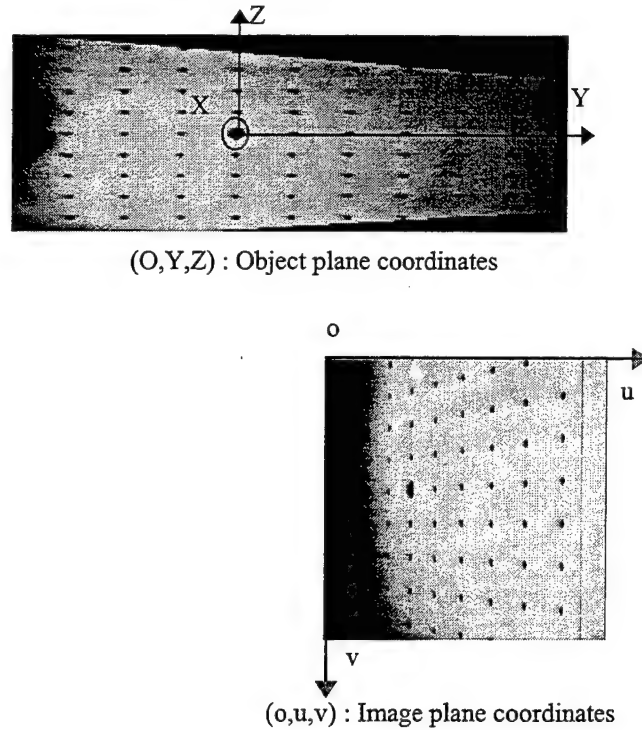


Figure 15 : Image and object-coordinates systems

Applying this process to images of the grid is useful to check the accuracy of image-to-object mapping. Dot spacing is compared to the effective distances : a mean error of 0.1 mm was achieved here on a field of $250(Y) \times 100(Z)$ mm². If the coincidence between input and output images is not perfect everywhere in the measurement plane, ((L)) matrices will be slightly different for each view.

All images will be mapped in the object plane before processing steps involving input and output views, because correspondence between these images is straightforward. In the outlook of a 3C system, this transformation is all the more essential, to ensure the matching of the three pairs of views. One more advantage is to present data in a coordinate system linked to the facility and free of any perspective effects. This processing step is easily and quickly implemented using specific Look Up Tables, integrated in Matrox Imaging Library.

c) In order to obtain the value of \vec{R} at each measurement point, the camera must be calibrated as regards the whole perspective projection of 3D space to 2D image plane

$$(su, sv, s)^t = ((M))(X, Y, Z, 1)^t \quad \text{Equation 4}$$

The orientation of the optical axis, the location of the perspective center, the equivalent focal length, ... can be derived from the 3x4 ((M)) matrix coefficients, which are calculated from the images of a 3D set of control points, obtained here by moving the grid perpendicular to its plane. The crossing of windows (wind tunnel, iodine cell,...) can be easily incorporated in this model, which makes the method accurate [11].

Finally, the maps of \bar{R} components are available : the R_x one is presented in Figure 16.

IMAGE DATA PROCESSING

Three different kinds of images, always simultaneously recorded for both cell-input and output (i,o) cameras, are necessary to fulfill the global D.G.V measurement process. Images are acquired and processed by a Genesis Matrox board.

- a) Background images (Bi,Bo) are acquired without any seeding in the wind tunnel. Stray light is generally negligible because glasses are shielded, and a green filter helps removing it. The recorded levels mostly represent the dark current values of the camera system.
- b) So-called « flat field correction » images (Fi,Fo) are taken by tuning the laser frequency outside the absorption curve, where Doppler effects are no longer visible by the iodine cell. A low speed flow is generated, and seeded.
- c) « Doppler images » (Di,Do) are images of the seeded flow, at a given Mach number.

Processing steps take place as follows :

1. Prior to any processing, images are corrected from pixel response non-uniformity, according to individual pixel level.
2. Background shots are always subtracted from other images. A mask is then applied to discard pixels which have intensity values outside a preset range : too bright pixels which may be close to the saturation level and too dark ones are rejected.
3. Input and output « Doppler images » must be divided by corresponding flat-field correction images in order to take into account the differences in optical paths on either view as well as differences in camera system parameters (gain, ...). Before this calculation, images are transformed in object-plane images as explained above. Then, the following formula can be applied to derive a « normalized » transmission ratio, on a pixel-by-pixel basis : $\tau = (Di-Bi) \cdot (Fo-Bo) / ((Do-Bo) \cdot (Fi-Bi))$
4. As the location and slope, versus frequency, of the iodine line are provided in real time by the specific device mentioned above, the Doppler shift can be accurately interpolated.
5. In our experimental configuration, \bar{V} can be easily deduced from Eq [2]. In general, a 1C device gives the component of \bar{V} on a Ri-Ei direction, local to pixel i. Three directions of projection are then necessary to restore \bar{V} .
6. Finally, images are low-pass filtered, with a 3x3 smoothing kernel.

RESULTS

The images presented here were taken with a pair of 8-bit analog cameras, because the SMD ones were not yet

available at the time of these first tests. Nevertheless, the global processing steps can be tested ; further results, obtained with 12-bit cameras, 1K² resolution, can only be better. In order to decrease photon shot noise, images were time-averaged during 0.64s, on 16 consecutive frames.

Images of different acquisition and processing steps are presented in Figure 16. Flat-field correction images are not uniform ; the intensity level decreases according to Y axis, because of the diverging sheet expansion, and shows a Gaussian profile versus Z. Optical defects generating brighter rays are visible too. The gain of the cell-output camera is adjusted to give a higher intensity level. Input and output views, which account for differences that are not due to Doppler effects, are really essential.

A pair of « Doppler images » is then presented at Mach M=0.6. The map of Doppler shifts Δf shows a Y-gradient which will be counterbalanced by the division by the R_x map, to yield a uniform velocity field V. The map of R_x component shows a significant variation according to Y : it ranges from 0.2 to 0.4, corresponding to an angle $12^\circ < \theta < 24^\circ$. The average velocity and its standard deviation are calculated from this last map. For Mach numbers ranging from 0.4 to 0.7, the accuracy on the mean velocity is close to 1 m/s, and the standard deviation varies from 3 to 6 m/s, as presented in Figure 17. These results constitute a validation of the whole measurement process : there is no patent bias in it. However, they deserve a more detailed analysis, which is being undertaken, to understand and master the error sources. Accuracy will be significantly improved by the use of 12-bit digital cameras.

Several viewing angles θ were tested but the decrease in scattered light intensity with θ limits the operating range to a few 20° , with these cameras (Figure 14). This geometrical configuration is not in favor of accuracy to restore V, but enables a measurement range of 800 m/s on the whole rising edge of the absorption curve.

CONCLUSION AND OUTLOOK

D.G.V., as is often reported, is a complex system to handle, where each element plays an important part on the final accuracy. Our first aim is to make it easy to use and efficient in wind tunnel experiments, for mean flow qualification. This kind of application should lead, in a nearby future, to a systematic use of DGV. In this context, some problems must still be deepened, as seeding in large scale facilities, stray lights coming from reflection on models, optical accesses, wall approach, mechanical stability,... After these promising results, a new series of experiments will be conducted in T2, then, at a larger scale, in a subsonic wind tunnel, with a model. Meanwhile, the 3C system is being designed, on the basis of three receiving optics, to ensure simultaneous measurements of the three velocity components.

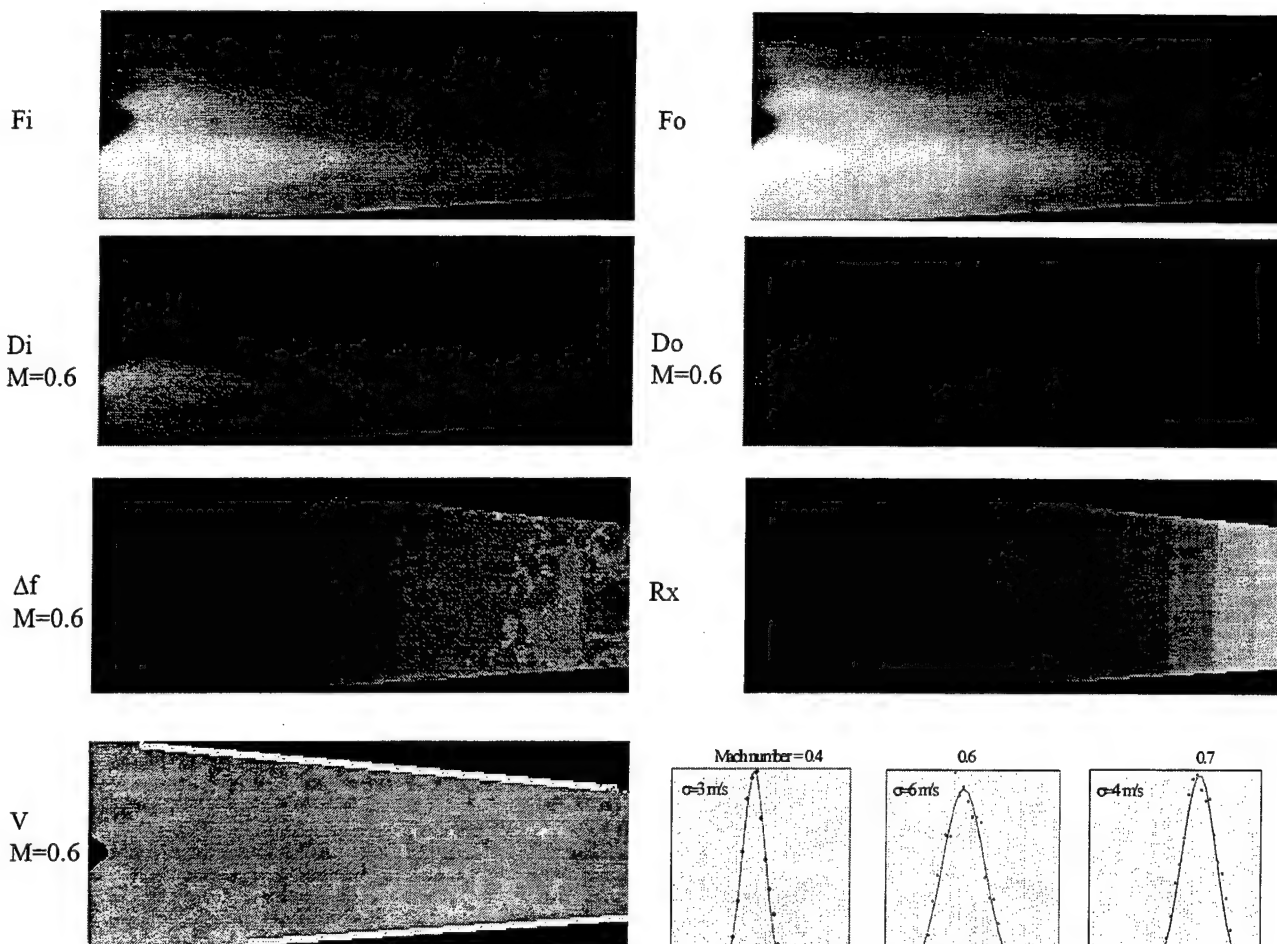


Figure 16 : Input and output images of the acquisition and processing steps.

The authors would like to acknowledge DGA/SPAE for its financial support, and their colleagues of T2 wind tunnel team and of the Optics Department of ONERA Toulouse Center for their help and advice.

REFERENCES

- [1] Komine, H., Brosnan, S.J., Litton, A.B., Stappaerts, E.A., *Real-time, Doppler Global Velocimetry*, AIAA Paper 91-0337, 29th Aerospace Sciences Meeting, Reno, Jan 91.
- [2] Beutner, T., Elliott, G., Mosedale, A., Carter, C. : *Doppler Global Velocimetry Applications in Large Scales Facilities*, 20th AIAA Advanced Measurement and Ground Testing Technology Conference, Albuquerque, June 1998.
- [3] Roehle, I., Wilhert C., Shodl, R. : *Applications of 3D Doppler Global Velocimetry in Turbo-machinery*, 8th International Symposium on Flow Visualisation, 1998.
- [4] Mc Kenzie, R., *Planar Doppler Velocimetry for Large-Scale Wind Tunnel Applications*, AGARD Fluid Dynamic Panel, Paper n°9, Seattle Sept 97.
- [5] Mc Kenzie, R., *Measurement Capabilities of planar Doppler Velocimetry using pulsed lasers*, Applied Optics, Vol.35, n°6, Feb96.

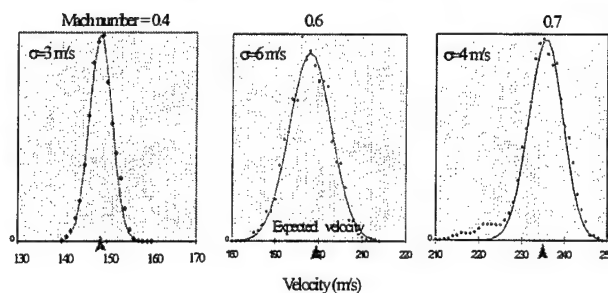


Figure 17 : Histograms of calculated velocities

- [6] Reinath, M. : *Doppler Global Velocimetry Development for the Large Wind Tunnels at Ames Research Center*, NASA Technical Memorandum, Sept 97.
- [7] Meyers, J., Fleming, G., Gorton, S., Berry, J. : *Instantaneous Rotor Wake Measurements Using Doppler Global Velocimetry*, 9th International Symposium on Applications of Laser Techniques to Fluid Mechanics, Lisbon Jul 98.
- [8] Arnette, S., Samimy, M., Elliott, G. : *2C Planar Doppler Velocimetry in the Compressible Turbulent Boundary Layer*. Experiments in Fluids n°24 p323-332 1998.
- [9] Naylor, S. : *Development and Accuracy Determination of a 3C Doppler Global Velocimeter*. Ph.D Dissertation, West Virginia University, Morgantown, Jul 98
- [10] Andelfinger, R., Photon Transfer Curve Statistics and CCD characterization, Application note, www.smd.com
- [11] Lempereur, C., Barricau, P., Mathé, J.M., Mignosi, A., *Développement d'un Système de Vélocimétrie Doppler Globale*, Technical Reports, ONERA DMAE TME Jan 99, Jun 99.

EXPERIMENTAL INVESTIGATIONS ON VORTEX BREAKDOWN OVER DELTA WINGS WITH DOPPLER GLOBAL VELOCIMETRY

Förstermann, M., Bütefisch, K. A.
German Aerospace Center
Institut für Strömungsmechanik
Bunsenstr. 10, D-37073 Göttingen, Germany

ABSTRACT

The fluid dynamic properties of the flow over a delta wing are still not yet fully understood. Recent numerical simulations have shown that the stability of the vortices could be best judged and observed by resolving the unsteady velocity distributions of the axial velocity vector component in the vortex core region.

For an experimental validation of these numerical results it is necessary to obtain the three dimensional velocity distribution in the vortex core. Obtaining the velocity distribution should work without influencing the flow because the stability property is very sensitive against any disturbance in the flow.

A non intrusive optical technique is chosen as adequate to measure the velocity distribution: Doppler Global Velocimetry. It is based on the Doppler shift of laser light due to scattering at moving particles. By extensively seeding the flow with these particles it was possible to determine the unsteady three dimensional velocity distribution in the vortex core.

The experiment shows a good agreement with the numerically predicted flow structures.

1. INTRODUCTION

The fluid dynamic properties of the flow over a delta wing are still not fully understood [1]. Even at small angles of attack the flow separates at the leading edge where a vortex sheet rolls up into a vortex core above the wing [6]. The vortex stability has a significant influence on the lift of the wing. Recent numerical simulations [12] have shown, that particularly the fluid dynamic properties in the vortex core could give more information about a beginning instability. For an experimental validation of these numerical results it is necessary to measure the three dimensional velocity distribution in the vortex core. These measurements have to be carried out at least in a two dimensional plane to obtain planar fluid dynamic relations between the different parts of the vortex. Furthermore obtaining the velocity distribution should

work without influencing the flow, therefore a non intrusive method is eligible.

With the improvements in laser technique and increasing computer performance, optical measurement methods, which work non intrusive, have succeeded in fluid dynamics.

There are a lot of different optical methods to get velocity information but most of them have problems to obtain velocity information from the vortex core [4]. The difficulty is caused by the principle of achieving velocity information by seeding the flow with particles. The velocity of these seeding particles leads then to the velocity of the particle surrounding flow. In the vortex core most of these particles are driven away from the center by centrifugal force. Therefore the number of particles is low in the vortex core compared to the other parts of the vortex, in the vortex core only the small particles with a comparable low scattering cross section remain. Under these circumstances it is difficult to obtain the particles velocity using optical methods like LDV or PIV.

Doppler Global Velocimetry (DGV, PDV) is chosen as adequate because with this measurement technique it is possible to acquire a velocity distribution of the flow even in the region of the vortex core. The technique is based on the doppler frequency shift of laser light scattered by seeding particles [7]. An optical filter (absorption line filter) turns the frequency shift into a transmission distribution. The measured transmission gives the velocity [10]. It is not necessary to analyse single particles. The velocity is calculated by the cumulated scattered light of multiple particles. Therefore it is possible to achieve velocity informations even from the region of the vortex core by the cumulated scattered light of many small particles. With the used measurement system it is possible to measure only one component of the three dimensional velocity vector in the observed plane. The three dimensional velocity information is achieved by three measurements which are taken successively. With each single of the latter measurements it is possible to obtain informations of unsteady flow phenomena from the core of the vortex. A sophisticated designed computer system which processes the image

data, allows an online evaluation of the velocity distribution. The problem of stability of laser light frequency was solved by simultaneously observing the frequency of the laser light and the transmission of scattered light during data acquisition [2]. Therefore it was possible to determine the velocity without any reference. In the following paper the results of the three dimensional velocity field are presented for different angles of attack and different shapes of delta wings. The numerically found stability criterias of vortex breakdown are confirmed. The stability of the vortex could be observed best by the velocity distribution in the axial direction of the vortex. Furthermore there are regions of back flow near the center of the vortex core if instability occurs. The dependence of vortex instability on angle of attack and moreover the dependence on aspect ratio [11] was confirmed.

The advantage of this setup of the Doppler Global method is the speed of obtaining velocity data. It is possible to judge on vortex stability with only one set of pictures which takes only 1/120 second to record.

2. VORTEX STABILITY PROBLEM OF DELTA WINGS

The velocity distribution over a pitching delta wing differs to a great extent to different forms of wings. Even at small angles of attack the flow separates at the leading

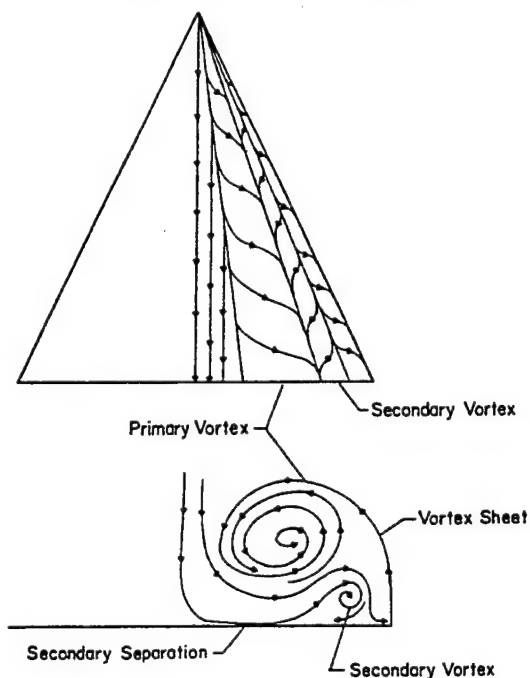


Figure 1 : Flow field topology over delta wing [9]

edge where a vortex sheet rolls up into a vortex core above the wing [6]. Figure 1 shows schematically this separation.

The vortices induce an increase in velocity in the vortex region above the wing. This increase of velocity leads to an additional aerodynamic lift which could get as much as sixty percent of the total lift [1]. Under certain circumstances the entire velocity distribution over a delta wing changes: the vortices burst. The cores of the vortices enlarge and the velocity therein decreases rapidly. As a consequence the aerodynamic lift decreases as well. The vortex breakdown could start on one wing chord further downstream than on the other [1] which causes undesirable taxiing of the wing. This undesired phenomenon and the rapid loss of lift lead to a great effort in experimental and numerical investigations to understand the vortex breakdown. Although the latter is not yet fully understood, one could draw some conclusions based on recent publications:

There are two different types of vortex breakdown [12]:

- bubble-type: formation of a bursting bubble with expanded vortex core, the velocity in the vortex core decreases rapidly and forms a stagnation point on the vortex axis; this breakdown type goes along with a restricted region of backflow near the center of the vortex axis.
- spiral-type: the direction of the flow of the vortex core leaves the center vortex axis and flows in a spiral-type-form around it as long as the vortex center flow diminishes

The onset of vortex breakdown over the delta wing depends on different conditions [11][12]:

- the smaller the angle of attack the closer is the formation point of vortex breakdown to the apex
- the bigger the sweep of the wing the closer is the formation point of vortex breakdown to the apex.
- the vortex breakdown is an unsteady flow phenomena (figure 2, the point of vortex breakdown over the delta wing changes with time)

In order to proof these numerical calculations it is necessary to set up an experiment which allows to measure a three dimensional velocity distribution on a short time scale. Therefore Doppler Global Velocimetry is chosen which could provide three dimensional velocity information in a chosen plane over the delta wing. The advantage of this measurement technique is its ability to obtain velocity information even of the vortex core region.

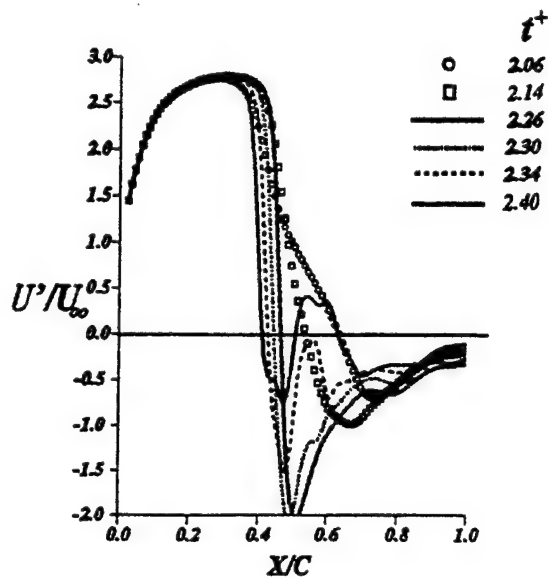


Figure 2 : Numerical calculations of the axial component of the vortex velocity distribution [12] with non-dimensional time $t^+ = tU_\infty/C$ with C as wing chord

3. DOPPLER GLOBAL VELOCIMETRY

Basic Principles

The technique is based on the doppler frequency shift of laser light scattered by seeding particles [7]. Compared to the frequency of laser light the doppler frequency shift of scattered light is very small. Therefore a spectroscopic method is chosen to resolve this shift. A cell containing iodine gas is used as an optical filter for the scattered light. An absorption line of iodine, which frequency region lies within the laser light frequency ν_0 turns the frequency of the scattered light into a transmission distribution. By simultaneously observing the laser light frequency and measuring the transmission of scattered light from moving particles through a iodine cell it is possible to determine the doppler frequency shift with an calibrated absorption line (figure 3) [10]. The order of magnitude of the doppler shift $\Delta\nu$ is dependent on the scattering angle Ψ (figure 4) between the propagation direction of the laser beam \vec{l} , the scattering light receiving direction $\vec{\delta}$ and the velocity \vec{v}

$$\Delta\nu(v) = 2(lv/\lambda) \cos(\psi/2) \quad (1)$$

with λ as laser light wavelength and v as velocity. Due to the limited broadness of the absorption line the range of measurable velocity is restricted and dependent on the scattering angle ψ .

A camera system consisting of two CCD-cameras is used as a receiver unit for the scattered light (figure 5). One camera receives the scattered light through the iodine cell, the other receives the light without filtering in order to get a total transmission by dividing the two camera images.

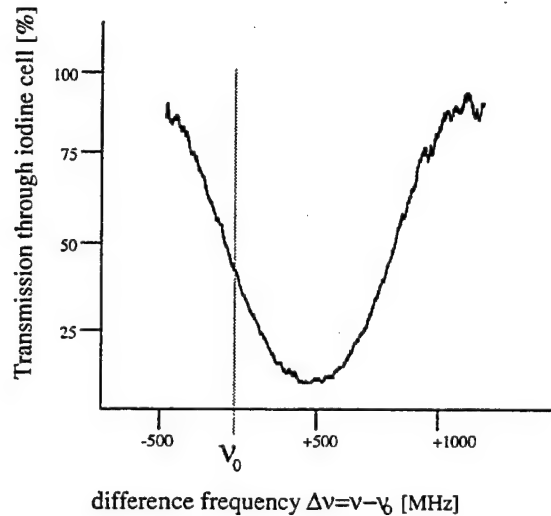


Figure 3: Absorption line of iodine

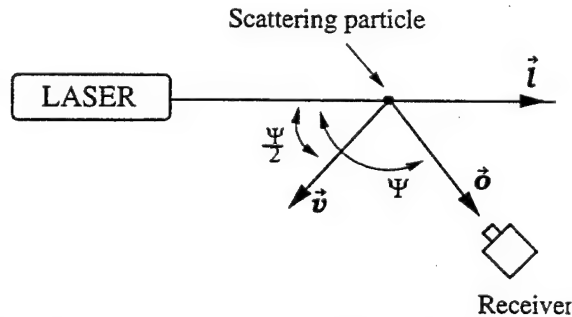


Figure 4: Determination of the direction of the measured velocity component

The characteristics of the transmission curve of the absorption line filter is very sensible of the experimental environment. It is dependant on the amount of pure iodine in the iodine cell, its vapour pressure and its dimensions [3]. Therefore it is eligible to calibrate the iodine cells used under experimental conditions. The calibration is done with the same laser which is used for the doppler global velocimetry measurements. Into its cavity an etalon is placed which ensures a small bandwidth

of laser light frequency. By slowly heating up the etalon the laser light frequency changes in steps. The frequency steps are dependent on the resonator modes of the used laser. For calibrating an iodine cell the laser light is observed by an optical setup containing two photodiodes and the cell (figure 6).

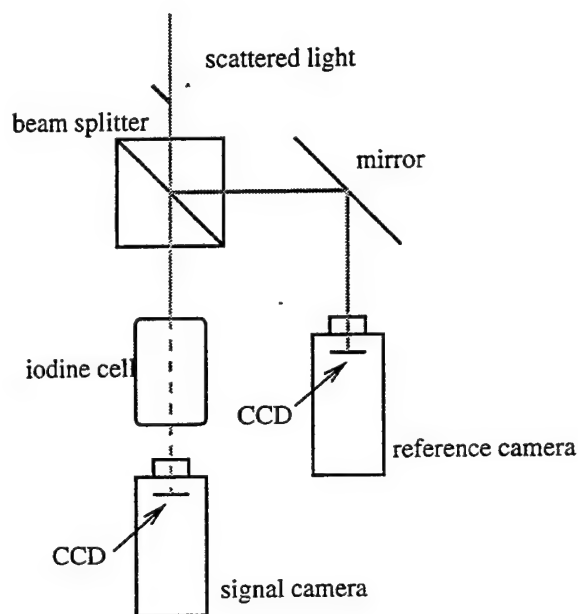


Figure 5: schematic setup of a DGV receiver unit

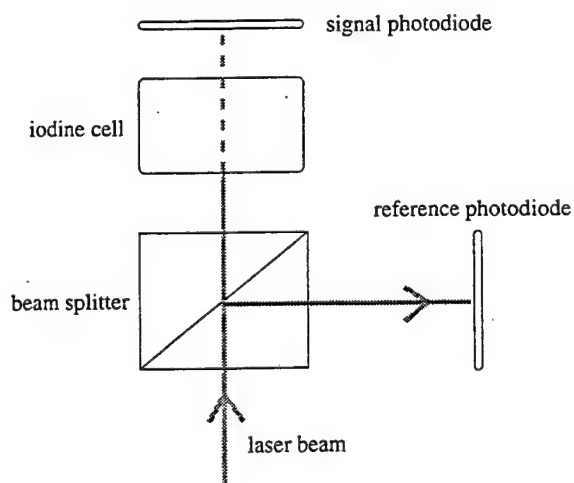


Figure 6: schematic setup for calibrating the iodine cell transmission curve and for determining the laser light frequency

Determination of the absorption line filter

The signal photodiode collects the iodine cell filtered laser light, the reference photodiode is used for normalization. By dividing the two photodiode signals one gets the absolute transmission value of the iodine cell. Figure 7 shows the change of transmission in time while heating up the etalon. Each step in transmission represents a change of resonator mode of the laser light frequency which amounts to 147 MHz for the Argon-Ion CW laser used. A polynomial fit of these obtained frequency steps and a frequency shift according to minimum correction yields the transmission -- frequency dependance of the iodine cell (figure 8).

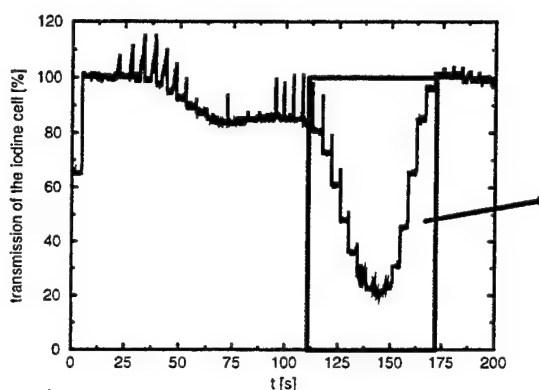


Figure 7: transmission of the laser light through the iodine cell during frequency change by heating up the etalon

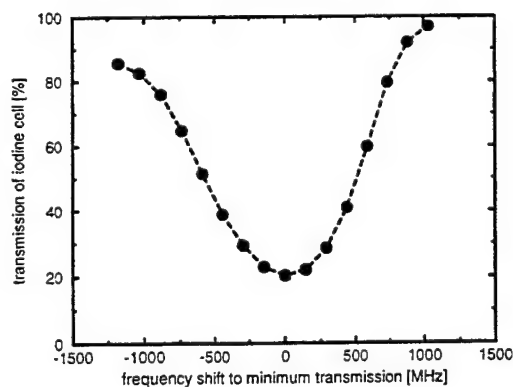


Figure 8: calibration curve of the absorption line filter

Laser light frequency observation

In order to determine the absolute doppler frequency shift it is necessary to observe the laser light frequency ν_0 simultaneously with the DGV measurement of the flow field [2]. Therefore two calibrated iodine cells are used, one cell in the DGV setup (figure 5) and one in a setup as shown in figure 6 to observe the laser light frequency by measuring the transmission of a separated laser beam and comparing this transmission to the calibrated values. By staying on one slope of the transmission curve one gets an absolute frequency shift to the frequency of minimum transmission.

Camera alignment and dewarping

Signal and reference camera are CCD cameras with 572×768 pixels. Each signal camera pixel contains a velocity information by comparing it to the belonging reference camera pixel. Therefore the views of the two cameras have to be aligned in order to find the matching pixels. The alignment is done by placing a grid in the observation plane of the laser light sheet (see chapter 3) and by adjusting the camera positions until both see the same part of the grid. By taking a picture of the grid it is possible to dewarp the cameras' sight of view into an absolute coordinate system.

After aligning and dewarping one could calculate the velocity distribution for the entire observed plane. The procedure to obtain a single velocity information is explained in figure 9.

First the two grey values of the two matching pixels are divided. The calculated transmission is converted with the calibrated transmission curve into a frequency shift (relative to minimum transmission). By subtracting the shift of the laser light frequency one obtains the absolute doppler shift. This shift set in the doppler formula yields the absolute velocity for the single pixel.

Computer setup for online evaluation

It was possible to set up a computer system which could calculate and show the velocity distribution of the observed plane with more than 24 Hz on a monitor. The two videosignals of the two cameras are turned into grey values by the framegrabbers. These grey values are processed in an arithmetic logical unit. It divides the two signals and scales the result to an adequate magnitude. The result is shown online as a velocity information on a monitor. The dividing and scaling is done with the help of a lookup table. It contains every combination of two greyscales and their velocity value. The lookup table is calculated before the measurement starts. Therefore the speed of calculating increases to an extent that it is possible to provide an online velocity distribution with more than 24 Hz. The computer setup is shown in figure 10.

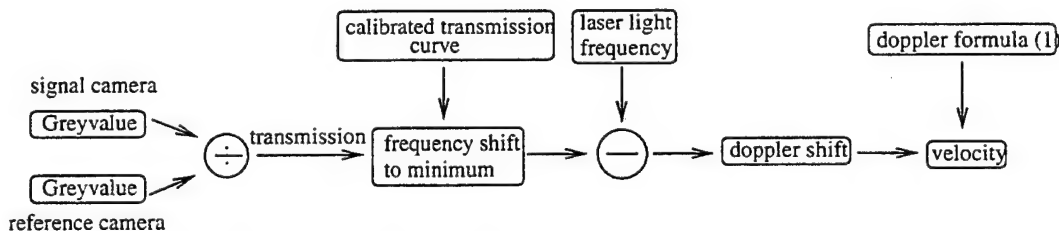


Figure 9: Determination of the velocity information

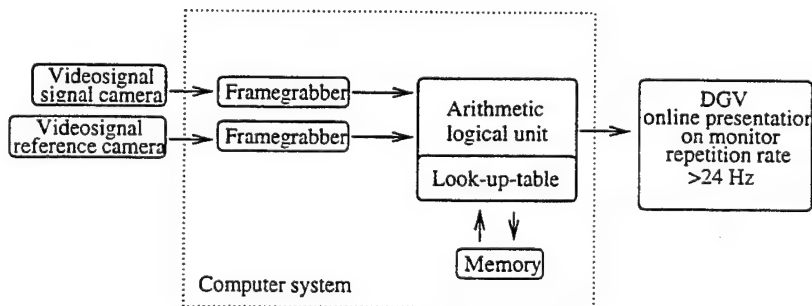


Figure 10 Computer system for online evaluation
Determination of the velocity distribution

4. WIND TUNNEL EXPERIMENTS

Windtunnel setup

The used Eiffel-type windtunnel has a test section of $10 \times 10 \text{ cm}^2$ and its maximum free stream velocity is 35 m/s . During the measurement the free stream velocity is held constantly at 30.5 m/s by observing the antechamber pressure. The seeding was introduced by a fog generator into the antechamber. Two different delta wings were used, one with 65° sweep and 50 mm wing chord, the other with 75° sweep and 50 mm wing chord. The velocity distributions were taken at 60% and 80% of total wing chord (downflow). The angles of attack were 15° and 20° .

Optical setup for three dimensional velocity data acquisition

To obtain scattered light from particles in a chosen plane the laser light sheet technique is used [4]. In order to achieve a three-dimensional velocity distribution of the chosen plane the laser light has to generate the laser light sheet from three different directions. Thus the changing propagation direction \vec{l} creates three different directions (see formula (1)) of the measured velocity component v (figure 11). The undewarped reference camera image is shown in figure 12. The scattered light intensity decreases rapidly in the vortex core.

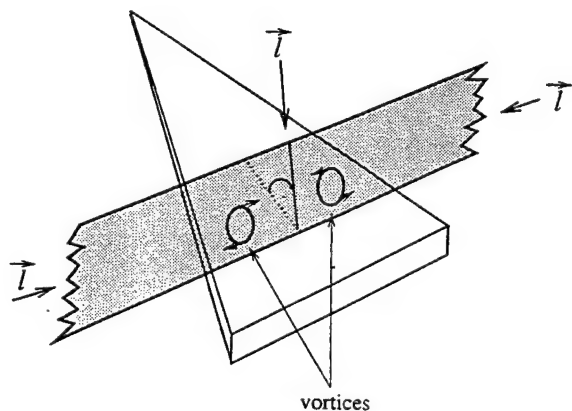


Figure 11: Optical setup for three dimensional velocity data acquisition by changing the laser light propagation direction \vec{l} which creates the laser light sheet

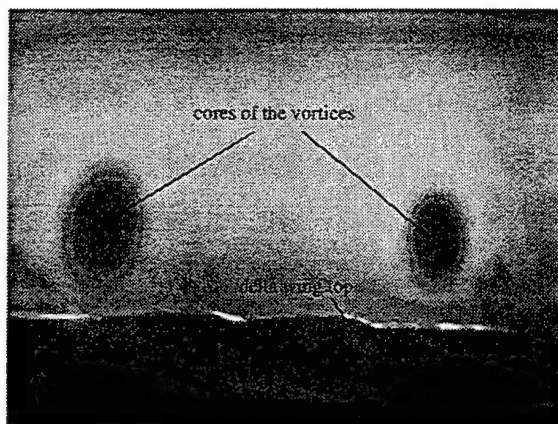


Figure 12: Undewarped reference camera image of the laser light sheet over a delta wing

5. RESULTS

Velocity distribution of one velocity component

The dewarped velocity distribution of a single velocity component calculated from the reference and signal image of the lightsheet (figure 11) is shown in figure 13. Due to the dewarping process it is possible to determine absolute coordinates of the velocity information of the flow field. The accurateness of the velocity information of a single point is as high as $1/10 \text{ mm}$. The main part of the direction of the shown velocity vector in figure 13 points from left to right. Therefore the flow field topology of the vortices are easy to see. The left vortex rotates clockwise which causes a positive velocity value close to the delta wing and a negative velocity value on the opposite side of the vortex. The right vortex rotates anticlockwise, therefore the velocity distribution is vice versa. The velocity distribution represents the result of a single pair of signal and reference camera images taken with a camera shutter time of $1/60$ second.

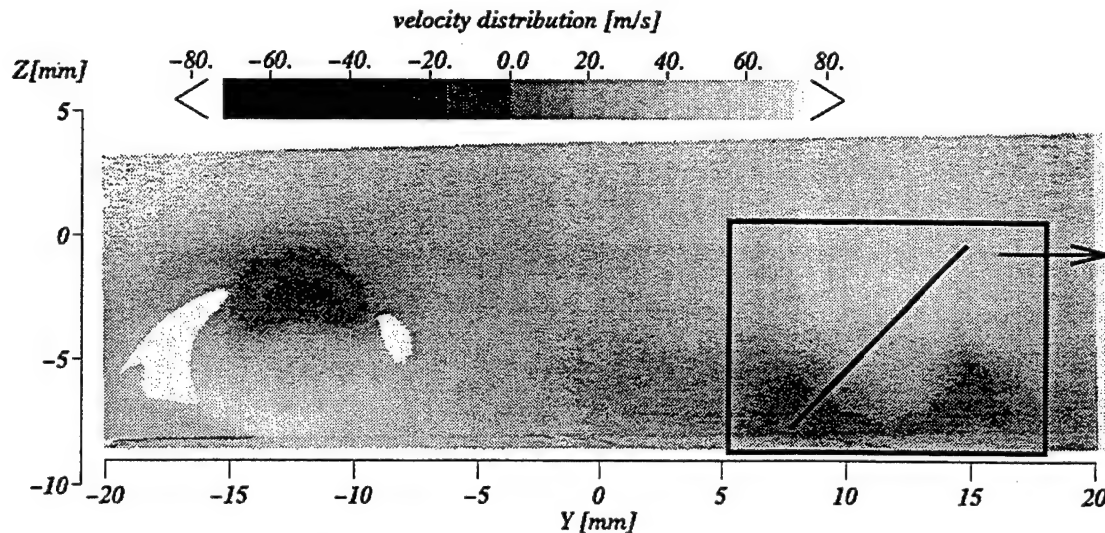


Figure 13: Velocity distribution of one velocity component directing mainly from right to left. The white parts contain no velocity information due to the limited range of the used cameras. The following investigations are restricted to the area in the black square and the black line respectively

Time dependence of each velocity component

For the coordinate transformation of these successively measured velocity distributions of the chosen velocity vector components into a rectangle coordinate system it is important that the velocity distribution of each velocity component is not changing significantly with time. This fact can only be assumed for stable vortices (figure 2). Moreover the change of velocity with time differs from the observed velocity component and from the observed flow region. The magnitude of velocity change is bigger for the axial velocity vector component and for the region of the vortex core compared to velocity vector components which are rectangular to the vortex axis (figure 13) and to the regions further away from the vortex core. This dependence is shown by calculating the standard deviation of the successively measured velocity distributions of each velocity component (figure 14).

In the vortex core region the standard deviation increases from approximately 5m/s outside the vortex core to 15m/s inside for the axial velocity vector component. The velocity distribution of the vector component rectangular to the vortex axis shows much less time and region fluctuations. The standard deviation for the latter velocity distribution is not more than 5m/s.

The standard deviation shows the dependence of vortex stability to time dependence as well. The magnitude of standard deviation for the axial velocity component is much less for stable vortices whereas the standard deviation for the velocity component rectangular to the vortex axis does not change to a great extent. In order to get a more precise understanding of the vortex breakdown

it is therefore needful to investigate the time dependence of the axial velocity vector component.

Velocity distribution of the axial velocity vector component

Time sequence of the velocity distribution of an unstable vortex

The velocity distribution of a unstable vortex does change to a great extent with time. Figure 15 shows the change of velocity along the cross section of the vortex core. The observed cross section is shown in figure 13. Another instability criteria could be observed in this sequence -- the region of backwards flow which size and form is changing with time.

Time sequence of the velocity distribution of a stable vortex

The more stable the vortex is the higher is the axial velocity component. Figure 16 shows the increase of speed of this velocity vector component compared to the unstable case shown in figure 15. Backward flow in the vortex core is not observed. The increase in stability is caused by the observed position which is closer to the apex. The time between two successively taken velocity distributions is 50ms and the exposure time of the camera chip is 8ms.

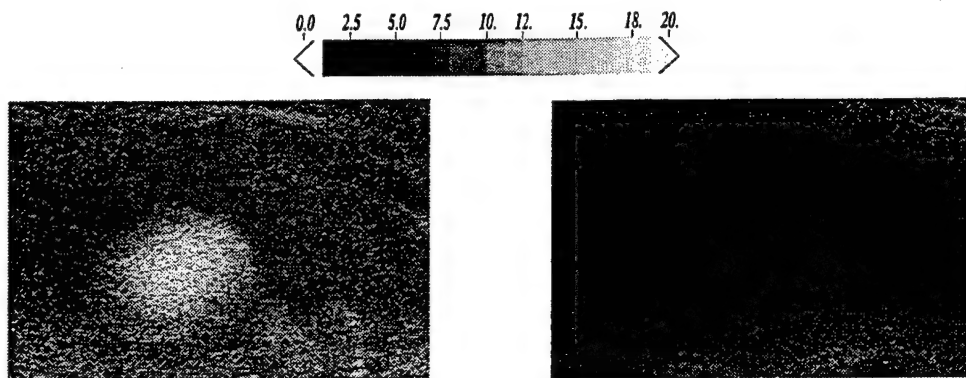


Figure 14: Standard deviation of the velocity distribution of an unstable vortex. The left figure shows the standard deviation for the axial velocity component. The increase of standard deviation in the region of the vortex core is due to the vortex instability (see also figure 15). The right figure shows the distribution of the velocity vector component rectangular to the vortex axis. The sweep of the delta wing was 65° , angle of attack 15° and the observed plane at 80% of wing chord.

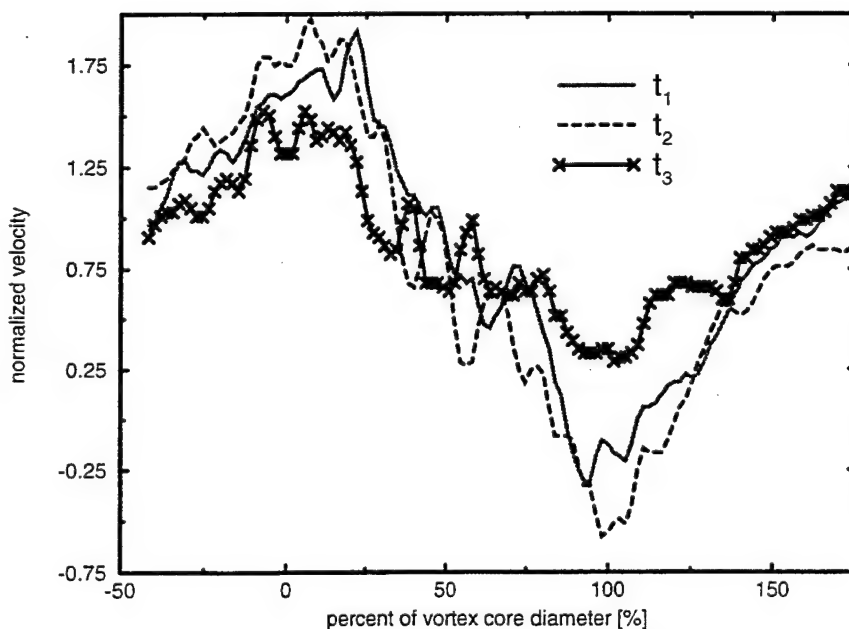


Figure 15: Time sequence of the velocity distribution of an unstable vortex for a 65° sweep and 15° angle of attack delta wing at 80% of wing chord. The velocity distribution is changing with time. Backwards flow in the vortex core is observed.

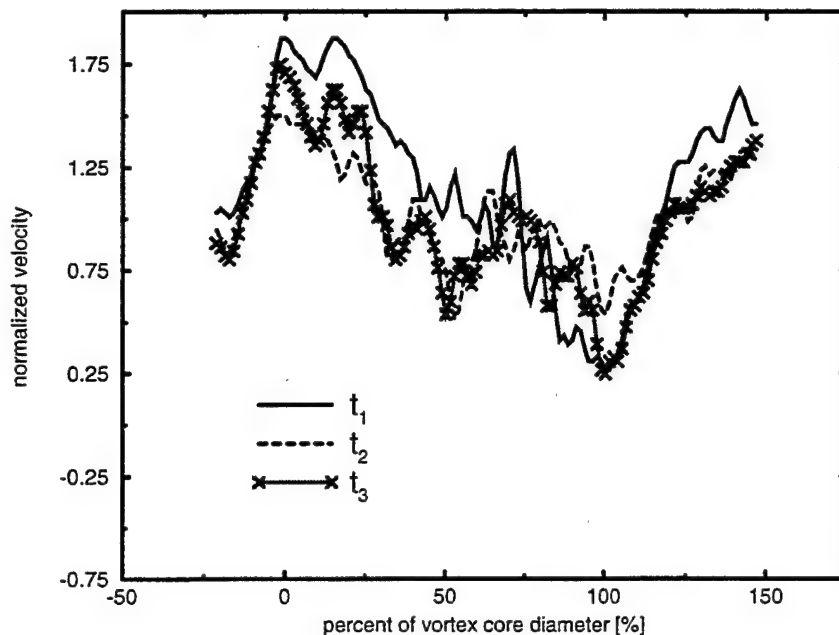


Figure 16 : Time sequence of the velocity distribution of a stable vortex of a delta wing with 65° sweep and 20° angle of attack at 60% of wing chord. The velocity distribution is not changing to a great extent with time. Backwards flow in the vortex core is not observed, the vortex is stable.

6. CONCLUSIONS

The presented Doppler Global Velocimetry technique allows the determination of the unsteady three-dimensional velocity distribution in a chosen plane over an inclined delta wing. With the obtained results it was possible to confirm theoretical vortex stability criteria and furthermore confirm the numerical simulations of bubble type breakdown mechanism calculated by Visbal.

The used DGV-system provides quasi instantaneous flow field velocity information with more than 20 Hz at less than 10 ms exposure time for each velocity distribution. The accuracy of resolving flow field structures was as high as $1/10 \text{ mm}^2$ with less than $\pm 3 \text{ m/s}$ measurement uncertainty. The problem of laser light frequency fluctuations was solved by monitoring the laser light frequency simultaneously with the experiments instead of stabilizing the laser. The DGV-technique allows the determination of the three-dimensional velocity distribution even in the region of the vortex core although the particle density is reduced.

The investigations have shown that the vortex stability could be best judged by measuring the velocity

distribution of the axial velocity vector component. Backward flow in the vortex core region and the increase of change of the velocity vector value with time are the most obvious signs of vortex breakdown found by the investigations presented in this paper. The effects of delta wing sweep and angle of attack on vortex breakdown could be observed and confirm the theoretical work by Sforza, Visbal and Hummel.

7. ACKNOWLEDGEMENTS

The authors gratefully acknowledge the help of Dr. Riehle of the Physikalisch-Technische-Bundesanstalt (PTB) in Braunschweig for his support in the filling of the iodine cells.

They also would like to thank Mr. Schodl, Mr. Röhle and Mr. Wolf for their helpful support in designing the measurement system.

8. REFERENCES

- [1] ALTHAUS ; W. ; BRÜCKER, CH. ; WEIMER, M. : *Fluid Vortices*. Kluwer Academic Publishers, Dordrecht, 1995.
- [2] BÜTEFISCH, K. A. : *Verfahren zur Bestimmung der Geschwindigkeit einer Strömung*. German Patent P 44 26 956.0-09, 1994.
- [3] CHAN, V : S. S. ; HEYES, A. L. ; ROBINSON D. I. ; TURNER, J. T. : *Iodine absorption filters for Doppler Global Velocimetry*. Meas. Sci. Technol., pp. 784-794, 1995.
- [4] ECKELMANN, H. : *Einführung in die Strömungsmeßtechnik*. Teubner, Stuttgart, 1997.
- [5] HSU, C.-H. ; LIU, C. H. : *Numerical simulation of the vortical flow over a round-edged double delta wing*, Southeastern Conference on Theoretical and Applied Mechanics, 1988.
- [6] HUMMEL, D. : *Untersuchungen über das Aufplatzen der Wirbel an schlanken Deltaflügeln*. Z. Flugwiss. 13, 1965.
- [7] KOMINE, H. : *System for measuring velocity field of fluid flow utilizing a laser doppler spectral image converter*. United States Patent No. 4919536
- [8] MEYERS, J : F. : *Doppler Global Velocimetry : A New Way To Look At Velocity*. ASME, pp. 289-296, 1991.
- [9] REYNOLDS, W. C. ; CARR, L. W. : *Review of unsteady, driven, separated flows*. AIAA 85-2424, 1985.
- [10] RÖHLE, I. ; SCHODL, R. : *Evaluation of the accuracy of the Doppler Global technique*. Proc. Opt. Methods and Data Process. in Heat and Fluid Flow (City Univ. London), pp. 155-161, 1996.
- [11] SFORZA, P. M. ; STASI, W. ; PAZIENZA, W. ; SMORTO, M. : *Flow measurement in leading-edge devices*. AIAA J., 116 : pp. 218-224, 1978.
- [12] VISBAL, M. R. : *Computational study of vortex breakdown on a pitching delta wing*. AIAA 24th Fluid Dynamics Conference, Orlando, 1993.

FLOW VELOCITIES VISUALIZATION USING DOPPLER PICTURE INTERFERENCE VELOCIMETRY

F. Seiler, A. George, F. Leopold, J. Srulijes, G. Smeets

French-German Research Institute of Saint-Louis (ISL)
5, Rue du Général Cassagnou, F-68301 Saint-Louis, France

Abstract

An improved technique for visualizing a velocity field in an entire plane has been developed by taking "Doppler Velocimetry Pictures" using Michelson interferometry (DPV). The Doppler pictures give information about the instantaneous local velocities of tracers passing through a light sheet. The Doppler shift of the frequency of the light scattered by tracer particles is modified by a Michelson interferometer into varying light intensities. The initial interference fringe system is transformed by flow velocities. Two different techniques for the treatment of the images are presented. The first one is based on the shift of the fringe system, the second one uses the different light intensity distribution of the fringe system. For both cases the Doppler pictures are taken by CCD cameras and the images are computer-processed for velocity presentation.

1 INTRODUCTION

In order to take pictures of the velocity distribution, e.g. in a light sheet crossing a gas flow, some measuring techniques have been developed. Particle Image Velocimetry (PIV) and Doppler Global Velocimetry (DGV) are well-known tools for this purpose. A new velocity visualization technique was developed by Oertel et al. [1] 1981 at ISL. The frequency of the light scattered by tracer particles passing through a light sheet is shifted by the Doppler effect. This Doppler shift leads to a change of the light intensity distribution at the exit of the Michelson interferometer (see Seiler et al. [2]-[4]). The changes in the light intensity distribution can be directly related to the velocities of the tracer particles. This method, called Doppler Picture Interference Velocimetry (DPV), has been developed and two techniques, processing the interference image of the Doppler picture, will be described herein.

2 PRINCIPLE OF DPV TECHNIQUE

2.1 Doppler Effect

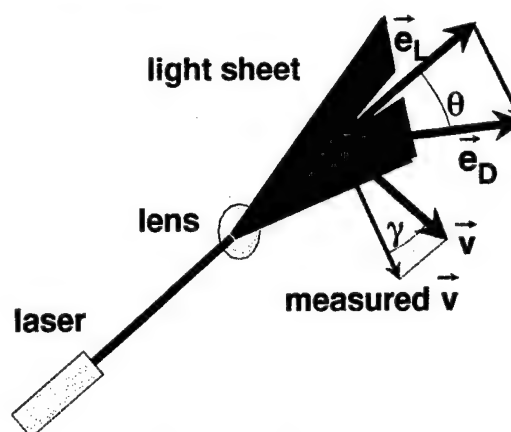


Fig. 1. Doppler effect

In order to calculate the tracer velocity \vec{v} , the well-known formula of single beam velocimetry is used with the angles γ and θ . In figure 1 \vec{e}_L denotes the vector situated between the light source (L) and the tracer particles (P), and the vector \vec{e}_D is directed from the tracers to the Michelson interferometer detector (D). θ is the angle between the two unit vectors \vec{e}_L and \vec{e}_D . The velocity component of the flow vector \vec{v} is measured in the direction of the difference vector $\vec{e}_D - \vec{e}_L$. The angle γ is defined by the velocity vector \vec{v} and its measured component, as shown in figure 1. The Doppler frequency shift can be expressed as follows:

$$\frac{dv_L}{v_L} = \frac{\vec{v}(\vec{e}_D - \vec{e}_L)}{c} = 2 \frac{v}{c} \cos \gamma \sin \frac{\theta}{2} \quad (1)$$

In order to be able to visualize the velocity distribution, the plane Σ crossing the gas flow seeded with tracer particles, is illuminated by a light sheet of frequency ν_L .

2.2 Michelson interferometer

The light from these tracer particles is focused into a special Michelson interferometer (see fig. 2). The light scattered is Doppler-shifted to ν_D in the case of moving tracers. The frequency variations $d\nu_L = \nu_D - \nu_L$ of the scattered light lead to changes $d(\Delta\phi)$ of the phase difference $\Delta\phi$ between the light waves returning from the two legs of the Michelson interferometer. (L) denotes the light source, (D) the detector, i.e. the Michelson interferometer. The $d(\Delta\phi)$ shift causes variations dI of the interference light intensity I illuminating the plane Σ' (plane Σ and Σ' see fig. 3). The light intensity distribution gives information on the frequency shift depending on the tracer velocity.

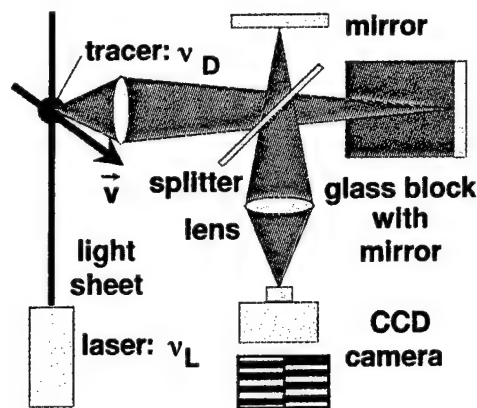


Fig. 2. Principle sketch of the DPV technique

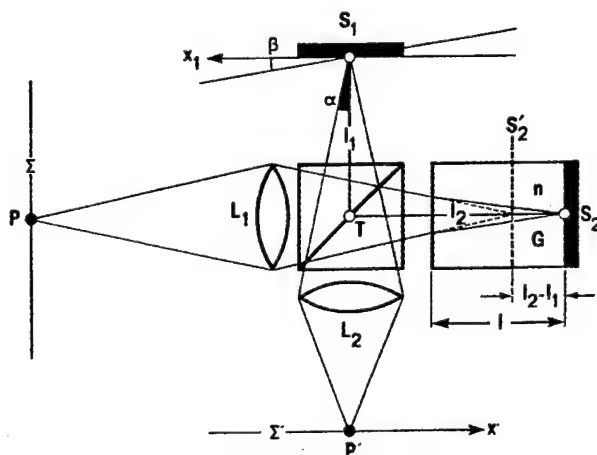


Fig. 3. Michelson interferometer

The Michelson interferometer (fig. 3) consists of a beam-splitter cube T with a semi transparent mirror, the two mirrors S_1 and S_2 and the glass block G between S_2 and T. The scattered light coming from the object plane Σ and passing through lens L_1 is divided by the beam splitter into two components of equal intensity. These two parts are focussed by lens L_1 on S_1 and S_2 respectively. With lens L_2 the image of the object plane Σ on S_1 and S_2 is transferred to the image plane Σ' .

The Michelson interferometer works as a frequency shift detector (spectrometer) and its mechanism is described below. The light intensity I in the image plane Σ' (light interference) depends on the phase difference $\Delta\phi$ between the light waves returning from the two legs (1) and (2) as follows:

$$I = \hat{I} \cos^2 \frac{\Delta\phi}{2}. \quad (2)$$

The phase difference $\Delta\phi$ is defined as a function of the optical path difference $\Delta\phi$, the light source frequency ν_L and the speed of light c :

$$\frac{\Delta\phi}{2\pi} = \nu_L \frac{\Delta\phi}{c}. \quad (3)$$

Differentiation leads to the following expression with λ_0 being the vacuum wavelength of the scattered light:

$$d\left(\frac{\Delta\phi}{2\pi}\right) = \frac{\Delta\phi}{\lambda_0} \frac{d\nu_L}{\nu_L}. \quad (4)$$

In order to obtain detectable variations of $d(\Delta\phi)$ and consequently visible variations dI of the light intensity on the plane Σ' with small Doppler shifts $d\nu_L$, the optical path difference $\Delta\phi$ between the two legs of the Michelson interferometer has to be sufficiently large. For example, by using different glass blocks the following velocities for a fringe shift of one fringe spacing can be obtained:

$\Delta\phi$ [cm]	V [m s ⁻¹]
5.0	772
10.0	386
20.0	193
40.0	96
100.0	39

Tab. 1 Velocity as a function of the optical path difference

2.3 Experimental setup for a rotating disc

The periphery of the disc is illuminated by light from a 1 W Ar⁺-laser from a direction nearly perpendicular to the axis of rotation. The scattered light is observed in the back scattered direction (see principle sketch in fig. 4).

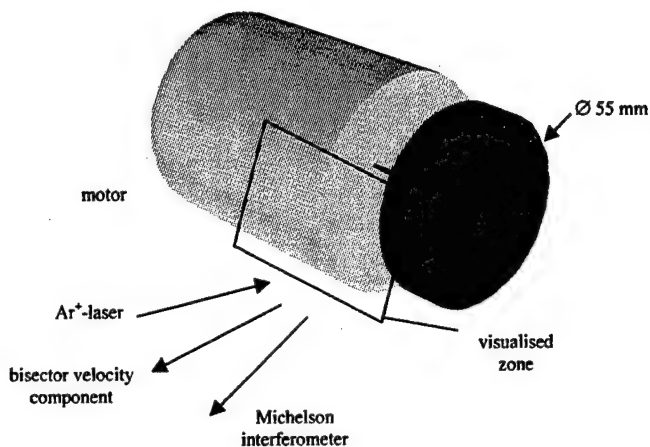


Fig. 4: Setup of the rotating disc

For the rotating disc, the velocity vector of the "scattering surface particles" is tangential to the surface. This tangential velocity vector is composed of a component in the direction the bisector situated the illumination and observation directions (Michelson interferometer) and into a perpendicular part which is of no influence.

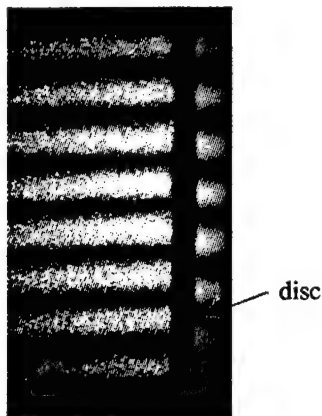


Fig. 5 Interference image with rotating disc

The measured bisector velocity component \bar{v} is, according to equation (1), proportional to the Doppler shift $d\nu_t = \nu_D - \nu_L$ processed by the Michelson interferometer.

3 TREATMENT OF THE INTERFERENCE IMAGE

3.1 Velocity evaluation based on the shift of the fringe system

Generally the light intensity distribution on the object is not homogeneous. In gas flows seeded with particles the variations of the scattered light intensity due to particle density fluctuations can be very large. On the contrary the Doppler shift is very small. In this paper two different techniques for solving this problem are proposed. For the first technique, the interference fringes have been adjusted by turning the mirror S_1 by a small angle β , as shown in figure 3.

Then straight and parallel interference fringes appear in the Doppler picture, as seen in fig. 5. The fringe light intensity variation depends on the $\Delta\phi$ according to the \cos^2 - distribution in equation (2). At $\Delta\phi = \pi, 3\pi, \dots$, the light intensity is nearly equal to 0, forming equidistant dark lines in the fringe system.

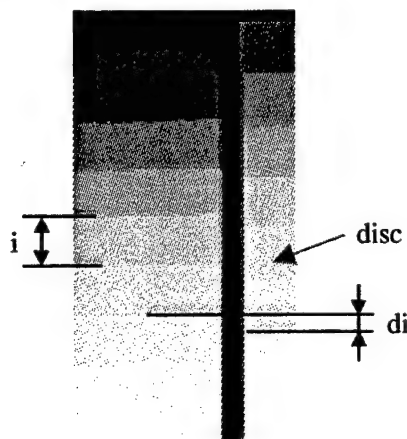


Fig. 6 Treated Doppler picture for the fringe shift detection (right: motionless, left: rotating disc)

At the dark lines, the light intensity I is a minimum and is independent of the intensity \hat{I} of the scattered light. For the evaluation of the fringe Doppler pictures, only the dark lines are considered. This means that only the areas of the Doppler picture which have the smallest light intensity are noninfluenced by the light fluctuations and therefore give exact information about the frequency shift and the tracer velocity distribution in the Doppler picture. Therefore, only the shift of the lines in the middle of the dark fringes has been used to determine the fringe shift "di" which is proportional to $d(\Delta\phi)$:

$$\frac{di}{i} = \frac{d(\Delta\phi)}{2\pi}, \quad (5)$$

where i denotes the unshifted fringe spacing. In order to detect the fringe shift, two Doppler pictures, one showing the rotating disc and the other of the motionless disc, have to be taken into account. Then both pictures are treated in the same way. Beginning in the upper left-hand corner of the images a phase shift $\Delta\phi$ of 2π is added, every time a new pair of dark and bright fringes occurs (fig. 6).

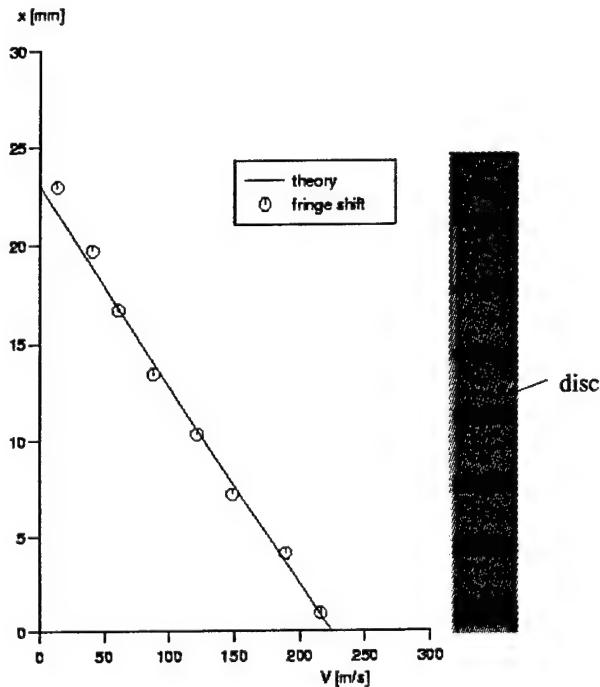


Fig. 7 Evaluation of the velocities for the fringe shift detection (rotating axis: $x = 23$ mm)

The fringe shift is determined by the subtraction of these two images. In figure 7 the result of this technique is presented. A Doppler picture processed in this way only visualizes the considered velocity field discontinuously. Nevertheless, the measured velocities correspond very well to the theoretical values.

3.2 Velocity evaluation based on the light intensity distribution of the fringe system

Two different procedures are here applied in order to evaluate the velocity at each pixel of the CCD Camera. At first each interference system is normalised with the actual light distribution captured by a reference camera. Mismatched depths of field optical distortion caused by lens aberrations, imperfections of the beam-splitters and mirrors, non-uniformity of the pixel distribution and element orientation are factors which make the exact overlay of the interference and reference images very difficult (Meyers [5]). Therefore after every alignment of

the optical system, several images of the calibration card placed in the light sheet plane are recorded.

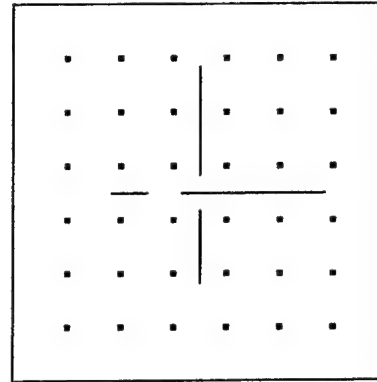


Fig. 8 Calibration card

The calibration card consists of 4 different lines and 36 grid points. The 4 lines were detected with an RLC algorithm developed by A. Schneider [6]. By means of the information concerning the position and the orientation of these lines, the image is correctly aligned. Due to the grid points several sets of linear equations can be established in order to move the recorded grid points of the calibration card from their imaged to their ideal positions. In order to get an accurate transformation of the grey values, an interpolation technique described by Schumacher [7] is applied in order to determine the grey values between the neighbouring pixels.

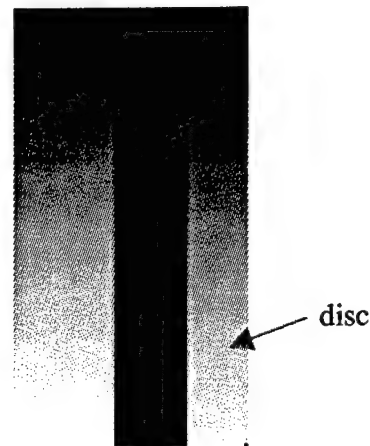


Fig. 9 Treated Doppler picture for the grey value detection (right: motionless, left: rotating disc)

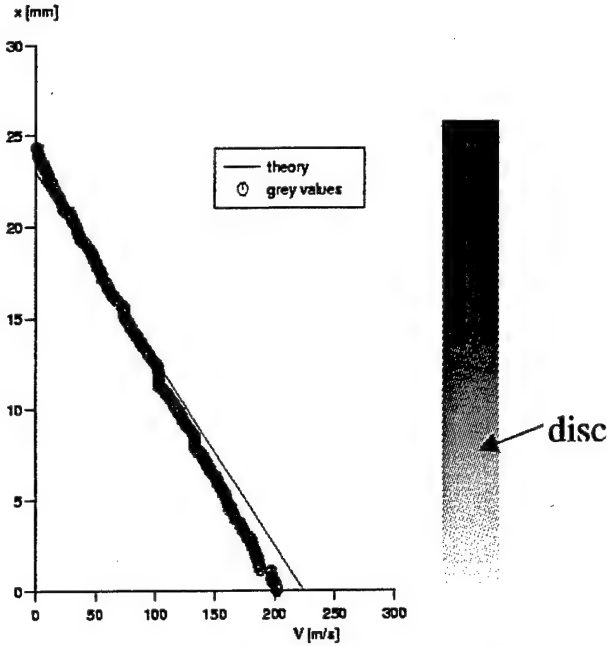


Fig. 10 Velocity distribution for every pixel
(rotating axis: $x = 23$ mm)

In order to avoid problems due to the variation of the light intensities on the interference images, several pictures have been taken in which the fringe system is slightly shifted. In this way the maximal G_{max} and minimal G_{min} grey values for every pixel can be established. This finally leads to the following expression for every grey value:

$$G_{(x,y)} = G_{min} + (G_{max} - G_{min}) \cos^2\left(\frac{\pi \Delta \phi}{\lambda}\right) \quad (6)$$

In order to assume $I_n = \frac{G_{(x,y)} - G_{min}}{G_{max} - G_{min}}$ the equation (6) is transform to:

$$v \Delta \phi = \frac{c}{2\pi} \arccos(2I_n - 1) \pm n \quad n = 1, 2, 3, \dots \quad (7)$$

If the disc remains motionless, the constant n and all other variables of the following equation can be determined:

$$(v_L \Delta \phi)^{ref} = \frac{c}{2\pi} \arccos(2I_n^{ref} - 1) \pm n \quad (8)$$

Finally, assuming a small difference between the laser frequency and the dopplershifted one detected by the Michelson interferometer, the equation can be transformed into:

$$\frac{dv_L}{v_L} = \frac{v \Delta \phi - (v_L \Delta \phi)^{ref}}{(v_L \Delta \phi)^{ref}} \quad (9)$$

In order to avoid problems, if the displacement of the fringes is more than one fringe spacing 2π is added at each point, where $I = 0$, as shown in chapter 3.1. Figure 9 shows the Doppler picture treated in the way described below and figure 10 represents the velocities at each pixel of the image.

3.3 Improvement of data processing

The quality of the electronic results could be improved in a number of ways. For example, the "wash-out effect" of the Doppler picture fringes should be reduced. This means that the contrast C of the Doppler pictures must be improved. The definition for the contrast C is:

$$C = \frac{I_{max} - I_{min}}{I_{max}} \quad (10)$$

The improvement of the contrast can be obtained by limiting the angle α (see fig. 3) to a maximum value of about 4° as described by Oertel et al. [1]. This would allow the image system to work with less noise and improved visibility. To make the resolution better, the camera should zoom an area as small as possible and generate the best pixel resolution available at the moment, e.g. 1024×1024 pixels per sensitive CCD-chip area.

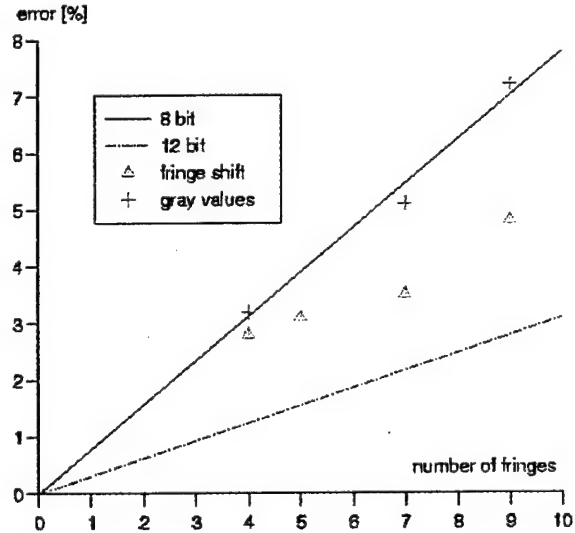


Fig. 11 Mean errors versus number of fringes per image

In figure 11 the errors in the different test cases are shown. The errors for the measured velocities, using the grey value distribution, are more important than for the fringe shift detection. Especially, in the region where the light intensity distribution is near the maximum or the minimum, the errors increase. The line represents the estimated error for a certain number of fringes for an 8-bit

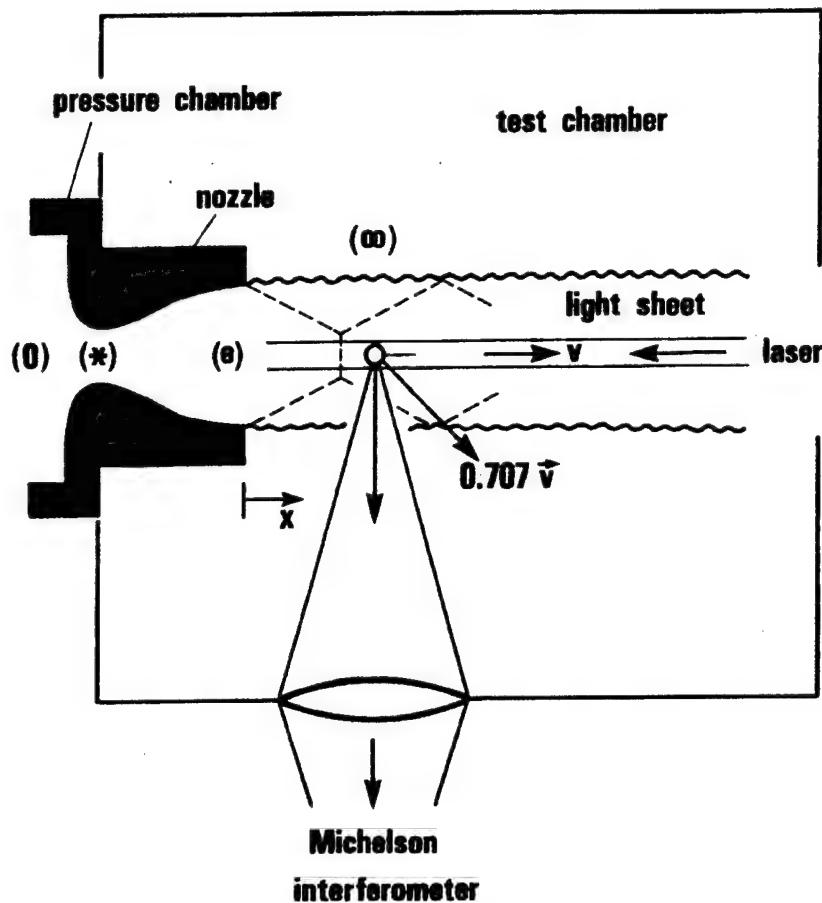


Fig. 12 Schematic presentation of the nozzle

camera with 512×512 pixels. The use of a 12-bit camera can help to considerably decrease the error for the evaluation of the velocities from grey values (dashed line).

4 APPLICATION TO A FREE JET

Fig. 12 shows the experimental setup of a free jet issuing from a nozzle. The nozzle exit diameter was $D_e = 2.5$ mm. The jets are produced by blowing the gas (carbon dioxide) out of a stagnation chamber into the atmosphere. The tracer particles are condensed carbon dioxide particles.

The beam of a 1 W Ar^+ -laser is transformed to a light sheet with a cross-section of $0.5 \text{ mm} \times 15 \text{ mm}$, passing vertically through the longitudinal axis of the jet. The angle between the interferometer and the flow direction is adjusted to 90° . A glass block with a length of 180 mm and a refractive index of $n = 1.52$ is used.

Figure 13 represents the Doppler pictures taken at the nozzle exit at a pressure of $p = 20$ bar in the stagnation chamber. The image (fig. 14) taken by the reference camera shows the shocks generated by the underexpansion. Unfortunately, due to the shock strength, the temperature increases and the carbon dioxide particles disappear in a small region behind the shock wave. Figure 15 shows the Doppler picture normalized by the reference image. Both evaluation techniques are applied in order to determine the velocities (fig. 16). On the right-hand side, due to the shift of the fringe system, the velocity profiles could be seen directly. On the other side, the technique based on the grey values, is applied. The velocities determined in this way on the center line in figure 17 correspond very well to the one-dimensional theory. On the right-hand side the velocity distribution, based on the fringe shift detection, is shown along different horizontal lines. The velocities along the center line, which are very low behind the shock, increase. In contrary the velocities close to the free jet border decrease.

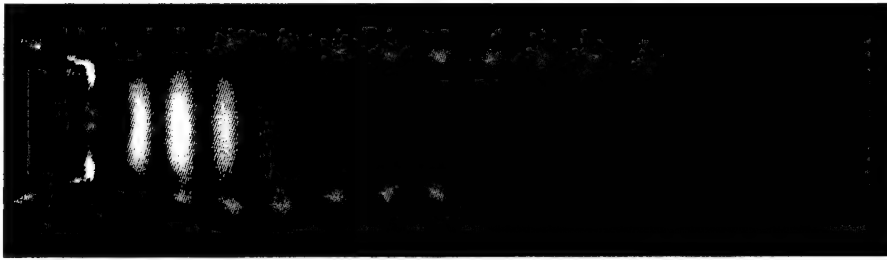


Fig. 13 Interference image of the free jet



Fig. 14 Light intensity of the flow field

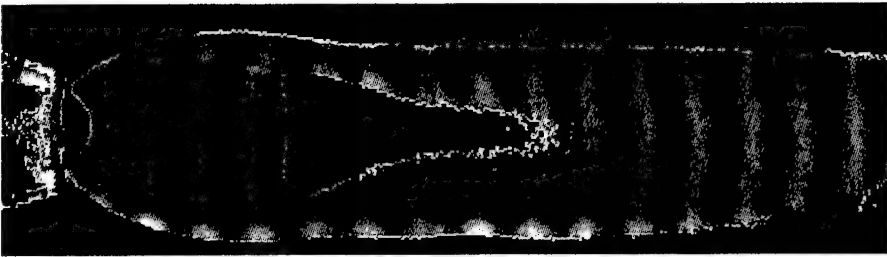


Fig. 15 Normalised interference image

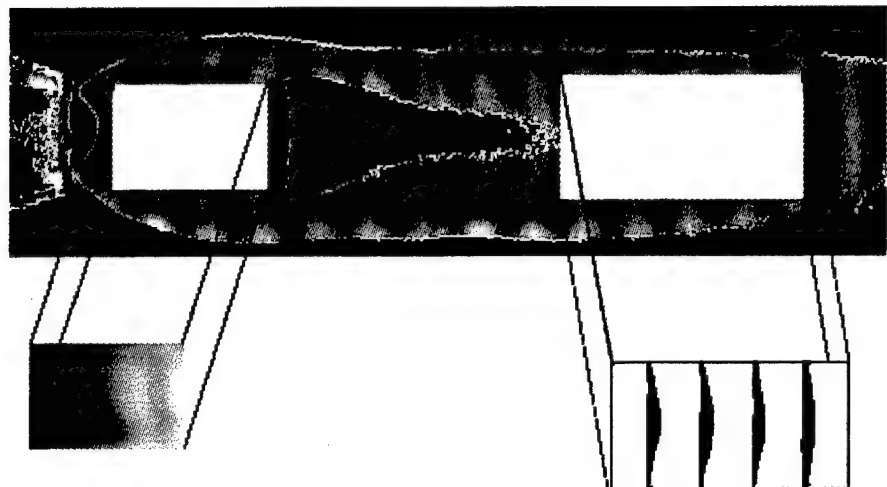


Fig. 16 Evaluation of the velocities
(left: grey values, right: fringe shift)

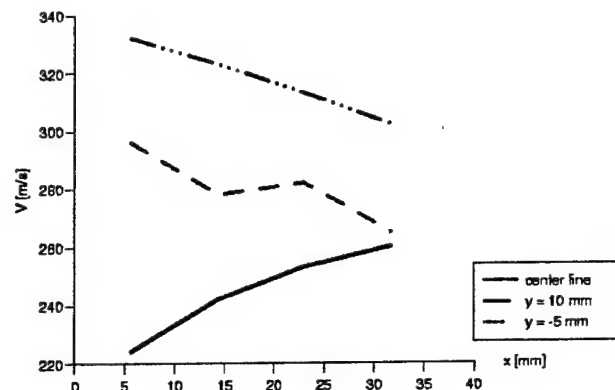
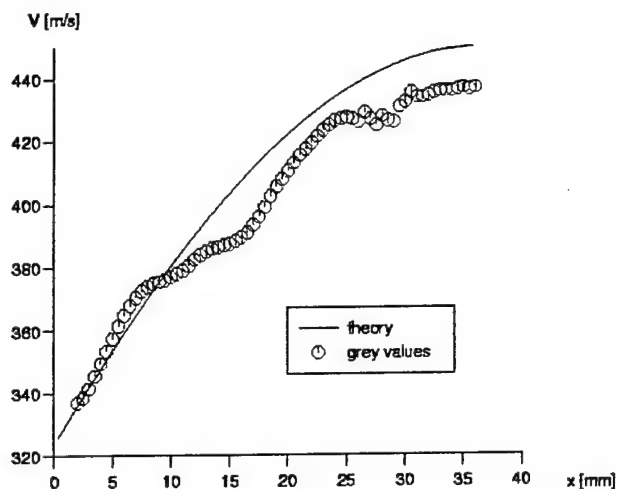


Fig. 17 Velocities along different horizontal lines
(left: velocity distribution on the center line, right: evaluation of the velocities for the fringe shift detection)

5 CONCLUSION

The Doppler Interference Picture Velocimetry (DPV) technique began in 1981. The method, which uses the shifts of interference fringes for flow velocity visualization, gives us the possibility of becoming in the dark fringe region independent of varying light intensities resulting from the inhomogeneous distribution of tracer particles. Therefore, only a discontinuous interpretation of the Doppler pictures is possible.

The concept, using the grey values, is a very powerful tool allowing to obtain information at any point of the plane crossing the flow. In future a 12-bit camera will help to increase the accuracy considerably. This work will be continued with the use of DPV for various flow phenomena, e.g. free jets, shocks and wakes behind bodies.

ACKNOWLEDGEMENT

The authors wish to thank A. L. Schneider and E. Bacher for their help and useful suggestions throughout this work.

REFERENCES

- [1] Oertel H., Seiler F., George A., Visualisierung von Geschwindigkeitsfeldern mit Dopplerbildern. ISL-report R 115/82, 1982
- [2] Seiler F., Oertel H., Visualization of velocity fields with Doppler-pictures. Proc. of the 3rd Int. Symp. on Flow Visualization, Ann Arbor, Michigan, USA, 1983
- [3] Seiler F., Srulijes J., George A., A Doppler-picture camera for velocity field visualization. Proc. of the 12th Int. Congress on Instrumentation in Aerospace Simulation Facilities, Williamsburg, VA, USA, 1987
- [4] Seiler F., Srulijes J., George A., Principles of laser velocimetry with Doppler-pictures. Proc. of SPIE's 36th Annual Int. Symp. on Optical and Optoelectronic Science and Eng., San Diego, California, USA, 1991
- [5] Meyers J. F., Doppler Global Velocimetry the next generation, AIAA 92-3897, 1992
- [6] Schneider A. L., Konturverfolgung und Merkmalsgewinnung von Binärbildern mit Hilfe des RLC-Verfahrens, Diplomarbeit, Fachhochschule Ravensburg-Weingarten, 1987.
- [7] Schumacher D., Graphics Gems III; pp.8, Oxford University Press, 1996

MEASUREMENT TECHNOLOGY OF THE IMPACT OF ALUMINA LIQUID PARTICLES ON A HOT SURFACE

Escure C., Vardelle M., Grimaud A., Fauchais P.

Université de Limoges, Laboratoire SPCTS (Science des Procédés Céramiques et Traitements de Surface),
UMR 6638

ABSTRACT

The aim of this study, carried out in the frame of the ASSM (Aerodynamics of Segmented Solid Motors) research program, is a better understanding of the phenomena that govern the interactions between liquid alumina particles and a hot surface or liquid alumina film. To achieve it, a complex experimental device has been designed and built.

- In a controlled argon atmosphere chamber are set two plasma torches and a reclining substrate. This set-up allows the use of carbon-carbon substrates. The first plasma torch produces molten alumina particles, and the second one heats the substrate up to 2300K.

- An optical diagnostic characterizes the in-flight parameters of a single particle : its size and velocity by PDA (Particle Doppler Anemometry) and its temperature by two-color fast (100 ns) pyrometry.

- An imaging technique monitors the impact mode : splashing, deposition or rebound. For the latter the rebounding angle and velocity can be measured. A laser beam is used for visualization of trajectories in a narrow wavelength band-pass.

For each droplet, its size, velocity and temperature are measured and impact is observed. The goal is to investigate how the impact mode is influenced by these parameters.

I - INTRODUCTION

The in flight propulsion of the Ariane V rocket is produced by the very powerful Vulcain engine. However, at take off, the two enormous propellant boosters, constituting the first stage of the rocket, furnish more than 90% of the thrust. Each of them contains 230 tons of propergol - giving the boosters name : P230 - and produces a thrust of about 5300kN.

In order to increase the engine performance, the propergol is enriched with aluminum : an amount of 18 to 20 wt.% of aluminum in the propellant allows increasing the specific impulsion of 6 to 8%.

Nevertheless, during the combustion of the propergol, the aluminum is oxidized and alumina is produced. According

to the high temperature in the booster, the alumina is in a liquid state. The liquid alumina particles impact on the internal wall of the engine, and they form a puddle on the rear part of the booster. After the complete burning of the propellant, about two tons of alumina are deposited in each booster. This confirms the presence of an important puddle of alumina that may be harmful to the working of the engine due to different phenomena that may appear :

- massive ejection of matter leading to a decrease of the thrust

- movement of the puddle
- dissymmetry between the two engine
- overload

...

Many numerical studies [1,2] try to simulate this phenomenon, yet they face the problem of the alumina droplets' behavior impacting a surface. The prediction of the impact behavior has to be supported by experimental studies. Actually, many studies have already been done, and others have been initiated in the ASSM program concerning the impact phenomenon, but none of them deals with alumina. Our goal is thus to study the behavior of an alumina droplet impacting on a solid or liquid surface.

II - THE PARTICLE-WALL INTERACTION PHENOMENON

II.1 - The impact theory and the dimensionless numbers

The impact phenomenon of a liquid particle on a solid or liquid surface is quite complex. Indeed, the particle's behavior depends on many parameters that are either intrinsic or extrinsic :

- the first ones correspond to the characteristics of the particle at impact : size, velocity, but also density, viscosity, surface tension... that depend themselves on other parameters such as the particle temperature.

- the others are mainly those of the impact surface : state (liquid or solid), temperature, roughness...

The phenomenon has to be considered from an energetical point of view [1]. When the droplet impacts the surface, a little part of its kinetic energy is lost, but the main part is changed into deformation energy. It is this residual energy that has to be considered :

- if the deformation is weak and if the residual energy is sufficient, the droplet will recover a spherical shape under the effect of surface tension forces and will leave the surface : a rebound occurs.
- if the deformation of the droplet due to the impact is very important, the energy is not high enough for the droplet to recover a spherical shape and leave the substrate : it forms a deposit.
- if the droplet's deformation is too important, the surface tension forces will not be sufficient to keep the cohesion of the particle. It breaks into several droplets that leave the surface : it is the splashing phenomenon.

In order to assure a better understanding of these phenomena and maybe to predict the behavior of an impacting droplet, several dimensionless numbers are used :

The Reynolds number :
$$Re = \frac{\rho_p \cdot d_p \cdot v_p}{\mu_p}$$

The Weber number :
$$We = \frac{\rho_p \cdot d_p \cdot v_p^2}{\sigma_p}$$

The Sommerfeld parameter :
$$K = \sqrt{We} \sqrt{Re}$$

Where the following parameters are related to the impacting particle :

- ρ_p : density
- d_p : diameter
- v_p : incident normal velocity
- μ_p : viscosity
- σ_p : surface tension

II.2 – Interaction between a droplet and a cold substrate

Mundo, Sommerfeld and Tropea [3] are among the first who have studied this phenomenon. The experiment consisted in impacting water or ethanol droplets onto a dry, cold surface. These particles had diameters between 60 and 150 μm and velocities between 12 and 18 m/s. The incident angle could vary. The deposition and splashing phenomena occurred. The correlation they found led them to the definition of the Sommerfeld parameter K : they determined that the transition between deposition and splashing always occurred for a K number equal to 57.7.

A more recent study has been made by Lavergne and Platet [4], in near experimental conditions using ethanol droplets on a copper substrate. Thanks to this experiment, a new particle behavior after the impact has been observed : the rebound. The authors have also used the Sommerfeld parameter for their correlation and they have shown that the limit between rebound and deposition occurred for $K=3$. Moreover, their experiment has

confirmed the value of 57.7 for the deposition-splashing boundary.

II.3 – Interaction between a droplet and a hot surface

Another important parameter has to be taken into account when considering the impact of a droplet on a hot surface : the surface temperature. In impact phenomena, we can talk about high temperature for the substrate when it is above the boiling point of the particle's material. When the substrate temperature exceeds the droplet's boiling point, it may reach the Leidenfrost temperature where the droplet is partially vaporized when impacting the hot surface. Thus, a fine vapor film is formed on which the droplet may rebound more easily.

II.4 – Impact on a liquid film

In this case, the liquid film may react like the vapor layer : it damps down the droplet, thus rebounds may also be observed. Nevertheless, it is usually difficult to distinguish between the case in which the droplet rebounds on the liquid film and that in which liquid is detached from the film by the impact and forms new droplets. This mechanism has been observed by Engel [5] who also showed that the mass of the resulting droplet after the impact might be 2 to 4 times that of the incident droplet. This demonstrates that liquid has been pulled out of the film. This phenomenon is called « spattering ».

Another study made by Platet and Lavergne has allowed characterizing this phenomenon [6]. Using the Sommerfeld parameter, they showed that the boundaries between the different impact mechanisms are slightly shifted with the film thickness, and that spattering occurred for $K \approx 35.5$.

II.5 – The particle-wall interaction in our experimental conditions

For these experiments, we use alumina droplets and the substrate is usually a carbon-carbon composite (or stainless steel for the first experiments) which temperature is about 2000K. However, the substrate has to be considered as "cold", indeed its temperature is below the boiling temperature of alumina (about 3800K), and so below the alumina Leidenfrost temperature. Nevertheless, a vapor film may be present at the droplet-wall interface, but it is not the result of the Leidenfrost phenomenon. It may be due to the presence of a vapor cloud that usually surrounds a plasma sprayed particle, or to a possible degassing of the composite substrate.

On the assumption that alumina reacts like other liquids already tested as seen before (water, ethanol), the aim is to check whether the Sommerfeld parameter K, which gives excellent correlations for these liquids, may be applied to describe the impact behavior of alumina. This parameter may be expressed with the characteristics of the liquid material :

$$\Rightarrow K = \frac{\rho_p^{3/4} \cdot d_p^{3/4} \cdot v_p^{5/4}}{\sigma_p^{1/2} \cdot \mu_p^{1/4}}$$

The values of ρ_p , μ_p , σ_p used are the following one (Glorieux [7]).

$$\rho_p = (3,15-1,12 \cdot 10^{-4} \cdot T) \cdot 10^3 \text{ Kg/m}^3$$

for $(2300 < T < 3200K)$ [8]

$$\mu_p = 6.83 \times 10^{-8} \times T \times \exp\left(\frac{110 \times 10^3}{8.32 \times T}\right) \text{ Pa.s}$$

for $(2300 < T < 2550K)$ [9]

$$\sigma_p = (1563-0,5 \cdot T + 43,2 \cdot 10^{-6} \cdot T^2) \cdot 10^{-3} \text{ N/m}$$

for $(2300 < T < 3000K)$ [10]

Thus, the Sommerfeld parameter of an alumina particle depends only on the size, the velocity and the temperature of the droplet. These parameters will be measured prior to the impact.

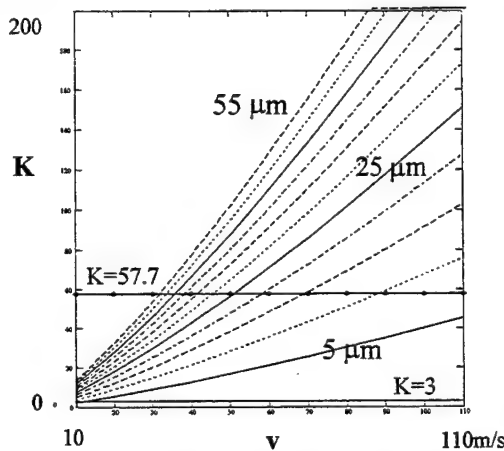


Figure 1 : evolution of K with the particle velocity for $5 < d < 55 \mu\text{m}$ ($T=2500K$)

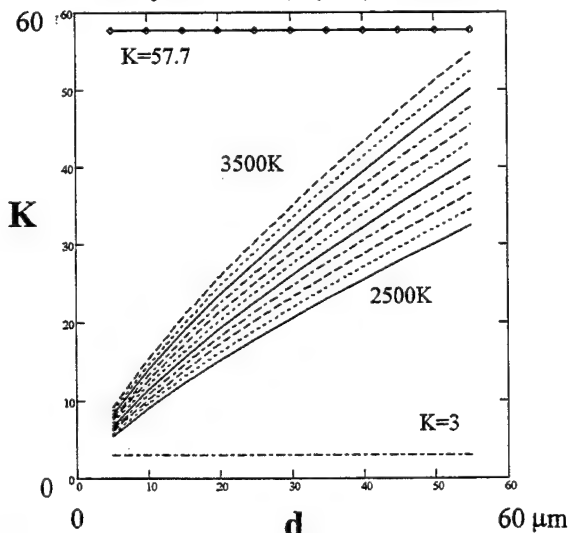


Figure 2 : evolution of K with the droplet size for $2500 < T < 3500K$ ($v=20 \text{ m/s}$)

For a specific value of temperature, as the velocity is multiplied by 10, K is multiplied by about 20, and when the diameter is multiplied by 10, K is multiplied by 5. For a specific value of the diameter, K is only multiplied by 1.5 when the temperature is increased of 1000K.

Thus the Sommerfeld parameters calculated with our experimental conditions (fig.1 and 2) increases with, by order of importance, the particle velocity, its size, and its temperature (this last point can be seen in figure 2 : the different curves are very close).

III - EXPERIMENTAL SETUP

III.1 - The droplet generator

In order to generate liquid alumina droplets, a plasma torch is used. This device has been chosen because of the high energy density provided ($>10^{10} \text{ W/m}^3$).

The principle of a plasma torch is presented in figure 3. An electrical arc strikes between the conical-shaped cathode made with thoriated tungsten and the copper nozzle-shaped anode surrounding the cathode. As the gas is blown through this electric arc, it is ionized and a plasma is created. The plasma exits from the nozzle at a very high speed, less than 2000 m/s, and at a temperature higher than 10000K. The created environment is very powerful, and ideal for the melting of nearly all kind of materials including refractory ones. The solid alumina particles are introduced into the plasma at the exit of the nozzle where they are quickly melted and accelerated.

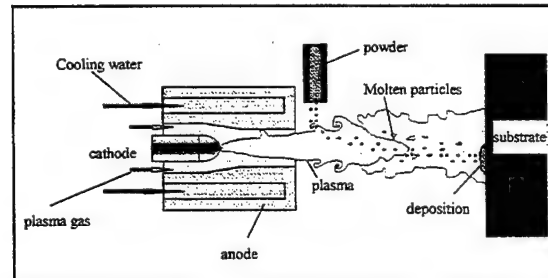


Figure 3 : principle of a plasma torch

The plasma environment is not homogeneous, important velocity and temperature gradients are present, mainly radially. Moreover, the fluctuations of the arc root may induce voltage variations and thus power variations resulting in a fluctuations of the isotherms (see fig. 4 and 5).

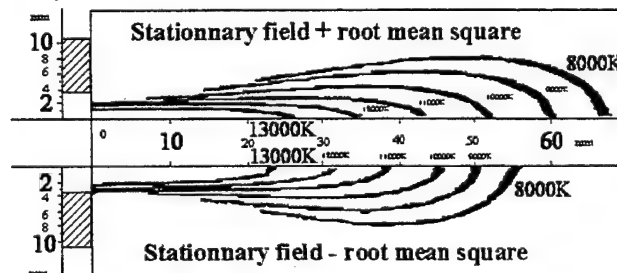


Figure 4 : temperature gradients in a plasma jet : (emission spectroscopy measurements)

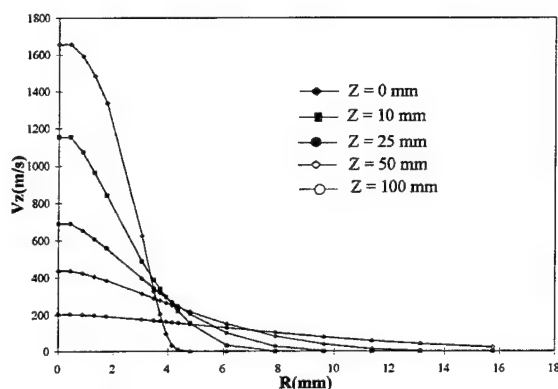


Figure 5 : example of radial evolution of the axial velocity of the plasma jet

For a specific value of the distance Z from the nozzle exit, the greatest velocity is obtained on the torch axis. However, the farther from the axis, the weaker is the plasma velocity. Finally, the plasma extends when moving away from the nozzle exit.

The two main characteristics of the droplets are their velocity and temperature. They are influenced by many parameters among which the particles' size, morphology and density but also the plasma flow parameters. These characteristics of the plasma depend on many parameters : the plasma composition (Ar, N₂, Ar-N₂, Ar-He, Ar-H₂...), the ratio of each gas, their mass flow rate, the arc current, the surrounding atmosphere... The following curves (fig. 6, 7) have been obtained by a simulation program developed in the laboratory [11]. The experimental conditions are :

- particle diameter = 37 μ m
- plasma mixture : Ar-H₂ (in the figure, 45/15 for example means 45 slm of Argon and 15 slm of hydrogen)
- nozzle internal diameter = 7 mm
- ambient atmosphere : air
- arc current : 300 – 600A

The particle velocity increases mainly with the arc current and the total gas mass flow rate (see fig. 6).

The particle temperature increases with the hydrogen volume percentage and the arc current (see fig.7). Yet, the main factor is the hydrogen volume percentage according to the corresponding increase of the thermal conductivity and heat transfer. Above 80mm, the temperature gap between the different experimental conditions is only 300K, when the velocity gap is about 200m/s. The available velocity range is wider than the particle temperature range. These results show that plasma torch is the well adapted tool for studying the various impact modes. Indeed, the velocity has a greater influence than the temperature on the Sommerfeld parameter (cf. § II.5). Another important parameter is the surrounding atmosphere composition : if the ambient gas is argon, the obtained plasma jets are longer and wider than those obtained in atmospheric plasma spraying. Thus the energy transferred to the particles is more important, and the droplets are hotter and faster.

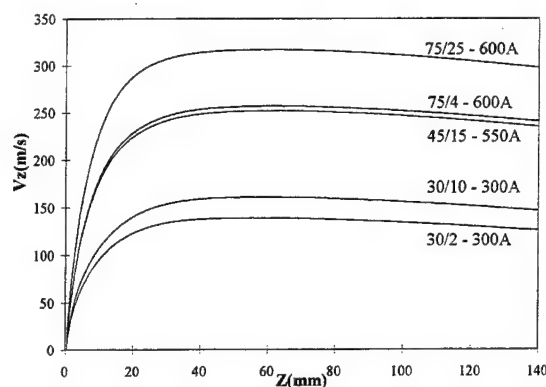


Figure 6 : axial evolution of the particle velocity for different plasma conditions along a mean trajectory

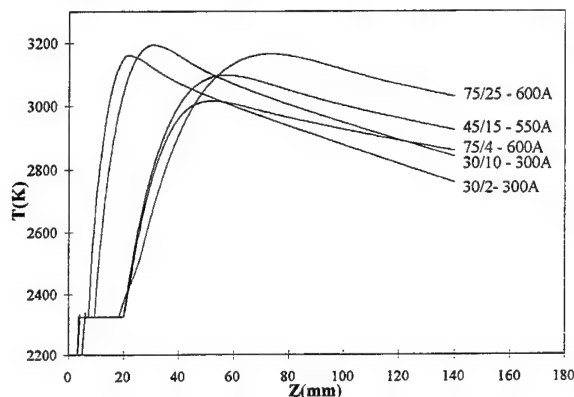


Figure 7 : axial evolution of the particle temperature for different plasma conditions along a mean trajectory

In our experiment, it is necessary to work under inert atmosphere, such as argon, to avoid oxidation of the carbon-carbon substrate. The plasma torch and the substrate are placed into a controlled atmosphere chamber. Moreover, we wish to work using a hot surface (about 1500-2000K) or a liquid film. In order to control this temperature independently of the plasma flow, a second plasma torch has been set in the chamber.

III.2 - Measurement device

Our goal is to observe the impact of a droplet of which we have previously determined the size, velocity and temperature (see fig.8).

III.2.1 – Velocity and size measurement

The Phase Doppler Anemometry method (PDA method) is used. This method is based on the Doppler effect on an alumina droplet that diffuses light as it crosses a system of interferential fringes (fringe spacing : 12 μ m). The experimental device is composed of two elements : an emission device with an argon laser ($\lambda = 514.5$ nm) and a detection device to monitor the diffused light. This one includes two optical heads equipped with optical fibers and filters to eliminate parasite light emitted by the plasma

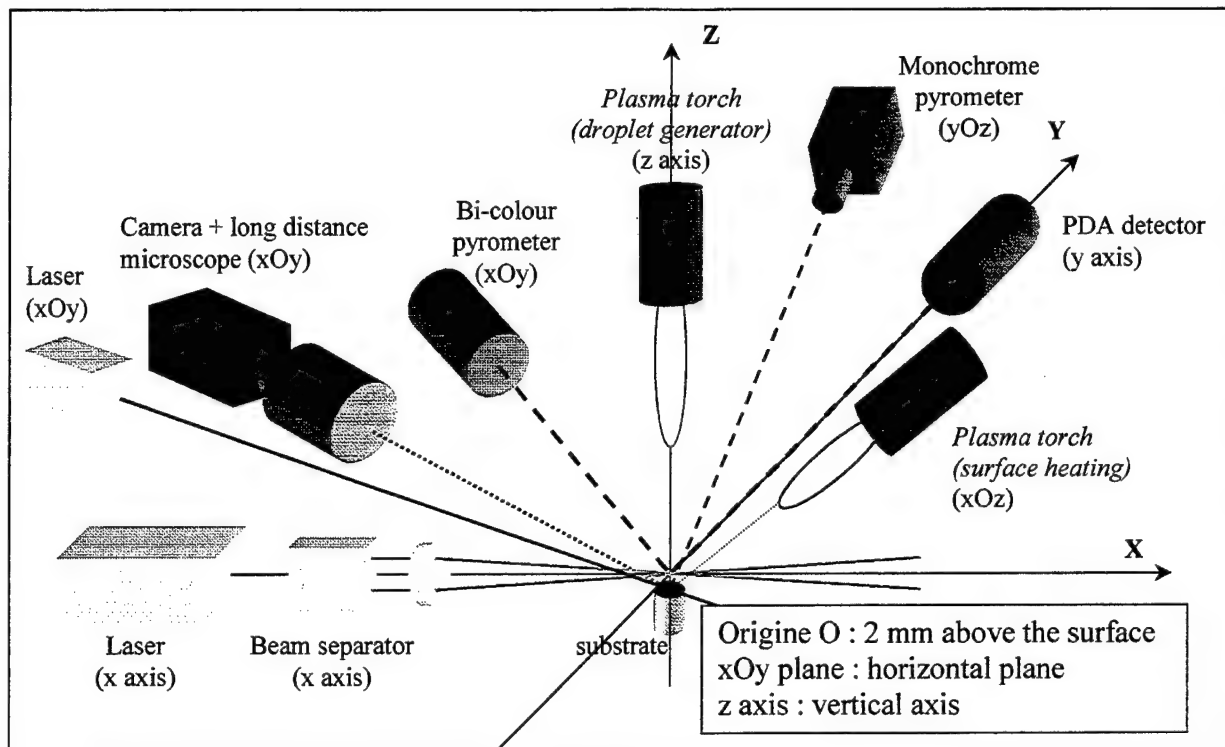


Figure 8 : the experiential set-up

itself or by its reflections on the substrate. The two luminous signals are sent to photomultipliers.

The angle between the incident laser beams and the detector has to be about 135°. The working distance of the detector is 400 mm, imposed by the size of the spraying chamber.

The measurement volume can be assimilated to a cylinder of 400µm in diameter and 1.5mm in length (fig.9).

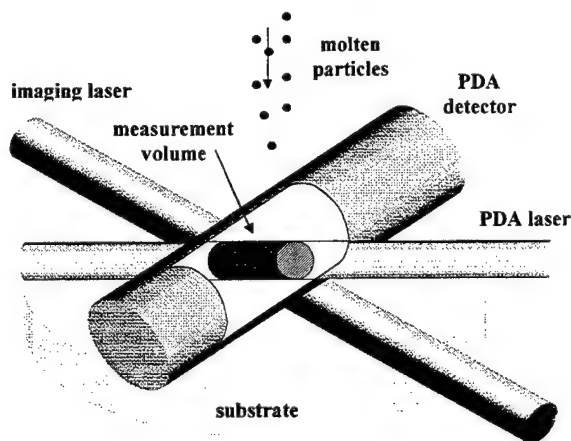


Figure 9 : The detection area

The Doppler bursts created by the photomultipliers are filtered between 5 and 50 MHz, which correspond to a velocity between 45 and 450 m/s. A numerical signal is then created using an oscilloscope connected to a computer via an IEEE bus. The data acquisition software performs a Fourier transformer and yields the cross

spectral density. The signal frequency is then determined (peak in the power density function) as well as the phase (ratio of the imaginary to the real part of the position of the peak-frequency). The particle velocity is calculated from the signal frequency.

The phase displacement $\Delta\Phi$ between the two signals is directly a function of the particle diameter according to the following relationship :

$$\frac{\Delta\Phi}{d} = \frac{\pi \cdot n_c}{\lambda_l} \times 2\Delta$$

$\Delta\Phi$: phase displacement (in degrees)

d : particle diameter

n_c : refraction factor of the environment = 1

λ_l : laser wavelength = 514.5nm

Δ : constant function of the geometrical parameters of the experimental set-up

III.2.2 - Particle temperature measurement

The particle temperature prior to the impact is measured thanks to a two color fast pyrometer (resolution time : 100ns). The pyrometer principle is based on the analysis of the thermal radiation emitted by the molten particle. It is focalized at about 1.5 mm above the impact surface. The optical signal collected is transmitted to a monochromator by an optical fiber. The signal is then filtered at two wavelengths (632.8 and 832.8 nm) and the two resulting signals are sent to two photomultipliers. The output signals are filtered, amplified and sent to an oscilloscope where they can be visualized.

The signals collected are function of the luminous power Ψ emitted by the liquid droplets :

$$\Psi(\lambda, T, \Sigma) = \Sigma \cdot K \cdot C_1 \cdot \varepsilon(\lambda, T) \cdot \lambda^{-5} \cdot (\exp(\frac{C_2}{\lambda \cdot T}) - 1)^{-1}$$

Ψ : luminous power (W)

λ : wavelength (m)

T : temperature (K)

Σ : emitting surface (m²)

K : constant of the optical and electrical line

$C_1 = 3.741 \cdot 10^{-16} \text{ W.m}^2$

$C_2 = 1.4388 \cdot 10^{-2} \text{ m.K}$

ε : material emissivity

The ratio of the two signals is calculated in order to eliminate geometrical, optical and electrical parameters. Considering that molten alumina behaves like a gray body, it can postulated that the alumina emissivity is quite the same at the two considered wavelengths. The ratio depends therefore only on the particle temperature. In a practical way, the particle temperature is calculated by :

$$T = C_2 \frac{\lambda_1 - \lambda_2}{\lambda_1 \cdot \lambda_2} \cdot \frac{1}{\ln(R(T)) + 5 \cdot \ln(\frac{\lambda_1}{\lambda_2})}$$

Nevertheless, the correlation made after the calibration of the pyrometer has shown that the alumina temperature might be estimated with an excellent accuracy by a linear expression. Thus, in the calculation software, this more simple linear expression is used.

$$T = A \cdot R(T) + B \quad \text{with} \quad \begin{matrix} A = 666.9 \\ B = 1174.5 \end{matrix}$$

III.2.3 - Surface temperature measurement

The surface temperature control is made thanks to a commercial monochromatic pyrometer (spectral response : 4.80 - 5.30 μm). The captor is an electro-optical device that collects the infrared energy emitted by an object. The angle between the pyrometer head and the horizontal plane is 40°. This allows to determine the surface temperature on a horizontal substrate, but also on a surface sloped towards the pyrometer. The distance between the pyrometer and the substrate is about 500mm. The pyrometer aims the surface through a window made with fluorine calcium. The infrared energy received by the pyrometer head is processed by a lock-in amplifier. The surface temperature is then calculated, taking into account the material emissivity, and displayed. The response time is about one second.

III.2.4 - The imaging set-up

In order to visualize the impact of a liquid alumina droplet on a substrate and to determine the impact mode, we have to use a complex imaging device. It includes :

- a fast CCD camera
 - 12 bits dynamic at 12.5MHz readout frequency
 - resolution : 1280*1024 pixels
 - exposure/delay time : 1ms ... 1000s
 - multiple exposure possibility
 - Peltier cooling

- this camera is controlled by a computer via an interface-board.

- a long distance objective

Because of the chamber size, the working distance of the camera is about 400mm and moreover, the monitoring area is weak (about 500 μm). A long distance microscope has to be used (maximum magnification : 80 times).

- a lighting device

As the radiation of one liquid alumina particle is very weak, it is difficult to observe droplets directly. They are lit thanks to a blue laser beam ($\lambda=488\text{nm}$). The minimum laser power required to light the particles is about 2W. Furthermore, the camera may be equipped with an optical filter which working wavelength is that the laser, subduing the parasite plasma light.

In order to observe the impact phenomenon, the axis of the camera has to be in the surface plane and stay in this plane when the target is rotated (to obtain impact with an incident angle below 90°). Thus the camera axis has also to be the substrate rotating axis, tangential to the impact surface. The laser beam axis must be as close as possible to this axis. The angles between the two axis are about a few degrees.

III.2.5 - Synchronization

It is based on the passing of the particle through the measurement volume of the PDA device. One of the Doppler bursts is sent to a timing device. If the signal exceeds the minimum threshold, a 5V TTL signal is created. This pulse is sent to triggers of the two oscilloscopes (velocity and size, and temperature measurements) and to the camera acquisition card.

For only the particle triggering the set-up, are obtained the impact image on the computer, the speed and size signal on the first oscilloscope and the temperature signal on the second oscilloscope. These signals are immediately sent to a second computer where they are processed in order to obtain the desired parameters.

IV - FIRST RESULTS

The results presented here are given as examples of the device possibilities, mainly concerning the imaging point of view.

Experimental conditions :

- torch parameters : those given in section III.1
- substrate : stainless steel
- spaying distance : 100mm
- the second plasma torch is off. That means that the surface temperature is about 600K.

The exposure time is 200 μs .

IV.1 - Typical result example

The figure 10 presents the two voltage temperature signals produced by a single particle passing through the detection area of the pyrometer.

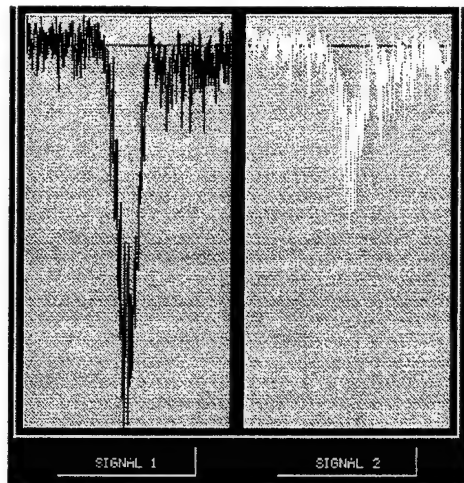


Figure 10 : typical temperature signal

The size and velocity data are stored and introduced in this program for viewing. In this case, the particle characteristics are :

$$v = 99 \text{ m/s}$$

$$d = 33 \text{ }\mu\text{m}$$

$$T = 3061 \text{ K}$$

The corresponding Sommerfeld parameter is $K=224$.

The photograph produced by the corresponding particle passing through the detection area is given in figure 11. The particle can be observed, but it is quite difficult to understand its behavior, even if, according to its Sommerfeld parameter, we can suppose that the droplet splashed on the surface.

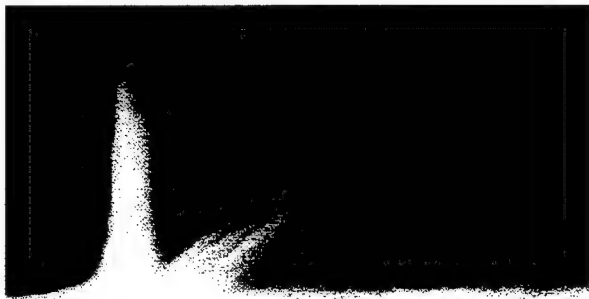


Figure 11 : example of impact

IV.2 - Different particle impact behaviors

• rebound example

This case has been obtained with an Argon plasma (less powerful than an Ar/H₂ one)

If the particle trajectory (see fig. 12) seems to become bigger after rebounding, this is only due to the fact that the



Figure 12 : example of rebound

rebound does not happen in the camera focalization plane (perpendicular to the camera axis because of the weak optical depth).

The particle parameters measured are :

$$v = 123 \text{ m/s}$$

$$d = 4 \text{ }\mu\text{m}$$

$$T = 2000 \text{ K}$$

The droplet behavior (rebound) may be explained by the weak particle temperature. This low temperature might be a direct consequence of the low size of the droplet. A little droplet has a low thermal inertia and cools quickly when it is far from the nozzle exit. However, the particle may be in a semi-molten state by reason of the supercooling phenomenon. Thus, according to this particular state and to its low size, the particle may rebound (because of the uncertainty concerning the particle state, the K parameter is not calculated).

• deposition example

After the impact, no clear particle trace is observed (see fig. 13). We can suppose that the droplet has been deposited on the substrate.

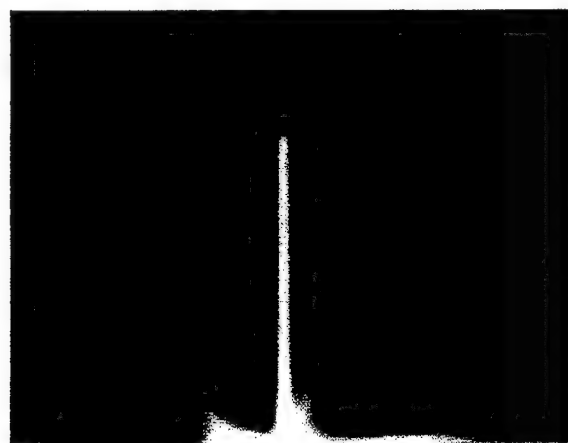


Figure 13 : example of deposition

• splashing example

On the photograph shown in figure 14, the end of the incident trajectory can be observed as well as numerous



Figure 14 : example of splashing

traces after the impact. These traces should correspond to several ejected droplets : a splashing occurs. This is confirmed by the particle parameters :

$$v = 104 \text{ m/s}$$

$$d = 76 \text{ }\mu\text{m}$$

$$T = 2990 \text{ K}$$

These parameters correspond to a splashing behaviour according to the Sommerfeld's model : $K=430$.

V - CONCLUSION

The experimental set-up is quite complex. In particular, working under a controlled atmosphere lead to setting the substrate and the two plasma torches in a closed chamber. Moreover, the detection devices are consequently far from the working area (about 400mm), which complicates a little more the adjustment of the laser beams and of the detection devices, which are already complex and that must be very precise.

The problem of the synchronization of the different detection elements is also quite critical. For a result to be valid, for one particle, the anemometry and the pyrometry signals have to be "correct" as well as the image. Nowadays, the triggering is only made on the anemometry signal. It might be necessary to trigger on a coincidence signal corresponding at once to a correct anemometry signal and a correct pyrometry signal.

Nevertheless, some experimental results have already been obtained. Experiments have to be multiplied in order to get statistical results and make correlations.

ACKNOWLEDGEMENTS

This work has been carried out with the support of the CNES (Centre National d'Etudes Spatiales) the SEP (Société Européenne de Propulsion) and the ONERA (Office National d'Etudes et de Recherches Aeronautiques).

REFERENCES

- [1] N. CESCO, *Etude et modélisation de l'écoulement diphasique à l'intérieur des propulseurs à poudre*, Thèse de doctorat, Ecole Nationale Supérieure de l'Aéronautique et de l'Espace, Novembre 1997
- [2] T. PEVERGNE, P. LE HELLEY, *Simulation des impacts de particules et du dépôt dans le MPS P230*, 3^{ème} Colloque R&T, « Ecoulements internes en propulsion solide », Vol 2, pp.201-210, Poitiers, mars 1998
- [3] C. MUNDO, M. SOMMERFELD, C. TROPEA, *Experimental studies of deposition and splashing of small liquid droplets impinging on a flat surface*, ICLASS-94, Rouen, Paper I-18, 1994
- [4] G. LAVERGNE, B. PLATET, *Etude de l'impact de gouttes sur une paroi chauffante*, Rapport final, N°1/2401/CERT/DERMES, 1991
- [5] O. ENGEL, *Initial Pressure, Initial Flow Velocity, and the Time Dependence of the Crater Depth in Fluid Impacts*, Journal of Applied Physics, vol 38, 10, pp 3935-3940, 1967
- [6] B. PLATET, G. LAVERGNE, *Caractérisation des phénomènes d'interaction goutte-paroi*, 3^{ème} Colloque R&T, « Ecoulements internes en propulsion solide », Vol 2, pp. 231-242, Poitiers, mars 1998
- [7] B. GLORIEUX, J.C. RIFFLET, C. PULVIN, F. MILLOT, J.P. COUTURES, *Propriétés thermodynamiques de l'alumine liquide*, Note technique NT1-PhC-ASSM6 CRPHT/CNRS, mai 1997
- [8] COUTURES J.P., RIFLET J.C., FLORIAN P., MASSIOT D., *Rev. Int. Hautes Temp. Refract.*, Fr, 29, 123, 1994
- [9] URBAIN G., *Rev. Int. Hautes Temp. Refract.*, Fr, 19, 55, 1982
- [10] SHPIL'RAIN E.E., YAKIMOVITCH K.A., TSATSARKIN A, *High temp; High Pressure*, 11(5), 894, 1974
- [11] S. BERNARD, *Etude numérique de l'accélération et du chauffage d'une particule injectée dans un écoulement plasma*, Rapport de DEA de l'université de Limoges, 1997

3-Component-Doppler-Laser-2-Focus : A new kind of three component velocimeter

I. Roehle, G. Karpinski, R. Schodl

Institute for Propulsion Technology, German Aerospace Center (DLR), Cologne.

Abstract

The conventional Laser-Two-Focus (L2F) method measures the two components of the flow vector in the plane normal to the optical axis by measuring the time of flight of particles crossing the two laser beams in the probe volume. Recently a new three component system was developed, named 3D-Doppler-L2F, which operates with the same confocal optical set-up as the two component L2F system, thus enabling three component measurements even under difficult conditions, for example in centrifugal compressors. The technique combines the L2F with the technique of the Doppler Global Velocimeter. The set-up of a 3D-Doppler-L2F, especially designed for 3D-velocity measurements in a turbine is presented as well as measurement results from a free jet.

Introduction

The process of enhancement of modern compressor and turbine technology is strongly in need of accurate, reliable and detailed experimental velocity data from the flow inside these turbomachinery components. Non-intrusive state-of-the-art techniques for this purpose are L2F, LDA and PIV. Often, the most severe problem is the limited optical access to the flow. This is especially true when 3C-measurements are required, that is measurements of all three components of the velocity vector.

To date the 2-Component-Laser-Two-Focus technique (L2F) has been suited best in overcoming serious access problems, since it is a back scattering technique with a confocal optical beam path [1]. Furthermore it is capable of measuring very close to walls and windows (down to 0.3 mm) and is capable of detecting very small particles (typ. 0.2 μm diameter) which can follow very strong accelerations. This technique is limited to turbulence levels of 30 % and to two component measurements.

For three component velocity measurements a combination of two 2C-L2F Systems, called 3C-L2F, was used in the past (figure 1) [2]. The two optical axis of these two systems form an angle of 16° . The cone, formed by the path of the scattered light detected by the two optics, has an angle of 28° . This receiving aperture is larger than the aperture of the conventional 2D-L2F with an angle of 11° .

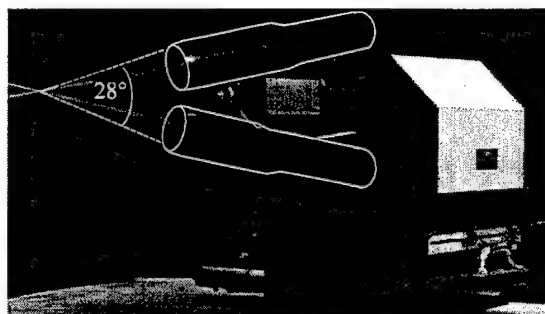


Figure 1: Photograph of the 3D-L2F.

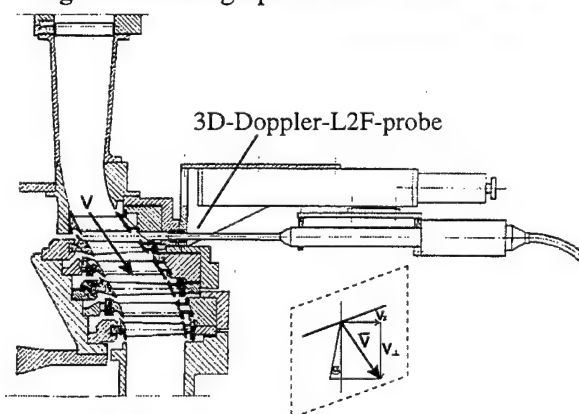


Figure 2: Application of the 3D-Doppler-L2F (probe version) to a turbine test rig.

Even though this 3C-L2F is well suited for turbomachinery measurements in general, there are extreme cases, in which there is insufficient space to place the optical head of the system.

The set-up of the 3C-System is not confocal, which cases difficulties when measuring through an inclined window.

For these reasons a new kind of three-component velocimeter was developed. It is a combination of the conventional 2C-L2F and the Doppler Global Velocimetry technique (DGV) to a so called 3C-Doppler-L2F [3]. This system has the same confocal set-up as the 2C-System, which makes it well suited to overcome serious access problems.

A first application of this anemometer is shown in figure 2. The flow in the stator blade channel of a three stage turbine will be investigated. Therefore an L2F probe was constructed with an diameter of only 14 mm and a working distance of 58 mm. In this application the flow velocity vector has a strong radial flow component towards the probe. That is the reason why 3C-measurements are needed in this particular experiment.

Principle of the 3D-Doppler-L2F

The 3D-Doppler-L2F measures the two velocity components in the plane vertical to the optical axis, called focal plane, by applying the time of flight technique (figure 3). The third velocity component in the direction of the optical axis causes a Doppler shift, which is analysed by the DGV-technique [4].

Principle of the L2F

The L2F is a statistical time of flight technique. It measures the velocity of particles in the fluid. Two laser beams are focused down to two spots separated by a distance of typically 100 μm to 300 μm . If a particle passes these two spots, it causes two successive scattered light pulses (figure 3). The scattered light is detected by appropriate receiving optics with photomultipliers (figure 4). The velocity of the particle can be derived from the time between the two pulses and the distance of the two focus points.

For successful measurements, it is necessary that the velocity vector of the particle is in the plane formed by the two laser beams. All other particles generate random time of flight measurements. If the turbulence is not too high (below 30%) the peak of these events can be identified in a histogram. The random events create a statistical background noise without significant peaks.

The inclination of the plane formed by the two laser beams is called the angle α . After a measurement at a certain angle α , α is changed

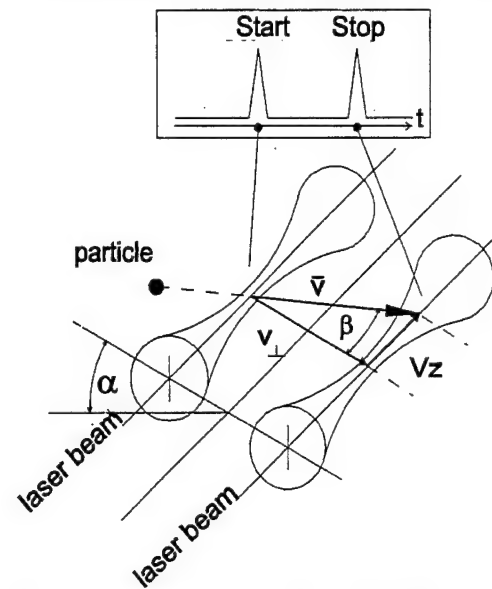


Figure 3: Probe volume of the L2F.

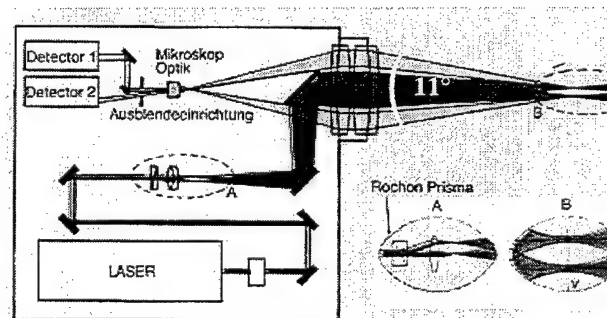


Figure 4: Schematic of the 2D-L2F optic.

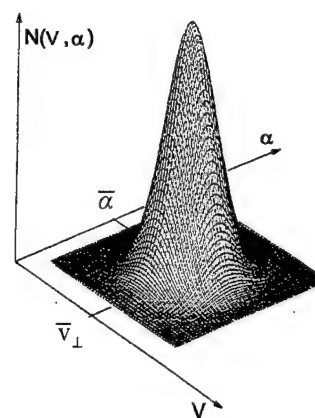


Figure 5: Two dimensional frequency distribution.

to $\alpha + \Delta\alpha$, that means the plane of the two laser beams is turned slightly around the optical axis and the measurement is repeated. In this way a 2C-Histogram is acquired (figure 5). The maximum of this distribution is at the point $(\bar{v}_\perp, \bar{\alpha})$, that means the maximum marks

average velocity magnitude \bar{v}_\perp in the plane vertical to the optical axis and the average flow angle $\bar{\alpha}$.

The flow component in the direction of the optical axis, the component v_z can not be measured this way.

Principle of the Doppler Measurement

The third component v_z cause a Doppler shift $\Delta v = v - v_0$ of the scattered light frequency v in respect to the laser frequency v_0 . In backward scattering the shift equals the equation

$$\Delta v = 2 \cdot v_0 \frac{v_z}{c}$$

The basic idea is to analyse this frequency shift by measuring the transmission of the light through an iodine cell which serves as a frequency to intensity converter (figure 6). An iodine cell is made from silica glas, evacuated and filled with iodine vapour. Molecular iodine has strong absorption lines which interfere for example with the 514 nm line of an Argon ion laser. If the laser frequency v_0 is looked to the slop of such an absorption line, the scattered light will be weakened by the factor $T(v)$. T is the transmission of the cell and is defined as the fraction of the light intensity before and after passing the cell. $T(v)$ is a function of the light frequency v .

Therefor the frequency v of the scattered light can be determined by measuring its transmission passed the iodine cell. Two detectors are required. One to measure the light intensity before and one to measure the light intensity after the cell.

If the transmission profile $T(v)$ is known, v can be derived this way. If the frequency v_0 of the laser is also known, the Doppler shift is derived from

$$\Delta v = v - v_0$$

Set-up of the 3D-Doppler-L2F

The set-up of the system is shown in figure 7. A frequency stabilised argon ion laser with intercavity etalon is used as a light source. The etalon is a thick, slightly inclined glass plate, thermalised by an electric oven. Its purpose is

to allow single mode operation of the laser. The etalon is optimised for the 514 nm line of

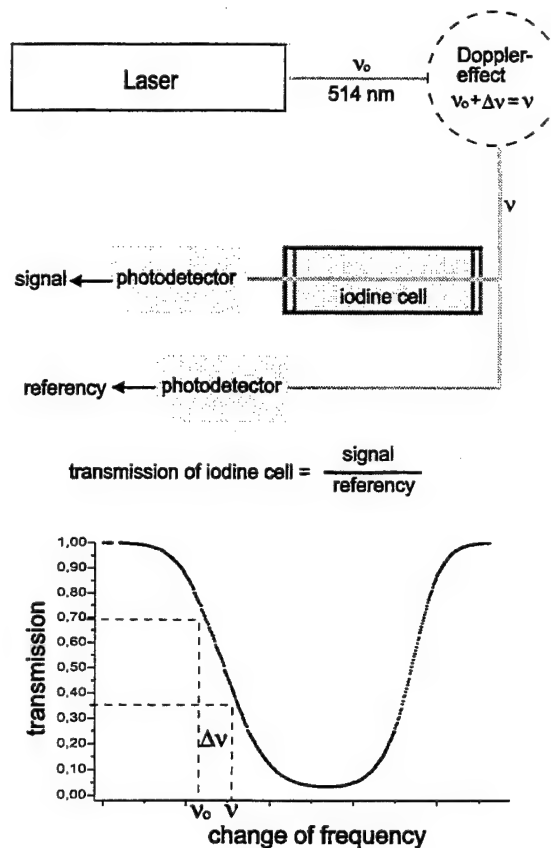


Figure 6: Principle of the Doppler measurement.

the laser. There is no prism in the resonator. Therefore the laser is active on several colours at the same time. Single mode operation is only achieved for the 514 nm line.

The laser light is coupled into a single mode fibre and transferred to a miniature L2F- probe. The lens f_1 (see figure 7) is used to collimate the divergent beam coming out of the fibre. A colour dispersing prism in front lens f_2 focuses the multi colour beam down to spatially separate focus points of different colour. As a consequence of the chromatic imperfections of the lens f_2 , the focus points are not only located at different positions in flow direction (x-direction), but also at different positions on the optical axis (z-position). Although this is a disturbing effect in general, it is highly appreciated in the context of the turbine measurements, mentioned in the introduction. As shown in Figure 1, the main flow direction is not perpendicular to the

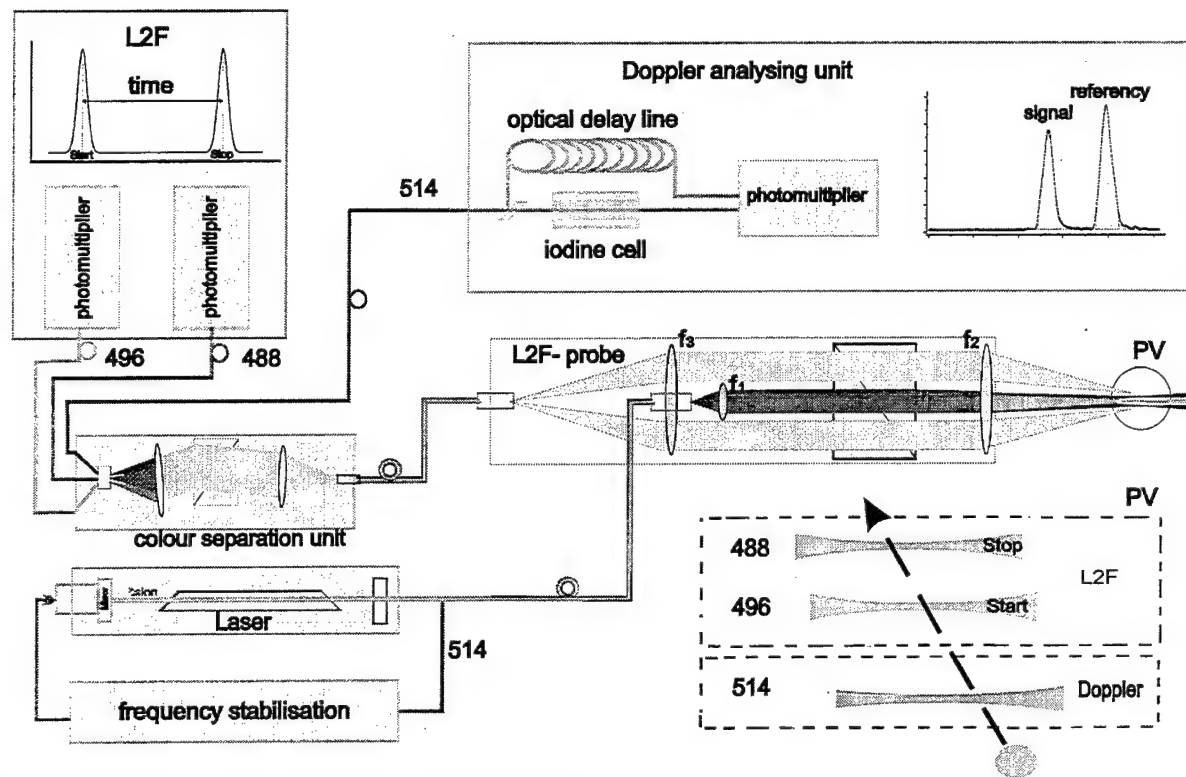


Figure 7: Schematic of the 3D-Doppler-L2F optics.

optical axes of the L2F-probe; in contrast to standard L2F-applications. The angle between the optical axes and the main flow direction is about 60° . In this way the spatial arrangement of the focus points and the main flow direction are well adapted to each other.

The lens l_2 is also used to collect the scattered light emitted by the particles when passing the focus points. This light passes the colour dispersing prism as well, so that the different colours are recombined into one beam. Lens f_3 focuses the recombined multi-colour beam on a multi mode fibre. This fibre carries the light to a colour separation and detection unit. By an arrangement of two lenses f_4 and f_5 and a second dispersing prism the different colours of the detected light are separately launched into these set fibres. The scattered light pulses from the 488 nm focus point and from the 496 nm focus point is carried to photomultipliers directly. These generate the start and stop signal for the L2F time of flight measurement.

The Doppler analysing unit

The third fibre carries the scattered light of the 514 nm line to the doppler analysing unit. In this unit the light is split by a non polarising beam splitter. Half of the light pulse passes the iodine cell, the other part is sent through a long

multimode fibre, which serves as an optical delay line. Both pulses are detected by the same photomultiplier with a time delay given by the fibre. The amplitude ratio of these pulses is proportional to the transmission $T(v)$ of the iodine cell, from which the scattered light frequency can be derived:

$$\frac{\text{iodine} - \text{signal}}{\text{reference} - \text{signal}} = T(v) \Rightarrow v$$

An important and new aspect of this set-up is the use of the "delay fibre". Previous tests have shown, that the more common set-up with two photo multipliers, one for the signal with iodine cell and one for the reference measurement, causes problems because of time depending sensitivity differences of the two physically different detectors. With only one detector, sensitivity changes due to temperature effects and due to changes of the amplitude of the supply voltage influence both signals in the same way.

The signals are collected and digitalised by a 400 MHz transient recorder card placed in a PC and the further signal processing is done by software.

Doppler Signal processing

The two peaks of each pair of signals have similar (but not equal) shape and a constant time distance of 645 ns arising from the delay line, corresponding to the delay of the fibre with a length of 120 m. The transmission passed the iodine cell is determined by the fraction of the time integrals of the two signals:

$$T = \text{const.} \cdot \frac{\int_{t_1}^{t_2} I(t) dt}{\int_{t_3}^{t_4} I(t) dt}$$

Since the signals show a certain noise level, the integration is restricted to the time interval in which the signal amplitude larger than at a certain minimum Intensity. This minimum Intensity was chosen to be 13% (e^{-2}) of the maximum amplitude of the signal (figure 8). Both signals are integrated over a time interval of equal length. The integration ranges are set by the stronger one of the two signal. The constant time distance of 645 ns is then taken into account to fix the integration ranges for the weaker pulse.

$$t_3 = t_1 + 645 \text{ ns}$$

$$t_4 = t_2 + 645 \text{ ns}$$

For technical reasons, the photomultiplier signal has an offset which needs to be subtracted from the signals. The offset level is measured before or after the two pulses, depending whether the first or the second pulse has triggered the event. 100 values are averaged to determine the offset.

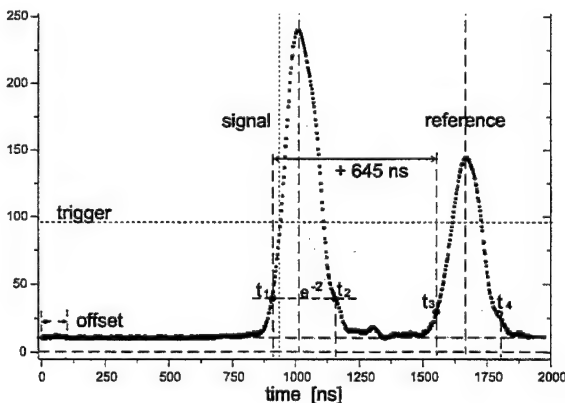


Figure 8: Integration intervals of the two pulses.

The signal processing of the time of flight measurement is not different from other kinds of L2F- Systems [1],[2]. In the presented

System it is performed independently from the determination of the v_z component, although 3D-correlations should be feasible in principle.

Frequency Stabilisation

An Ar⁺-Lasers with Etalon operating at 514 nm wavelength is in general suited as a light sources for 3D-Doppler-L2F measurements (an alternative could be a frequency- doubled YAG laser operating at 532 nm). Its insufficient frequency stability, however, must be improved. Necessary requirements for accurate Doppler measurements are to adjust the laser frequency ν_0 to the transmission profile $T(\nu)$ of the iodine cell very precisely and to keep it very stable during the measurement procedure.

The following example gives an estimation of the required stability: A resolution of 1 m/s in the direction of v_z equals to a frequency shift of $\Delta\nu = 3.8$ MHz.

The Etalon selects one mode of the ≈ 70 modes of the laser. It functions as a second resonator inside the laser resonator. The mode which matches best the optical length l_0 of the etalon is weakened least. In this way the laser is running monomode.

$$l_0 = l(T) \cdot n(T)$$

l = geometrical length of the etalon

l_0 = optical length

n = refractive index

T = temperature

The mode can be chosen and changed by changing the temperature of the Etalon. In this way the laser 'hops' from one mode to the other in steps of the free spectral range FSR (typically 150 MHz).

$$FSR = \frac{c}{2L}$$

c : Speed of light

L : length of laser resonator

The laser mode has a very small line width but a time dependent fast frequency jitter and long term drift. The jitter has an amplitude of typically 4 MHz with a jitter frequency in the range of 1 KHz. This jitter was not compensated in the presented set-up.

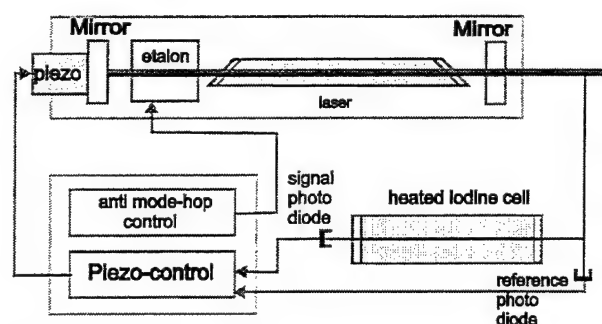


Figure 9: The control loops of the frequency stabilisation.

The long term drifts may be up to 100 MHz/Minute, in other words, the long term drift may be very large compared to the Doppler shift of 3.8 MHz per 1 m/s. Therefore it is necessary to compensate the long term frequency drift with a controller.

By placing the rear mirror of the resonator on a piezo translator the resonator length can be actively controlled thereby stabilising the laser frequency (figure 9). The change in frequency is directly proportional to the change in length of the resonator:

$$\Delta\nu = \nu_0 \Delta L / L \quad L = \text{Resonator length}$$

To stabilise the laser frequency, a reference frequency measurement is needed. A simple approach to this problem is to use the Doppler broadened line of a second iodine cell that serves as a reference.

In full analogy to the DGV measurement, the laser frequency is determined by measuring the fraction T of the laser beam intensity before and after the iodine cell. A PID controller stabilises this T to a fixed value (figure 10). Apart of this the etalon temperature also needs to be stabilised in order to avoid mode hops.

Etalon anti mode-hop control

A slight frequency modulation with a modulation amplitude of about 2 MHz and a frequency of about 500 Hz is used to stabilize the etalon transmission. By detecting the laser output power with an lock-in amplifier, the first derivative of the modulated laser power is generated and fed in a PI-controller to tune the etalon to maximum transmission (figure 10). In this way the transmission of the intercavity etalon is stabilised on the laser frequency to avoid mode hopping and to be able to tune the

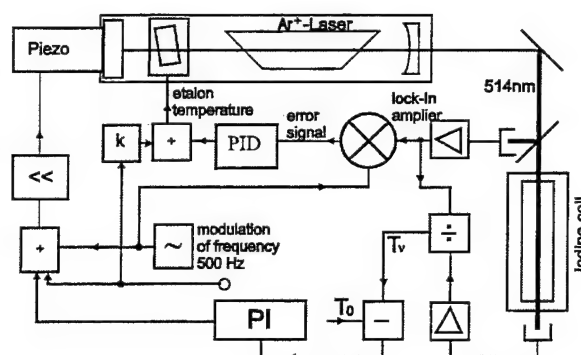


Figure 10: Detailed block schematics of the control system. The parts with grey background are software realised.

laser over frequency intervals greater than the free spectral range of the laser.

Calibration of the iodine cells

The iodine cells are filled with a small amount of iodine. At a certain temperature T_{Sat} the iodine crystal is fully evaporated. The cell is operated above this temperature level, so that the vapour density inside the cell is constant and independent of the exact temperature.

The frequency positions of the absorption lines of iodine are determined by the quantum mechanics of the molecule. They are very well known and very insensitive to any kind of outer influences. In contrast to this, the strength and the width of these lines is very sensitive to the temperature changes and to changes of the gas pressure inside the iodine cell. In addition to this the presents of other gases influences the shape of these lines as well.

Because of this, the transmission profile of each cell needs to be calibrated individually.

The set-up for the calibration is shown in figure 12. Two argon lasers are needed; the first laser is stabilised as described above while the second laser is pre-stabilised on an interferometer. This interferometer is continuously and linearly tuned in frequency. In this way the laser is tuned in frequency as well. The light of the two lasers is coupled into a single mode fibre which serves as a mixer. Because of the two different light frequencies a beat frequency arises, which equals the frequency difference

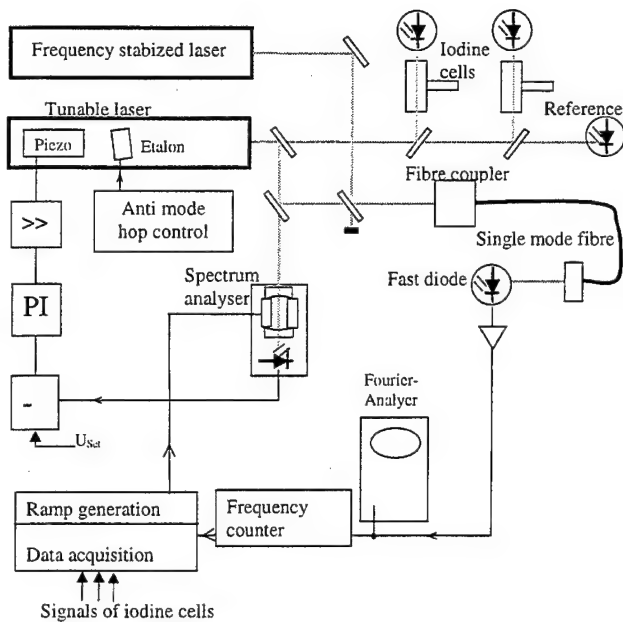


Figure 11: Optical and electronic schematics of the iodine cell calibration set-up.

between the two lasers. This difference frequency is measured with a frequency counter.

The light of the scanning laser is also used to measure the transmission of the iodine cells. While the laser is tuned, a data acquisition board in a PC acquires the cell Transmission T as well as the difference frequency ν . In this way the transmission profile $T(\nu)$ of several iodine cells is measured (figure 12).

Choice of iodine lines in respect of measurements in the turbine

In the planed turbine measurement the main flow vector will have a mean component v_z of about 90 m/s in the direction of the L2F- probe. This velocity will cause a mean Doppler shift of about + 340 MHz. Because of this, two iodine cells with different temperature T_{Sat} and therefore with a different width of the transmission profile were chosen (figure 13). The left side of the cell with the larger width is used to stabilise the frequency ν_0 of the laser. The left side of the cell with the smaller width is used for the Doppler measurement. In this way the working point of both, the frequency stabilisation and of the Doppler measurement are located in the center of the slope of the corresponding profile, were the accuracy of the

frequency measurement is best. Further more a high flexibility is achieved this way.

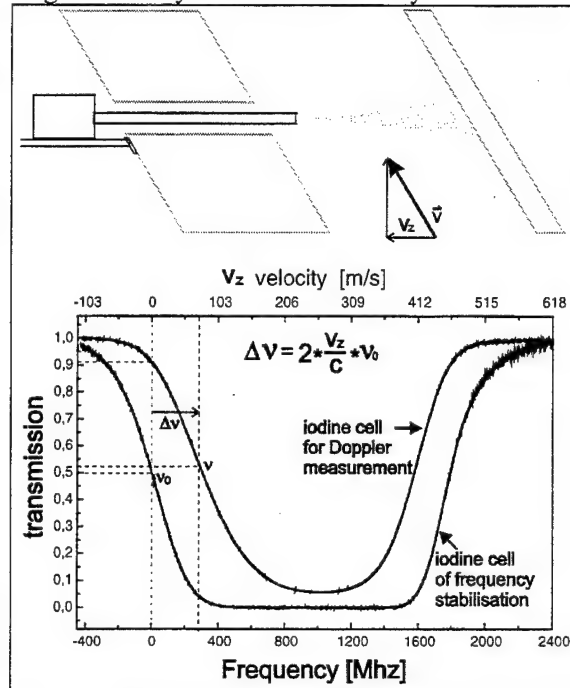


Figure 12: The calibration curves of the two iodine cells, used for the measurements in the turbine. The different width of the profiles is well adapted to the expected mean doppler shift caused by the velocity component v_z .

First tests on a free jet

The set-up of the 3C- Doppler L2F system was tested on the flow of a free jet. The reference velocity component v_z was calculated from the jet velocity and the inclination angle β between the free jet nozzle and the optical axes of the anemometer, which is shown in Figure 13 together with the results of the tests. The velocity component v_z measured with the 3C-Doppler- L2F is plotted against the theoretical velocity v_z . Each point represents the average value of 1000 particles. The scattering of the measured values is about ± 1 m/s and independent of the magnitude of the velocity. The relative measurement uncertainty therefore depends on the magnitude of the velocity.

This result was also verified in a second experiment: At a fixed velocity the reproducibility of the value \bar{v}_z was investigated. In a period of one hour each 10.000 successive events were averaged. The data rate was about 1000 Hz, therefore it took about 10 seconds to

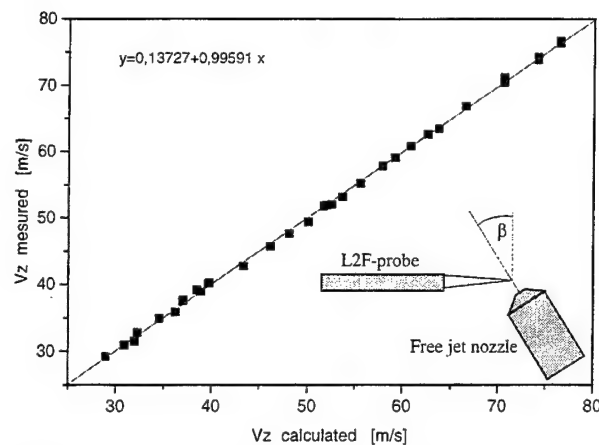


Figure 13: Measurement of the component v_z versus the calculated velocity of a free jet. The jet axis was inclined relative to the axis of the 3D-Doppler L2F.

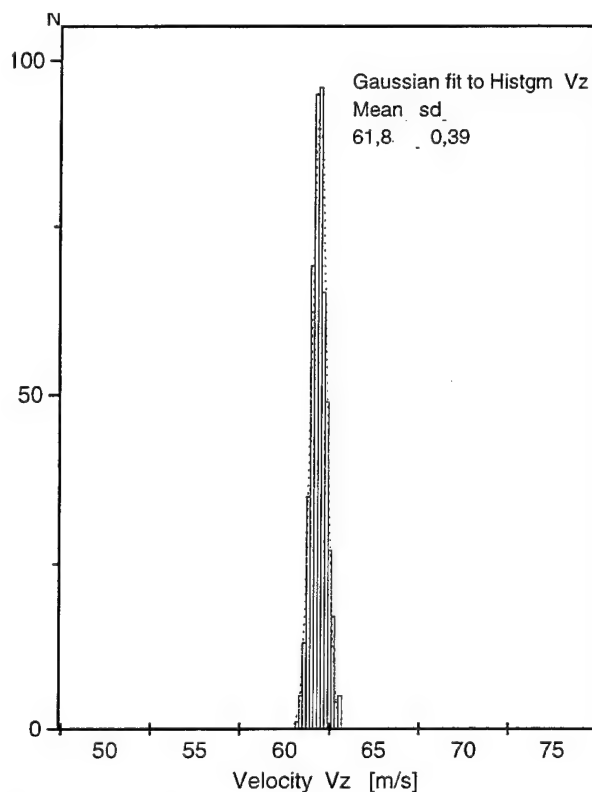


Figure 14: Frequency distribution of the velocity \bar{v}_z , averaged over 10.0000 events (≈ 10 s). The whole histogram data was acquired within a time period of one hour.

acquire 10.0000 events. Figure 14 shows the frequency distribution of \bar{v}_z . The standard deviation is only ± 0.5 m/s. The reproducibility of the averaged Doppler measurement is obviously very good. It is even better than the measurement with the turned nozzle. In that experiment the uncertainty of the determination

of the angle β was even larger than the uncertainty of the doppler measurement.

Instrumental artificial turbulence

At a given velocity v_z of 74.9 m/s with an estimated turbulence of ± 1.1 m/s a number of 10.000 events was acquired. Figure 14 shows a histogram of the number of particles measured at a certain velocity versus the velocity. The distribution has a standard deviation of 4.6 m/s. This value is larger than the estimated turbulence in the flow. Therefore we consider the value of 4.6 m/s to be the instrumental turbulence, presumably caused by the short time frequency fluctuations of the laser, which could not be eliminated by the selected control method.

This experiment shows, that the 3C-Doppler – L2F should at least be capable of measuring the 3C- turbulence, when the turbulence level is above $\approx \pm 4$ m/s.

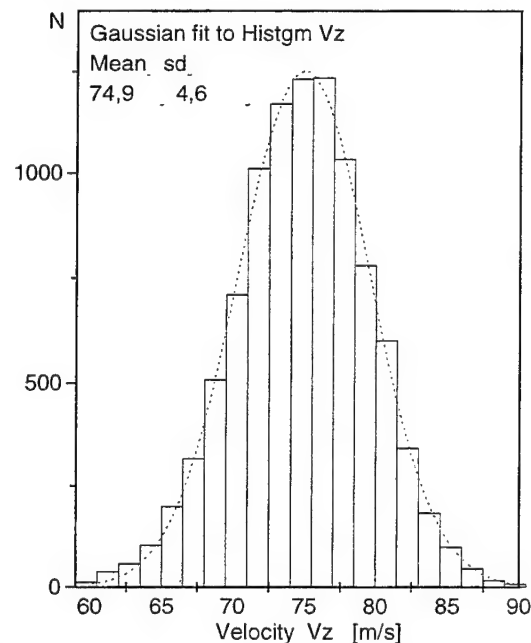


Figure 14: Frequency distribution of velocity measurements of single particles. This diagram shows, that the 3D-Doppler L2F shows an artificial turbulence level of about 4.5 m/s.

With the presented set-up the data processing of the time of flight measurement (magnitude and flow angle) and the determination of the v_z component are performed independently. Therefore correlated measurements of the turbulence of the three velocity components can not be carried out, but are in general possible.

Conclusions and Outlook

A 3C-Doppler-L2F probe is described with the unique feature of being operational in internal flows via a single optical access port of a very small viewing angle of only 11° . The L2F probe is a result of a combination of the time of flight principle and the direct measurement of the frequency of the Doppler shifted scattered light. The on axis velocity component is measured independently from the two other components. The measurement uncertainty of mean values is ± 0.5 m/s, the lowest value of the standard deviation is determined by the instrumental broadening of about 4.5 m/s.

The main reason for this rather high value are presumably the short time frequency fluctuations of the laser, which could not be eliminated by the selected control method. Control methods for the reduction of the remaining fluctuations are in process. A more detailed error analysis is in preparation.

For the application in a turbine rig the electronics are extended with synchronisation devices, which enable phase-looked measurements behind and within rotating components.

Literature

- [1] Schodl, R.: *A Laser-two Focus Velocimeter for Automatic Flow Vector Measurement in the Rotating Components of Turbomachines*, Measurement methods in rotating components of turbomachines, ASME, New York, 1980.
- [2] Schodl, R.: *Laser-Two-Focus velocimetry: Two and Three dimensional techniques*, VKI Lecture Series on Advanced Measurement Techniques, D/1998/0238/455, VKI LS 1998-06, Brussels, 1998.
- [3] Roehle, I., Schodl, R.: *Method for Measuring Flow Vectors in Gas Flow*, UK-Patent GB 2 295 670 A, 1995.
- [4] Röhle, I.: *Three dimensional Doppler Global Velocimetry in the flow of a fuel spray.. nozzle and in the wake region of a car*, Flow Measurement and Instrumentation (Journal), Volume 7, Number 3/4, September/December 1996.

APPLICATION OF 3 COMPONENT LASER-DOPPLER VELOCIMETRY IN TRANSONIC FLOW OVER A DELTA WING

T.J. Möller¹, A. Wiedemann¹, K.A. Bütefisch¹, F. Micheli², D. Scholz³, K. Sjörs⁴

¹Deutsches Zentrum für Luft- und Raumfahrt e.V. (DLR), Institut für Strömungsmechanik, Bunsenstraße 10,
D-37073 Göttingen, Germany

²ONERA Chalais Meudon, Fundamental and Experimental Aerodynamics Department,
8, Rue de Vertugadins, F-92195 Meudon, France

³Instituto Nacional de Técnica aeroespacial (INTA),
Carretera de Alalvir, kp. 4, E-28850 Torrejón de Ardoz, Madrid, Spain

⁴The Aeronautical Research Institute of Sweden (FFA),
SE-161 11 Bromma, Sweden

Abstract

In the development of numerical codes for the prediction of aerodynamic flows is a strong need to obtain reliable flow field data which is suited to validate turbulence models used in numerical calculations. In three dimensional boundary layers Laser-Doppler Velocimetry (LDV) is the appropriate technique usually applied to obtain this kind of data. Since LDV, being a single point measurement technique, is a time consuming method, it is desirable to have the ability to make use of data from different experiments and research groups. Therefore it is necessary to have a standard to compare experimental results obtained by different LDV processors and to define a consistent mathematical algorithm to process data from the different LDV experiments. This is the objective of the present paper. In an European activity four different research groups have conducted common experiments in industrial wind tunnels and finally compared the results to qualify LDV for the application in industrial wind tunnel and to define a standard to compare LDV data coming from different sources.

Introduction

In the development of numerical codes for the prediction of aerodynamic flows there is a strong need to obtain reliable flow field data which is suited to validate turbulence models used in numerical calculations. To determine turbulent boundary layers utilising time averaged Navier-Stokes calculations turbulent model are necessary. Hence velocity data of the three dimensional turbulent boundary layer is of interest to validate the applied turbulence models.

Hummel [1] noted that vortex flow generated by a delta wing are very sensitive to any disturbances. Therefore this

kind of investigation cannot be performed using probes, e.g. hot wire probes, hence optical measurement techniques have to be applied. In three dimensional boundary layer flows LDV is the most appropriate technique usually applied to obtain these kind of data. Since LDV, being a single point measurement technique, is a time consuming method, it is desirable to have the ability to make use of data from different research groups. Therefore it is necessary to have a rational basis to compare measurements executed with different LDV processors and to define a consistent mathematical algorithm to process data from different LDV experiments. This was the objective of a common experiment of four European research teams from ONERA, INTA, FFA and DLR with the aims to conduct common experiments, to compare the results from the different teams to qualify LDV for industrial wind tunnel applications and to define a standard to compare LDV data from different origins. The present paper shows first results of the common investigation of this four European teams.

Experimental Set up

Wind tunnel

The experiments were carried out in the Transonic wind tunnel in Göttingen (DNW-TWG). The DNW-TWG is a continuously working wind tunnel with three exchangeable test section for subsonic, transonic and supersonic speed range. During the experiments the transonic test section with perforated walls has been applied. The flow can be observed through two glass windows. The test section size is 1.0 m x 1.0 m. The wind tunnel has been operated by a fixed Mach number of 0.85. The axial compressor has an electric power supply of 12 MW. In [2] further technical

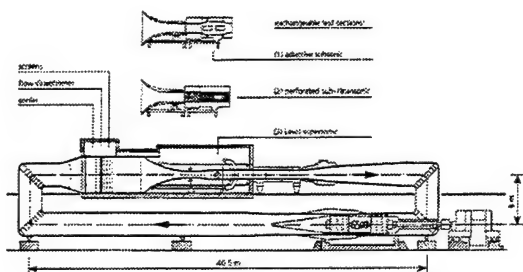


Figure 1: Sketch of the DNW-TWG

details can be found.

Model parameters

A wind tunnel model used in the framework of the Vortex Flow Experiment has been utilised in the present experiments. Elseenaar et al. [3] describe the model in detail. The model is fixed on a stiff sting who can be moved vertically and horizontally. The model has a sweep angle $\Lambda = 65^\circ$ and a length of 432.94 mm, the corresponding Reynolds number based on the model length is $6.24 \cdot 10^6$. The angle of incidence was 10° and 15° for the presented experiments. Figure 2 shows a sketch of the applied model.

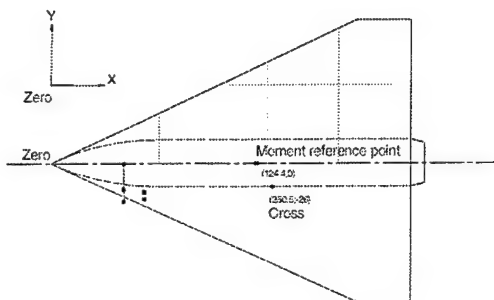


Figure 2: Sketch of the VoMo model and used coordinate system

Seeding System

A seeding system developed by DLR Göttingen has been employed during the experiments. The mean diameter of the particles produced by the atomiser is $1\mu\text{m}$. In [4] the principle of this type of atomiser is explained in detail. The particles are added to the flow in the settling chamber

of the TWG. By a numerical calculation it has been estimated the $1\mu\text{m}$ particles follow velocity fluctuations of the continuous flow in the investigated flow region sufficiently. The behaviour of particles in a gas flow is governed by particle inertia and the interaction with the turbulent fluid surrounding it. Consider a small diameter in the range of μm , rigid, spherical particle the inertia of such a particle can be characterised by its aerodynamic particle response time τ_p . It is defined for a particle with radius r as:

$$\tau_p = \frac{2}{9} \frac{r^2 \rho_p}{\nu \rho_f}$$

Where ρ_p denotes the particle density, the ρ_f fluid density, the r particle radius and ν the fluid viscosity. This expression can be interpreted as the time needed for the particle to react to fluctuations of velocity of the continuous phase. The above definition is based on flow in the Stokes regime. To calculate the trajectory of an individual particle the following instantaneous particle equations have to be solved numerically:

$$\frac{d\bar{U}_p}{dt} = \frac{[\bar{U}_f(y(t), y) - \bar{U}_p]c_d}{\tau} - g\delta_{i3}$$

$$\frac{d\bar{x}}{dt} = \bar{U}_p$$

Where U_f denotes the fluid velocity, U_p is the velocity of the particle, δ denotes the Kronecker symbol and c_d is an empirical non-Stokesian correlation for the drag factor which is given by:

$$c_d = \frac{24}{\text{Re}_p} (1 + 0.15 \text{Re}_p^{0.687})$$

The calculation has been performed for particles with $1\mu\text{m}$ diameter and yield to the above described results. Details about this calculations can be found in [5,6]

LDV Set-up

The DLR LDV system is a three component system. Figure 3 shows a sketch of the applied set-up. The system has been specially adapted to the environment of the TWG. Furthermore CAD simulations of the optical path have been performed in advance to define an optical set-up which allows measurements close to the surface. As a light source an Argon-Ion Laser with 6W all lines is applied. The LDV operates in a back scatter set-up. The

present set-up has a focal length of 1.75 m and an angle of diffusion of 6° . The Bragg shift frequency was 40 MHz. The probe volume is typically $220\mu\text{m}$ in diameter, with $15\mu\text{m}$ fringe spacing. This leads to typical frequencies of the Doppler signal of 60 MHz. The scattered light is collected by a lens optic with 180 mm aperture. In [7] the system is explained in detail. Four different LDV processors have been connected to the photo multipliers of the LDV system. To distribute the signal of each photo multiplier to all four groups an electronic device has been developed. This device allows to divide the signal from each single photo multipliers into four signal streams with amplification 1. Hence it was possible to provide each participating group with the electrical signals from the photo multipliers without decreasing signal amplitude.

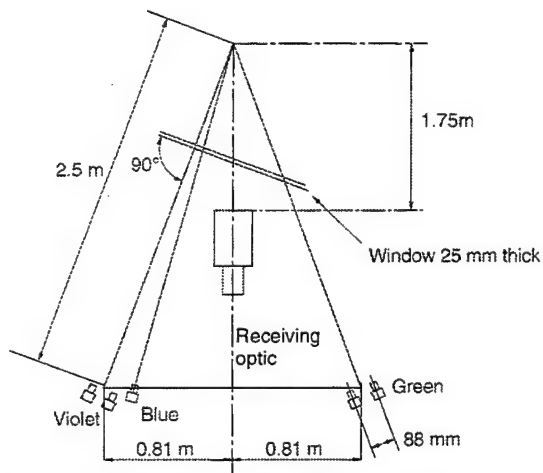


Figure 3: Sketch of the DLR three component LDV system

LDV processors

In the present experiments four different LDV processors have been applied. TSI counter 1990 [8], TSI IFA 750, TSI IFA 755 [9] and Aerometrics DSA [10] have been used. Hence different signal evaluation schemes, i.e. counter type, autocorrelator type (IFA 750, 755) and one type using the Fourier transform to determine the Doppler frequency out of the LDV signal (Aerometrics DSA), have been employed in the presented experiments. Thus the influence of the different strategies of the system could be investigated in the present study. Jensen [11] compared in a simulation the IFA counter 1990 and TSI IFA 750 system. From a theoretical comparison of signal processing of LDV bursts in the time and frequency domain Lading [12] expects that for signals with low SNR the determination of LDV bursts using the Fourier transform should lead to more reliable results. Ibrahim et

al. [13] studied in a simulation the algorithm to evaluate LDV burst realised in the DSA. They predict that it should be possible to evaluate LDV signal with low SNR. But comparisons of different LDV processors in the environment of industrial wind tunnels are rarely found in the literature.

Position monitoring system

To determine the vertical position of the model the DLR position monitoring system has been employed in the TWG. A detailed description of the system can be found in [14]. The system is capable to acquire data with frequencies up to 500 Hz. The spatial resolution of the system is better than 0.02 mm.

The object or a part of it is focused, by means of an optical system, onto an image plane, where a line CCD sensor is placed. The output voltage of the sensor is proportional to the local light intensities. With the array oriented perpendicular to the object contour, the contrast of the object against a lighted background results in an obvious rise or drop of the signal along the array. Making use of the adaptable reference threshold voltage this analogous signal is converted into a binary signal, the dark-light step then indicating the position of the object contour parallel to the direction of orientation of the sensor array and perpendicular to the direction of view.

For LDV measurements position data has to be recorded simultaneously with LDV data storage which is controlled by data rate and not by fixed time intervals. The digital position data is therefore continuously converted into analogous voltage which can be recorded by most LDV processors. This permitting storage of latest position data synchronously with LDV data. The DLR LDV system can record three analogous signals, hence it is possible to record the displacement of the model in all six degrees of freedom. In the present experiments the vertical position of the model was monitored.

Results

LDV measurements

The results from the experiments were processed by a unique code based on the ONERA code. Table 1 shows results obtained in the free flow. On the average velocities, the agreement is rather good, within the traditional 1% uncertainty (3 m/s here) for the main component. For the vertical component W, the agreement is also quite good. But for the transverse horizontal component V, the disagreement between systems is substantial, although within the 3 m/s band.

Table 1 : Comparison of mean velocity measurements

	Team	U [m/s]	V [m/s]	W [m/s]
Point 1	DSA	307,8	-45,9	-8,5
	TSI	304,2	-32,3	-5,8
	counter			
	IFA 750	304,9	-31,1	-8,9
Point 2	IFA 755	305,9	-29,9	-7,6
	DSA	300,7	-4,2	17,7
	TSI	297,7	5,9	21,2
	counter			
Point 3	IFA 750	300,7	-1,4	19,8
	IFA 755	301,7	1,2	18,4
	DSA	303,9	-26,1	0,9
	TSI	303,2	-22,5	5,1
	counter			
	IFA 750	303,3	-18,9	2,8
	IFA 755	304,6	-17,3	1,0

Table 2 : Comparison of variance measurements

	Team	U' [m/s]	V' [m/s]	W' [m/s]
Point 1	DSA	9,1	21,7	9,6
	counter	10,4	21,2	10,9
	IFA 750	27,4	36,8	12,0
	IFA 755	9,8	16,9	8,3
Point 2	DSA	17,1	32,1	11,7
	counter	11,8	20,1	13,1
	IFA 750	77,6	101,0	16,5
	IFA 755	9,4	17,0	19,1
Point 3	DSA	12,4	23,5	12,7
	counter	11,9	28,4	9,8
	IFA 750	35,0	76,0	24,5
	IFA 755	10,0	18,8	13,2

There are large differences on the variance (table 2) between the systems. The DSA was adjusted manually for each single measurement point during the test, while the IFA's relied on their internal algorithm to do the work. There was slight differences in the adjustment of the IFA's which could explain a part of the differences in the results. The counter had difficulties to measure the signals with low SNR.

In figure 4-6 the velocities at $x = 131.3$ mm and $y = 12.5$ mm are shown. The closest position of the probe volume to the model surface is 0.8 mm. Also in the

boundary layer good agreement of the velocity data for U and W, like in the free flow can be found. But for the V

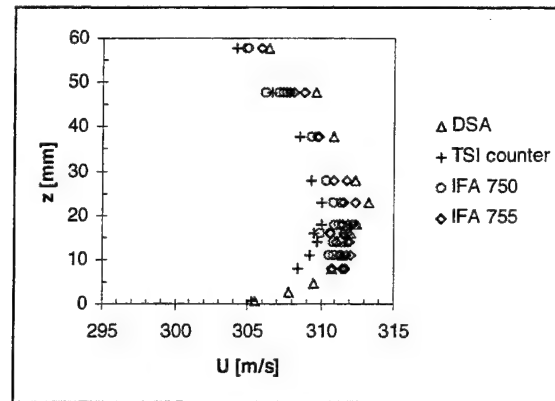


Figure 4: Velocity profile for U at $x=131.3$ mm and $y=-12.5$ mm

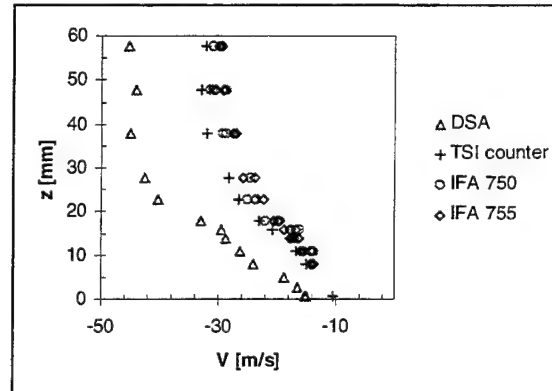


Figure 5: Velocity profile for V at $x=131.3$ mm and $y=-12.5$ mm

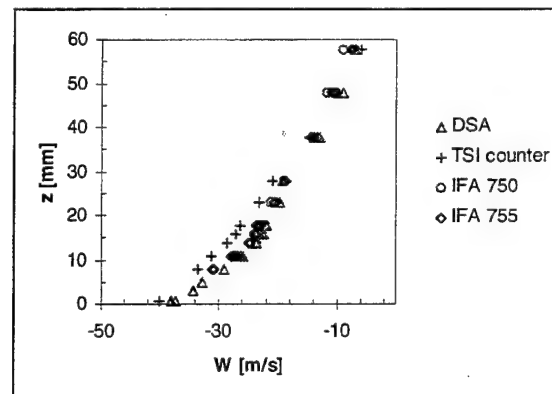


Figure 6: Velocity profile for W at $x=131.3$ mm and $y=-12.5$ mm

component the data of the DSA shows significant deviation from the results obtained by the three other system. This can not explained in the moment. Since this discrepancy is also found in the frequency data this is not the result of the post processing procedure. The velocity data from the other processors in opposite are within a 1% interval.

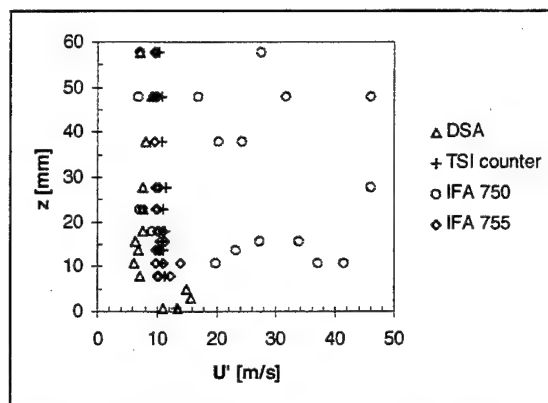


Figure 7: RMS values U' at $x = 131.3$ mm and $y = -12.5$ mm

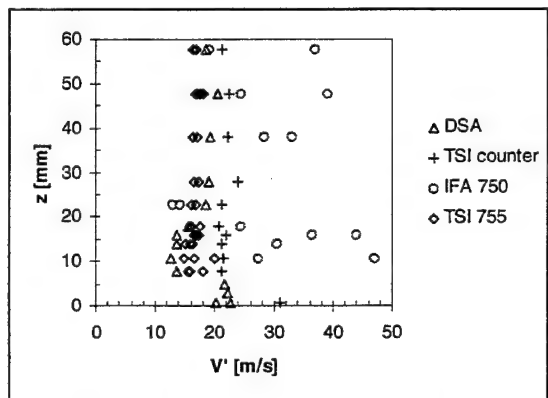


Figure 8: RMS values V' at $x = 131.3$ mm and $y = -12.5$ mm

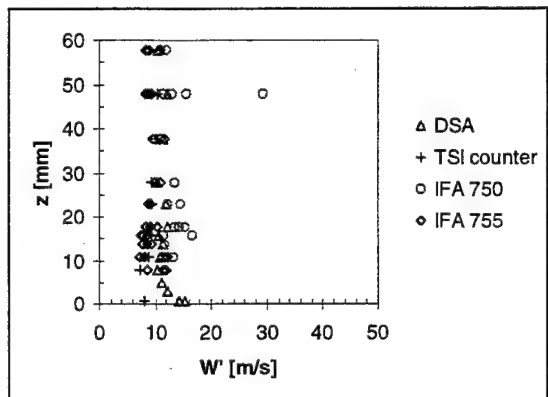


Figure 9: RMS values W' at $x = 131.3$ mm and $y = -12.5$ mm

Figure 7-9 show the RMS values for the same stream wise position. Here the data obtained by the IFA 750 shows significant scattering of the standard deviation values. This could be explained by the low number of samples for each single measurement, due to the low data rate of the IFA 750 for this measurements. The results acquired by the other system in opposite are in good agreement. Beside these findings it can clearly be seen, that the data for the RMS values show significant different turbulence intensity for the three velocity components. This results has to be considered in numerical calculations of this kind of flow fields.

model position monitoring

The data from the position monitoring system is recorded simultaneously to the LDA measurements. Figure 10 shows a typical result of the position monitoring. The maximum amplitude of the vibration is 0.2 mm. Hence the influence of the motion of the model on the boundary layer flow could be neglected during further processing of the LDA data if the boundary layer is significantly larger than the amplitude of the model vibration. In the present study the model vibration is not yet took into account. It can be seen that a typical frequency of 19 Hz (s. fig. 11) can be obtained from the data. This is the frequency of the whole

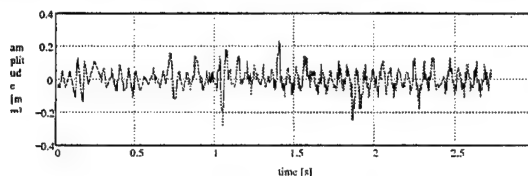


Figure 10: Time signal of the model position

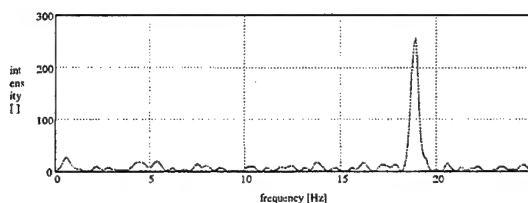


Figure 11: Frequency analysis of the model position

system mounting the model in the wind tunnel and the model itself.

Conclusions

The boundary layer of a delta wing in a transonic flow has been successfully investigated by means of 3 component Laser Doppler Velocimetry. The data obtained by the position monitoring system show a maximum vibration amplitude of the model of 0.2 mm and typical frequency of 19 Hz. Hence the influence of the motion of the model

was neglected during the evaluation of the LDV data. It is shown the 3D LDV system and the position monitoring system have been successfully adapted to this problem. Velocity data as well as turbulent quantities have been successfully acquired close to the surface of the model.

The comparison of the different LDV processor shows no uniform result. Obviously the counter system has difficulties to determine signals with low SNR ratio correctly. But also between the other systems there are significant differences in the velocity data. Especially the velocity fluctuation data shows remarkable differences. These results could confirm the conclusions by Lading, and Ibrahim et al. which predict the presented behaviour which is found in our investigations.

Acknowledgments

We would like to thank DASA for providing the VoMo Model. Furthermore like the authors to thank the wind tunnel crew of the TWG for their support.

References

- [1] Hummel, D.: Untersuchungen über das Aufplatzen der Wirbel an schlanken Deltaflügeln. Z. Flugwiss. 13, 158-168, 1965
- [2] Binder, B., Riethmüller, L., Tusche, S., Wulf, R.: Modernisierung des Transsonischen Windkanals in Göttingen. DGLR Jahrbuch Band I, 237-249, 1992
- [3] Elsenaar, A., Hjelmberg, L., Bütetisch, K.-A., Bannink, W.J.: The international vortex flow experiment. AGARD-CP-437. Vol.1, 9-1 – 9-23, 1988
- [4] Melling, : Tracer particles and seeding for particle image velocimetry. Meas. Sci. Technol., Vol. 8 Number 12, 1406-1416, 1997
- [5] Möller, T.J., Bütetisch, K.A.: Numerical and experimental investigation of a gas-particle wake flow of a bluff body. Proceeding 3rd European Fluid Mechanics Conference, Göttingen, 244, 1997
- [6] Thomas, P.J., Bütetisch, K.A., Sauerland, K.H.: On the motion of particles in a fluid under the influence of a large velocity gradient. Experiments in Fluids, 14:42-48, 1993
- [7] Seelhorst U., Bütetisch, K.A., Sauerland, K.H.: Three Component Laser-Doppler Anemometer development for large wind tunnel. ICIASF '93 Record, pp. 33.1-33.7, 1993
- [8] Model 1990C Counter-type Signal Processor Instruction Manual, P/N 1990256, TSI Inc. St. Paul, MN, USA, 1985
- [9] TSI, Model IFA 755 Digital Burst Correlator Instruction Manual revision B, January 1997
- [10] Aerometrics Doppler Signal Analyzer Installation Manual, Sunnyvale, CA, USA, Aerometrics Inc., 1991
- [11] Jenson, L.: Automatic digital signal processor for LDV. Proc. Fourth International Conference on Laser Anemometry – Advances and Applications, 5-9 August Cleveland, Ohio., 617-628, 1991
- [12] Lading, L.: Spectral analysis versus counting. Proc. International Symposium on Laser Anemometry. 17-22 November Miami Beach, ASME paper, 189-196, 1985
- [13] Ibrahim, K.M., Wertheimer, G.D., Bachalo, W.: Signal processing considerations for low signal-to-noise ratio laser Doppler and phase Doppler signals. Proc. of the Fourth International Conference on Laser Anemometry – Advances and Applications, 5-9 August, Cleveland, Ohio, 685-692, 1991
- [14] Grauer-Carstensen, H.: A Versatile Model Monitoring System, Rev. Sci. Instrum., 65 (2), 481-484, 1994

SESSION : 4

SENSITIVE PAINT TECHNIQUES I

**STATUS OF PRESSURE-SENSITIVE
PAIN TECHNOLOGY AT NAL**

Dr. Keisuke ASAI

Head, Aero-Thermodynamics Laboratory
Aerodynamics Division
National Aerospace Laboratory
7-44-1 Jindaiji - Higashi
Chofu, Tokyo 182-8522
JAPAN

*Paper not available
at time of printing*

COMPARISON OF LUMINESCENT PAINTS MEASUREMENT SYSTEMS

Marianne Guille, John P. Sullivan
School of Aeronautics and Astronautics
Purdue University, West Lafayette, IN, USA

Jim Holmes
Aerodynamics and Hydrodynamics Centre
Defense Evaluation and Research Agency, Bedford, UK

ABSTRACT

Techniques based on luminescent paints are a way to obtain the pressure and/or temperature distribution over a surface. Measurement systems associated with these techniques consist of an illumination source, a detector to measure the luminescence emitted by the paint coated on the surface and a procedure to relate luminescence to pressure or temperature, which all differ from one system to the other.

Experiments are done at Purdue University using different luminescent paints measurement systems to obtain pressure and temperature distributions from a jet impinging obliquely on a flat plate. A cooperation between Purdue University and DERA makes it possible to group three systems for comparison. They include the CCD camera system and the laser scanning system developed at Purdue University, and the DERA fluorescent lifetime imaging (FLIM) system.

INTRODUCTION

Luminescent paint coatings are used extensively in experimental aerodynamics for measurement of pressure and temperature. Models are coated with the paint, which is then excited by an illumination source. The luminescent intensity and fluorescent lifetime of the paint can be related to pressure or temperature. Different measurement systems exist in order to implement this concept.

Experiments are performed on an obliquely impinging jet at Purdue University. Intensity-based measurements are made with a scientific grade CCD camera system. Phase-based measurements are taken with a laser scanning system, and a modulated CCD camera produces fluorescent lifetime images (FLIM).

Compared with the CCD camera systems, which give a complete pressure or temperature distribution, the laser scanning system gives only a point by point value of pressure or temperature. The FLIM technique and the

phase-based measurements are both related to lifetime, and don't require the reference data necessary for the intensity-based method.

The choice of system and technique usually depends on the experiment conducted. However, the jet experiment is easy to implement and is well adapted to all the different systems under consideration. Results are presented and compared for the three systems.

PSP AND TSP BACKGROUND

Temperature sensitive paint (TSP) and pressure sensitive paint (PSP) techniques are based on thermal and oxygen quenching respectively, which occur in molecular photoluminescence (fluorescence and phosphorescence). Through these processes, the luminescent intensity or fluorescent lifetime of the paint excited by light can be associated with pressure or temperature.

The paint is usually made using luminescent molecules mixed with a solvent and a binder. It is then coated on the surface of the model, using either a paintbrush or a spray gun. As it dries, the solvent evaporates leaving a uniform coating. Short wavelength light, in the excitation range of the luminescent molecule, causes the paint to emit light at a longer wavelength. A photo-detector measures the resulting emission. A simple schematic of the TSP/PSP operation is shown in Fig1.

DESCRIPTION OF THE DIFFERENT SYSTEMS

The measurement systems are the same for both the TSPs and PSPs. The essential elements of the systems include illumination source, optical filters, photo-detectors, and data acquisition/processing units.

CCD intensity method

Intensity based imaging is the simplest and most widely used technique for acquiring pressure and temperature sensitive paints images. The surface is illuminated with

a continuous light source and the paint luminescence is normally detected by a cooled, charge-coupled device (CCD), camera [1]. The general setup for intensity based imaging is shown in Fig 2.

Both a wind-on image (at temperature and pressure to be determined) and a wind-off image (at a known uniform temperature and pressure) are obtained. The intensity ratio (IR) between the wind-on image, corresponding to a map of intensity I , and the wind-off image, corresponding to a map of the reference intensity I_{ref} is taken, yielding a relative luminescent intensity image. The surface temperature or pressure can be computed from the relative luminescent intensity image and a suitable calibration.

For pressure sensitive paint:

$$\begin{aligned} IR &= I_{ref}/I \\ P/P_{ref} &= f_1(IR) \end{aligned} \quad (1)$$

For temperature sensitive paint:

$$\begin{aligned} IR &= I/I_{ref} \\ T &= f_2(IR) \end{aligned} \quad (2)$$

In equations (1) and (2), functions f_1 and f_2 are obtained from the calibrations. They can be simple linear equations or higher degree polynomials to fit the calibration data as accurately as possible. Also, if temperature effects are considered for the pressure paint, a correction for temperature can be done if temperature is taken into account in the function f_1 .

The image ratio eliminates the effects of spatial non-uniformity in illumination light, coating thickness, and luminophore concentration. However, any wind-on model displacement will make direct pixel computation inaccurate, since pixels will be shifted from their original location. Small registration errors [2] between the two images can be corrected by computer image transformation [3].

The illumination source for the intensity-based measurements is a 15W GE Blacklight (UV).

The camera is a Photometrics scientific-grade CCD, model Sensys. The CCD in the camera is constantly cooled down by a Peltier cooler. The camera produces an analog signal that uses a 12-bit ADC (4096 gray levels). The 0.4s readout rate is limited by the ADC conversion rate of 1Mpixel/sec. Each image is 768 x 512 pixels with a pixel size of 9μm x 9μm and a number of electrons per pixel well of 80,000.

The camera is controlled by a PC. The software for data acquisition is called PMIS. The exposure time is usually set to use the full range of the CCD pixel well. This exposure time for these experiments is in the range 200-500 ms, depending on the brightness of the paint used. Eight images are averaged for each measurement.

The data reduction of the images is done using Matlab. A pressure or temperature map of the entire surface is obtained using the flow off and the flow on images and the calibration coefficients in a Matlab program written specifically for the task.

FLIM method

Fluorescent lifetime imaging uses a modulated light source to illuminate the paint [4]. The system developed at DERA consists of an array of modulated blue light emitting diodes and a solid state phase-sensitive CCD camera, Fig.3. The lifetime of the paint can be computed by making two measurements of the fluorescent intensity at different phases relative to the excitation light source [5]. However, the measurement of intensity cannot be instantaneous, so must be performed using two gates. To minimize the exposure time, the gate widths are made as large as possible. One solution is to make one gate in-phase, between 0 and π , and the second gate out-of-phase, between π and 2π . This is illustrated in Fig 4 and 5. The FLIM method relies on the ability of the modulation to alter the paint's effective sensitivity to pressure or temperature. Hence, the intensity emitted by the paint can be written in the following form:

$$\begin{aligned} I_{in-phase} &= I(1 + 2m_o/(\pi + 4f^2\pi^3\tau^2)) \\ I_{out-of-phase} &= I(1 - 2m_o/(\pi + 4f^2\pi^3\tau^2)) \end{aligned} \quad (3)$$

Where f is the frequency of modulation, t is time and m_o is the modulation depth of the fluorescence. I is proportional to the lifetime τ (which depends on pressure or temperature):

$$I/I_o = \tau/\tau_o = f_3(P, T) \quad (4)$$

I_o is the intensity at lifetime τ_o corresponding to vacuum. Images taken in phase with the light source are less sensitive than the ones taken with the intensity-based method. Images taken out of phase are more sensitive. The ratio of these images then gives a measurement of pressure or temperature, by eliminating I_o .

The imaging system consists of a Photonic Research System thermo-electric cooled camera head [6] with c-mount lens adapter, a modulation control box with analog to digital converter, and a personal computer, Fig 6. The interface cable between the control box and camera must be kept as short as possible due to the high frequency modulation signals carried. The computer interface to the control box is via a standard parallel port.

The personal computer runs IMAGEX software specifically developed for sensitive paint imaging. This allows live fluorescent lifetime imaging, by alternately acquiring the in-phase and out-of-phase images. The

image ratio is automatically computed and the display updated in real time. Pixel binning can be used to reduce the image download time and increase the frame rate. An analysis mode allows stored images to be retrieved and processed. Images can be captured at any time either by keyboard command, or through an RS-232 link to the wind-tunnel host computer.

The CCD full well capacity is limited to 80,000 electrons per pixel. The camera can be modulated at up to 300 kHz with better than 95% modulation depth, tested directly by imaging an LED light source. The control box contains a computer controlled frequency source, ADC, computer interface and the modulation electronics. The ADC supplied is 12 bits. The image readout rate is limited by the data rate of the link between the control box and computer.

The Photonic Research System LED array used as a modulated light source for the FLIM system is composed of 100 blue LEDs, Fig 7. The spectrum of the recently available ultra-bright Light Emitting Diode (LED) sources is well suited to the excitation of the paint. Fig 8 shows the spectral output of the LED lamp and should be compared to the excitation spectrum of the paint shown in Fig 11.

The approximate size of the lamp is 9 cm x 11 cm x 14 cm with the LED array covering an area of 75 mm x 75 mm. The field of illumination diverges at 30°. The lamp consumes approximately 0.7 A at 28 V DC, when on, and is modulated by a 5 V TTL signal. The output is 7 W m⁻² at a distance of 50 cm. The stability of the lamps is 0.1% per hour under laboratory conditions after a 5 minute warm up period.

A single set of two images at a modulation frequency of 150 kHz is used in all the following experimental sections. Each image has an exposure time of about 1s and a 1s readout time.

Laser scanning system

A schematic of the laser scanning system is shown in Fig 9. The plate supporting the whole system is mounted on two rotary stages, allowing the laser to scan the surface of the paint, one point at a time. This laser excites the paint and luminescence is detected by a low noise photo-detector (e.g. a Photo Multiplier Tube), equipped with a long pass filter. The photo-detector signal is processed to obtain temperature and pressure using a lock-in amplifier and a PC.

The scanning system can be used for both intensity-based and phase-based measurements. A modulator is used for both methods. The intensity-based technique is similar to the one used with the CCD camera, but the excitation signal (laser) is modulated at a frequency of around 1kHz, and then the emitted intensity is demodulated and measured by the lock-in amplifier. This technique helps to get rid of ambient noise, such as

the 60Hz signal that would come from any residual light in the room where the experiment is performed. For the phase-based measurements, the laser is modulated at a frequency depending on the paint used. The luminescent intensity emitted by the paint has the same frequency, and the phase lag between the excitation signal and the emitted signal is measured (Fig 9). A phase calibration is used to obtain pressure or temperature. In the case of the paint used here, the modulation frequency is set to 80kHz. The measurement of the phase (θ) is based on the equation:

$$\tan\theta = 2\pi f\tau \quad (5)$$

Labview programs control the laser scanning system via an IEEE 488 (GPIB) interface for the lock-in amplifier and a RS/232 serial interface for the rotary stages.

The laser scanning system is shown in Fig 10. The laser used in the laser scanning system is a 50mW, 532nm diode laser and the photodetector a Hamamatsu PMT. The scanning rate depends on the integration time (set on the lock-in amplifier) as well as the number of values averaged for each point (set with the Labview program). Ideally, the scanning rate should be as fast as possible without affecting the quality of the data. This is not so much an issue for the jet experiment as it is for other experiments such as the acquisition of in flight data over a wing currently in progress at Purdue University.

The surface pressure or temperature is obtained off-line using a Matlab program.

EXPERIMENTAL SETUP

Paints

Two luminescent paints are used, a pressure sensitive paint and a temperature sensitive paint. Both paints are based on a Ruthenium complex. The pressure paint is Bathophenanthroline Ruthenium Chloride in GE RTV 110, and the temperature paint Tris(2,2'-bipyridyl) Dichlororuthenium Hexahydrate in Clear Cote. These paints were chosen especially for their ability to fluoresce when exposed to wavelengths in a range including UV, blue and green (Fig 11), therefore being compatible with the different measurement systems used. Calibrations for these paints are shown in Fig 12 to 17. Fig 12 and 15 show intensity calibrations of the temperature and the pressure paints for use with the intensity-based CCD camera system. In Fig 13 and 16, temperature and pressure calibrations are presented for the FLIM system. And, finally, phase calibrations of the TSP and PSP in Fig 14 and 17 are used for the laser scanning system. To reduce the data, the different calibrations are fitted to a polynomial curve using Matlab. In the pressure data, temperature correction techniques are used for all the measurements systems.

The influence of temperature is known from the pressure calibrations done at different temperatures.

Jet setup

The experimental setup for the CCD camera/scanning system comparison is shown in Fig 18. It consists of a jet impinging on a flat plate, which can be positioned at different angles and different impingement distances independently, relatively to the jet. The settling chamber of the jet is a 12.5-cm diameter by 30-cm cylinder. The total pressure in the settling chamber can be varied up to around 400 kPa. A regulator controlling the air supply from the Purdue ASL PAC air system sets this pressure, and a 1300 Pa resolution Heise gauge provides monitoring. The total temperature in the chamber is measured with a J-type thermocouple. The nozzle used is a converging nozzle with an exit diameter of 0.5cm.

Two square aluminum plates (40cm x 40cm x 1.25cm) are used in the experiments, each one coated with one of the paints. The paints are sprayed onto white Mylar (model airplane covering), applied on the aluminum plates.

This jet setup was selected because it is geometrically simple. Also, the ability to vary the total pressure and the impingement angle makes it easy to control the surface temperature and pressure.

RESULTS AND DISCUSSION

Studying the behavior of an impinging jet on a flat plate depending on the physical conditions (impingement distance, angle and jet pressure) has been done in the past, [7,8,9]. However, the main emphasis in this paper is the comparison of different PSP/TSP measurement systems. The testing conditions for this experiment are an impingement distance of 5 cm, impingement angle of 10 degrees and a chamber static pressure p_0 of 340kPa. The corresponding values of pressure, temperature and Mach number at the exit of the nozzle and the atmospheric conditions are presented in the following table:

P_0 (kPa)	T_0 (K)	P_{exit} (kPa)	T_{exit} (K)	M_{exit}	P_{atm} (kPa)	T_{atm} (K)
340	300	179.5	250	1	100	300

The flow is induced by the difference between the total pressure in the chamber and the back pressure (downstream pressure outside) which is equal to atmospheric pressure. The pressure ratio $p_{exit}/p_{atm}=1.8$ indicates that the jet is underexpanded. This will induce a series of expansion waves in the flow at the exit of the nozzle. This configuration represents a difficult case for the PSP since it involves large temperature variations and strong pressure gradients across shock waves.

The data taken is presented in Fig 19 to 25. In the case of the temperature paint, temperature distributions are obtained with the intensity-based CCD camera system (Fig 19), the FLIM system (Fig 20) and the laser scanning system (Fig 25). Pressure measurements are performed with all the systems (Fig 21, 22 and 23) and are complemented by the use of pressure taps, for a pressure distribution along the centerline of the jet. All the dimensions are normalized to the diameter of the nozzle (D) and the origin of the coordinate system is chosen to be the geometric impingement point of the jet. For temperature data, raw temperature is presented whereas a pressure coefficient is used for pressure data. C_p is calculated as follows:

$$C_p = (p - p_{atm}) / q_{exit} \quad (6)$$

A Schlieren image (Fig 24) helps to understand better the flow field associated with the experiment. And finally, Fig 25 and Fig 26 give all the different results for temperature and pressure respectively, along the centerline of the jet.

Intensity-based/FLIM camera systems

Compared with the intensity-based method, the FLIM system is not sensitive to non-uniform illumination, paint thickness, photo-degradation, dust and model motion. Therefore, it doesn't require a flow off picture like the intensity-based method does. The same conclusions can be drawn when comparing the intensity-based and phase-based methods for the scanning system. For the images taken here, the total exposure time for the intensity-based method is 4s maximum (a maximum of 500ms per image times 8 images added). For the FLIM system, it also takes 4s (1s for in-phase and 1s for out-of-phase, plus 2x1s for readout). Overall, the need to take two images for the FLIM system coupled with the fact that data is only taken during half of the time increases the wind-on acquisition time by a large factor for the FLIM system.

The comparison between the intensity-based CCD camera system and the FLIM system shows that the images obtained with the FLIM system are noisier. Lower CCD resolution and no frame averaging for the FLIM system can explain this. In addition, as discussed by Liu et al in a study on uncertainty analysis for CCD camera systems, [10], signal to noise ratio is better for the intensity-based method. In conclusion, the FLIM system should be able to reach a resolution comparable to the one of the intensity-based CCD camera systems if image-averaging techniques were used.

Camera systems/laser scanning system

The pressure and temperature distributions obtained with the laser scanning system and the phase-based

method is shown in Fig 23 and Fig 25. Compared with camera systems (intensity-based and FLIM), the laser scanning system has some advantages, but also drawbacks. The laser scanning system can be used for measurements in a facility where optical access is very limited and the CCD camera system is difficult to use. It provides uniform illumination over a surface by scanning a single light spot. In order to obtain a complete pressure map, the laser spot is scanned over the surface. However, it currently takes more time to get a pressure or temperature distribution with the scanning system. As a positive point, many types of enhancing techniques (filtering...) are available for the laser scanning system, for example, through the use of a lock-in amplifier. This means that the system can be easily adapted for measurement of luminescent lifetime or phase shift if a pulsed laser or modulated laser is used. These kinds of techniques offer the advantages of eliminating the need for a reference.

Luminescent paints measurement systems/pressure taps

In Fig 25, the temperature data on the centerline of the jet obtained with the different systems looks very similar except for the region closest to the nozzle where there is a discrepancy between the scanning system and the camera systems. There is also a difference between the two camera systems towards the downstream region. Fig 26 presents a comparison of the PSP data with pressure tap data along the centerline of the jet. Qualitatively, the pressure coefficients obtained with the measurement systems follow the trend of the pressure taps, even though significant errors can be seen in this figure. This is mostly due to temperature effects, which are not corrected entirely. Although not totally accurate compared to pressure taps, luminescent paints measurement systems have at least the advantage of offering a complete pressure distribution. More generally, the application of the temperature and pressure sensitive paints offers the possibility of being significantly less expensive than conventional instrumentation.

CONCLUSION

A set of pressure and temperature data for an underexpanded obliquely impinging jet is presented for comparison of three luminescent paints measurement systems. For both the temperature and the pressure data, significant errors are encountered. Temperature effects are primarily responsible for these problems.

The FLIM system would require more time than the intensity-based CCD camera system for an equal resolution, but offers the advantage of not needing a flow-off image. The laser scanning system has advantages compared to the camera systems, the main

one being its ability to be used in environments where a camera could not. Knowing the comparable quality of the different systems and the advantages and disadvantages of each one, a system should be selected depending on the testing conditions for a given experiment. This choice would more precisely depend on three factors: optical access of the facility, possibility to take a flow off reference (model motion) and time available to do the measurement.

Acknowledgement

The authors would like to thank Tianshu Liu for his advice concerning data comparison and his useful information for uncertainty analysis of camera systems.

References

- [1] Moris, M.J. et al, "Aerodynamic Applications of Pressure Sensitive Paint", AIAA paper 92-0264, January 1992.
- [2] Bell, J.H., Mc Lachlan, B.G., "Image Registration for Luminescent Paint Sensors", AIAA Paper 93-0178, January 1993.
- [3] Donovan, J.F. et al, "Data Analysis Techniques for Pressure and Temperature Sensitive Paints", AIAA Paper 93-0176, January 1993.
- [4] Holmes, J.W., "Analysis of Radiometric, Lifetime and Fluorescent Imaging", The Aeronautical Journal, Paper 2306, p189-194, April 1998.
- [5] Morgan, C.G., "Measurement of Luminescence", US Patent 5,459,323, October 1995.
- [6] Morgan, C.G., Mitchel, A.C., Murray, J.G., Wolf, E.J., "New Approaches to Lifetime-resolved Luminescence Imaging", Journal of Fluorescence Vol7, No 1, 1997.
- [7] Donaldson, C.D., Snedeker, R.S., "A Study of free Jet Impingement", Journal of Fluid Mechanics, vol. 45, part 2, 1971.
- [8] Lamont, P.J., Hunt, B.L., "The Impingement of Underexpanded, Axisymmetric Jets on Perpendicular and Inclined Flat Plates", Journal of fluid Mechanics, vol. 100, no. 3, p.471-511, 1980.
- [9] Crafton, J., Lachendro, N., Guille, M., Sullivan, J.P., Jordan, J.D., "Application of Temperature and Pressure Sensitive Paint to an Obliquely Impinging Jet", AIAA Paper 99-0387, January 1999.
- [10] Liu, T., Guille, M., Sullivan, J.P., "Uncertainty Analysis of Pressure Sensitive Paint Measurement", AIAA Paper 99-3785, June 1999, to be published.

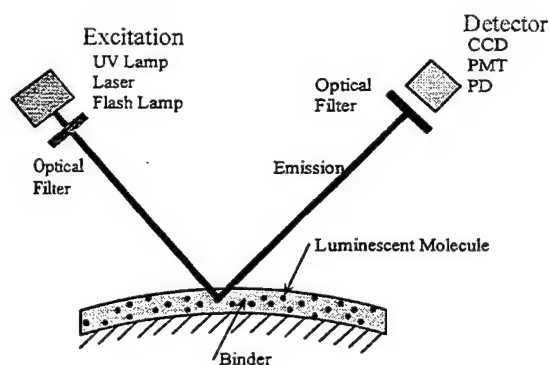


Figure 1 Basic PSP/TSP operation

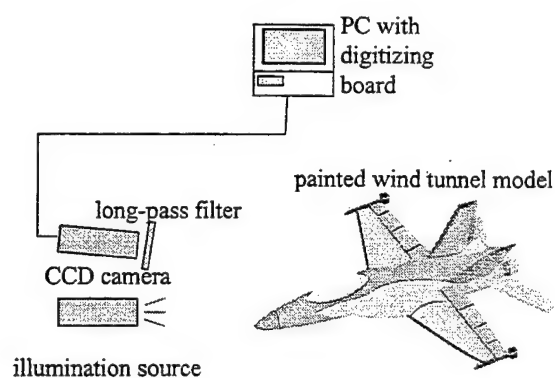


Figure 2 Intensity based CCD camera system

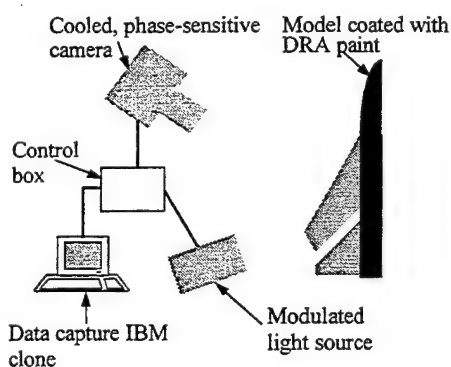


Figure 3 Schematic of FLIM system

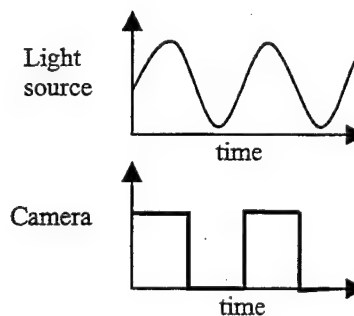


Figure 4 In-phase gate for the FLIM system

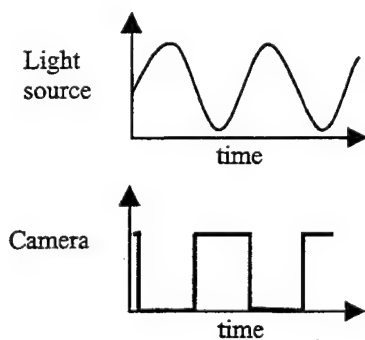


Figure 5 Out-of-phase gate for the FLIM system

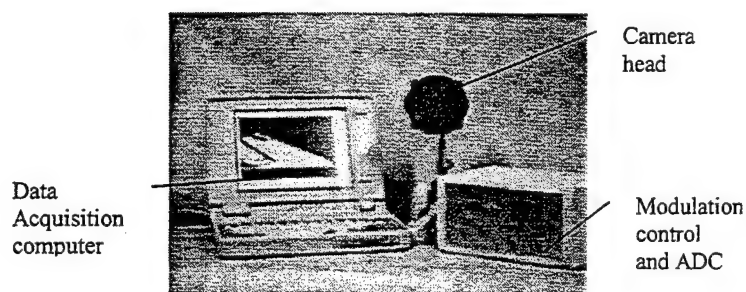


Figure 6 Modulated camera system

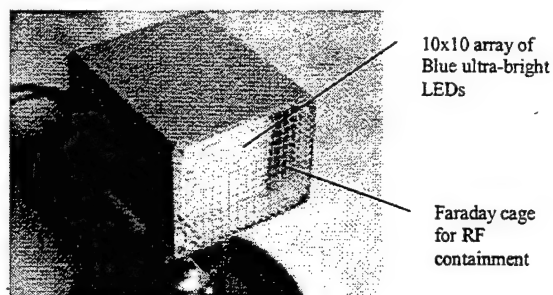


Figure 7 Picture of 100 light emitting diode source

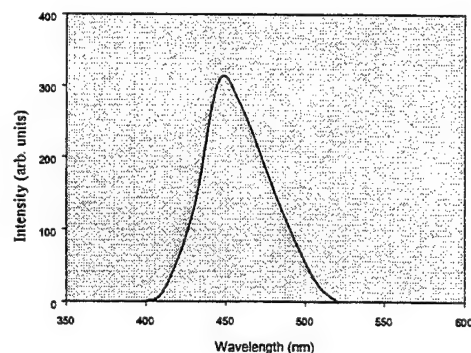


Figure 8 Spectral output of LED source

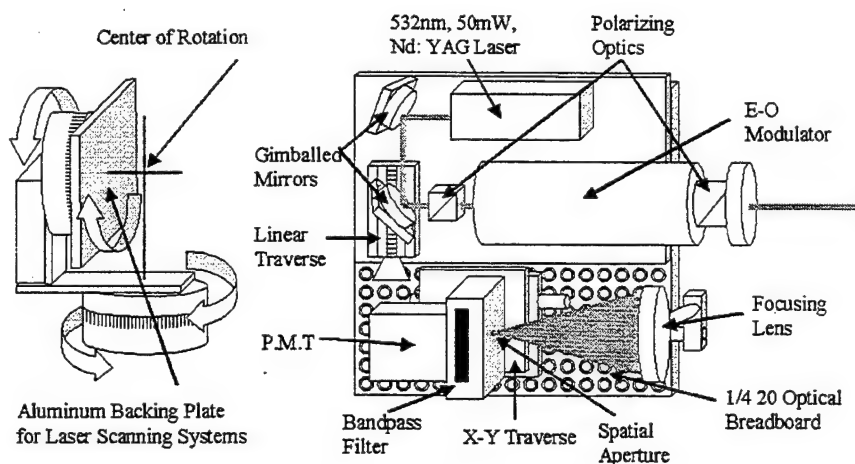


Figure 9 Schematic of laser scanning system and phase based measurement technique

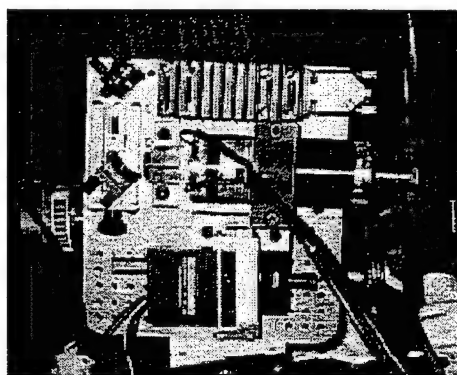


Figure 10 Laser scanning system at Purdue University

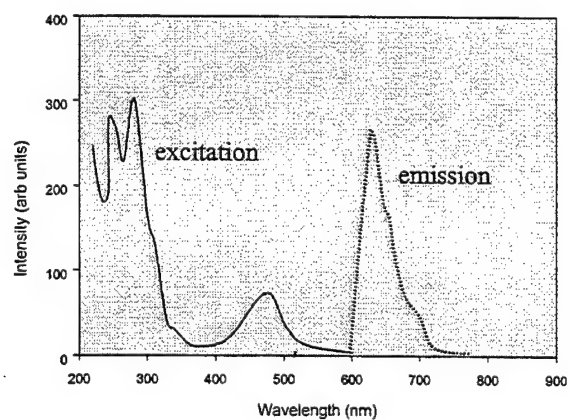


Figure 11 Excitation and emission spectra for Ruthenium-based molecules

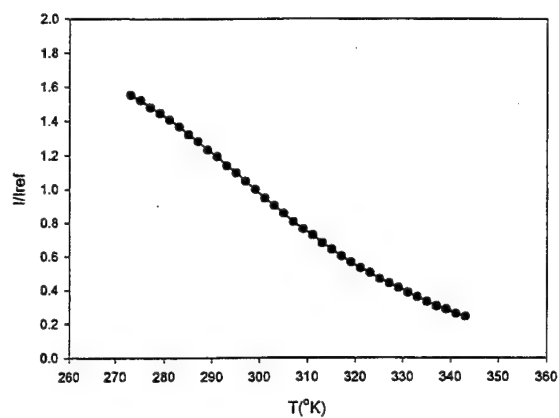


Figure 12 Intensity calibration of the temperature point

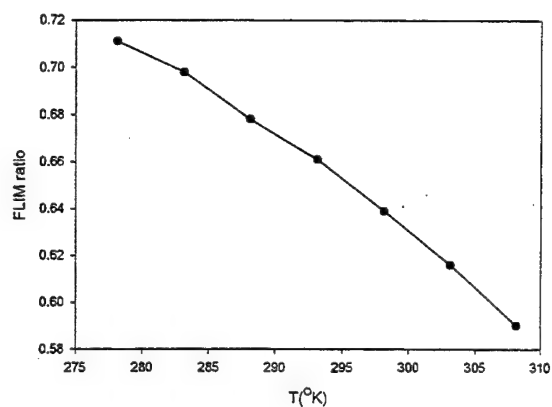


Figure 13 FLIM calibration of the temperature point

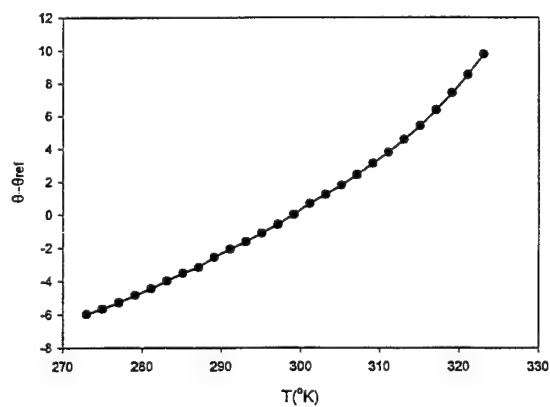


Figure 14 Phase calibration of the temperature point

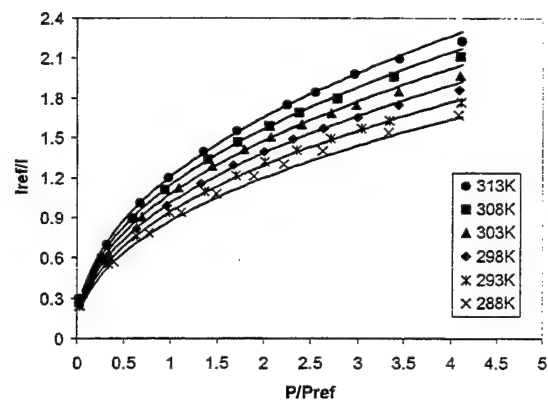


Figure 15 Intensity calibration of the pressure point

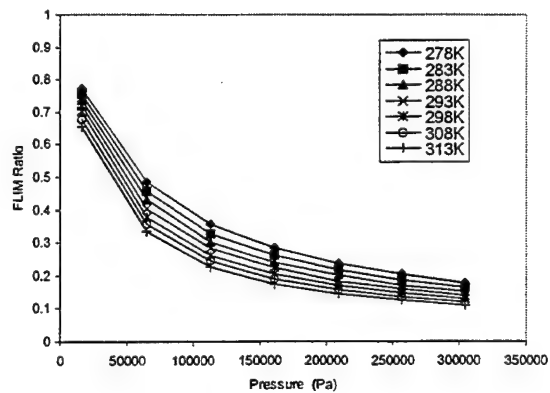


Figure 16 FLIM calibration of the pressure point

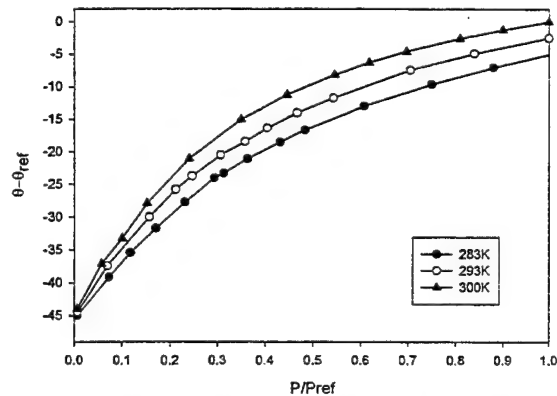


Figure 17 Phase calibration of the pressure point

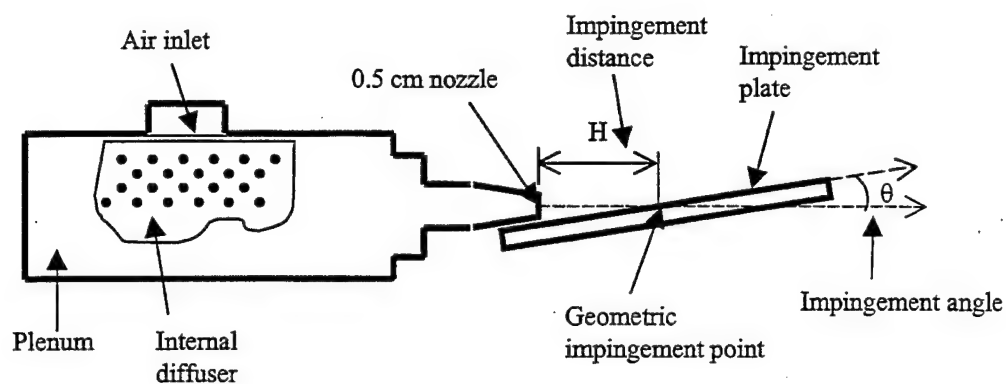


Figure 18 Experimental setup

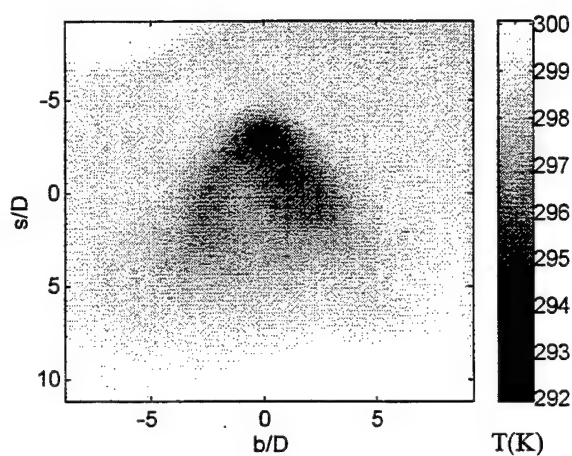


Figure 19 Temperature distribution with the intensity-based CCD camera system

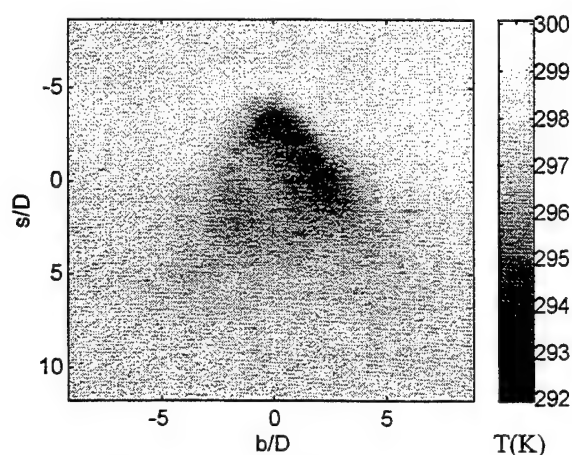


Figure 20 Temperature distribution with the FLIM system

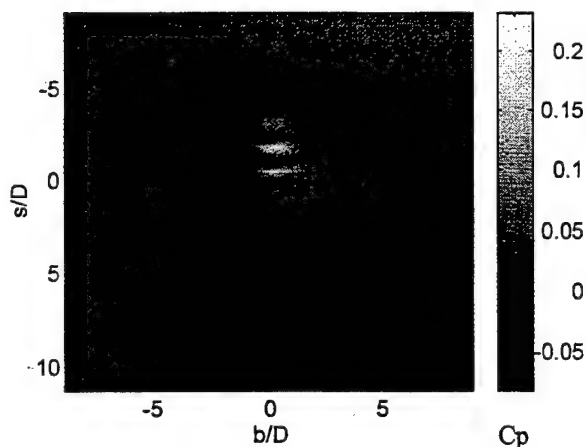


Figure 21 C_p distribution with the intensity-based intensity-based CCD camera system

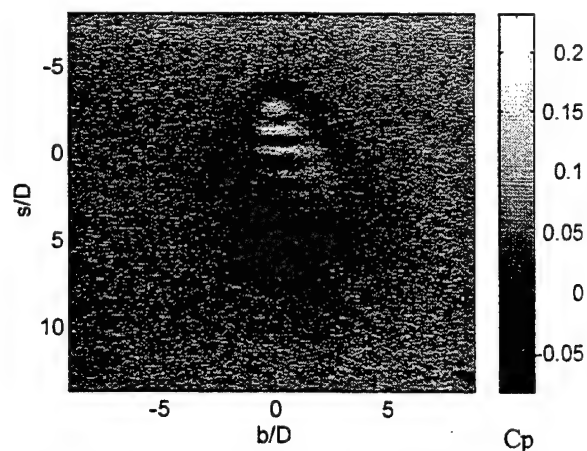


Figure 22 C_p distribution with the FLIM system

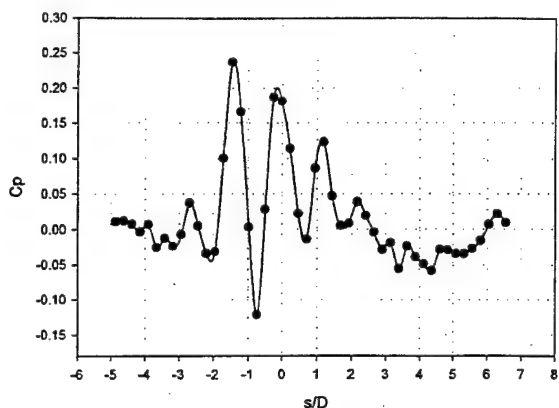


Figure 23 C_p distribution on the centerline with the laser scanning system

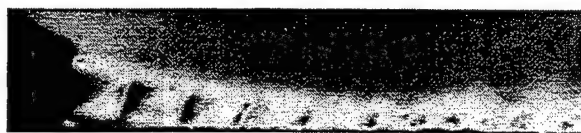


Figure 24 Schlieren flow visualization

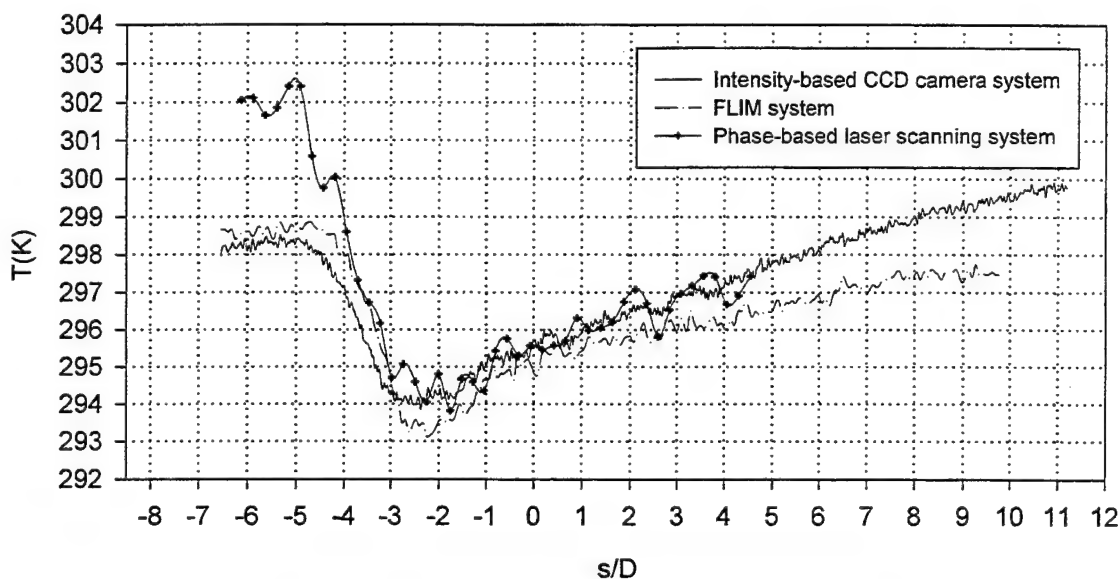


Figure 25 Temperature comparison of all the systems

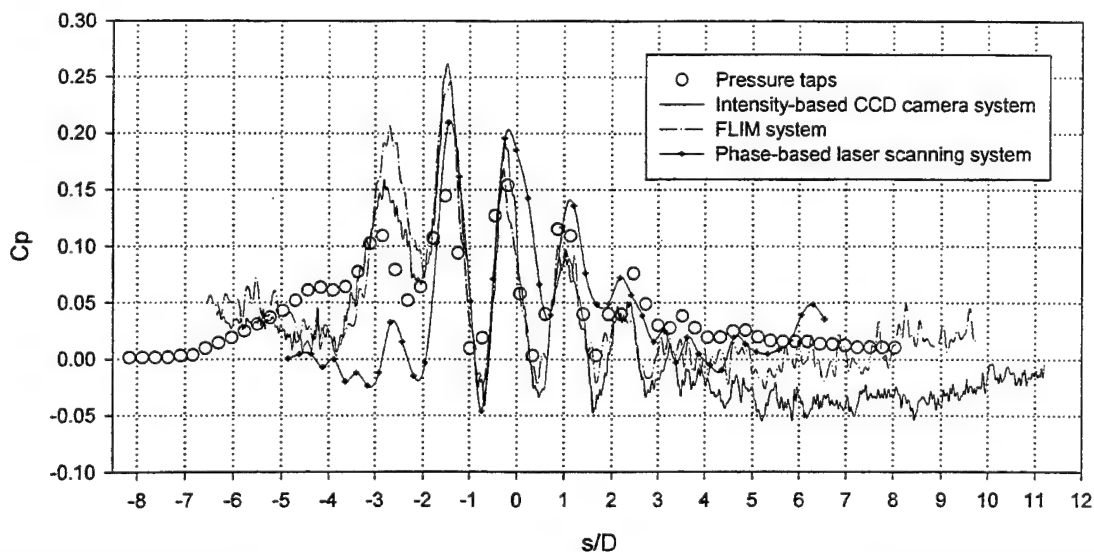


Figure 26 Pressure comparison with the pressure taps

THE RECENT METHODS FOR SURFACE PRESSURE AND SKIN FRICTION MEASUREMENTS ON THE MODELS.

A.Bykov, V.Kulesh, A.Orlov, V.Pesetsky

Central Aero-Hydrodynamics Institute, Zhukovsky, Russia

ABSTRACT

The work presents experimental and theoretical evaluations of the ultimate measurement possibilities and application fields of the PSP and mechanical skin friction gages. PSP provides visualization and measurement of the pressure distribution on the model surface without usual pressure taps. The mechanical skin friction gages have been developed for point measurements of the friction stresses on the surface. It was made attempt to unite small sizes of hot-wire film gage with possibility for direct measurements of the skin friction as in balances with a floating element. The results of the evaluations are illustrated by the examples of pressure distribution measurements on the surface of the different aircraft models, propeller blades in transonic and supersonic wind tunnels, and by measurements of the skin friction on the test section walls of the trans- and supersonic wind tunnels and on the wing surface of the supersonic transport aircraft model.

INTRODUCTION

Pressure distribution measurement on the surface of an aircraft model is one of the main problems of experimental aerodynamics. With the help of pressure distribution field it is possible to state flow separation zones, shock wave position, loads distribution, to visualize aerodynamic interference between aircraft components and to understand in common the influence of such effects on integral aircraft characteristics. The classic taps measurements of pressure distributions are very complex and expensive due to model itself and pressure measurement techniques. That is why the pressure taps measurements cannot be widely used as aircraft instrument. A PSP Technology, based on well-known phenomenon of oxygen quenching, permits to solve this problem [7-25]. The PSP method allows to obtain the pressure distribution practically on the total surface of the standard models, for example, on the model for balance experiments and to make experiments in parallel with another testing. Usually three dimensional flow field structures are overcomplicated in third - time dimension, by some non-stationary effects. PSP provides possibility

of quantitative visualization not only the panoramic pressure field on the total model but its evolution.

The precise measurement of skin friction gains in ever increasing importance because of a rising contribution of skin shear to the total drag of current speed wide-body aircraft. Both direct and indirect methods are used to measure skin friction. The indirect methods, based on the similarity laws for velocity profiles near the wall (Preston method, Stanton method, bar/ledge method) or on the analogue between skin friction and heat transfer (thermal and hot-wire anemometry methods) [1-3], necessitate, as a rule, preliminary calibration, often at site, under conditions close to test ones. The basic disadvantage of the first group of methods concerns a disturbed flow over the wall at the place of their application because its concept implies the action on the flow. The film hot-wire anemometers to measure skin friction disturb the flow the least and in view of this they are most suitable for delicate experiments. Besides, they enable turbulent skin friction fluctuations to be estimated. But a serious weakness of this method is inadequate control over heat transfer towards the wall, which restricts severely their application to measure moderate skin friction.

Among the direct methods, the method of floating-frame balance, providing most reliable results, finds the widest application. However, even most space-saving similar balances (Cistler and Laval [4]) feature, along with excellent performance, too great sizes; besides, they imply significant deterioration of the model surface and observance of precautions when applied (for example, the absence of drastic flow non-stationarities and considerable temperature gradients). Therefore, they are unsuitable for mass experiments.

The current aerodynamic experiment dictates measurements of skin friction over the total surface of almost all components in flow: wing, fuselage etc. This requires the application of a great number of discrete skin friction gages, which deteriorate the surface under study as little as possible and do not disturb the flow.

The suggested method to measure skin friction combines the advantages of the floating-frame balance (direct skin on shear measurement) and the film hot-wire skin friction gages (small sizes, low inertia). It allows the development of small-size mechanical skin friction gages (MSF). The

method was proposed by A.Orlov in 1987 to be published in 1990.

PRINCIPLE OF OPERATION

The principle of operation of small-size mechanical skin friction gages is based on the application of a thin elastic polymer layer as a flexible system to transform the tangential force to a shear. The lower surface of the elastic polymer layer makes contact with the gage base or directly with a surface to be investigated (Figure 1).

The tangential force F acts on the external surface of the elastic layer to shear it with respect to the lower surface in the force direction by the value of

$$\Delta x = h\tau/G, \quad (1)$$

where h is the elastic layer thickness, G is the shear modulus, $\tau = F/S$ is the desired tangential stress, S is the external elastic layer surface area.

The shear Δx of the external elastic layer surface can be converted into electric signals by applying various well-known methods, for example, optical, capacitance methods etc. Existing polymer materials feature a wide range of shear modulus values thus providing considerable opportunity to choose a characteristic shear value Δx depending on the method of its measurement and test conditions. In the present paper, the polymer layers with the shear modulus G in the range ($10^{-1} \div 1$ gf/cm²) were used to measure skin shear up to 10 gf/cm². This technology makes it possible to develop small-size mechanical skin friction gages for aerodynamic and hydrodynamic applications.

Optofiber small-size mechanical skin friction gage

There are many various optical methods of measuring small displacements (Moire method, interference method etc.) which can be applied to develop optical MSF gages. The paper [5] describes the optical light guide-based method of measuring small displacements designed for floating-frame balance. We employed a similar method of measuring elastic layer shears in our technology of the optofiber small-size mechanical skin friction gage (OMSF). Figure 2 presents the general view of an optofiber mechanical skin friction gage. It consists of a MSF transducer 1 with a three-core optofiber cable 2 and a single signal-conditioning unit (SCU) 3 to convert the optical signal into a standard electric signal. The optical scheme of the MSF transducer 1 is given in Figure 3.

The optofiber cable 2 has one central light guide 2.1 used to transmit the initial light flux to the MSF transducer and two signal light guides 2.2 and 2.3 transmitting the differential optical signal to the SCU. The case 1.1 of the

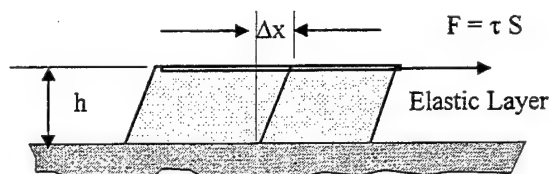


Figure 1

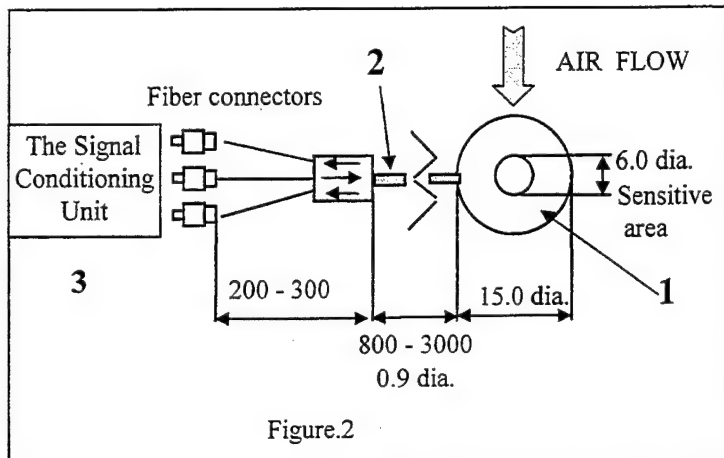


Figure.2

MSF transducer contains an elastic polymer layer 1.2 with a sensitive plate 1.3 on its external surface and an

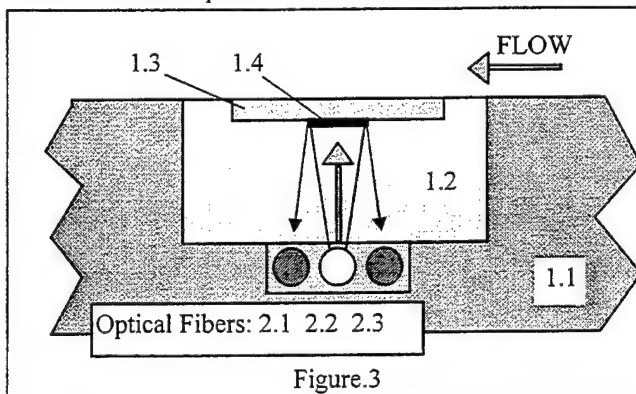


Figure.3

optical sensing element (a mirror band 1.4 on the sensitive plate) to provide optical communication and redistribution of the light fluxes from the central light guide output to the inputs of a pair of the signal light guides depending on the shear Δx of the elastic layer. The SCU includes an infrared light-emitting diode as a source of the initial light flux and a pair of receiving photodiodes connected, respectively, to the central and signal light guides via special connectors, and an electronic circuit to amplify and normalize the photodiode signals.

The analysis reveals that a similar gage does not respond to the tangential force directed along the mirror band of the sensitive plate. It senses only the vector component of

the skin friction stress τ in the direction \mathbf{n} perpendicular to the mirror band. In this case, the effective elastic layer shear Δx is in proportion to the scalar product of the vectors τ and \mathbf{n} :

$$\Delta x = \mathbf{h}(\tau \mathbf{n}) / G.$$

The relationship between the light fluxes I_1 and I_2 at the signal light guide outputs and the shear Δx at small values of Δx can be represented by a linear function

$$I_1 \approx I_{01} (1 + k_1 \Delta x);$$

$$I_2 \approx I_{02} (1 - k_2 \Delta x),$$

where k_1 and k_2 are the constants, and I_{01} and I_{02} are the light fluxes at the signal light guide outputs at $\Delta x = 0$. The values of I_{01} and I_{02} are not constant to vary slowly with time due to the light guide radiation instability and the dependence of the light guide transmission factor on the light guide deformation. Because all the optical fibers are placed in one cable and their deformations are similar, while the influence of the light guide instability for two signal light guides is the same; it is believed that the ratio

$$\hat{I} = I_{02} / I_{01} \text{ is constant.}$$

The electronic circuit to amplify and normalize the photodiode signals provides the conversion of the form

$$U = \frac{I_1 - I_2}{I_1 + I_2} = \frac{1 - \hat{I} + (k_1 + \hat{I} \cdot k_2) \cdot \Delta x}{1 + \hat{I} + (k_1 - \hat{I} \cdot k_2) \cdot \Delta x},$$

which allows such a balance of the photodiode signals that $k_1 - \hat{I} k_2 = 0$; besides, "zero" of the output signal can be regulated. In so doing, it is possible to achieve a direct proportionality of the output signal to a desired shear Δx . Reversal of the shear force direction results in changing the output signal sign.

This principle underlies the optofiber small-size mechanical skin friction gage OMSF-0.4 designed for $\pm 10 \text{ gf/cm}^2$ with the MSF transducer 15mm in diameter and 0.4mm in thickness (Table 1), the sensitive plate shear corresponding to a nominal skin friction stress value being $\sim 5 \mu\text{m}$.

Capacitance MSF

The capacitance method of transforming the tangential shear Δx to an electric signal implies that the elastic layer lies between two thin plates. The lower plate is attached to the gage base, while the upper plate represents a sensitive plate subjected to the action of a desired tangential stress. A raster in the form of metallized bands constituting a pair of electrodes is applied to each plate (Figure 4). In total, the plates form a system of four flat capacitors a connected in a capacitance bridge. Apart from the main operating bridge capacitance's C_1 and C_2 , the circuit includes interelectrode capacitance's C_3 on

each plate and shunt capacitance's C_4 of the lead conductors (assume that they are the same). Let the plates have the form of a square with a side of L , the width of the metallized bands of the raster be equal to d , the space between the adjacent metallized bands be b and the raster period be $\Lambda = d + b$. Then on each plate we have two

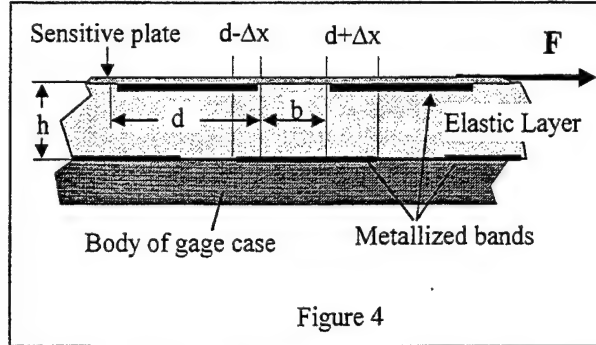


Figure 4

electrodes each comprising $L/2\Lambda$ metallized bands of a total area of $L^2/2\Lambda$. In the initial state, the electrodes of different plates overlap each other thus forming flat capacitors. Assuming that the elastic layer thickness h is much smaller than the band period Λ the capacitance of each capacitor is equal to $C_0 = \epsilon_0 \epsilon L (d - b) / 4\Lambda h$, where ϵ is the dielectric constant of the elastic layer material and ϵ_0 is the dielectric constant of vacuum. The shear Δx increases the overlapping area for one pair and decreases it for the other by $\Delta x L^2 / 2\Lambda$, therefore, the main operating bridge capacitance's C_1 and C_2 can be expressed as follows:

$$C_{1,2} = C_0 (1 \pm \Delta x / \Lambda) = C_0 \pm \Delta C.$$

The application of the two-conductor line model under the assumption that the effective conductor radius is a half of the conductor width $d/2$ and the relative dielectric constant of the polymer ϵ and the plate material are the same gives estimates for the interelectrode capacitance's

$$C_3 \approx 2\pi / \ln 2 \cdot C_0 \cdot h / d \approx 2.27 C_0 \cdot h / d.$$

The electric signal U at the output of this capacitance bridge is proportional to ΔC :

$$U \sim U_0 \Delta C = U_0 2\Delta x / (d - b),$$

where U_0 is the bridge supply voltage.

The signal/noise ratio of a similar gage is in proportion to the capacitance C_0 of the electrodes forming the capacitance bridge and in inverse proportion to the total capacitance $C \approx C_0 + C_3 + C_4$ of the system of the capacitors, lead conductors and input capacitance's of the amplifiers, i.e.:

$$S/N \sim \frac{2\Delta x}{d - b} \frac{C_0}{C_0 + C_3 + C_4} = \frac{2\Delta x}{(d - b)(1 + 2.27 h/d) + 4\Lambda h C_4 / L^2}$$

From this it is inferred that for the signal/noise ratio to be increased it is necessary to reduce the raster period Λ , ratio h/d and, first of all, the capacitance C_4 . To do this,

the electronic amplifying device should be placed in the immediate vicinity of the capacitor plates, for example, inside the MSF transducer case.

The general view of the capacitance mechanical skin

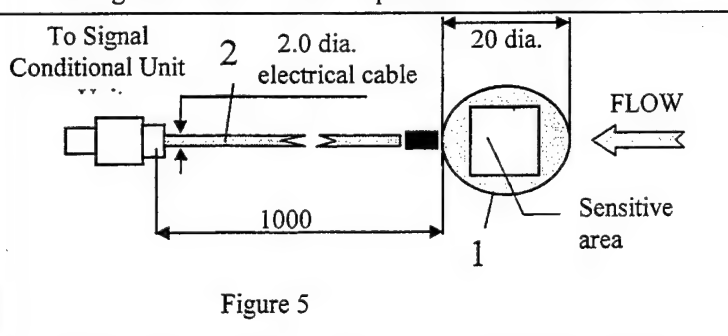


Figure 5

friction gage is given in Figure 5. The capacitance MSF gage consists of a MSF transducer 1 with an electric cable 2 and a signal control unit.

INVESTIGATION OF MSF GAGES ON TEST SECTION WALLS

The initial investigations of the MSF gages were carried out in a well-studied gradientless flow over the test section walls. The tests were conducted in a transonic 2.5 m-diameter wind tunnel and in a supersonic 2.25x2.25m wind tunnel. The turbulent boundary layer in the regions of testing MSF gages was 100mm thickness; therefore, the methodical requirements for the gage installation were satisfied rather easily.

Test equipment

The mounting plate A and the mounting plate B were manufactured for the transonic and supersonic wind tunnels, respectively. Two OMSFI-0.4 gages and one static pressure gage were installed flush with the surface of the plate A with a diameter of 130mm. The plate B 315 mm in diameter was provided with (Figure 6):

- 4 OMSF gages (N1, 2, 3 and 4);
- a tap to measure static pressure fluctuations by the DMI gage;
- a tap to measure mean static pressures by the IKD 800 gage;
- AD590 temperature gage

Experiment

The OMSF gages were investigated at the following flow parameters:

Transonic wind tunnel

Table 1.

M	Re/lm, mln	P _{static} , kPa	T ₀ , K°
0.3÷0.86	6.08÷12.55	95.8÷62.8	308÷321

Supersonic wind tunnel

The OMSF gages were studied in the range of M=0.8÷2.0, but multiple tests were conducted only at M=2.0.

Table 2.

M	Re/lm, mln	P _{static} , kPa	T ₀ , K°
2.02	23.62	25.30	293 to 283
2.03	24.20	24.50	294 to 281
2.03	24.20	24.96	289
2.02	24.78	24.90	282
2.03	24.02	24.57	287

The measurements were begun several seconds before the wind tunnel start and finished after its stop.

In investigating the OMSF gages (mounting plate A) in the transonic wind tunnel, the electric signals were recorded continuously at a scanning frequency of 60Hz. Besides, one of two OMSF gages was scanned at a frequency of 1.5kHz. Each series contained 1000 samples. The number of series in runs was varied from 5 to 25.

In investigating OMSF gages (mounting plate B) in the supersonic wind tunnel, the signals were digitized and recorded using an ADC by series. Two gages from four were scanned at a frequency of 1kHz with buffer capacity of 1000 samples, while two other gages were scanned at a frequency of 15 kHz with buffer capacity of 800 samples. The number of the series during the experiment was varied from 10 to 15. The gage signals were continuously recorded on the tape recorder. These signals were

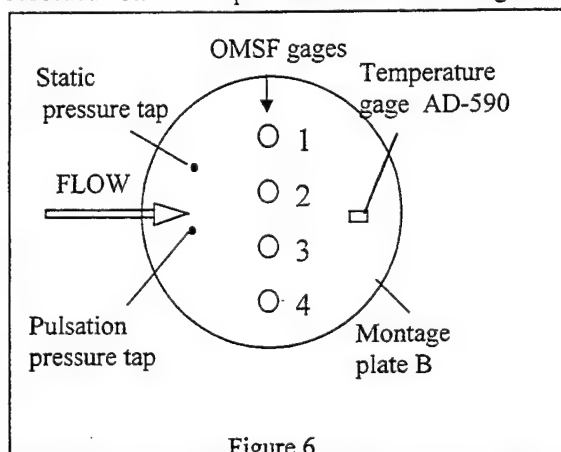


Figure 6

digitized using a high-speed ADC on completion of the experiment.

After the wind tunnel experiments, the information was processed with due consideration of the calibration coefficients obtained for the OMSF gages. The OMSF gages were calibrated after the experiments with the mounting plate taken off from the test section wall. The corrections for the temperature dependence of the sensitivity coefficient to amount to 0.3%/deg were also applied. The measurement data processing procedure

included the zero shifts, which was assumed to be linear over the wind tunnel operation time.

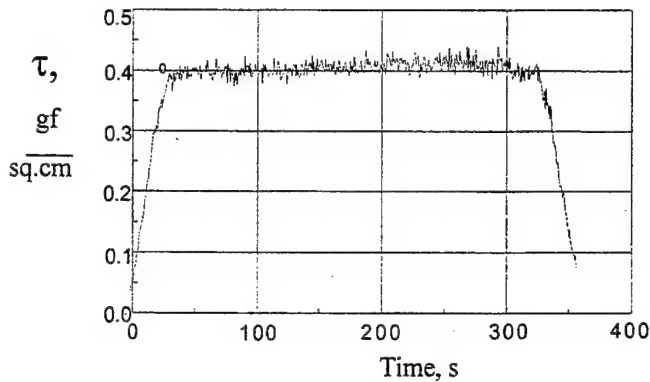


Figure 7

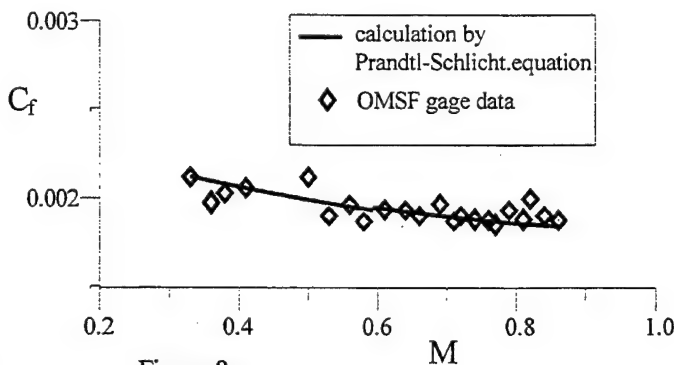


Figure 8

Mean skin friction stresses.

Transonic wind tunnel.

The time history of the skin friction stress is presented in

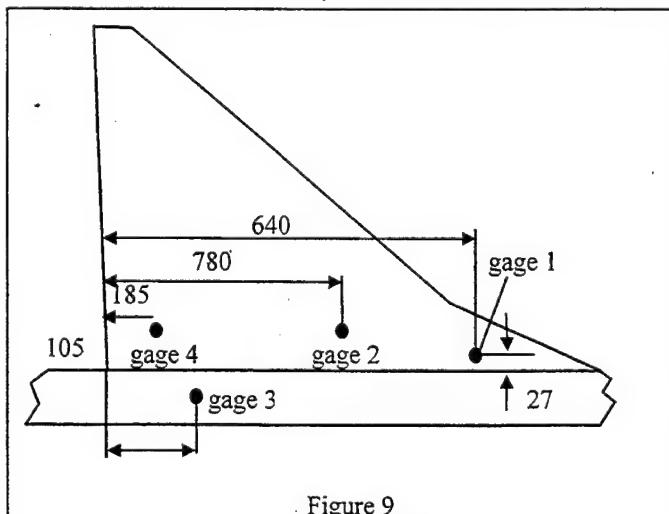


Figure 9

Figure 7 at $M=0.62$ with the time laid off on the abscissa

axis and the skin friction stress on the ordinate axis. Figure 8 illustrates the skin friction coefficient based on the skin friction stress values measured by one of the OMSF gages installed on the mounting plate A as a function of the number M . The skin friction coefficients calculated by the Prandtl-Schlichting equation including the compressibility effect are also presented in this figure. In this case, the standard deviation from the mean value is not in excess of $\pm 3\%$.

Supersonic wind tunnel

The skin friction coefficients derived using each 4 OMSF gages installed on the mounting plate B are compared with the data obtained by E.Efimov [6]. E.Efimov made measurements of the skin friction stress at the same place of the supersonic test section wall using the floating-frame balance at Mach numbers ranging from 0.5 to 3.66. In addition, he measured the velocity profile, the boundary layer thickness, displacement thickness and momentum thickness. Proceeding from these data, local values of $Re(x)$ and resulting skin friction coefficient C_f were calculated. The skin friction coefficients C_f obtained by applying each of 4 OMSF gages were averaged over 5 runs. The below table summarizes the relative standard deviations for each OMSF gages, the averaged values $\langle C_f \rangle$ and the skin friction coefficients C_f measured by E.Efimov at $M=2$.

Gage #	Standard Deviations of OMSF gage skin friction coefficient, %	$\langle C_f \rangle$	Efimov's skin friction coefficients
1	9.8	0.001354	0.00132
2	5.5	0.001365	
3	8.5	0.00120	
4	7.8	0.001354	

Unfortunately, the supersonic test section flow contained oil, water and dust drops, therefore, the OMSF gages gave too high skin friction coefficient values. In further runs, the flow became increasingly purer and the gage readings were closer to real values.

INVESTIGATIONS OF OMSF GAGES IN SUPERSONIC WIND TUNNEL ON SUPERSONIC CIVIL AIRCRAFT MODEL

Test equipment

The OMSF gages were tried for measurements of the skin friction stress on a supersonic civil aircraft model (1:25 Tu-144 aircraft model). To do this, 4 OMSFT1-0.4 gages were mounted on the model surface (Figure 9) and 3 OMSFT1-0.4 gages on the wing.

Measurement results

The tests were conducted in accordance with the parameter matrix given in Table 2. Figure 10 shows the time variations in the shear stress measured by the gages #1 and #4.

But it is quite obvious that the gage #1 experienced much more intense action of the non-air phase than the gage #4. It can be assumed that the solid and liquid particles of the non-air phase went through the thin boundary layer to act directly upon the sensitive plate of the gage #1.

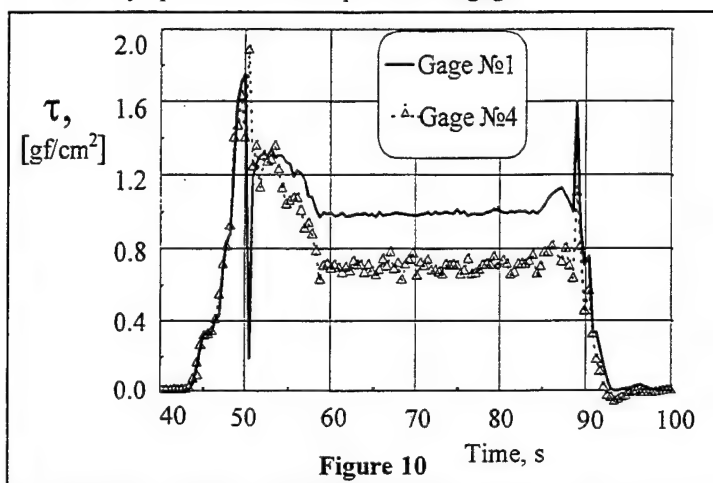


Figure 10

Besides, a shock wave acted upon the gages during the test starts and stops which is well seen in Figure 13. The action of the pressure gradient $\text{grad}P$, on the gage readings is also obvious. In this case, the vector of $\text{grad}P$ and the skin friction stress vector are opposite in direction.

The OMSF gages installed on the model featured the zero drift; therefore, the OMSF gage readings were recorded before and after the wind tunnel start. The zero instability was taken into account in processing the measurement data. The zero drift during a run was assumed to be linear.

The OMSF gages were calibrated by applying a tangential force using weights immediately on the model on completion of the wind tunnel operation.

The skin friction stresses obtained on the wing of the TU-144 model by the OMSF gages were compared with the predictions made for a flat plate.

PSP MEASUREMENT CONCEPT

Luminescence intensity I of PSP-coating is inversely proportional to the pressure p and is directly proportional to excitation light intensity and to the coating thickness. To exclude the influence of excitation light intensity and coating thickness to the measurement result, the ratio of reference image at known (wind-off) condition to

operating image at unknown (wind-on) condition must be taken [9]. The surface pressure in the point i can be determined from PSP calibration characteristic:

$$p(i) = A + BI_{ref}(i) + C(I_{ref}(i)/I(i))^2$$

Coefficients A , B and C are determined from PSP calibration in laboratory and are assumed to be the same for all points of PSP-coating. Above expression also assumes that: a) model position and shape at wind-on condition is the same as at wind-off condition; b) excitation light distribution remains the same during the test; c) excitation light energy at wind-off exposition is equal to the energy at wind-off exposition; d) there are not any scattering particles in the airflow and on the model surface (dust, fog, smoke etc.). PSP technology is detailed in Refs. [7-11].

EXPERIMENTAL RESULTS

Aerodynamic loads

Aerodynamic loads by PSP were investigated in T-112 blowdown wind tunnel on the canard aircraft configuration at $M=0.8$ and 1.2 and angle-of-attack from 0° up to 23° . The T-112 wind tunnel has a rectangular $0.6\text{m} \times 0.6\text{m}$ test section with a hole perforation on its sell and bottom and non-perforated side walls. Figure 11 shows pressure field distribution at $M=0.8$ and 1.2 on 5° , 9° , 15° and 23° angle-of-attack on upper surface canard

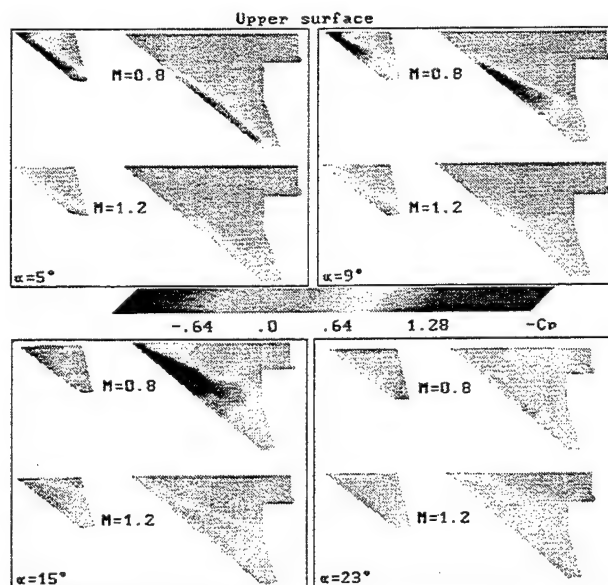


Figure 11

configuration. Simultaneously we measured normal force acting on canard. Figure 12 shows comparison of normal forces acting on a canard measured by internal strain gage

balance and calculated from pressure distributions for upper and lower surfaces of a canard at $M=1.2$. The agreement between measured by internal balance and by PSP is very good.

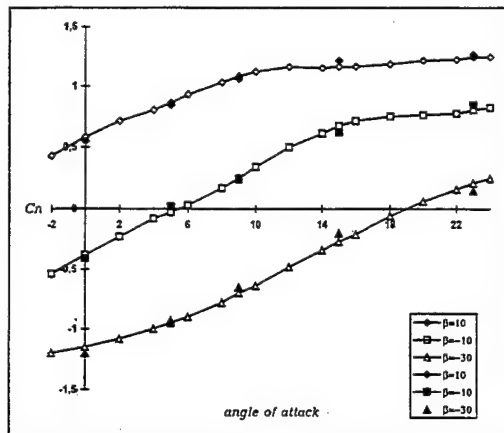


Figure 12

Black marks -PSP measurements.
White marks - strain gage balance.

Unsteady flow on the wing upper surface

Time evolution of the pressure fields was investigated on the training aircraft Yak-130 model at $M=0.5-0.9$ in transonic T-106 wind tunnel. T-106 wind tunnel has a circular test section with a diameter 2.48 m.

Time evolution of the pressure field was more apparent at Mach number 0.7. C_p fields presented on Figure 13 have been chosen to show maximum detectable variations in C_p field topologies. Pike suction zone near leading edge at angle-of-attack $\alpha=10^\circ$ are usually divided in two parts (sometimes three) with boundary point attached to leading edge and migrating along it. C_p distributions along wing span at 5% of local wing chord are presented on Figure 14 demonstrate the magnitude of spatial and amplitude fluctuations.

Propeller blades

Pressure distribution on the front surface of rotating blades of model of propellers was measure in T-104 wind tunnel. T-104 is an open-jet subsonic wind tunnel of 7 meters nozzle diameter allowing to get flow speed in the range of 0-120 m/sec [14].

The model was twin-blade propeller model of 0.65 m diameter having sweptback blades from the rotor of coaxial propeller CB-27M. The model was investigated in whole flow speed range of T-104 wind tunnel at rotation frequency 7000 rpm at different installation angles of blades $\beta=15^\circ, 22.5^\circ, 30^\circ, 40^\circ$ (β -blade installation angle at relative radius $r/R=0.75$). This

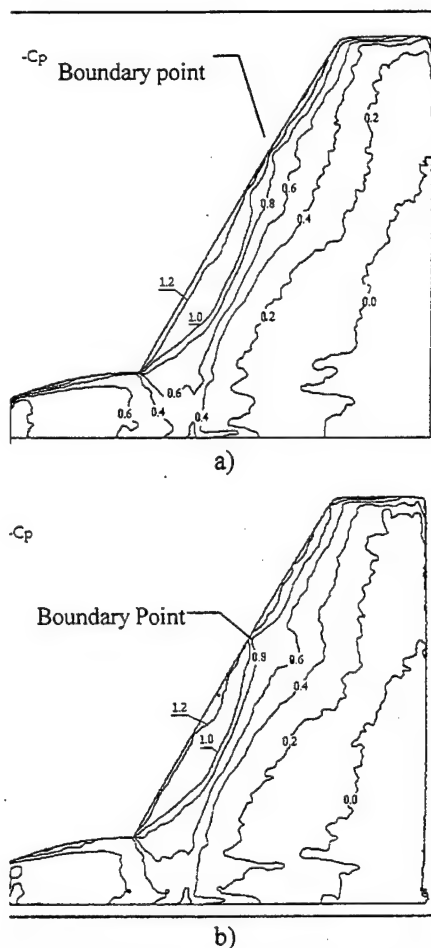


Figure 13 C_p fields at $M=0.7$ and $\alpha=10^\circ$ in different moments

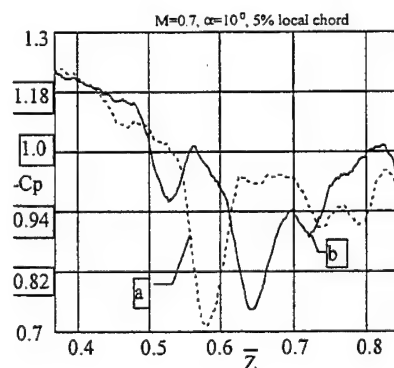


Figure 14

rotation frequency of propeller model corresponds to the full-scale blade speed. Figure 15 presents pressure distributions on the blade installed at the angle $\beta=40^\circ$ at different flow speeds $V=20, 40, 60, 90$ m/sec, and Figure 16 presents pressure distributions on the blade installed at different angles $\beta=15^\circ, 22.5^\circ, 30^\circ$ at the absence of flow. These figures show the change of flow structure about

blade surface depending on installation angle and flow speed.

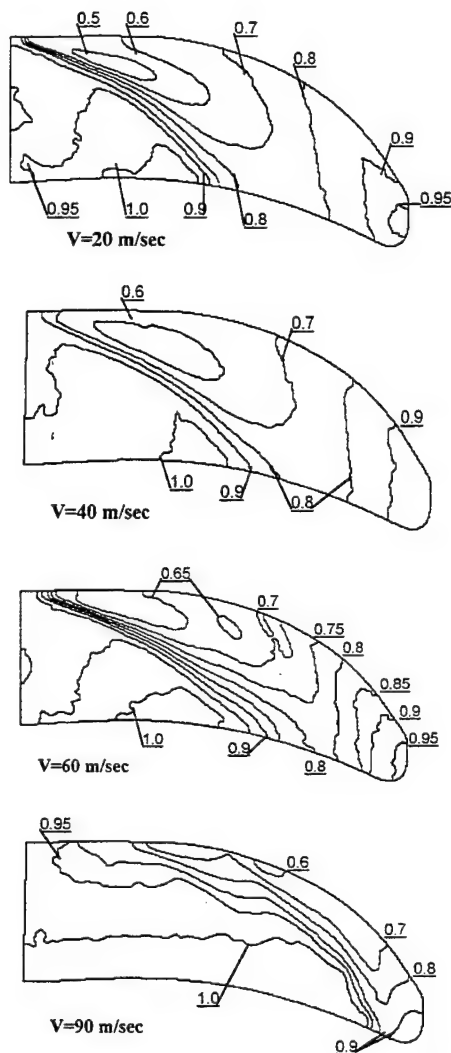


Figure 15. Pressure distributions (in bar) on a blade of CB-27M propeller at installation angle $\beta = 40^\circ$ and rotation frequency $n = 7000 \text{ rpm}$ at different flow speeds

CONCLUSIONS

- (1) The OMSF gages are capable for normal operation in the range of $M=0.3 \div 2$ including the action of shock waves occurring during the wind tunnel start and stop.
- (2) The rms deviation of skin friction stresses is $\pm 3\%$ in tests on the test section wall in the range of $M=0.3 \div 0.86$ and $Re = 6 \times 10^6 \div 12 \times 10^6$ based on 1 meter.

- (3) The skin friction stresses measured on the industrial aircraft model in the supersonic wind tunnel are in good agreement with the predictions made on the flat plate.
- (4) The OMSFT1-0.4 gages enable the skin friction fluctuations to be evaluated in the wind tunnel conditions at 0-3.0 kHz.

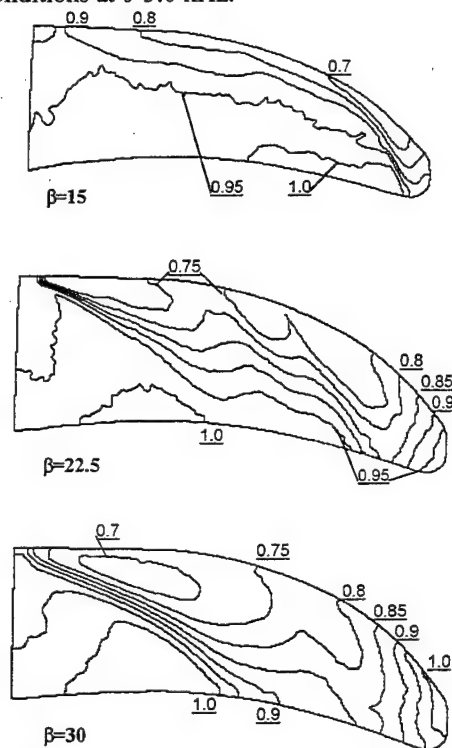


Figure 16. Pressure distributions (in bar) on a blade of CB-27M propeller at flow speed $V=0 \text{ m/sec}$ and rotation frequency $n = 700 \text{ rpm}$ at different installation angles

- (5) Pressure Sensitive Paint permits to investigate unsteady separated flow on the aircraft models.
- (6) The investigations prove that PSP technology is extremely attractive method of pressure measurements on rotating blades, fast enough, cheap and universal.

REFERENCES

1. Winter K.G., "An outline of the techniques available for the measurement of skin friction in turbulent boundary layers"; Progress in aerospace sciences, v.18, p.1-57, 1977.
2. Settles G. S., "Recent skin friction techniques for compressible flows", AIAA Paper, No.1099, 1986.
3. Nitsche W., Haberland C., Thunker R. "Comparative investigation on friction drag measuring techniques

- in experimental aerodynamics", ICAS-84-2.4.1, p.391.
4. Elfstrom G.M., "Indirect measurement of turbulent skin friction", Quart. Bull. Division of Mech. Engineering and the Nat. Establishment, 1/1-31/111, No.1, p.21-51, 1979.
 5. Frank W. Cuomo, Robert S. Kidwell, Andong Hu, "A fiber optic sensor sensitive to normal pressure and stress", SPIE Optical Testing and Metrology, Vol.661, pp.234-239, 1986
 6. Efimov E.S., "The drag of technological vehicle surface roughness and superstructures in a turbulent boundary layer at $M=0.5-3.6$ ", (in Russian), Trudy TsAGI, 1970.
 7. Bykov A.P., Orlov A.A., Mosharov V.E., Pesetsky V.A., Radchenko V.N., Sorokin A.V., Fonov S.D., Alaty L., Colucci V. "Application of Luminescence Quenching for Pressure Field Measurements on the Model Surface in a Wind Tunnel", conference "Wind Tunnels and Wind Tunnel Testing Techniques", South Hempton, September 1992.
 8. Troyanovsky I., Sadovskii N., Kuzmin M., Mosharov V., Orlov A., Radchenko V., Fonov S. "Set of Luminescence Pressure Sensors-LIPS for Aerospace Research", 1st European conference on optical chemical sensors and biosensors, Graz, Austria 12-15 April 1992. Sensors and Actuators B, 11 (1993) 201-206.
 9. Bykov A., Mosharov V., Orlov A., Pesetsky V., Radchenko V., Matyash S., Fonov S., Kuzmin M., Sadovskii N., "Optical surface pressure measurements: accuracy and application field evaluation", 73rd AGARD Fluid Dynamics Panel Meeting and Symposium on Wall Interference, Support Interference and Flow Field Measurements, Brussels, Belgium 4-7 October 1993, AGARD-CP-535.
 10. Mosharov V., Orlov A., Radchenko V., Kuzmin M., Sadovskii N., "Luminescent Pressure Sensors for Aerospace Research: Diffusion-Controlled Characteristics", 2nd European conference on optical chemical sensors and biosensors, Firenze, Italy, 19-21 April 1994.
 11. Andreev A.O., Bykov A.P., Ipatov M.W., Kabin S.V., Nushtaev P.D., Orlov A.A., Mosharov V.E., Radchenko V.N., Pesetsky V.A., Fonov S.D., "Pressure fields investigation by LPS technology on the aerospacecraft model", J.Phys. III France 4 (1994) 2317-2337.
 12. Bykov A., Fonov S., Mosharov V., Orlov A., Pesetsky V., Radchenko V. "Investigation of the airflow around aircraft model at high and intermediate angle of attack with pressure sensitive paint", 20th Congress of the ICAS, Sorrento, Napoli, Italy, 8-13 September, 1996
 13. Lifshitz Yu., Fonov S., Morozov A., Orlov A., Radchenko V., Pesetsky V., "A Study of Transonic Winglet-Wing Flow with Light Intensity Pressure Sensors", TsAGI's preprint No. 78, 1993.
 14. Bykov A., Fonov S., Kishalov A., Mosharov V., Orlov A., Ostroukhov S., Radchenko V., "Application of Luminescent Pressure Sensor Technology to Propellers", TsAGI's preprint No 99, 1995.
 15. Bykov A., Fonov S., Mosharov V., Orlov A., Pesetsky V., Radchenko V., "Study Result for the Application of Two-Component PSP Technology to Aerodynamic Experiment", 81st AGARD Fluid Dynamics Panel Symposium on Advanced Aerodynamic Measurement Technology, Seattle, United States, 22-25 September 1997, AGARG-CP-601.
 16. Lyonnet M., Deléglise B., Grenat G., Bykov A., Mosharov V., Orlov A., Fonov S., "The Two-Component PSP Investigation on Civil Aircraft Model in S2MA Wind Tunnel", 81st AGARD Fluid Dynamics Panel Symposium on Advanced Aerodynamic Measurement Technology, Seattle, United States, 22-25 September 1997, AGARG-CP-601.
 17. Kavandi J., Callis J., Gouterman M., Khalil G., Wright D., Green E., Burns D., McLachlan B. "Luminescent Barometry in Wind Tunnels", Rev. Sci. Instruments, 61(11), pp. 3340-3347, November 1990.
 18. McLachlan B.G., Kavandi J.L., Callis J.B., Gouterman M., Green E., Khalil G., "Surface pressure field mapping using luminescent coatings", Experiments in Fluids 14, 33-41(1993).
 19. Baron A.E., Danielson J.D.S., Gouterman M., Wan J.R., McLachlan B., "Submillisecond response times of oxygen-quenched luminescent coatings", Rev. Sci. Instrum. 64 (12), Dec. 1993.
 20. Crites R.C., Benne M.E., Morris M.J., Donovan J.F. "Optical Surface Pressure Measurements: Initial Experience in the MCAIR PSTWT", conference "Wind Tunnels and Wind Tunnel Testing Techniques", South Hempton, September 1992.
 21. Morris M.J., Donovan J.F. "Application of Pressure- and Temperature - Sensitive Paints to High-Speed Flows", 25th AIAA Fluid Dynamics Conference, June 20-23, 1994/ Colorado Springs, CO, AIAA Paper No 2231, 1994
 22. Jagharhi A.J., Mitchell M., Burkett C., Sealey S. "Wind Tunnel Application of Pressure Sensitive Paint at NASA Langley Research Center (8-foot TPT & 7'x10' HST)", NASA LaRC IRD ATMB, June 15, 1993.
 23. Sellers M.E., Brill J.A., "Demonstration Test of Pressure Sensitive Paint in the AEDC 16-ft

Transonic Wind Tunnel Using the TST Model", 18th AIAA Aerospace Ground Testing Conference, June 20-23, 1994/ Colorado Springs, CO, AIAA Paper No 2231, 1994.

24. Engler R.H., Hartmann K., Schulze B. "Aerodynamic Assessment of an Optical Pressure Measurement System (OPMS) by Comparison with Conventional Pressure Measurements in High Speed Wind Tunnel", 14th ICIASF Congress, October 27-31, 1991, Rockville, MD
25. Burns S.P., Sullivan J.P., "The Use of Pressure Sensitive Paints on Rotating Machinery", 16th ICIASF Congress, July 18-21, 1995, Dayton, Ohio.

Pressure and Temperature Measurements with a Dual-Luminophor Coating

Bruce F. Carroll and James P. Hubner*

Department of Aerospace Engineering, Mechanics & Engineering Science
University of Florida
Gainesville FL, 32611-6250

*Joint appointment with AeroChem Corporation

Kirk Schanze and Joanne Bedlek

Department of Chemistry
University of Florida
Gainesville, FL 32611-7200

Martin Morris

Department of Mechanical Engineering
Bradley University
Peoria, IL 61625

Abstract - Data reduction requirements for dual-luminophor pressure/temperature sensitive paints (P/TSP) are explored through the use of principal component analysis. The dual-luminophor coating contains one luminophor which primarily responds to temperature and one which responds to both temperature and pressure. The analysis indicates that a two-factor reduced order model based on two fundamental spectra represents the majority of the luminescence response but cannot properly account for mutual interaction effects between the luminophors. The inclusion of a third factor appears to sufficiently model the mutual interaction effects. This work indicates that P/TSP data reduction procedures based on principal component analysis are promising for improving the accuracy of the measurements. The potential to remove the requirement of a wind-off reference image and to reject high frequency noise is also indicated.

INTRODUCTION

Pressure and Temperature Sensitive Paints, PSP and TSP, are luminescent coatings for which the luminescence intensity varies with pressure and temperature, respectively. As has been well documented in the literature, PSP coatings also display undesirable temperature sensitivities [1] which can cause significant errors in the pressure determination. Various techniques to correct for the temperature effects exist [2,3]; however, the temperature field must be measured concurrently with the pressure field to implement these corrections. Increasing interest has been placed on the development of multi-luminophor coatings that provide spectrally resolved indications of pressure, temperature, and/or reference intensity. The purpose of this paper is

to explore data reduction requirements for dual-luminophor pressure/temperature sensitive paints.

CHARACTERISTICS OF PSP AND P/TSP

The temperature and pressure dependence of a typical PSP is shown in Figure 1 which illustrates the change in emission intensity, I_{em} , with both pressure and temperature. A schematic of this PSP coating is shown in Figure 2 where a luminophor is dispersed within an oxygen permeable binder. The emission intensity of a particular coating depends primarily on three variables: pressure, temperature and excitation intensity/coating thickness. Spatial variations in excitation intensity and coating thickness are usually corrected by using an intensity ratio between a reference condition and the run condition, as presented in Figure 1. The pressure dependence of the PSP arises from oxygen quenching of the luminescence. The quenching rate, and hence the luminescence intensity, is proportional to the oxygen concentration within the coating which is related to the partial pressure of oxygen at the solid/gas interface. The temperature dependence of the PSP coating arises from two primary sources. First the diffusion of oxygen through the polymer binder is a temperature dependent process. This affects the ability of the oxygen to migrate to and quench luminophor molecules. Secondly, quenching of the luminescence due to energy transfer directly from the luminophor to the binder is a temperature dependent process. As seen in Figure 1, the temperature dependence of the PSP coating is significant and can cause unacceptably large errors in many flow conditions.

A dual-luminophor T/PSP system is shown schematically in Figure 3. Two luminophors are selected such that one exhibits a pressure sensitivity (along with an unwanted temperature sensitivity) and the second luminophor exhibits a strong temperature sensitivity but little if any pressure sensitivity. Spectroscopic data for a dual luminophor system is shown in Figures 4a and 4b: the first for a constant pressure condition and the second for a constant temperature condition.

DATA ANALYSIS REQUIREMENTS

Appropriate data reduction procedures for single-component PSP have been developed. However, the data reduction requirements for a dual- or multi-component P/TSP system are unclear. One approach is to use an optical band-pass filter to generate two data sets - one for the temperature dependent region of the spectra and the other for the pressure/temperature region. Simple ratios between a reference and run condition are then formed and data reduction procedures analogous to single component PSP and TSP are used. This approach may yield useful results for some applications but fails to account for mutual interactions between the luminophors. In this paper, we have chosen to approach the data reduction question with the use of principal component analysis. In this approach, the individual component contributions (or factors) are extracted from the total emission spectra. Secondary contributions due to mutual interactions between the luminophors or contributions from a third or fourth luminophor may also be extracted from the data.

A brief overview of the principal component analysis follows. A spectrally resolved data matrix is obtained from the CCD camera (alternately from a spectrometer) using a series of optical filters. Each pixel on the CCD supplies spectral data for a single environmental condition (i.e. pressure and temperature condition). Thus the data matrix may be expressed as

$$S = S_{\lambda n} \quad (1)$$

where S is a two dimensional array of measured intensities, λ is the wavelength, and n is the environmental condition (i.e. pixel number). The columns of S give the spectral distribution of each pixel of the camera. We make the assumption that S may be represented by the product of a principal component array, F , and a contributions array, A ,

$$S = S_{\lambda n} = FA = F_{\lambda k} A_{kn} \quad (2)$$

In this expression, k is the number of factors used to represent the complete data set, S . Thus, our goal is to generate a reduced order model with k important factors used to represent S . Intuitively for a two-luminophor system, with no mutual interaction between luminophors, we expect $k = 2$ to adequately represent the data. For this ideal system, F , would be the fundamental luminescence spectra of each luminophor in the two-luminophor system and A would be an attenuation multiplier that accounts for variations in environmental parameters (i.e. pressure, temperature, coating thickness, etc.).

The next steps in the principal component analysis follow the approaches outlined by Lawton & Sylvestre [4] and Malinowski & Howery[5]. The data matrix, S , is normalized such that for each value of n the sum over λ yields unity. This is done to avoid numerical problems with the matrix manipulations. The normalization also eliminates the need of forming a ratio of the data to a reference condition. A covariance matrix, Z , is defined by

$$Z \equiv SS^T \quad (3)$$

The covariance matrix is then diagonalized by finding a matrix, V , such that

$$V^{-1}ZV = E \quad (4)$$

The columns of V are mutually orthogonal eigenvectors and the diagonal elements of E are the eigenvalues (off diagonal elements of E are zero). Making use of the orthogonality of V (i.e. $V^T = V^{-1}$) one can show that

$$A = V^T S \quad (5)$$

and

$$F = V \quad (6)$$

The product FA is an abstract model for the data matrix S in that it does not necessarily represent the data in any physically meaningful format. Also note that since the problem has been overdetermined, the eigenvectors, V , contain extraneous data corresponding to noise. However, the eigenvectors that correspond to the largest eigenvalues contain the "important" information. Stated another way, each eigenvector represents an abstract factor that contributes to the spectral data set. A large eigenvalue indicates the corresponding eigenvector is an important contribution to the data while a small eigenvalue indicates the corresponding eigenvector is unimportant. By neglecting unimportant eigenvectors we achieve a mathematically

compact representation of the data. These effects are illustrated in Figures 5 and 6. These figures were obtained by applying the procedure above to spectroscopic data similar to that in Figure 4. Figure 5 gives the relative magnitudes of the first five eigenvalues. The first two eigenvalues are orders of magnitude larger than the other eigenvalues. Thus it appears reasonable to "compress" the model by setting the eigenvalues past the first two to zero. This is equivalent to setting $k = 2$ in Eq. (2) and nulling the appropriate matrix elements in Eqs. (5) and (6). We will refer to the reduced or compressed model for S as S' which for $k = 2$ is given by

$$S' = S'_{\lambda n} = F_{\lambda k} A_{kn} \text{ with } k = 1, 2. \quad (7)$$

Note that the data set S' is still a λ by n matrix but F and A have been reduced in size from Eqs. (5) and (6). Figure 6 shows the first two eigenvectors which correspond to the first two principal components in matrix F . While the sum of the two abstract spectra give a reasonable representation of the data, the negative values in second vector near a wavelength of 625 nm are clearly unrealistic for a luminescence process.

Various procedures exist to rotate or transform the eigenvectors in such a way as to extract physically important information from the data set. For our data set we expect that one rotated eigenvector should describe the temperature sensing luminophor and the other rotated eigenvector should represent the pressure sensing luminophor. Complete details of the coordinate transformation process will not be presented, but an illustration for a single environmental condition (i.e. single pixel or single value of n) will be helpful. Our original data matrix was represented by the product $S = FA$. If we limit our attention to a single environmental condition and consider only $k = 2$ factors we can write the spectra $S'(\lambda)$ as

$$S'(\lambda) = A_1(n)F_1(\lambda) + A_2(n)F_2(\lambda) \quad (8)$$

where $F_1(\lambda)$ and $F_2(\lambda)$ are the principal components found in the first two columns of F and $A_1(n)$ and $A_2(n)$ are the corresponding elements of A for a particular value of n . Thus the combined spectra, $S'(\lambda)$ is simply a linear combination of the two fundamental (abstract) spectra, $F_1(\lambda)$ and $F_2(\lambda)$. The information regarding the environmental parameter, n , is contained in the n -pairs of attenuation or contribution parameters ($A_1(n)$, $A_2(n)$). Since the individual spectra are uniquely defined by the ($A_1(n)$, $A_2(n)$) pairs, the entire data set may be represented on a two-dimensional plot of $A_1(n)$ vs $A_2(n)$. Defining a generalized set of contribution parameters,

(ξ_1, ξ_2), the range of possible spectra are represented on a graph of (ξ_1, ξ_2) = ($A_1(n)$, $A_2(n)$) pairs. This is done in Figure 7 where the compressed data is represented as solid square symbols. The linear representation of the data, with very little scatter, in the two-dimensional (ξ_1, ξ_2) solution space indicates that a two-factor system provides a reasonable representation of the data. Coordinate transformations of the abstract principal vectors, F , may be obtained by finding new (ξ_1, ξ_2) pairs that fall along the straight line defined by the data. Our goal is to find rotated vectors, denoted f , that have more physical significance than the principal abstract vectors, F . The rotated f are formed as a linear combination of the principal abstract vectors

$$f_i(\lambda) = \xi_{1,i}F_1(\lambda) + \xi_{2,i}F_2(\lambda). \quad (9)$$

Once the vectors f_i are obtained and the matrix f is formed then a new contribution matrix, a , is obtained from the relation

$$S' = fa. \quad (10)$$

For a two-term representation ($k = 2$) we will obtain $f_1(\lambda)$ and $f_2(\lambda)$ referred to as factor 1 and factor 2, respectively. Constraints are placed upon the new (ξ_1, ξ_2) pairs to represent physical limitations:

- I) The transformed factors, $f(\lambda)$ must be non-negative to represent realistic spectra from a luminophor.
- II) The attenuation multipliers, ξ_1, ξ_2 , must be non-negative.
- III) The transformed vectors, which correspond to actual luminescence spectra, are minimized at appropriate end points.

Conditions (I) and (II) are required for any physically realizable system of luminophors. Condition (III) is based on our knowledge of the luminescence spectra for each luminophor in isolation. These constraints are shown as open circles in Figure 7 and the open triangles represent the most physically realistic spectral distributions for the transformed factors, f . Figure 8 also illustrates these concepts. The transformed vectors $f_1(\lambda)$ and $f_2(\lambda)$ are plotted for the two constraint conditions and the most realistic condition. Factor 1, centered about 500 nm, represents a temperature sensing luminophor and factor 2, centered about 625 nm, represents a pressure sensing luminophor. While all the curves shown satisfy constraints (I) and (II), the darker curves also satisfy the constraint (III).

Using the factors $f_1(\lambda)$ and $f_2(\lambda)$, the resulting combined spectra, $S'(\lambda)$ is obtained using Eq. (10) and shown in Figure 9 for a single environmental condition. The thin line is the model representation, $S'(\lambda)$, of the raw data, $S(\lambda)$, shown in bold line. We see that the model representation of the data set provides a reasonable representation of the original data, but some errors exist. In an absolute difference sense the error between $[S(\lambda)-S'(\lambda)]$ is 7%, which propagates to a pressure error of a similar magnitude. The compression process is responsible for this error and one sees that even though the third eigenvalue in the abstract solution space was only 0.1% relative contribution, the third and higher factors contribute 7% of the total luminescence response.

To explore this further, the raw data spectra over a range of environmental parameters, $n = 0$ to 19, is plotted in Figure 10. This data set is then represented by a two-factor and a three-factor model in Figures 11 and 12, respectively. The primary region of difference between the two models is highlighted by a circle on both figures. The three-factor model more accurately captures the true behavior. The average percent error for each environmental condition, n , is plotted in Figure 13. The two-factor model has errors ranging from 1 to 9% while the three-factor system consistently provides errors below 2%. Thus, including the third factor, which accounts for interactions between the two luminophors, is important to minimize errors. An additional benefit of the principal component analysis is noise rejection. The high frequency noise apparent in Figure 10 has been reduced in Figures 11 and 12.

CONCLUSIONS

Data reduction requirements for a dual-component pressure/temperature sensitive paint were investigated using principal component analysis techniques. Principal component analysis provides a robust tool for characterizing the spectral distributions of multi-component luminescence sensors. The dual-luminophor P/TSP was found to have two primary physical factors. One was predominately temperature sensitive while the second was both pressure and temperature sensitive. Mutual interaction effects, especially noticeable in the overlap between the spectra of the two factors, were modeled well by the inclusion of a third factor. This indicates that simple ratio based data reduction techniques may not be able to accurately characterize multi-luminophor sensor systems.

An added benefit of the principal component analysis is that it tends to reject noise from the data set. The technique also has the potential of eliminating the

need for a wind-off reference image. Further work needs to be done to combine the principal component analysis with calibration procedures to provide a complete data analysis tool for multi-luminophor sensor systems. The impact of the data collection optical band-pass filter width on the data analysis requires further study. A P/TSP coating that exhibits three strong principal components should provide sufficient information to determine pressure and temperature without a wind-off reference.

REFERENCES

- [1] Schanze, K. S., Carroll, B. F., Korotkevitch, S., and Morris, M. J., "Temperature Dependence of Pressure Sensitive Paints," *AIAA Journal*, Vol. 35, No. 2, pp. 306-310, Feb. 1997.
- [2] Hubner, J. P., Carroll, B. F., Schanze, K. S., "Temperature Compensation Model for Pressure-Sensitive Paint," FEDSM97-3470, ASME Fluids Engineering Division Summer Meeting, Jun. 1997.
- [3] Woodmansee, M. A., and Dutton, J. C., "Treating Temperature-Sensitivity Effects of Pressure-Sensitive Paint Measurements," *Experiments in Fluids*, Vol. 24, pp. 163-174, 1998.
- [4] Lawton, W. H., and Sylvestre, E. A., "Self Modeling Curve Resolution," *Technometrics*, Vol. 13, pp. 617-633, 1971.
- [5] Malinowski, E. R., and Howery, D. G., *Factor Analysis in Chemistry*, John Wiley & Sons, New York, 1980.

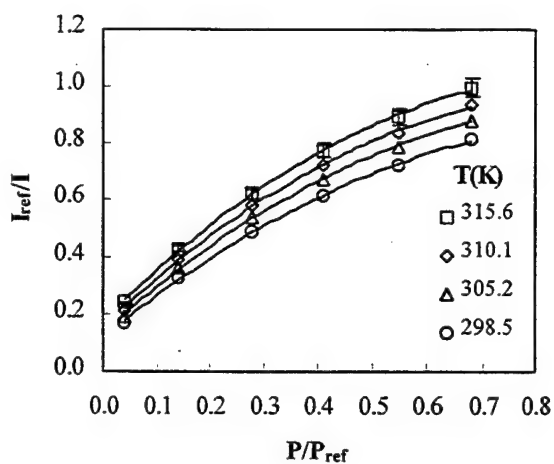


Figure 1. Variation of ratioed luminescence emission intensity with pressure and temperature.

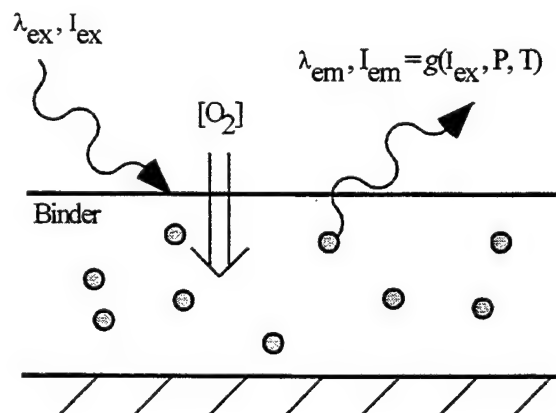


Figure 2. Schematic of a typical single-luminophor PSP.

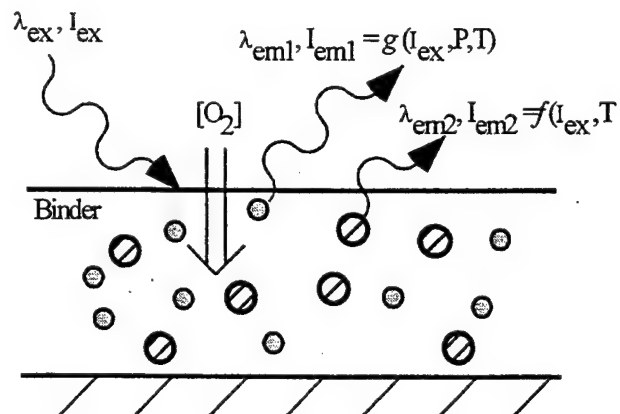


Figure 3. Schematic of a dual-luminophor pressure/pressure sensitive paint (P/TSP).

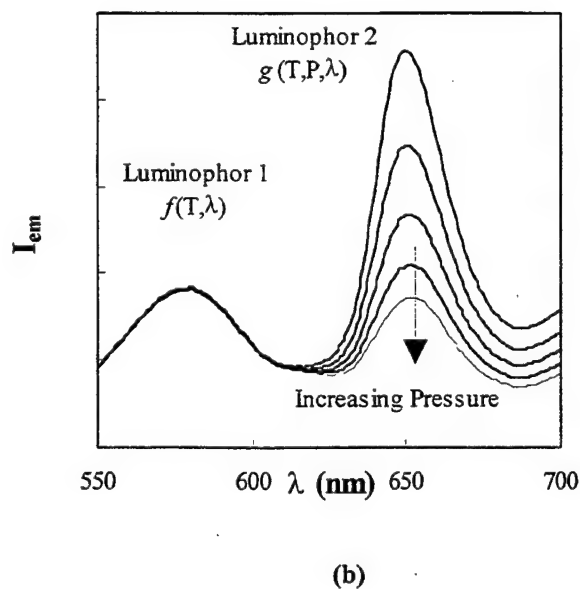
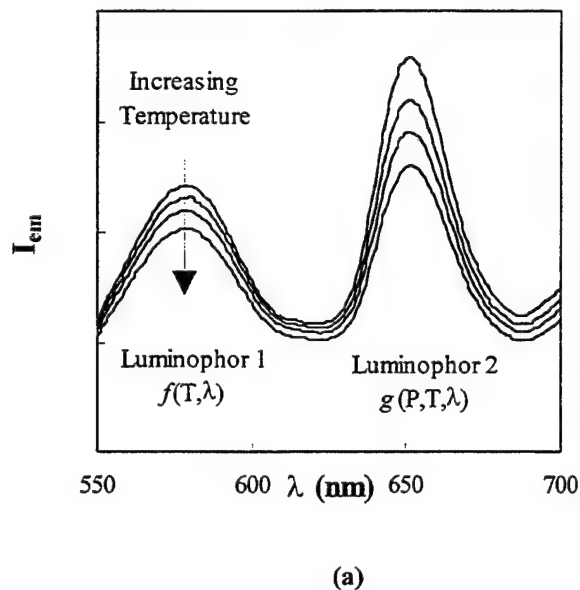


Figure 4. Spectroscopic data for a dual-luminophor temperature/pressure sensitive paint; (a) constant pressure with changing temperature, (b) constant temperature with changing pressure.

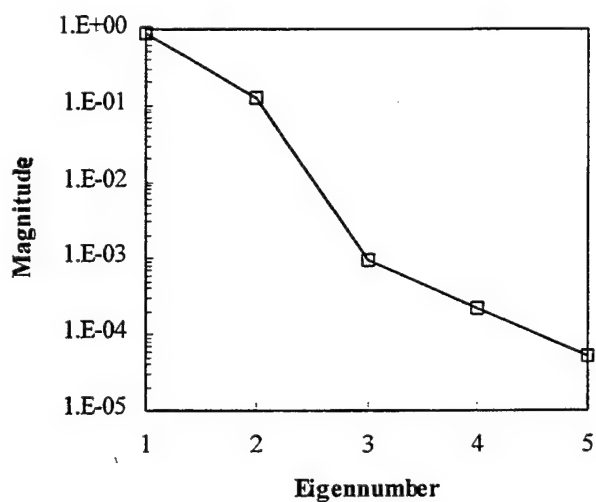


Figure 5. Relative magnitude of eigenvalues normalized such that the sum of the eigenvalues is unity.

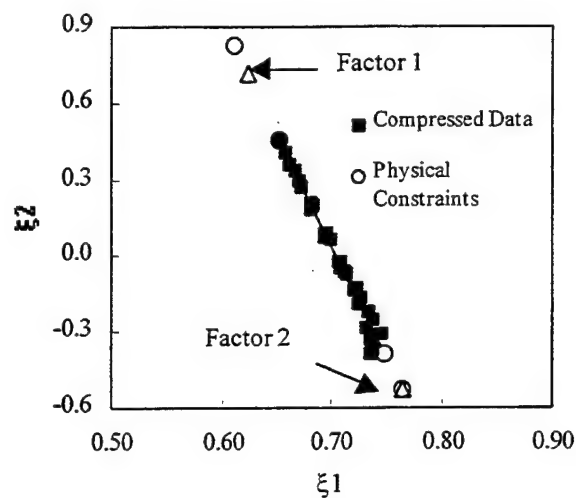


Figure 7. Generalized contribution parameters for a two-factor model of the data. The solid squares identify the data set representation based on the principal components for the range of environmental parameters in the data set. The open circles denote the transformed vectors that meet physically realistic constraints (I & II). The open triangles denote factors 1 and 2 which are the most physically realistic transformed vectors (III).

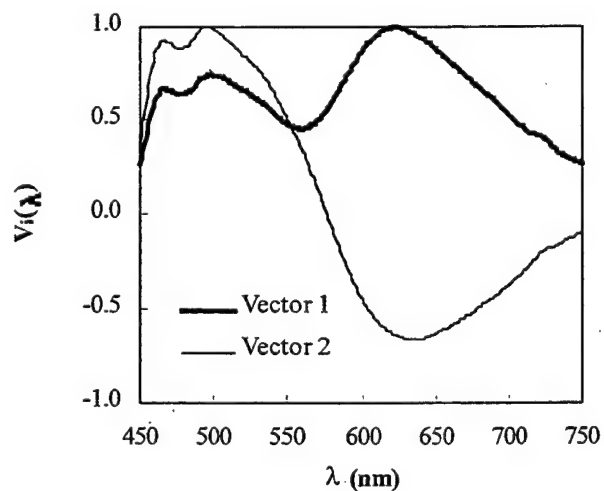


Figure 6. First two eigenvectors corresponding to the two largest eigenvalues in Figure 5. These are the abstract principal components of the data set.

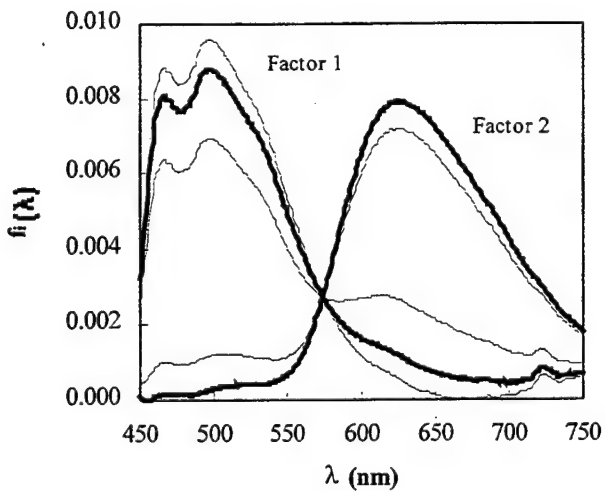


Figure 8. Transformed factors showing the range of physically possible solutions (light curves) and the most physically satisfactory solution (dark curve).

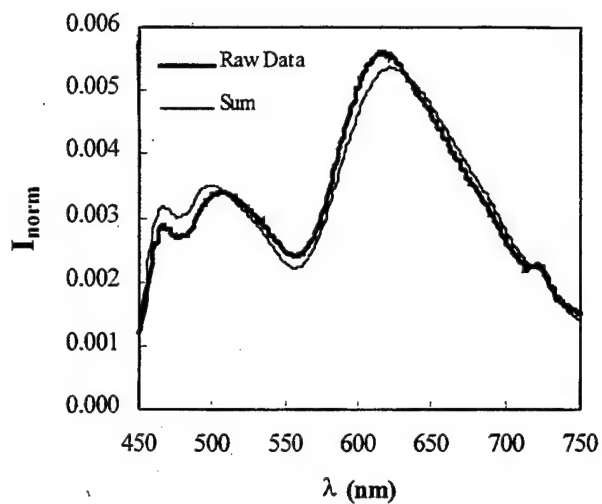


Figure 9. Reconstructed (combined) spectral response from the two-factor model at a set environmental condition. The dark line is the original data set.

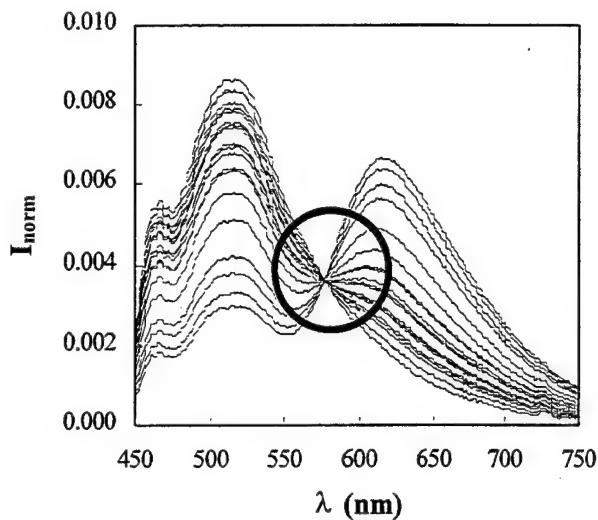


Figure 11. Two-factor model representation of the spectral data in Figure 10.

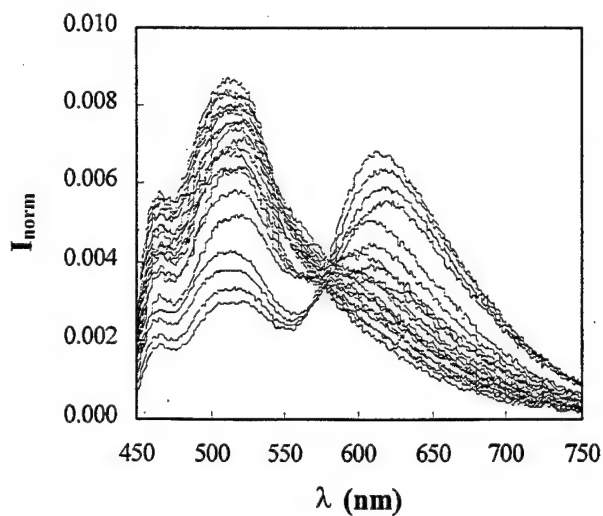


Figure 10. Original spectral data for $n = 20$ environmental conditions.

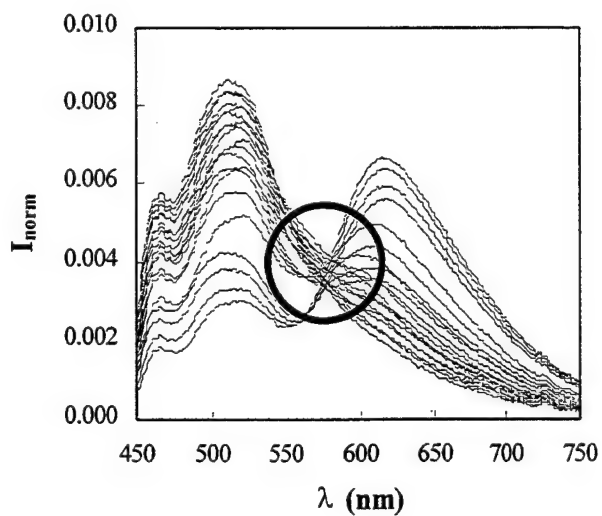


Figure 12. Three-factor model representation of the spectral data in Figure 10.

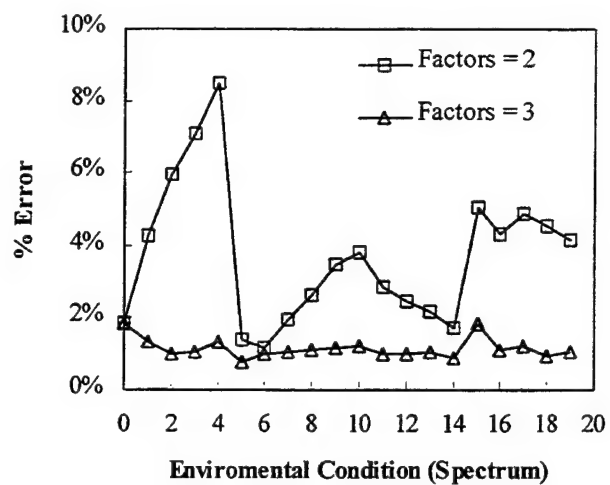


Figure 13. Average percentage error over the spectra for each of the 20 environmental conditions in Figure 10. Squares give the error for the two-factor model in Figure 11 and triangles give the error for the three-factor model in Figure 12.

VORTICAL FLOW FIELD INVESTIGATION USING A TWO-COMPONENT PRESSURE SENSITIVE PAINT AT LOW SPEED

M.C. Mérienne, F. Bouvier
ONERA/DAFE,
BP n°72, 92322 Châtillon Cedex, France

ABSTRACT

A two-component pressure sensitive paint has been designed to perform wind tunnel tests in low speed flow. In order to increase the measurement accuracy, the sources of errors have been reduced by using a low temperature sensitive paint. Furthermore, this PSP allows to measure the variations of the excitation light between wind-on and wind-off images by means of the second component, insensitive to pressure.

The PSP is applied on an non-instrumented delta wing model and pressure data are obtained by using separate calibration on small samples of paint. PSP images present some defects of non-uniformity due to a problem with the paint itself. Pressure fields are obtained from 50 down to 24m/s. Comparison between measurements obtained with pressure taps and PSP results on separated tests shows a significant shift due to the paint calibration.

INTRODUCTION

Pressure sensitive paint (PSP) is becoming an attractive technique for measuring surface pressure in wind tunnel testing. The time saving in model manufacturing and the resolution of this method has originated a strong interest in the United-States, Russia and Europe.

Since the 1980's, the technique has been successfully applied in various flow conditions from low speed to hypersonic flow, including tests on rotating turbine blades. In low speed flows, where pressure variations generated by the airflow are very small, the measurement accuracy tends to become very poor leading to the relatively small signal-to-noise ratios.

The involved phenomenon in PSP is a photochemical process: some luminescent coatings absorb the energy of the incident light (UV or visible light), and release part of it at a longer wavelength. As this luminescence can be quenched by oxygen, the increasing air pressure tends to decrease the emitted intensity.

Unfortunately, two major factors can reduce the accuracy of the pressure measurements : the temperature [1, 2] and

the variation of the excitation intensity during the test [3]. The sources of the temperature sensitivity are inherently connected to the photoluminescence process and the paint used. A careful selection of the luminescent dye can significantly reduce the influence of the temperature. The intensity method used for PSP measurements requires to perform a ratio between a reference image and a test image. But during the test, the model location changes under aerodynamic loads. Due to this displacement, the illumination field is modified and the same physical point doesn't receive the same excitation light intensity for the two images.

The PSP described in this paper is specially designed for low speed flows. The idea of using a binary paint has already been developed by a Russian team and applied under transonic flow conditions [4]. The paint contains a second luminescent component, insensitive to pressure, used to measure the variation of the excitation light intensity. The binary paint is calibrated in a special pressure chamber. Then optical pressure measurements are made on a delta wing model tested at very low speeds. Quantitative results are obtained without any pressure tap measurement.

PSP FEATURES

Paint formulation

The paint has been developed at ONERA and contains two luminescent components. The luminescence of the first one is quenched by oxygen. The pyren molecule has been chosen for three reasons : relatively high quantum efficiency (0.6), good pressure sensitivity (90% per bar) and low temperature sensitivity (<0.1% per degree). Previous works [5], carried out in laboratory, relate in details the behavior of pyren molecule (and more particularly the effect of its concentration and the associated silicone resin) on the emission spectra. The optimum formulation was found to be 7mM pyren in RTV118 (General Electric) silicone resin.

PSP luminescence is inversely proportional to the pressure and directly proportional to excitation light intensity and to the thickness of the paint. To eliminate the influence of excitation light and thickness, the pressure field is

computed from the ratio of two luminescent intensity images, one recorded at uniform and known pressure (wind-off) and one recorded at unknown conditions (wind-on). During the test, the model location changes under aerodynamic loads and it is necessary to realign the two images. This operation is carried out with a dedicated software developed at ONERA [6] which uses markers placed on the model surface. Nevertheless the resection software is unable to correct for the illumination field modified by the model displacement. Excitation light distribution is not uniform on the model, so any displacement of the model changes the excitation light intensity on the model surface. As the light intensity at a given distance of the light source is inversely proportional to the square of this distance, a 1% change in the distance leads to 2% change in excitation light intensity. Furthermore, this change depends on the point location.

This is the reason why a second component, insensitive to pressure, is added to the paint as a reference to correct for local variations of illumination. It is an europium-activated yttrium oxysulfide ($Y_2O_2S:Eu$) with a strong emission in the red range. As the luminescence of pyren is in blue light, there is no interference between the two emissions.

For each measurement point, two images have to be acquired. The concentration of the reference luminophore is chosen in order to have almost the same intensity on the two images.

Paint calibration

The paint calibration is performed in laboratory in a pressure chamber. Intensity measurements, in laboratory or wind tunnel, require scientific and low noise instrumentation. Excitation light is provided by a Mercury light source, filtered in the ultraviolet range (320 ± 15 nm) connected to a liquid fiber. The measurements are achieved with a cooled numerical CCD camera – PRINCETON Site 512 back illuminated detector. The camera is also used for spectral measurements when fitted with a spectrograph ACTON Spectra-Pro 150.

Spectral analysis is a key tool for measuring the variation of luminescence versus the wavelength. The ratio of two spectra at different pressures leads to the pressure sensitivity versus the wavelength. In the two-component paint, it allows to find out the range of luminescence insensitive to pressure (the red luminescence) and to choose the filter suitable for the reference measurement. The emission spectra, recorded at ambient pressure and under vacuum (figure 1), shows that the pressure sensitivity is observed in a large range (between 400nm and 600nm), while the reference measurement is focused

in the red part (around 620nm). In practice, the spectral range of the filters used is respectively 430-510nm and 620-630nm.

The calibration procedure requires to measure the intensity for the two spectral ranges : I_b for the blue image and I_r for the red image. The ratio I_b/I_r is performed. The result gives an information on pressure corrected from local variations of illumination but it doesn't takes into account local variations of concentration between the two components. So, it keeps necessary to divide the image I_b/I_r with the same ratio computed from measurements obtained under reference pressure (I_{b0}/I_{r0}). Pressure sensitivities, obtained for the two emission ranges, are presented in figure 2.

The pyren molecule has been chosen for its low sensitivity to temperature. When using the blue filter described previously (430-510nm), this sensitivity is equal to - 0.35% per degree (figure 3). The reference component added in the PSP has a comparable temperature sensitivity. Consequently, the ratio I_b/I_r enables the temperature sensitivity to be reduced to 0.02% per degree. This is the second advantage of the two-component paint.

The drawback of using the pyren as pressure sensor is due to the fact that this molecule has a tendency to evaporate. This leads to a decrease of luminescent intensity with time which is accelerated at low pressure level (below 100mbar) and increased temperature (above 40°C).

The calibration of the paint is performed in a reduced pressure range, between 0.8 and 1 bar, corresponding to the pressure gradients in low speed flow. Under these conditions, the relation between pressure and intensity is linear. The temperature in the test section is controlled so as the variation between the reference and the run images is below one degree. Consequently, no temperature correction is required.

Finally, the Stern-Volmer law, including the reference measurement, obtained with the second component, is expressed as:

$$\frac{P}{P_0} = A + B \frac{I_{b0}}{I_b} \frac{I_r}{I_{r0}}$$

Where the ratio I_r/I_{r0} represents the correction of illumination. The subscript 0 indicates the measurements at the reference conditions, at ambient pressure P_0 . The curves presented in figure 4 are obtained on samples painted at the same time as the model under testing.

EXPERIMENTAL SET-UP AND PROCEDURES

Experimental Set-up

A schematic view of the experimental set-up is shown in figure 5. The experiment is conducted in the low-speed wind tunnel F2 located at the ONERA Fauga-Mauzac center. This is a closed-circuit type wind tunnel and the test section is $1.8 \times 1.4\text{m}^2$ in cross section.

The model under study is a delta wing with a 70° sweep angles and root chord of 950mm. The model is equipped with two nozzles for tangential blowing near the apex on the leeward surface. The goal is the control of the leading edge vortex breakdown location. This model is not instrumented. Figure 6 illustrates the wind tunnel model and its dimension. Another model, with the same geometry as this one but equipped with 232 pressure taps, has been studied in previous works [7] for conventional static pressure measurements. Comparisons with PSP measurements are done with these results.

The pressure sensitive paint is sprayed with an airbrush over a white paint (Sacothersm 900) applied first as a screen layer on the model upper surface. The polymerization of the PSP is completed after 12 hours at ambient conditions. The total thickness of the coating is around $40\mu\text{m}$. In order to allow accurate alignment between images for data processing, 14 markers are implemented on the model surface.

The angle of attack is set at 27 degrees and the flow velocity is investigated from 50m/s down to 24m/s. A repeatability test is carried out at 40m/s with an additional run with tangential blowing at 1.8g/s.

The measurement system is placed at the upper wall of the test section. The UV illumination is achieved with the optical fiber fixed through a hole in the wall inside the test section and the camera is located outside the window on the top of the test section (figure 7). The camera is equipped with a 24mm Nikon camera lens on which a filter holder is fixed. In order to avoid reflections and to reduce the darkness in the test section, the lateral windows are painted with a black paint and wood panels are placed on the outside. Data acquisition and remote control (lamp shutter and filter holder) are achieved with a Pentium 120T Personal Computer located in the wind tunnel control room.

Data acquisition

A dark image obtained with the lamp shutter closed is recorded before the test and will be subtracted to every run images. The level of darkness represents 1% of the

signal recorded at ambient pressure. Reference images at ambient pressure are recorded before and after each run. When the thermal equilibrium is reached in the wind tunnel, the temperature is checked with an accuracy of one degree. In practice, the reference image taken after the run, fan motor turned off and free-stream velocity in the test section near zero, is used for data processing. This is done to minimize the temperature difference of the model surface between the wind-off and wind-on conditions. By this way, the maximum temperature shift between the reference and the run images is equal to 2°C .

Owing to the fact that the pressure gradients at low speed are very small, the data acquisition procedure is optimized. Firstly, the dynamic range of the camera is fully used by increasing the exposure time up from 10 to 60s. Second, twenty images are recorded for each measurement point.

Data reduction

Data reduction is carried out using a home made software (AFIX) able to produce pressure maps and to extract data relatively to physical coordinates on the model. The processing sequence is described below.

1. The average of the twenty images is performed for the reference and run images, red and blue separately.
2. Dark images are subtracted.
3. The reference and run images are normalized, which means that the blue image is divided by the red image.
4. Each run ratio obtained is realign with the reference ratio (see below for the details about this processing).
5. The normalized reference image is divided by the normalized run image.
6. The result is converted into pressure data using the calibration coefficients previously performed in laboratory.
7. Data are extracted relating to physical coordinates in the model.

An automatic image alignment (step 4) is performed as follows:

- The marker positions on the reference image are recognized.
- Each marker is associated to a physical point in the model.
- The camera attitude and location relative to the model are identified. This is used for data extraction on step 7.
- Marker positions are recognized on the run image and linked to the markers in the reference image.

- The alignment is done by a polynomial transformation (which provides good results on a plane model).

RESULTS AND DISCUSSIONS

PSP results at different speeds

PSP images are presented at four speeds, at 24, 30, 40 and 50m/s in figure 8. The images are not smoothed after data processing and markers remain visible. The images reveal a problem of paint uniformity on the model surface. The paint was prepared 3 days before application on the model and it was observed that the viscosity changed showing a beginning of polymerization. Furthermore, as the reference component added to the paint remains in suspension in the resin, it is necessary to agitate the mixture continuously while painting. These two reasons explain the bad uniformity of the coating on the model surface. Nevertheless, the leading-edge vortices are clearly visible from 50m/s down to 30m/s. At 24m/s, the vortices are too weak to be visible. The maximum pressure gradient measured at this speed is indeed 40mbar. PSP image obtained with tangential blowing at 40m/s has a lower noise level.

The correction made by the reference component is illustrate in figure 9. The first image presents the coefficient I_r/I_{r0} and shows a variation of illumination between the left and the right part of the wing. In the second image, performed only with the blue component I_{b0}/I_b (pyren), the leading-edge vortices are not symmetrical. Comparison has to be made with the third image which is the second one corrected by the coefficient I_r/I_{r0} . The resulting image in pressure is presented figure 8, at 40m/s.

Data extracted from the images presented in figure 8 are obtained without low-passed filtering in 3 transverse sections normal to the root chord. The figure 10 presents the row at 500mm in abscissa from the leading-edge and illustrates the improvement due to temporal image averaging. The residual noise observed on the extracted curves represents around 2.5mbar at 30m/s. Figures 11, 12 and 13 show the curves obtained at 250, 500 and 750mm from the leading-edge for each velocity. Marker location can be identified on some curves. The noise level is almost the same for the three velocities. Its amplitude represents 10mbar.

Pressure data located along vortex axis have been extracted (figure 14) with and without tangential blowing. Blowing smoothes the data and the pressure levels are

lower. A more interesting effect of blowing is that the two vortices become symmetrical.

Comparison with pressure taps

Uncertainties concerning the calibration remain. Calibration has been carried out, 18 days after the wind tunnel tests, on the two samples painted at the same time as the model. The samples differ by their thickness (screen layer + active layer) : 35 μ m for the first one and 50 μ m for the second one. The calibration curves presented in figure 4 have different slopes for the two samples. A shift of 40mbar is observed for the identical luminescence ratio ($I_0/I=0.9$) at a pressure level equal to 0.8bar.

A comparison with pressure taps (obtained on another model under separated tests) is presented in figure 15. PSP data are presented upon the two calibration coefficients (from figure 4). The influence of the pressure sensitivity on the results is clearly visible.

When using in-situ calibration [1, 2, 3], the PSP results are always in the measurement range of the pressure taps. In the presented case, the accuracy of the calibration process (shift and slope) determines the accuracy of the final results.

Paint degradation

As mentioned previously, the drawback of this PSP is due to the fact that the pyren molecule has a tendency to evaporate. This was observed during the wind tunnel tests where the decrease of luminescence between two consecutive runs for the first day is equal to 2%, and only 1% for the second day. But the degradation between the two consecutive days, after 24 hours in the wind tunnel, is equal to 10%. This contributes to PSP results lower than expected.

CONCLUSIONS

A two-component paint has been designed and tested for wind tunnel tests at low speed flow. The first component is pressure sensitive with a good quantum efficiency and a low sensitivity to temperature. The second component is used to correct the variation of illumination and is insensitive to pressure. Unfortunately, these interesting features are hidden by some problem of application and calibration.

Accuracy of PSP measurements in low speed flows is closely dependent of all sources of errors. It is essential to reduce the noise by image average. The temperature and the variation of illumination, as well as image alignment, have to be controlled.

Other tests have to be carried out in order to improve the use of the two-component paint and to produce accurate results.

ACKNOWLEDGEMENT

The authors would like to express their sincerest thanks to the members of the F2 wind tunnel team who contributed to the best accomplishment of the tests.

REFERENCES

1. Rickard S.J., Washburn A.E., Morris M.J. Donovan J.F., *Pressure Sensitive Paint Studies of Vortical Flow at Low Speed*, SAE Technical paper series, n°951989, Aerotech'95, Los Angeles (USA), September 18-21, 1995.
2. Shimbo Y., Mehta R.D., Cantwell B.J. *Vortical Flow Field Investigation using the Pressure Sensitive Paint at Low Speed*, AIAA 97-0388, 1997.
3. Brown O.C., Mehta R.D., Cantwell B.J., *Low-Speed Flow Studies using the Pressure Sensitive Paint technique*, 81st AGARD/FDP Symposium on Advanced Aerodynamic Measurement Technology, Seattle (USA), September 22-25, 1997.
4. Lyonnet M., Deléglise B., Grenat G., Bukov A., Mosharov V., Orlov A., Fonov S., *The Two-Component PSP Investigation on a Civil Aircraft Model in S2MA Wind Tunnel*, 81st AGARD/FDP Symposium on Advanced Aerodynamic Measurement Technology, Seattle (USA), September 22-25, 1997.
5. Mébarki Y., Mérienne M.C., *PSP Application on a Supersonic Aerospike Nozzle*, PSP Workshop, Seattle (USA), October 6-8, 1998.
6. Le Sant Y., Deléglise B., Mébarki Y., *An Automatic Image Alignment Method Applied to Pressure Sensitive Paint Measurements*, 17th ICIASF, Monterey (USA), September 29-October 2, 1997.
7. Mitchell A., Barberis D., Déleroy J., *Oscillation of Vortex Breakdown Location and its Control by Tangential Blowing*, AIAA 98-2914, 29th Fluid Dynamics Conference, June 15-18, 1998.

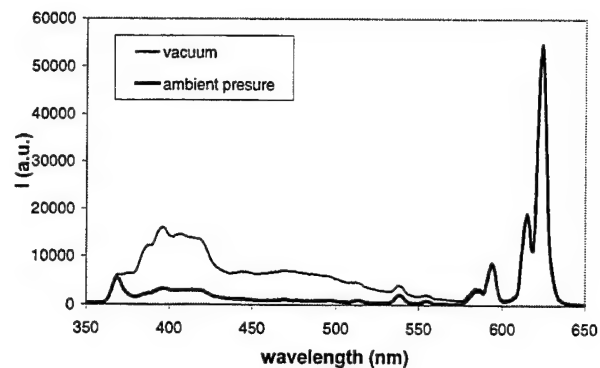


Figure 1 : Emission spectra of the two-component paint at ambient pressure and vacuum.

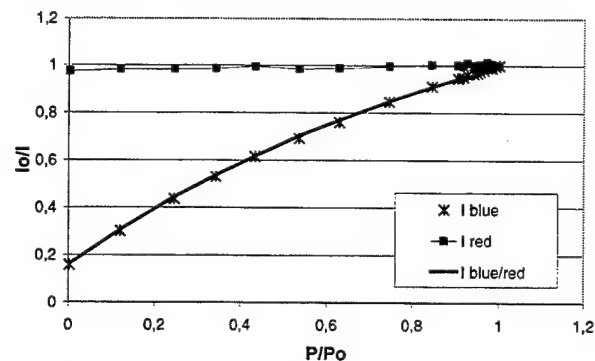


Figure 2 : Pressure sensitivity of the two-component paint

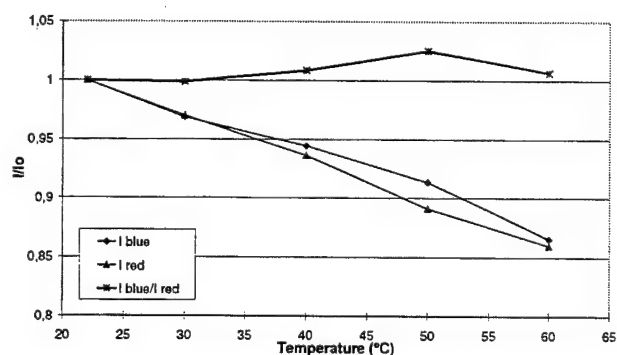


Figure 3 : Temperature sensitivity of the two-component paint.

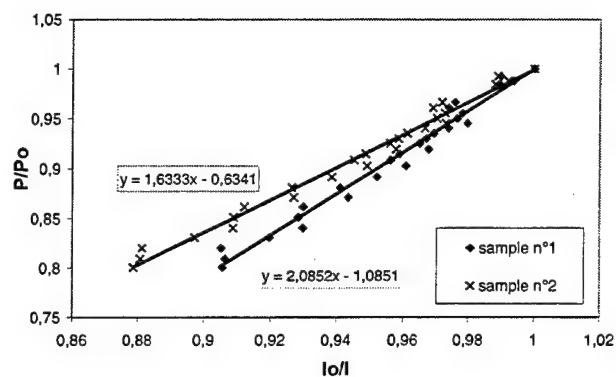


Figure 4 : Calibration of the paint

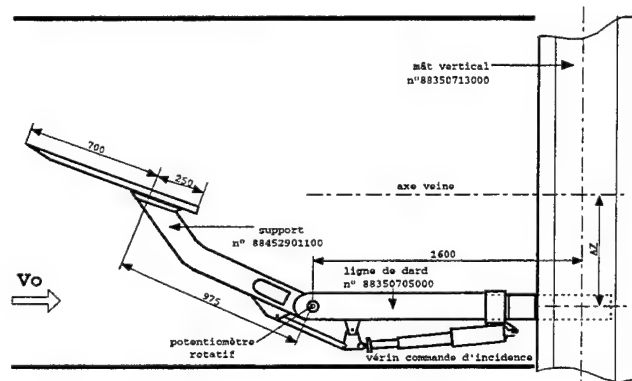


Figure 5 : Experimental set-up in the test section (F2 CFM wind tunnel).

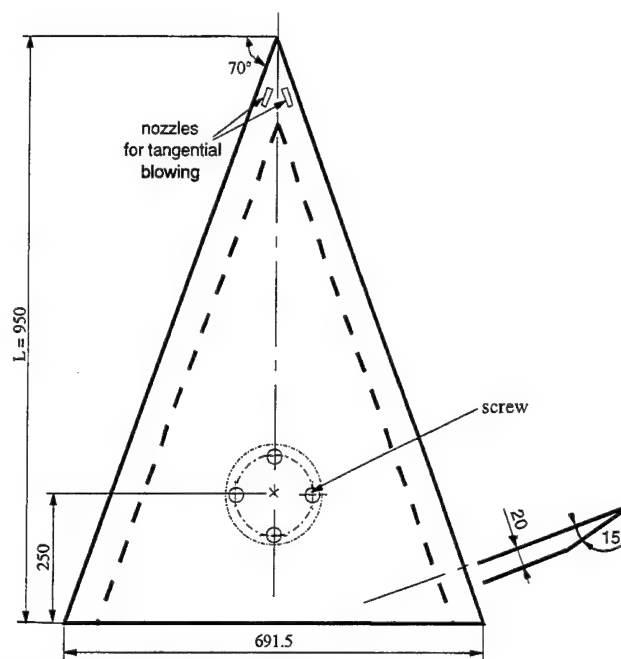


Figure 6 : Delta wing model

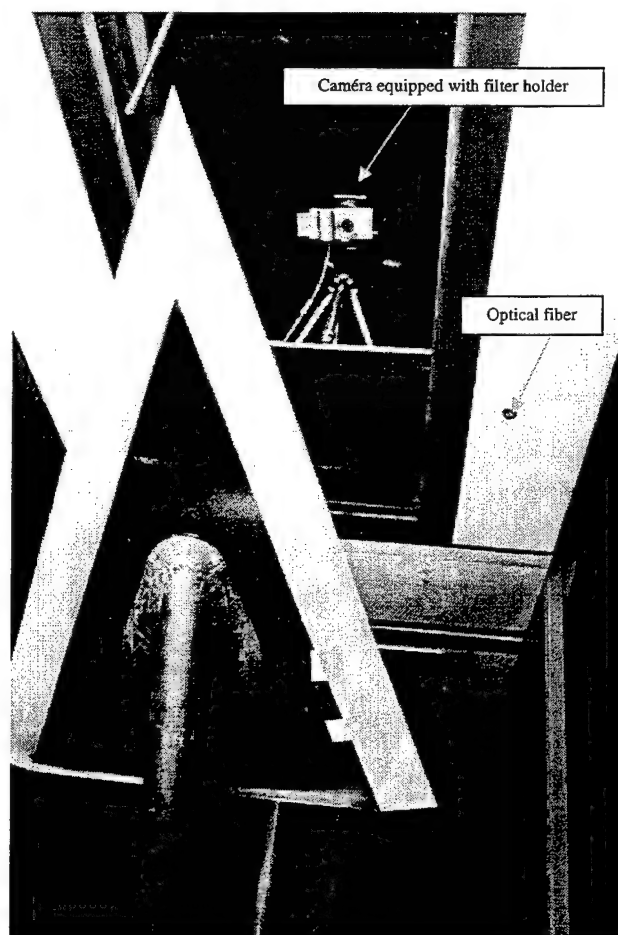
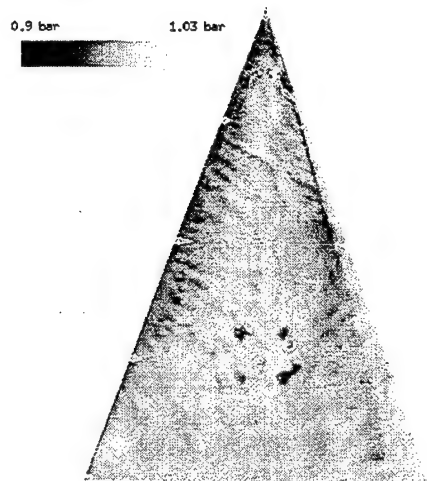
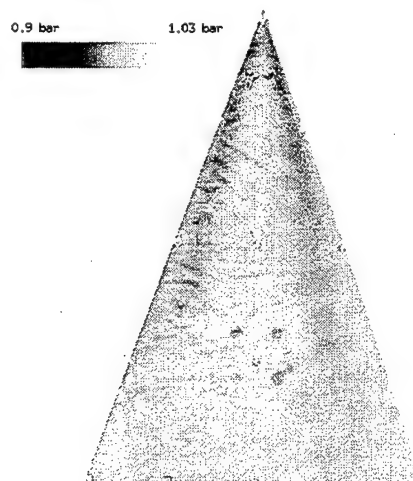


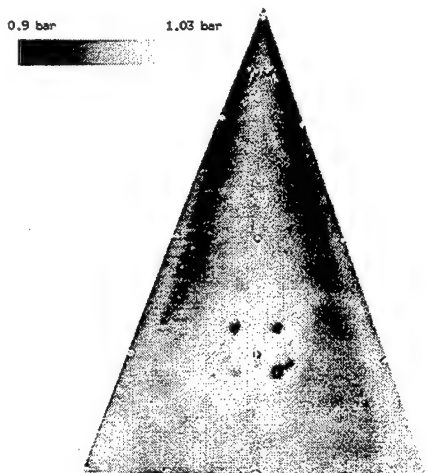
Figure 7 : Measurement system in the test section



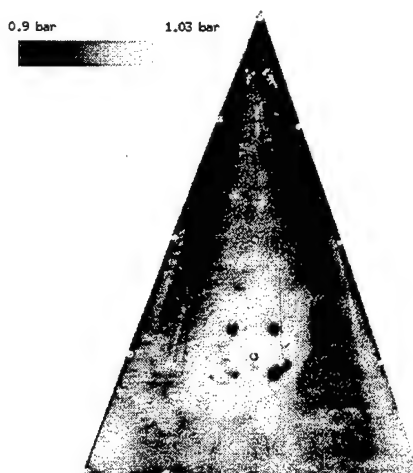
24m/s



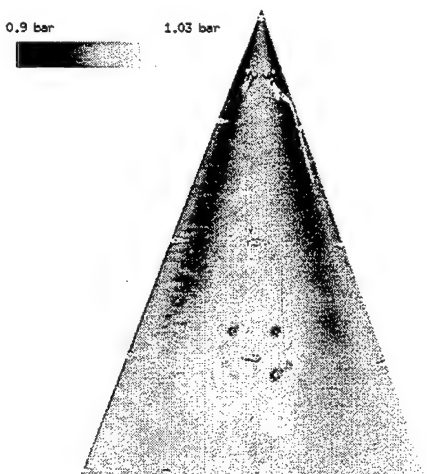
30m/s



40m/s

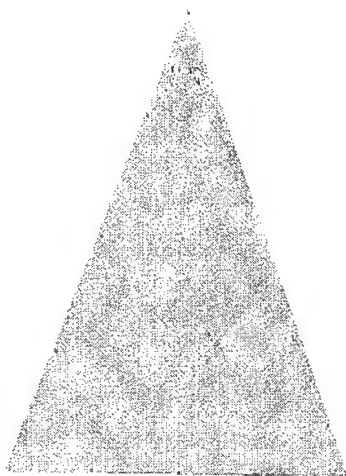


50m/s

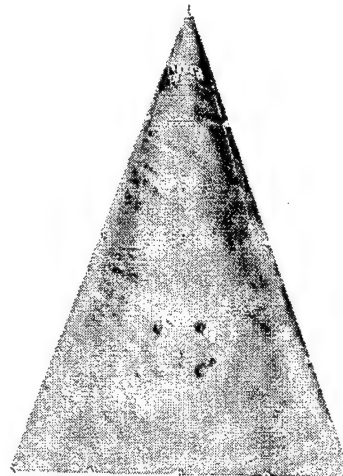


40m/s with tangential blowing

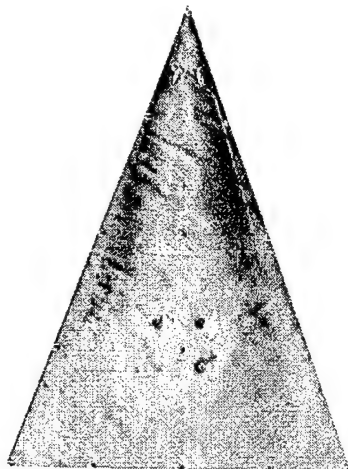
Figure 8 : PSP images at different velocities.



Raw image I_r/I_{r0}



Raw image I_{b0}/I_b



Raw image with the correction of illumination

Figure 9 : Correction of illumination in raw images at 40m/s

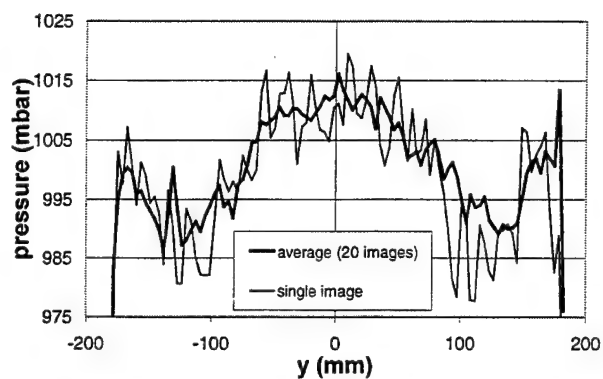


Figure 10 : Effect of temporal image averaging at 30m/s, $x=500$ mm.

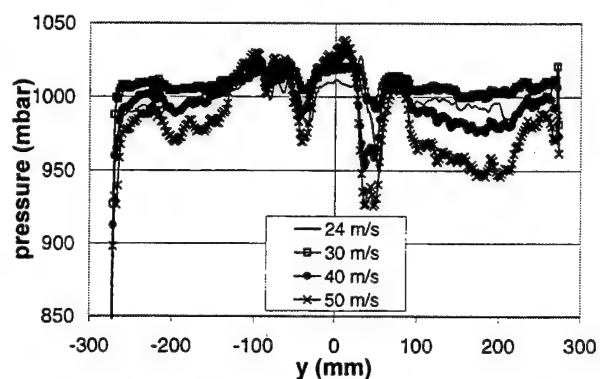


Figure 13 : Extracted data at $x = 750$ mm.

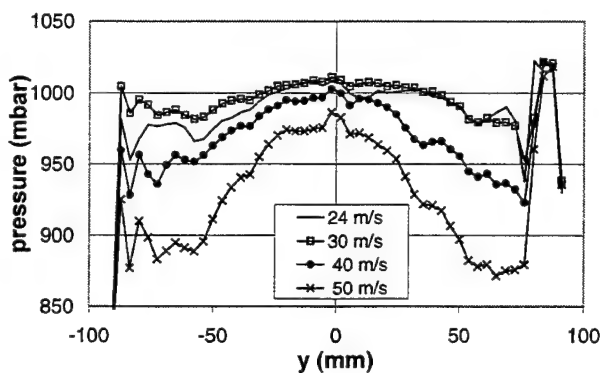


Figure 11 : Extracted data at $x = 250$ mm.

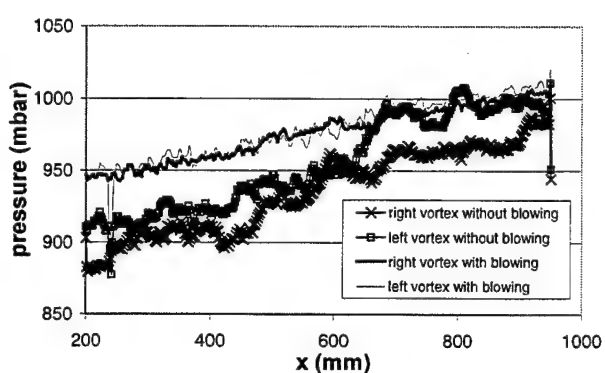


Figure 14 : Extracted data along vortex axis at 40m/s.

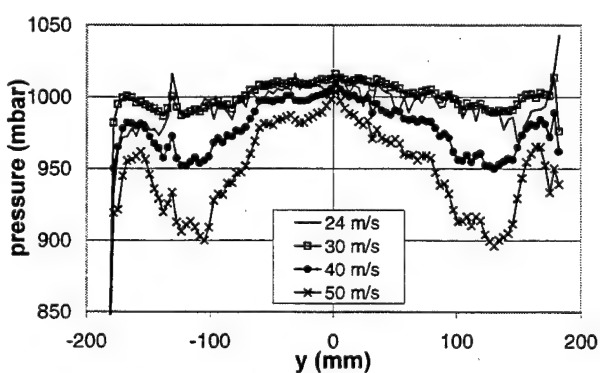


Figure 12: Extracted data at $x = 500$ mm

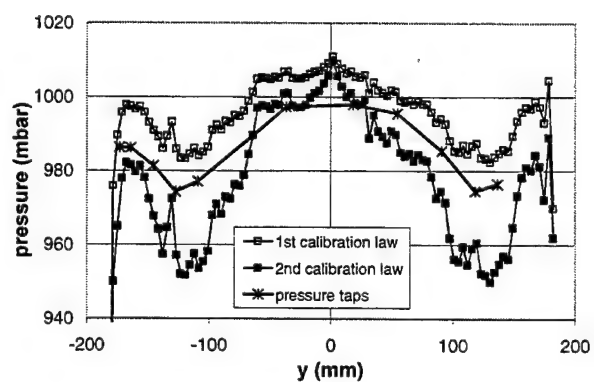


Figure 15 : Comparison with pressure taps at $x = 500$ mm and 40m/s.

SESSION : 5

SENSITIVE PAINT TECHNIQUES II

IMPLEMENTING PRESSURE-SENSITIVE PAINT IN THE AFRL SUBSONIC AERODYNAMIC RESEARCH LABORATORY

Gary A. Dale and Henry D. Baust
AFRL Air Vehicles Directorate, WPAFB, OH

Gary A. Clinehens*
WPAFB, OH

ABSTRACT

Research and development conducted to enable pressure-sensitive paint (PSP) measurements to be made in the Air Force Research Laboratory (AFRL) Subsonic Aerodynamic Research Laboratory (SARL) is described. In addition to the fundamental challenges of making PSP measurements in low speed flows, the unique characteristics of the SARL, and how they further challenge the technique, are presented. The design and performance specifications of ultrastable illumination sources, based on arrays of blue light emitting diodes, are given. The characteristics of sol-gel-based PSPs, which offer a number of advantages for low speed measurements, are provided. A highly adaptable system for rigidly mounting and easily positioning and aiming the lamps and camera is described. A process whereby as many as four regions of interest, in the camera field of view, are displayed real-time for monitoring model thermal stability and facility ambient light contamination is shown. Other operational aspects of deploying PSP in SARL are also described.

INTRODUCTION

There is growing acceptance of pressure- and temperature-sensitive paint (PSP and TSP) measurements in aerodynamic testing. These techniques [1-3] employ photoluminescent coatings applied to the test article of interest that is then imaged with a photodetector, often a scientific grade CCD camera. The resulting 2-D image, when reduced to pressure or temperature, provides greatly enhanced understanding of the flow phenomena.

Pressure-sensitive paint is becoming routine in transonic and supersonic wind tunnel testing where the oxygen concentrations are low and therefore the luminescence of the paint is adequate to achieve accurate measurements. The challenge in using PSP at low speeds is one of inadequate signal-to-noise ratio. Low speeds, near

atmospheric conditions, result in small photoluminescent signals and diminished paint sensitivity. Typical pressure sensitive paints are approximately 90% quenched at atmosphere, i.e. the intensity at atmospheric pressure is just 10% that of its maximum at vacuum. In this region the pressure sensitivity is on the order of 0.30-0.35% per kPa. The low paint signal can be overwhelmed by other factors such as paint temperature sensitivity and illumination variations. The temperature sensitivity of a 'good' PSP is on the order of 1%/°C, meaning that a temperature change of a few degrees can produce an intensity change equivalent to a full scale pressure change at low speed.

FACILITY DESCRIPTION

The AFRL SARL [4], Figure 1, is a 2.1 by 3.0-meter atmospheric indraft wind tunnel that operates at Mach Numbers ranging from 0.1 to 0.5. The requirement to implement pressure sensitive paint (PSP) in SARL brings with it a number of challenges, some being particular to the technique and others related to the facility itself.

The SARL was designed for employing optical-based flow diagnostics such as PSP. The test section is comprised of 56% windows, permitting exceptional optical access over the length of the 4.6-meter long test section. The windows are positioned such that a full 360-degree view of the test article is possible. A retractable 'tent' is positioned over the test section when employing intensity-based diagnostics to minimize the effect of ambient light on the measurement. Unfortunately, being an indraft facility, ambient light is also introduced to the test section from both upstream and downstream. Figure 2 is a photograph taken in the test section, looking downstream, showing ambient light being transmitted past the fan blades and stators, and reflected from the interior of the diffuser and test section. The figure also shows some of the test section windows. An air deflector, Figure 3, mounted on the drive motor

* SelectTech Services Corporation, Centerville, OH USA

tower, further complicates this light contamination. The air deflector, not shown in Figure 1, is made of galvanized steel and reflects sky light through the diffuser and into the test section. The resulting light contamination, constantly changing, is a function of the position of the moon or sun and the degree of cloud cover. Light contamination from upstream, Figure 4, is significantly less than that from downstream because of the filtering effects of the honeycomb and anti-turbulence screens in the facility inlet. The developments to overcome the challenges inherent to making quality PSP measurements in low speed flows and those posed by the design of the facility follow.

PSP RELATED DEVELOPMENTS

Ultra-Stable Illumination

The illumination sources used for PSP measurements are analogous to the excitation voltage of a transducer - any change in illumination produces a change in paint output that is indistinguishable from pressure induced changes. As such, temporal illumination stability is critical, particularly for low speed measurements. An atmospheric wind tunnel at Mach 0.5 has a free stream static pressure only 14 kPa below ambient. At this ΔP the change in paint intensity is only on the order of 5%. Assuming the requirement is to resolve one-fiftieth of this pressure change, measuring intensity changes of 0.10% is required. Clearly illumination stability is critical.

Ultrastable lamps, based on arrays of blue light emitting diodes (LEDs), have been developed. The arrays utilize 15° (divergence) LEDs¹ that are 8 mm long and 5 mm in diameter. A single LED produces 1,500 millicandles at the rated forward current of .020 ampere and has a quoted lifetime of 100,000 hours. Newer LEDs produce 5,000 millicandles at the same current. As shown in Figure 5, emission is centered at 460 nm. Each lamp utilizes 73 LEDs mounted on a custom-made 50-mm diameter circuit board. Lamp construction is based on 50-mm copper tubing components, which are inexpensive, easy to machine, and a convenient size for standard optical filters, lenses, etc. Figure 6 shows the LED array and inner housing for the array and optics. A 250-mm focal length lens, mounted in front of the LED array, provides some collimating effect. Although predominantly blue, the LEDs do emit light at longer wavelengths. A short-wave pass filter is used to block these longer wavelengths which, although very small in

comparison to the blue emission, are significant compared to the red paint emission. A muffin fan is attached to the back of the outer housing. A 50-mm iris, which mounts to the front of the outer housing, is used to adjust lamp output. Figure 7 is a photograph of the major components of the lamp and a sectional drawing of the lamp is shown in Figure 8. The assembled lamp is 89-mm in diameter by 114-mm long.

The presence of resistors in the LED circuit, although required, introduces instability in the lamp output. As the resistor temperature increases under load the resistance increases resulting in an effective decrease in drive current and reduced lamp output. The muffin fan supplies cooling air to the resistor side of the circuit board. Figure 9 shows normalized lamp intensity data, taken at 10-second intervals. The data show the LED achieves output intensity within 0.5% of final intensity within 4 minutes. After a warm-up of approximately 20 minutes the lamp output is stable to within $\pm 0.10\%$. The cooling fan has a flow rate of 13 cubic feet per minute, however, no attempt was made to investigate the minimum flow rate required and it is suspected a lower flow-rate fan may be sufficient to maintain long term lamp output stability. For comparison, the output of a quartz tungsten halogen (QTH) lamp is also shown in Figure 9. The QTH lamp output is unstable with occasional spikes in output as high as 1.0%. LED and QTH lamp characteristics are summarized in Table 1.

	QTH Lamp	LED Lamp
Lifetime	10 hours	100,000 hours
Relative Output	1.0	1.8
Power	100 watts	7.5 watts
Stability	> 3.0%	$\pm 0.10\%$

Source: Oriel Corporation Catalog [5]

Table 1. LED and QTH Lamp Comparison

When deployed for a PSP experiment, the LED lamps are powered by a regulated DC power supply. By utilizing a relay and a simple circuit of 5 ohm, 5 watt, shunt resistors, the power supply can be constantly on and loaded, either with the shunt resistors or the LED lamps. This permits the power supply to be set at the appropriate level and left on throughout a test period. The lamps can then be turned off when not needed, minimizing photodegradation, and the same output can be repeated when the lamps are turned on again. This minimizes the necessity to adjust exposure time and f-stop to optimize the signal collected by the camera.

¹ Nichia NSPB500S

A device was developed for the LED lamps to make it easier to optimize the position of their illumination field on the model. Uniformity of test article illumination is necessary to achieve the highest quality pressure measurement. If a broad range of luminescent intensities exist on the surface the camera must be adjusted for the most intense luminescence. In effect, the resolution of luminescence measurement is set by the most intense luminescence because the dynamic range of the camera A/D converter must be distributed over this level. The 'aiming' device consists of an inexpensive laser pointer and an adapter to mount it to the front of the LED lamp. As shown in Figure 10, the device projects the laser beam along the centerline of the lamp, designating the location of the center of the lamp illumination field.

Paint Development

The focus of PSP development for SARL has been on sol-gel-based paints [6]. The sol-gel process permits formation of controlled-pore glasses at ambient pressure and temperature. The ability to control the porosity makes it possible to develop coatings with pores large enough to permit oxygen diffusion. This can be accomplished even while probe loading is increased, without clustering of the probe molecules. This ability to tune the porosity of the matrix and adjust probe loading affords the possibility to adjust the sensitivity of the resulting PSP. Figure 11 indicates how varying the porosity of the sol-gel to vary oxygen diffusivity effects the sensitivity tuning. Probe loading is a constant in Figure 11. An aerosol-based deposition technique has been developed to apply the sol-gel-based paints to test articles, resulting in thin (2 μm), uniform films that are smooth and robust. The PSPs are applied over a commercially available white base coat that improves sol-gel adherence, eliminates substrate-induced quenching, masks surface irregularities, and minimize temperature sensitivity. Sol-gel-based PSPs are characterized by high thermal stability and, therefore, exhibit very low temperature-dependent viscosity changes. The sol-gel-based paints are also fast drying; their pressure sensitivity stabilizes approximately 30 minutes after application, and easily removed with mild solvent (e.g. alcohol).

OPERATIONAL ASPECTS

Significant effort has been devoted to making the acquisition of PSP data in SARL minimally obtrusive to the customer. This has focused on minimizing the time required to mount equipment, prepare the test article for painting, mask the test section, paint the model, and

begin the process of acquiring PSP data. This effort has manifested itself in several ways.

Equipment Mounting and Adjustment

Optical rails and related components², Figure 12, have been employed to make rigid installation of lamps and cameras fast while permitting the flexibility required to optimize illumination and imaging. The rails are cylindrical aluminum extrusions, 80 mm in diameter, with four longitudinal reinforcing ribs. These 10-mm thick ribs provide four symmetrical clamping surfaces for the mating components and significantly increase the rigidity of the rail. Long rails are mounted permanently to the top and sides of the SARL test section exterior. Shorter rails and related components are used as necessary for the unique configuration required for each test. Figure 13, a photograph taken from outside the test section, shows the camera and several lamps mounted on the top of the facility. Figure 14, a photograph taken from inside the test section, shows the lamps and camera mounted at the top windows as well as lamps mounted in the top corner windows.

Painting Preparations

Although very desirable for optical access, protecting the expanse of windows in SARL presents a challenge when applying PSP to the model in-place, as is most often the requirement. Affixing masking material to the test section walls with tape is impractical because of the oily residue left by the smoke used for flow visualization. A means to affix the masking material to the walls magnetically was developed to overcome this difficulty and to reduce the time required to prepare the test section for painting the model. This approach uses clear plastic sheets sized to fit sections of windows. The sheets have pockets formed along the entire perimeter that hold 51-mm wide strip magnets. These masking sheets are reusable and, being transparent, do not block the external work lighting for the test section. Figure 15 shows a corner of one of these masking panels in place in the test section with the magnetic edge pulled back at one corner. Figure 16 is a photograph of the test section, looking upstream, completely masked for painting. Two people can mask the entire test section in 10-15 minutes. Although not readily evident, Figure 16 also shows the temporary test section floor. The floor puts the model at a convenient height for applying the PSP and provides a flat surface for setting the tripod-mounted portable coordinate measurement system for measuring the location of reference targets and pressure taps. The floor

² Series X95, Newport Corporation, Irvine, CA, USA

is built in lightweight, interlocking, aluminum sections and can be installed and removed in minutes.

Ambient Light and Thermal Stability

To mitigate the contamination from ambient light as much as possible the inside of the diffuser has been painted flat black. The air deflector on the motor tower will also be painted flat black. While these measures, combined with testing at night, will help minimize the ambient light problem, additional steps are required. To help account for the remaining ambient light a compensation process is employed. This involves adding a reference area on the support sting, in the camera field of view, of reflective tape which is insensitive to pressure and temperature. The 'Reference ROI', as shown in Figure 17, is used to compensate model image data. Figure 18 is a plot of the body ROI data taken over an entire run; during daylight hours, from before fan start until after the post-run wind-off image acquisition was completed. The upper plot is the uncorrected average intensities from the body ROI region on the test article shown in Figure 17. While the huge changes include effects due to pressure, temperature, and ambient light variations, the majority of the changes are due to the latter. Much of this effect can be compensated for by monitoring the ambient light with the 'Reference ROI' on the sting. The lower plot ('Corrected ROI') in Figure 18 is the 'Body ROI' corrected for ambient light changes as determined from the 'Reference ROI' on the sting.

As the temperature induced intensity changes can easily be on the same magnitude as those due to pressure in low speed flows, accounting for thermal effects is critical. Research is ongoing to develop PSPs with minimal temperature sensitivity and on bi-luminophor paints for temperature compensation. As these paints have not been deployed to date, another ROI technique is used to help minimize temperature effects. The objective is to determine when the test article reaches thermal equilibrium and data acquisition can begin. As many as four ROIs, consisting of rectangular regions of a few hundred pixels each, can be defined on the test article. The pixels are averaged to give a mean value for each ROI and the 'Reference ROI' value is subtracted to account for ambient light changes. The resulting data are plotted real-time and monitored on-line to determine when the model has stabilized thermally, meaning data acquisition can begin.

SUMMARY

The challenge in using PSP at low-speeds is one of inadequate signal-to-noise ratio. In addition to the

problems inherent to low speed work, there are facility specific challenges to deploying PSP in the SARL. Lamps based on arrays of light emitting diodes (LEDs) were developed which exhibit long term output stability ($\pm 0.10\%$). These lamps are powered by a regulated DC power supply and employ a simple circuit allowing the power supply to be set at a designated output and left on throughout a period of testing, further improving the long term stability of the LED lamp output and making it easier to achieve optimal exposures with the camera. To help optimize the illumination of the test article, and therefore the quality of the measurement, an aiming device was developed for the LED lamps. Optical rails and related components have been employed to make rigid installation of lamps and cameras fast while permitting the flexibility required to optimize illumination and imaging. Research on sol-gel-based paints has resulted in coatings that can be tailored for porosity and dye loading. An aerosol-based deposition technique has been developed to apply the sol-gel-based paints to test articles, resulting in thin ($2\ \mu\text{m}$), uniform films that are smooth, robust, rapidly applied, and easily removed. A method to compensate for ambient light contamination in the pressure measurements has been developed. This involves adding a ROI on reflective tape which is insensitive to pressure and temperature. The 'Reference ROI' is used to compensate model pressure data. Another ROI technique is used to help minimize temperature effects by determining when the test article is at thermal equilibrium. These ROIs consist of rectangular regions of a few hundred pixels each. The pixels for ROIs on the test article are averaged to give a mean value for each. After subtracting the 'Reference ROI', these ROI values are plotted real-time and monitored on-line to determine when the model has stabilized thermally and data acquisition can begin.

ACKNOWLEDGEMENTS

The authors would like to acknowledge: Dr. Alan E. Baron, PhotoSense, for his encouragement to examine blue LEDs as a candidate for ultrastable illumination sources; Mr. Daryl Trump, Innovative Scientific Solutions Inc. (ISSI), for his assistance in characterizing the performance of the LED lamps; Dr. Jeffrey D. Jordan and Dr. A. Neal Watkins, ISSI for the sol-gel-based paint development.

REFERENCES

- [1] J. Kavandi, J.B. Callis, M.P. Gouterman, G. Khalil, D. Wright, E. Green, D. Burns, and B.G. McLachlan, "Luminescent Barometry in Wind Tunnels," *Review of Scientific Instruments* 61(11), 3340-3349, 1990.
- [2] M.J. Morris, J.F. Donovan, J.T. Kegelman, S.D. Schwab, R.L. Levy, R.C. Crites, "Aerodynamic Applications of Pressure Sensitive Paint," AIAA Paper 92-0264.
- [3] B.G. McLachlan, J.H. Bell, "Pressure-Sensitive Paint in Aerodynamic Testing," *Experimental Thermal and Fluid Science*, Vol. 10, 470-485, 1995.
- [4] T. Tighe, "Subsonic Wind Tunnel Design for Low Turbulence and Flow Visualization Capabilities," AIAA Paper 88-4672.
- [5] Light Sources Catalog, Oriel Corporation, Stratford, CT
- [6] J.D. Jordan, A.N. Watkins, W.L. Weaver, G.A. Dale, K.R. Navarra, "Sol-Gel-Based Pressure-Sensitive Paint Development," AIAA Paper 99-0566.

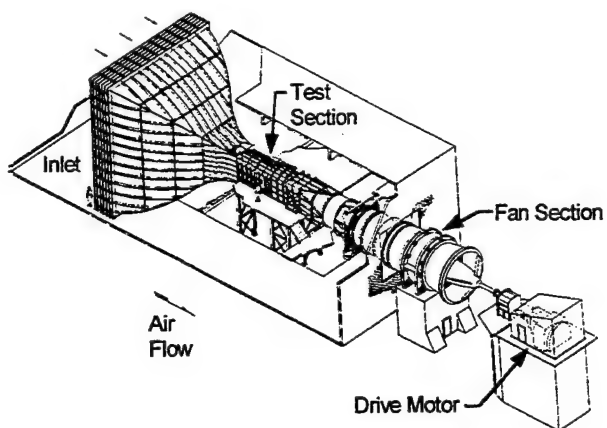


Figure 1. AFRL Subsonic Aerodynamic Research Laboratory

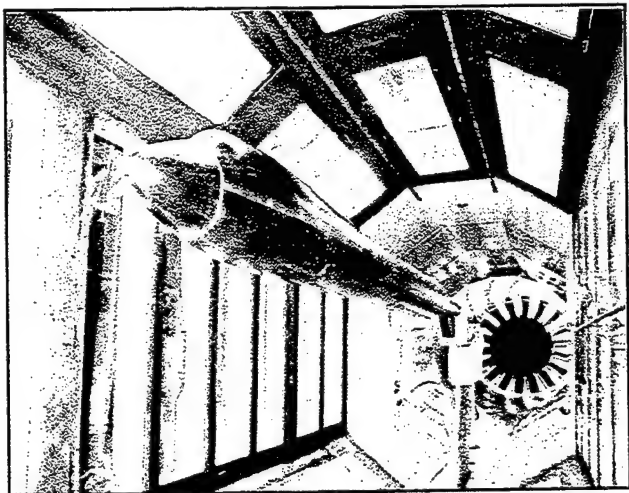


Figure 2. SARL Test Section (looking downstream)

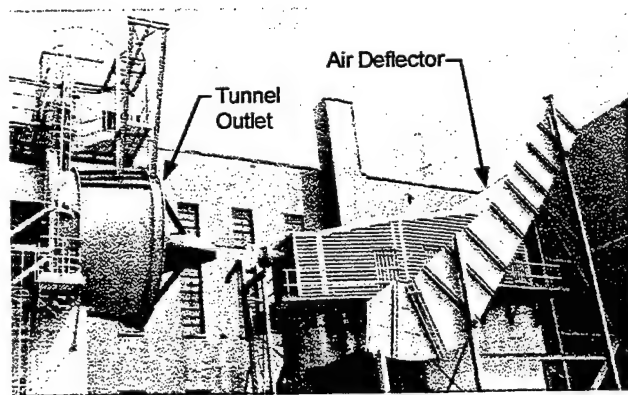


Figure 3. Air Deflector

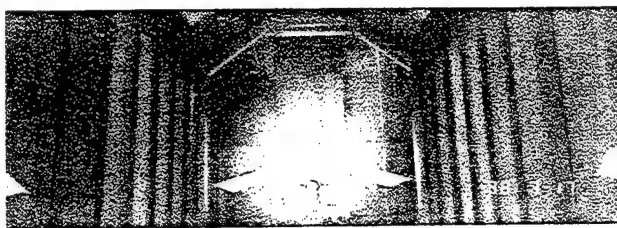


Figure 4. SARL Test Section (looking upstream)

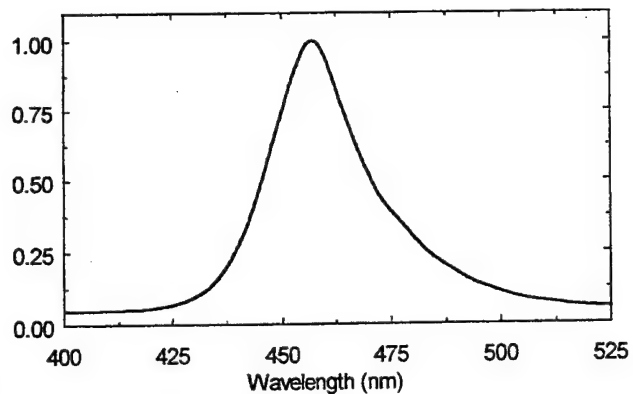


Figure 5. Normalized Emission Spectrum of Blue LED



Figure 6. LED Array Assembly (left) and Inner Housing for LED Array and Optics



Figure 7. Major Components. From Top Clockwise: Muffin Fan, Inner Housing Assembly, Iris, Outer Housing

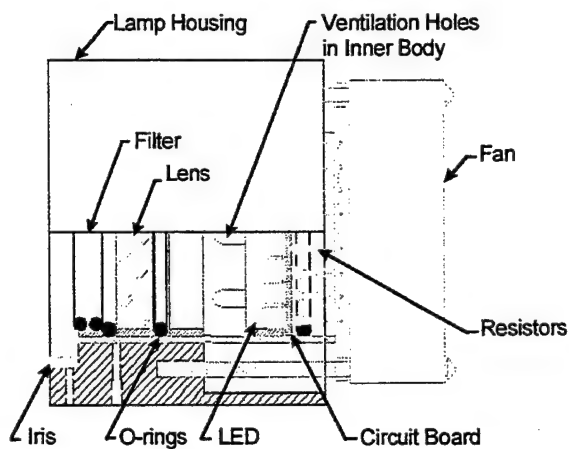


Figure 8. Cross Section of LED Lamp

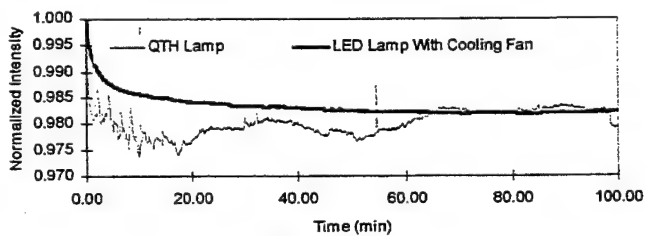


Figure 9. Output Stability of QTH and LED Lamps



Figure 10. Laser Aiming Device for LED Lamps

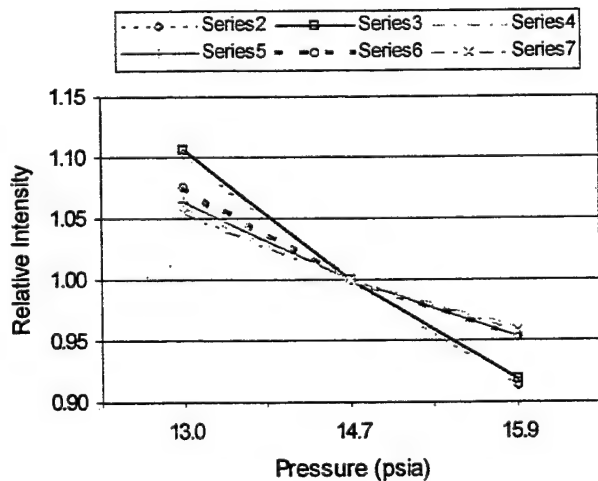


Figure 11. Sol-Gel-Based Paint Tunability

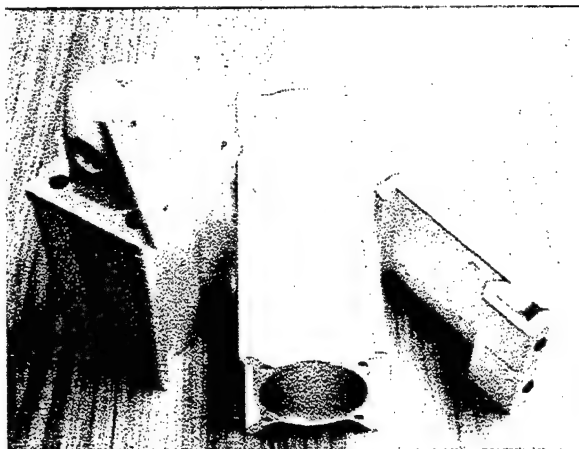


Figure 12. Optical Rails and Components for Mounting Lamps and Cameras

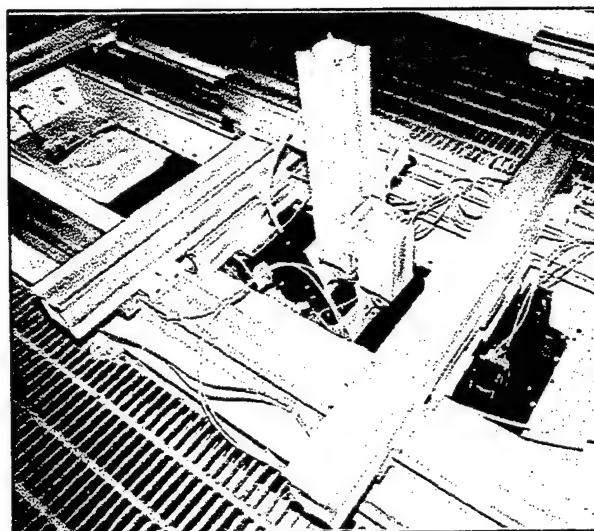


Figure 13. Top of Tunnel: Lamps and Camera Mounted On Optical Rails and Adapters

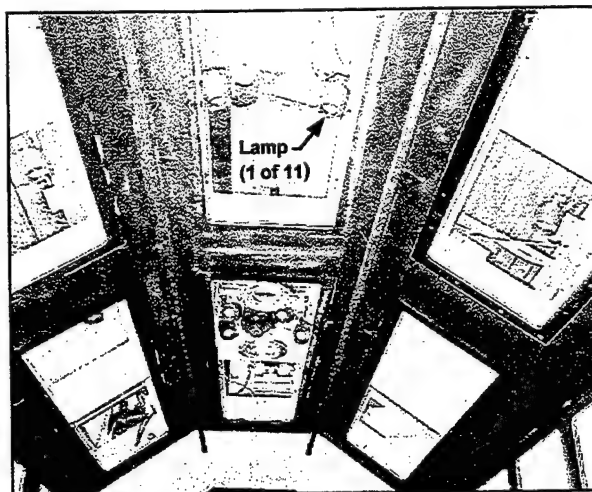


Figure 14. Inside Test Section Looking Up: Lamps and Camera

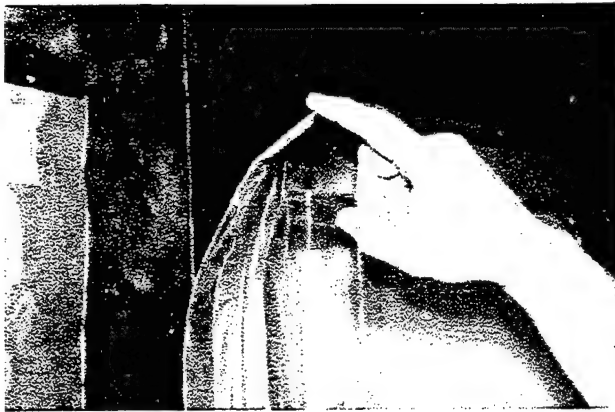


Figure 15. Corner of Magnetic Masking Sheet



Figure 16. SARL Test Section Masked Using Magnetically Attached, Reusable, Plastic Sheetting

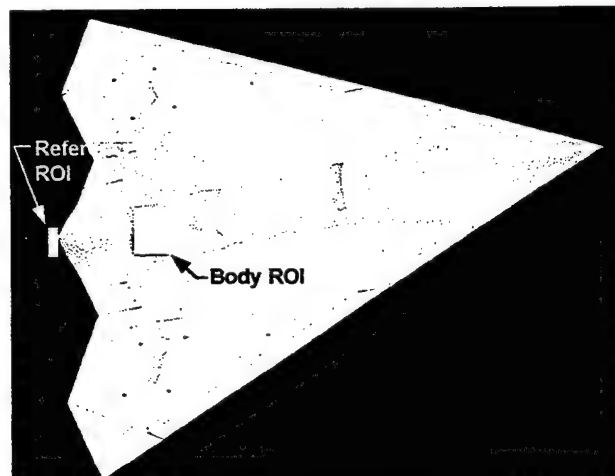


Figure 17. Image of Test Article with Regions of Interest (ROI)

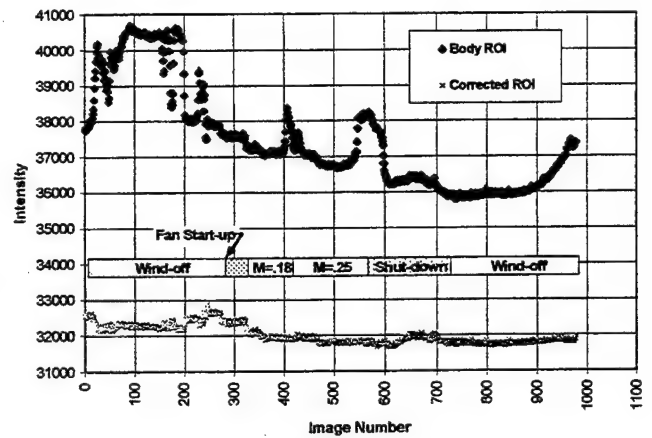


Figure 18. Corrected and Uncorrected Body ROI Intensities

PRESSURE-SENSITIVE-PAINT MEASUREMENTS IN A LARGE-SCALE COMMERCIAL-ENGINE TEST STAND

Jeffrey D. Jordan, A. Neal Watkins, John C. P. N. Davis, and William L. Weaver
Innovative Scientific Solutions, Inc.
2766 Indian Ripple Road
Dayton, OH 45440-3638

Gary A. Dale and Kelly R. Navarra
Air Force Research Laboratory
Wright-Patterson AFB, OH 45433

Justin R. Urban, Wayne E. Devoid, and Richard A. Strange
Pratt & Whitney
400 Main St., M/S 121-02
East Hartford, CT 06108

ABSTRACT

This paper presents the application of pressure-sensitive paint (PSP) measurement technology to a large-scale commercial turbine-engine test stand. In this work, the test article is the engine-inlet bell mouth. A sol-gel-based PSP is applied to the inlet and illuminated using the blue (460-nm) output of eleven LED arrays. PSP data are acquired using a scientific-grade CCD camera. The application of PSP measurements in the engine-test-stand environment requires test instrumentation to be fixed within a housing located upstream of the test article. Challenges associated with performing PSP measurements in this hostile environment are discussed, with focus on the strategies implemented to recover surface-pressure distributions on the engine-inlet bell mouth.

INTRODUCTION

The accurate determination of spatially continuous pressure and temperature distributions on aerodynamic test surfaces is critical for the understanding of complex-flow mechanisms and high-cycle-fatigue (HCF)-related phenomena and for comparison with computational-fluid-dynamics (CFD) predictions. Conventional pressure measurements are based on pressure taps and electronically scanned transducers. Although these approaches provide accurate pressure information, pressure taps are limited to providing data at discrete points. In addition, integration of an adequate population of taps on a test surface can be time consuming, labor intensive, and expensive.

The ability to make an accurate determination of pressure and temperature distributions over an aerodynamic surface based on the emitted luminescence signal from a coating has attracted much attention in the aerospace community [1-14]. PSP measurements exploit the oxygen (O_2) sensitivity of luminescence probe molecules dispersed within gas-permeable binder materials. The mechanism for temperature-sensitive-paint (TSP) sensitivity is based on thermal-deactivation processes inherent in the probe species and temperature-dependent viscosity changes of the binder [15].

If the test surface under study is surrounded by an

atmosphere containing O₂ (e.g., air), the experimental intensity (I) and lifetime (τ) can be described as a function of O₂ partial pressure (P_{O2}) and the pressure exerted on the test surface within a Stern-Volmer framework [15]

$$\frac{\tau_0}{\tau} = \frac{I_0}{I} = 1 + K_{SV} P_{O_2} = 1 + k_q \tau_0 P_{O_2} \quad (1)$$

In this expression I and τ represent the luminescence intensity and the excited-state lifetime at a given P_{O2}, respectively. The subscript 0 denotes measurements in the absence of quencher (vacuum). K_{SV} is the Stern-Volmer quenching constant that provides a measure of the sensitivity of the luminescent species to O₂. The bimolecular quenching constant (k_q) reflects the quenching-process efficiency.

For intensity-based pressure measurements, it is often convenient to use a modified form of the Stern-Volmer expression that replaces the vacuum calibration (i.e., 0) with a reference standard

$$\frac{I_{ref}}{I} = A(T) + B(T) \frac{P}{P_{ref}} \quad (2)$$

In this approach, the reference intensity (I_{ref}) at a given reference pressure (P_{ref}) is divided by the luminescence intensity (I) at some test condition (P) over the region of interest. The coefficients A and B are determined experimentally for a given paint formulation and are a function of temperature (T). Calibration of this intensity ratio (I_{ref}/I) is then correlated with the output of a two-dimensional detector. In practice, the intensities are generally sampled over the surface of interest by a detector array such as a charge-coupled-device (CCD) camera. With today's CCD cameras having a million or more pixels, this technique provides a spatially continuous surface-pressure measurement with unequaled spatial resolution. The output of the CCD array can be visually represented as a two-dimensional image, with the luminescence corresponding to a gray or false-color scale.

The salient criteria that determine paint selection include output intensity, pressure and temperature sensitivity and stability, ease of application and removal, hazardous-material concerns, frequency response, and surface roughness. These characteristics are considered when developing a paint for a given application.

We have pursued the development of paints based on sol-gel-derived thin-film technology. Application of sol-gel-derived composites to PSP technology offers several attractive features. First, sol-gel-derived coatings are characterized by high thermal stability and, therefore, exhibit very low temperature-dependent viscosity changes. Second, the aerosol-based deposition technique allows the formation of thin, uniform films that are optically transparent, robust, and smooth [13]. Furthermore, these coatings can be easily removed by destabilizing the base coat with a mild solvent (e.g., alcohol), which leaves the test surface unaffected. Third, sol-gel thin films exhibit excellent loading capabilities, allowing multiple probe species to be incorporated into the same film at high concentration for increasing output signals. Finally, novel thin-film architectures have been designed that provide a convenient means of optimizing the sensitivity of these composite coatings for the specific pressure and temperature regimes of interest.

In-Situ Calibration

To minimize temperature effects, pressure-tap data are often correlated with the intensity-ratio values of the surface-coated PSP. In this fashion, the tap data correct for illumination and temperature effects inherent in the PSP signal. To demonstrate the capability of this approach under low-speed-flow conditions, a sol-gel-based PSP was tested in the 0.3-m wind tunnel at NASA Langley Research Center in Hampton VA, which is used for testing two-dimensional airfoil sections and other models at high Reynolds numbers. This test was run under ambient-temperature air at low speed (M < 0.5). The model was a supercritical airfoil. A platinum meso-tetra (pentafluorophenyl) porphine [Pt(TfPP)]-based sol-gel low-speed PSP was applied to a portion of the model, with nine registration marks subsequently being drawn on the paint with permanent marker, as shown in Figure 1.

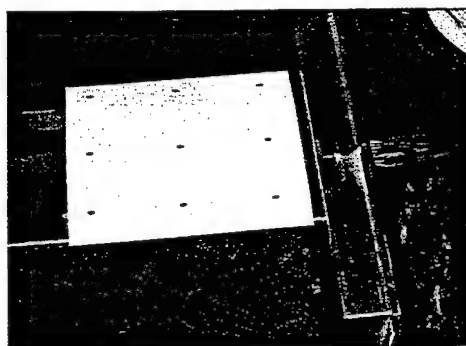


Figure 1. Pt(TfPP)-based sol-gel PSP applied to a model in the 0.3-m wind tunnel at NASA Langley.

Images were acquired using a 512 x 512 14-bit CCD camera with the model at 10° alpha under wind-off conditions and at Mach numbers of 0.15, 0.25, and 0.50 (ambient air). The data were analyzed by Langley personnel using a commercially available software package and the in-situ calibration method; the results are shown in Figure 2.

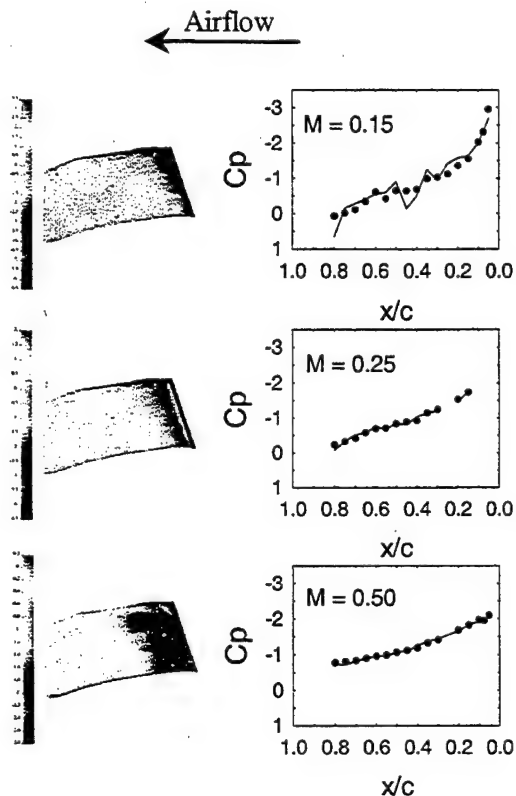


Figure 2. Pressure distribution across chord of SC3 model at three velocities.

The plots to the right of each image show a comparison of the pressure coefficient (C_p) recovered from the pressure tap (points) and PSP data (line). Good correlation was observed at $M = 0.25$ and 0.50 , with slight deviation at the lowest velocity investigated ($M = 0.15$), demonstrating the capability of PSP-based techniques for the measurement of 2D surface-pressure distributions at low velocity.

These results illustrate the utility of PSP measurements for the investigation of low-speed-flow aerodynamics. Transitioning this technology to the large-scale engine test cell introduces several additional challenges associated with the high-mass flow, high vibration, and large source-to-target distances. The remaining sections of this paper will discuss the strategies and mechanisms

employed to recover accurate surface-pressure distributions in this relatively hostile environment.

TEST SETUP

The deployment of PSP measurements in an engine test cell required two phases of setup: 1) model preparation and painting and 2) instrumentation installation and alignment. The following subsections summarize the steps taken to deploy PSP measurements within an engine test cell at Pratt & Whitney, East Hartford, CT.

PSP Application

A photograph of the engine-inlet bell housing in the test cell is shown in Figure 3.

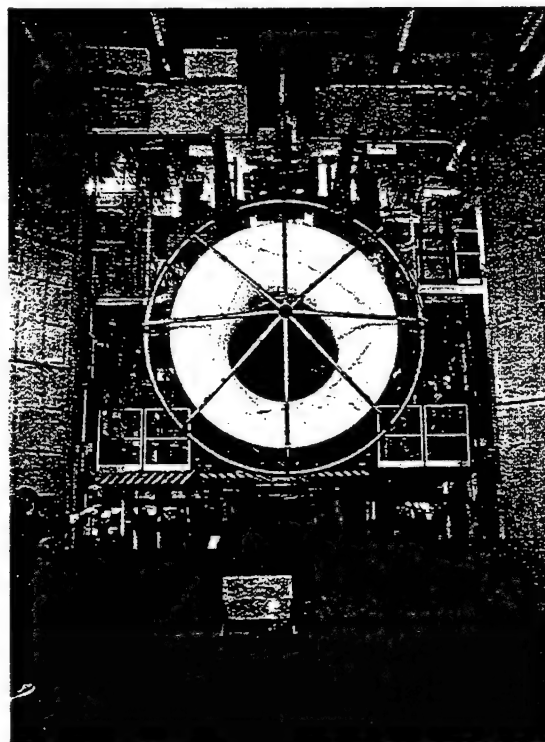


Figure 3. Engine-inlet bell housing within test cell.

The internal diameter of the bell mouth tested was ~ 75 in. (1.9 m). The spherical structure located upstream of the engine inlet (wagon wheel) was used to mount pressure and temperature transducers. For this test, two symmetrical regions of the upper surface of the bell housing were painted with a low-speed sol-gel-based PSP, indicated by the upper regions on the bell mouth in Figure 4.

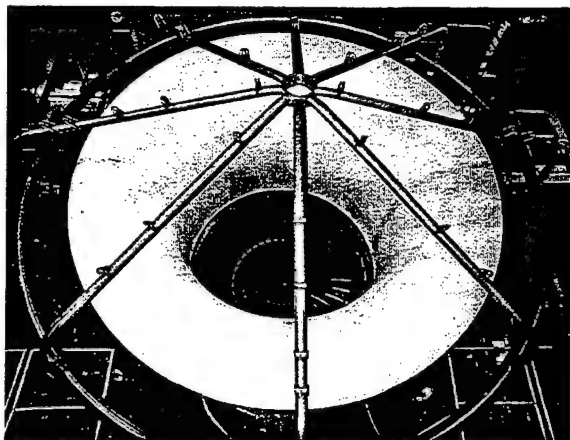


Figure 4. Painted engine-inlet bell mouth from the instrumentation housing (22 ft).

Prior to PSP application, the engine-inlet surface was first cleaned with alcohol and a lint-free cloth. The surrounding area was then masked to prevent overspray from contacting the unpainted areas of the bell housing, the fan blades, the pressure and temperature transducers, and the wagon-wheel structure located upstream of the inlet. A white base coat was applied and allowed to dry for ~1 hr prior to deposition of the sol-gel PSP. Finally, registration (fiducial) marks were drawn on the painted surface in a grid formation and the precise locations determined using a coordinate mapping system (CMS). These data allow reference images acquired under isobaric and isothermal conditions (wind off) to be registered and accurately ratioed with the spatially distorted images acquired at condition (wind-on).

Hardware Installation

The high-mass flow encountered within large-scale engine test cells requires that precautionary measures be taken to prevent the ingestion of diagnostic instrumentation components that would cause engine damage and/or catastrophic failure. To that end, the housing structure shown in Figure 5 was designed and constructed by Pratt & Whitney personnel.

The instrumentation housing was designed to support the mounting of eleven LED-based illumination sources and a scientific-grade CCD camera and controller (16-bit, 512 x 512, back-lit, slow-scan CCD). The individual lamp mounts allowed each unit to be rotated and translated within the structure for alignment purposes.

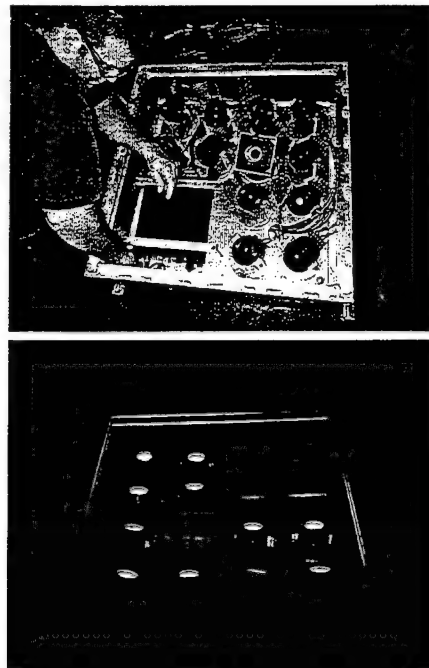


Figure 5. LED lamps and CCD camera being installed within the instrumentation housing (upper) and in operation (lower).

Once installed and aligned, a transparent shield (1-in. thick) was installed within a groove in the housing to isolate the instrumentation from the flow. The housing structure was mounted on two, 3-ft I-beam sections that were bolted to the test-cell floor at a distance of ~22 ft (6.7 m) from the PSP-coated surface. Cables were run from a cutout in the back of the housing to the LED-array power supply which was located behind the test-cell picture frame and downstream of the engine inlet.

The LED-lamp output was controlled using a break-out box wired to the control room. The CCD camera was operated remotely via a fiber-optic serial interface.

EXPERIMENTAL PROCEDURE

Steady-state PSP data were acquired under three experimental conditions: ground idle, flight idle, and cruise, representing 1500, 6000, and 10000 lb of thrust, respectively. Single-shot PSP images were also acquired while the engine thrust was ramped from 6000 to 26,000 lb. During steady-state test operation, PSP, pressure tap, and thermocouple data were acquired simultaneously. Fifteen PSP and background (lamp-off) images were collected at each run condition for later post processing.

DATA ANALYSIS

PSP Image Registration

Image registration is an area of active research in the PSP community. Currently deployed PSP systems require that intensity (I) images collected at condition (wind-on) be ratioed to images collected at an isobaric (wind-off) condition ($I_{\text{wind-off}} / I_{\text{wind-on}}$). Test-article deflection and warping between the wind-on and wind-off conditions result in systematic errors in the calculated intensity ratio. Identical image locations on the model rather than identical CCD camera pixel locations must be ratioed.

In practice, image processing for paint-sensor systems falls into two categories—image registration and image resection. Image registration is concerned with the effects of model movement and deformation on the calculation of the $I_{\text{wind-off}}/I_{\text{wind-on}}$ ratio; image resection involves the accurate placement of the resulting two-dimensional image of pressure values on a three-dimensional wire-mesh model grid for spatial quantitative visualization. Algorithms for image registration and image resection in the area of PSP appear in the published literature [16, 17]. For simple image translation, x and y coordinates of a given pixel in the wind-on image are related to the pixel coordinates of the identical model location in the wind-off image (x' and y') through the transforms in Eq. 3, where m is a magnification factor and s_x and s_y represent the x and y components of the shift, respectively.

$$x = R_x(x', y') = mx' + s_x \quad (3a)$$

$$y = R_y(x', y') = my' + s_y \quad (3b)$$

To account for model bending, Eq. 3 is extended to a set of second-order equations appearing in Eq. 4.

$$x = \sum_{i,j=0}^2 a_{i,j} x'^i y'^j \quad (i+j \leq 2) \quad (4a)$$

$$y = \sum_{i,j=0}^2 b_{i,j} x'^i y'^j \quad (i+j \leq 2) \quad (4b)$$

The coefficients $a_{i,j}$ and $b_{i,j}$ can be determined by using at least six pairs of known image locations in the wind-off and wind-on images $[(x,y),(x',y')]$ pairs] and solving for the coefficients using a least-squares fitting algorithm. These image locations are typically well-defined model features or registration marks placed on the model. After the coefficients have been determined, the shifted x and y pixel coordinates are calculated, and the pixel values of the registered wind-on image are calculated by linear interpolation of the pixel intensities in the actual wind-on image. The intensity ratio of the $I_{\text{wind-off}}$ to the registered $I_{\text{wind-on}}$ yields the corrected values.

The process of image resection has its basis in the area of photogrammetry [18-21]. Image resection is the process of recovering the three-dimensional coordinates of a surface from a two-dimensional image of the surface. This process is used in the PSP technique for accurate placement of the calculated pressure values on a three-dimensional wire-mesh model of the test article to extract three-dimensional quantitative surface-pressure information. Bell and McLachlan [17] have demonstrated the utility of the Direct Linear Transform (DLT) [21] formulation for the process of image resection. The x and y coordinates of the two-dimensional CCD-camera image are translated into X , Y , and Z model coordinates via Eq. 5.

$$x = \frac{L_1 X + L_2 Y + L_3 Z + L_4}{L_9 X + L_{10} Y + L_{11} Z + 1} \quad (5a)$$

$$y = \frac{L_5 X + L_6 Y + L_7 Z + L_8}{L_9 X + L_{10} Y + L_{11} Z + 1} \quad (5b)$$

The 11 DLT unknown coefficients in Eq. 5 can be determined using the same six pairs of registration marks that were used for image registration. Information required from the six pairs is the X , Y , and Z coordinates of the registration marks in model space and the two-dimensional x , y coordinates of the registration marks in the CCD-camera image. The location of the x , y pixel coordinates is obtained from inspection of the CCD-camera image. The X , Y , Z model coordinates are obtained independently using a CMS. Armed with the six registration marks of known 2-D and 3-D coordinates, one can uniquely determine the coefficients in Eq. 5 by solving the resulting system of linear algebraic equations.

QPED Registration Method

We are currently investigating the development of new algorithms to aid in the image-registration process. The study involves evaluating the utility of automated techniques that have potential for performing image registration in an unattended and non-user-assisted algorithm. The algorithm under development is called Quantum Pixel Energy Distribution (QPED) [22]. This algorithm is based on the discrete pixel-based architecture of the CCD camera and is intended to augment the linear-interpolation algorithm used for fractional-pixel image shifting.

The QPED process is used as the foundation for an optimizing search algorithm. In this algorithm, a matrix of x , y shift values for each pixel (QPED matrix) in a wind-off image are adjusted on a pixel-by-pixel basis. The resulting pixel-shifted image (QPED image) is ratioed with the wind-on image, and the quality of the resulting intensity-ratio image is assessed. The QPED matrix values are adjusted until the optimal condition is found.

For the present experiments, the QPED algorithm was used for image registration and the results compared with those obtained using the registration functions included in the commercially available PSP data-reduction software.

RESULTS

Figure 6 shows the engine inlet bell mouth under illumination from the 11 LED sources located within the instrumentation housing (image lower left).

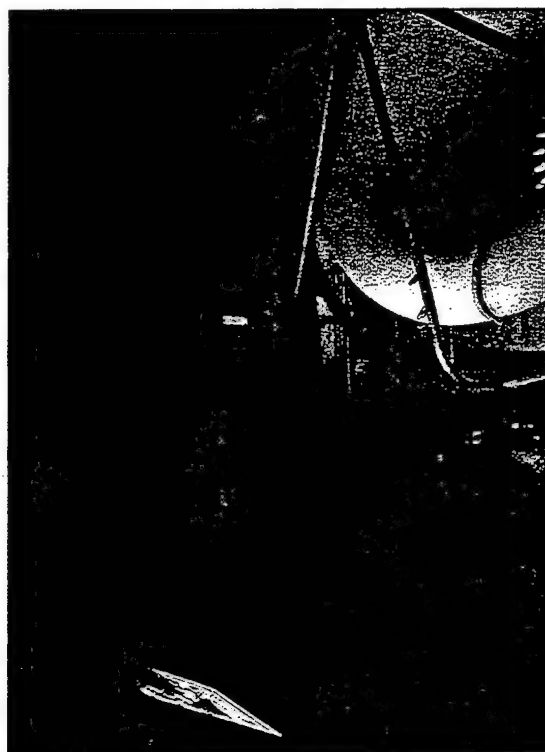
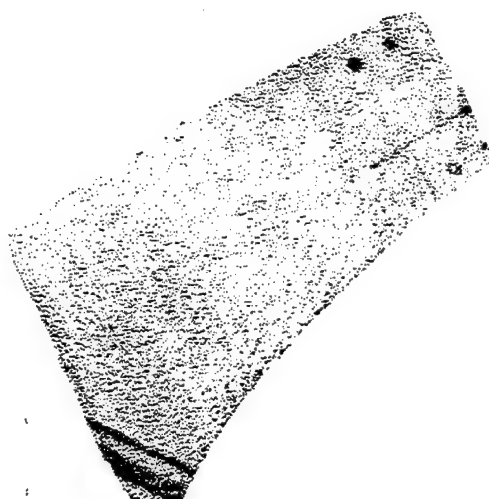


Figure 6. Engine inlet illuminated using 11 LED-based illumination sources at a distance of 22 ft.

During PSP data acquisition, all non-essential test-cell lights were turned off to mitigate background. For PSP data post processing, the ground-idle condition was used as the wind-off reference and ratioed with the images acquired under each test condition. To facilitate the resection of PSP data to a three-dimensional grid, the commercially available software package maps the two-dimensional CCD image acquired under each test condition to the wind-off data. The QPED algorithm maintains the capability of using either condition as the target, and for these experiments mapped the static wind-off data to the wind-on images. This practice allows visualization of the aerodynamic-load-induced deformation of the test article. The left-hand portion of the painted regions was obscured under test conditions and was removed from the image. A CFD grid was not available to allow image resection to a three-dimensional model. Pressure data were available from a single tap located on the surface of the bell mouth near the fan. The pressure results at this point were correlated with the intensity-ratio data from the PSP, providing a one-point in-situ calibration. This analysis was performed for a single PSP image

acquired at the 10,000-lb thrust condition, and the results are shown in Figure 7.



12.0 12.8 13.7 14.5 15.3 16.2 17.0

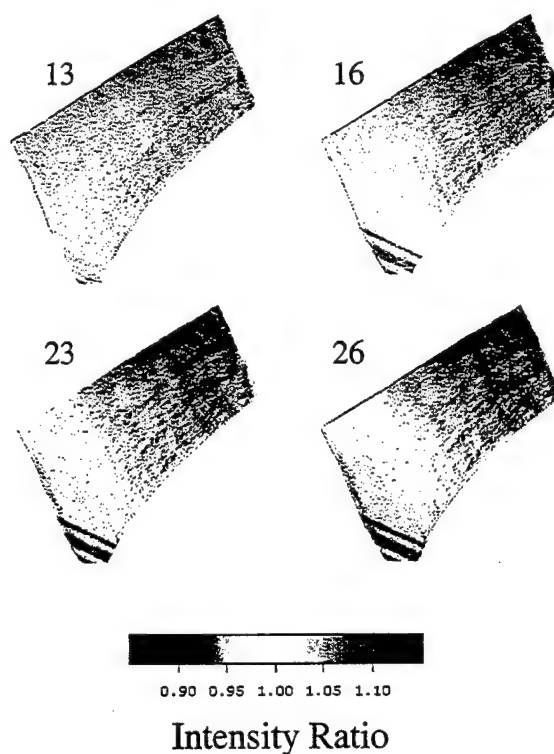
Pressure (psia)

Figure 7. Temperature-corrected PSP image at 10000 lb of thrust.

The PSP image shows that the pressure near the leading edge in the stagnation region is consistent with the ambient pressure (~14.8 psia) in the test cell. The pressure decreases with increasing velocity as the flow is accelerated through the inlet toward the engine fan. The total recovered pressure differential from the bell mouth leading to the trailing edge is ~1.2 psi. The striped region in the image lower left corresponds to a shadow from the wagon wheel that was not removed in the post processing.

PSP images acquired as the engine was accelerated through 26,000 lb of thrust were registered using the QPED algorithm and ratioed with the images acquired under ground idle; four of these are shown in Figure 8.

The intensity-ratio images range in thrust from 13,000 to 26,000 lb. Intensity ratios greater than one indicate



0.90 0.95 1.00 1.05 1.10

Intensity Ratio

Figure 8. PSP intensity-ratio images as a function of thrust (1000 lb).

higher than ambient pressures and/or temperatures, and vice versa for values lower than one. For these tests, pressure-tap data were not acquired; this prevented the application of in-situ calibration methods. Nonetheless, it is clear from these data that as the engine thrust increases, the magnitude of the pressure/temperature distributions increases on both the leading and trailing edges. Together these results show the feasibility of performing PSP measurements using LED-based illumination sources in large-scale test-engine environments.

The registration capabilities of the newly developed QPED algorithm were compared to the standard registration functions utilized in the commercially available software using data acquired at 26,000 lb of thrust. Figure 9 shows the two ratioed images on identical scales.

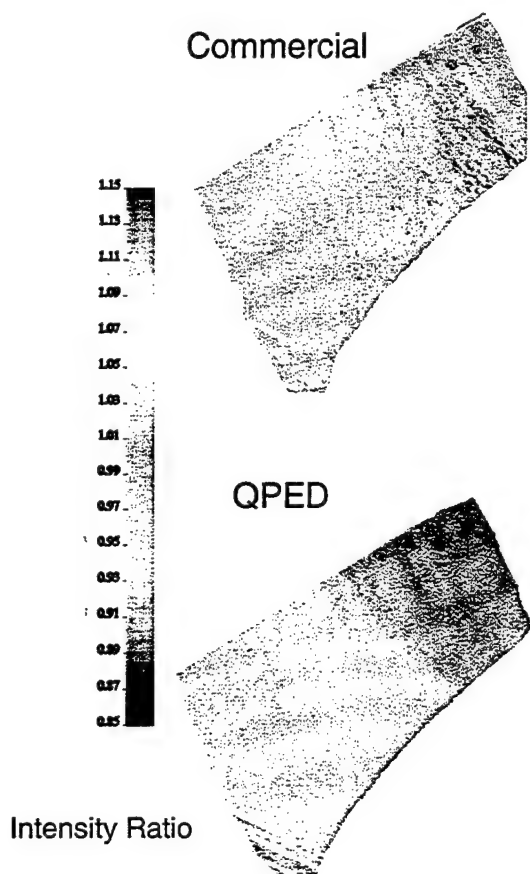


Figure 9. PSP intensity-ratio images at 26,000 lb of thrust registered using commercially available (top) and QPED (bottom) software.

It should be noted that of the twelve registration marks placed on the painted area, only seven were visible to the camera; model displacement during operation caused them to be obscured by the wagon wheel. The QPED registration was accomplished without the use of registration targets with known x, y, z positions. Image features including pressure taps, edges, and surface topography were used to register the images.

SUMMARY

To our knowledge, these results represent the first successful deployment of PSP measurements in a large-scale commercial-engine test stand. Challenges associated with the high source-to-target distances (22 ft), the high mass flow, severe vibration, and large test-article displacement between the wind-off and wind-on conditions were overcome to recover surface-pressure distributions on an engine-inlet bell mouth. Current efforts focus on the development of PSPs that contain

an additional probe species that is sensitive to temperature only. These paints will provide a means of decoupling the effects of pressure and temperature in PSP measurements without pressure-tap data being necessary to perform in-situ calibration. Additional efforts are focused on optimizing PSPs and measurement techniques for rotating turbomachinery components in the latter stages of the turbine engine.

REFERENCES

1. Kavandi, J., Callis, J., Gouterman, M., Khalil, G., Wright, D., Green, E., Burns, D., and McLachlan, B., "Luminescence Barometry in Wind Tunnels," *Review of Scientific Instruments* **61**(11), 3340-3349 (1990).
2. Morris, M., Donovan, J., Kegelmann, J., Schwab, S., Levy, R., and Crites, R., "Aerodynamic Applications of Pressure Sensitive Paint," AIAA Paper 92-0264.
3. McLachlan, B., and Bell, J., "Pressure-Sensitive Paint in Aerodynamic Testing," *Experimental Thermal and Fluid Science*, **10**, 470-485 (1995).
4. Liu, T., Campbell, B., Burns, S., and Sullivan, J., "Temperature- and Pressure-Sensitive Luminescent Paints in Aerodynamics," *Applied Mechanics Reviews* **50**(4), 227-246 (1997).
5. Erausquin, R., Jr., Cunningham, C., Sullivan, J., Asai, K., Kanda, H., Kunimasu, T., and Iijima, Y., "Cryogenic Pressure Sensitive Fluorescent Paint Systems," AIAA Paper 98-0588.
6. Asai, K., Kanda, H., and Kunimasu, T., "Detection of Boundary-Layer Transition in a Cryogenic Wind Tunnel by Using Luminescent Paint," AIAA Paper 96-2185.
7. Asai, K., Kanda, H., Cunningham, C., Erausquin, R., Sullivan, J., "Surface Pressure Measurement in a Cryogenic Wind Tunnel by Using Luminescent Coating," ICIASF, Monterey, CA, 1997.
8. Shimbo, Y., Mehta, R., Cantwell, B., "Vortical Flow Field Investigation Using the Pressure Sensitive Paint Technique at Low Speed," AIAA Paper 97-0388.
9. Torgerson, S., Liu, T., Sullivan, J., "Use of Pressure Sensitive Paints in Low Speed Flows," AIAA Paper 96-2184.
10. Carroll, B., Abbitt, J., Lukas, E., and Morris, M., "Pressure Sensitive Paint Response to a Step Pressure Change," AIAA Paper 95-0483.
11. Winslow, N., Carroll, B., Setzer, F., "Frequency Response of Pressure Sensitive Paints," AIAA Paper 96-1967.
12. Baron, A., Danielson, S., Gouterman, M., Wan, J., Callis, J., and McLachlan, B., "Submillisecond Response Times of Oxygen-Quenched

- Luminescent Coatings," *Review of Scientific Instruments* 64(12), 3394-3402 (1993).
13. Jordan, J., "Development and Application of Sol-Gel-Derived Platforms for Chemical and Biological Sensing," Ph.D. Dissertation, State University of New York at Buffalo, NY, May 1997, and references therein.
 14. Navarra, K., "Development of the Pressure Sensitive-Paint Technique for Turbomachinery Applications," Master's Thesis, Virginia Polytechnic Institute and State University, Blacksburg, VA, May 1997.
 15. Lakowicz, J., *Principles of Fluorescence Spectroscopy* (Plenum Press, New York, 1983).
 16. Donovan, J., Morris, M., Pal, A., Benne, M., and Crites, R., "Data Analysis Techniques for Pressure- and Temperature-Sensitive Paint," AIAA Paper No. 93-0176.
 17. Bell, J., and McLachlan, B., "Image Registration for Luminescent Paint Sensors," AIAA Paper No. 93-0178.
 18. Slama, C., Ed., *Manual of Photogrammetry*, 4th Ed. (American Society of Photogrammetry, Falls Church, VA, 1980).
 19. Wolf, P., *Elements of Photogrammetry* (McGraw Hill, New York, 1974).
 20. Marzan, G., and Karara, H., "A Computer Program for Direct Linear Transformation Solution of the Collinearity Condition, and Some Applications of It," in *Proc. ASP Symp. on Close-Range Photogrammetric Systems* (1975), p. 420.
 21. Abdel-Aziz, Y., and Karara, H., "Direct Linear Transformation From Comparator Coordinates into Object Space Coordinates," in *Proc. ASP/UI Symp. on Close-Range Photogrammetric Systems* (1971), p. 1.
 22. Weaver, W, Jordan, J., Dale, G., and Navarra, K., "Data-Analysis Methods for the Development and Deployment of Pressure-Sensitive Paints," AIAA Paper No. 99-0565.

ACKNOWLEDGMENTS

The authors acknowledge Mr. Gary Clinehens of SelectTech Corporation for his LED lamp expertise and Mr. Henry Baust of AFRL/VA for assistance with the data analysis using the commercially available software. This work was supported by the U.S. Air Force under Contracts F33615-95-C-2507 and F33615-98-C-3012 and by Pratt & Whitney, East Hartford, CT.

PRESSURE SENSITIVE PAINT MEASUREMENTS ON A WING MODEL IN A LOW-SPEED WIND TUNNEL

Christian KLEIN, Rolf H. ENGLER, Sergey D. FONOV, Ole TRINKS

DLR-Göttingen, GERMANY

ABSTRACT

Pressure field measurements on a wing profile are conducted to evaluate the accuracy of a measurement system using the so called "binary" or "two-color" Pressure Sensitive Paint (PSP) for low-speed (40-60 m/sec) environments. A part of the wing surface was coated with a binary paint. Two different light sources, a high pressure Xenon-flash lamp and a nitrogen laser were used for the excitation of the paint. The resulting fluorescence fields were acquired by a 16-bit CCD slow-scan camera. In front of this camera two different optical devices, a filter-shifting system or alternative a beam-splitting system, each of them were equipped with appropriate optical filters to separate the two different spectral emission wavelength of the paint, were used. Results shows that this optical pressure measurement system is able to resolve the small pressure changes on the model surface. Due to model movement and model deformation in between the image acquisition of the "wind-off" and "wind-on" images the necessity to use a binary paint for precise pressure measurements is clearly visible. These PSP-System working with binary paint can achieve pressure resolution in the region of 1 mbar.

NOMENCLATURE

I = luminescence intensity
 K_q = quenching constant
 PO_2 = partial pressure of oxygen
 p = local static pressure
 A, B, C = calibration coefficients of a paint
 t = response time
 l = thickness of the binder layer
 D = diffusion coefficient of oxygen
 Λ = aspect ratio

SUBSCRIPTS

0 = absence of oxygen (vacuum conditions)
 ref = reference condition

INTRODUCTION

The physical basis of all Pressure Sensitive Paint (PSP) formulations is the oxygen-quenching process in which excited luminophore molecules are deactivated by oxygen. Luminophore molecules are placed in a binder layer on the model surface and are excited by an appropriate light source. Oxygen from airflow can diffuse into the binder layer and the oxygen

concentration in the layer is the function of local static pressure on the upper surface of the binder. Resulting luminescent intensity distribution reveals the static pressure distribution on the model [1]. The PSP method gives quantitative as well as qualitative pressure distribution images of the complete observed model surfaces [2] without significant disturbances. This method could be used also for flow visualization and to provide detailed aerodynamic quantitative static pressure information about the models aerodynamics. The PSP techniques have been widely used in wind tunnels for investigations in transonic - and supersonic flow [3]. For these fields of interest, the absolute pressure changes on the model surface are rather large. Therefore changes in the detectable luminescence levels are also large. Low-speed flows ($Ma < 0.3$) in comparison to the transonic - and supersonic flows produce relatively small pressure changes on the models surface and therefore the variation of luminescence levels due to pressure change is quite small. However, there exist already pressure measurements in low-speed flows using the different existing PSP techniques:

Group	Model	Ma	Δp_{max} [psi]
Morris et al. [4]	Delta wing	0.17	0.3
McLachlan et al. [5]	NACA 0012	0.30	1
INTECO [6]	Car-model	0.12	0.12
Sullivan [7]	Jet interaction		3
Brown et al. [8]	NACA 0012	0.03-0.15	0.1

Table 1: Previously PSP measurements in low-speed flow

In the here described experiment the measurement system and data processing algorithms were optimized to achieve a good signal-to-noise ratio (SNR) and to reduce the influence of possible measurement errors. With this system, reliable experimental results were obtained for flow velocities down to $U_\infty = 40 \text{ m/s}$. Presented results shows the influence of possible error sources of the PSP technique. The PSP data were compared with those of the conventional pressure taps. Finally, several aerodynamic effects on the investigated wing profile are given.

PSP BASIS

PSP techniques are based on the deactivation of photochemical-excited organic molecules, so called luminophores, by oxygen molecules. This oxygen-quenching process of luminescence was first discovered

and described by Kautsky and Hirsch [9] in 1935 and will be briefly reviewed in this paragraph. The behavior of photoluminescence of a luminophore quenched by oxygen molecules can be described by the Stern-Volmer relation [1]:

$$I_0/I = 1 + K_q PO_2, \quad (1)$$

where I_0 is the photoluminescence in the absence of oxygen (vacuum), I the detected photoluminescence, K_q the quenching constant, and PO_2 is the partial pressure of oxygen. K_q is a function of temperature.

In the widely-used pressure sensitive paint formulations, the luminophores (e.g. ruthenium, Pyren) are located in a polymeric binder material (e.g. silicon rubber). The binder compound is permeable to the oxygen molecules. To calculate the static pressure values from a measured intensity distribution for such paint formulations the second order approximation is more useful:

$$p = A(T) + B(T)(I_{ref}/I) + C(T)(I_{ref}/I)^2, \quad (2)$$

where p is the local static pressure, A, B and C are temperature dependent calibration coefficients of the pressure sensitive paint formulation, which can be determined in laboratory or pressurized wind-tunnel and I_{ref} is the corresponding intensity value for a constant reference pressure. Thus, using a ratio of images taken at two pressure conditions ("wind on" and "wind off") allows determining of static pressures over the surface of interest. A problem that occurs when using PSP in this intensity method is the model displacements, uncertainties of the temperature field on the model surface, excitation light non-stability, the spread of exposure time, and the luminescence light scattering on the adjacent model parts or test section walls (self illumination). Aerodynamic forces acting on the model change their position relative to the light source and image acquisition system. Alignment of "wind off" and "wind on" images does not totally eliminate influence of model displacement and deformation [2] and [10]. Influence of the temperature field uncertainties can be minimized by direct measurements of the temperature distributions on the model surface, by using PSP formulations with small temperature sensitivity or (and) by estimation of the temperature field on the base of measured pressure fields and some assumption about heat flux on the model surface [11]. A more detailed description of different pressure sensitive paint formulations as well as a more complex theoretical background is presented in [11], [12] and [13].

WIND TUNNEL AND MODEL

The presented measurements were performed in the Low-Speed-Wind-Tunnel (LSWT) of DaimlerChrysler Aerospace in Bremen. This Eiffel-type wind tunnel with a test section of 2.1m x 2.1m is a continuously driven facility operating at flow speeds between $U_\infty=6$ and 75m/s. The final image acquisition procedure was

started 10 minutes after the wind tunnel was turned on, to stabilize the flow temperature in order to minimize the temperature influence to the PSP coating. After this warm-up phase the flow temperature in the test section was measured with $25 \pm 2^\circ\text{C}$. For all PSP tests a wall plate element, Fig. 1, was built for the fast implementation of the excitation illuminators and the CCD camera. As known, daylight or other ambient light can disturb the final result obtained by the PSP-System. In order to exclude this influences, all sources of ambient light were covered by light-absorption material. In addition, the test section inside was coated with light-absorption material. Therefore also self-reflection effects from the emission light of the paint at the test-section walls can be excluded.

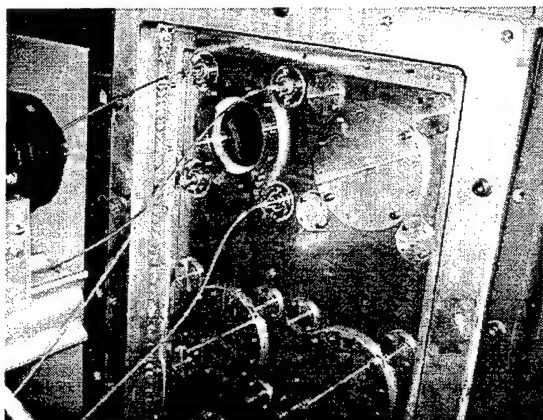


Fig. 1 Observation window, illuminators and camera

The investigated model surface is a part of the suction side of a wing with a constant profile (Swept-Constant-Chord-Half-wing, SCCH). Fig. 2 shows a photo of the mounted model on the upper test-section wall. In this photo, the so called "clean-wing" configuration is presented. Also different slats and flaps could be fixed on this type of the model.

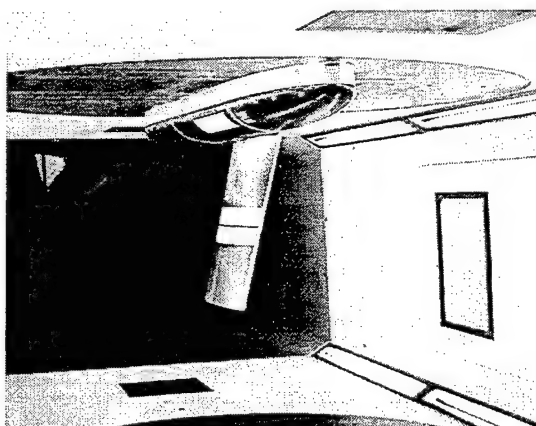


Fig. 2 Investigated model in the test section with PSP coated areas

In Fig. 2 the PSP coated area of the investigated model is visible on the wing. Along the small non-coated strip in the middle conventional pressure taps are located. A

PSI-System as conventional pressure acquisition system for PSP comparison was used. The geometry of the SCCH model and the location of the section of the pressure orifices are given in Fig. 3.

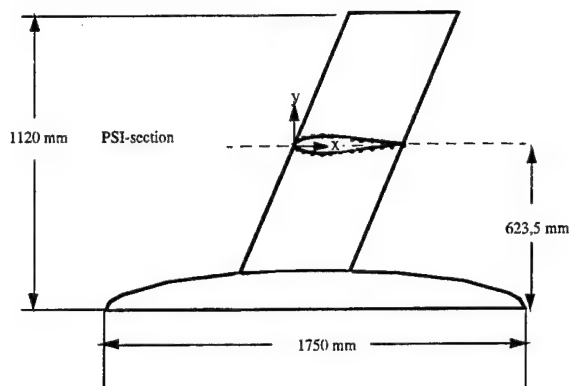


Fig. 3 Geometry of SCCH model

EXPERIMENTAL SETUP

A Xenon-flash lamp or a nitrogen-laser, each equipped with four fiber optics, for illumination and a scientific grade 16-bit, 1024x1024pixel CCD slow-scan camera for image acquisition were used. In this arrangement exposure times of approximately 10s for a typical distance of 1.6m between the camera and the model could be realized for each pair of "blue"/"red" images. Details about "binary paint" are given in chapter PAINT.

Such pairs of images were either acquired sequentially by the camera using a filter-shifter or in parallel by a multi-viewer (beam-splitter system) in front of the camera lens. In fact, the filter-shifting approach does not totally eliminate time non-stability of the light source but is affordable by taking the long exposure time into consideration. A multi-viewer will overcome these time non-stabilities of the light source at all, but a small viewing angle must be accepted because two images of 400x400pixel will be finally projected to the 1024x1024pixel array – see Fig. 4. Therefore not the complete PSP coated area could be detected for this test.

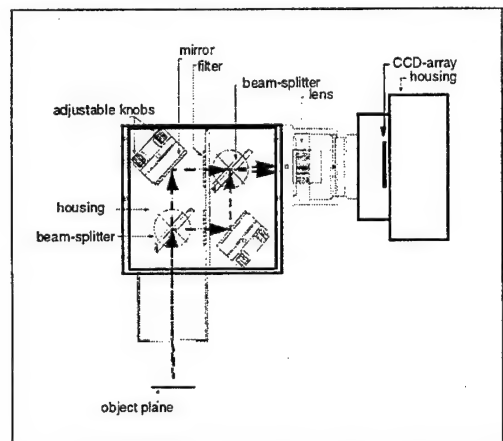


Fig. 4 Multi viewer for "binary paint" test

Fig. 5 shows the basic PSP system composition for this wind tunnel test. All different devices of the system (data-acquisition, data-processing, synchronization of CCD camera and excitation light) were controlled via PC. In front of the camera lens, either the filter-shifter or multi-viewer was installed.

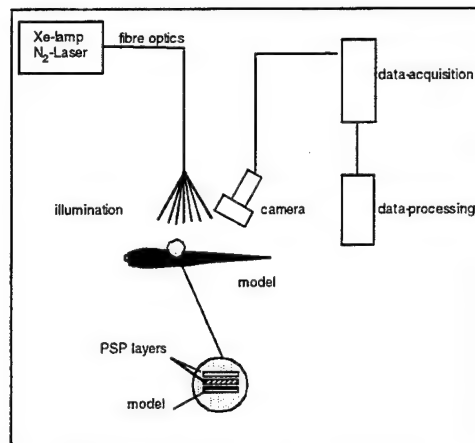


Fig. 5 Schematic diagram of experimental set-up

PAINT

The B1 binary paint formulation from Optrod, based on Pyren as luminophore, was used for the measurements. This paint consists of a screen layer, adhesive layer and an active layer with a total thickness about 50 μm and a response time 0.5s [11]. A typical calibration curve for a Pyren-based paint is presented in Fig. 6.

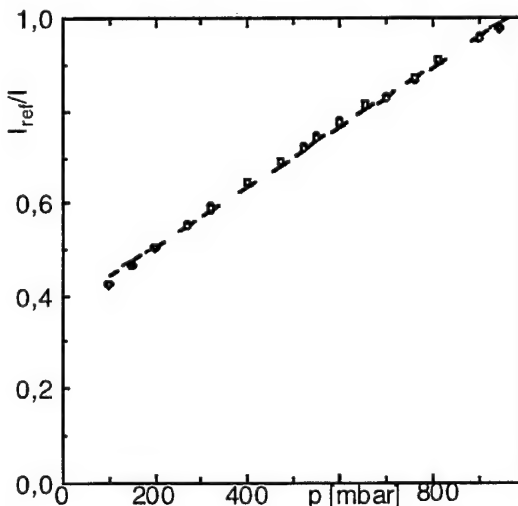


Fig. 6 Calibration curve for a Pyren-based paint, $T=\text{const.}$

The emission of the PSP depends on the excitation intensity, see (1). That means instabilities of the excitation light, model movements or model deformations relative to the light source will lead directly to an error in the pressure measurements. To minimize these errors the excitation intensity should be measured simultaneously during taking the image which is related to the pressure changing will be acquired. This

can be done globally, on several locations on which the excitation intensity is mirrored ("intensity-mirror"). More detailed excitation intensity information can be obtained using the binary paint composition. This binary paint provides the possibility to acquire simultaneously additional reference image, which contains information about local excitation intensity. The excitation intensity fluctuations for the Xenon-flash lamp or the nitrogen-laser integrated for an exposure time of 1 sec can be estimated as 1%. That provides significant input in the measurement error without using a binary paint. Fig. 7 shows the emission spectra of the binary paint that was used for different absolute pressures.

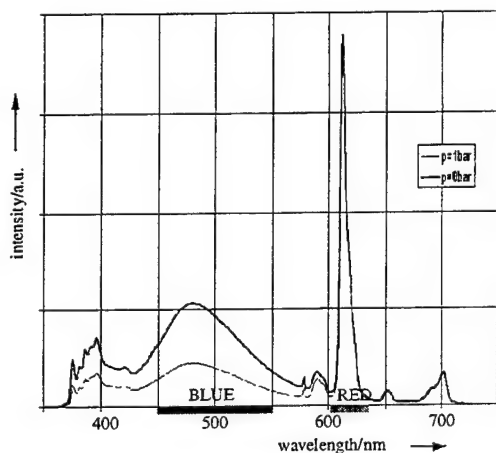


Fig. 7 Emission spectra of binary paint for different absolute pressures and constant temperature

The emission band from 425 to 550 nm is used to acquire pressure sensitive images ("blue" images) and the emission band from 610 nm to 630 nm is used to obtain the excitation-reference images ("red" images).

Since pressure sensitive paints are also sensitive to temperature, the temperature of the flow was controlled during the run to minimize the temperature effect on the luminescence painting. The model surface temperature during the run was also measured in several points with PT100 thermocouples. The maximum fluctuation of the temperature for all measurements was in about 1°C. The required accuracy for pressure measurements in the low-speed regime must be better than 0.1 mbar. For Pyren-based PSP formulations this pressure resolution requires 0.05% of relative intensity resolution. Pyren-based PSP formulations has a temperature coefficient in the range of 0.2 to 0.5%/°C. In this case uncertainties of 1°C of the static temperature distribution on the model surface creates a significant error of about 1 mbar. Therefore one of the most important remaining systematic errors for the PSP measurements comes from temperature influences.

Quantum and read-out noise of the CCD camera referred to maximum dynamic range can be estimated as 0.2%. Taking into account that to calculate relative intensity it is necessary to use six images (three: blue, red and dark

images for "wind-off" conditions and the same three for "wind-on" conditions) the error of relative intensity will be not less than 0.4%. Thus there are two possibilities to improve intensity accuracy measurements: to average appropriate number of all necessary images, which is a time consuming operation, or to use additional spatial filtering that finally reduces the spatial resolution. The pressure distribution on the SCCH gives the possibility to use appropriate spatial filter without significant loss of resolution.

The data processing of the set of the final PSP images must be able to match the related images (blue/red). For this procedure position markers were placed on the model surface. These position markers can be seen as non-emitting areas in all the images. After detecting these markers a alignment procedure was used to match the images. Finally, the 2-dimensional pressure information, that was acquired in the CCD plane, must be transformed onto the 3-dimensional surface-grid of the model. This transformation is called resection. To run this procedure in automatically manner the physical coordinates of the position markers were measured and mathematically transformed to the position markers in the CCD plane.

RESULTS

In a first step of the investigations, the data-processing system used few points for the excitation intensity normalizing procedure (global correction). This test should give information about the influence of the model movement and model deformation for the final PSP results. A typical PSP result for this kind of image-processing is presented in Fig. 8. The SCCH model in this case was equipped with a slat and a flap in the so called high-lift configuration. The flow parameters are $U_\infty=60\text{m/s}$ and $\alpha=16^\circ$. In this figure, the pressure coefficient on the model surface is presented. Obviously the PSP-System is able to visualize pressure differences, because of the expected suction areas on the slat and on the main part of the wing are clearly visible.

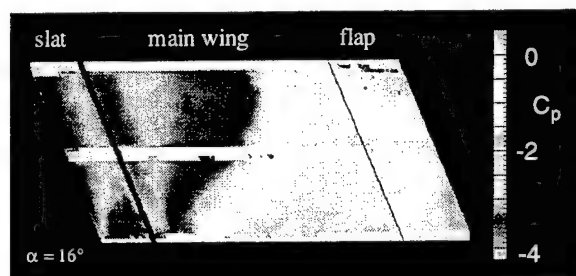


Fig. 8 Pressure coefficient on the model surface for $U_\infty=60\text{m/s}$, $\alpha=16^\circ$ with global intensity correction

The comparison of the PSP- and PSI result for the same test case is given in Fig. 9. This quantitative comparison indicates that with the global excitation intensity correction especially the areas of high decompression will not be measured correctly. Therefore, a non-binary

paint can be used in low-speed flows only for visualization, when model movement or model deformation are possible effects.

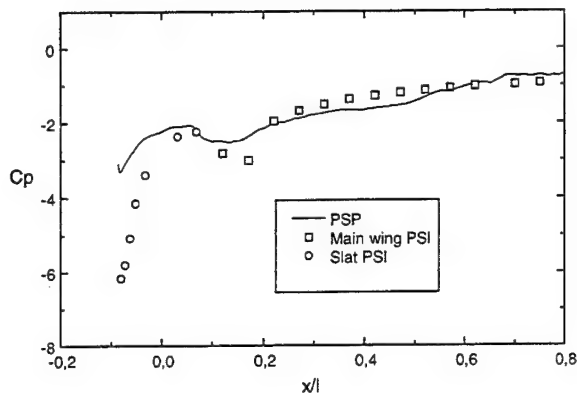


Fig. 9 Comparison of PSP and PSI measured pressure coefficients for $U_{\infty}=60\text{m/s}$, $\alpha=16^\circ$ with global intensity correction

In a second step of the experiments, the total set of the six images were taken using the filter-shifter in front of the camera lens. In **Fig. 10** a typical PSP result using this technique is presented. For a direct comparison of the now obtained results and the previous one, the model and flow parameters were chosen as in **Fig. 8**. In **Fig. 10**, again all the expected decompression areas on the slat and main-wing part are clearly visible.

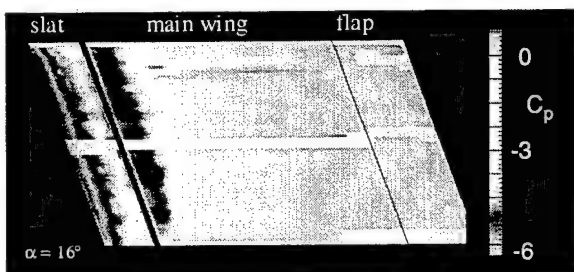


Fig. 10 Pressure coefficient on the model surface for $U_{\infty}=60\text{m/s}$, $\alpha=16^\circ$ using filter-shifter

For comparison of accuracy of the PSP-System using the binary paint and detailed local intensity correction, in **Fig. 11** the PSP- and the PSI results are presented. In this case now, the PSP-System is able to measure the pressure distribution on the slat and on the first 20% of the main wing correctly. The presented comparison in **Fig. 11** shows rather rough PSP results. This fluctuation gives an impression of the possible SNR of the PSP setup used, for single measurement of blue/red images. This means that no image averaging method was used to reach a higher SNR. Due to the fact, that the pairs of blue/red images were acquired sequentially, the non-stability of the light source can create some measurement error. The error in average using the filter-shifter can be given with $\Delta C_p=0.5$.

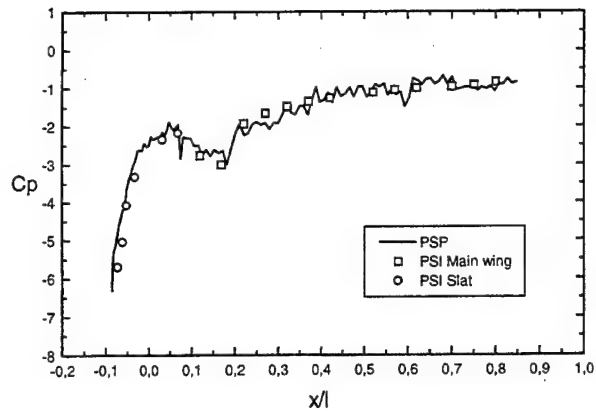


Fig. 11 Comparison of PSP and PSI measured pressure coefficients for $U_{\infty}=60\text{m/s}$, $\alpha=16^\circ$ using filter-shifter

Finally, the possible influence of the non-stability of the light source was excluded, using the multi-viewer in front of the lens to acquire the blue/red images simultaneously on the same CCD array. Because of the above already mentioned smaller viewing angle of this a optical device, only the so called "clean-wing" configuration, that means the main wing without slat and flap, can be seen with an acceptable spatial resolution. In comparison to the images obtained with the filter-shifter the spatial resolution in this case is diminished by a factor of 6: from 1024×1024 pixel down to 400×400 pixel. In **Fig. 12** a PSP result obtained with the multi-viewer for the flow parameters of $U_{\infty}=60\text{m/s}$ and $\alpha=16^\circ$ is presented. Here, the pressure coefficient on the model surface is presented.

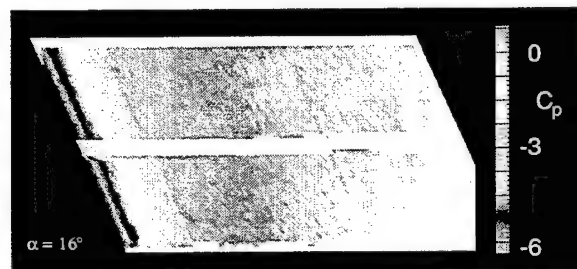


Fig. 12 Pressure coefficient on the model surface for $U_{\infty}=60\text{m/s}$, $\alpha=16^\circ$, using multi-viewer

In **Fig. 13** the comparison of the PSP results obtained by the multi-viewer, the filter-shifter and the results obtained by the PSI-System for $U_{\infty}=60\text{m/s}$ and $\alpha=16^\circ$ for the "clean-wing" configuration is given. Especially near the leading edge of the SCCH model, the multi-viewer shows a better accuracy than the filter-shifter. As a result from this figure it can be stated that the simultaneous acquisition of the blue/red images exclude the error created by non-stabilities of the light source. These measurements also shows a good agreement for the flow speed of $U_{\infty}=40\text{m/s}$. The error in average in the case where the multi-viewer was used can be given with $\Delta C_p=0.1$.

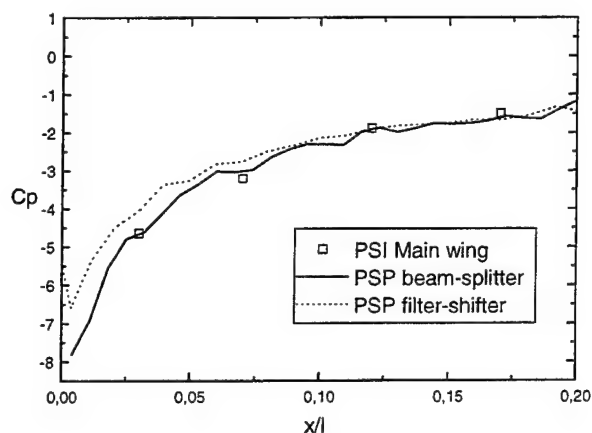


Fig. 13 Comparison of PSP and PSI measured pressure coefficients for $U_{\infty}=60\text{m/s}$, $\alpha=16^{\circ}$ using multi-viewer

CONCLUSIONS

Due to model movement between the "wind-off" and "wind-on" conditions the necessity to use a binary-paint formulation, which allow to measure a pressure image and an excitation-reference image simultaneously, was shown. The possible different kinds of data acquisition systems were presented. To achieve the maximum accuracy of the PSP results, the pressure and reference images must be acquired simultaneously. With such an experimental set-up, pressure resolution of $\Delta C_p=0.1$ was reached. Obtained results shows that the designed PSP-System can be used for pressure measurements at flow velocities down to 40m/sec. For low-speed measurements the run conditions must be carefully controlled (temperature/dust) and the signal-to-noise ratio must be optimized. Therefore spatial-filtering procedures or image-averaging procedures must be applied for PSP measurements in low-speed flows.

REFERENCES

- [1] Vollan, A. & Alati, L. (1991). A New Optical Pressure Measurement System, 14th ICIASF Congress, Rockville, MD.
- [2] Engler, R.H. & Klein, Chr. (1997). First Results Using the New DLR PSP System –Intensity and Lifetime Measurements, Conference "Wind Tunnels and Wind Tunnel Test Techniques", Cambridge UK, ISBN 185768 048 0.
- [3] Engler, R.H., Hartmann, K., Troyanovski, I. & Vollan, A. (1992). Description and assessment of a new optical pressure measurement system (OPMS) demonstrated in the high speed wind tunnel of DLR in Göttingen, DLR-FB 92-24.
- [4] Morris, M.J., Donovan, J.K. Kegelmann, J.T., Schwab, S.D., Levy, R.L. & Crites, R.C. (1993). Aerodynamic Applications of Pressure Sensitive Paint, AIAA Journal, Vol. 31, No.3, 419-425.
- [5] McLachlan, B.G., Kavandi, J.L., Callis, J.B., Gouterman, M., Green, E. & Khalil, G. (1993). Surface Pressure Field Mapping Using Luminescent Coatings, Experiments in Fluids 14, 33-41.
- [6] INTECO Report (1994). OPMS low speed test at Mercedes-Benz, Sindelfingen.
- [7] Torgenson, S.D., Tianshu, L., Sullivan, J.P. (1996). Use of Pressure Sensitive Paints in Low Speed Flows, 19th AIAA Advanced Measurement and Ground Testing Technology Conference, 6/1996, New Orleans, LA,
- [8] Brown, O.C., Mehta, R.D. Cantwell, B.J. Low-Speed Flow Studies Using Pressure Sensitive Paint Technique.
- [9] Kautsky, H. & Hirsch, A. (1935). Nachweis geringster Sauerstoffmengen durch Phosphoreszenztilgung, Z. f. anorg. Und allg. Chemie, Band 222, 126-134.
- [10] Le Sant, Y., Delegise, B., Mebarki, Y. & Merienne, M-C. (1997). An Automatic Image Alignment Method Applied to Pressure Sensitive Paint Measurements, 17th ICIASF Congress, Monterey, CA., USA.
- [11] Fonov, S.D., Radchenko, V.N. & Mosharov, V.E. (1997). Luminescent Pressure Sensors in Aerodynamic Experiments, TsAGI's books, No. 8005.
- [12] Holmes, J.W. (1997). Optical Pressure Measurement (PSP), Presentation on Modern Optical Flow Measurement Advanced School, Udine, Italy, October 1997.
- [13] Engler R.H. (1995). Further Developments of Pressure Sensitive Paint for Non Flat Models in Steady Transonic Flow and Unsteady Conditions, 16th ICIASF Congress, Dayton, Ohio, USA.

APPLICATION OF THE DIRECT PSP-LIFETIME METHOD ON PYREN-BASED PAINT AS A COMPLETION OF THE EXISTING DLR PSP SYSTEM

O. Trinks, R. H. Engler, Chr. Klein, S. Fonov
DLR Göttingen, Germany

ABSTRACT

Pressure Sensitive Paint (PSP) provides a pressure map on the whole surface of a wind tunnel model without transducers and tubing. In principle there are two different ways to gather experimental data – by using the fluorescent decay time of excited luminophore molecules (lifetime method) or by detecting its integrated fluorescent emission (intensity method). During the last five years PSP measurements utilizing the intensity of the luminescence are performed at DLR with pyren-based paints. This paint is characterized by its low temperature sensitivity and high quantum efficiency - due to these qualities the lifetime technique is also developed for this paint type. PSP measurements utilizing the lifetime of the luminescence are independent to particles in the flow (dust, oil, condensed water, etc.), changing in density, light source instabilities and light reflection and less sensitive to the model movements because there is no need for a reference image. The short luminescence decay time of pyren in the order of 50 ns gives the possibility to investigate fast flow processes (pressure measurements on helicopter blades, propellers, turbines, etc.). Using the same paint for the intensity as well as the lifetime technique a simultaneously application will complete the existing PSP system.

INTRODUCTION

Pressure sensitive paints (PSP) have evolved quickly in few years and were applicated in several wind-tunnel facilities for aircraft models tests [1]. All PSP formulations are basing on the phenomenon of deactivation photoexcited molecules of mainly organic luminophores by oxygen molecules. To gather experimental data from pressure sensitive paint it is possible to use either the intensity or the lifetime method [2]. If the paint is illuminated with a pulse of light the integrated intensity of the luminescence gives a measure of the partial pressure of oxygen and hence the pressure of air. On the other hand the luminescence will decay exponentially with a characteristic lifetime which is also a function of oxygen partial pressure. PSP applications utilizing the lifetime of the luminescence offer several advantages in comparison to intensity based methods because this technique is no more sensitive to light source instabilities, particles in the flow like dust, oil and condensed water and changing in flow density [2]. Furthermore self illumination has less influence to measurements and no reference image (wind-off) is

required. As such, the lifetime technique makes PSP applications feasible on rotating or moving surfaces where it would be impossible or difficult to acquire a reference image. In [Figure 1](#) typical luminescence decay curves at different pressure values are shown for paints on the basis of ruthenium and pyren, respectively. Both luminophores are differently sensitive to temperature and pressure at different excitation wave lengths. Using pyren as pressure sensitive molecule with a typical lifetime in the order of only 50 ns makes the lifetime technique well suited to investigate fast flow phenomena such as present in turbines, on the surface of helicopter blades or propellers.

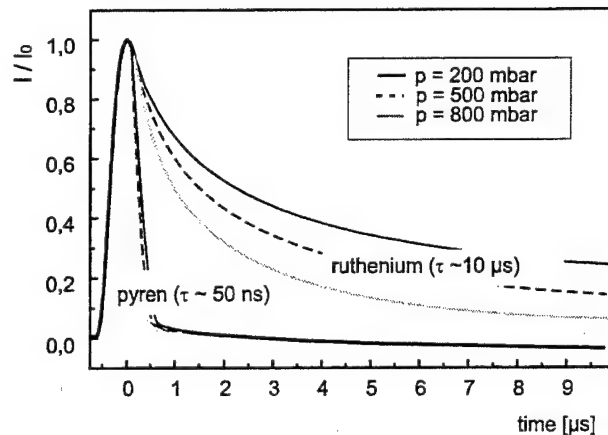


Figure 1: Luminescence decay curves for ruthenium and pyren based paint for different pressure values

In addition to model deformation and light reflection the temperature influence is an essential factor affecting an accuracy of pressure measurements by all PSP methods. The temperature sensitivity and temperature hysteresis of the used paint can lead to significant errors and corrections must be applied. Paint which contains pyren as luminophore is characterized by its low temperature sensitivity making it well suited for PSP applications. At DLR pyren-based paints are therefore used since several years for PSP measurements basing on the luminescent intensity method in transonic, subsonic and even in low-speed wind tunnel facilities [3],[4],[5]. The paint (B1-paint; OPTROD Ltd.) has a temperature sensitivity of 0,2%/°C and can be excited with UV light from a Xe-flash lamp or nitrogen laser ($\lambda = 337$ nm), its luminescence emission for different temperature and pressure values is spectrally resolved shown in [Figure 2](#).

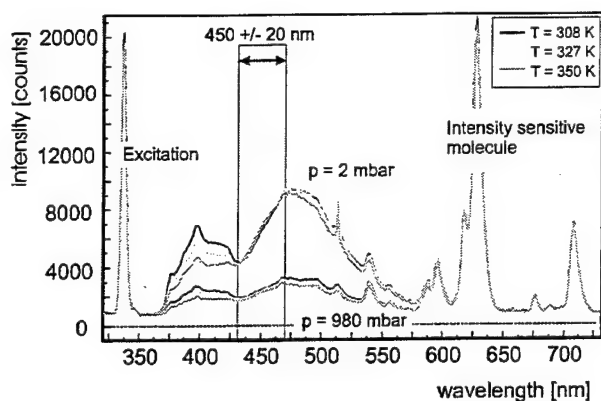


Figure 2: Emission spectra and temperature sensitivity of pyren-based paint (B1, OPTROD Ltd.) excited with a nitrogen laser ($\lambda = 337$ nm) for different pressure values

EXPERIMENTAL SETUP

The setup for pressure measurements using the lifetime method is schematically shown in Figure 3. The paint is illuminated with a pulse of a 250 μ W nitrogen laser ($\lambda_{\text{excitation}} = 337$ nm) using an optical fiber and the emitted luminescence was taken at (450 ± 20) nm by an optical bandpass to minimize the temperature effect as emphasized in Figure 2. The spectral response of the photomultiplier is also optimized at this wavelength range. The luminescence lifetime of excited pyren molecules is in the order of 50 ns making for data acquisition a 1 GHz transient recorder and a fast responding photomultiplier with an anode pulse rise time less than 0.7 ns and an electron-transit time in the order of 0.2 ns necessary. Since this setup allows point wise measurements a scanning laser system is used to acquire a two-dimensional pressure distribution on a PSP-coated surface.

Lifetime Measurements

Investigations made in a calibration chamber shows that the oxygen sensitive luminophores of the pyren-based paint can be used for pressure measurements by using the lifetime technique as well as the intensity method. The intensity of the luminescence emission I can be approximated by an exponential decay (equation [1])

$$I(t) = I_0 \cdot \exp(-t / \tau) \quad (1)$$

where I_0 is the intensity at time $t = 0$ and τ the lifetime of the luminescence emission. Assumed that the decay curve of oxygen sensitive luminophore is single exponential the luminophore lifetime dependent only on pressure and is independent on excitation light intensity as shown in the Stern-Volmer equation [2].

$$\frac{\tau_{\text{ref}}}{\tau_p} = A + B \cdot \frac{P}{P_{\text{ref}}} = \frac{I_{\text{ref}}}{I_p} \quad (2)$$

This relation equates both luminescent lifetime ratio ($\tau_{\text{ref}} / \tau_p$) and the luminescent intensity ratio (I_{ref} / I_p) where τ is the lifetime, the subscript "ref" indicates the reference condition where the pressure value is known, and A and B are properties of the specific paint system. The Stern-Volmer plot for paint containing pyren as pressure sensitive luminophore obtained via the lifetime method is shown in Figure 4.

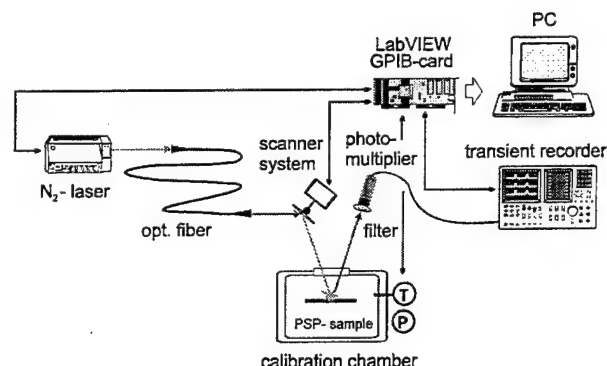


Figure 3: Test setup for point wise PSP measurements using the luminescence lifetime method

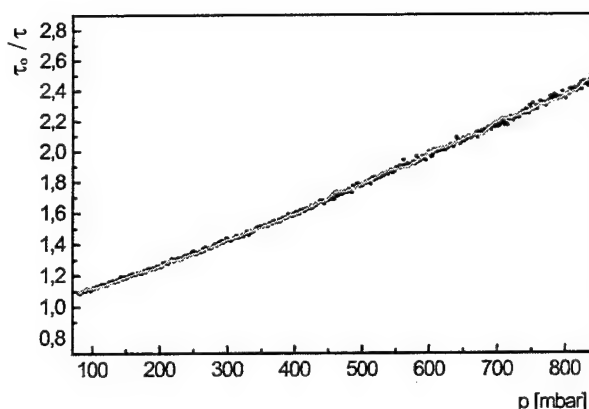


Figure 4: Stern-Volmer plot for pyren-based paint obtained with the lifetime technique

In consideration the lifetime technique is developed for the same paint which is still used for intensity measurements both PSP methods can be applicable simultaneously to complete each other. To compute lifetime values for each decay curve in average 50 measurement points were used to obtain the best exponential fit. Typical luminescence decay curves for three different pressure values are shown in Figure 5 and Figure 6 with linear and logarithm divided y-axes, respectively. The time window is emphasized where the decay curves are exponential and the lifetime values are obtained. Since with increasing pressure values the intensity of the fluorescence emission becomes more and more lower for different pressure ranges a weighted time gate setting is under development to get a better accuracy of the calculated pressure values.

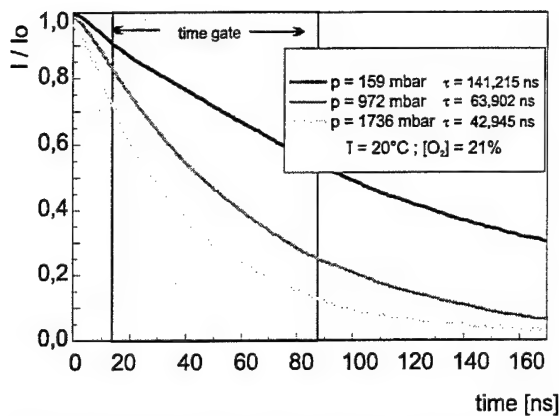


Figure 5: Linear scaled luminescence decay curves of pyren-based paint for three different pressure values

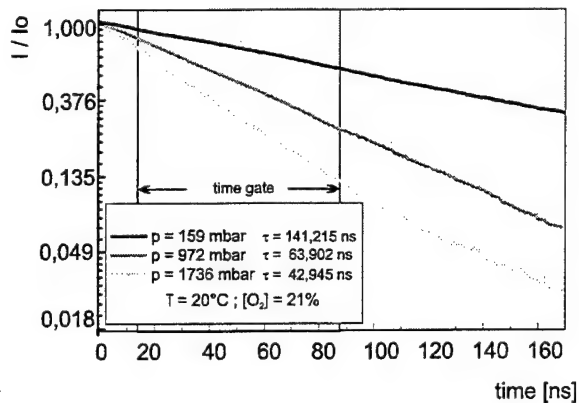


Figure 6: Exponential scaled luminescence decay curves of pyren-based paint for three different pressure values to optimize the time gate setting

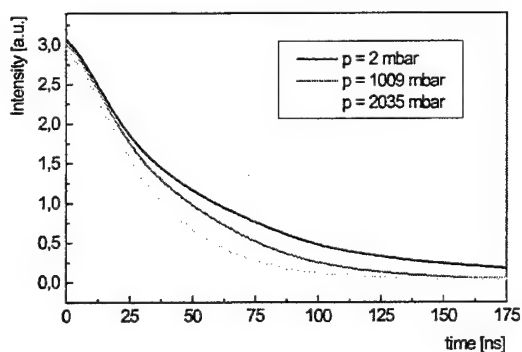


Figure 7: Luminescence decay curves for different pressure values in the wavelength range 450±20 nm

spectral range around 500 nm (see Figure 2) the luminescence decay time is between 430 – 470 nm more pressure sensitive and accurate.

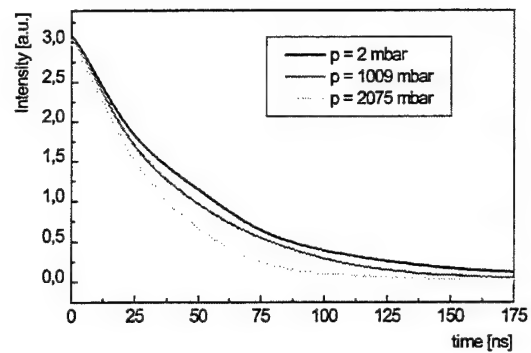


Figure 8: Luminescence decay curves for different pressure values in the wavelength range 500±20 nm

To estimate the measurement accuracy of the lifetime method several investigations in the calibration chamber have been performed. In this case the accuracy is not degraded by model movements due to the real wind tunnel measurements, thermal errors have not been considered and the observed decay curves are not averaged. In [Figure 9](#) the pressure values for different pressure levels obtained via the lifetime technique (y-axis) from the pressure values in the calibration chamber (x-axis) are shown. In general the pressure values are calculated from the decay curves by using a fixed time gate as emphasized in [Figure 5/6](#) - this gives a standard deviation of about 17 mbar. With increasing pressure values the obtained decay curves become more noisy because the intensity of the fluorescence emission drops down. This results in an increasing of the uncertainty of estimated lifetime and pressure values, respectively. To obtain better accuracy for data evaluation different routines (esp. multi exponential curve fitting) are under development. Furthermore the signal-to-noise ratio for the measurement system must be optimized.

To optimize the pressure sensitivity of the PSP lifetime technique luminescence decay curves for different spectral ranges and pressure values between 1 and 2000 mbar are obtained. For 450±20 nm and 500±20 nm the results are shown in [Figure 7](#) and [Figure 8](#), respectively. Although the emission of the used paint has a maximum in the

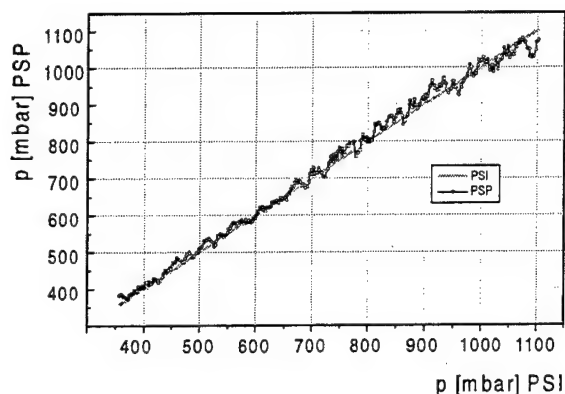


Figure 9: Lifetime results in comparison with PSI measurements

Since the developed PSP technique obtains point wise measurement data, a scanning laser system is used to acquire a pressure map. First investigations with the scanning lifetime system were made on a nitrogen jet (nozzle diameter 0.3 mm) which was directed on an oblique PSP coated surface. By using a well focused laser point for paint excitation a spatial resolution better than 0.15 mm² can easily be obtained. The visualization of a nitrogen jet (nozzle diameter: 0.3 mm) is shown in [Figure 10](#).

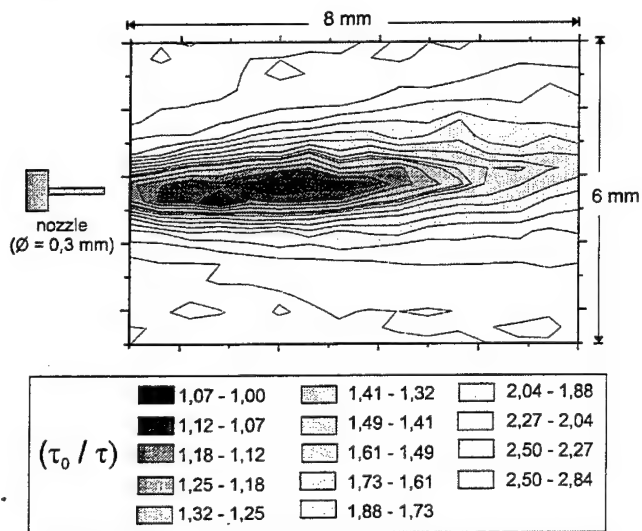


Figure 10: Visualization of a nitrogen jet directed on a PSP sample using the scanning lifetime method

CONCLUSION

Investigations in a calibration chamber and on a nitrogen jet stream show that the developed lifetime technique can be applied to the same pyren-based paint which is used for PSP intensity measurements at DLR. This paint is characterized by its low temperature sensitivity (0.2 %/°C)

but high quantum efficiency. Due to the fast luminescence decay of pyren (~50 ns) the PSP lifetime technique can be applied to objects whose positions in the field of view cannot be reproduced under wind-off conditions because there is no need for a second reference image, whereas intensity PSP measurements require both wind-on and wind-off measurements. Other advantages include the non-sensitivity to displacement, dust, paint degradation and ambient light (esp. reflection). Since the lifetime technique can be applied simultaneously with the existing intensity PSP system, this technique leads to a good completion of the existing Intensity-PSP-system.

REFERENCES

- [1] S. D. Fonov, V. N. Radchenko, V. E. Mosharov: *Luminescent Pressure Sensors in Aerodynamic Experiments*; TsAGI's books, No. 8005, 1997.
- [2] J. W. Holmes: *Optical Pressure Measurement (PSP)*, Presentation on Modern Optical Flow Measurement Advanced School, Udine, Italy, October 1997.
- [3] R. H. Engler, Chr. Klein: *First Results Using the New DLR PSP system – intensity and lifetime measurements*; Conference "Wind Tunnels and Wind Tunnel Test Techniques", Cambridge UK 1997, ISBN 185768 048 0.
- [4] Chr. Klein: *Einsatz einer druckempfindlichen Beschichtung (PSP) zur Bestimmung des momentanen Druckfeldes von Modellen im Windkanal*, Dissertation University Göttingen, Germany, DLR-Forschungsbericht 97-55, ISSN 1434-8454, 1997.
- [5] Chr. Klein, R. H. Engler, S. D. Fonov, O. Trinks: *Pressure Sensitive Paint Application In Low-Speed Flows*; Presentation on 13th Australasian Fluid Mechanics Conference, Monash University, Melbourne, Australia, 13-18 December 1998.

Pressure Sensitive Paint for Oscillating Pressure Fields Measurements.

S.D. Fonov, R.H. Engler, Chr. Klein
Deutsches Zentrum für Luft- und Raumfahrt (DLR) e.V.
Institut für Strömungsmechanik, Göttingen, Germany

S.V. Mihailov, V.E. Mosharov, V.P. Kulesh, V.N. Radchenko
TsAGI, Zhukowsky, Russia

E. Schairer,
NASA Ames Research Center, Moffett Field, California, USA

Summary

The paper describes the main problems encountered during investigations of the oscillating pressure fields by the Fast Binary Pressure Sensitive Paint (FBPSP). This formulation has response time in the millisecond range and provides compensation of the model displacements and excitation light instability. Measurement methodology, theoretical and experimental estimations of the FBPSP dynamic characteristics are presented. It is shown that FBPSP formulation can be used for oscillation frequencies up to 20-40Hz but requires dynamic compensation of the resulting pressure fields. The experimental results obtained on the pitching wing model at Mach numbers 0.3 and oscillation frequencies 0 and 20Hz are presented and discussed.

Introduction

The Pressure Sensitive Paint (PSP) method provides a good opportunity for investigation of unsteady flows. Dynamic parameters of PSP (response time) and measurement system (time, amplitude and spatial resolutions) are determined to determine the ultimate accuracy and should be involved into data processing scheme.

Background

The PSP layer is a two-dimensional array of oxygen sensors, each of them consisting of a polymer binder with the luminophore molecules dissolved in it. The oxygen molecules from the airflow can diffuse into polymer layer. Radiationless energy transfer from the excited luminophore molecules to the oxygen-quenching phenomenon governs the luminescent output. Quenching of luminescence is controlled by the diffusion of the oxygen in the polymer binder of PSP. As a result such PSP characteristics as pressure and temperature sensitivity, time response of PSP to the change of external pressure and spatial resolution are diffusion-controlled.

An analysis of these diffusion-controlled characteristics was presented in earlier papers [1, 2 and 4] where it was shown that PSP response in the time domain is determined by oxygen diffusion

characteristic time τ (h - paint thickness, D - oxygen diffusion coefficient)

$$\tau = \frac{4h^2}{\pi^2 D} \quad (1)$$

and by optical density of the PSP layer d . Theoretical estimations of typical response functions are presented on Fig. 1

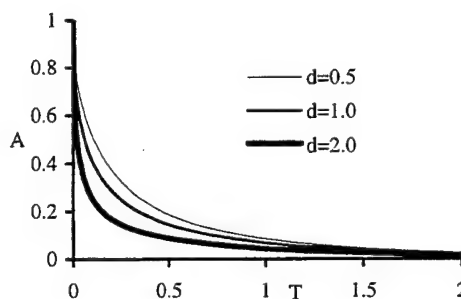


Fig. 1. Theoretical estimations of the PSP response function.
(d - optical density, $T = t/\tau$ - normalized time)

Amplitude-Frequency Characteristics (AFC) and the Phase-Frequency Characteristics (PFC) are presented on Fig. 2) and Fig. 3 (in these figures

$$W = 2\omega h^2/D = \omega\tau\pi^2/2)$$

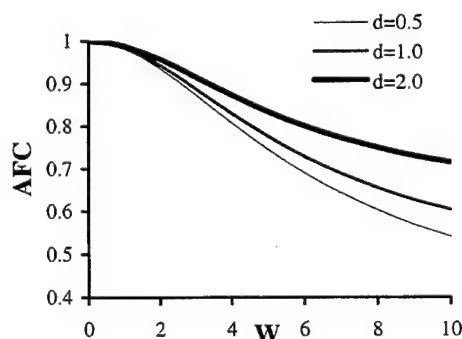


Fig. 2. Amplitude-Frequency Characteristic of PSP.
(d - optical density, W - normalized frequency)

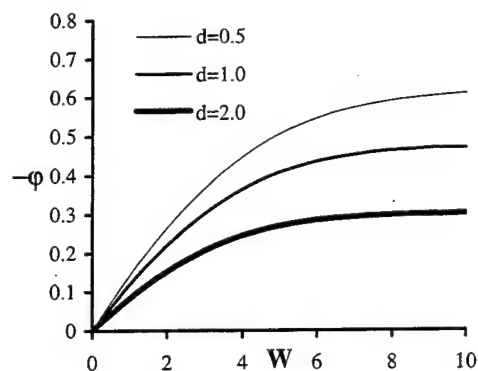


Fig. 3. Phase-Frequency Characteristic of PSP
(d -optical density, W -normalized frequency)

Fast Binary Paint Formulation

The standard approach to compensate the excitation light fluctuation and the model displacements is to use second reference luminophore, which is insensitive to the pressure and having luminescent output in the another spectrum region relative to active luminophore [4]. Direct measurements of the PSP response time show that response time in region 2-10 ms can be achieved for the paint layer having thickness about 2-6 μm . Such small thickness creates difficulties in implantation of the reference luminophore in the active layer. Usually the reference luminophore is a crystallophosphore grains having dimensions about 1-5 μm that creates significant ruthless of the active layer in the case of the direct implantation. The possible solution is to use additional polymer layer binding the reference luminophore crystals as a substrate of the active layer. Optical density of the active layer should be in the region 0.3-0.5 to provide appropriate excitation level for reference component. Plots presented on

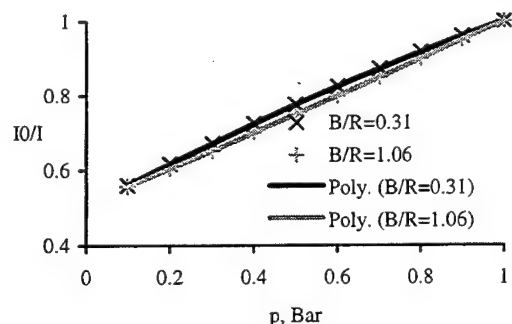


Fig. 4. Calibration characteristics of Binary Fast PSP

Fig. 4 and 5 shows that PSP calibration parameters in this case are the functions of the relative luminescent output of reference (R) and active (B) components. It means that calibration parameters will be a function of the spatial distribution of the paint thickness. Temperature sensitivities of the reference and active components have the same sign

that is resulted in some temperature self compensation in the normalized signal.

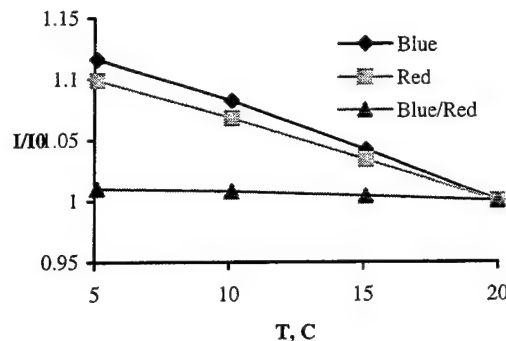


Fig. 5. Temperature sensitivity of Binary Fast PSP

Laboratory setup for investigation of PSP response to the step pressure change was described in [4] (Fig.6). The topside of the tube cell was closed by a cellulose membrane and an air was evacuated from the cell. A needle destroyed the membrane and movement of a shock wave inside the tube was initiated. The pressure relaxation time in the cell was estimated in a range of 50-200 μs , while some sonic waves could also appear in this cell with the main frequency about of 2000Hz that was determined by the length of the tube. A continuous luminescent UV lamp performed the excitation of the PSP sample. A photomultiplier tube acquired the luminescence intensity and its output signal was digitized.

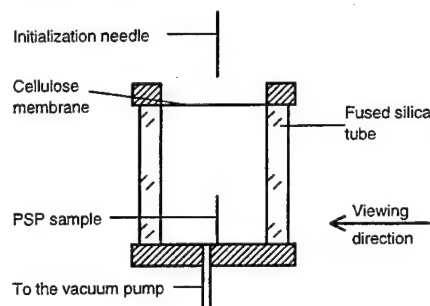


Fig. 6. Schematic of a cell for investigation of PSP response to the step pressure change

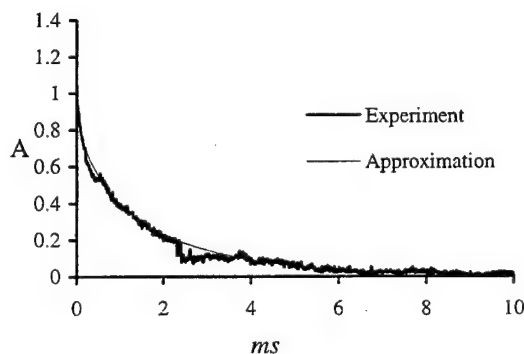


Fig. 7. Time response of PSP F2 to the step pressure change, $\tau=2.6\text{ms}$

Fig.7 presents the time response of the PSP to the step pressure change. This response corresponds to the theoretical predictions with characteristic time $\tau=2.6\text{ms}$. The response time of 99% relaxation of luminescence intensity is equal to 6.5ms. AFC of this PSP is equal to 0.99 at frequency 7Hz and 0.7 at 70Hz. thus this PSP can be used for unsteady pressure measurements at the frequency up to few dozens Hz. Some samples of very thin PSP type F2 was prepared and tested in this cell. Their characteristic times were of the order of $100\div300\mu\text{s}$.

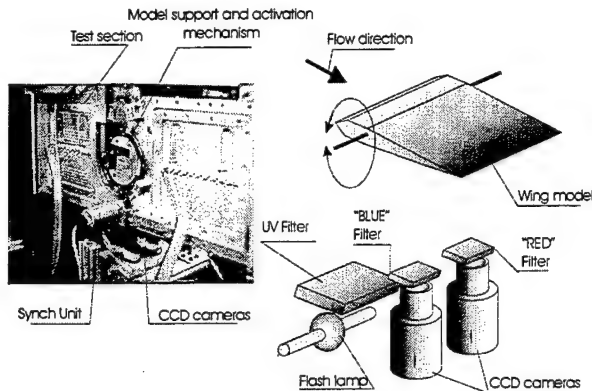


Fig. 8. Schematics of the test setup for PSP measurements on the oscillating model

Experimental Setup

A test setup assembled in the NASA Ames wind tunnel to fulfill PSP measurements on an oscillating model is presented in Fig.8. The wing model has NACA0012 profile with 6-inch chord and 5% relative thickness. The pitching harmonic oscillations were created by an actuator mechanism, which provides oscillation frequency from 0 to 20Hz with pitching amplitude up to 10° . The central section of the model was covered by fast binary PSP. A pulsed light source was used for PSP excitation at certain phases of the model position. Flash duration of 1msec was enough for measurements at the models oscillating frequencies up to $20\div30\text{Hz}$. Two digital CCD cameras with appropriate filters acquired the pressure sensitive and reference luminescence intensities.

Pressure field investigations on the pitching model

Measurements were conducted at oscillation frequencies 0, 5, 10 and 20Hz and a flow Mach numbers 0.3 and 0.45. Image information was acquired for angles of attack from -10° to $+10^\circ$ with 2° step. During each image acquisition cycle flash lamp was ignited at a predetermined angle of attack and two images were acquired using separate CCD cameras with appropriate glass filters. Reference images were acquired at the same angle of attack

without flow. After image alignment procedure C_p fields were calculated and these fields were transferred to the grid model of the wing section. Special markers were applied to the model surface for the image alignment and resection procedures.

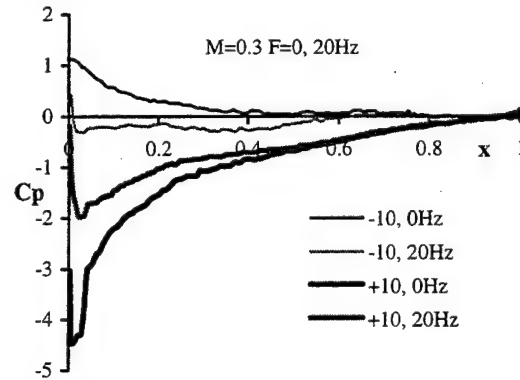


Fig. 9 C_p distributions (x-normalized coordinates along the wing chord)

Plots in Fig.9 show C_p distributions along a wing chord for $+10^\circ$ -10° angles of attack, $M=0.3$ for oscillation frequency $F=20\text{Hz}$ and under static environment. Estimated mean response time 8ms corresponds to a cutoff frequency of 20Hz, which means that for the model oscillation frequency of 20Hz this paint realization can resolve only several harmonics and actual AFC&PFC characteristics of the paint should be taken into consideration. This model was not equipped with a conventional pressure measurement system but pressure distributions obtained for zero frequency are in a good agreement with the pressure distributions for this profile type. As mentioned above PSP response time is a function of the paint thickness. Paint thickness distribution can be estimated by a luminescent output distribution normalized on an excitation light distribution. This distribution for centerline of the painted strip is presented on Fig. 10.

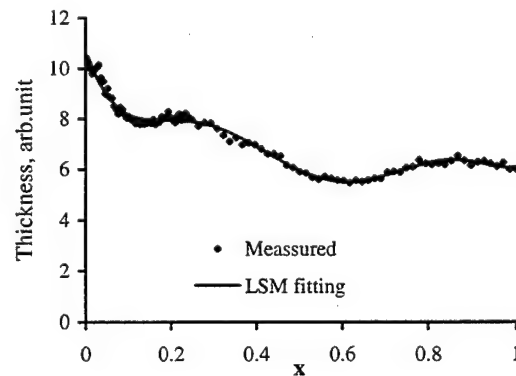


Fig. 10. Estimation of the thickness of PSP active layer along the wing chord

Resulting AFC and PFC distributions for 20Hz frequency and higher harmonics are shown on Fig.

11 and 12. These estimations can be used for dynamic compensation of the measured pressure distribution as its shown on Fig. 13 and 14 for the first harmonic of the C_p distribution obtained for $M=0.3$ and oscillation frequency 20Hz.

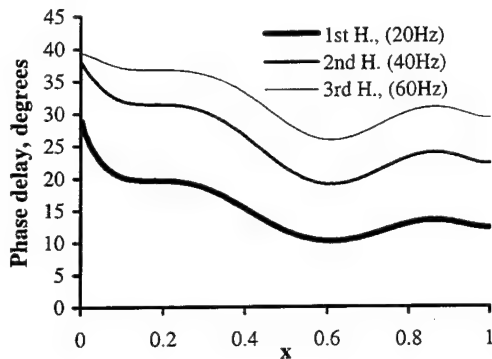


Fig. 11. Phase delay distributions for the first three harmonics

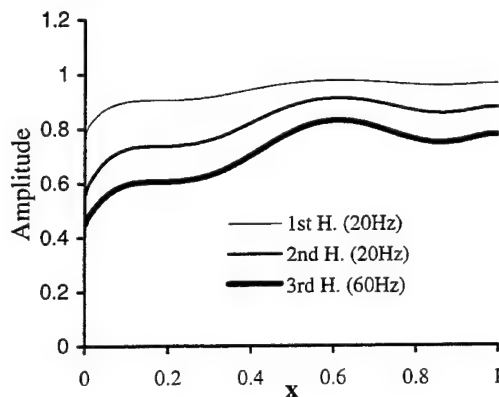


Fig. 12. Amplitude fade distributions for the first three harmonics

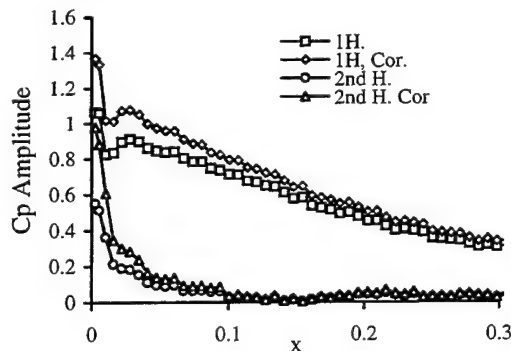


Fig. 13. C_p amplitude corrections for 1st and 2nd harmonics

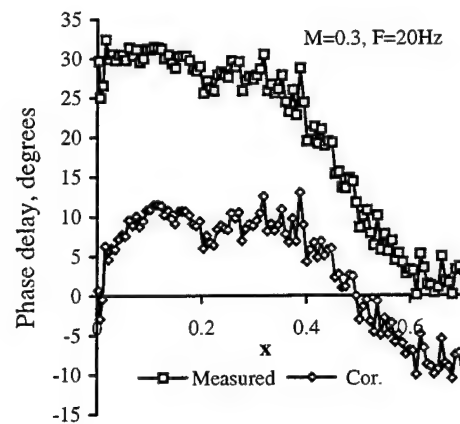


Fig. 14. Phase Delay Correction for the 1st harmonic

Conclusion

Theoretical estimations and experimental research show that binary fast PSP can be used for pressure field investigations on the oscillating models at frequencies up to 20-40Hz. Taking into consideration of the dynamic parameters of the paint can increase the measurement accuracy. Binary composition compensates the influence of the model movement and excitation light instability.

Acknowledgement

The tests presented here were sponsored by the US Army Research Office, Contract DAAH04-96-1-0469, "Development and Experimental Investigation of the PSP Technique for Pressure Field Measurements on Helicopter Blades." Significant contributions to the realization of this program are attributed to Dr. W.J. McCroskey (AFD NASA Ames Research Center).

References

- [1] V. Mosharov, A. Orlov, V. Radchenko, M. Kuzmin, N. Sadovskii, "Luminescent Pressure Sensors for Aerospace Research: Diffusion-Controlled Characteristics." 2nd European Conference on Optical Chemical Sensors and Biosensors, Firenze, Italy, April 19-21, 1994.
- [2] B.F. Carroll, J.D. Abbitt, E.W. Lukas, M.J. Morris, "Pressure Sensitive Paint Response to a Step Pressure Change." AIAA Paper 95-0483, Jan. 1995.
- [3] OPTROD Ltd, Dugin str. Zhukovsky, Moscow reg., 140160 Russia. Fax: 07 095 939 0290, e-mail address: optrod@photo.chem.msu.su Attn. Mosharov
- [4] S. Fonov, R.H. Engler, Chr. Klein, V. Mosharov, V. Radchenko, Application of the PSP for Investigation of the Oscillating Pressure Fields, Proc. of AIAA Congress, Albuquerque, Ca, 1998

SESSION : 6

FLIGHT INSTRUMENTATION

LDA System for In-Flight Local Velocity Measurements on Airplane Wings

S. Becker, F. Durst and H. Lienhart

LSTM Erlangen, Institute of Fluid Mechanics, University of Erlangen-Nuremberg,

Cauerstrasse 4, D-91058 Erlangen, Germany

ABSTRACT

The development of laminar wing technology requires wind tunnel studies with numerical flow simulations and in-flight measurements. A strategy for in-flight flow measurements is outlined. It is shown that laser Doppler anemometry (LDA) is well suited for providing the desired local velocity information, but must be specifically adapted for the various spatial, geometrical, and power constraints imposed by the test aircraft. This program yielded two optical units suitable for in-flight velocity measurements on airplane wings. Laboratory and free flight measurements studying boundary layer transition on an airplane wing downstream of an excitation source were successfully carried out and a summary of results is presented. Finally, suggestions for further advancements of LDA systems are proposed.

1. Introduction

Research and development work in aircraft aerodynamics to date has been heavily based upon wind tunnel investigations, even though it has been known that the test facilities employed did not provide the required flow conditions to yield directly applicable design information. For instance, the size of wind tunnel test sections employed were usually too small and the velocities too low to yield Reynolds numbers comparable to those for free flight. Thus, reliable methods to predict boundary layer transition are not yet available for realistic flight environments, and the identification and quantification of the relevant parameters, like pressure gradient, wing geometry, surface curvature, sweep angle, Mach number, heat and mass transfer at the surface, etc. are far from being complete. For the studies of laminar to turbulent transition, individual wind tunnels inherently introduce their own specific spectrum of flow disturbances and hence, their laminar to turbulent transition data can be effected by 'wind tunnel noise'. Therefore, results of wind

tunnel studies yielding design parameters for laminar wings have to be verified by flight experiments. For this task there is a pronounced need for advanced measuring techniques that are nonintrusive and reliable in the harsh environment of flight. Several techniques have been developed in past years, e.g., hot film arrays, piezo foils, and infra red cameras for transition detection. All of these techniques are only capable of acquiring information directly on the wall surface, whereas LDA may give an insight into the complete boundary layer and the surrounding flow velocity field. However, typical LDA instrumentation does not perform adequately in the environment of in-flight testing.

2. Layout of inflight LDA- systems

The test aeroplane for the present studies consisted of a GROB 109B, a two-seat powered sail plane equipped with a 'wing glove' on its starboard wing. The size and design of the plane imposed very stringent restrictions upon the weight and space available for the optical and electronic components, as well as upon the permissible power consumption of the measuring system.

The first approach employed a LDA probe with an integral design. The probe used an integrated semiconductor laser diode as the light source with a semiconductor photodetector and operated in direct backscatter (Durst, Lienhart and Müllers [1]). Figure 1 is a cross-sectional view of the design of this LDA. The system incorporated a laser diode and collimator assembly which was temperature controlled by Peltier elements, thereby stabilizing both the wavelength of the laser and the alignment of the collimator. An avalanche photo diode was mounted between the two parallel laser beams together with its signal amplifiers. The beam paths are diverted by a 45°- mirror and the entire LDA assembly was mounted in such a way that it could be rotated by a DC motor in the wing pod. This construction design

permitted traversing of the measuring control volume perpendicular to the wing surface and allowed clamping the system on top of the wing glove at an arbitrary chordwise position.

This LDA system design proved to be very reliable and stable, and maintained optical and mechanical alignment at free flight conditions. The experience gained during the in-flight measurements with this LDA design can be summarized as follows:

- local velocity measurements in the flow surrounding a flying aircraft were feasible, however, the data rate in tests performed in the free atmosphere without any hazes or clouds was quite low and not sufficient for some desired studies, e.g. for spectral analytical studies of Tollmien-Schlichting instabilities, and
- it was concluded that this difficulty resulted from the low concentration of aerosols in the atmosphere that are needed as scattering particles.

In order to examine this hypothesis the concentration and diameter distribution of natural aerosols in the atmosphere were investigated using a cascade impactor. In Figure 2 a particle diameter distribution measured during flight tests is presented. The results showed a very steep increase of concentration for particles of very small size. Therefore the conclusion is clear that, in the absence of artificial seeding, the data rate could only be improved if one succeeded in detecting signals from particles of diameters less than about $d_p = 0.5 - 1 \mu\text{m}$, which was about the limit for the semiconductor LDA probe.

The above findings led to the development of an improved LDA system. The emphasis of this new design was to maximize the measured signal generated by very small particles. To this end, all design parameters influencing the scattered light intensity were analysed using the theory of light scattering by small particles (Naqwi and Durst [2]). The new system features a laser diode-pumped frequency-doubled Nd-YAG laser, which provided higher light power at a shorter wave length, when compared to the semiconductor laser used in the first design, while still having low electrical power consumption. The power of scattered light for very small particles is governed by Rayleigh's law and varies with the fourth power of particle diameter divided by wave length (d_p/λ). Replacing the semiconductor laser ($\lambda = 830 \text{ nm}$) by a frequency-doubled Nd-YAG-laser ($\lambda = 532 \text{ nm}$) resulted in an increase of about a factor of six in scattered light power. The output power available with a Nd-YAG laser was about 400 mW, but since it was not longer possible to integrate the laser

into the probe design, losses of about 40 % due to the fibre optic cable needed to be considered. This was more than compensated for by a reduction of the beam waist diameter in the crossing volume. The final gain of light power in the measuring control volume was a factor of about 12. A near forward scatter arrangement was adopted for the receiving optics, which provided an additional one order of magnitude increase in signal power for the smallest particle size and about two order for the larger ones.

This resulted in an unconventional probe design. It employed the narrow gap between wing and wing glove for the optical components and the beam path was diverted twice by mirrors for both the transmitting and the receiving path. As sketched in Figure 3 all optics apart from the upper mirrors were placed underneath the wing glove surface and only these mirrors are protruding. Therefore, the distortion of the flow induced by the measuring system was minimal. The optics were mounted on a traversing mechanism that allowed automated measurements of boundary layer profiles. The compact design of the probe, the integral machining of its mechanical structure from titanium, and the way it is clamped to the wing glove ensured mechanical and optical stability and, thus, prevented misalignment during flight experiments due to vibration, bending of the wing, and stresses due to changes in temperature. Figure 4 shows the LDA system in actual flight tests.

3. In-flight arrangements

The laser, traversing controller, photomultiplier, power supplies, and signal acquisition and processing unit completed the measuring system. The LDA probe was connected to the laser and the photodetector by monomode and multimode glass fibre cables, respectively. Figure 5 gives an overview of the instrumentation distributed in different locations of the airplane. It indicates that the wing glove mounted on the starboard wing was equipped with the LDA probe and traversing system, as well as the transition excitation source. The loud speaker drivers for the excitation source and the controller for traversing were located in the underwing station. The laser, photodetector and signal processor (Burst Spectrum Analyzer – BSA) were mounted on the instrumentation platform behind the pilots' seats. The port wing carried the flight data acquisition system of the test aircraft, which was described in detail by Erb, Ewald and Roth [3]. All systems were automatically controlled by

the onboard computer in the cockpit. The computer ran the different programs in multitasking operation, in this way simultaneous data acquisition could be performed. The battery that powered the instrumentation allowed about 20 min of run time per flight.

During in-flight testing the rate of validated velocity data was approximately 200 Hz for clear atmospheric weather conditions and several kHz for hazy weather. The major atmospheric parameter influencing the validated data rate was the humidity of the air. Experiments carried out at flight levels above the inversion layer yielded significantly lower data rates than flights below the inversion. Nevertheless, in all conditions sufficient data could be obtained during flight experiments to provide useful boundary layer information.

4. Results of boundary layer measurements on an airplane wing

Windtunnel flat plate boundary layer transition measurements were performed by Lienhart and Becker [4] before performing in-flight investigations. In order to demonstrate the performance of the new LDA system to detect Tollmien-Schlichting waves an excitation source for small flow disturbances was installed in the test wing section. This source consisted of six small circles of holes on the wing glove along a span-wise line at 27 % of the chord length. These circles are connected to a loudspeaker driver mounted in the underwing station. The excitation frequency was set to 900 Hz that corresponded to the frequency of maximum amplification according to a stability computation. To map the span-wise velocity distribution of the boundary layer, the six circles were successively excited rather than traversing the LDA system.

A measured boundary layer velocity profile without any excitation is presented in Figure 6. It displays mean velocity distribution and turbulence intensity. This measurement was taken in the boundary layer on the wing glove at a chord length position of 42.5 %. The position was chosen to be in the region of laminar flow.

Some results of flight tests with a wave train introduced by the excitation source are additionally shown in Figure 6. Whereas the influence of the wave train in the mean velocities could hardly be identified, the turbulence intensities were significantly increased with introduced excitation and showed the characteristic peaks of a transitional stage. There are profiles of mean velocity and turbulence intensity at different span-wise positions. The

greatest increase of the turbulence intensity could be observed at a distance of 20 mm from the symmetry plane. This corresponded to an angle of lateral growth of the disturbance of about 6°.

During good weather conditions data rates could be achieved that allowed a direct calculation of the power spectral density function from the velocity-time series via Fourier transformation. For lower data rates, amplitude and phase angle of the Tollmien-Schlichting wave at any location in the boundary layer were analysed using harmonic analysis of the time series. Figure 7 shows the amplitude of the Tollmien-Schlichting wave in comparison to the results of the Direct Numerical Simulation (DNS) carry out by Stemmer, et al [5]. It shows good agreement with the numerical results in the location and size of the peak turbulence intensities in the boundary layer. Differences are located close to the wall, probably caused by three-dimensional effects of the wave on the end of the linear stability region.

CONCLUDING REMARKS AND OUTLOOK

The present paper summarizes the development of a new LDA system optimized to be small, light, robust, and capable of detecting signals from very small scattering particles. Typical results of in-flight measurements are presented. The mean stream-wise velocities, rms values of turbulent velocity fluctuations, and energy spectra of the fluctuating components were measured.

There is still room for further development and related work. Whereas the optical system design was optimized for in-flight measurements in the present research efforts, conventional LDA signal processing equipment was employed. Future work should concentrate on developing LDA electronic systems that are small in size, light in weight, and robust, so that they can be reliably operated under flight conditions. It should also aim for a reduction of power consumption of the electronic systems to permit long duration measurements in small airplanes of the kind employed in this research work.

ACKNOWLEDGEMENTS

The authors gratefully acknowledge the financial support they received for their research work through the DFG (German Science Foundation). The authors are also thankful to the Institute of Aerodynamics of the University of Darmstadt for making the test airplane available to accomplish the in-flight measurements, and the University

of Stuttgart for performing the Direct Numerical Simulations.

REFERENCES

- [1] Durst, F., Lienhart, H., and Müller R., "Application of a semiconductor LDA for inflight measurements," *Proc. 6th Int. Symp. Appl. Laser Anemometry to Fluid Mech., Lisbon, 1992*
- [2] Naqwi, A., and Durst, F., "Light Scattering Applied to LDA and PDA Measurements, Part I: Theory and Numerical Treatments," *Particle and Particle Systems Characterization*, VCH Verlag, 1991, pp. 245 - 258

- [3] Erb, P., Ewald, B., and Roth, M.: "Flight Experiment Guidance Technique for Research on Transition with G109b Aircraft of the Technische Hochschule Darmstadt", *New Results in Numerical and Experimental Fluid Mechanics, NNFM60*, Vieweg Verlag, 1996, pp. 143 - 150
- [4] Lienhart, H., and Becker, S., "LDA Untersuchungen in transitionalen Grenzschichten," *Proceedings 9. DGLR - Fach - Symposium, Erlangen*, DGLR-Bericht 94-04, 1994
- [5] Stemmer, C., Kloker, M., and Wagner, S., "DNS of Harmonic Point Source Disturbances in an Airfoil Boundary Layer", *AIAA Paper 98-2436*, , 29th AIAA Fluid Dynamics Conference, Albuquerque, NM, 1998

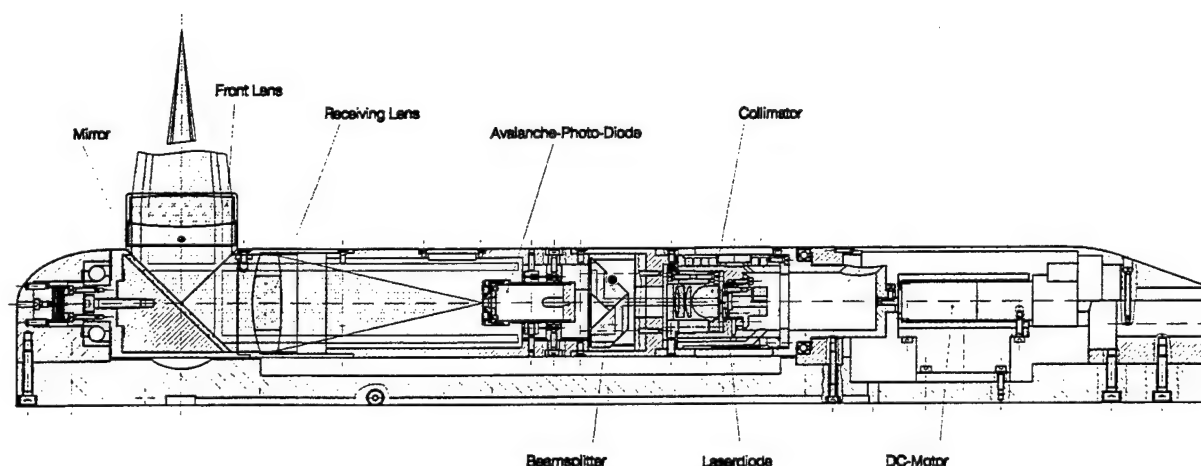


Fig. 1: Cross sectional view of the semiconductor LDA probe

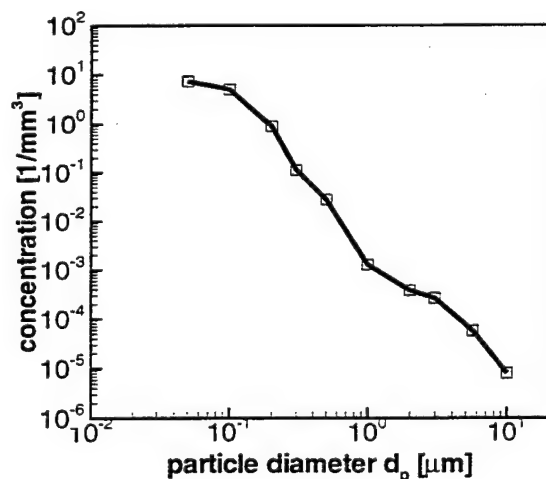


Fig. 2: Particle diameter distribution in the atmosphere measured with a cascade impactor

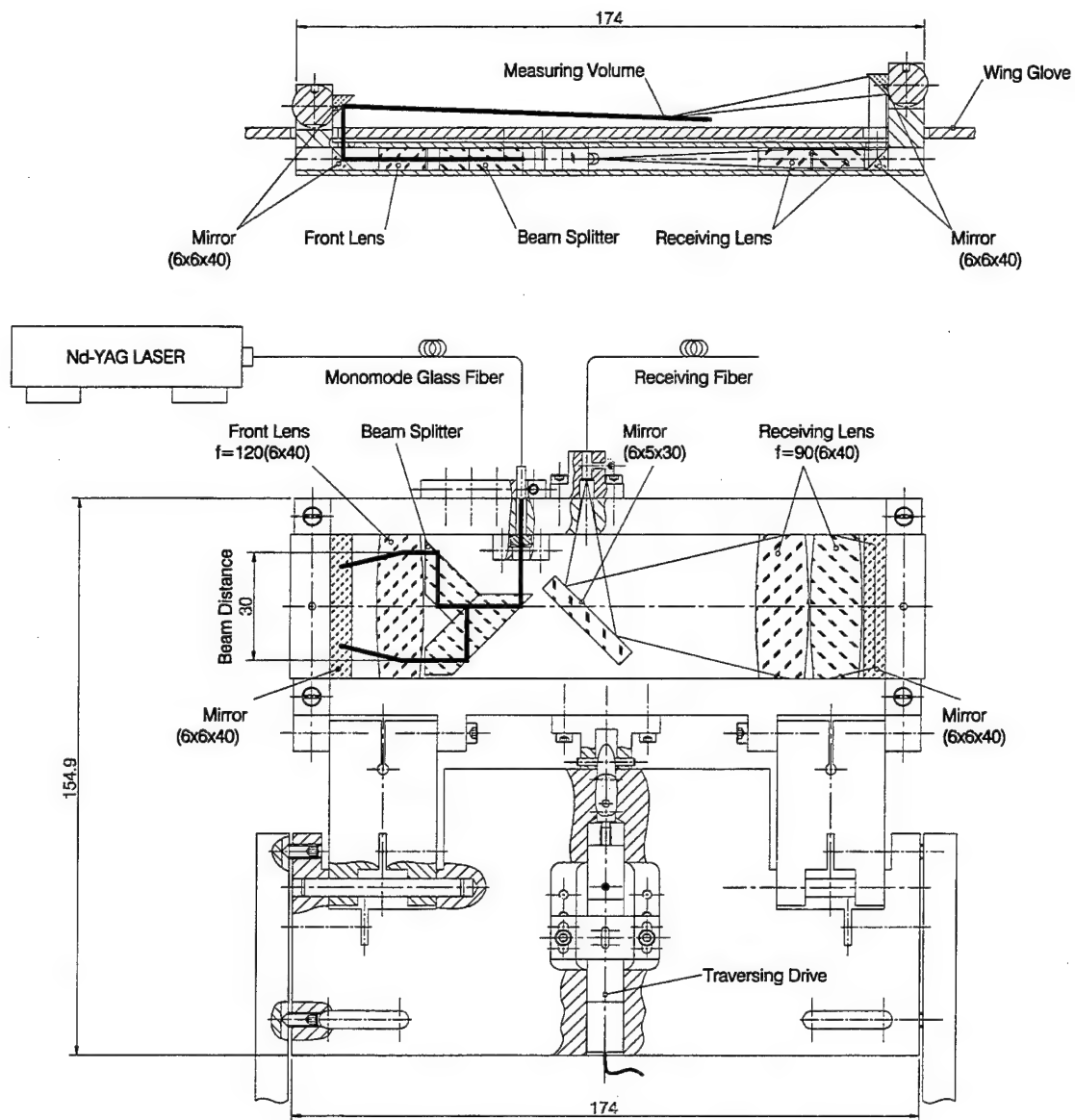


Fig. 3: Cross sectional view of LDA probe for in-flight measurements

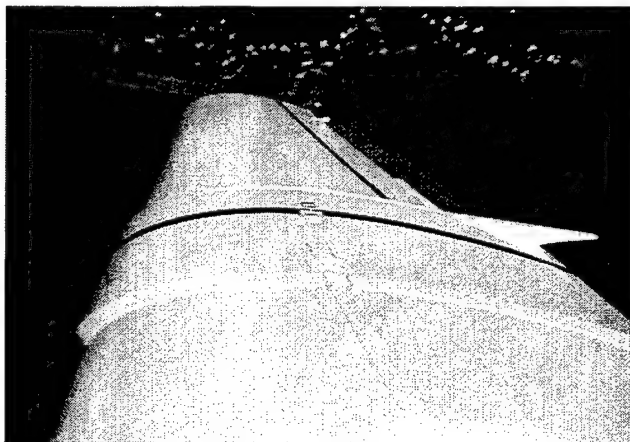


Fig. 4: LDA system during in-flight tests

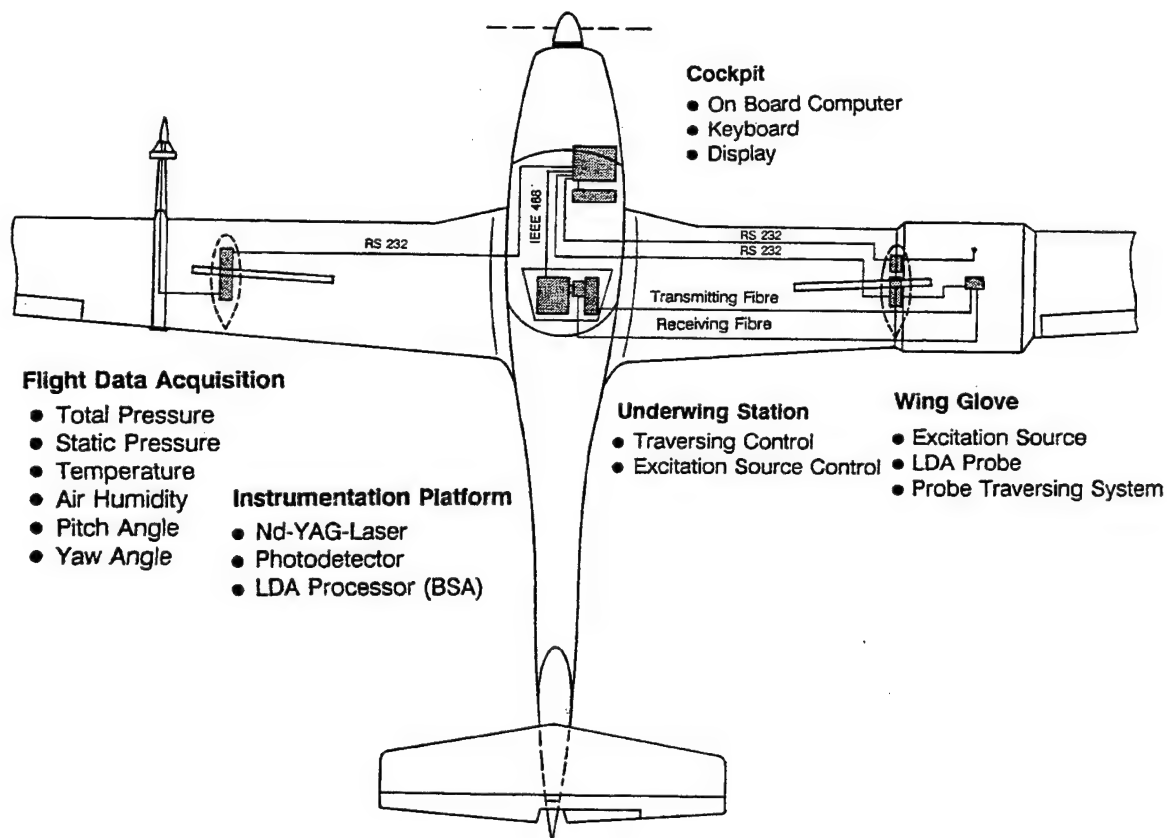


Fig. 5: Arrangement of instrumentation for in-flight tests

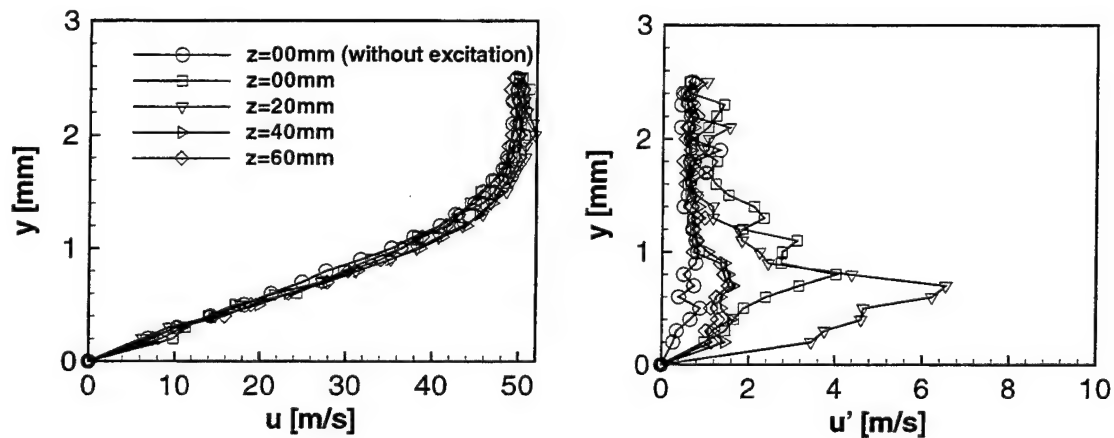


Fig. 6: Mean velocity and turbulence intensities at different spanwise positions with and without excitation

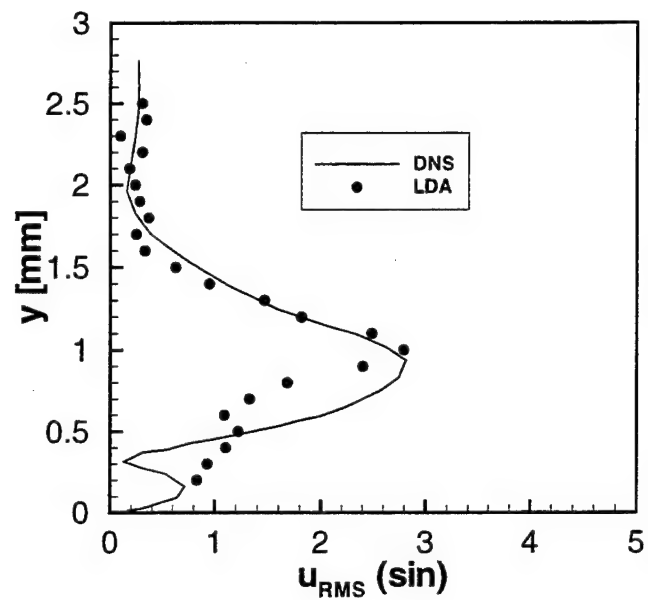


Fig. 7: Turbulence intensity of the Tollmien-Schlichting wave in Comparison with DNS calculations

DEVELOPMENT AND APPLICATIONS OF A RAPID FLIGHT TEST PROTOTYPING SYSTEM FOR UNMANNED AIR VEHICLES[†]

E.Hallberg, J.Komlosy, T.Rivers, M.Watson, D.Meeks, J.Lentz, I.Kaminer, O.Yakimenko[‡]

Department of Aeronautical and Astronautical Engineering, Naval Postgraduate School, Monterey, CA 93943, USA

This paper describes the development of a rapid prototyping system for flight testing of guidance, navigation, and control algorithms for unmanned air vehicles. The system affords a small team the ability to rapidly prototype new theoretical concepts and flight test their performance in realistic mission scenarios. The paper describes the software and hardware tools adopted for system development and discusses their application to the proof of concept flight test demonstration of a new integrated guidance and control algorithm for the Frog UAV.

1. INTRODUCTION

The past two decades have witnessed a dramatic increase in the utilization of Unmanned Air Vehicles (UAVs) by the armed forces, both in the US and abroad. More recently, many researchers in the academic community have realized the usefulness of UAVs both as teaching and research tools. The development of UAVs and their flight control systems requires addressing a number of engineering problems in a wide range of issues that include weight and energy restrictions, portability, risk factors, electronic interference, vibrations and manpower, to name but a few. Furthermore, the testing of new algorithms, sensor packages, and vehicles is truly a multi-disciplinary effort that borrows from many branches of the engineering sciences that include aeronautic, electrical, and computer engineering. This effort is costly and time consuming, and has the potential for catastrophic failure. When successfully done, however, it provides developmental information, insight, and field data that are unavailable from other sources. Since all theoretical and numerical results must be verified by some form of experiment, flight-testing is clearly the best way to achieve those goals.

Motivated by these considerations, and as a contribution towards the development of a versatile set-up for advanced UAV system design and testing, the Naval Postgraduate School has recently completed the development of a Rapid Flight Test Prototyping System (RFTPS) for a prototype UAV named Frog. This paper describes the complete RFTPS system that utilizes the Frog UAV and a portable ground station, and explains how it is being used as a rapid proof-of-concept tool for testing new guidance, navigation, and control algorithms for air vehicles. The paper starts with a general discussion of the RFTPS including the main motivation behind its development, system capabilities, cost and safety requirements, and hardware

description. The second part focuses on the software structure and capabilities including modeling of the Frog UAV and a novel integrated guidance and control (IGC) algorithms for precise trajectory tracking design. Then, it is shown how the RFTPS was used to develop and flight-test the IGC system. The full capabilities of the RFTPS are demonstrated when the new algorithm is taken from theoretical development to flight test on the UAV Frog operated by the UAV Lab at the Naval Postgraduate School. Finally work in progress is briefly discussed.

2. HARDWARE DESCRIPTION

The RFTPS [1] consists of a test bed unmanned air vehicle equipped with an avionics suite necessary for autonomous flight, and a ground station responsible for flight control of the UAV and flight data collection, as shown in Figures 1 and 2, respectively. A functional block diagram of the RFTPS is shown in Figure 3. The key decision when designing the RFTPS was to use off-the-shelf technology as much as possible, thus exploiting the economy of scale of a number of commercial industries. Furthermore, since the UAV development program is to span many years and to draw on the talents of the NPS students in the future, the RFTPS emphasizes high-level algorithm design. Low-level code and device driver generation is therefore kept to a minimum, the vast majority of the code "writing" being done via autocode tools. The system architecture is open, providing the ability to add, remove, or change real time input/output (I/O). Computational power can be increased as mission requirements dictate. The telemetry links are secure, yet low power and unobtrusive to the public, thus dispensing with the need for special authorizations from government authorities. The onboard components are lightweight and low power, allowing for the inclusion of additional payload.

2.1. RFTPS capabilities

The RFTPS provides the following capabilities.

1. Within the RFTPS environment, one can synthesize, analyze and simulate guidance, navigation, control, and mission management algorithms using a high-level development language;
2. Algorithms are seamlessly moved from the high level design and simulation environment to the real time processor;
3. The RFTPS utilizes industry standard I/O including digital to analog, analog to digital, serial, and pulse width modulation capabilities;

[†] This work was supported in part by Code Air 4.0T, Naval Air Systems Command under Maritime Avionics Subsystems Technology Program (MAST) and by National Research Council.

[‡] Aviation and Aeronautic Academy of Sciences, 40 Leningradskiy prospect, Moscow 125190, Russia. Currently on National Research Council tenure at the Naval Postgraduate School.

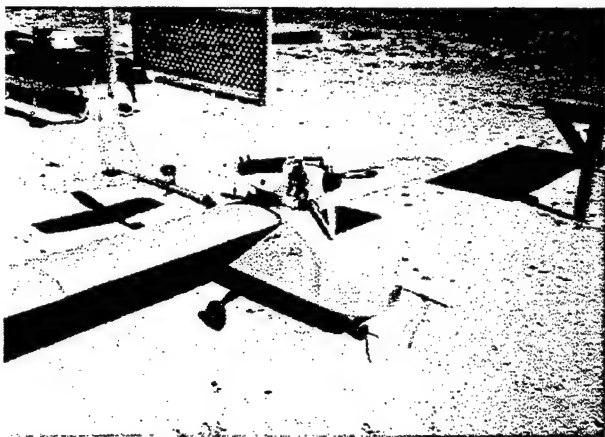


Figure 1. UAV Frog at the NPS

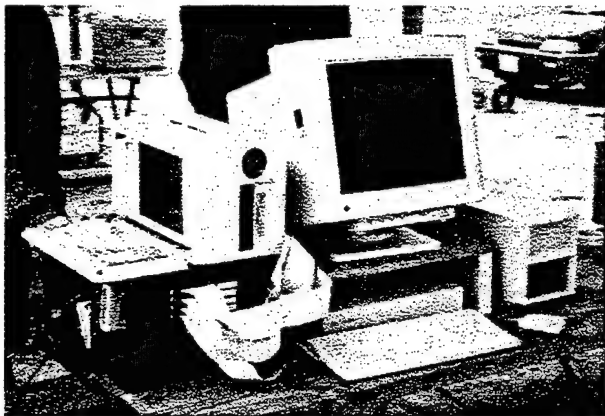


Figure 2. The RFTPS's base station in use at the airfield

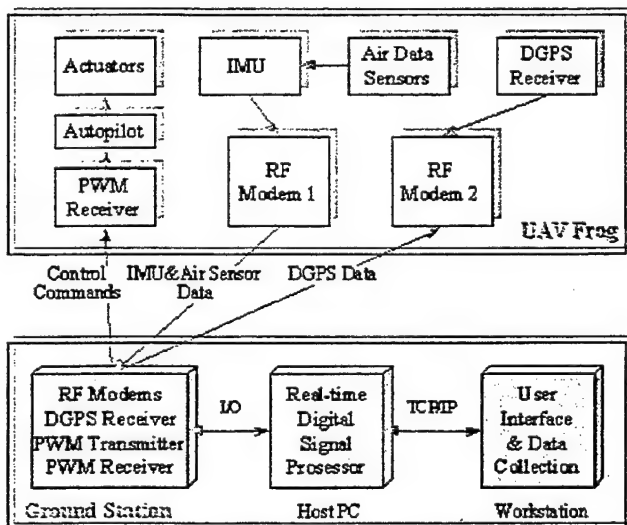


Figure 3. RFTPS hardware architecture

4. The RFTPS is portable, easily fitting in a van. In general, testing will occur at fields away from the immediate vicinity of the Naval Postgraduate School;
5. The unmanned air vehicle can be flown manually, autonomously, for using a combination of the two. For instance, automatic control of the lateral axis can be tested while the elevator and throttle are controlled manually;

6. All I/O and internal algorithm variables can be monitored, collected, and analyzed within the RFTPS environment.

2.2. Cost, Safety and Other Considerations

Cost and risk are two leading, and at times competing concerns that had to be effectively handled. Since all initial testing of new algorithms or vehicle systems is expected to occur within line of sight at all times, a pulse width modulated (PWM) remote control system manufactured by Futaba was chosen. Testing of a new control algorithm is similar to handing over control of the aircraft to a student pilot. The algorithm should have full freedom to perform, yet adequate safeguards must exist in case it fails. With some modifications, the extensive master-slave flight training capabilities built in to the existing RC transmitters were exploited. A significant portion of the cost of the RFTPS resides in the real time processor, I/O board and modules, and in the host computer. In spite of their compactness, the weight and power requirements of these components are significant when compared to on-board power and payload available. In order to gain additional payload and manage the risk associated with the loss of an expensive computer package, the real time controller was kept on the ground. Sensor and control links to the real time controller were bridged via RF components described later.

2.3. Components

The centerpiece of the RFTPS ground station is the AC100/C30 system from Integrated Systems Incorporated (Figure 4). The key feature of this product is its autocode tools. With a relatively short time available for research, emphasis had to be shifted from codewriting, debugging, and maintenance to algorithm development.

Communication with the real time processor is via an Ethernet bus using TCP/IP protocol. The AC100/C30 software provides extensive animation tools for building graphical user interfaces (GUI). By appropriate design of these interfaces, the flight test team can monitor, modify, and control the actions of the real time processor. The GUI resides on the workstation. Communication between the workstation and the real time processor is via the Ethernet connection, and is managed by a host PC. Additionally, the host PC provides power to the real time processor, as well as utilities for compiling, linking, and downloading the C-code. The I/O consists of four multi-mode, bi-directional, serial ports utilizing RS-232 protocol, a 16 channel PWM port capable of measuring up to sixteen PWM signals or generating up to six PWM signals, and a six channel digital-to-analog converter. The I/O modules are hosted by the same PC that holds the real time processor, a single Texas Instruments Digital Signal Processor (TMS320C30) (Figure 5).

The Frog UAV (Figure 1) is rectangular top-wing monoplaner with NACA2415 profile. It has a wingspan of 10.6 ft, reference wing area 17.6 ft², and its typical take-off weight is 90 lbs including up to 25 lbs payload. Maximal lift-to-drag ratio is equal to 7. Its performance is characterized by 50 miles range, 1 hr endurance, 90 ft/s speed,

and 5000 ft ceiling. The control configuration of the Frog is conventional with three independent surfaces (elevator, aileron, rudder) and a throttle. Manual control is provided via a Futaba, dual conversion, PWM transmitter utilizing the portion of the radio spectrum reserved for Radio Controlled (RC) flight, 72.030 MHz to 72.990 MHz. Precautions entail a search of the electronic spectrum utilizing a hand held spectrum analyzer, as well as standard procedures employed by RC hobbyists to avoid two individuals selecting the same frequency locally. Built-in capabilities of the transmitter include the ability to transmit one or more signals from a slave transmitter. The slave transmitter is a modified Futaba transmitter where the manual control effectors have been replaced by a direct connection to the digital-to-analog I/O module (Figure 6). Thus, an exogenous source (RFTPS) can be given control of one, some, or all of the control actuators of the aircraft using the same RC link currently controlling the aircraft. The aircraft is also equipped with the BTA autopilot. The sensor suite onboard the air vehicle consists of an inertial measurement unit (IMU), differential GPS (DGPS) receiver, elevator, aileron, and rudder actuator position sensors, and angle of attack, side slip angle, pitot-static, and static pressure air data sensors. The IMU includes a three axis rate gyro, three axis accelerometer, magnetic heading indicator, and a two axis pendulum that measure the vehicle's angular rates, accelerations, and

attitude, respectively. The sensor data are processed by a navigation filter inside the IMU. Errors of the resulting estimates are summarized in Table 1 [1]. The IMU also provides a four channel analog-to-digital (A/D) converter which is used to capture data from any four of the following sensors: elevator, aileron, rudder actuator position, angle of attack, side slip angle, dynamic pressure, or static pressure.



Figure 4. AC100/C30

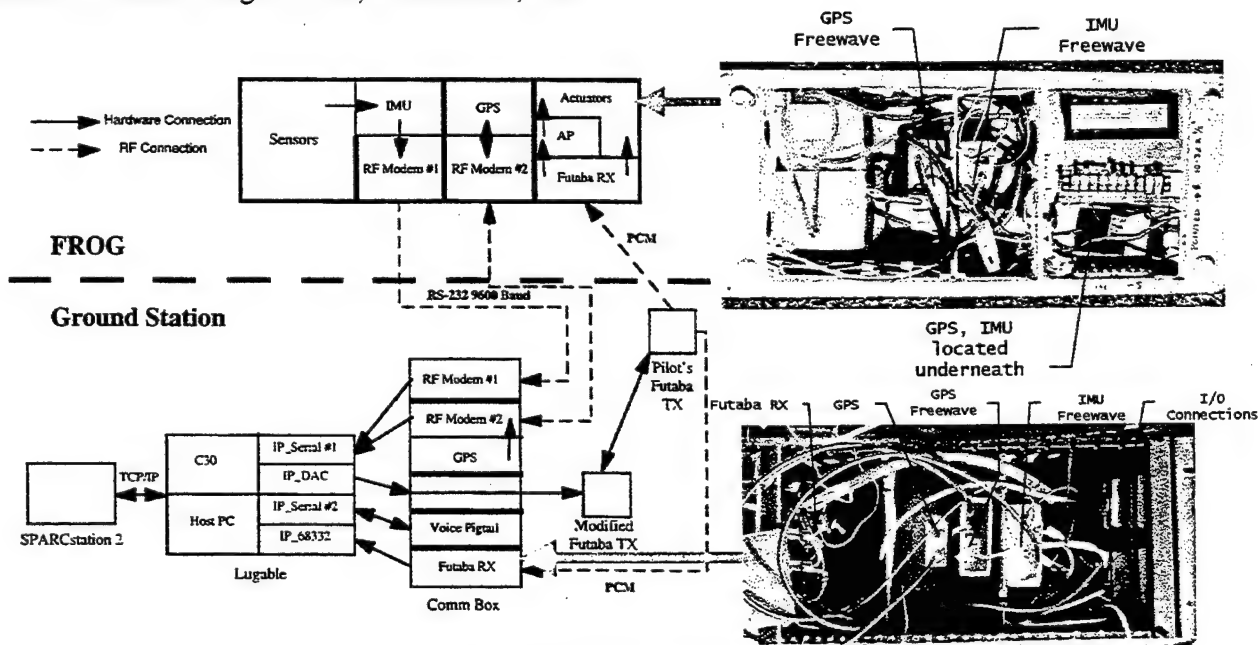


Figure 5. Hardware interface

The DGPS receiver on the aircraft receives differential corrections from the DGPS receiver installed on the ground station. The RMS errors inherent in the position estimates provided by this system can be found in Table 2.

Communication between the sensors and the real time processor is accomplished via two full duplex RF serial links. Frog is equipped with two low power, matched,

spread spectrum RF modems that provide up to 115 Kbaud rates at over 10 miles range. They require no license, and can be used anywhere in the United States. The data obtained by the IMU are sent to the ground station via one of the RF modems at 9600 baud. This results in an update rate of 25 Hz for the IMU sensor data. The GPS receiver onboard the aircraft uses the full duplex capability of the second RF modem to send position information

to the ground station and to receive differential corrections from the DGPS receiver on the ground. The update rate for GPS data is 1 Hz.

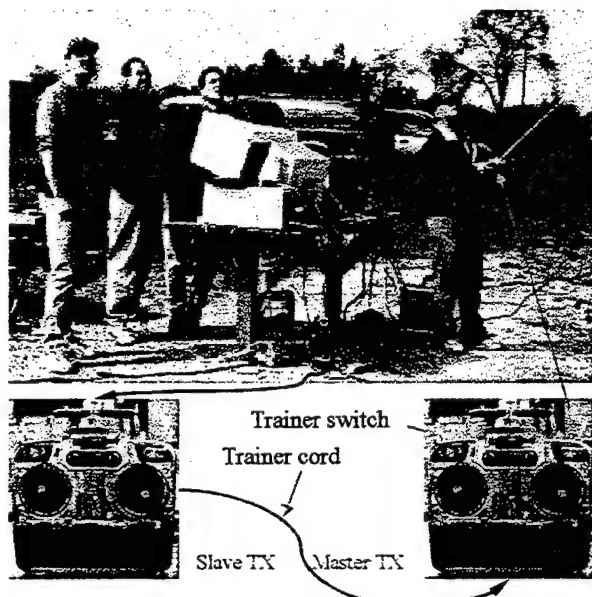


Figure 6. Futaba transmitters interface

Power for the onboard avionics is supplied from a lithium-ion battery. The battery provides 6 hours of continuous use. The power budget of the onboard components is shown in Table 3.

Table 1. IMU Error Budget

Sensor Estimates	Errors (% of full-scale)
Attitude	$\pm 2\%$
Angular rates	$\pm 2\%$
Accelerations	$\pm 1\%$

Table 2. DGPS Error Budget

Position Estimates	RMS Errors
lateral	3 meters
longitudinal	3 meters
vertical	5 meters

Table 3. Power Budget of Onboard Components

	Voltage	Current	Power
IMU	24 Volts	400 Milliamps	9.6 Watts
GPS	12 Volts	250 Milliamps	3.0 Watts
Telemetry 1	24 Volts	300 Milliamps	7.2 Watts
Telemetry 2	24 Volts	300 Milliamps	7.2 Watts
Total Required			27 Watts
Battery			≥ 200 Watts

3. SOFTWARE DESCRIPTION

The AC100/C30 utilizes "Xmath/SystemBuild", a graphical programming environment that uses a high-level block

diagram paradigm for modeling of linear and nonlinear systems. Within the "Xmath/SystemBuild" environment, algorithms can be built, simulated, tested, and debugged. Real-time code can then be generated for execution on the real time processor. Currently, the "Xmath/SystemBuild" environment resides on a Sun workstation.

3.1. Rapid Prototyping

A rapid prototyping system is an aid to the engineering process that allows the engineer to quickly design, test, and implement a control process. The MATRIX_x Product Family of software tools is a commercial system that provides a set of integrated tools to accomplish this task. The functionality of each MATRIX_x tool is shown in Figure 7a. Xmath/SystemBuild is an interrelated program set similar to MATLAB/Simulink. The RealSim GUI, shown in Figure 7b, provides overall control by stepping the user through the design process from initial formulation to the actual real-time implementation of the control systems.

Xmath is the computational element that provides analysis and control simulation functions. SystemBuild is the graphical, interactive program that uses both pre-defined and user defined blocks as modeling system elements. The autocode feature is a powerful time saving capability that generates high level C code based on the system built in the graphical System/Build environment. Once the code is generated it is sent to the host computer via FTP. The host computer compiler generates the object code and the link produces the executable code for the target processor. The animation builder enables the user to build a graphical interface with the control system that allows real-time inputs as well as display of system outputs during both ground and flight-testing. The hardware connection editor is used to associate system inputs and outputs with external hardware. The final feature of the RealSim GUI is "download and run". This feature loads the executable code into the target processor and prepares for real-time operation.

3.2. Frog UAV Model

A complete nonlinear 6-DOF model of the Frog, BTA autopilot and onboard sensors has been developed. Figure 8 includes the block diagram of the model in SystemBuild environment, and Figure 9 represent an example with involved sensor (vision camera) model.

3.3. GUI Description

As mentioned above RealSim GUI provides simple and effective design tool. Besides simulation and flight control algorithms (like those shown in Figures 8 and 9) flight critical information can be represented in convenient cognitive form using a system of hierarchical menu-displays (see example on Figure 10).

3.3. Data Collection and Representation

Test data acquired during simulation or flight test can be easily stored in any format, processed, analyzed, and presented in convenient cognitive form. This allows the use of both embedded and newly created tools.

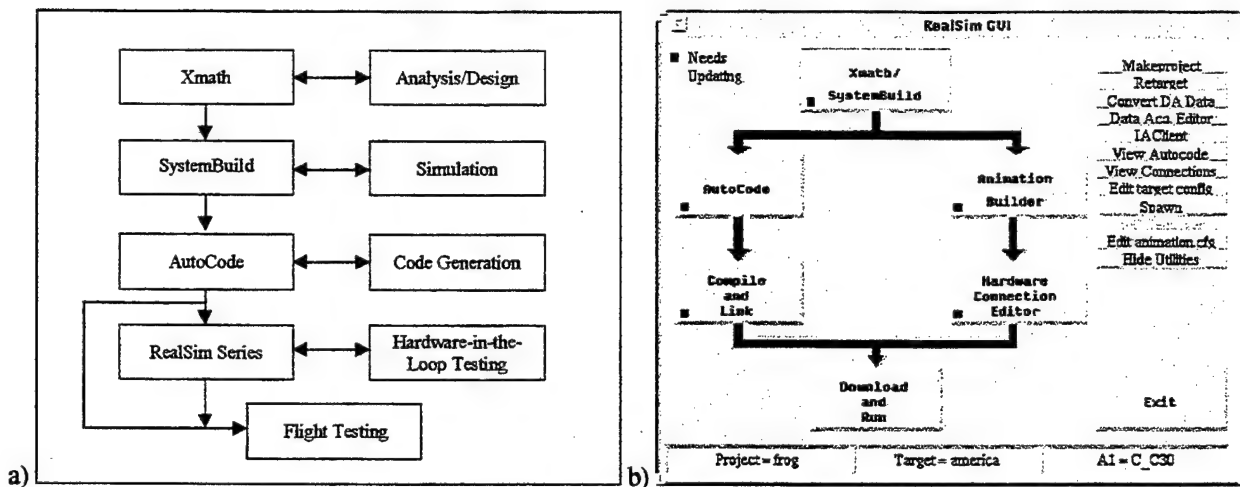


Figure 7. RealSim functions (a) and GUI (b)

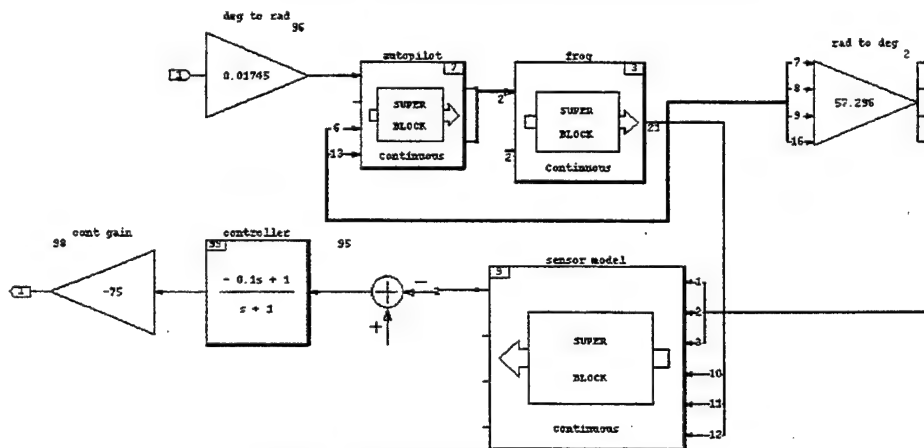


Figure 8. Frog UAV model block-scheme

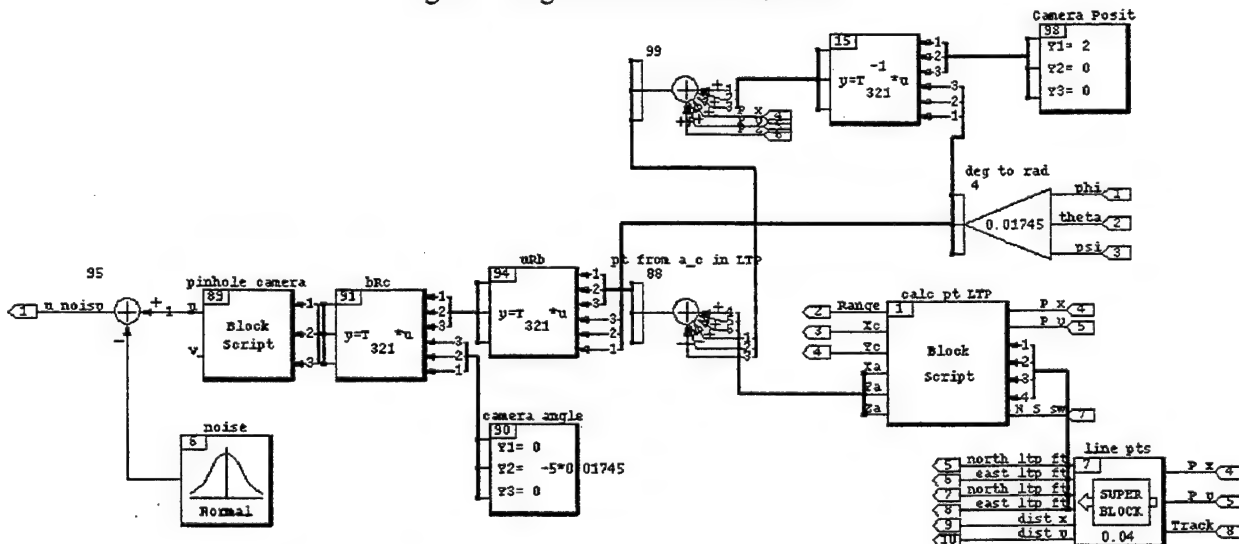


Figure 9. Vision based guidance algorithm block-scheme

4. APPLICATIONS

Recent applications of RFTPS are discussed in this section.

4.1. Frog Model Derivation

Initially, dynamic model of the Frog was developed using analytical methods [2]. Then a series of flight tests were

conducted to test the validity of the analytical model. The control surface inputs and the corresponding aircraft response measured by various IMU sensors were stored by the RFTPS and used for parameter identification.

The conventional configuration of the Frog suggested that the parameter identification problem could be decoupled

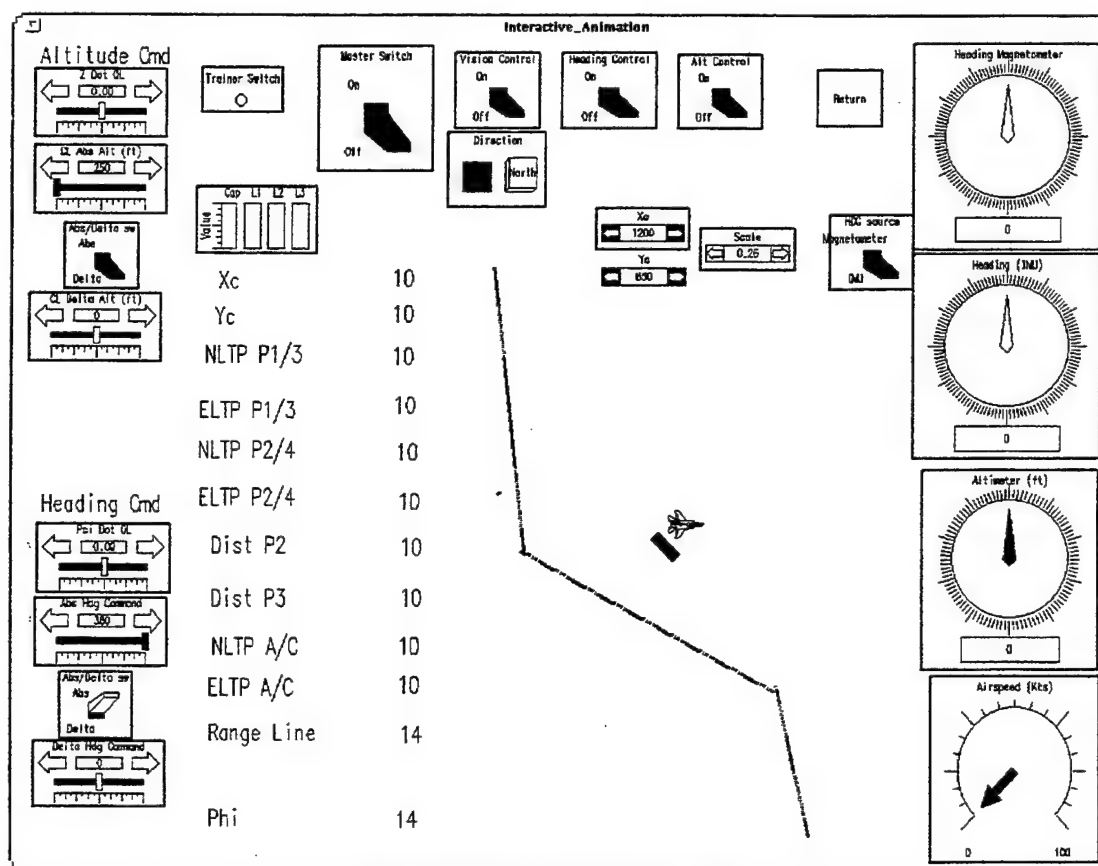


Figure 10. Flight display submenu

by identifying longitudinal and lateral/directional dynamics separately. Maximum likelihood parameter identification was used to refine existing analytical estimates of the stability and control derivatives. The results for a few key longitudinal stability derivatives are compared to analytic estimates in Table 4. Figure 11 compares pitch rate response of the refined model to an elevator doublet with in flight response of the Frog.

Table 4. Comparison of selected longitudinal derivatives

Derivative	Analytic	Experimental	Δ , %
C_{L_u}	4.3	4.09	5.13
C_{M_u}	-0.417	-0.557	-25.1
$C_{L_{\dot{u}}}$	-1.12	-0.391	186
$C_{M_{\dot{u}}}$	-1.62	-1.05	54.3

Similar process was repeated for the lateral axis. Aileron and rudder doublets were executed while aileron and rudder position, roll and yaw rates, and sideslip angle were measured. Results, for a few key lateral stability derivatives, are compared to analytic estimates in Table 5. Table 6 shows eigenvalues of the complete longitudinal and lateral models of the Frog at a typical cruise condition.

4.2. Autopilot Model Identification

The control laws of the BTA autopilot were identified as well. The autopilot is a "black box" containing both sensors and controller logic. The intent was to model the unit

as closely as possible without disassembling it. Since autopilot controls vertical speed using elevators and yaw rate using ailerons it was natural to decouple the problem into an identification problem for the lateral and longitudinal channels separately.

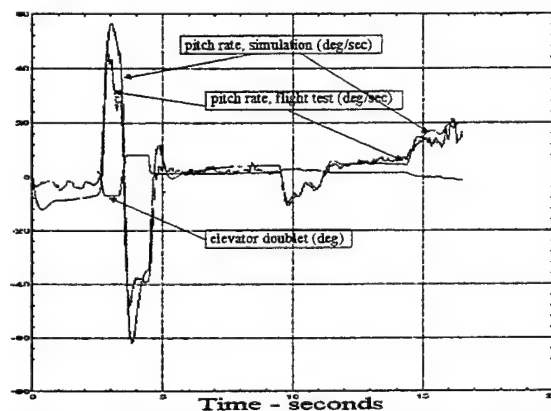


Figure 11. Pitch rate response to an elevator doublet

Table 5. Comparison of selected lateral derivatives

Derivative	Analytic	Experimental	Δ , %
C_{Y_p}	-0.31	-0.987	-68.6
C_{l_p}	-0.051	-0.094	-45.7
C_{N_p}	0.058	0.176	-67.0
$C_{l_{\dot{p}}}$	0.181	0.339	-24.3

Table 6. Open loop eigenvalues of the Frog

Eigenvalue	Damping	Frequency, rad/sec
-0.1730	1.0000	0.1740
-0.0398+0.4104i	0.0966	0.4123
-0.0398-0.4104i		
-0.6645+2.8205i	0.2293	2.8977
-0.6645-2.8205i		
-3.3526	1.0000	3.3526
-3.2295+4.0951i	0.6192	5.2153
-3.2295-4.0951i		

The lateral channel employs a rate gyro to track yaw rate commands via feedback to the ailerons. The general structure is shown in Figure 12.

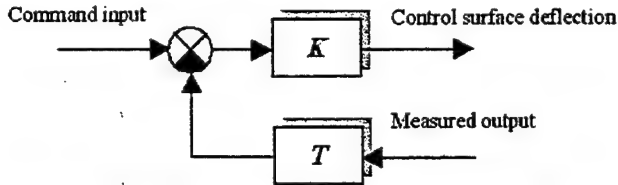


Fig 12. Generalized autopilot structure (for each channel)

In order to identify the dynamics of the block labeled T , the unit was rotated at differing yaw rates. This provided a variable frequency signal to the feedback path with a frequency content covering 0 to 20 radians per second. The commanded yaw rate was held constant. The feedback loop was broken at the summing junction of command and measured signals, and the feedback signal was captured. Parameter identification algorithms were used to determine that the feedback loop dynamics could be approximated by the following transfer function:

$$T_{lat}(s) = \frac{1 - 0.1s}{s + 1}$$

With the autopilot on, a step command in yaw rate was transmitted to the vehicle in flight. Vehicle yaw rate, as measured by the IMU, was recorded and used to estimate the value of the gain K_{lat} at 0.25 (see Figure 13).

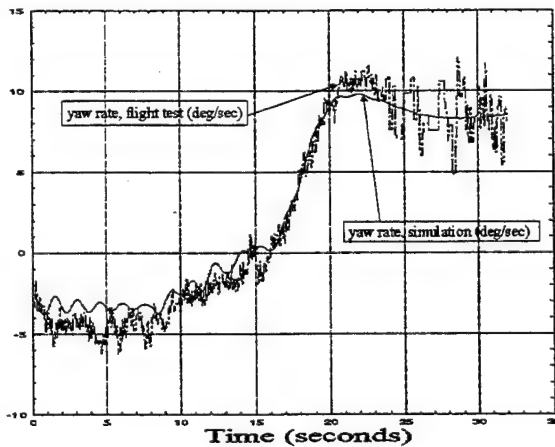


Figure 13. Yaw rate response to a step signal sent to the autopilot's lateral channel

The longitudinal channel of the autopilot senses the rate of change of static pressure in order to control the vehicle's vertical velocity via feedback to the elevator. Flight test data capturing the response of the vehicle to a step input in climb rate command was used for model identification. The structure of longitudinal channel occurs to be the same with $T_{lon}(s) = \frac{0.45s}{s + 0.45}$ and $K_{lon} = 0.25$.

4.3 Path Following Algorithm Development

In this section we present the results of the design and flight testing of nonlinear inertial path following algorithms using RFTPS. Figures 14-16 show the generalized feedback diagram and examples of these IGC algorithms flight-test results.

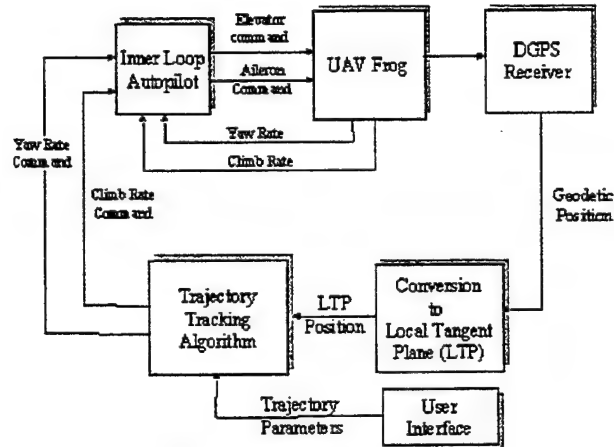


Figure 14. Feedback diagram

Figure 15 presents flight test and simulation results of tracking of a circle in presence of turbulence [3].

Figure 16a includes a map of a river to be tracked by a vision based tracking algorithm [4]. Figure 16b shows the results of tracking of a corresponding trajectory by a vision based guidance algorithm.

4.4. Voice control experiment

In this section we briefly discuss the voice control experiment using ViA Wearable PC [5]. The Voice Control System (VCS) was comprised principally of commercially available components. In addition to the standard RFTPS, the VCS required the use of a laptop computer to translate commands between the ViA Wearable PC and the Sun workstation. The VCS software programs that run on the laptop and wearable computers are the only custom made components of the system. Figure 17 provides an overview of the RFTPS including the additional equipment associated with the VCS.

The ViA Wearable system features two methods of entering commands during normal operation. Commands may be entered in the traditional manual method utilizing the touchscreen display (Figure 18) or with voice via the Audio Headset and voice recognition software. Table 7 illustrates a set of available commands.

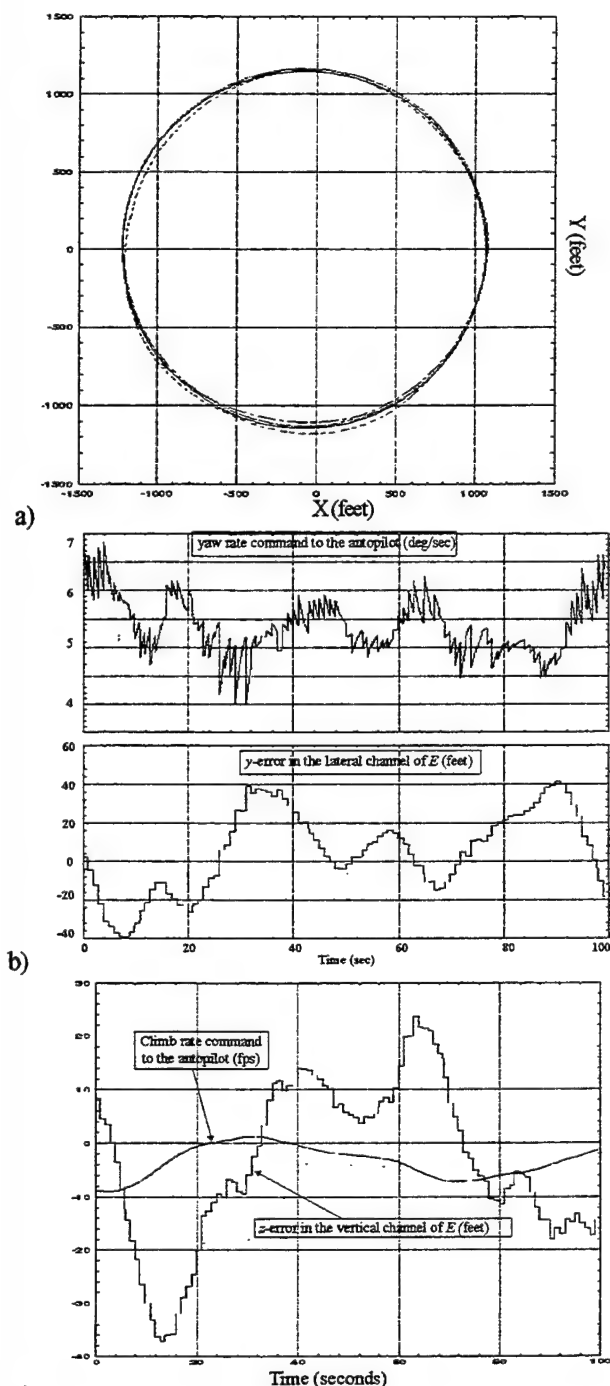


Figure 15. Flight test results of circle tracking (a): lateral errors and control commands (b), vertical errors and control commands (c)

The ViA Wearable and voice recognition software performed exceptionally well. Once the user determines the proper microphone placement and speaking volume level, the software recognized almost 100% of voice commands. Figure 19a illustrates the lateral commands and resulting aircraft response for one of the test runs. The top graph represents the input command from the VCS before it is augmented by the variable gain. A value of one represents a standard rate right turn; negative one a standard rate left

turn. The middle graph is the resulting PWM Futaba command transmitted. The final graph shows GPS heading and demonstrates that the aircraft does indeed turn in the direction commanded. Figure 19b details the longitudinal results for the same run. Here, a value of negative one represents a full climb; -0.5 represents a half rate descent.

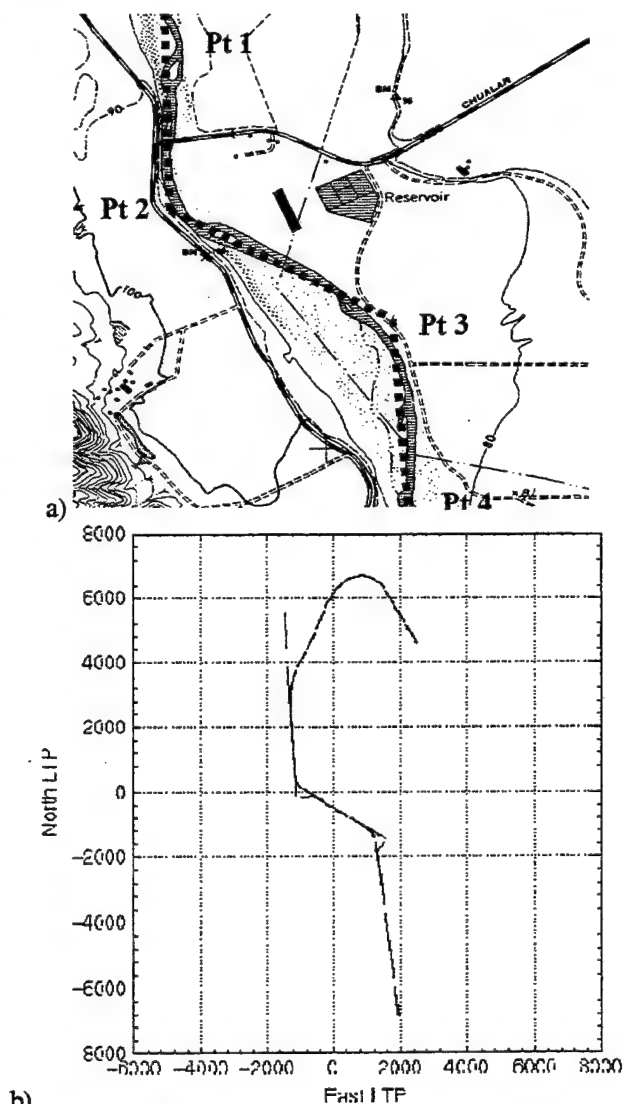


Figure 16. Map fragment with river approximation (a), and its tracking result (b)

5. WORK IN PROGRESS

This section discusses work in progress and future research to be accomplished using RFTPS.

Hardware-in-the-loop testing of the actuators determined their bandwidth to be an order of magnitude higher than the available BTA autopilot bandwidths. Since the BTA autopilot seems to be the limiting factor in achievable performance of the guidance and control algorithms work is directed towards replacing it with a dedicated computer. In addition frame grabbing and image processing cards are being integrated into RFTPS.

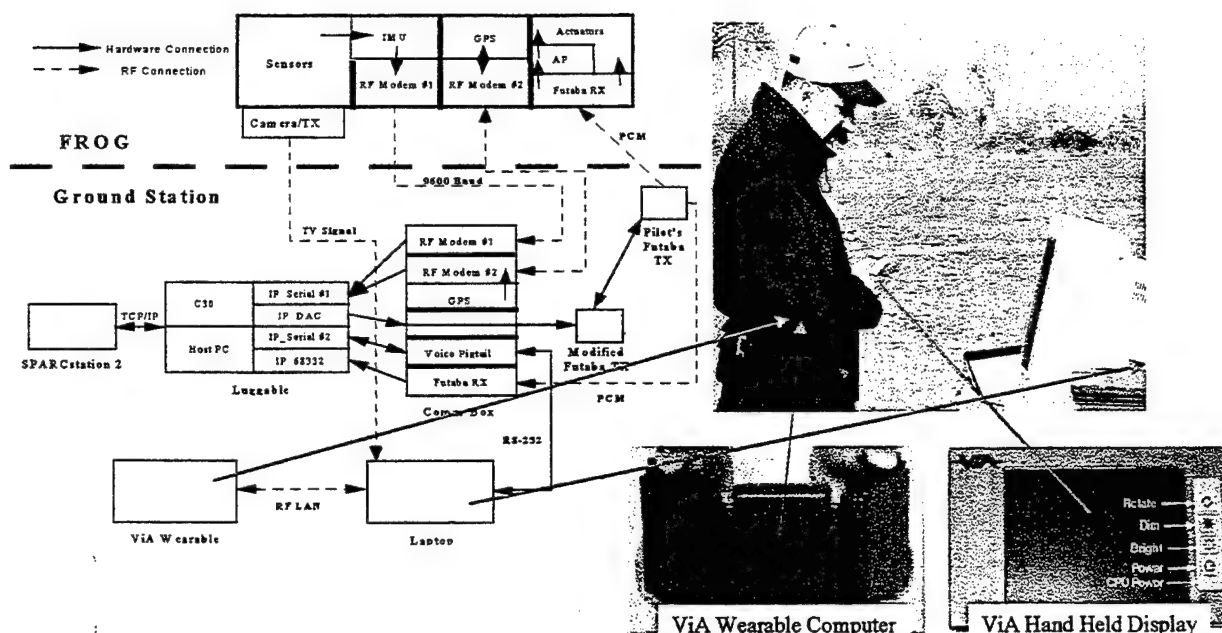


Figure 17. VCS architecture overview

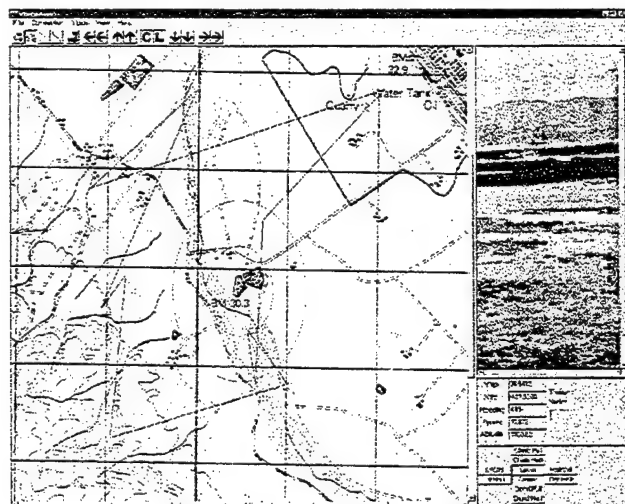


Figure 18. Touchscreen display

Table 7. The set of available commands

Voice command	Action command
"RIGHT STANDARD"	Standard rate right turn
"RIGHT HALF"	Half rate right turn
"LEFT STANDARD"	Standard rate left turn
"LEFT HALF"	Half rate left turn
"CENTER"	Constant heading
"CLIMB FULL"	Standard rate climb
"CLIMB HALF"	Half rate climb
"DESCEND FULL"	Standard rate descent
"DESCEND HALF"	Half rate descent
"LEVEL"	Constant altitude

5.1. RFTPS Upgrade

At present another FROG UAV is being equipped with more precise sensors, including Humphrey vertical gyro, Trimble DGPS, 8-12 micron IR and visible spectrum video cameras.

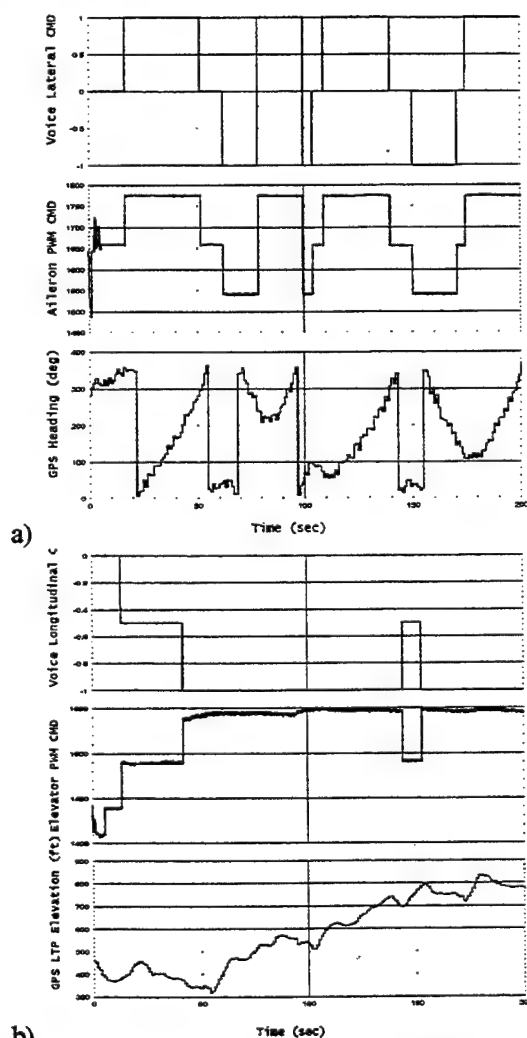


Figure 19. Examples of lateral and longitudinal commands performing

5.2. Onboard Image Processing and Trajectory Formation Algorithms Design

The hardware and software upgrades discussed will support new work in the areas of passive sensor-based navigation and real-time optimal trajectory generation and tracking.

Available passive sensor suite includes vision/IR sensors (Figure 20), IMU, DGPS, air data. These sensors will be used to demonstrate the capabilities of new navigation algorithms that integrate vision, GPS and inertial sensors and explicitly address

- performance measures compatible with the sensor specifications and with control system requirements,
- the nonlinear nature of the underlying sensor geometry (e.g., vision sensors),
- physical characteristics of the sensors,
- multi-rate nature of the data generated by the passive sensors,
- robustness with respect to out-of-frame events and occlusions.

Another area to be supported by upgraded RFTPS is to flight test real-time optimal trajectory generation algorithms [6] with new cognitive image capability (Figure 21), which were already implemented in cockpit transformed training system [7].

Combined solution of these problems will lead to a new autonomous landing capability using passive sensors for the Frog.



Figure 20. Example of vision camera use during landing operation

CONCLUSIONS

In conclusion it can be stated that designed RFTPS showed itself as a powerful, portable, rugged, effective in the field and in the lab. It ensures safety and reliability at controlling an aircraft and provides excellent opportunities for rapid flight testing of sensors and new algorithms.

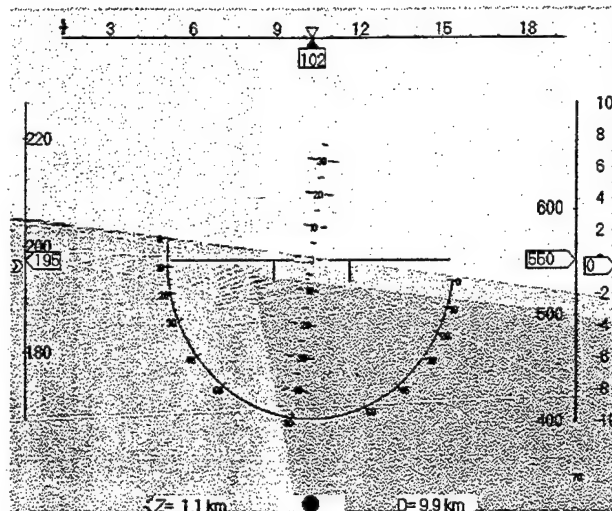


Figure 21. Example of operator's control actions support image (road-in the sky)

REFERENCES

1. Hallberg, E., Kaminer, I., and Pascoal, A. "Development of a Flight Test System for UAV's", IEEE Control Systems, Feb 1999.
2. Papageorgiou, E., "Development of a Dynamic Model for a UAV", Master's Thesis, Naval Postgraduate School, March 1997.
3. Kaminer, I., Pascoal, A., Hallberg, E., and Silvestre, C., "Trajectory Tracking for Autonomous Vehicles: An Integrated Approach to Guidance and Control," AIAA Journal of Guidance, Control and Dynamics, January-February 1998.
4. Watson, M., "Vision Guidance Controller for Unmanned Air Vehicle," Master's Thesis, Naval Postgraduate School, December 1998.
5. Komlosy, J., "Application of rapid prototyping to the design and testing of UAV flight controls systems," Master's Thesis, Naval Postgraduate School, March 1998.
6. Yakimenko, O., "Shortcut-time spatial trajectories on-board optimization and their cognitive head-up display visualization for pilot's control actions during maneuvering support," Collection of technical papers of 17th ICIASF, Monterey, CA, 1997.
7. Firsov, A., and Yakimenko, O., "Mobile adaptive training system for pilot's on-board pre-flight preparation and tactical thinking training," Proceedings of 10th International Training and Education Conference, The Hague, The Netherlands, 1999.

AN OPTICAL TECHNIQUE FOR DETECTING FATIGUE CRACKS IN AEROSPACE STRUCTURES

David Banaszak
Gary A. Dale
AFRL Air Vehicles Directorate, WPAFB

A. Neal Watkins
Jeffrey D. Jordan
ISSI, Dayton, OH

ABSTRACT

The development of a field-deployable non-intrusive optical-based crack-detection and -measurement system based on temperature-sensitive-paint (TSP) technology is described. The TSP developed is based on a platinum porphyrin immobilized in a sol-gel-derived thin film. For this test, the TSP is deposited on top of an aluminum plate that is then subjected to dynamic fatigue through the use of an electrodynamic shaker. Detection of cracks in the aluminum is accomplished by monitoring the changes in the surface temperature of the plate as it was excited at its resonant frequency. Visualization and measurement of the cracks is easily accomplished in near real time using this method. Finally, this method is compared with conventional thermography, and the results indicate that for aluminum, the surface-temperature change was below the resolution of conventional instrumentation.

INTRODUCTION

Detection of cracks and measurement of crack lengths represent critical requirements in the development of new materials and structures for airframe components that will operate under extreme conditions. Currently, an electrodynamic shaker employing out-of-plane excitation is used to fatigue aircraft materials and structures. During dynamic-fatigue tests, the occurrence of a crack is the only criterion for the generation of stress-versus-cycles-to-failure curves for various structural materials. A failure is defined as a resonant-frequency shift of a fixed percentage. Through the use of out-of-plane excitation, the structural test community is currently investigating methods of determining crack length versus cycles that are similar to the techniques used for tension/compression fatigue tests [1-2]. However, the cracks grow very rapidly, the vibration of the structure does not allow test personnel to view the crack length versus time or test cycles, and the crack is usually extremely thin and, thus, detecting/resolving it using

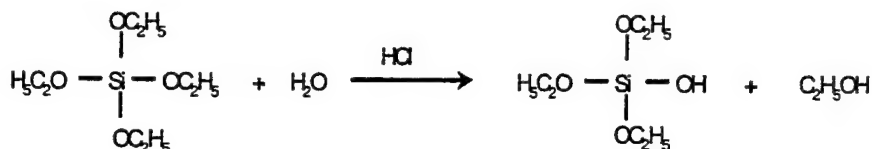
conventional video capture techniques is extremely difficult. To overcome these limitations, test personnel must stop the test to measure the crack length; this affects the input levels and the meaning of the number of cycles of excitation.

However, it has been noted that a substantial change in the surface temperature occurs as dynamic-fatigue increases. The initiation and growth of the crack may provide a way for the surface to relieve the added stress due to out-of-plane excitation. One possible method of detecting cracks and measuring crack lengths involves the use of a thermography system based on an infrared camera. Drawbacks to this technique include the substantial cost of such systems (well over \$100,000 for adequate range and sensitivity) and the large background signal due to ambient heat sources.

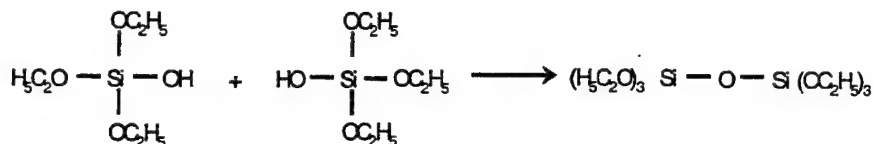
This effort is an extension of the pressure-sensitive-paint (PSP) approach for determining surface pressures in a wind tunnel. In this approach, luminescent molecules are dispersed within a binder, or paint, that is applied to the test model of interest. Illumination of the PSP coating with the appropriate excitation frequency induces lower-energy light emission from the PSP, with amplitude inversely proportional to the partial pressure of oxygen (P_{O_2}). Because oxygen is a fixed-fraction of air, PSP-based systems provide a means of making non-intrusive, full-field surface-pressure measurements at relatively low cost very early in the design cycle.

One of the major obstacles in the full exploitation of PSP technology is the temperature sensitivity of the luminescent molecule. Commonly, the temperature sensitivity of many PSP systems is actually greater than the pressure sensitivity. This is due, in large part, to the increase in the inherent non-radiative decay processes in the probe molecule. To compensate for the temperature sensitivity of PSPs, several attempts to create a temperature-sensitive-paint (TSP) have been reported [3-4]. In these approaches the pressure sensitivity of the

Hydrolysis TEOS, tetraethylorthosilicate



Condensation



Polycondensation

Formation of 3D matrix

Aging/Drying

Expulsion of solvent
Composite strength increased

Figure 1. Sol-gel processing chemistry.

paint is minimized or eliminated, leaving only the temperature sensitivity.

EXPERIMENTAL

Temperature-Sensitive-Paint Optimization

In the design of TSP coatings, the polymeric support dictates the thermal and mechanical stability, adherence characteristics, and surface roughness while contributing to the temperature sensitivity. Control of these parameters would allow the formation of TSP systems ideally suited for test conditions of interest. Sol-gel processing has been shown to be a viable method for the creation of optically transparent, inorganic matrices at relatively mild conditions. The stability and porosity of these films can be manipulated by simply changing the sol-gel processing conditions. Typically, the sol-gel film is deposited on top of a white base coat produced by commercially available white spray paints. The base coat serves to stabilize the probe-doped active sol-gel layer, improve adherence of the sol-gel layer, and provide a screen layer suitable for uniform deposition of the sol-gel layer.

The sol-gel process allows the formation of controlled-pore glasses under ambient conditions of temperature and pressure. Sol-gel processing involves the transition of a solution phase into a gel, followed by densification and loss of solvent. This results in a solid, optically transparent glass. The five-step process as shown in Figure 1 represents the sol-gel chemistry.

The process is initiated by the acid- or base-catalyzed hydrolysis of a metal or semi-metal alkoxide such as tetraethylorthosilicate (TEOS) to form the hydrated product. Condensation of these moieties results in the formation of metal-oxygen-metal bonds (Si-O-Si) and a colloidal mixture termed a sol. Polycondensation of these species results in the formation of a three-dimensional network and macroscopic solid, as defined by the gelation point. Subsequent aging and drying of the composite film causes the expulsion of solvent from the matrix, increasing the composite strength. Host composites for chemical-sensing applications can be easily produced in this manner by incorporating recognition elements (RE, e.g., probe molecules) directly into the sol-gel precursor solution, followed by thin-film deposition. In this manner, the RE is entrapped within the porous matrix, and a significant population remains accessible to the external analyte. In addition, the molar ratio of sol-gel precursors, hydrolysis time and temperature, and drying conditions affect the sol-gel processing chemistry and, thus, the physicochemical properties of the final composite (e.g., porosity, polarity). Also, the ambient processing conditions allow the incorporation of luminescent probe species that would otherwise thermally decompose under conventional glass technology.

Several advantages result from the use of sol-gel-based composites as binders. First, sol-gel-derived coatings exhibit high thermal stability, making them more capable of withstanding extreme environments than comparable organic binders. Second, a deposition technique that



Figure 2. Sol-gel-derived temperature-sensitive-coating architecture.

allows the formation of thin, uniform films has recently been developed and has been shown to produce optically transparent, robust composites that possess low surface roughness. Changing the film thickness and surface roughness can effect changes in the temperature sensitivity. Finally, it should be noted that these coatings can be easily removed from most materials by simply destabilizing the base coat with mild solvent, leaving the test surface unaffected.

The use of sol-gel-derived composite coatings as platforms for chemical and biological sensors has been demonstrated [5-11]. Typically, successful applications of these coatings involve deposition onto substrates such as glass or quartz. For adapting this technology to surfaces of various metallic and ceramic substances, the coating architecture illustrated in Figure 2 was developed. In this approach, a bare surface is cleaned and coated with a white base-coat layer. The base coat serves to improve the adherence of the sol-gel layer to the surface, eliminate substrate-induced quenching of the luminescent probe, and mask test-surface irregularities.

Several molecules have been investigated as possible temperature sensors, based on the following criteria: increased temperature sensitivity, negligible pressure sensitivity, spectrally separate emission from the pressure sensor than from the temperature sensor, and ability to be used in the same paint matrix as the pressure sensor [3]. Obviously, these criteria are based on using the TSP in conjunction with a PSP. Without the PSP, many of these criteria can be relaxed. In fact, only the first two (increased temperature sensitivity and negligible pressure sensitivity) become the limiting factors in TSP development. Various molecules have been used as temperature sensors, including rhodamine laser dyes [3] and europium and ruthenium compounds [4]. In the case of the latter two sets of materials, the paint is coated with an oxygen-impermeable membrane to reduce the pressure sensitivity.

One compound for the development of TSPs is platinum mesotetra(pentafluorophenyl)porphine [Pt(TfPP)], which has been used in various matrices as a PSP. The

temperature sensitivity of Pt(TfPP) in a sol-gel matrix is shown in Figure 3.

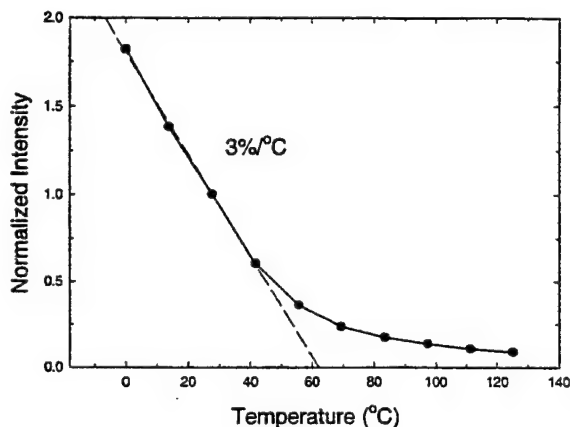


Figure 3. Temperature sensitivity of Pt(TfPP) immobilized in a sol-gel matrix at ambient pressure.

These results show that Pt(TfPP)-based TSPs allow the investigation of materials up to about 60°C. The development of alternative probes that can maintain temperature sensitivity at higher temperatures is under investigation, with emphasis on currently available thermographic phosphors and analogous materials.

Instrumentation Setup

To validate the use of TSPs as a method for investigating dynamic fatigue of materials, an aluminum plate was coated with a white base coat followed by a Pt(TfPP)-based sol-gel TSP. The coated plate was then placed on an electrodynamic shaker and excited continuously at resonant frequency. Figure 4 shows a plate mounted on the shaker and the typical deflections experienced while vibrating. The excitation frequency was recorded on tape for determination of cycles versus time. Two accelerometers (A1 and A2) measuring motion in the plane of excitation and out of the plane of excitation were used to measure the amplitude of the excitation frequency experienced by the plate, and was also recorded on tape.

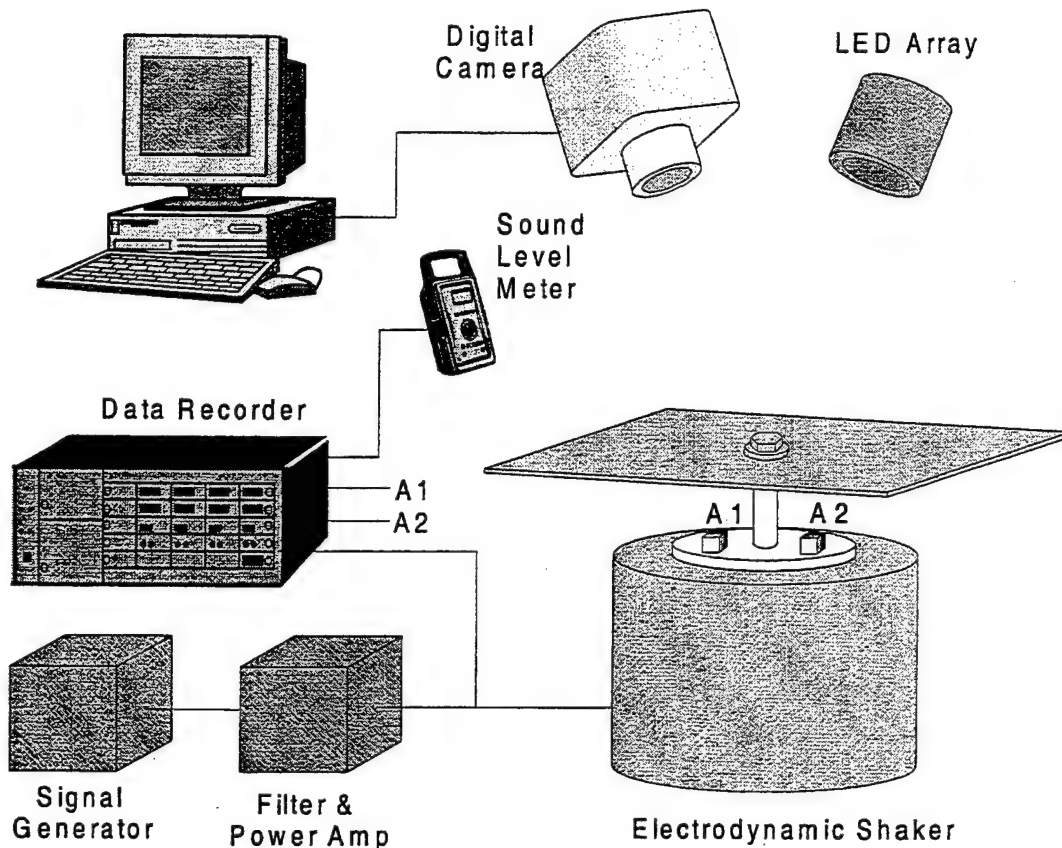


Figure 5. Schematic of instrumentation for visually detecting cracks induced by out-of-plane excitation.

To excite the TSP, blue light-emitting-diode arrays were placed above the electrodynamic shaker to illuminate as much of the surface as possible. A scientific-grade CCD camera was placed directly above the plate for image acquisition. Image acquisition was begun when the out-of-plane excitation frequency was applied to the aluminum plate. Images were then acquired every 10-15 s for about 9 min, the time required for the crack to initiate and grow to the edge of the plate. The instrumental setup is shown in detail in Figure 5.

EXPERIMENTAL RESULTS

Analysis of the images was accomplished by dividing each image by the initial image before the excitation frequency was applied. This serves as a measure of the intensity change resulting from the vibration of the aluminum plate. From the 52 images collected during the initial test, the crack length as a function of the number of excitation cycles can be calculated, similar to techniques used for linear tension/compression testing. The results are shown in Figure 6. Discontinuities in the data are due to manual tracking of the resonant-frequency and should be smoother with automatic tracking.

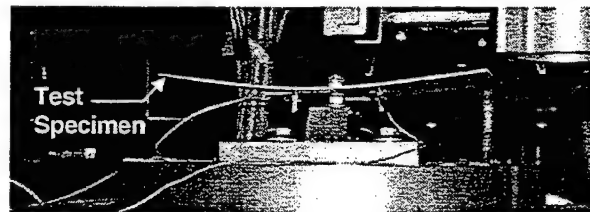


Figure 4. Aluminum plate placed on the electrodynamic shaker and showing typical deflections experienced by the plate during vibration.

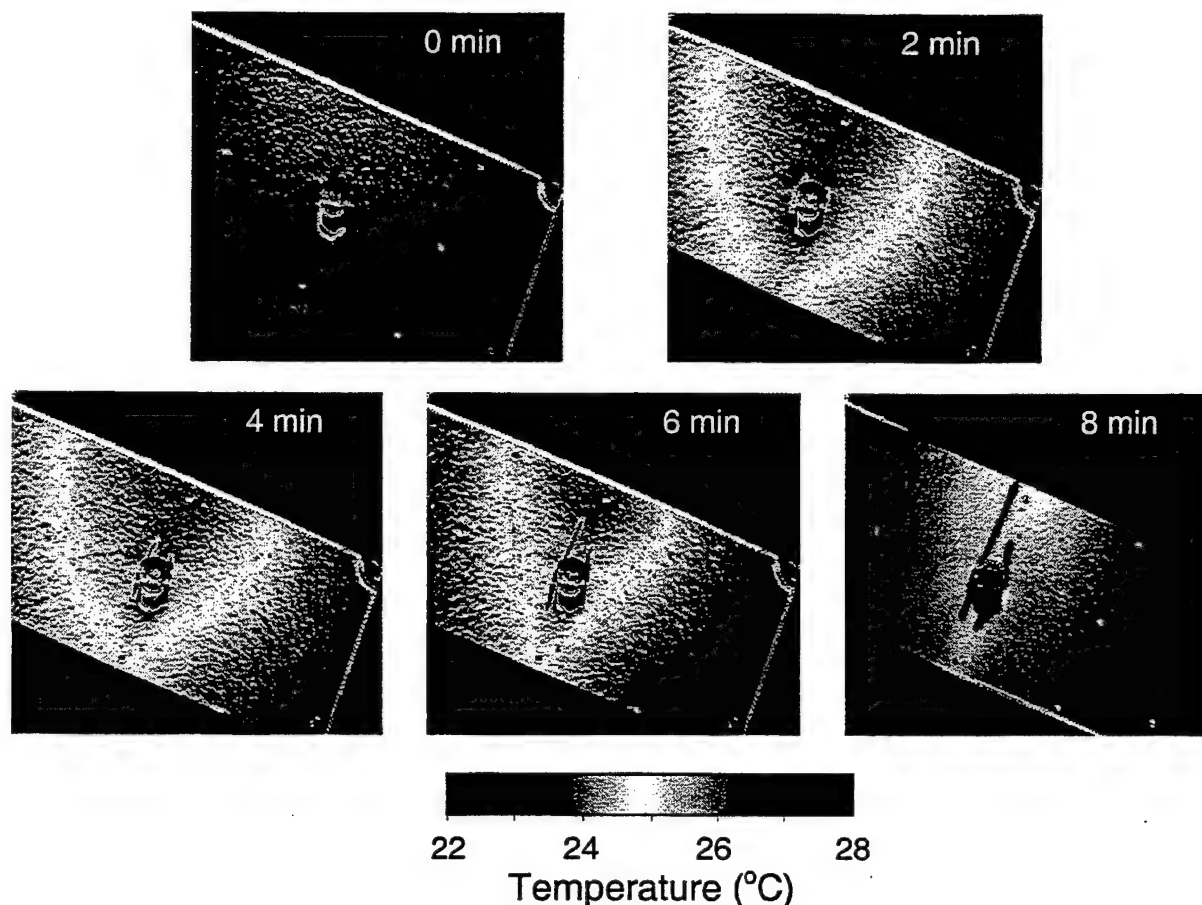


Figure 7. Temperature images showing the initiation and growth of cracks in the TSP-coated aluminum plate caused by out-of-plane excitation.

Since the experiment was conducted at ambient temperature and pressure, the temperature sensitivity calculated from Figure 3 can be used to determine the change in temperature across the surface with out-of-plane excitation. Figure 7 contains several images collected at different times, showing the progression of the cracks from the center hub to the edge of the plate.

It should be noted that this experiment was conducted using only one LED array for illumination. We believe that the observed increase in "temperature" on one side of the plate is simply an artifact due to uneven illumination. To investigate this possibility, more LED arrays were used to ensure even illumination across the surface of the aluminum plate. Also, a different camera giving approximately twice the resolution was used. This test was in support of a program to investigate methods of reducing the amount of sonic fatigue experienced by secondary aircraft structures. The result of the test is shown in Figure 8.

It is readily apparent that the increase in temperature observed in Figure 7 is absent with an even-illumination

field. Using an even-illumination field also allows observation of higher temperature regions at the stress concentrations at the crack tips, suggesting that the cracks relieve the added stress from out-of-plane

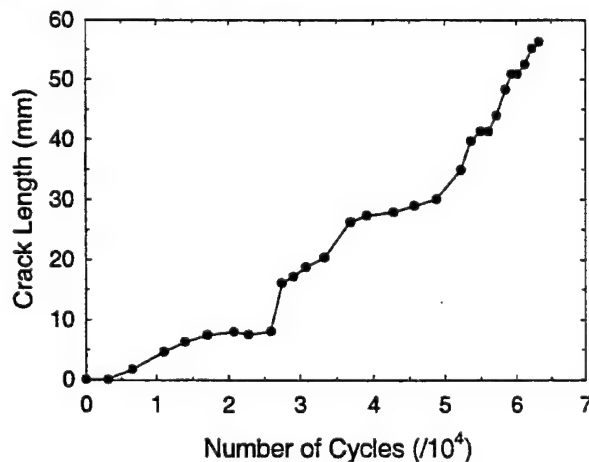


Figure 6. Crack length as a function of number of cycles in the test.

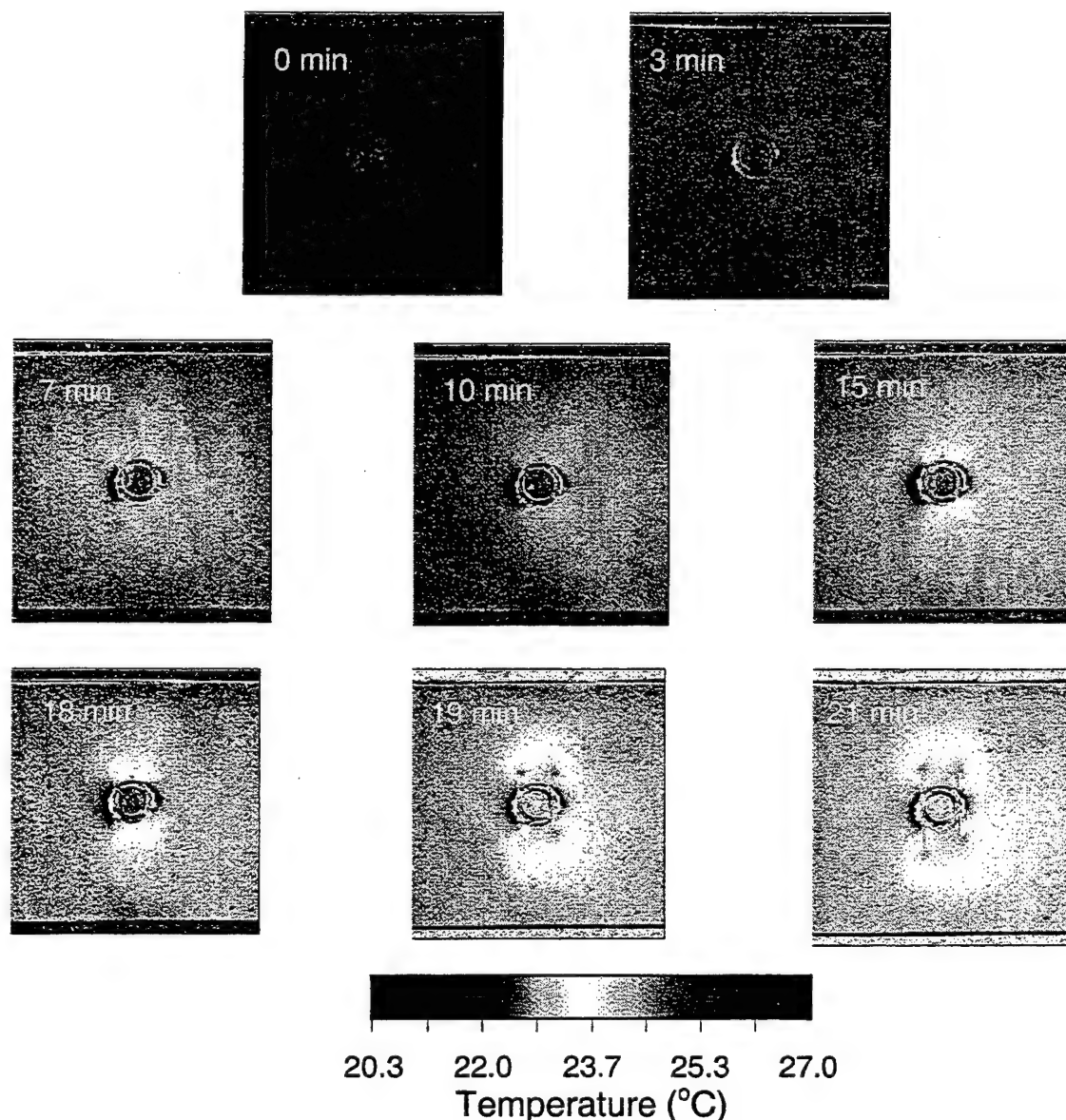


Figure 8. Temperature images collected using an even-illumination field.

excitation.

Finally, the TSP method for detecting and measuring cracks was compared with a commercially available thermography system. The advantages of using a thermography system are that images can be collected at an accelerated rate (approaching real time) and that the data are already cast as temperature. However, the expense of such systems (typically \$100,000 or more) and the large background signal due to ambient heat sources are major disadvantages. Furthermore, the small changes in temperature of the aluminum surface proved to be below the temperature resolution of the available thermography system; thus, no cracks were readily apparent in the recovered images (data not shown).

CONCLUSIONS

This effort demonstrates the potential of temperature-sensitive paints in applications involving testing of structural materials. Current testing methods often involve the use of out-of-plane excitation provided by an electrodynamic shaker. Using these methods, only the appearance of a crack in the surface can be used as the criterion for failure. However, because of the extreme vibration of the sample, real-time detection and measurement of cracks is difficult at best, requiring the test engineer to stop the test to make measurements. This affects the input levels and the meaning of the number of cycles of excitation.

The TSP method makes use of the changes in the surface temperature of the test article as dynamic fatigue increases. These changes are readily observable using standard data-reduction techniques, allowing the near-real-time detection and measurement of cracks on surfaces. This technique was demonstrated using aluminum plates, and was also found to be superior to standard thermography systems for measuring these relatively small temperature changes.

ACKNOWLEDGEMENTS

The authors gratefully acknowledge the efforts of Henry Baust for the development of the camera control macros as well as his efforts on data reduction and analysis. Gary Clinehens is thanked for his contributions to conducting the experiments, including the operation of the thermography system, and his many suggestions crucial to the success of the program. The authors are indebted to Mike Fabian for his efforts in the areas of experiment set-up, data acquisition, and vibrational spectral analysis.

REFERENCES

- (1) Schubbe, J.J., "Thickness Effects on a Cracked Aluminum Plate with Composite Patch Repair," Dissertation, Air Force Institute of Technology, AFIT/DS/ENY/97-2, 1997.
- (2) Gallinan, R. J., Galea, S. C., and Sanderson, S., "Finite Element Analysis of Bonded Repairs to Edge Cracks in Panels Subjected to Acoustic Excitation," *Composite Structures* **1997**, 38(1-4), 649.
- (3) Gallery, J., Gouterman, M., Callis, J., Khalil, G., McLachlan, B., and Bell, J., "Luminescent Thermometry for Aerodynamic Measurements," *Rev. Sci. Instrum.* **1994**, 65, 712.
- (4) Liu, T., Campbell, T., Burns, S., and Sullivan, J., "Temperature and Pressure Sensitive Luminescent Paints in Aerodynamics," *App. Mech. Rev.* **1997**, 50, 227.
- (5) Dave, B. C., Dave, B., Valnetine, J. S., and Zink, J. I., "Sol-Gel Preparation of Biosensors," *Anal.Chem.* **1994**, 66, 1120A.
- (6) Lev, O., Tsionsky, M., Rabinovich, L., Glezer, V., Sampath, S., Pankratov, I., and Gun, J., "Organically Modified Sol-Gel Sensors," *Anal.Chem.* **1995**, 67, 22A.
- (7) Ingersoll, C. M. and Bright, F. V., "Using Sol-Gel Based Platforms for Chemical Sensing," *CHEMTECH*, **1993**, 27, 26.
- (8) Jordan, J. D., Dunbar, R. A., and Bright, F. V., "Aerosol Generated Sol-Gel Derived Thin Films: Biosensor Platform," *Anal. Chim. Acta* **1996**, 332, 83.
- (9) Williams, A. K. and Hupp, J. T., "Sol-Gel Encapsulated Alcohol Dehydrogenase as a Versatile, Environmentally Stable Sensor for Alcohols and Aldehydes," *J. Am. Chem. Soc.* **1998**, 120, 4366.
- (10) Watkins, A. N., Wenner, B. R., Jordan, J. D., Xu, W., Demas, J. N., and Bright, F. V., "A Portable, Low Cost, Solid-State Luminescence-Based O₂ Sensor," *Appl. Spectrosc.* **1998**, 52, 750.
- (11) Jordan, J.D., Watkins, A. N., Trump, D. D., Weaver, W. L., Goss, L. P., Dale, G. A., and Clinehens, G. A., "Ultrastable Blue LED Illumination Sources for PSP Applications," 1998 IHPTET Turbine Engine Technology Symposium, Advanced Instrumentation Workshop, September 17, 1998.

Investigations on a Dynamic Forebody Flow Control System

Ernest Hanff

Institute for Aerospace Research, Ottawa, Canada

Richard Lee and Richard J. Kind
Carleton University, Ottawa, Canada

Abstract

A novel method is proposed for the dynamic manipulation of forebody vortices of high-performance aircraft during flight at high incidence to provide increased lateral controllability when the control authority available from conventional control surfaces is dramatically degraded due to severe flow separation. The method takes advantage of the inherently bi-stable nature of the forebody vortices by deliberately switching them between their two stable states at a high frequency. Duty cycle modulation of the alternating blowing from two forward facing nozzles is used to control the mean lateral aerodynamic forces and moments. A series of wind- and water-tunnel experiments on ogive-cylinders and a schematic aircraft configuration have shown that by appropriately placing the nozzles, it is possible to obtain a linear relationship between duty cycle and mean control load, a highly desirable characteristic from a flight control point of view.

Nomenclature

b span

C_n Yawing moment coefficient $\frac{n}{q_\infty S b}$

C_Y Side force coefficient $\frac{Y}{q_\infty S}$

d Nozzle diameter

D Fuselage base diameter

C_μ Coefficient of blowing momentum $\frac{\dot{m}_j V_j}{q_\infty S}$

q_∞ Freestream dynamic pressure

S Reference area $\frac{\pi D^2}{4}$

V_j Control jet velocity

α Angle of attack

σ Body axis inclination to freestream velocity

ω Control switching circular frequency

Ω Control switching reduced frequency $\frac{\omega D}{U_\infty}$

Introduction

The flight envelope of high-performance aircraft is restricted by limitations in lateral controllability at high angles of attack, conditions under which control authority obtainable from conventional control surfaces is seriously degraded due to the presence of severe flow separation. The recognition of this phenomenon has led to a search for alternate lateral control methods, such as thrust vectoring and flow control mechanisms.

Long pointed forebodies typical of modern high-performance aircraft shed strong vortices that have a major effect on the overall flow around the vehicle and thus on the airloads as well. They tend to assume asymmetric positions over a significant range of angle of attack (Fig. 1), causing unacceptably large lateral loads that must be avoided. The conventional approach to reduce this problem is to choose appropriate forebody geometries and/or incorporate wing leading-edge extensions (LEXs) to delay the onset of asymmetric vortex shedding.

The capacity these vortices have in generating substantial airloads, however, offers the attractive possibility of exploiting them to significantly enhance controllability at high incidence. Of particular interest is the fact that small flow perturbations in the vicinity of the forebody apex can have a dramatic effect on the positions of the vortices, thus providing a potentially effective flow control mechanism.

Such forebody vortex manipulation has been investigated for several years, with most implementations being quasi-steady in which the airloads are generated by forcing the forebody vortices to assume prescribed positions relative to the forebody in order to generate the desired airloads [1]. This approach, however, requires that the above mentioned bi-stable nature of the vortices be first overcome, for example by proper tailoring of the forebody geometry or the use of strakes, to force them to acquire a symmetrical stance. The desired loads are then generated by introducing mechanical or pneumatic perturbations to move them to an asymmetrical position. This approach has the drawbacks that considerable power may be required to overcome the artificially induced symmetry and the behavior of the airloads in terms of the control parameter may be highly non-linear, which would result in complex and even unreliable control laws.

As an alternative to the quasi-steady forebody flow control approach, a novel dynamic method has been proposed by the authors, which has the potential of avoiding the above problems [2],[3],[4],[5]. Rather than suppressing the bi-stable arrangement of the vortices, advantage is taken of the fact that minute perturbations are sufficient to cause the arrangement to switch state. Specifically, the forebody vortices are deliberately switched back and forth between their two stable states at a sufficiently high frequency such that the aircraft cannot respond significantly to the resulting instantaneous loads because of its large inertia. The aircraft does, however, respond to the time-averaged loads generated by the manipulation. These loads are, in turn, controlled by varying the fraction of the switching-cycle period during which the vortices are in one or the

other state, i.e. by modulating the switching duty cycle. The concept is illustrated in Fig. 2.

In order to investigate the practicality of the dynamic flow control method, preliminary water tunnel experiments were conducted on an ogive-cylinder configuration which demonstrated the potential of the proposed flow control method [2]. Very low blowing was required to switch the orientation of the vortices and their short response time suggested that sufficiently high switching frequencies could be achieved. In view of these results, more comprehensive wind tunnel experiments were conducted on a scaled-up version of the model (Fig. 3). The side force coefficient as a function of steady blowing through one nozzle for different angles of attack is shown in Fig. 4, where it can be observed that a very small blowing coefficient is required to cause a reversal in the side force, and that additional blowing does not significantly affect the resulting force. The side force and yawing moment due to steady blowing through one nozzle ($C_{\mu} = 0.00066$) are shown in Fig. 5. The symmetry of the loads for blowing from either nozzle indicates that the baseline loads resulting from the inherent asymmetry of the vortices, are effectively overcome. Similar results at higher Reynolds number did not exhibit the same degree of symmetry. A possible reason for such behavior is that the nozzles were located too far aft, such that the influence of the weak control jets did not reach sufficiently far into the apex to act effectively.

The effect of blowing duty cycle on the side force and yawing moment for various angles of attack and at a reduced switching reduced frequency $\Omega = 0.32$ is shown in Fig. 6. The curves exhibit remarkable linearity, which as already mentioned, is of importance from a flight control perspective. It should be pointed out that, in view of the side force behavior, the change in slope for the yawing moment as a function of angle of attack, is due to the fact that the center of pressure moves across the moment reference center. It was decided, on the basis of the encouraging results obtained with the forebody geometry, to test the flow control method on a more representative schematic aircraft configuration. The experimental arrangement, instrumentation, and highlights of results are of these tests are discussed in the following sections.

Experimental setup

Force and moment as well as surface oil flow investigations were performed in a 2m x 3m low speed wind tunnel, whereas off-surface flow visualization experiments, required to gain a better understanding of the flow, particularly near the forebody apex, were performed at a 50 cm by 75 cm water tunnel.

Wind-tunnel experiments

A view of the experimental setup in the IAR 2m x 3m low speed wind tunnel is shown in Fig. 7. The angle of attack is obtained by synchronously rotating the test section roof and floor turntables that support the vertical strut, while sideslip is obtained by rolling the sting about its axis. The length of the sting was selected such that

the model would be situated as far as possible from the vertical strut to minimize support interference effects, while ensuring that at high angles of attack (70° - 80°) the model tip would not be too close to the test section wall, to avoid significant wall interference. As a result of these requirements and the given radii of the turntables, the model moves away from the wind-tunnel centerline as the angle of attack is increased. The model is mounted on a specially made single-piece construction five-component balance (no axial force) located at the end of the sting.

Although it would have been best to retain the original forebody geometry to avoid changing too many parameters in these experiments, practical considerations dictated that an existing model be used after modifying it to accommodate the flow control system. The model, originally built for dynamic experiments, has a 65° delta wing, cylindrical forebody and vertical tail (Fig. 8). The wings and vertical tail are made of multi-layer graphite composite skin and foam core, the fuselage is entirely graphite composite and the forebody is made of a thin aluminum alloy shell. This type of construction was dictated by the requirement for high strength and stiffness with a minimum of weight, imposed by the conditions encountered in advanced dynamic testing.

Flow control is provided by alternatively blowing through two forward facing nozzles (1.5 mm internal diameter) located near the forebody apex. Switching of the blowing from side to side is accomplished by means of two high-speed solenoid operated pneumatic valves, each in series with one of the nozzles and located within the forebody, which divert the flow arriving through a common air line fed through the hollow sting and balance. Mass flow rate is measured by observing the pressure drop across 0.75 mm orifices on each of the nozzle supply lines and controlled by adjusting the supply pressure. Fig. 9 shows the flow control switching arrangement installed on the mounting bracket which also supports the flow sensors. Given the differences in response time between the valves as well as between opening and closing times, each valve is independently driven by signals tailored to ensure a simultaneous switching of the flow through both nozzles in spite of the fact that the valves are operating near their limit of dynamic capabilities. A number of interchangeable forebody tips divided into three families with different axial nozzle locations, and several angular locations, were used in order to determine the optimum geometry for best control. A listing of the tips is shown in Table 1, where the angular location is defined with respect to the leeward meridian.

Two orthogonally oriented accelerometers, also mounted on the above bracket, are used to monitor the model vibration. As a safety measure, a circuit constantly senses the accelerometer outputs, so that, as is discussed below, if a certain threshold is exceeded, a large flow coefficient is automatically applied through one of the nozzles to suppress the motion.

The data system, used to acquire the data is tailored to effectively handle the large amount of information produced by dynamic tests, such that the wind tunnel

can be efficiently utilized. It is based on a dual processor system with a real-time UNIX operating system for maximum flexibility and performance.

Generally the data of interest consists of forces, moments and pressures coherent with the model motion or, in this case, with the control blowing. The signals are typically contaminated by noise, mainly due to flow unsteadiness and model vibration, which must be minimized to obtain representative results. This is accomplished by ensemble averaging the signals obtained over a number of control blowing cycles, which in turn requires that the data be sampled synchronously with the blowing. During the experiment the operator uses a real time display of the ensemble averaged signals to assess the duration of the data acquisition process. Initially the ensemble average varies a great deal from one record to the next but this difference gradually decreases until there are no more perceptible changes, at which time the sampling process is stopped. Typically sampling for thirty seconds to one minute is sufficient for the ensemble average to reach its final value. Repeatability of the results has been found to be excellent. For the present experiments, the required average of the loads over a blowing cycle is obtained by averaging the points on the final ensemble average.

Surface oil flow visualization tests were also conducted as part of the wind-tunnel experiments in order to better understand the behavior of the flow and thus infer ways to more effectively control it. A mixture of titanium dioxide and oil was used. Its viscosity was controlled by choosing the appropriate type of oil, such that the skin friction patterns established themselves when the freestream velocity had reached its desired value. Videos were taken during the pattern development and still photographs upon completion of the runs, which imposed the additional requirement that the surface oil pattern not change during the slowing down of the wind tunnel flow.

Water-tunnel experiments

Previous wind-tunnel tests on the ogive cylinder model demonstrated that laser sheet smoke flow visualization was ineffective for observing the small scale phenomena taking place in the vicinity of the model tip [3]. Since these phenomena are the ones that largely dictate the flow behavior elsewhere, off-surface flow visualization tests were performed in the University of Ottawa water tunnel. Because of the relatively small size of the water tunnel, the model used in these tests was just the forebody of the schematic aircraft tested in the wind tunnel. Flow visualization was accomplished by releasing fluorescent dye upstream of the model tip and/or by adding dye to the nozzle control flow. The dye was pressure fed and the flow controlled with appropriate valves. A broad range of control blowing coefficients was used to investigate some unexpected phenomena observed in the wind-tunnel tests.

Results and discussion

As already mentioned, the experiments on the schematic aircraft model were motivated by the good results obtained in the earlier tests on an ogive cylinder

configuration and by the desirability of clarifying the effect of the presence of lifting surfaces on the effectiveness of the control method and its observed Reynolds number dependence.

Given the well known importance of even micro asymmetries at the model apex in determining the vortex behavior, the position of the nozzles was moved as much forward as practical relative to the one used in the previous forebody experiments, such that the control jets would act where they could have the most influence. The effect of blowing coefficient under steady blowing through one nozzle for $\alpha = 45^\circ$ and $U_\infty = 40$ m/s is shown in Fig. 10. The small asymmetry around the origin reflects the fact that with no blowing the port and starboard vortices are lifted off and attached respectively. A blowing coefficient of $C_\mu \sim 0.0004$ through the starboard nozzle is sufficient to reverse the state of the vortices. Above this value of C_μ a plateau is reached where additional blowing has no effect, until a certain threshold in the blowing coefficient is reached, where a force and moment reversal occurs. This unexpected result was found to be present with all the tips tested. The threshold C_μ value, however, is larger for nozzles located further aft, which may explain why the reversal was not observed in the earlier experiments. The cause of the reversal appears to have been elucidated by means of the water-tunnel flow visualization tests.

A water-tunnel flow visualization image obtained with low blowing (with dye) from the port nozzle and with dye released upstream of the model tip is shown in Fig. 11(a), where it is observed that the flow from the nozzle becomes entrained in the core of the port side vortex which lifts off the model surface, while the starboard vortex remains close to the model surface, leading to a positive side force, corresponding to the "normal" situation. Fig. 11(b) depicts a laser sheet frontal view of the vortices at a downstream station using fluorescent dye. Fig. 12(a) and Fig. 12(b) on the other hand, show the same views for a higher blowing coefficient. In this case the control jet penetrates through the shear layer and does not become entrained in the vortex, yielding the "reversed" position of the vortices and reversed loads.

The side force and yawing moment as a function of angle of attack for a steady blowing coefficients below and above the reversal threshold are shown in Fig. 13 and Fig. 14 respectively. It can be observed that in both cases the yawing moment baseline asymmetry is overcome by blowing, which is not the case with the side force as demonstrated by the asymmetry of the latter for port and starboard blowing. This effect can be explained by the fact that most of the side force created by the vortices is applied on the forebody, which due to the long arm length with respect to the model moment center, results in a significant yawing moment. The side force asymmetry of about $\Delta C_y = 0.007$ is of little practical consequence and appears to be due to contributions unrelated to the blowing and acting near the resolving center, thus not producing a significant yawing moment.

The same reversal in the loads shown in the previous figures is present under dynamic conditions when the blowing is switched between the nozzles. Fig. 15 shows the effect of duty cycle for $C_{\mu}=0.005$ which exceeds the threshold value. Again it is interesting to note the good linearity of the yawing moment in terms of the blowing duty cycle.

During the experiments, particularly at higher speeds, under some combinations of angle of attack, freestream velocity and forebody tip, lateral oscillations were induced which quickly diverged to unacceptable amplitudes (over 2 cm at the model tip). Concern for the structural integrity of the balance and support system (particularly the sting) prevented testing over a variety of conditions that were included in the original test schedule. The observed vibration frequency of approximately 30 Hz corresponds to the resonance frequency of the model-support system in the model yaw plane. It appears that the vibration is caused by a positive feedback between the motion-induced sideslip (up to 10°) which can force the vortices to switch state and the resulting reversal in the side force. This hypothesis seems to be corroborated by the fact that a strong steady blowing through one of the nozzles suppressed the oscillation, apparently by overcoming the tendency of the vortices to switch states due to the induced sideslip. If the suspected mechanism is indeed the reason for the oscillation, the problem is an artifact of the experiment as it relies on the restoring force provided by the stiffness of the support system, which would not be present under flight conditions.

Although the experiments on the schematic aircraft model were generally successful in that they corroborated the potential viability of the proposed control mechanism on a more realistic configuration, vibration problems encountered during the tests prevented the use of higher wind speeds to establish the effectiveness of the method at higher Reynolds number. The peculiar reversal of the vortex states for blowing exceeding a threshold value appears to be due to the control jets penetrating through the shear layer near the forebody apex. This phenomenon is probably connected to the fact that the nozzles are located significantly further forward than in the earlier experiments, but it is also possible that the considerably smaller tip half angle (12.8° vs 28° in the earlier model) may also influence this process.

Conclusions

- Preliminary tests on a schematic aircraft configuration suggest that the proposed dynamic forebody flow control method is feasible on realistic configurations
- Although very little blowing is necessary to control the vortex states, an unexpected reversal was found when blowing exceeds a particular threshold value. This value was found to be lower the closer the nozzles were to the forebody apex
- The evidence indicates that the reversal occurs when the blowing jet penetrates the free shear layer

before it rolls up into the forebody vortex. Blowing coefficients either well above or well below the threshold value must therefore be used to avoid this undesirable reversal

- Vibration problems encountered under some conditions, particularly at higher speeds prevented assessing the effectiveness of the control method at higher Reynolds number. The vibration problem however, seems to be an artifact of the experiment inasmuch as it requires a mechanical resonance at a certain frequency that would not be present in actual flight
- The importance of the small forebody tip half angle on the above two phenomena remains to be established

References

- Malcolm, G., "Forebody Vortex Control - A Progress Review" AIAA Paper 93-3540, August, 1993
- Alexan, K., Hanff, E.S. and Kind, R.J., "Water-Tunnel Investigations of Dynamic Manipulation of Forebody Vortices", AIAA Paper 94-0503, Jan., 1994
- Lee, R., Hanff, E.S. and Kind, R.J., "Wind-Tunnel Investigation of Dynamic Manipulation of Forebody Vortices", AIAA Paper 95-1794, June, 1995
- Hanff, E.S., Lee, R. and Kind, R.J., "A Dynamic Forebody Flow Manipulation Method for Lateral Control", NPU/AIAA AFM Paper 96-043, June, 1996.
- Lee, R., Hanff, E.S. and Kind, R.J., "The Dynamic Manipulation of Forebody Vortices on a 65° Delta-Wing Model", CASI Aerodynamics Symposium, May, 1999

Table 1: Nozzle locations

Tip ID	Nozzles axial location [x/D]	Nozzles angular location [°]
6-1	0.095	60
2-2	0.095	45
9-3	0.159	61
4	0.159	57
11-5	0.159	53
1-7	0.159	45
8	0.159	41
5-9	0.159	37
10	0.159	33
11	0.159	29
12	0.247	50
3-13	0.247	45
14	0.247	40
15	No nozzles	

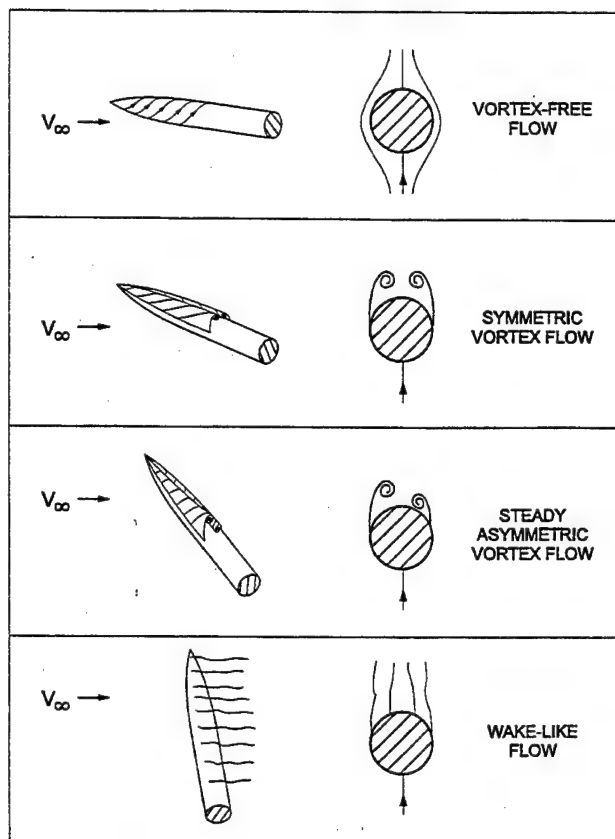
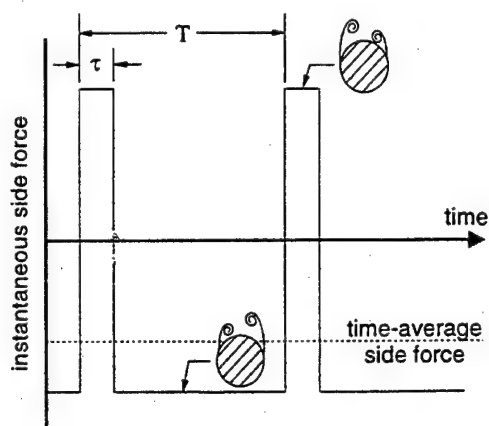
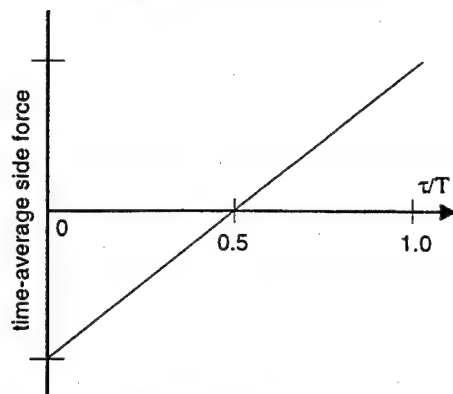


Fig. 1 Effect of angle of attack on forebody vortices



(a) Side force time history



(b) Expected variation of time-average side force with duty cycle

Fig. 2 Principle of dynamic forebody vortex manipulation

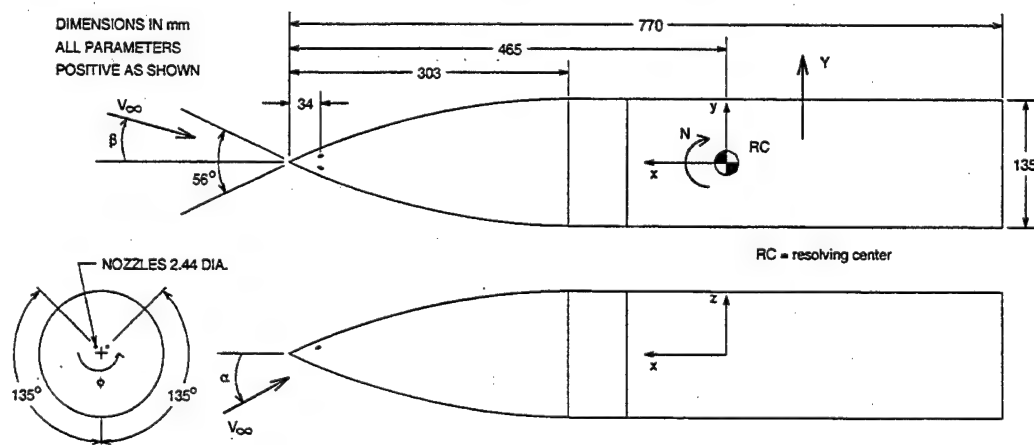


Fig. 3 Ogive-cylinder model used in preliminary tests

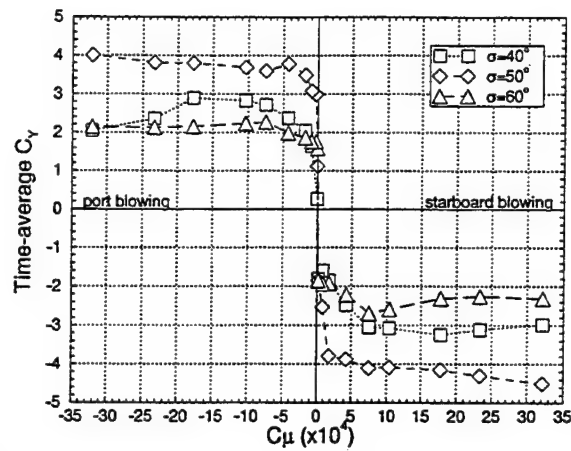


Fig. 4 Effect of blowing coefficient and angle-of-attack on side force. ($Re_D = 176000$)

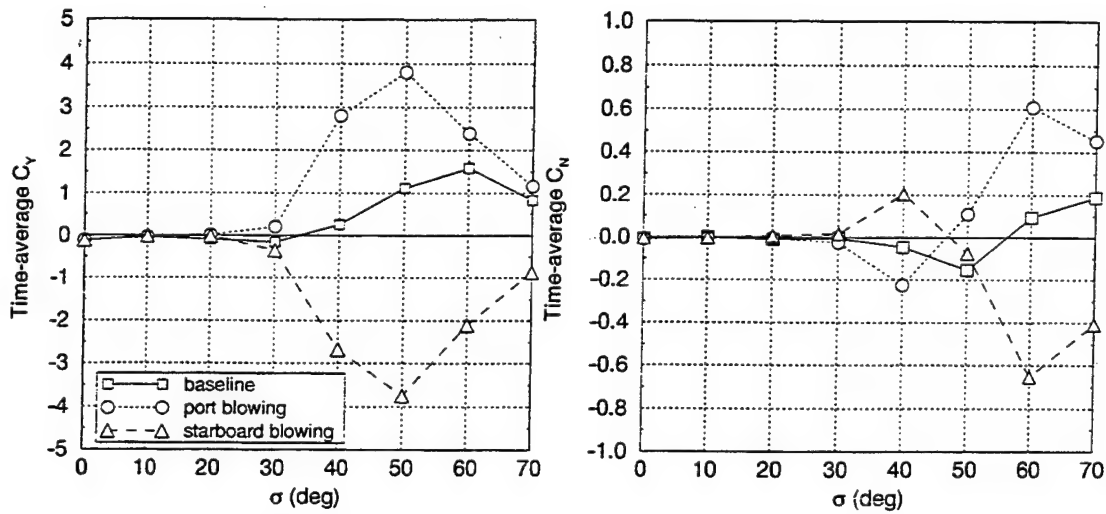


Fig. 5 Side force and yawing moment on ogive cylinder for steady blowing ($C_\mu = 0.00066$, $Re_D = 176,000$)

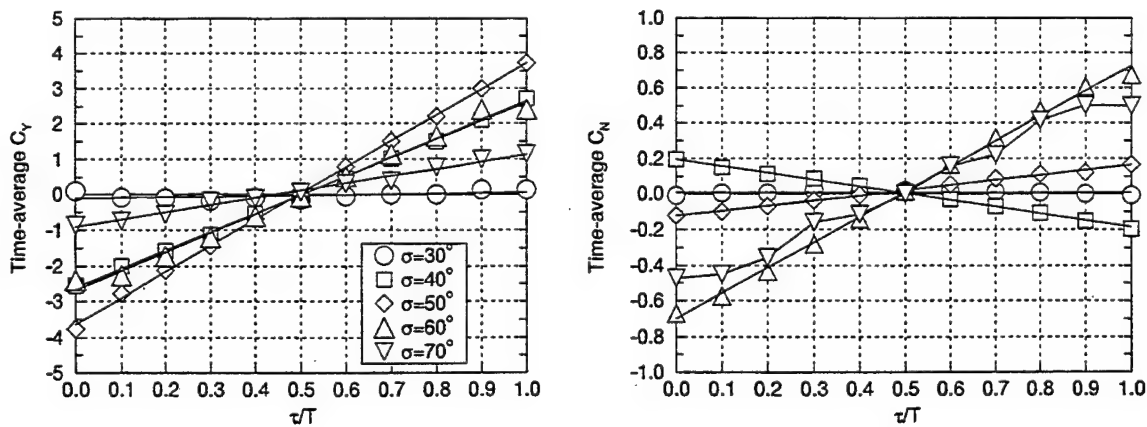


Fig. 6 Effect of port duty cycle on side force and yawing moment. ($C_\mu = 0.00066$, $Re_D = 176,000$, $\Omega = 0.32$)

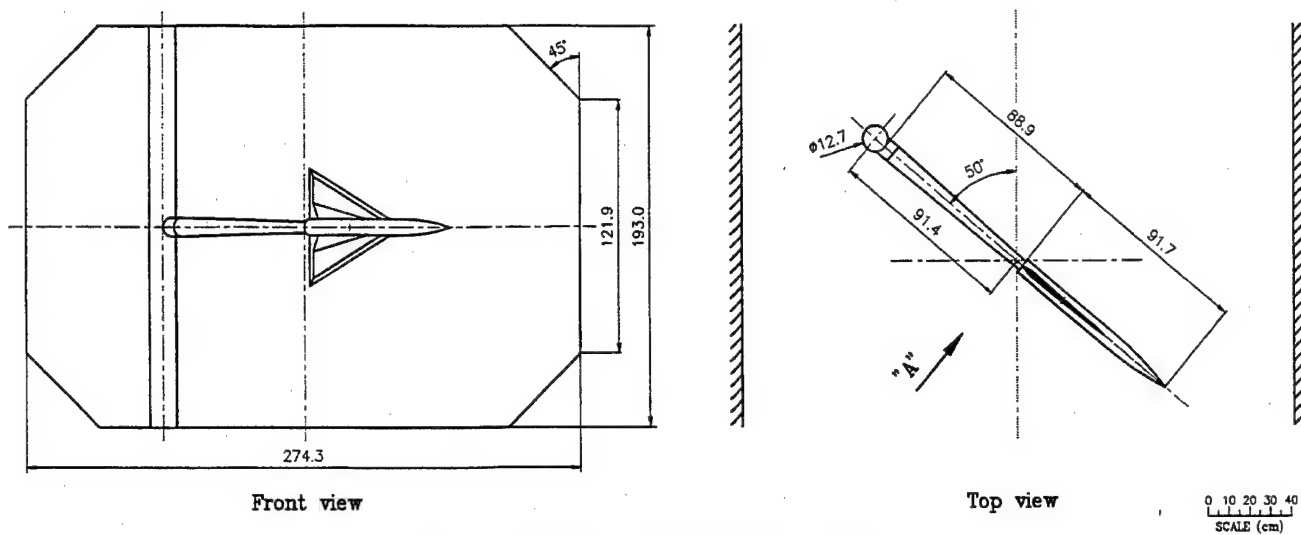


Fig. 7 Experimental setup in IAR's wind tunnel

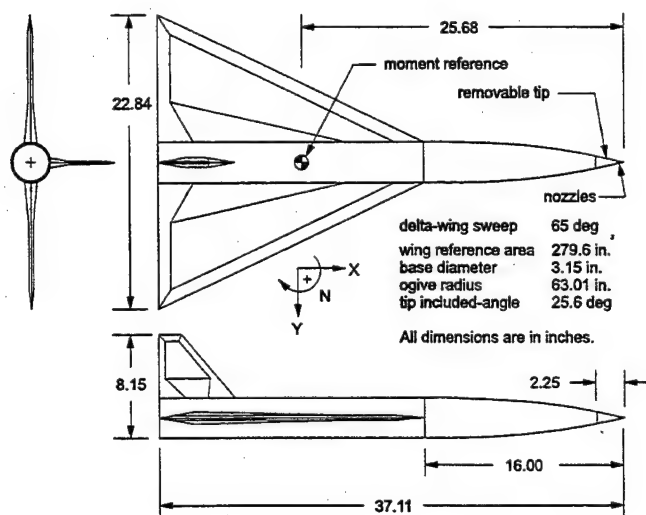


Fig. 8 Schematic aircraft model

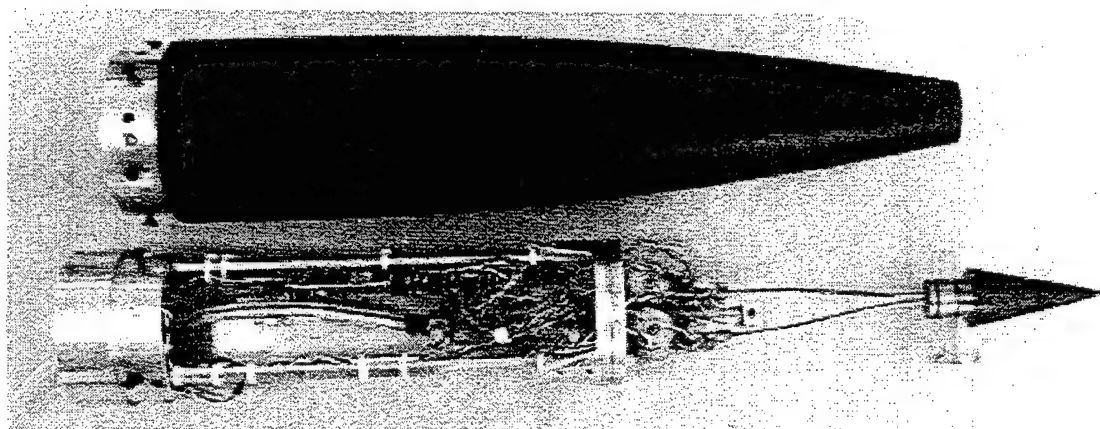


Fig. 9 Flow control switching arrangement

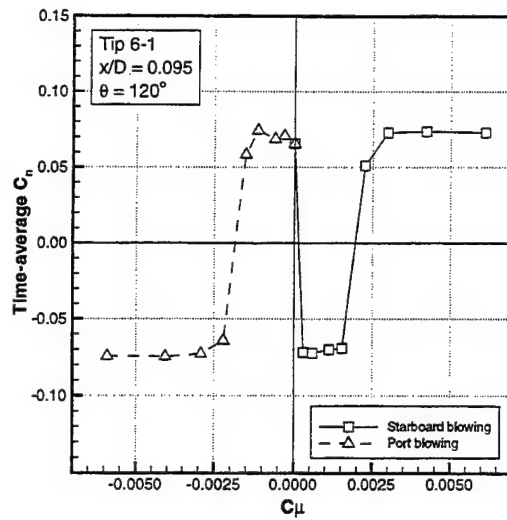


Fig. 10 Effect of steady blowing on yawing moment (Schematic aircraft model, $Re_D=196000$, $\alpha=45^\circ$)

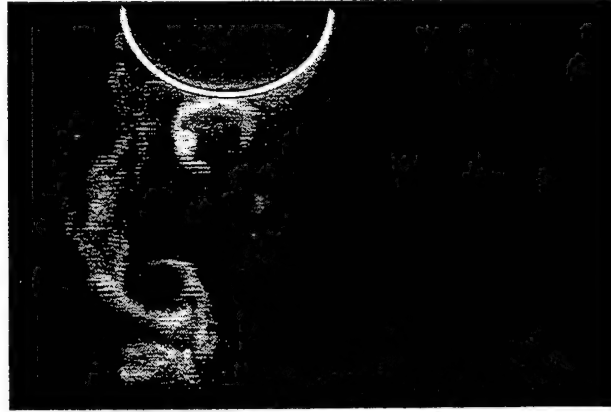
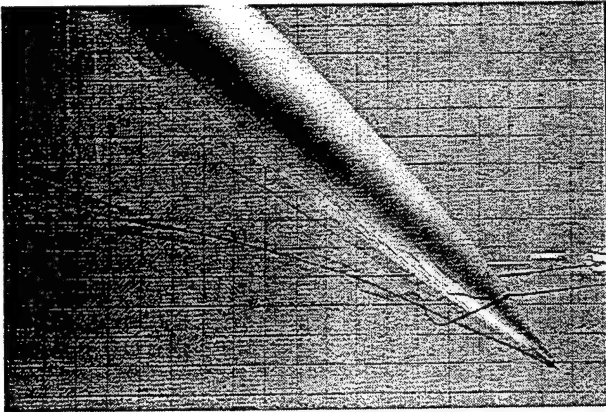


Fig. 11 Water tunnel flow visualization (Tip 2-2, $\alpha = 45^\circ$, C_μ below threshold level)

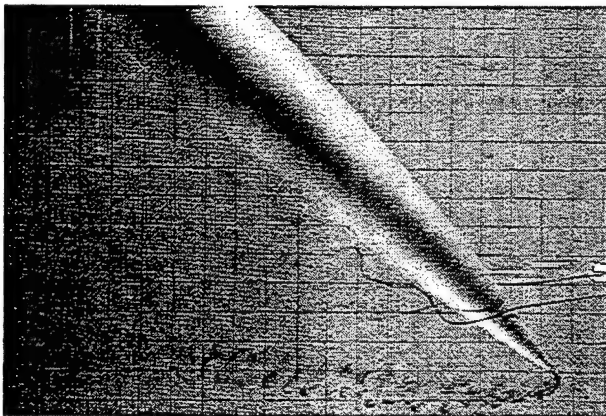


Fig. 12 Water tunnel flow visualization (Tip 2-2, $\alpha = 45^\circ$, C_μ above threshold level)

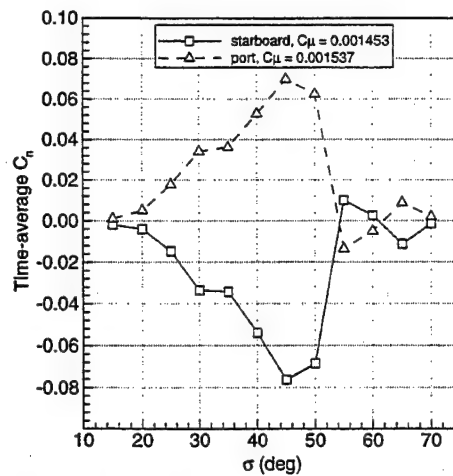
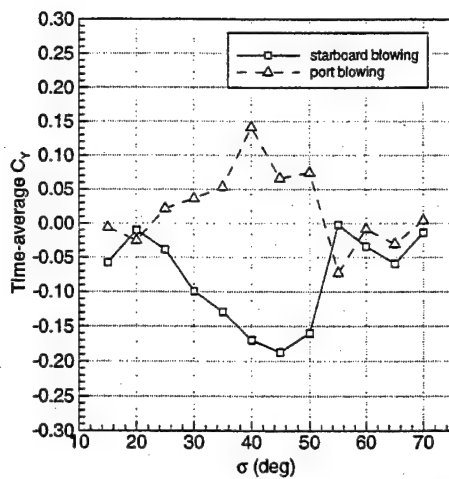


Fig. 13 Effect of steady blowing on side force and yawing moment ($Re_D=100000$, $C_{\mu}=0.0015$)

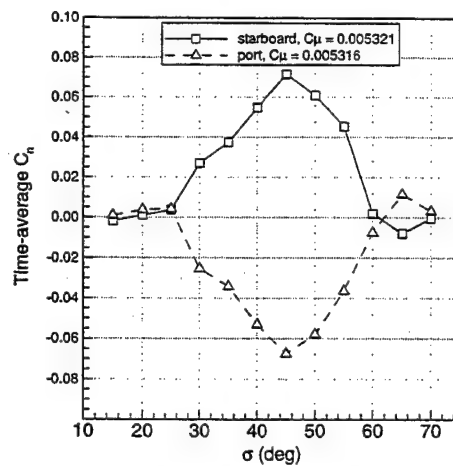
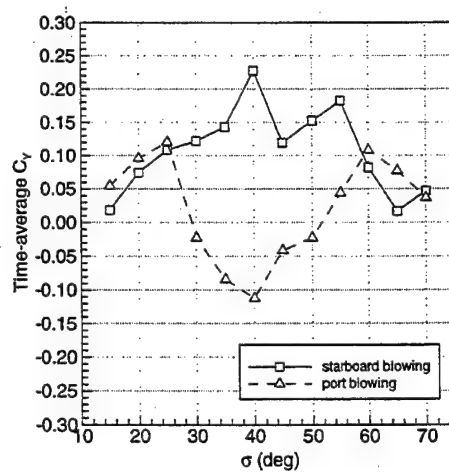


Fig. 14 Effect of steady blowing on side force and yawing moment ($Re_D=100000$, $C_{\mu}=0.0053$)

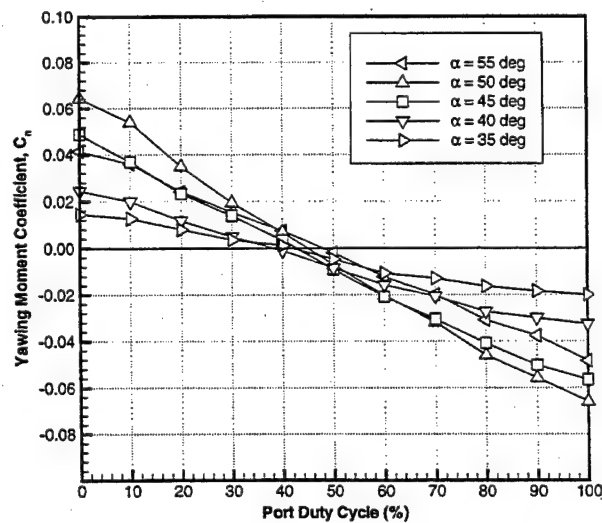


Fig. 15 Effect of blowing duty cycle on average yawing moment ($Re_D=196000$, $C_{\mu} = 0.00237$)

NEW ONERA SET-UPS FOR THE CHARACTERIZATION OF THE RESISTANCE OF MATERIALS TO LIQUID AND SOLID IMPACTS

by A.A. Déom, M. Lemistre and D.L. Balageas
ONERA, 29 Avenue de la Division Leclerc, F92320 Chatillon CEDEX

ABSTRACT

ONERA is involved in rain erosion studies since 1973. Rotating arms were used firstly to characterize the resistance of the materials with droplet velocities in the range 200-300 m/s. In the 1990's, the Cavendish Laboratory in Cambridge developed a new apparatus, called MIJA (Multiple Impact Jet Apparatus), which can automatically produce water jets at high velocities. ONERA is using a MIJA apparatus in its Chatillon Center since 1994. The set-up was first validated in the range 200-300 m/s by comparison with rotating arm results. It is used now up to 600 m/s. The possibility of characterizing in-shape samples like radomes, as well as the determination of the influence of temperature and stress in the samples were studied. A second water jet apparatus called SIJA, is used since mid 1998. It allows rain erosion resistance measurements up to 1000 m/s.

Our possibility of characterization of material impact resistance was completed by an other set-up called SPARC (Solid Particle Rebound Characterization apparatus) devoted to solid particle impact studies up to 190 m/s. Thanks to a bidimensionnal velocimetry laser measurement, SPARC allows the determination of the angle and of the velocity of rebound of a solid particle on a target.

CHARACTERIZATION OF THE RAIN EROSION RESISTANCE OF MATERIALS

Introduction

With the increasing speed of military planes and missiles, rain erosion becomes a more and more difficult problem. The rain erosion resistance of the materials of a plane or of a missile exposed to heavy rain conditions must be known before drawing a project.

In-flight rain erosion characterization of materials is expansive and the knowledge of the parameters of the encountered rain necessitates numerous and sophisticated apparatus.

On-ground measurements using simulation apparatus are easier and cheaper. One can cite some of the different available systems : rotating arms, linear tracks, wind tunnels, water jet generators.

Linear tracks (i.e. Holloman track in the US), and wind tunnels are huge set-up, quite expansive, whose main interest is the possibility to test realistic structures and, for some of them, at very high velocities. They must be used in the final step of a development program.

Rotating arms are less expensive. Such set-ups are available in USA (Wright-Paterson AFB...), in Germany

(Dornier rig), in Sweden (SAAB-SCANIA rig), in England (DERA rig).

For twenty years, the Cavendish Laboratory in Cambridge has developed single impact water jet generators (SIJA) interesting to characterize the resistance of a material to a liquid impact. More recently this group manufactured the multiple impact generator MIJA. With such an apparatus it is possible to obtain rain erosion data in the laboratory, thus at a cheaper cost. ONERA operates a MIJA since mid 1994 and a SIJA since mid 1998.

MIJA Set-up

brief description

A full description of MIJA can be found in [1]. One can see figure 1 a photo of MIJA set up. MIJA is enclosed in a soundproof cabinet in order to minimize the noise produced by the waterjet itself and the pumping device.



Figure 1 : MIJA apparatus

A jet of water is produced by applying a pressure of several bars in the system, which involves a main pressure vessel, a discharge tube, a nylon piston, a titanium shaft, and a thin nozzle. The sample is exposed to the jet thanks to X-Y stages positioning it randomly to simulate the erratic impacts of a real rain.

Aside, the electronics racks controlling the system and a microcomputer can be seen. All the parameters of the impact are given to the operator thanks to a userfriendly software and all experimental conditions effectively obtained are shown on the monitor and stored.

MIJA characteristics

The apparatus generates successive waterjets which impact the specimen whose rain erosion resistance has to be determined. The 0.8 mm-dia. nozzle throat generates water jets composed of a 2 mm-dia. half sphere followed by a cylindrical queue 1 mm in diameter and 8 to 10 mm long.

The velocity of each water jet, measured by optical fibres barriers, is depending mainly on the pressure introduced in the main pressure vessel. For the maximum value, 6.8 bars, the water jet velocity goes up to 600 m/s. The maximum repetition rate is 12 shots/mn. The sample diameter can go up to 100 mm.

Rain simulated by MIJA

The shape of the water particles delivered by MIJA being not spherical like a "conventional droplet", it was necessary to define an equivalence between MIJA jets and spherical droplets. The Cavendish lab established a correlation between the real velocity of the jet and the velocity of a 2 mm-dia. droplet producing the same damage. The correlation is given in figure 2. The problem is in the definition of the damage chosen for the comparison (see later).

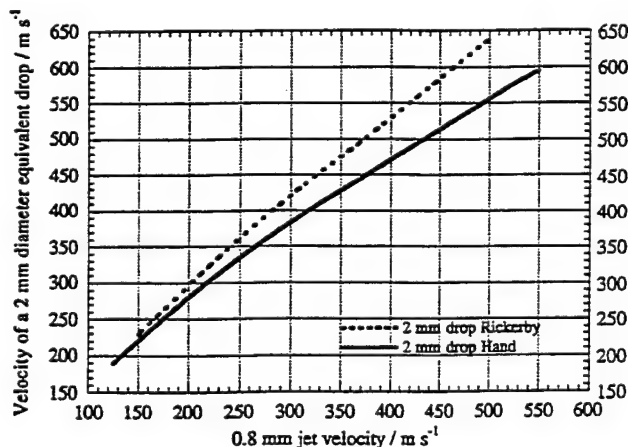


Fig. 2 : Conversion chart from a 0.8 mm dia. throat nozzle MIJA water jet threshold velocity to that of a 2 mm drop using the correlations obtained by Hand (1987) et Rickerby (1976).

The rain erosion resistance of a material is given by the rain exposure time which creates a given level of degradation (mass loss, loss of transmission...). With MIJA there is no continuous flow of rain droplets as in a real rain. Thus we have to convert the number of impacts per unit surface into a corresponding exposure time of rain.

One can easily show [2] that the equivalent rain exposure time \bar{t} can be determined from the number of impacts generated by MIJA using the formula :

$$\bar{t} = 10^6 N (D_g)^3 / 1,5 (D_i)^2 V$$

where \bar{t} is the equivalent normalized rain exposure time (s) corresponding to a normalized water concentration $C_0 = 10^{-3} \text{ kg/m}^3$, N the number of MIJA impacts produced on the sample, D_g the equivalent MIJA droplet diameter (m), D_i the diameter of the part of the sample exposed to MIJA impacts (m), V the MIJA equivalent droplet velocity (m/s).

Figure 3 shows as an example the evolution of the front face of a ZnS sample when increasing the cumulative number of impacts, i.e. the cumulative rain exposure time. This degradation of the material observed in the visible (photography) is accompanied by a decrease of its infrared transmission. We will particularly notice the time $\bar{t}_{0.1}$ corresponding to a 10% loss of transmission (optical incubation time) .

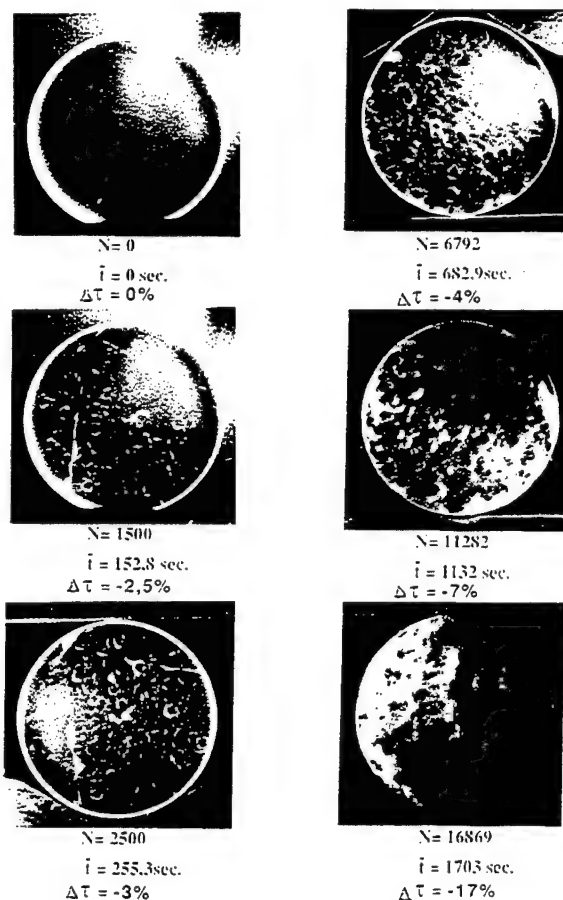


Fig. 3 : Evolution with number N of MIJA impacts and corresponding normalized equivalent rain exposure time \bar{t} of a ZnS sample and of its transmission τ in the 8-12 μm range (nozzle throat dia. 0.8 mm, $V_{\text{jet}} = 162 \text{ m/s}$, $V_{\text{equ. 2 mm droplet}} = 196 \text{ m/s}$)

Validation of MIJA in the range 200-300 ms⁻¹ by comparison with rotating arms

Different experiments were conducted to determine :

- if MIJA can produce materials degradations qualitatively comparable to those obtained with rotating arms,
- if MIJA rain erosion resistance ranking of materials is in good accordance with previous measurements obtained with rotating arms,
- if, for a given material, rain erosion data from MIJA is in good accordance with previous rotating arm measurements.

We used as reference rain erosion results of infrared materials tested with the SAAB-SCANIA rotating arm. ZnS, Ge and MgF₂ samples were eroded using MIJA with about the same velocities used with the SAAB-SCANIA rotating arm. The mean droplets diameter used with the rotating arm was 2 mm that corresponds to the diameter of the front head of a MIJA jet.

For ZnS and Ge samples, no evident difference in the morphology of the degradations can be seen between the rig and MIJA. For MgF₂ samples, precisely monocrystalline MgF₂, one can see a little difference between MIJA and SAAB degradations. Numerous degradations due to small particle impact diameter can be seen with the SAAB rig.

The velocity dependence of the normalized 3.5-6 μ m range optical incubation time $\bar{t}_{0.1}$ obtained with the two facilities is compared in fig 4 for the three materials.

For MIJA measurements, the velocity of the equivalent 2mm droplet diameter was calculated using Hand correlation previously presented. For the three materials and in the two optical ranges, it appears an overestimation of their rain erosion resistance in comparison with SAAB results.

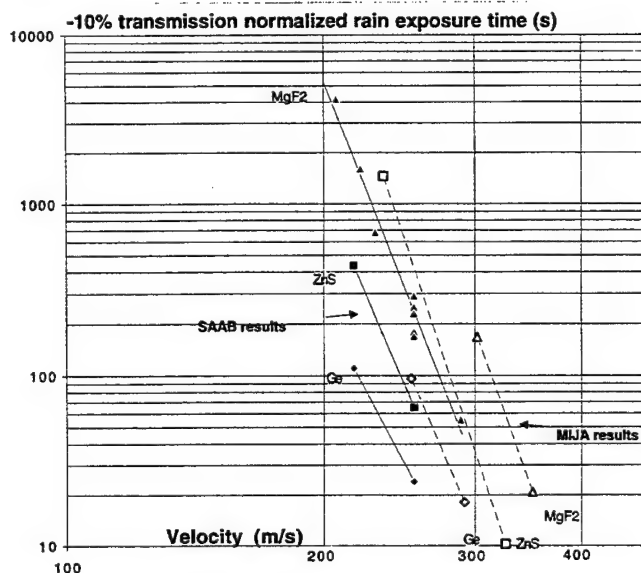


Fig. 4: Comparison for three IR materials of the dependance of the normalized characteristic optical time $\bar{t}_{0.1}$ (transmission range 3.5 - 6 μ m) on the droplet velocity measured with MIJA (dashed lines) and with the SAAB rotating arm (full lines). For MIJA the equivalent 2 mm drop velocities were determined using Hand correlation.

Consequently, we searched if it was possible to find a simple relation, between the MIJA jet velocities and the droplets velocities, owing a better agreement between MIJA and SAAB results.

The following law : $V_{\text{equ.}} = 1.21 V_{\text{jet}}$ was found to give the best agreement between MIJA and SAAB results for the transmission measurements in the 3.5-6 μ m range (figure 5). For the 8-12 μ m range, we found that the same law but with a coefficient equal to 1.26 was the best.

When taking into account the low number of experimental points, the difference in the multiplication factor is not significant and we will keep the first law.

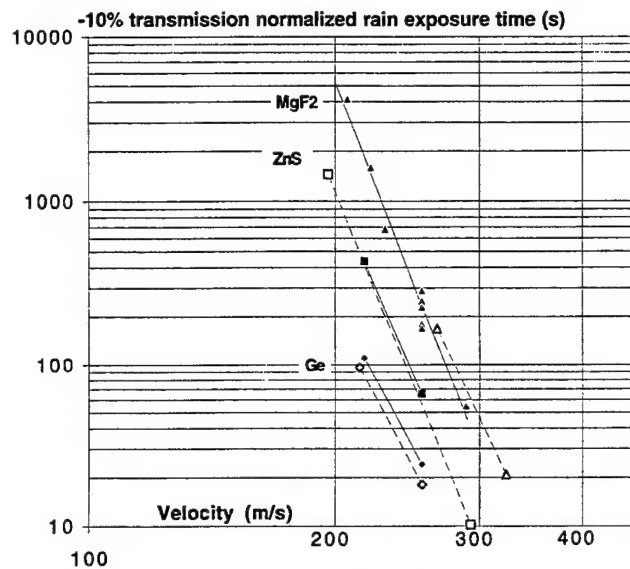


Fig. 5 : Same as Fig. 4, but for MIJA the equivalent 2 mm drop velocities were determined using the relation : $V_{\text{equ.}} = 1.21 V_{\text{jet}}$.

One can see figure 6 a comparison between Hand, Rickerby and ONERA laws. The discrepancies between ONERA correlation and the previous laws is not surprising since the types of damages used for comparing jets and droplets are not the same :

- very early damages for Hand and Rickerby laws,
- optical incubation time for ONERA.

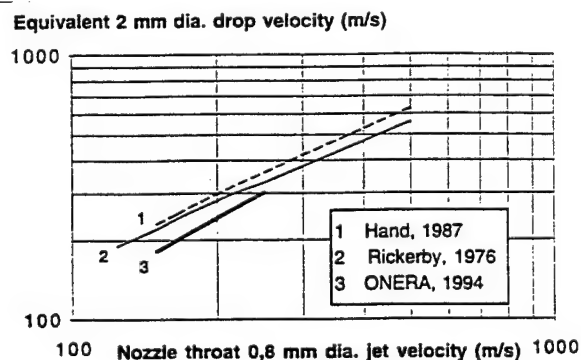


Fig. 6 : Comparison of the correlation curves between MIJA jet velocity and equivalent 2 mm drop velocity.

One can notice anyway that the extrapolation of the ONERA law to higher velocities gives something intermediate between Rickerby and Hand laws.

Rain erosion resistance characterization using MIJA up to 600 ms⁻¹

One can see figure 7 the results of the characterization using MIJA of sapphire up to 610 ms⁻¹, and a comparison of the results with the DORNIER rig. For a same velocity, the characteristic optical time $\overline{t}_{0.1}$ is higher with the German rig which is in good accordance with the respective diameters of the particles used: 2 mm for the water jet generator and 0.5 mm for the DORNIER rig.

Characteristic optical time $\overline{t}_{0.1}$ (m/s)

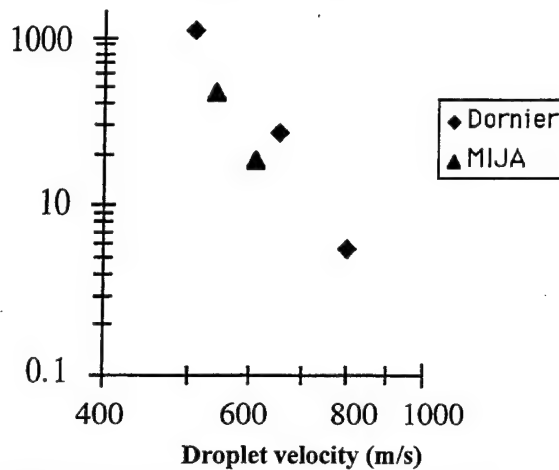


Fig. 7 : Comparison with sapphire of water jet measurements using MIJA and of previous DORNIER rig measurements.

In-shape samples characterization

The large volume between MIJA nozzle and the X,Y stages gives the possibility to test in-shape samples like small radomes (Figure 8).

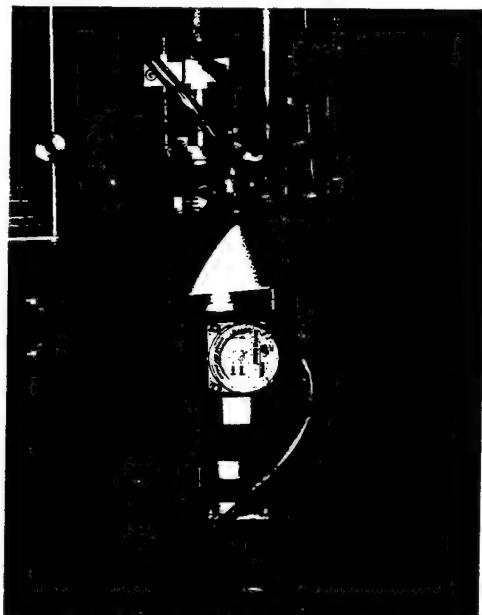


Fig. 8 : Characterization using MIJA of the rain erosion resistance of a small coated radome.

In that case, the three X,Y,Z orthogonal stages are moving step by step, taking into account the profile of the radome, in order to keep a constant value of the distance between the output of the nozzle and the radome. There is a limitation in the angle between the direction of the jet and the tangent at the profile at the impact point which must not exceed 45°.

Influence of the inflight environmental conditions such as temperature and stress

Special holders were built owing the possibility to make erosion measurements with heated samples up to 200°C or samples under stress [3]. One can notice the large influence of these two parameters on the rain erosion resistance of the tested materials [4].

SIJA Set-up

SIJA (Single Impact Jet Apparatus) is also a water jet generator. The liquid impact jet gun is a converted 0.22 inch air rifle. A gas reservoir filled from a compressed gas cylinder is attached to the breech via a fast action solenoid valve. At the extremity of the gun barrel is put a nozzle filled with water and closed by a neoprene diaphragm. When firing the solenoid valve, the lead slug put in the breech is propelled in the gun barrel and hurts at high velocity the neopren diaphragm producing a water jet. The jet moves at high velocity and impacts the front face of the sample whose rain resistance must be determined. The use of this technique allows a range of velocities between 100 and 1000 m/s. Jet velocities are measured by means of optical fibers barriers.

One can see figure 9 a comparison with sapphire of first SIJA measurements to MIJA and DORNIER rig measurements previously presented in figure 7.

Characteristic optical time $\overline{t}_{0.1}$ (m/s)

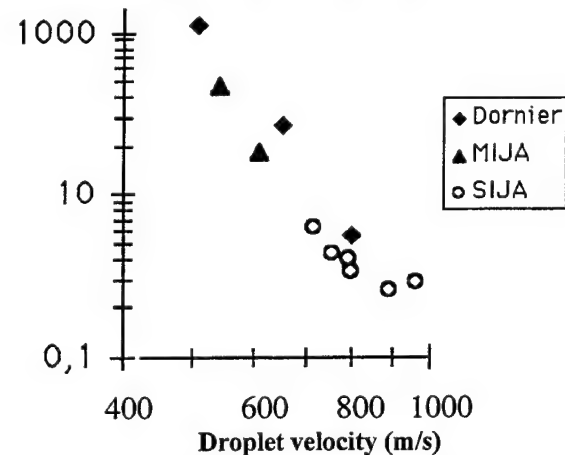


Figure 9: Comparison with sapphire of water jet measurements with 2 mm dia. droplets and DORNIER rig measurements with 0.5 mm droplets.

CHARACTERIZATION OF THE SOLID IMPACT RESISTANCE OF MATERIALS

Generalities

The SPARC (Solid Particle Rebound Characterisation Apparatus) has been designed at ONERA in order to characterize erosion resistance of aircraft and rotorcraft engines by sand. This new test facility allows to produce a continuous flow of calibrated solid particles having a velocity up to 180 m.s^{-1} and to impact a solid target without any residual airflow. The 2-D velocity distribution of impacting and reflected particles is measured.

This facility is composed of an aerodynamics set-up generating the flow of particles and of a velocity measurement system.

After a description of the test facility, results obtained during qualification test are given; several examples of vectorial mapping of the reflected particles velocity are shown.

Aerodynamics set-up

Low velocity calibrated particles (20 m.s^{-1}), are injected upstream of the supersonic nozzle, supplied by an absolute pressure of 1 bar. At the nozzle exit, the air flow mach number being greater than mach 1, the particles are carried along the accelerating pipe and the diphasic flow (air + particles) penetrates in the low pressure chamber (LPC on fig. 10) connected to a vacuum pump. Inside the low pressure chamber, a small pipe located exactly in the axis of the diphasic flow, is connected to an experimental enclosure (EE on fig. 10) where the absolute static pressure is 1 bar. The dynamic pressure of the air flow being 1 bar, in the entrance of the small pipe, there is equality of the two pressures (air flow dynamic pressure = static pressure) and the air velocity is null. So, only the particles penetrate into the experimental enclosure and impact the target. The air flow is entirely evacuated by the vacuum pump.

Note that, since the experiment enclosure is entirely sealed (except the small pipe), there is no air flow inside, and the particles impact without turbulence.

Velocity measurement set-up

The velocity measurement set-up is a fringes laser velocimeter [5]. Two beams of coherent light stemming from the same laser and covering optical paths of similar length, are self crossing in the velocity measurement point, where a system of interference fringes appears. When a particle is crossing this fringes system, a modulated light signal is produced. The measurement of the frequency of

the modulation allows to determine one component of the particle velocity V_i given by :

$$V_i = f \cdot I \quad (1)$$

where f is the measured frequency and I is the interfringes distance. The sign of the considered velocity component can be found by an artificial fringe displacement obtained by a Bragg cell inserted in the path of one of the two beams, so that the relationship (1) becomes :

$$V_i = f \cdot I - V d_i \quad (2)$$

where $V d_i$ is the magnitude of the fringe displacement velocity.

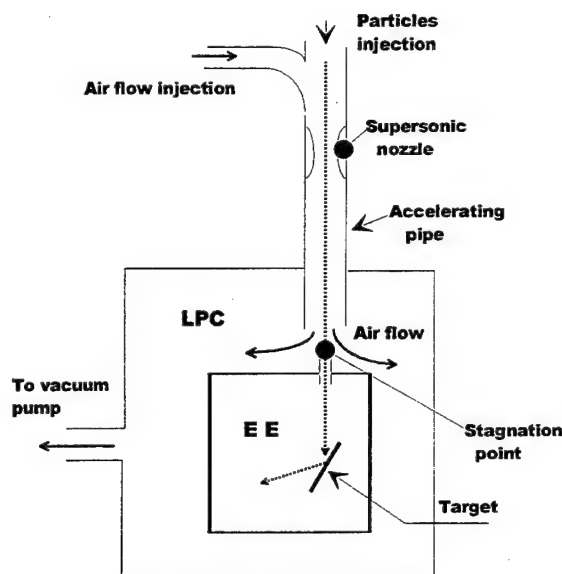


Fig. 10 . Schematic diagram of aerodynamics set-up.

The presence, at the same point, of two fringe systems of different wavelengths and directions allows to measure simultaneously the two components of the particle velocity. The two pairs of beams are constituted of the two most intense wavelengths, green ($\lambda = 0.5145 \mu\text{m}$) and blue ($\lambda = 0.488 \mu\text{m}$) of an ionised argon laser. The measurement volume (that can be displaced in the particle flow), corresponding to what photodetector sees, appears like a sphere having a diameter of some hundreds of μm . The photodetector is made of a telescope coupled with two photomultipliers each tuned on one used wavelength. The precision order of this process is $\pm 1.6 \%$ on each component, from 20 m.s^{-1} to 200 m.s^{-1} .

For each measurement point, one performs the acquisition of 1000 to 2000 velocity vectors, the processing of these data allowing then to compute average velocity components and different statistical values.

The whole of the velocimeter (laser, optical setting and photo detector) being slaved in position, it is possible to

perform velocity measurements at several locations, which allows to draw a mapping of the field velocity. The accuracy of the position setting is $\pm 50 \mu\text{m}$, the accuracy of the position measurement is $\pm 10 \mu\text{m}$.

Qualification tests

The velocity qualification test of the set-up has been performed with three diameters of particles : $80 \mu\text{m}$, $200 \mu\text{m}$ and $600 \mu\text{m}$. In order to determine the divergence of the particle flow, three measurement points in the incident flow have been investigated (see figure 11), one on the axis of the particles flow (point A) and one on each side of this axis, distant from 5 mm (points B and C). The distance between the line of the measurement points and the theoretical impact point of the particles is 30 mm, the target being removed from the experiment enclosure. The two measured velocity components are V_z and V_x , V_z being the main component, parallel to the axis of the particle flow.

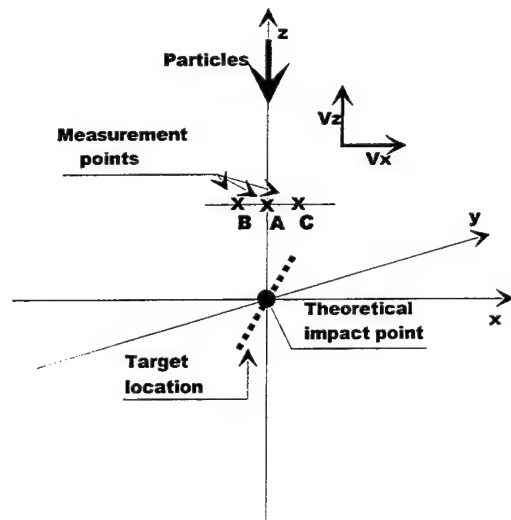
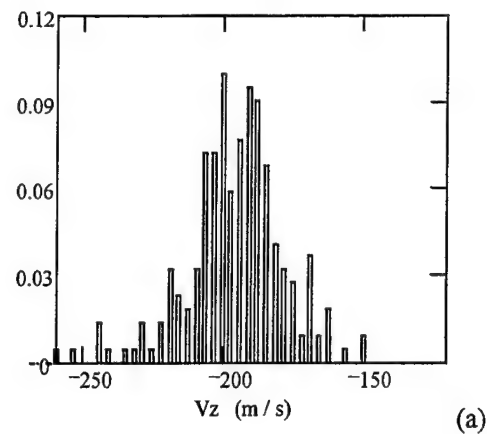


Fig. 11. Location of the velocity measurement points in the injected particle flow.

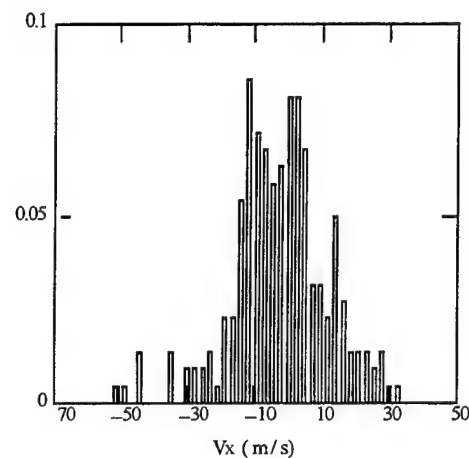
Figures 12 (a, b, c) show the histograms of velocities for particles of $200 \mu\text{m}$ of diameter, measured at the point A and calculated on 40 ranks. Velocities are in m.s^{-1} and the number of particles in each rank is normalized to the number of counted particles. The two channels of the velocimeter being synchronised, each particle simultaneously identified by the two channels is characterised by its two velocity components. So it is quite possible to compute the velocity vector for each particle. Figure 12 (c) shows the histogram of modulus of velocity vectors. The mean calculated velocity is 195 m.s^{-1} , the standard deviation being 18.5 m.s^{-1} .

Figure 13 is a vectorial representation of the divergence of the particle flow (for the same diameter $200 \mu\text{m}$), i. e. the mean computed magnitude for each measurement point

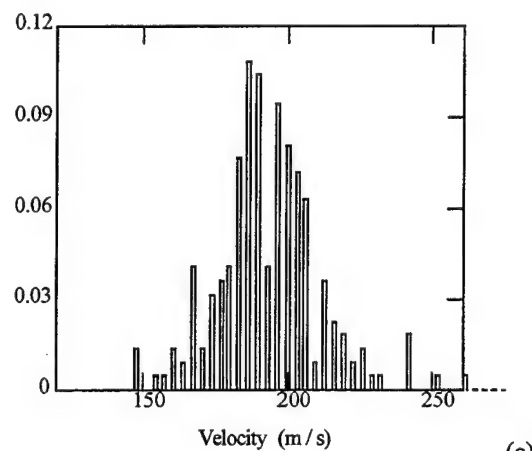
(A, B and C). The velocity modulus is given in m.s^{-1} , and the angles are in degrees. We can see that the divergence is extremely weak : 4° between points A and B and, 1.6° between points A and C.



(a)



(b)



(c)

Fig. 12. Histograms of velocities measured at the point A, for particles of $200 \mu\text{m}$ of diameter ; (a) V_z component, (b) V_x component, (c) modulus.

Table 1 gives the main characteristics of velocity and divergence obtained for each diameter of particles. Several tests with nozzle in function but without injection of

particle, have been performed to determine the residual turbulence in the experiment enclosure, with and without target. In this configuration, the velocimeter performs the velocity measurement on the dust particles present in the enclosure. The main results of this investigation are the following : the measured magnitudes are included between 0 and 5 m.s⁻¹, with an angle that seems perfectly random, and the presence or the absence of target does not change anything to these values.

To conclude about the qualification test, we can say that the phenomenon of solid particle impact can be studied in the almost total absence of residual turbulence.

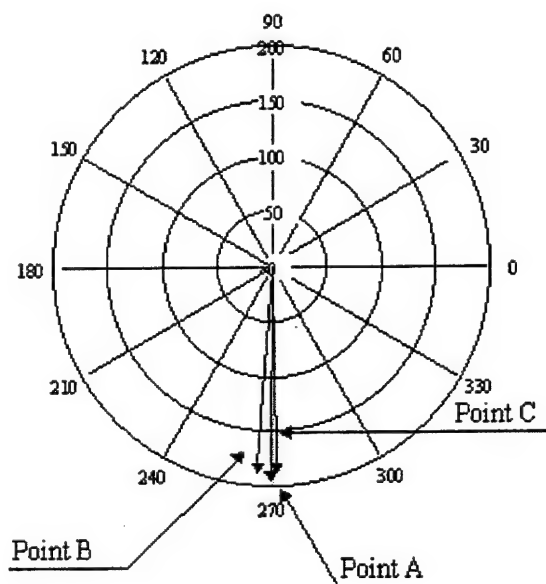


Fig. 13. Vectorial representation of particle flow.

Table 1. Velocity performances obtained for three diameters of particles.

Particle diameter (μm)	80	200	600
Mean velocity (m/s)	163	195	153
Standard deviation (m/s)	25.0	18.5	23.5
Mean angle (degrees)	270	270	271
Angle Standard deviation (degrees)	6.0	4.5	5.5
Particle flow divergence (degrees)	+0.5 -5.5	+1.5 -4.0	+2.5 -5.0

Rebound of particles study

As part of the study of the phenomenon of solid particle rebound on metallic targets, several tests have been achieved with three diameters of particles ($\delta = 80 \mu\text{m}$, $200 \mu\text{m}$ and $600 \mu\text{m}$). For each diameter of particle, different incidence angles β_i have been used from 15° to 75° (the incidence angle being the angle formed by the direction of the particle flow and the surface of the target).

In each test configuration (δ and β_i), 15 velocity measurement points have been characterised, 3 in the incident flow, having the same location during the qualification tests, and 12 in the rebound region (see figure 14).

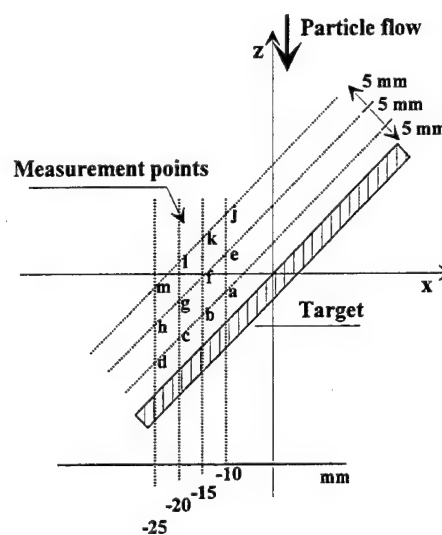


Fig. 14. Location of the measurement points in the rebound.

Getting the velocity component in the rebound from the measurement is not easy. Indeed, after impact, particles are fragmented and can collide with particles of incident flow, which can be seen on the obtained histograms by the presence of more than one population. So it is necessary, before computing the velocity vector, to perform a signal processing in order to remove the particles having characteristics not representative of the studied phenomenon, mainly the particles having a velocity component $V_z > 100 \text{ m.s}^{-1}$. This process allows then to compute the mean velocity vector for each measurement point, then to calculate, for each configuration (δ , β_i), the four significant parameters : incident velocity V_i , mean rebound velocity V_r , incident angle β_i and mean rebound angle β_r and finally to draw the diagrams : $V_r/V_i = f(\beta_i)$ and $\beta_r/\beta_i = f(\beta_i)$.

This process allows also to draw a map of the vectorial velocity field, for each measurement configuration. As an

example figures 15 (a), (b) and (c) show respectively the obtained diagrams in the three configurations.

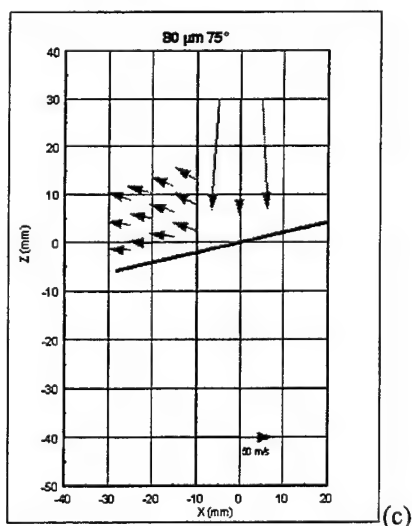
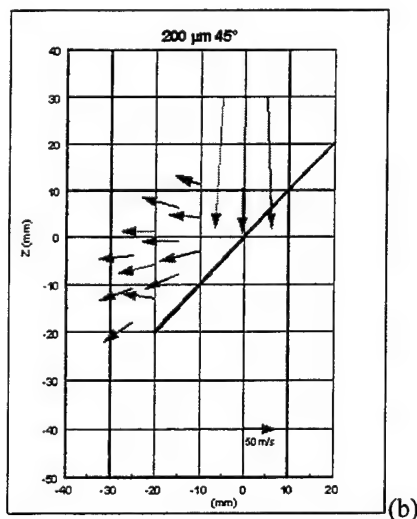
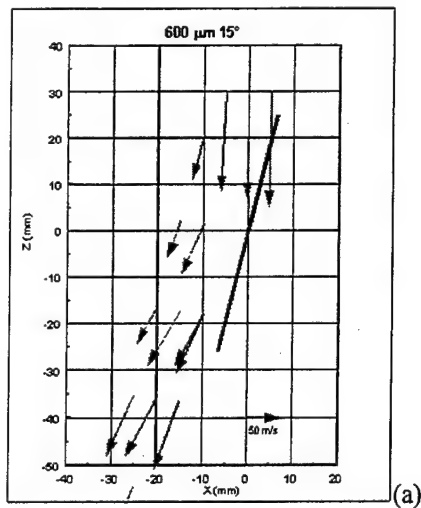


Fig. 15. Vectorial velocity fields ; (a) $\delta = 600 \mu\text{m}$, $\beta_i = 15^\circ$,
(b) $\delta = 200 \mu\text{m}$, $\beta_i = 45^\circ$, (c) $\delta = 80 \mu\text{m}$, $\beta_i = 75^\circ$.

CONCLUSIONS

MIJA and SIJA set-up allow the possibility of the measurement in the lab of the rain erosion resistance of materials from 100 to 1000 m/s. Characterizations can be performed but also more fundamental studies bent to high velocity impacts physics.

ONERA has designed and built a test facility to study the erosion phenomenon due to solid particles impact. This facility allows to reach a particle mean impact velocity up to 195 m.s^{-1} for given working parameters ; the main interest of the device is that no residual airflow exists at the target level.

Among the different velocity measurement techniques studied, the fringes laser velocimetry technique used is the one that allows to draw the trajectory; moreover the major advantage of the device is its working easiness.

REFERENCES

- [1] C. Seward, J. Pickles and J.E. Field,
Single and multiple impact jet apparatus and results
Proceedings of the SPIE's 1990 Tech. Symp. "Window and Dome Technologies and Materials II", vol. 1326, pp 280-290
 - [2] A. Déom, D.L. Balageas,
Rain erosion resistance of infrared materials, comparison of rotating arms results and multiple impact jet apparatus (MIJA) measurements. Proceedings of the 8th European Electromagnetic Structures Conference, Nottingham (G.B.), September 6-7, 1995.
 - [3] A. Déom, D.L. Balageas, F. Laturelle, G. Gardette, G. Freydefont
Sensitivity of rain erosion resistance of infrared materials to environmental conditions such as temperature and stress. Proceedings of the SPIE's 1990 Technical Symposium on "Optical and Optoelectronic Applied Science and Engineering", San Diego (USA), July 8-13 1990.
 - [4] A. Déom, A. Luc, S. Amara and D.L. Balageas
Towards more realistic erosion simulation for high velocity E.M. and I.R. windows
To be published in the Proceedings of the 9th Int. Conf. on Erosion by Liquid and Solid Impact, Cambridge (U.K.), 13-17 September 1998.
- REFERENCES (for SPARC)
- [5] M. Lemistre, D. Soulevant, F. Micheli and A. A. Déom.
New test facility for sand erosion studies. 9th International Conference on Erosion by Liquid and Solid Impact, ELSI IX, Cambridge, England, september 1998.

INCOMPRESSIBLE AERODYNAMICS OF A PLANETARY ENTRY CAPSULE

Ö. Karatekin, R. Voets, J-M. Charbonnier, F. Y. Wang

von Kármán Institute for Fluid Dynamics, Chaussée de Waterloo 72
B-1640 Rhode-St-Genèse, Belgium

ABSTRACT

The methodology and the assorted experimental techniques utilized in the aerodynamic investigation of a planetary entry capsule at low speed are presented. The combination of novel and classical instrumentations permitted the description of topology and off surface features that are important in the study of terminal capsule aerodynamics. In addition, suggestions on future commercial development of sensors conducive for general blunt body studies are made.

INTRODUCTION

The recent international interests in earth re-entry (i.e., ARD, Stardust, OREX) and interplanetary probes (i.e., Huygens, Mars Sample Return) motivate the re-examination of dynamic stability issue for new generation planetary entry capsules. Previous studies on planetary vehicles such as the Apollo, Viking and Stardust showed that these blunt bodies often exhibit dynamic instabilities during the final phase of their missions, and if no active measures were taken, would likely to result in a tumbling motion. In order to achieve stability, planetary entry capsules have resorted to deploy stabilizing drogue chutes at conditions as demanding as Mach 2. The deployment of a parachute at high speeds results in a heavier capsule and decreases the landing accuracy. The cause of the instability is not well understood, however Baillion [1] and Ericsson and Reding [2] have shown that both surface separation and near-wake flow are the contributing factors. The present paper will describe the methodology and the assortment of experimental techniques used to study the aerodynamics of a representative capsule in transonic and subsonic flow regimes where the problem of dynamic stability is known to be more pronounced. The selected model is an Apollo Command Module of Block I, whose dimensions and center of gravity are presented in Figure 1. The heat shield forward position corresponds to an angle of attack of 180° and the incidence decreases in counterclockwise direction.

The dynamic stability testing techniques will be reviewed briefly in the first part. After the description of the design of a new experimental campaign at low, several measurement techniques and their applicabilities to the

current problem will be discussed and some preliminary results will be presented.

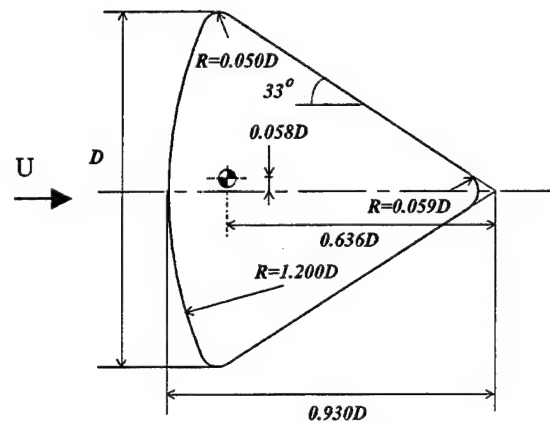


Figure 1: Geometry of the capsule model.

DYNAMIC STABILITY TESTS

Common methods of measuring dynamic derivatives include forced and free oscillation tests, rotary balances, the tests in aero-ballistic or hypervelocity ranges, free-flight and spin tunnel experiments [1], [3]. In order to properly predict the motion of a vehicle, data on dynamic stability derivatives at representative flight conditions are required.

The proper simulation of dynamic stability derivatives rely on satisfying a set of similitude requirements derived from dimensional analysis [4]. When predicting static characteristics, similarities in Mach and Reynolds numbers are the only requirements. This is not the case for dynamic testing where additional and sometimes conflicting similarity parameters are needed [5]. When the model is dynamically tested, similitudes in reduced angular velocity, inertia, buoyancy and frequencies need to be satisfied as well.

Experiments are often simplified further by using a single degree of freedom set-up and the application of small perturbation theory in data analysis. The derivatives are then calculated either from the time history of the model's motion (i.e., free rotation tests) or from measurements of

forces and angular displacements (i.e., forced and free oscillation tests).

The aerodynamic stability testing of bluff bodies needs special attention due to wake effects and large amplitude motions [1]. Free-to-tumble set-ups have been proposed as a suitable experimental tool in the characterization of capsule's dynamic behavior. In this technique the model is free to rotate around an axis passing through its theoretical center of gravity.

A free-to-tumble set-up developed for the VKI S1 transonic/supersonic wind tunnel is presented in Figure 2. The transverse rod is mounted on two ball bearings and linked to the encoder in one side and to a release system on the other side.

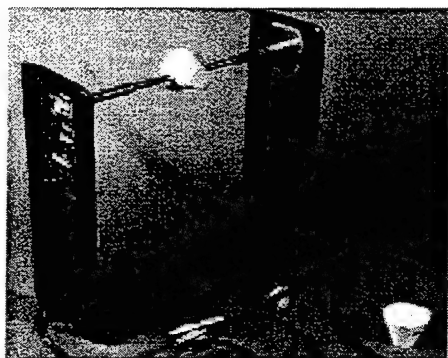


Figure 2: Free-to-tumble set-up.

Using this set-up, Paris and Charbonnier [6] have studied the dynamic behavior of various capsules in subsonic and transonic conditions. Representative results from a $M=0.5$ test campaign is given in Figure 3 where the data in phase plane $(\theta, \dot{\theta})$ have been obtained by the superposition of several individual free-to-tumble releases. The advantage of this form of representation is to put in evidence the critical points such as the stable positions, bifurcation points and limit cycles. The results showed that the aerodynamic stability weakens with decreasing speed and the model is dynamically stable only in a small range of angle of attack.

In order to understand the mechanisms influencing dynamic stability, the investigation of separation patterns and associated unsteady flow phenomena are indispensable. Such studies are not easy tasks due to the difficulties applying techniques such as Laser Doppler Velocimetry (LDV) and Particle Image Velocimetry (PIV) in high speed vortex dominated flows. Consequently there is a lack of information on the flow patterns around capsule shapes at terminal speeds. Wang et. al. [7] consequently examined the possibility of using low speed

facilities to extract the most salient features present at higher subsonic Mach numbers. The study revealed that incompressible flow pattern is representative of the entire subsonic regime. Time averaged flow field in the wake, aerodynamic forces acting on the model and unsteady flow features in incompressible flow were subsequently studied and summarized in [8],[9].

Another interest in low speed experiments comes from the fact that upcoming planetary sample-return capsules missions demand stable subsonic flights without the assistance of a parachute [10].

$\dot{\theta}$ (degree/sec)

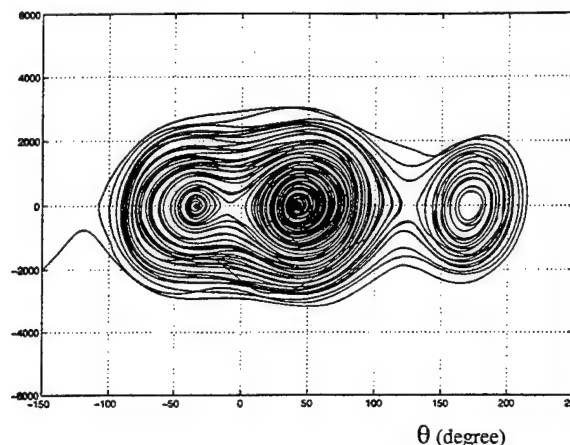


Figure 3: Free-to-tumble results.

SET-UP FOR LOW SPEED EXPERIMENTS

Wind Tunnel

The experiments were performed in VKI L1 wind tunnel with a open test section of three meters diameter (Figure 4). The speed can be varied continuously between 10 to 60 m/s. The resulting Reynolds number range based on maximum diameter of the model is between 2×10^5 and 1.2×10^6 .

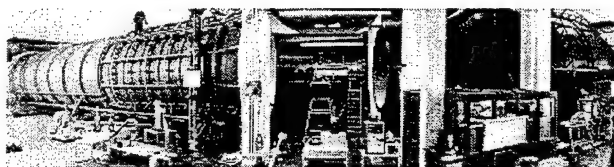


Figure 4: VKI L1 Wind Tunnel.

Model

The model in VKI L1 tunnel has a maximum diameter of

0.3 meter which is one order of magnitude bigger compared to previously performed PIV, LDV and dynamic stability tests. The larger size permits the examination of surface phenomenon in greater detail. The model is installed in a specially manufactured set-up including a transverse support mechanism passing through its theoretical center of gravity. The side supports are integrated in a "box" where the surface pressure values at the walls and boundary layer profiles at several locations were measured. It ensures a proper definition of the flow field boundary conditions for later numerical efforts.

Free-to-tumble

The VKI free-to-tumble set-up initially designed for VKI S1 transonic/supersonic wind tunnel (Figure 2) has been scaled up for the VKI L1 wind tunnel. The transverse rod is of stainless steel construction and has a diameter of 0.17D. It is supported on both sides by roll bearings. The model can be free-to-rotate for dynamic tests or fixed as required for the measurement of wall pressures and aerodynamic forces and moment at a given incidence. The set-up is designed also to allow the use of a motor for forced oscillations where the dynamic behavior can be tested for a given forcing amplitude and frequency. The model incidences were measured with an encoder having a resolution of 0.18 degrees.

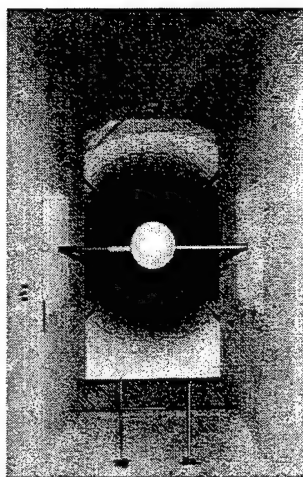


Figure 5: Model in the VKI-L1A tunnel.

Balances

The rotating mechanism can also be fitted with strain gauge balances on both sides for the measurement of the lift and the drag. In this type of system, the pitching moment will be measured using a torsion balance inserted in the transverse rod. The two side balances are based on two deformable parallelograms, one per component

equipped with 4 strain gauges each. The pitching moment balance is based on the torsion of a parallelepiped equipped with strain gauges.

Pressure Measurements

The model used for pressure measurements is of aluminum construction equipped with 490 pressure taps on two quarters of the surface (Figure 6). In order to measure the wall pressure, two scanivalves of 48 positions each are placed inside the model and the scanivalve tubings passed through the hollow transverse rod and connected to pressure transducers outside of the facility. Six sets of experiments are then required to measure the 490 pressure taps.

Flow Visualizations

In addition to the wall pressure measurements, oil flow visualizations (skin friction lines) were carried out with another model made out of foam. A mixture of petroleum, titanium-dioxide and oleic acid was used for the surface flow visualization. The model was painted to black to provide maximum contrast in the tests.

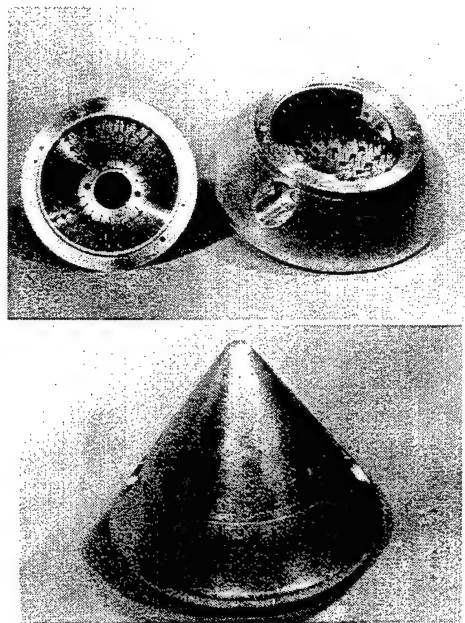


Figure 6: Experimental model for pressure measurements.

MEAN FLOW FIELD

The mean flow field investigation on the model surface is concentrated on three incidences: 180° (heat shield facing the flow), 165° (trim position) and 147° (upper surface of

the conical after-body aligned with the incoming flow direction). The flow velocities selected are 30 and 60 m/s corresponding to Reynolds number of 0.6×10^6 and 1.2×10^6 .

These angles of attack also correspond to the configurations tested in the VKI-L7+ wind tunnel at lower Reynolds number using Digital Image Particle Velocimetry (DPIV) and Laser Doppler Velocimetry (LDV) [8, 9].

Velocity Field

Wang et al. [9] obtained the mean flow in the symmetry plane by two-dimensional LDV measurements at three incidences (Figure 7). The corresponding Reynolds number was 4.5×10^5 . The "streamtrace" feature of the data visualization software was used to delineate the recirculating wake.

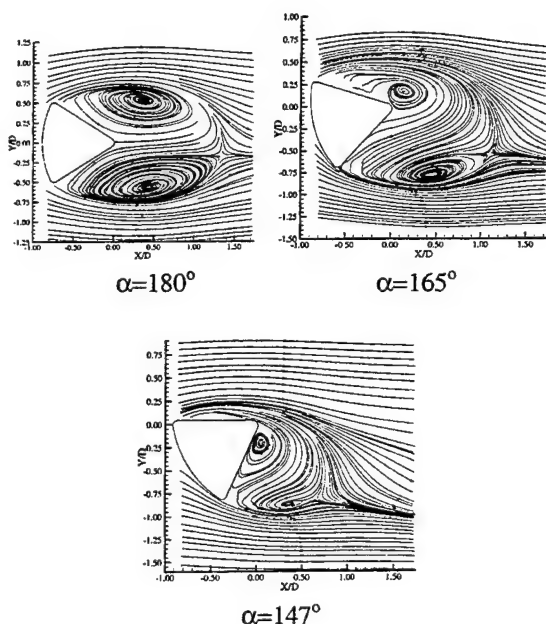


Figure 7: Mean flow field in the symmetry plane ($Re=4.5 \times 10^4$).

These flow-field studies conducted at lower speed the flow features obtained are not expected to be very Reynolds number sensitive since the separation is affixed on the cone-sphere junction which has a small radius of curvature. The possible influence of Reynolds number will be discussed in detail after the presentation of surface data.

For $\alpha=180^\circ$ and $\alpha=165^\circ$ the flow is separated from the cone-sphere junction of the model. At $\alpha=147^\circ$ the flow is probably attached at the upper surface conical part as suggested by the velocity vectors directed towards

downstream, even though it is not obvious in the streamtrace representation which suffers from the lack of data near the surface. In the downstream of the model, the recirculating region manifests itself in the center plane as two large counter rotating vortices. The size of the two vortices decreases with decreasing angle of attack. At $\alpha=147^\circ$ where the model's upper surface is aligned with the free-stream, both wake vortices are situated on the lower side of the model.

Surface Flow

Parameters and techniques for detecting the location of three-dimensional separations in subsonic flows were evaluated by several papers [11][12]. The surface measurements are performed to obtain local and global features of the wall flow phenomena such as pressure induced separation or boundary layer transition. The spatial and temporal characteristics of the measurement tools are important to obtain sufficient and reliable data bases that would help the understanding and control of relevant phenomena. Some of the commonly used techniques are: surface oil flow visualizations, infrared thermography, liquid crystals, hot-films, piezo-film sensors, pressure sensitive paints and pressure transducers. The application of these techniques to the present problem needs special care. For the three angles of attack investigated, the separated flow creates large recirculating areas on the conical part of the model where the skin friction forces and pressures have small amplitudes, which makes their investigation difficult.

Oil flow visualizations are simple to apply and provide indicators of separation lines in strongly separated flows. However due to the errors from gravity effects or interactions between the flow field and oil mixture, the oil flow data is suggested for qualitative interpretations of the flow only.

Surface flow characteristics are best ascertained by direct measurement of surface skin friction. Hot film sensor which rely on a relationship between heat transfer and skin friction have been widely used in subsonic flows. Wetzel et. al. [11] indicates that in cross-flow measurements the errors are typically around 10% and increases when the separation is weaker or it is formed more gradually.

Pressure data are often used to indicate the existence of massive separation where the profile becomes flat. However unless massive separation exists, the pressure is not an ideal separation indicator and the exact location of separation from surface pressure data can be ambiguous.

The oil flow visualizations are made for three angles of attack at a Reynolds number of 1.2×10^6 . The oil flow patterns on the heat shield and on the top of the conical after-body are shown in Figure 8.

When the model axis is aligned with the free stream with the heat shield facing the incoming flow ($\alpha=180^\circ$), the

stagnation point is located on the geometric center of the heat shield and the boundary layer detaches at the maximum diameter location producing a fully separated flow in the aft conical part of the capsule. As the angle of attack increases, the stagnation location moves toward the edge of the heat shield and the flow on the conical afterbody forms complex three-dimensional separation patterns. Two symmetrically placed focus points in the separated zone imply the existence of streamwise vortices in the near wake, verified separately in LDV measurements [9]. If the angle of attack is further increased, the stagnation point moves on the edge of the heat shield and the flow becomes attached on the conical part.

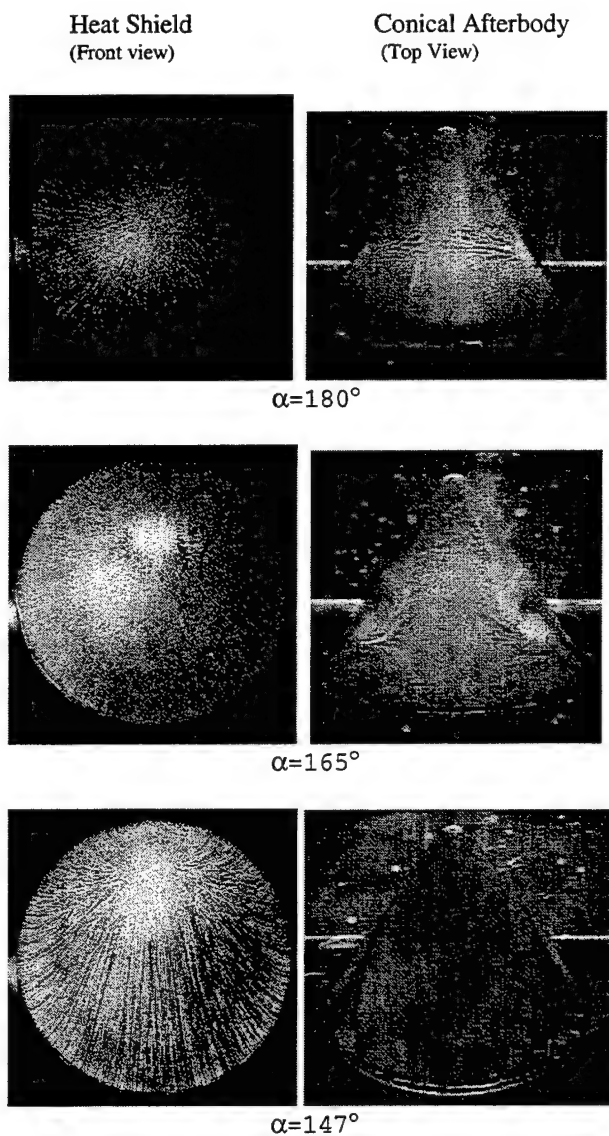


Figure 8: Oil flow visualizations

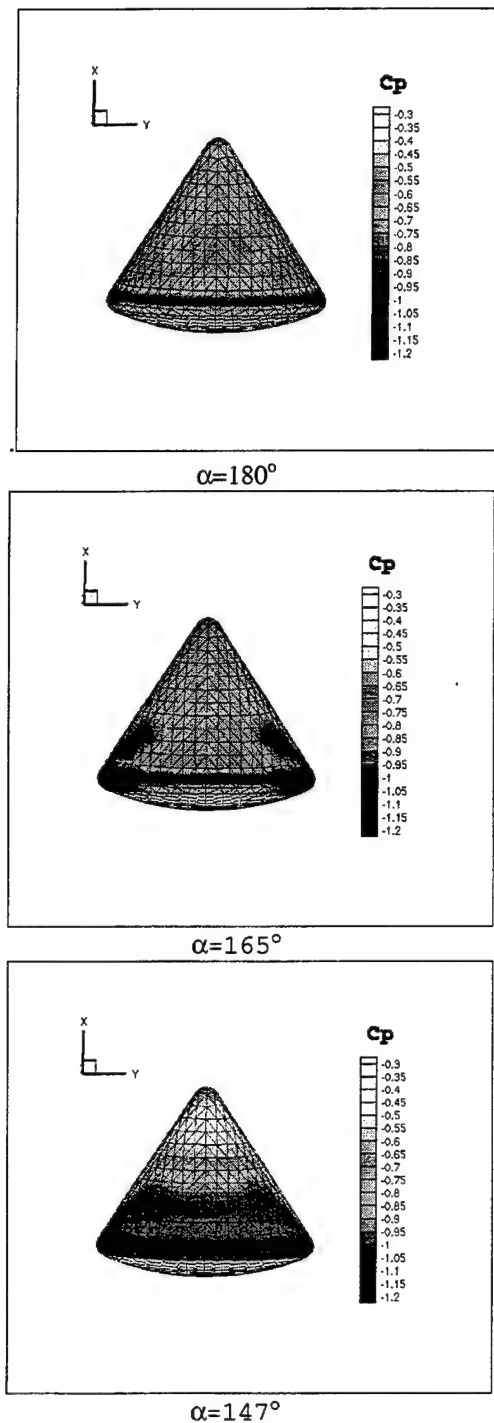


Figure 9: Pressure distribution on the conical part of the model at $Re=1.2 \times 10^6$ (Top view)

As discussed previously, the oil flow visualizations are qualitative measurement tools where the separated regions and stagnation locations are generally easy to locate.

However the location of critical points in the separated regions such as the vortex centers on the conical surface at $\alpha=165^\circ$ depend on the characteristics of the mixture. The asymmetry in the initial application of the mixture on the model surface may also modify the results causing asymmetric flow patterns. The oil flow pattern at $\alpha=180^\circ$ (Figure 8) indicate the presence of critical points on the conical afterbody. However in case of such low skin friction forces, the gravity forces acting on the oil can complicate the interpretation of the flow topology. With this respect the asymmetry between oil patterns on the top and bottom views is an indication of the influence of gravity force.

Due to the difficulties discussed above the experiments at $\alpha=165^\circ$ and at $\alpha=180^\circ$ were repeated several times. The visualizations at $\alpha=147^\circ$ were relatively simple due to the attached flow on the upper surface. Although oil flow visualizations provide the quickest global view of the surface phenomena they need to be supported by other experimental techniques before reaching some conclusion on the flow topology.

The surface pressure distribution on the model surface can yield the contribution of different parts of the model (i.e. spherical and conical parts) on the resulting forces and moments since the forces due to skin friction are negligible for blunt bodies. Since the resolution of surface pressure measurements determines the accuracy in these calculations, a large number of pressure taps were placed on the model surface as discussed previously.

The average surface pressure distribution were obtained for three angles of attack at two Reynolds numbers ($Re=0.6 \times 10^6$, and 1.2×10^6). The surface pressure contours on the conical after body at $Re=1.2 \times 10^6$ are presented in Figure 9 where the range of the contours is limited to $-0.3 < C_p < -1.2$ for visualization purposes. Therefore low pressures (minimum values are less than -2 at some points right after the shoulder of the heat shield) and the high pressures ($C_p > 0$ at the heat shield) are not shown.

$\alpha=180^\circ$ corresponds to axi-symmetric flow around the model. The minimum pressures are observed at the shoulder of the heat shield after which there is a sudden increase in pressure. On the conical after body the surface pressure variations are less than $\Delta C_p < 0.1$, resulting in a flat profile. There is no pattern indicating any critical point on the after body on the contrary to oil flow visualizations presented in Figure 8.

The flow on the conical after body stays separated at $\alpha=165^\circ$ as indicated by the flat profile of surface pressure values in the centerline of the model. The surface flow topology differs from the axi-symmetric case by the presence of two symmetrically placed low pressure regions. The low pressure centers correspond to the center of the vortices indicated by oil flow visualization (Figure 8).

The surface pressure level at $\alpha=147^\circ$ increases gradually starting from the edge of the heat shield where they have their minima. The gradual increase of the surface pressure continues until the vicinity of the nose where it reaches a maximum value. The profile is not flat and the flow remains attached on the upper surface as indicated also by the oil flow visualizations.

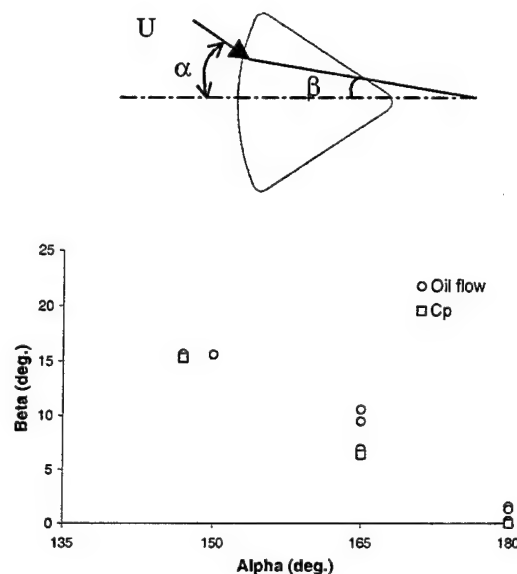
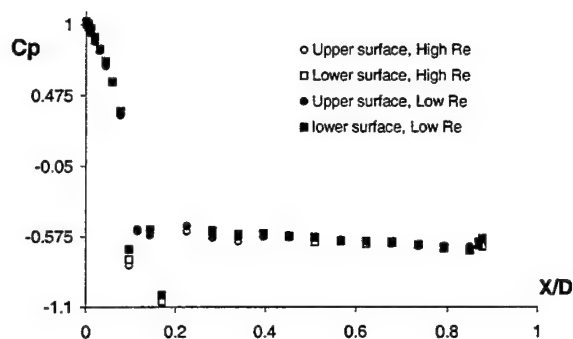


Figure 10: Stagnation position as a function of angle of attack

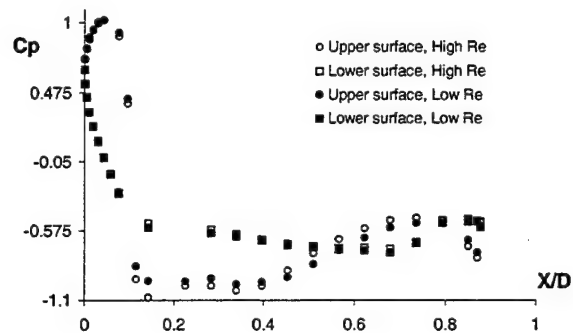
The variation of stagnation as determined from the oil patterns and pressure data with angle of attack is presented in Figure 10. The position of stagnation location moves linearly with angle of attack and is independent of the Reynolds number since the surface pressure measurements give the same β independently from Reynolds numbers for a given angle of attack. The oil flow data show the tendency to overestimate the stagnation location due to the errors in determination of β from oil flow visualizations pictures.

Reynolds Number Influence On C_p Distribution

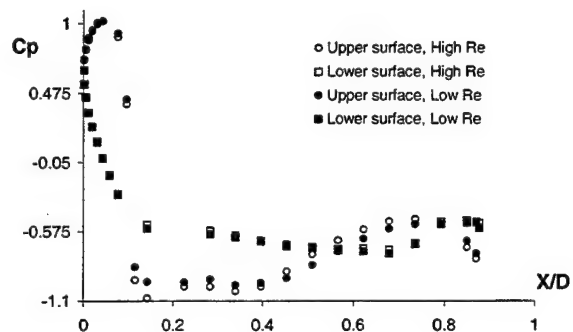
The surface pressure values on the symmetry plane are presented along the horizontal axis (i.e., X) normalized by the maximum diameter of the model for two Reynolds numbers (Figure 11). The position of the stagnation point is $X/D=0$ at $\alpha=180^\circ$ and moves downstream with decreasing angle of attack. The influence of Reynolds number is significant only at the shoulder of the heat shield and on the upper side of the conical after body at $\alpha=147^\circ$ where the flow on the surface is attached.



$\alpha=180^\circ$



$\alpha=165^\circ$



$\alpha=147^\circ$

Figure 11: C_p distribution on the conical part along the centerline

The additional flow visualization pictures (Figure 12) help to understand the distribution of pressure presented in Figure 11 for $\alpha=147^\circ$. The visualizations show that the surface flow on the upper surface is deflected towards the lower side in the neighborhood of the nose, which would cause an increase in lower side pressure.

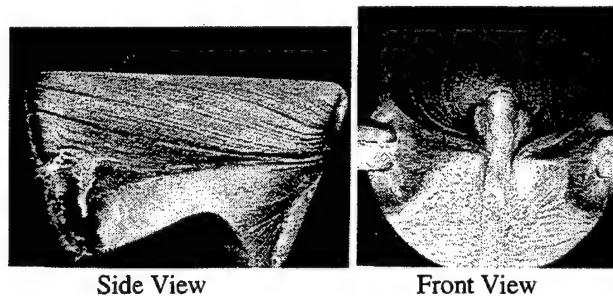


Figure 12: Oil flow visualization at $\alpha=147^\circ$

UNSTEADY FLOW

The flow field behind the capsule has similarities with a classical bluff body wake whose characteristics have been the subject of numerous studies [13]. The near wake of three-dimensional bluff bodies becomes more unsteady, hence more complex, with increasing Reynolds numbers. Large unsteady forces acting on the body result from the generation and shedding of coherent structures in the near wake.

In order to characterize the wake flow unsteadiness instantaneous PIV measurements were performed [8]. A typical PIV image is presented in Figure 13. From the analysis of these measurements, it becomes clear that the wake undergoes high level oscillations in the vertical plane visible by the movement of the velocity vectors. More precisely, the near wake of the model is characterized by two types of flow instabilities. The high frequency mode is a small scale instability associated with the rolling up of shear layers which manifests itself in elliptical vortex rings as it was clearly observed at lower Reynolds numbers (2000 compared to the order of 10^4 for the LDV and PIV measurements) in a water tunnel (Figure 14). The low frequency mode is connected with the alternating motion of the shear layers similar to the "fish tail" flapping behind a two dimensional body and corresponds to the vertical oscillation of the wake closure point. The non-dimensional frequency of this movement was measured to be $St=0.16$ whereas the high mode frequency is one order of magnitude higher, namely at $St=2.1$ [8]. From the dye flow visualization in Figure 14, it can be seen that the vortex rings loose their initial elliptical shapes and are destroyed rapidly because of azimuthal non-uniformities generating mutual inductions. After the breakdown, the upper portion of the ring vortices, identifiable as having negative vorticity, moves into the near wake and becomes part of the flow that impinges on the lower part of the capsule. This pseudo-periodic disturbance interferes the vehicle stability by introducing an amplification of the angle of attack oscillation magnitude.

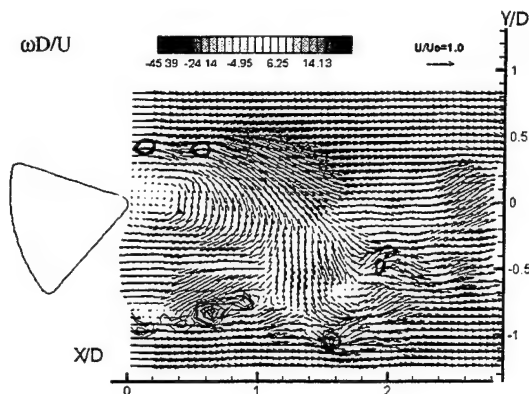


Figure 13: Instantaneous PIV image

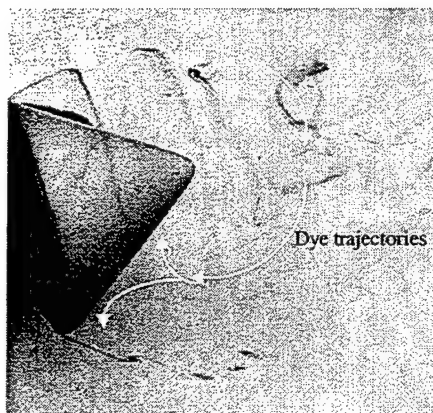


Figure 14: Water flow visualizations

Reynolds Number Influence On St

The data of non-dimensional wake frequency at $\alpha=180^\circ$ as a function of Reynolds number is given in Figure 15. The measurements at Reynolds numbers higher than 2×10^5 were made in the VKI L1 tunnel with a microphone placed approximately $1.5 D$ downstream of the model. The measurements at lower Reynolds number, namely in VKI L7+ wind tunnel and VKI water tunnel, were performed with hot-wire and dye flow visualization techniques, respectively.

The literature on blunt bodies such as sphere or circular cylinders suggest a sudden increase in St number which will correspond to a decrease in drag coefficient at the critical Reynolds number. The Reynolds number effect does not occur for blunt bodies such as square cylinders where the separation locations are fixed by the geometry [14]. For the angle of attack range investigated the separation is fixed on the cone-sphere junction of the model, hence the variation of St , similar to C_p data, does not show the influence of Reynolds number

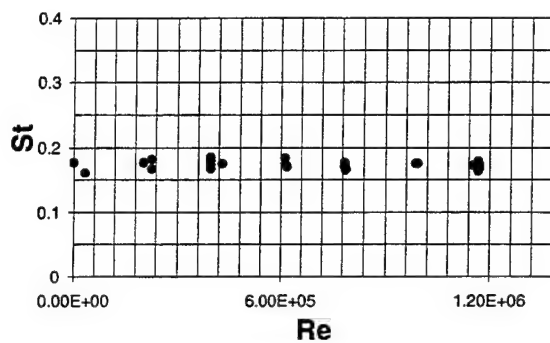


Figure 15: Variation of St with Reynolds number ($\alpha=180^\circ$)

Unsteady Surface Measurement Techniques

The interaction of the reattached wake and surface flow can be obtained through simultaneous measurements of surface data and velocity field. However the surface measurements involved with small models in unsteady turbulent subsonic flows are complex due to low pressure and skin friction forces. It is requested to measure pressure values of less than 2000 Pa with a frequency range of up to 1 kHz, based on the particularities of the current experiments. However the lowest range of the commercially available high frequency miniature pressure transducers are usually 1.4×10^4 - 3.4×10^4 Pa which is much larger than the range needed for the present study. Moreover the cost also limits the number of transducers that can be placed on the model. In the following part some of the unsteady measurement techniques that will be implemented in the present research will be presented.

Piezo-film

Thin unsteady pressure sensors based on polyvinylidene fluoride (PVDF) propose an economic solution for the measurement of unsteady pressures on small models at low air speeds. These sensors distinguish themselves by the existence of piezoelectric (generate charge when a mechanical stress applied) as well as pyroelectric (generate charge when a heat load is applied) properties. The foil is very thin ($9 \mu m < t < 100 \mu m$) and flexible so that it can be affixed on model surface without influencing the flow.

The development piezo-film sensors based on PVDF film has been initialized at VKI [15]. The film is covered by a thin layer of nickel cadmium alloy on both sides. The purpose of the metallization is to allow conductivity on the surface. A protective coating may also be applied. The wires were attached to the lead areas using conductive

epoxy. This assembly then flush mounted to the model surface using silicone. A schematic of the sensor is shown in Figure 16. Currently the work in instrumentation development is under progress to improve the performance of the home made piezo-film sensors

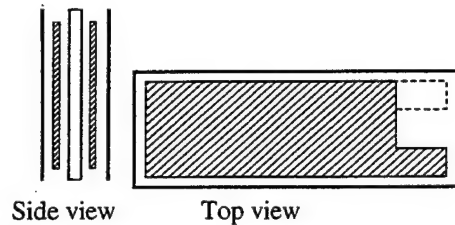


Figure 16: PVDF Sensor

Hot film

Flush mounting hot film sensors or surface mounted hot wires with high temporal and spatial resolutions provide another alternative. They are intended for measurements of wall shear stress, separation and transition locations in both laminar and turbulent boundary layers. They work on the same principle of relating the convective heat transfer from the active hot wire/hot film element to the corresponding velocity or velocity gradient at the wire location. The dynamic response which decreases with decreasing wall shear stress and thermal conductivity of the wall material [12] [16] make the use of hot film/wire on massively separated flows more complex.

Strain Gage Balance

The unsteady lift and drag forces will be measured by two parallel deflection type balances that will be incorporated at each end of the transverse support (Figure 17). The balances are designed to carry a maximum load of 250 N in drag and lift directions. Each parallelogram will be equipped with four strain gages. Typical deformation and stress levels as well as the eigen frequencies are calculated by a finite element analysis program in order to verify that the normal modes of the balance and flow induced frequencies are well apart from each other. In these calculation the maximums loads in vertical and horizontal directions are assumed to be applied in the central hole of the body. The results are presented in Table 1.

The range of the flow induced frequencies are pre-assumed based on the St number measurements made in the wake of the model in VKI L1 tunnel. The resulting frequencies for the three angles of attack investigated are:

15 Hz. < f < 30 Hz. at $V=30\text{m/s}$

30 Hz < f < 60 Hz. at $V=60\text{ m/s}$.

The smallest frequency given by the Modal analysis is very close to the upper limit of the expected frequencies. Modification of the design is therefore undergoing.

Table 1: Results of the Modal Analysis

Mode #	Eigen Frequency (Hz.)
Mode 1	75.7
Mode 2	100.9
Mode 3	144.6
Mode 4	273.4
Mode 5	366.7

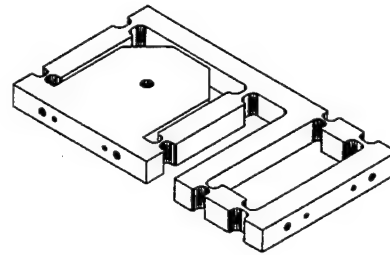


Figure 17: Parallelogram Balance

CONCLUSIONS

The experimental approach and the associated measurement techniques for the study of terminal aerodynamics of planetary entry vehicles are presented. The blunt geometry and the resulting large separated areas create a complex flow field, which demand a special methodology.

It is shown that most of the classical dynamic stability testing techniques used for slender bodies are not suitable for the capsule studies. Therefore for the investigation of the dynamic behavior of the model, a free-to-tumble set-up, which is initially tested in transonic flow is proposed. The experiments will be concentrated in incompressible flow where flow measurement tools are more available. The studies reveals that incompressible flow pattern is representative of the entire subsonic regime. Furthermore the preference of low speed experiments is supported by the missions of newly designed planetary entry vehicles which include subsonic regime.

A new free-to-tumble test set-up which is developed for VKI L1 low speed wind tunnel is presented. A major interest with the rig is also to measure vortex induced unsteady forces. The balance must be made sensitive enough, fast responding and stiff. The design of this

balance is greatly facilitated by finite element analysis, and the design iteration of the instrument is illustrated.

Initially, oil flow visualization experiments that provide quickest global view of the surface phenomena are performed around the stationary mode. This data together with the detailed surface pressure provided general surface flow characteristics on capsule body. The influence of Reynolds for the present geometry is found to be negligible as suggested from pressure distribution and St data.

Unsteady flow field investigations indicated the unsteadiness of the near wake and its interaction with the model surface. In order to have a better understanding of the nature this interaction, the possibility of applying several unsteady surface measurement techniques are discussed. However in the course of the study, it was borne out that there exists some limitations in the readily available commercial instruments, most notably, the lack of ability to measure unsteady pressures at low speed. Recommendations on future instrumentation development for general studies of blunt body flows are made.

ACKNOWLEDGEMENTS

The support from European Space Agency's GSTP Programme - Micro-Aerodynamics of Complex External and Internal Configurations is acknowledged with appreciation. The financial support from the NSF-NATO Grant Number DGE-9633933 for the fourth author, and the Scientific and Technical Research Council of Turkey for the first author are likewise gratefully acknowledged.

REFERENCES

- [1] Baillion M., "Blunt Bodies Aerodynamic Derivatives", in Capsule Aerothermodynamics, AGARD/VKI Special Course on Capsule Aerodynamics, von Karman Institute for Fluid Dynamics, Belgium, 1995.
- [2] Ericsson L. E. and Reding J. P., "Re-Entry Capsule Dynamics", J. Spacecraft Vol. 8, No. 6., 1971.
- [3] Orlik-Rukemann, K.J., 1981, "Review of Techniques for Determination of Dynamic Stability Parameters in Wind Tunnels" AGARD LS 114, 1981
- [4] Wolowicz C. H., Bowman, J. S. and Gilbert W. P., "Similitude Requirements and Scaling Relationships as Applied to Model Testing," NASA TP-1435, 1979.
- [5] Brandon, J. M. and Foster, J. V., "Recent Dynamic Measurements and Considerations for Aerodynamic Modelling of Fighter Airplane Configurations", AIAA Atmospheric Flight Mechanics Conference, Boston Massachusetts August 10-12 1998
- [6] Paris, S. and Charbonnier, J.-M., "Aerodynamic Force and Moment Measurements and Dynamic Characterization of an Apollo Capsule in the VKI-S1 Wind Tunnel," VKI Internal Note 107, 1997
- [7] Wang, F. Y., Charbonnier, J.-M., Karatekin, Ö., Paris, S., "The Utilization of Low Speed Facilities in Transonic Stability of Reentry Vehicles Research -An Evaluation", AIAA-98-2636, 16th AIAA Applied Aerodynamics Conference, Albuquerque NM, 1998
- [8] Karatekin, Ö., Wang, F. Y. and Charbonnier, J.-M., "Near-Wake of a Three-Dimensional Bluff Body at Angles of Attack," ASME Paper FEDSM98-5185, Proceedings of 1998 ASME Fluids Engineering Division Summer Meeting, Washington DC., June 1998.
- [9] Wang, F.Y.; Karatekin, Ö; Charbonnier, J.-M.: An experimental study of the flow-field around an Apollo capsule at low speed. 36th Aerospace Sciences Meeting & Exhibit, Reno (NV), USA, January 12-15, 1998. AIAA 98-0319
- [10] Desai, P. N., Mitcheltree, R. A., Cheatwood, F. Mc. N., "Entry Dispersion Analysis for the Stardust Comet Sample Return Capsule" AIAA GNC,AFM and MST Conference and Exhibit, August 11-13, New Orleans, LA., 1997.
- [11] Wetzel T.G., Simpson R.L., Chesnakas C.J., "Measurement of Three-Dimensional Crossflow Separation", AIAA Journal, Vol. 36, No. 4, April 1998.
- [12] Nitsche W., Suttan J., Haselbach F., Sturzebecher D., "Surface Forces Measurements with High Spatial and Temporal Resolution by Means of Liquid Crystal Foils, Pizofils and Surface Hot-Film Arrays" AGARD CP-601, 1997.
- [13] Sakamoto H. and Haniu, H., "A Study of Vortex shedding From Spheres in a Uniform Flow," Journal of Fluids Engineering, Vol. 112, pp. 386-392, 1990.
- [14] Delany N. K. and Sorensen E. N., "Low-Speed Drag of Cylinders of Various Shapes", NACA TN 3038, 1953
- [15] Claessens D. and Peeters K., "Development of Measurement Techniques for the Study of the Flow Over Oscillating Re-entry Capsule", Final year thesis, Louvain Institute of Technology Group T, von Karman Institute for Fluid dynamics, 1998.
- [16] Chew Y.T., Khoo B.C., Lim C.P., Teo C.J., "Dynamic Response of Hot-Wire Anemometer. Part II: A Flush-Mounted Hot-Wire and Hot-Film Probes for Wall Shear Stress Measurements", Meas. Sci. Technol., Vol 9., pp.764-778, 1998.

SESSION : 7

**WIND TUNNEL
MEASUREMENT TECHNIQUES**

A New Generation Traversing Rig with minimum Disturbances for a Closed Test Section of Subsonic Wind Tunnels

Taehun SEUNG



Division of Fluid Dynamics & Aerodynamics **SLA**
Department of Mechanical Engineering, Darmstadt University of Technology, Germany

Abstract

A probe traversing system developed for efficient operations in low speed wind tunnels has been developed. This traversing system of a new generation allows automatic scans of the entire test section with a wide variety of probes. The design of the rig considered both its stiffness and the aerodynamic interference. Special beam modules made of carbon fiber composite were developed for the main arm of the rig. When the rig is not in use, the beam modules can be easily dismantled from the base carriage and the entire system can move to a park position outside of the test section. The system exhibits high stability in positioning accuracy, eliminating the need for re-calibration before each application. The attainable positioning accuracy and the adjustable speed of traverse meet the demands of modern measuring instruments. The operating software 'AOSTA' (Advanced Operating System for the Traversing Appliance) controls not only the drive units of the system but also has an editor to generate the measuring grids. Grid generation is supported by graphic functions and a 'Teach-In' function to reduce the risk of collision between the probe and the model. 'AOSTA' runs in a Windows 98/NT environment and can communicate with a hierarchical computer via an IEEE488 interface, if required.

Introduction

Despite premature projections some years ago that the wind tunnel as a development facility will be superseded by greatly improved and accelerated CFD tools, its importance in the aerodynamic development process has remained undiminished. According to the statistics reproduced in figure 1, the hours of wind tunnel testing for airplane development have been steadily increasing over the last twenty years [6]. Nevertheless, it is not clear that the efficiency of wind tunnel studies has kept pace with the rapid improvements of modern measurement technologies.

The primary tasks during wind tunnel testing for aircraft development are the measurement of aerodynamic forces and moments on a model and the survey of the flow field around the model. The latter has gained importance in recent

years as a validation tool for CFD simulations and has also become more challenging due to the introduction of modern measuring techniques like PIV, LDA / PDA or DGV, in which fiber optic probes, illumination/recording devices or precision pressure transducers for use with pneumatic probes must be positioned within the test section. One of the main attractions of such flow field surveys is of course the possibility to determine the induced drag or to measure lift without the use of a balance.

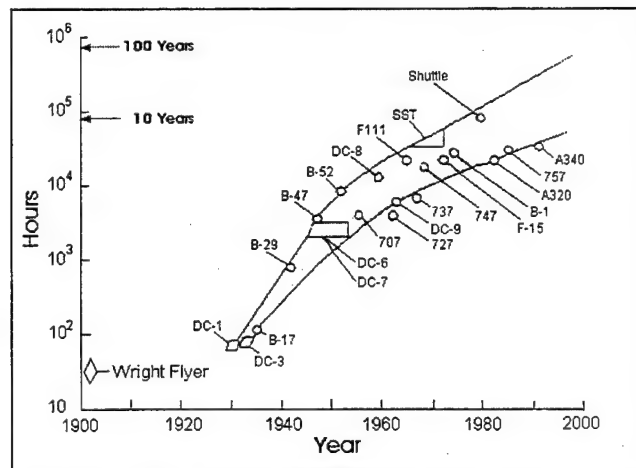


Fig. 1 Total testing hours in wind tunnels

Whereas the integration of strain gage balances on or in a model is not such a difficult task, the positioning of probes throughout the flow field introduces numerous problems. Not only must the aerodynamic interference be reduced to a minimum, also the demands on positioning accuracy are very high, especially when movement relative to the model is considered. Most traversing systems in subsonic facilities do not meet the demands set by modern measurement techniques and often very provisional solutions, as illustrated in figure 2 come into use. The main drawbacks of such provisional arrangements are high aerodynamic interference, low repeatability, low accuracy and tedious adjustment/calibration.

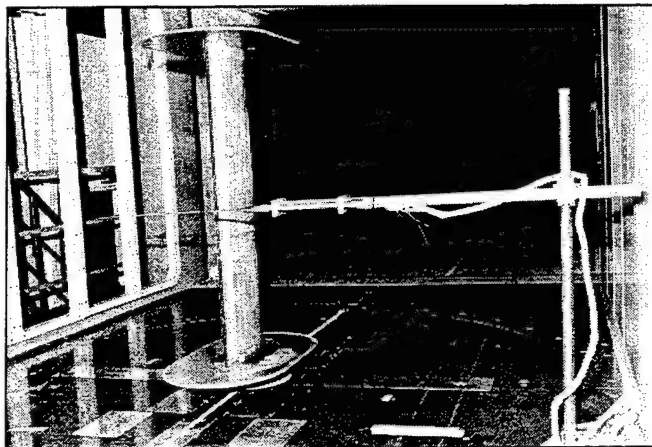


Fig. 2 Provisional positioning of a probe

Therefore there is a current need for advanced traversing rig concepts for low speed wind tunnels, which come closer to meeting the needs of modern measurement systems. A new solution for a traversing system, of which a prototype has been constructed and tested successfully at the wind tunnel of Technical University of Darmstadt, Germany, will be introduced in this contribution. This solution is particularly interesting, since it is also suitable for retrofitting.

Review of recent Traversing Rigs in some Subsonic Wind Tunnels

The state-of-the-art of traversing rigs can be discussed in terms of two different concepts: portable rigs which can be removed from the test section after the experiment and permanent installations. This contribution confines itself to the latter type, since the former has usually a stroke of less than 600 mm [18] and as such is not so suitable for large test sections. Furthermore, its aerodynamic interference is often large and is therefore not so interesting for closed test sections (for example such as [15]). Miniature portable systems are more appropriate for direct mounting on or in a model to measure the local flow conditions [16].

The two main characteristics to consider in evaluating traversing systems are the positioning accuracy and the aerodynamic interference. Aerodynamic interference can be minimized not only by component design but also by supporting the probe from downstream of the model. In fact most present designs used such a strategy.

In test sections with access from the top, the probe can be mounted on a vertical strut supported above the test section on a carriage with crossbar, which itself is traversed along the top side of the test section. Examples of such systems can be found at IVK, University of Stuttgart [10], [15] or in the wind tunnels of Volvo or BMW [16].

If access from the top is not readily available, more innovative solutions are necessary. The traversing rig of the 'Kirsten wind tunnel' at the University of Washington for example, is installed in the ceiling and uses moving sealing panels across the entire surface of the test section [8], [17]. It allows the vertical strut to be placed at any position of the ceiling area. However the design principle with a vertical strut often requires compensation against the mechanical backlash of the strut if the load due to the wind force is significant. This problem arises since the strut is mounted only at one end (cantilever). In some unfavorable cases, traversing rigs using this principle not only need to actively correct the position but may also require measures such as damping devices to reduce vibrations [10].

A variation of this principle foresees a horizontal boom instead of a vertical strut. The traversing rig of Airbus Bremen, Germany [13] or of Carleton University, Ottawa, Canada [9] are examples for such a system. However a horizontal support introduces also a bending of the arm due to its own weight, the amount of which varies according to the extended length of the arm.

These problems of exact positioning arise due to the inadequate stiffness of the strut or arm and can be overcome by fixing the strut on both ends. Traversing rigs such as in ONERA F1, ONERA S1MA or in NLR LST adopt such an arrangement [7], [14]. The disadvantage introduced is that the strut or arm can no longer be easily removed from the wind tunnel and is therefore less flexible.

Other solutions include a rotating arm attached to a movable carriage. However then the measurement position distribution follows a polar coordinate system and is often undesirable for post-processing. Conversion procedures into cartesian coordinates are often necessary, in many cases even for on-line acquisition. It is also inconvenient to have to remove the rotation arm when not in use or to re-adjust the system after re-mounting.

In summary, most present traversing systems meet requirements only through compromises. New solutions are required and welcome.

Principle of the new Traversing Rig

The new traversing rig concept is based on three axes of movement in a cartesian system and is illustrated in figure 3. Two synchronized horizontal tracks and a vertical strut mounted on the carriages of the horizontal tracks provide the basis of the this traversing rig. The horizontal tracks are installed between the test section and the diffuser, where

there is usually the so-called 'breathing gap' for a closed test section.

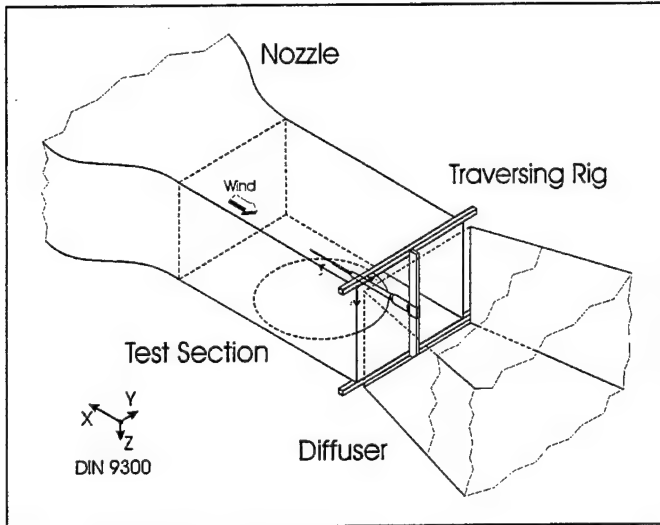


Fig. 3 Principle of new traversing rig mechanism

The horizontal tracks may be mounted on the outer frame of the test section so that they do not cause any disturbance in the flow field. The vertical strut also has its own carriage, on which a mast arm may be mounted. With a variable length of the mast arm it is possible to reach almost any relevant point inside the test section. When the traversing rig is not in use, the mast arm is dismantled from the carriage, allowing the carriage to return to its park position confined behind the wind tunnel side wall.

Using a forward looking boom/mast, the rig minimizes aerodynamic interference at the downstream plane of the probe. The cross-section of the traversing rig at this plane is only the cross-section of the boom, which decreases between the vertical strut and the probe holder at the tip. The vertical strut, being mounted both at the top and bottom, easily fulfills the most demanding requirements on stiffness, torsional stability and/or aerodynamic induced vibrations.

The length of the mast arm must be variable in order to reach all streamwise points within the test section. Either a telescopic solution or a modular extension solution can be considered to achieve this variability. A telescopic mast is certainly desirable from the convenience point of view, however the size necessary to achieve the required stiffness while still reaching all points in the test section is larger than allowable in terms of aerodynamic disturbance. Furthermore, the play in telescopic arms becomes unacceptable, especially at large extensions. Different mast arms for different test section segments would solve the problem, but is a costly

solution. A modular solution, in which the mast arm can be assembled from different available segments, reduces complexity in construction, but allows only a step by step change in probe position.

The problem of traversing in the streamwise direction (x coordinate) is solved in the new hybrid concept by combining the modular and telescopic solutions. A course positioning is achieved through the combination of mast arm segments and the fine positioning is handled by a telescopic final module.

Prototype, Practical Solutions

A prototype of this unique design concept has been successfully constructed and evaluated. It has been installed in the closed test section of the Low Speed Wind Tunnel (2900 X 2200 X 4800 mm) at the Darmstadt University of Technology, Germany. Positioning accuracy and operating speed are excellent and fulfill the requirements for measurements in the subsonic wind tunnel. Any position within the adjustment range of the x-axis (a streamwise 'slice', as described below under *Hybrid Beam*) can be reached within one minute. With the longest beam of over 4 meters, the movement of the probe support at the maximum speed of $V_{\infty} = 68$ m/s is hardly perceptible (less than ± 0.5 mm). The natural frequency lies in the range of 12 – 14 Hz. The mast arm and the vertical strut have shown excellent dynamic behavior during the evaluation phase.

The following description gives details of the construction and relates some of the experience which has been gained with this prototype over the past 4 years. Figure 4 shows a view of the prototype positioned between the nozzle and the diffuser.

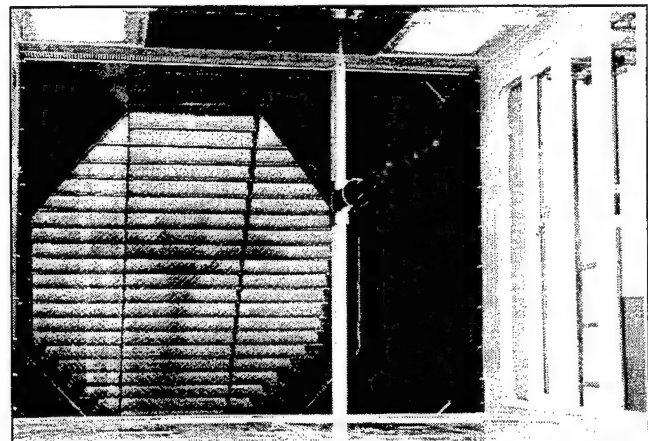


Fig. 4 Prototype at Darmstadt Univ. of Technology, Germany

Base of the Rig (Y- & Z-Traversing Unit)

Modern compact Linear Motion (LM) Guides of high performance were used for the base rig as y-tracks. They have quite low friction and offer high translation speeds at high positioning accuracy. These tracks are not seen in figure 4, since they are installed within the outer frame of the test section, in other words under the floor and in the ceiling respectively. Thus, they also do not cause any interference with the tunnel air flow.

These tracks are synchronized with each other through two no-slip hypoid bevel gears and a synchronization shaft as shown in figure 5. A vertical strut with a carriage (z-axis), is mounted on the supports, so that it can be moved across the test section from one side wall to the other. Behind each side wall a parking slot is provided. The LM tracks are long enough to bring the vertical strut laterally into any one of the parking slots. The parked strut does not disturb the pressure compensation at this 'breathing gap'. Flush mounted doors are installed on both parking slots. Using CamLocks the doors are easy to open and can be closed and locked within half a minute. Due to the parking slots it is neither necessary to dismantle nor to adjust the strut before each use. This reduces the set-up time and ensures high repeatability and accuracy of the probe positioning.

According to previous investigations [12], the 'breathing gap' must neither be completely open nor be completely covered. A certain percentage of the surface has to be perforated so that a pressure equalization is insured at all times. It is no problem to perforate the cover panels of the parking slots on the side walls, however the floor and ceiling elements must allow the vertical strut to pass through them. This problem was overcome using two perforated moving belts of aluminum which cover the lanes on the ceiling and

on the floor. Figure 6 illustrates the perforated moving belts, which work on similar principle as those of some machine tools. (Note that the perforation degree must be matched to the particular test section.)

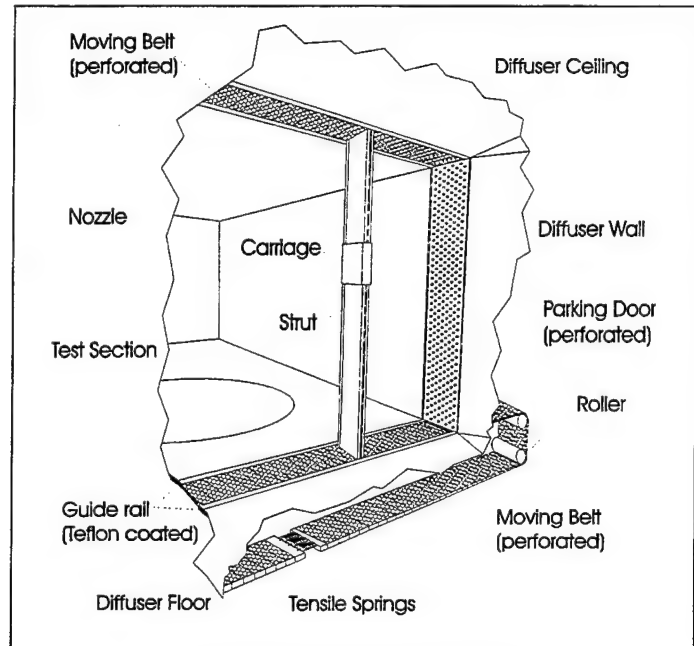


Fig. 6 Perforated moving belts

The vertical strut is a welded construction assembled from several steel profiles. For the vertical carriage two high performance guide rails are provided on the front and the rear end sides of the strut. The strut has also a no-slip ballscrew spindle inside. The structure of the strut was optimized with a Finite Element Method (FEM) program to obtain as narrow a width as possible while maintaining a high torsional stiffness. The blockage of the test section due to the presence of the strut amounts only to 2 %.

The electric cables and pneumatic hoses are carried in a guidance chain inside of the strut to avoid tangling and

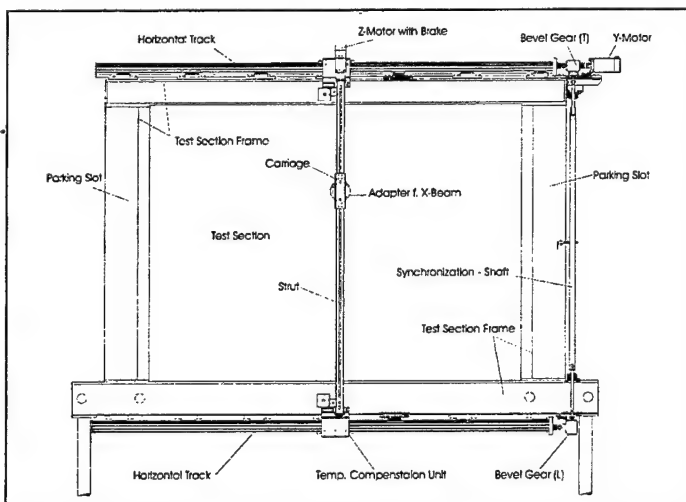


Fig. 5 Base of the rig, y- & z-traversing unit

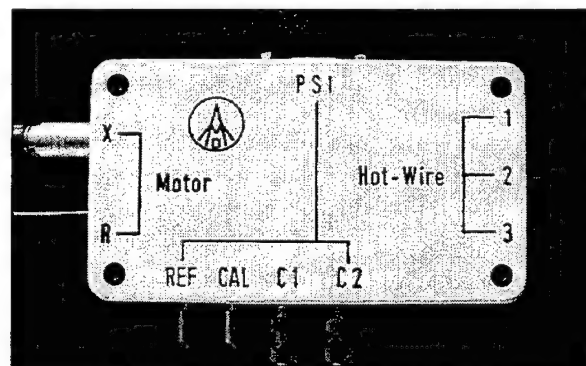


Fig. 7 Interface box on the carriage

snagging. The guidance chain also provides enough space to mount cables for the measuring equipment, e.g. ESP module of PSI system, three channels of hot wire probes, etc. Figure 7 shows the interface box on the carriage.

The outer surface of the strut must be covered. Two protecting bands of stainless steel are installed on the strut. Their working principle is similar to that of the moving belt mentioned above. Thus, the channel is always completely covered in spite of the movement of the vertical carriage. The upper and lower housings of the covering band, which are attached on the vertical strut, are shown in figure 5.

Hybrid Beam for X-Axis movement

As described before, a hybrid beam has to be attached to the carriage on the vertical strut as a horizontal mast arm. Special beam modules made of carbon fiber and steel adapters were constructed for the hybrid beam. The different lengths of the beam are realized by combinations of the modules and corresponding adapters.

Modular Arrangement for the Hybrid Beam

The entire length of the test section is divided for this arrangement into seven Y-Z-'slices', each of 420 mm width in the x direction. Each 'slice' has an overlap of 25 mm with neighboring 'slice'. Probes mounted on the tip of the beam (head module), can move telescopically up to 420 mm. In this way, an entire slice cross-section of the tunnel can be traversed automatically. Moving to the next slice requires a manual exchange of beam modules.

The particular length of the beam modules are chosen in such a way that no two modules have the same length. This arrangement of non-equidistant modules keeps the number of modules small, while maximizing the achievable distances. Figure 8 shows the mast modules and their combinations. Figure 9 illustrates the arrangement necessary if only equidistant modules were available. By comparing figures 8 and 9, it can be seen that the number of modules using non-equidistant lengths can be kept smaller and thus the system is more cost effective.

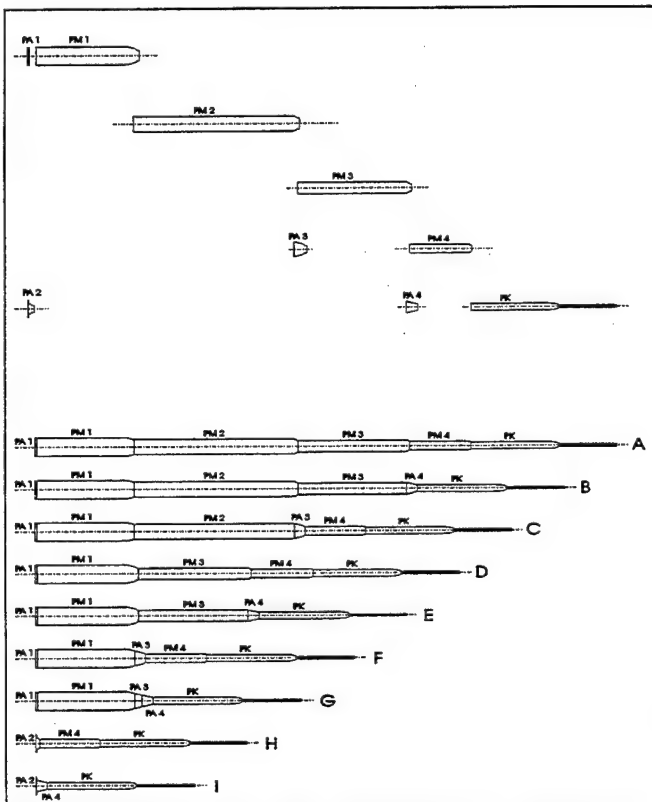


Fig. 8 Non-equidistant mast modules and their combinations

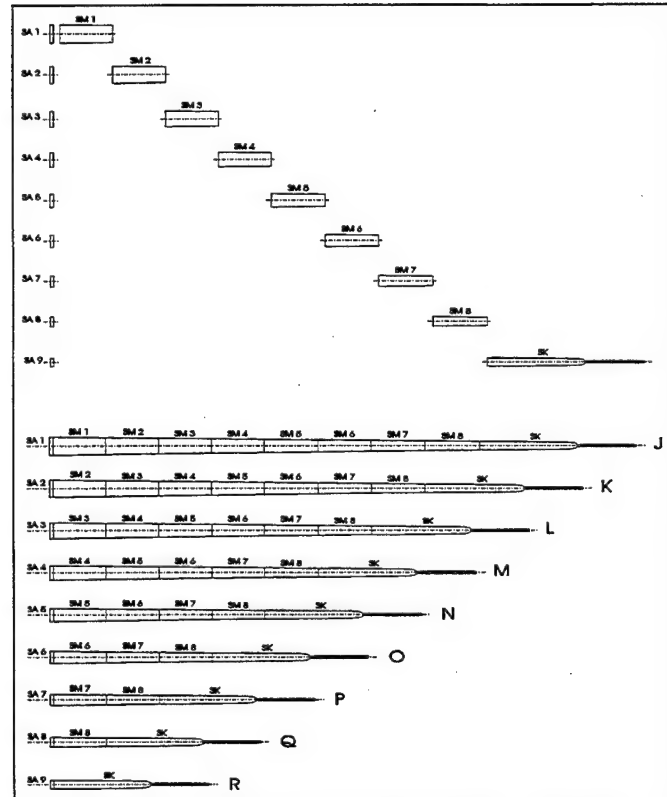


Fig. 9 Equidistant mast modules and their combinations

Actuator for varying the beam length

The rear module contains an actuator for traversing a probe in the flow direction automatically. (Figure 10a) The front module with a telescopic spline-pipe is connected to the ballscrew actuator at the rear module with a push-pull rod.

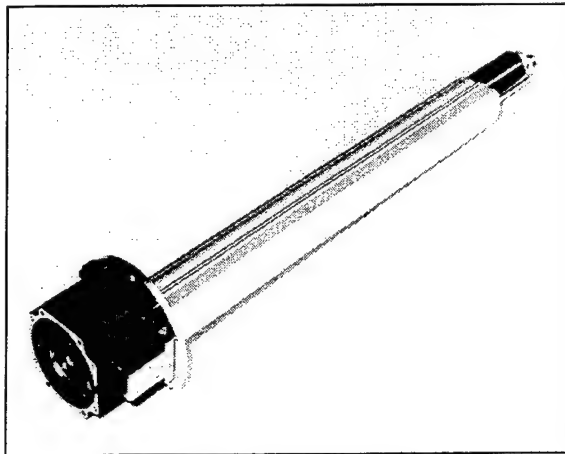


Fig. 10a The actuator

Figure 10b shows the actuator and how it works with a push-pull rod. The entire push-pull rod consists of three pieces. They are combined according to the chosen length of the mast arm. (Note that the push-pull rod in figure 10b requires two segments.)

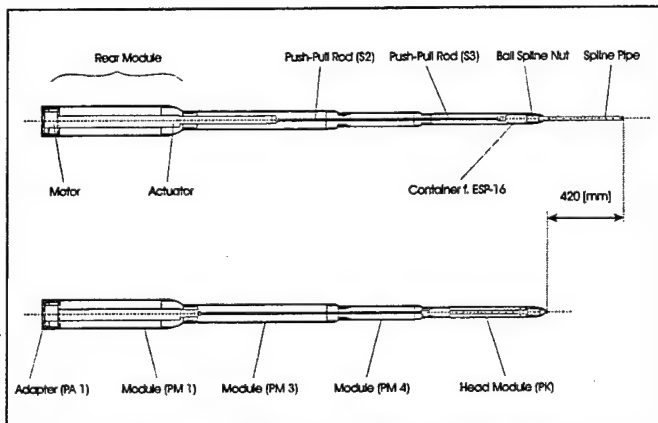


Fig. 10b Actuator and push-pull rods in the mast arm

The separation of the actuator from the telescopic pipe is necessary to keep the diameter of the final module small. This reduces flow disturbances near the probe and also improves the dynamic behavior of the system since moment of inertia of the mast arm is kept low.

As shown in figure 8 the beam is composed of eight

modules, which can be combined to achieve 9 different lengths. The actuator, together with the other two translation stages provides full-automatic movement in three coordinates. Only for the mast combinations H and I is the third stage inhibited, since the actuator cannot be mounted in the mast due to the lack of space. This reduced operation is referred to as semi-automatic.

Fixing the telescopic spline-pipe for semi-automatic operation

For the semi-automatic operation an attachment was constructed as shown in figure 11. By turning the cowling, the spline pipe can be fixed by a collet. Three balls and springs fix the cowling at the defined end position, so that the cowling does not turn alone and loosen the collet.

The notch marks on the spline-pipe give an orientation while adjusting the length (see the photo in figure 11). For the full automatic operation in three coordinates, such an attachment is not necessary since the driving unit exhibits a holding moment. Thus the collet must not block the spline-pipe. The fixing mechanism with three balls and springs keeps the cowling in place, so that the telescopic spline-pipe is always free to move.

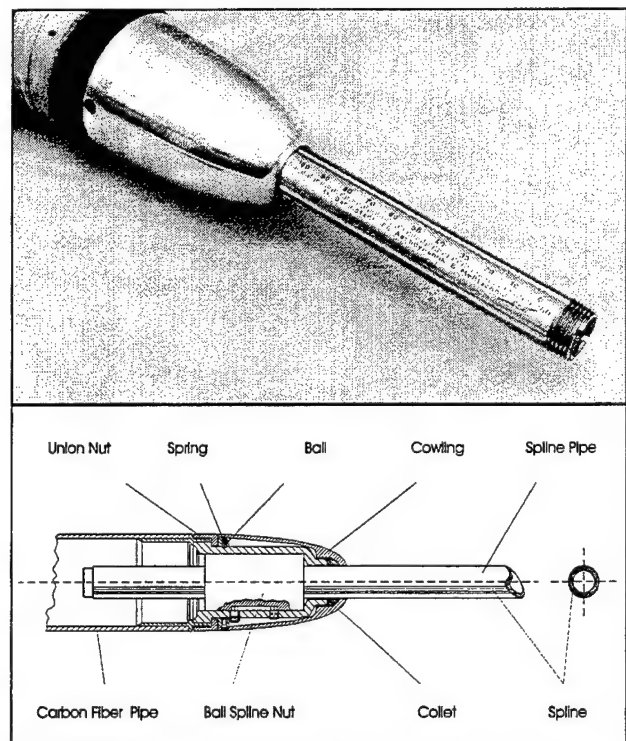


Fig. 11 Details of the head module (PK)

Adjusting Device for Alignment of the Rig and Probe

Adjusting the rig perpendicular to the flow is of great importance, as discussed in [8]. The problem not only involves alignment, but also bending of the mast arm. The use of carbon fiber composite minimizes the strain and stress in the mast arm due to the weight saving but nevertheless, a finite bending always remains. Figure 12 shows the magnitude of such positioning errors and a solution to this problem using a ball-joint adapted to the present prototype.

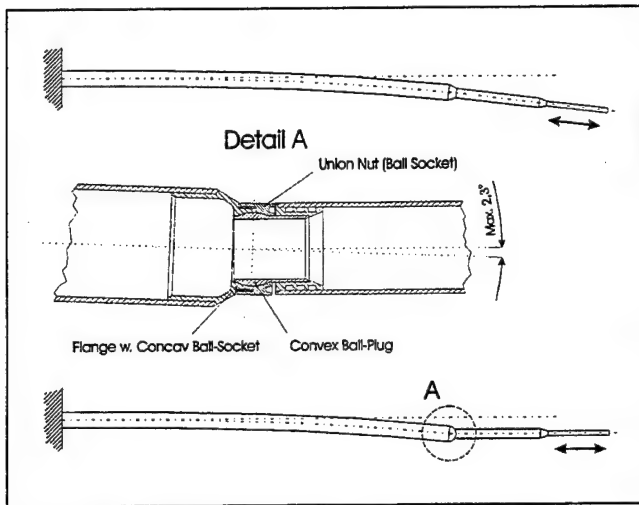


Fig. 12 Ball-joint system to align the mast tip

The principle of a laser based adjustment device developed for the prototype is shown in figure 13. This device consists of two parts. The first one is a reference beamer with a linear positioner, which may be mounted laterally on the carriage. The laser beam can be shifted parallel up and down by adjusting the linear positioner. This unit must be pre-aligned with reference to the flow. This master adjustment has to be

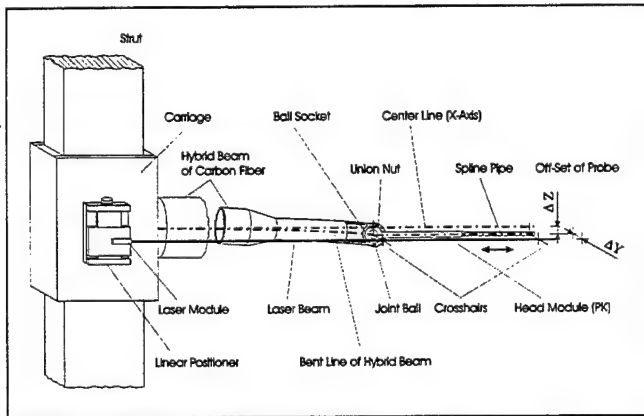


Fig. 13 Alignment of the Probe with a laser beam device

done only once, however. The second part is a fixing claw with two integrated leveling devices and height adjusting screws for all directions. With these adjusting screws the pipe can be aligned relative to the laser beam. After that the claw of heavy weight holds the telescopic pipe until the union nut at the ball-joint is fastened. (The claw is not shown in figure 13). During this alignment the offset of the probe in two directions can be determined (see figure 13).

Driving Unit / System Control

From the large variety of possible driving units for the three component directions a choice of three phase stepper motors has been made. They provide high accuracy with comparatively simple electronics with no need for closed loop control. Stepper motors with 1000 steps per revolution have been used for all three coordinates.

To improve dynamic performance, especially when rapid traverses are necessary, a sine-squared ramp function has been used for acceleration and deceleration. The motor for the z movement is equipped with a brake to prevent the vertical movement carriage from running to the tunnel floor when power is turned off. Figure 14 shows the stepper motors and a low level regulation processing unit. Power supplies for the motors and the entire control system, including the control unit for the z-brake, are integrated in this low level regulation processing unit. It is intended that this unit communicates with a high level regulator (control PC) via a serial RS-232 interface. However this unit can also

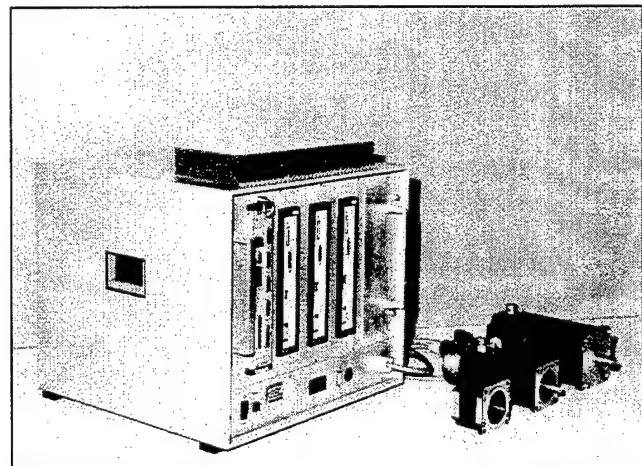


Fig. 14 Stepping motors and low level regulation processor drive all the three axes on its own.

Software

A software package named 'AOSTA' (Advanced Operating System for the Traversing Appliance) was developed to

drive and control the rig. It runs in the Windows 98/NT environment on a personal computer. The AOSTA software begins by connecting itself to the low level regulation processing unit via an RS-232 interface. AOSTA can communicate with the host computer of the wind tunnel via an IEEE 488 Interface. Commands for the traversing rig can also be given by the hierarchically higher host computer (micro VAX), if required.

AOSTA controls not only the driving units of the system but also has an editor, useful graphic functions etc. By using the editor of AOSTA the operator can define measuring grids in the virtual test section. Such measuring grids can be 0, 1, 2 or 3 dimensional. In other words they can be defined as a single point, a straight line, a surface or a spatial volume.

The orientation of the axes of the measuring grid follows normally that of the test section, but this is not mandatory. In some cases it is very useful to make the axes of the grid inclined to the test section reference co-ordinates or even more totally separated from the reference axes. For example the vortex of a wing tip could be measured with great time saving by defining a three dimensional measuring grid restricted by an oblique truncated pyramid. The grid can be aligned also parallel to the axes of the model, so that it has just the same angle of attack and the same angle of yaw as the model relative to the flow. In some cases this possibility is useful for comparison of the measurement data with CFD results. Due to the shifting of the grid center at a non-equidistant grid, the interesting part of the flow field can be measured with a higher resolution than the remaining parts. Figure 15 illustrates an oblique three-dimensional grid with a cosine distribution and a shifted vertical center.

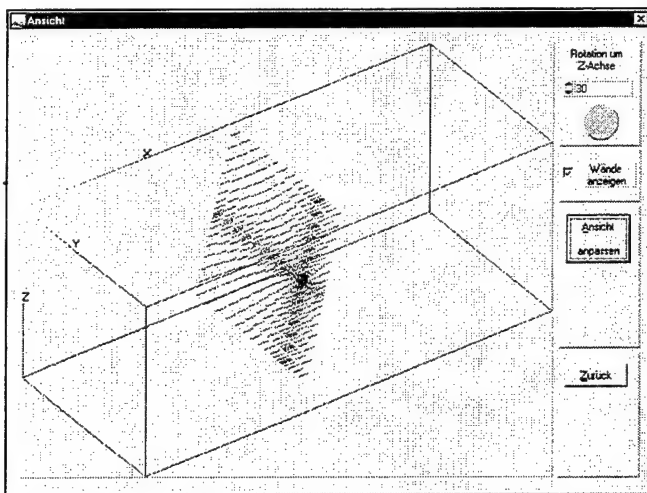


Fig. 15 An oblique three dimensional grid

Another important consideration when designing measurement grids is collision prevention, referring to possible collisions between the probe or traversing arm with a model. There are no universal solutions to this danger which can be easily programmed. Thus, a passive function 'Teach In' was adopted for the AOSTA software to avoid collisions. With this useful function the system can register any kind of model geometry in the test section. A probe (a dummy probe is recommended) can be led manually around the model contour with a hand held control unit (Joystick). The co-ordinates of corners or edges are saved by pushing a trigger switch on the hand held control unit (see figure 16).

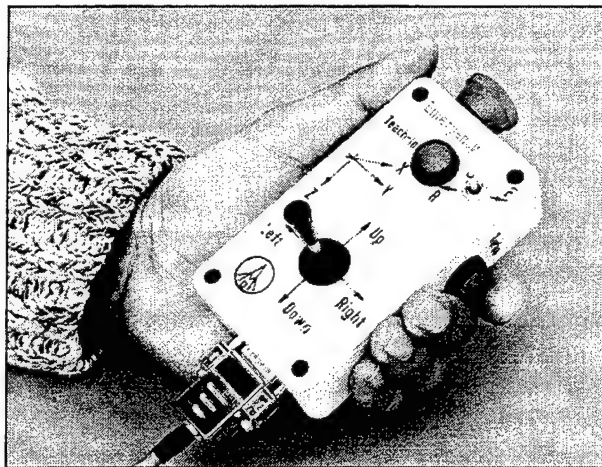


Fig. 16 A real hand held control unit with 9 functions.

A contour can also be optionally entered, for instance the model mounting support, inside of which movement of the probe is prohibited ('prohibited zone'). The co-ordinates of this zone are automatically excluded from the predefined measuring grid. Then, using a special algorithm which is similar to that of NC machine tools, AOSTA finds which way the measuring points should be approached without collision.

The operator has the choice to set some special options such as running precedence of axes, time delay, additional paths etc. The operator can check the errors in the path by monitoring the graphic simulation at any time. If required, he can add a dummy path point or let AOSTA suggest an alternative path. Figure 17 demonstrates the traversing path optimized around a wind tunnel model.

Both the contour and the path generated by the function 'Teach In' can be stored as an operating information file. This information will be used later when the same model is again installed in the test section. This saves set-up time and increases productivity and efficiency of the operation.

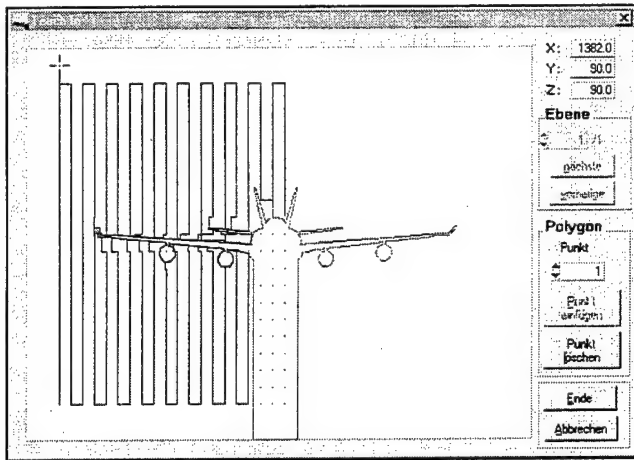


Fig. 17 Suggestion with an optimized traversing path

A notebook computer can take over the control from the PC during the 'Teach In' procedure inside the test section. Experience shows that the comparison between the visual simulation on the screen and the actual model in the test section is very helpful to prevent a malfunction due to misunderstandings. AOSTA also includes system diagnosis to inform the operator about the actual status of the entire system. Figure 18 shows an example for the system diagnosis. It is clear from this example, that the door of the left parking lot is actually open.

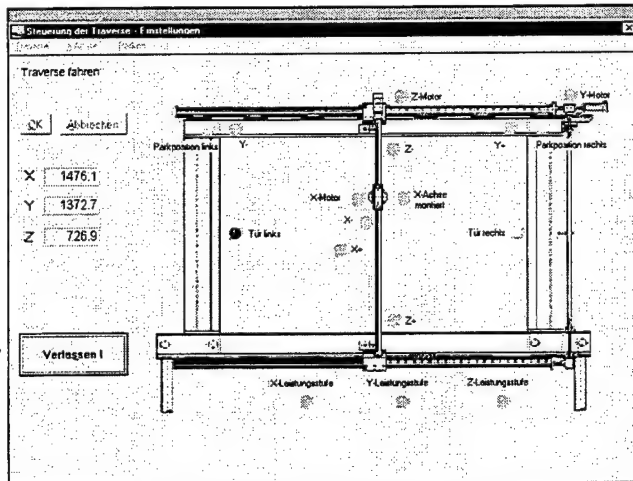


Fig. 18 Display of a system Status

The flexible structure of AOSTA allows easy integration of additional functions, for example procedures to take control of external measuring such as LDA, PIV or CTA equipment. Another possibility would be a fourth axis of movement, such as rotation of a probe. The corresponding probe

coordinates can still be monitored, once the axis of rotation is input to the program. Measurements can also be carried out in a polar co-ordinate system, if required. With such options, probes can be traversed in confined spaces, like between the engine nacelle, pylon and wing of a transport airplane configuration. Figure 19 shows preliminary construction of such a fourth rotation stage, which can be mounted on the mast tip.

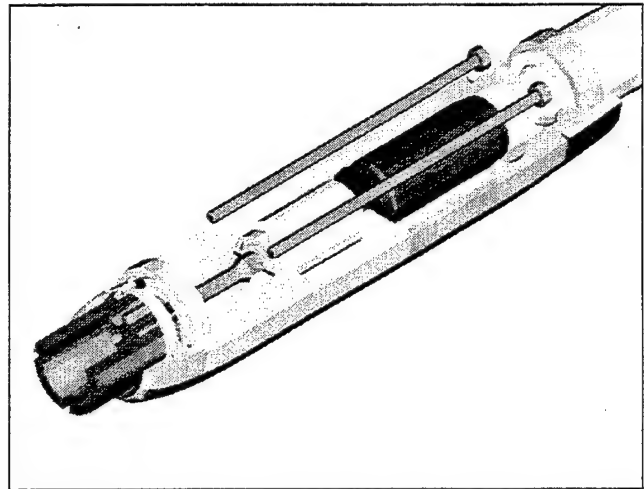


Fig. 19 Structure of a fourth rotation stage

Specifications

Low Speed Wind Tunnel at TU Darmstadt [20]

Type: atmospheric Göttinger Type (return circuit at 1 atm)

Test section (W*H*L): 2900 X 2200 X 4800 m³ / closed

Cross section : A = 6.38 m²

Contraction ratio: 5.2

Max. speed: $V_{max} = 68 \text{ m/s}$ (= 245 Km/h)

Fan Drive: 300 kW DC motor with a Hoffmann 6 blade rotor

max. Re-Number: 1.1 E6 (based on $0.1 \cdot \sqrt{A}$)

Established in 1935, modernized in 1974, 1986-1988

Prototype of the Traversing Rig at TU Darmstadt [1]

Available stroke of the axes in mm: X: 420, Y: 3240, Z: 2340

Operating range in mm: X: 737- 4135 Y: 2610, Z: 1910

Velocity: $V_X = 10 \text{ mm/s}$, $V_Y = 50 \text{ mm/s}$, $V_Z = 40 \text{ mm/s}$

Nominal Accuracy in mm: X: 0.004 Y: 0.02, Z: 0.01

Real repeatability in mm better than: X: 0.5, Y: 0.2, Z: 0.1

Natural frequency: 12-14 Hz

Max. weight of the entire traversing rig: 240 Kg

Max. weight of the x-mast: 28.2 Kg

Drive : 3-phase Stepping Motor for all the three axes

Projected surface normal to the flow: 0,1364 m²

Blockage of the test section due to the Traversing rig: 2 %

Dedication / Acknowledgements

The development work described in this paper was performed in the period 1995 - 1998 under the supervision of Prof. emeritus Dipl.-Ing. B. Ewald, to whom this contribution is dedicated on the occasion of his emeritus.

The author would also like to acknowledge the helpful discussions of cooperation of his colleagues at the TUD wind tunnel facility.

The proof-reading by Prof. Dr.-Ing. C. Tropea is also gratefully acknowledged.

References

1. Seung, T. : „Sondentraversiergerät neuer Generation für geschlossene Unterschall-Windkanal-Meßstrecken“, Bericht des FG Aerodynamik & Meßtechnik, TU Darmstadt, A615p / 98, 1998.
2. Seung, T. et Conrad, H. : „Automatisierung der Strömungsfeldmessung in geschlossenen Niedergeschwindigkeitswindkanal-Meßstrecken“, Kongreß VIP 98 „Virtuelle Instrumentierung in der Praxis“, ISBN: 3-7785-2729-0, Oktober, 1998.
3. Seung, T. : „Längenvariabler Mast für meßtechnischen Anwendungen im Windkanal als Sondenträgerarm“, Bericht des FG Aerodynamik & Meßtechnik, TU Darmstadt, A205 / 98, 1998.
4. Seung, T. : „Kartesisches Sondentraversiergerät mit einer aus der Windkanalmeßstrecke herausfahrbaren Teiltraverse“, Bericht des FG Aerodynamik & Meßtechnik, TU Darmstadt, A206 / 98, 1998.
5. Ewald, B. et Seung, T. : „Automation of flow field measurements in low speed wind tunnels with closed test sections“ ISASTI 98, Jakarta, Indonesia, September 1998.
6. Ewald, B. : „Die Rolle der Aerodynamik und des Windkanals bei der Entwicklung von Verkehrsflugzeugen“, Luft- u. Raumfahrt, Heft 2, 1995, Deutsche Gesellschaft für Luft- und Raumfahrt e. V.
7. Thibert, J. J. : „The GARTEUR High Lift Research Programme“, „Eternal Probe Traversing System“ in LST of Nationaal Lucht- en Ruimtevaartlaboratorium, Wind tunnel ONERA F1 (Toulouse, France), AGARD, CP-515, ISBN 92-835-0715-0, 1992.
8. Brune, G. W. : „Quantitative Three-Dimensional Low-Speed Wake Surveys“, 5th Symposium on Numerical and Physical Aspects of Aerodynamic Flows, California State University, Long Beach, CA, Jan. 1992.
9. El-Ramly Z. M. et Rainbird, W. J. : „Computer-Controlled System for the Investigation of the Flow behind Wings“, J. Aircraft, Vol. 14, No. 7, July, 1977.
10. Raagaard, Jacob : „Traversing System of Full-Scale Wind Tunnel“, , ICIAASF '95 Record, p43.1-43.7, 16th International Congress on Instrumentation in Aerospace simulation Facilities, IEEE Publication 95CH3482-7, ISBN 0-7803-2088-3, 1995.
11. van den BERG, B. : „Boundary Layer Measurements on a Two-Dimensional Wing with Flap“, Report NLR TR 79009 U, Nationaal Lucht- en Ruimtevaartlaboratorium, Holland, 1979.
12. Runge, F. : „Einfluß von Wandöffnungen hinter der Meßstrecke auf die Windkanalströmung“, Bericht des FG Aerodynamik & Meßtechnik, TU Darmstadt, 1996. A160 / 96.
13. Kreuzer, P. : „Weiterentwicklung und experimentelle Überprüfung eines 3-D Panelverfahrens im Falle einer Tragflügelanordnung mit Winglets“ Dissertation am FG Aerodynamik & Meßtechnik der TH Darmstadt 1993.
14. Henke, R. et Dreißler, U. : „Untersuchungen am Flugversuchsträger ATTAS mit Laminarhandschuh und dessen 1:2 Großmodell im DNW und S1“, p417-426, DGLR Jahrbuch 1981 I.
15. „Dantec Newsletter“, Special edition / 1996, Dantec Measurement Technology A/S, DK-2740 Skovlunde, Denmark.
16. „Dantec Newsletter“, Volume 4 no. 1 / 1997, Volume 4 no. 4 / 1997, Dantec Measurement Technology A/S, DK-2740 Skovlunde, Denmark.
17. „Modular aluminum traverse“, Dantec Newsletter, Volume 5 no. 1 / 1998, Volume 5 no. 3 / 1998, Dantec Measurement Technology A/S, DK-2740 Skovlunde, Denmark.
18. „56H00 Traversing System“, Publication. No. 4202 E, Dantec Measurement Technology A/S, DK-2740 Skovlunde, Denmark.
19. Technical Guide for „Kirsten Wind Tunnel“, University of Washington Aeronautical Laboratory, <http://www.aa.washington.edu/uwal/techinfo.html>, Standing: May 1999.
20. Ewald, B. : „The Subsonic Wind Tunnel of the Technical University of Darmstadt“, Report 166/96, Division of aerodynamics and Measuring Techniques, TU Darmstadt, May 1996.

18TH INTERNATIONAL CONGRESS ON INSTRUMENTATION IN AEROSPACE SIMULATION FACILITIES

ONERA

Toulouse

14.-17. June 1999

Klaus Hufnagel TUD
Rüdiger Rebstock DLR
Junnai Zhai DLR

Half-Model-Balance for the Cologne-Cryogenic-Wind-Tunnel Development and Test Results

SUMMARY

After the instrumentation of the Cologne Cryogenic Wind Tunnel (KKK), with internal balances, it has been a demand of the tunnel customers to make half model tests at high Reynolds numbers. The Mach number range from zero to 0.3 and the relative low costs with regard to the high Reynolds number made the KKK very attractive for half model testing. To realize this capability DLR and the Department of Aerodynamics and Measurement Techniques of the Darmstadt University of Technology (TUD) decided to develop a half-model-balance for the KKK in 1994. A very challenging task, because no previous attempt to solve this problem for a continuous running cryogenic wind tunnel was successful.

Fortunately the tests in the tunnel with the first balance (W519) we built were very successful. During the tests a lot of experience was made and some new problems appeared. The main problem was the unexpected great temperature gradient inside the balance, although there was a very sophisticated heating and insulating device around the balance.

At TUD a finite element study was made to design a new balance in such a way that the balance is more insensitive to temperature gradients.

Unfortunately the balance W519 was destroyed by an accident in the tunnel and we had to build a second one (W523) very quickly. All the things we learned had to be turned into practice very quickly without any tests in the laboratory. Finite element calculations turned out to be a very useful tool to solve this task.

In November 1997 we started to design and built the second balance and we finished it in August 1998. The

very short time for the manufacturing of 9 month was achieved by the use of a three dimensional EDM-machine and the change of the calibration procedure.

Instead of using weights as true calibration loads, we used the external balance of our low speed wind tunnel as a reference balance to give us the "true loads". By this method no realignment of the calibration model was necessary and the calibration process could be done in three weeks.

The accuracy of the new procedure, based on recalculation of the calibration loads, turned out to be better than the former one, because the accuracy of the external balance is one magnitude better than the required accuracy of the half model balance and there are no errors by misalignment.

The balance W523 could be delivered to the tunnel just in time and it was first used successfully in September 1998. The comparison between some measurements, made with the old balance and the new one, showed a very good correspondence of the results. The repeatability of polars with the new balance in the tunnel was about one drag and lift count.

BALANCE AND SUPPORT DESIGN

In 1995 Darmstadt University of Technology (TUD) designed a half model balance (W519 **Fig. 1**) for the Cologne-Cryogenic-Wind-Tunnel (KKK). This balance was the first successful half model balance in a cryogenic wind tunnel.

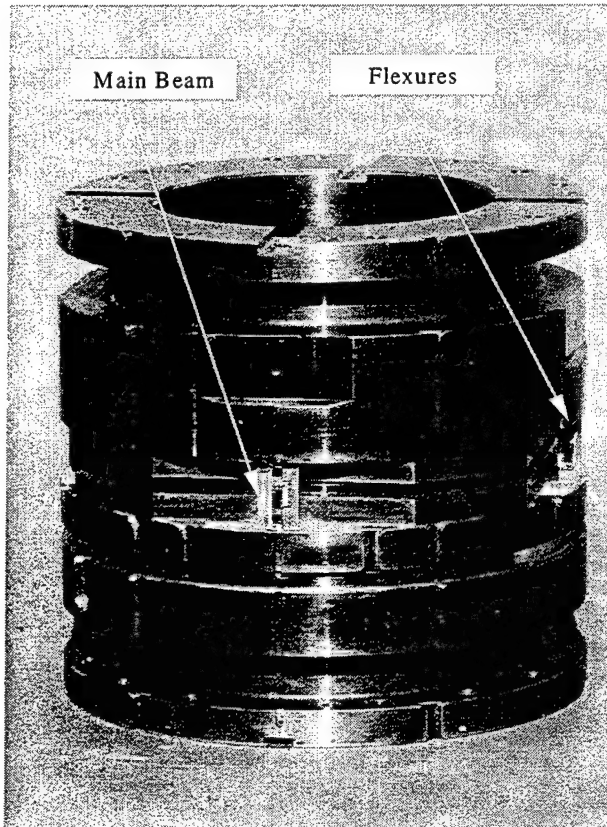


Fig. 1 Balance W519 First Half-Model-Balance of KKK

The balance was designed as a warm balance surrounded by a superinsulation with heating foils on the surface and connected to the model by a very sophisticated combination of insulators, heaters and thermal rectifiers (see Fig. 2)

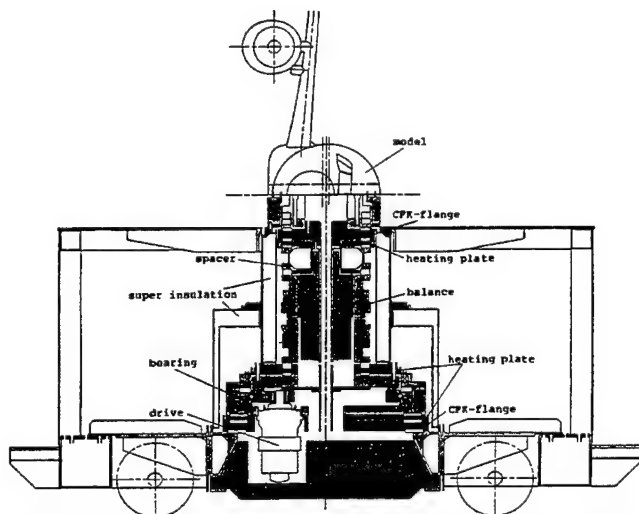


Fig. 2 Total arrangement of balance W519 in KKK- model cart.

This concept proved to be correct in several campaigns with half models of airbus type. Nevertheless there were

some unexpected temperature gradients inside the balance. these gradients could not be compensated by the heaters.

Fig. 3 shows that spacer and copper-plate temperature stays constant, while the temperature inside the balance is drifting . In some cases the drift was only very low (2...4 K), in some others the drift could be up to 10 K.

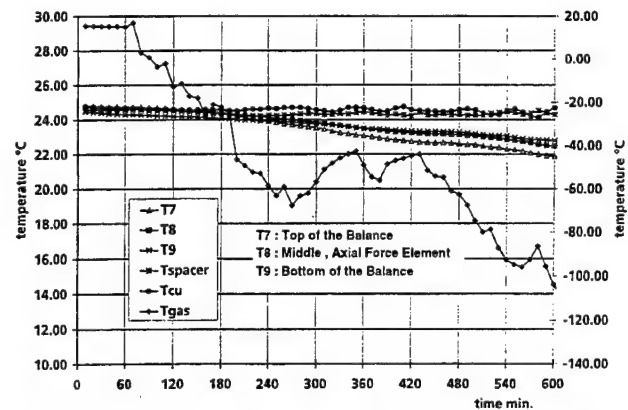


Fig. 3 Temperature versus Time inside Tunnel and Balance

These gradients are not very high, but they cause high axial force signals.

This signal could be compensated in the first balance by the use of four different beams for the axial force measurement,. These beams are placed symmetrically and so most of the error-signals are canceling out after their signals are summed up. We decided to use this complicated arrangement of four axial force bridges before we knew something about the gradients in the balance. But the experience with the internal balances showed, that the temperature gradient problem rises with the dimensions of the balance.

SECOND HALF MODEL BALANCE W526

Regarding these facts we tried to study these effects by a finite element analysis.

To have a common basis for all new designs we created some different temperature gradients and all the new designs were analyzed with respect to this temperature gradients. Also the new designs were compared with the results of the old balance.

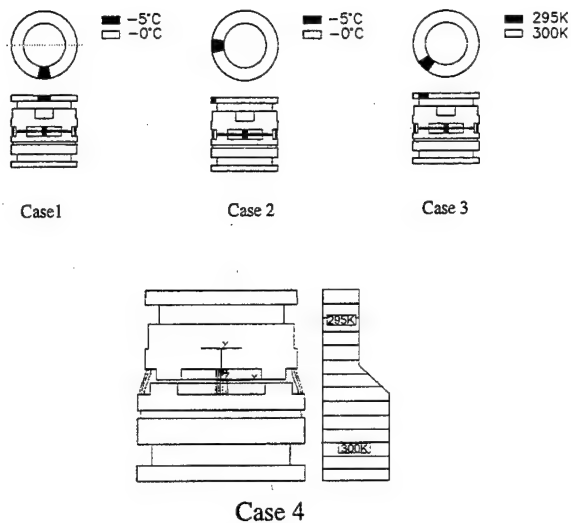


Fig. 4 Basic Temperature Gradients for the FE-Calculations

Fig. 4 shows the four different basic temperature gradients which may occur inside the balance and cause error-signals.

The first case is a difference of 5 K in the flange above the main measuring beam, the second case is a 5 K gradient in the flange above the parallelogram system and the third case is a 5 K gradient in the flange at the 45° degree position between parallelogram and main beam. In the fourth case a difference of 5 K between the upper and the lower main parts of the balance was assumed.

The result of this investigation was, that this four different gradients will cause deformation differences between the upper and the lower main ring of the balance which are equalized by deformations of the measuring- and parallelogram beams and so various signals due to gradients are generated.

The measures to prevent the balance from gradient sensitivity therefore must be more flexibility, a greater heat transfer resistance in the flange part of the balance and no heat radiation to the center rings by heating devices at the inner side of the super insulating box.

Heat transfer from the adapter to the balance could be reduced by a Teflon foil between the flanges and titanium instead of steel screws, which do have a three times lower thermal conductivity.

The flexibility of the flange and a further reduction of the heat conducting area was achieved by slots in the flange as shown in Fig. 5.

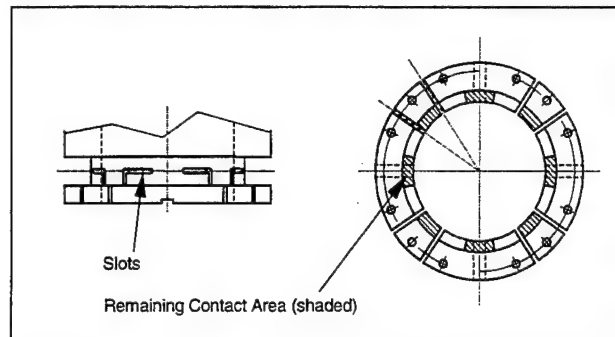


Fig. 5 Flange of Balance W526 with Slots

Finite element calculation showed that there will be a significant reduction in temperature gradient sensitivity by these measures, but the balance could not be totally protected against temperature gradients.

To compensate the remaining effect of temperature gradients in the axial force measurement we used separate strain gage bridges on each main beam and on the outer parallelogram springs. Now 6 different bridges are used for axial force measurement to optimize the effect of cancellation by summing up the signals. Two bridges in opposite position on the balance must have nearly the same sensitivity. This is achieved by the design of the measuring beam. The aim of the design was to get a uniform stress distribution in the area of the strain gage application under the load to be measured.

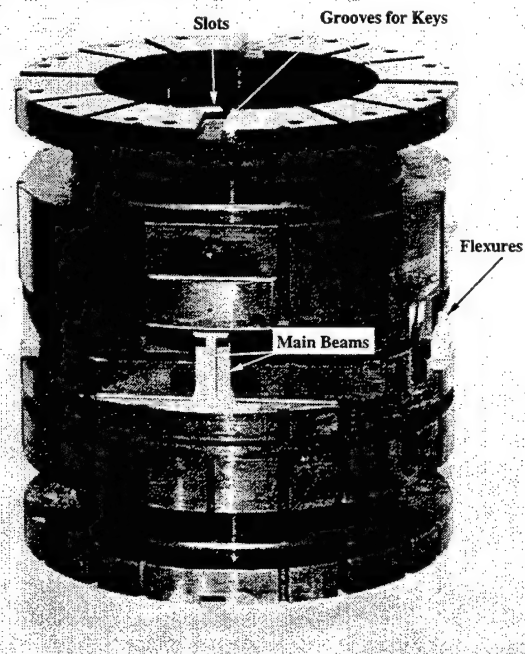


Fig. 6 Balance W526, ready machined

Machining of the balance was done by milling and EDM. Most of the work was done on a three dimensional

operating NC-EDM-machine. Most of the reduction of the time for the manufacturing process was gained by the use of this machine. A side effect of this machine is that the overall precision of the dimensions is better than on a conventional machine, because the balance stayed in position on the machine during the whole process. Therefore no aligning for the machining of different parts of the balance was necessary.

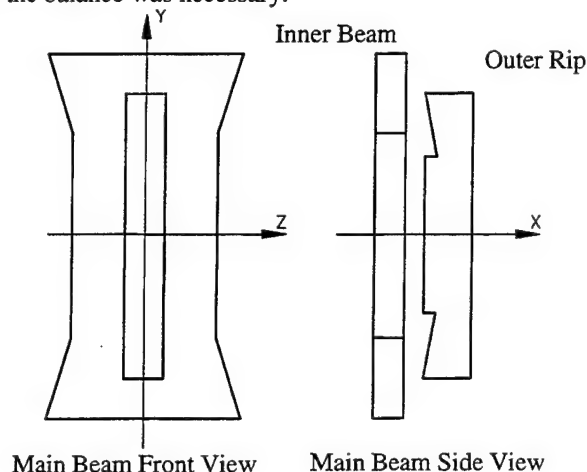


Fig. 7 Front and Side View of Main Measuring Beam

To get a uniform stress distribution the main beam must be cut in two parts (see Fig. 7). The outer rip carries one axial force bridge and one bridge of the yawing moment. The inner beam is used to measure lift and pitching moment.

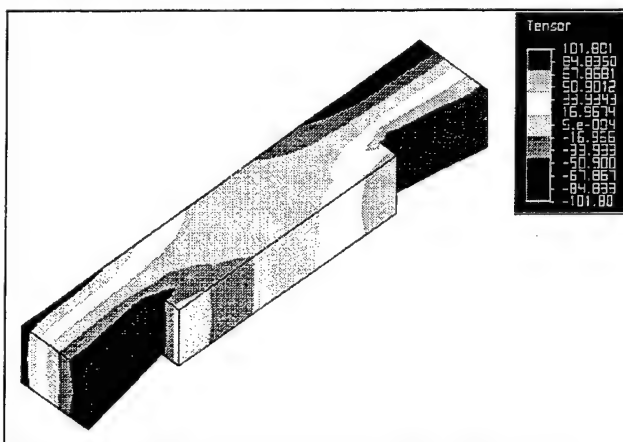


Fig. 8 Stress Distribution in outer Main Beam under Axial Force

Fig. 8 shows the stress distribution in the outer main beam under axial force and it can be seen, that over the area of strain gage application at the ends of the beam, stress distribution is very uniform.

For the measurement of the rolling moment and additional axial forces another eight bridges are installed on the outer flexures of the parallelogram system as shown in Fig. 9.

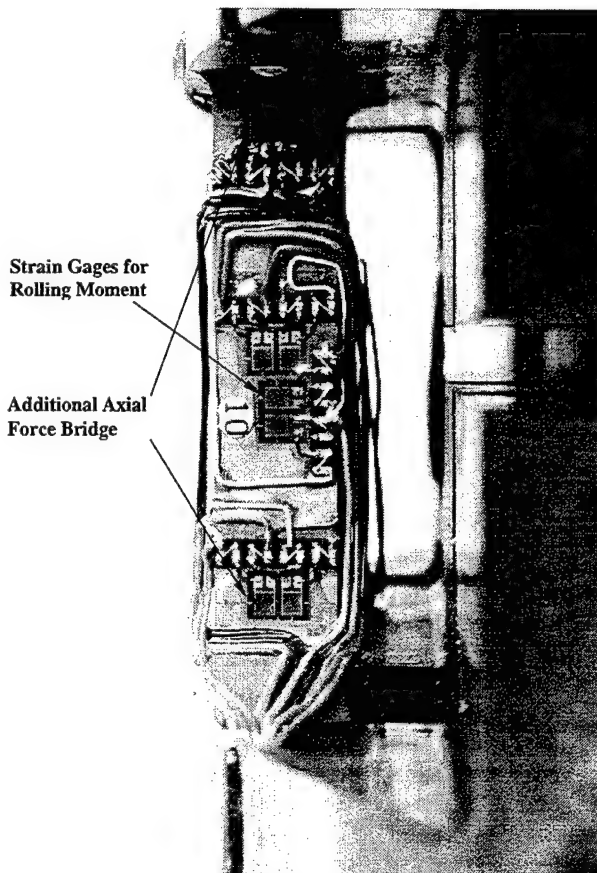


Fig. 9 Strain Gauge Application of Parallelogram Flexure

CALIBRATION OF THE BALANCE

The first half model balance (W519) we built for the KKK was calibrated on our calibration rig which is normally used to calibrate internal balances. The balance with its non metric end was mounted to the earth end of the rig and on the metric end a calibration model was fixed. Weights were applied via rods to this calibration model and the axis system of the model was realigned to the geodetic axis system (see Fig. 10).

To calibrate all forces, different setups of the balance must be made. In one position the balance was installed with its Y-axis vertical, like the real position in the tunnel. In the other setup the balance was mounted horizontally like it can be seen in Fig. 10. The result of this different mounting was a different zero loading of the balance that causes instability of the zero signals, which could not be corrected completely. The very lengthy realigning process causes a relative long time for the whole calibration of about three month. All these facts reduced the overall accuracy of the process.

Out of these experiences made with the first balance, we realized that we would not be able to finish the balance in time with this method of calibration. So we decided to change the calibration method.

Like in the new design of our calibration machine the metric end of the half model balance is now connected to the metric end of a reference balance and the non metric end of the half model balance is loaded with weights (see Fig. 11). As reference balance we used the external balance

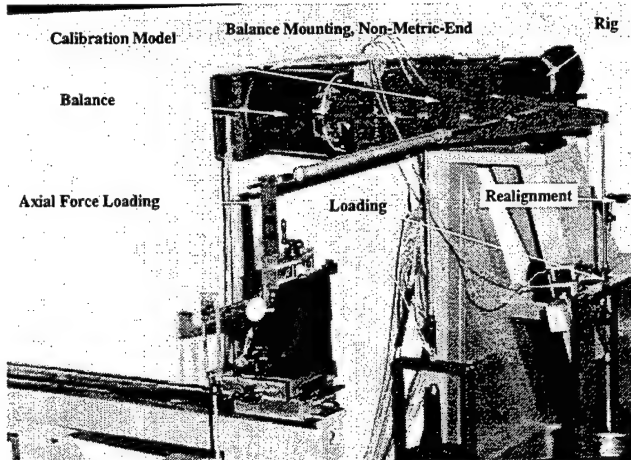


Fig. 10 Balance W519 Calibration Setup

of our low speed wind tunnel. The overall accuracy of this balance is about 0.025% F.S., which is good enough to get an accuracy of the half model balance of less than 0.1%.

The main advantage of this setup is, that there is no realignment of the loads after every change of a loading during the calibration, because the axis system of the half model balance and the reference balance are connected together. The real calibration loads are measured by the reference balance. The major disadvantage is, that no pure single load can be produced. Every change of a load will cause also little changes in some other components, but these changes are precisely measured by the external balance. Our algorithm which is used to compute the evaluation matrix is able to handle such data sets, so that the use of this calibration method promised to be successful.

In contrast to former calibrations we also changed the distribution of calibration loads. Normally equal load steps from zero to the nominal load are used during calibration. A analysis of the loads measured in the tunnel with the first balance showed, that there are some major areas between 50 % and 100 % which are used more than the other parts of the load range. In this areas we used smaller load steps and beside this areas we used larger ones to focus the data set on the most used part of the load range.

The measured data in the tunnel were also analyzed, to see which load combinations were measured the most. The choice of load combinations for the calibration was done according to the most frequent combinations in the tunnel.

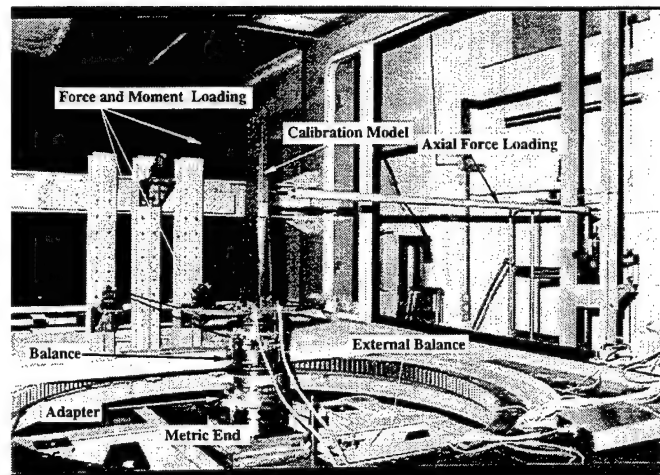


Fig. 11 Calibration Set Up of Balance W526

The goal was to fit the whole data set of the calibration as good as possible to the loads which occur during tunnel testing. This reduces the number of loads we have to apply for the calibration and gives the best fit of the evaluation matrix without having lower accuracy at the endpoints of the balance capacity.

The recalculation of the calibration data set of the first balance showed in most load sets a difference between the true loads and the calculated loads of about 0.1 % to 0.25 % and some sets had relative high difference of about 1 % full scale. The recalculation of the data set of the new balance showed differences of about 0.02% to 0.1% and in some cases up to 0.2 % relative to the measured loads of the external balance which do have a uncertainty itself.

Taking into account that the "true loads" measured by the external balance have an error itself, the accuracy obtained by the second method is better than by first one. Regarding the fact that the repeatability of both balances are the same, the error of the "true loads" of the first method must be higher. Therefore the error of the loading must be caused by the realigning and the long duration of the whole process, because the loads generated by calibrated weights do have only a small error itself.

COMPARISON OF OLD AND NEW BALANCE

The first few test with new the balance were made to check the repeatability of the whole system. Therefore one of the last configurations measured with the old balance was used

to ensure tunnel people and customer of the repeatability and the accuracy of the new balance.

In Fig. 12 two polars of the same configuration, one measured with the old balance W519 and the other one measured with the new balance W526, both at ambient temperature are shown. The correspondence of the two curves is very good.

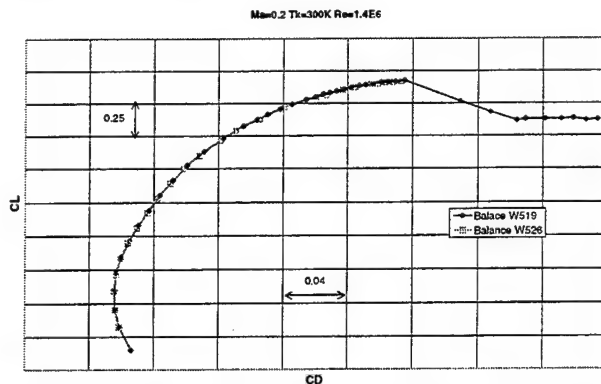


Fig. 12 Comparison of measured Polars at ambient Temperature

Also very good is the correspondence at low temperature (100 K) as Fig. 13 shows. No differences can be calculated because the values are measured not exactly at the same angle of attack. Repeatability of tunnel together with the new balance is about 1 drag- or lift count.

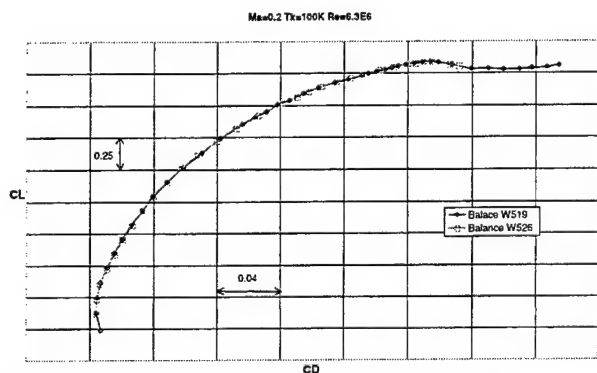


Fig. 13 Comparison of measured Polars at 100 K

CONCLUSIONS

A half model balance with a new design has been built and calibrated in the relative short period of 9 months. The risk of the new design could be minimized by use of finite element calculation to predict the characteristics of the new balance. The reduction of the time for the manufacturing process was achieved by the change of the calibration method and the use of a three dimensional NC-EDM-machine. The results of the development can be traced to

any other Half-Model-Balance at any nearly constant temperature level.

REFERENCES

- [1] Ewald, B.: *Grundsatzuntersuchung zum Temperatur-Verhalten von DMS- Axial-Kraftteilen*, BMFT LVW 8420 1 0, Nr. 10185 1985
- [2] Ewald, B. and Krenz, G.: *The Accuracy Problem of Airplane Development Force Testing in Cryogenic Wind Tunnels*, AIAA Paper 86-0776, Aerodynamic Testing Conference, March 1986
- [3] Ewald, B.: *Balance Accuracy and Repeatability as a Limiting Parameter in Aircraft Development Force Measurements in Conventional and Cryogenic Wind Tunnels*, AGARD FDP Symposium, Neapel, September, 1987
- [4] Ewald, B., Hufnagel, K. and Graewe, E.: *Internal Strain Gage Balances for Cryogenic Windtunnels*, ICAS- Congress, Sept. 92, Peking, Bericht A 100/92
- [5] Ewald, B.: *The Development of a Complete Internal Balance Testing Technology for Cryogenic and Conventional Wind Tunnels*, Pacific International Conference on Aerospace Science and Technology, September, 1993, Bericht A 119/93
- [6] Ewald, B., Hufnagel, K. and Zhai, J.: 'Advanced Force Measuring Technique in Cryogenic and in Conventional Wind Tunnels. Present Status and Further Development', the 2nd International Symposium on Aeronautical Science and Technology of Indonesia (ISASTI), Jakarta, Indonesia, June, 1996
- [7] Ferris, A. T.: *Cryogenic Strain Gage Techniques used in Force Balance Design for the National Transonic Facility*, NASA TM 87712, May 1986
- [8] Hufnagel, K.: *Entwicklung und Optimierung von sechs-Komponenten-DMS-Windkanalwaagen zum Einsatz unter Kryogenen Bedingungen*, Dissertation, 1995, TH Darmstadt
- [9] König, K.G.: *Eigenschaften metallischer Meßkörper für die Windkanalmeßtechnik*, Dissertation, 1993, TH Darmstadt
- [10] Rebstock, R.: *Development of Correction Procedure for Signals of Cryogenic Balances*, AGARD-R-812, February 1997

- [11]Rebstock. R.: *Half Model Testing at High Reynolds Number and Low Temperature in the Cryogenic Wind Tunnel Cologne (KKK)*, 17th ICIASF, September 1997
- [12]Viehweger, G. and Ewald, B.: *Half Model Testing in the Cologne Cryogenic Tunnel (KKK)*, AIAA-94-2511
- [13]Zhai, J., Ewald, B. and Hufnagel, K.: *An Investigation on the Interaction of Internal six-Component Wind Tunnel Balances with FEM*, 16th ICIASF Congress, July, 1995, Dayton, Ohio
- [14]Zhai, J., Ewald, B. and Hufnagel, K.: *Shape Optimization of the Internal Wind Tunnel balances Using Simulated Biological Growth Approches*, AIAA-96-2255, 19th AIAA Advanced Measurement and Ground Testing Technology, June, 1996, New Orleans, LA, USA
- [15]Zhai, J., Ewald, B. and Hufnagel, K.: *Optimization of the Performance of Internal Six-Component Strain-Gage balances with FEM*, ICAS-96-3.4.3, 20th Congress of ICAS, Sept. 1996, Sorrento, Italy
- [16]Zhai, J. and Hufnagel, K.: *Optimization of Internal Strain Gage Balances with Finite Elements Computation', the International Symposium on Strain Gage Balances, NASA Langley, VA, October, 1996*

A NEW APPROACH TO MEASURING MODEL DEFLECTION

R.K. van der Draai, R.P.M. van Schinkel, A. Telesca
NLR, Anthony Fokkerweg 2, 1059 CM Amsterdam, The Netherlands.

ABSTRACT

This paper illustrates results of a series of deformation measurements on a dummy wing which were performed in the NLR workshop. Two different Moire techniques are applied: the Painted Pattern Method, and the Projected Pattern Method. The out-of-plane distortions, obtained under different loads applied, are compared with those measured in five sections along the wing span using a 3D Co-ordinate Measuring Machine and with those predicted using a CAD system. Two examples of wind tunnel measurements are briefly discussed.

1. INTRODUCTION

A wind tunnel is the measuring device to create the aerodynamic controlled conditions (Mach, Po and To), in which a scaled model is placed.

In general, the main interest for researchers is the aerodynamic behavior of the model and its flow field, directly evaluated from measuring the aerodynamic forces and moments acting on the model. However, due to the aerodynamic loads on the model, it will be subjected to structural deformations.

That is the reason of the interest for customers of wind tunnels in measuring deformations of model surfaces under aerodynamic loads.

The Moire technique that is used for the measurement of deformations is relatively old.

In the past, the Fixed Grid, the Projected Grid and the Reflected Grid Method were already applied. In order to measure deformations in wind tunnels, the most common pattern used was the line type pattern and the image acquisition system was usually composed of a digital video camera and software developed especially for this purpose.

A new approach arrives from the analogy with Particle Image Velocimetry (PIV):

PIV

- Seeds are injected in the flow

- Seeds pass through a light sheet
- A CCD camera focuses on the sheet
- Two images are acquired
- The in-plane displacement can be derived, and from the time delay between pulses follows the velocity field

Moire

- Spots are painted or projected black on a dull white model surface
- A CCD camera focuses on the model surface
- Deformed and undeformed images are acquired
- The in-plane displacement can be derived, and applying calibration images follows the out-of-plane displacement

In the last years, this technique has been already used for several clients during experimental tests in the DNW-HST wind tunnel.

In order to improve the method and verify its limitations, in the NLR workshop a series of deformation measurements on a dummy wing were performed. Two different Moire techniques have been applied:

- A random pattern with black dots is projected, under an angle, on the side of the model that is painted dull white
- A random pattern with black dots is painted on the other side of the model

In both cases a CCD video camera is used to record the images of the surface, both deflected and undeflected. The shift of the pattern on that surface is a measure for the out-of-plane distortion of the wing, caused by the applied loads.

The images recorded for different load conditions are subsequently analysed and processed using a commercially available PIV data processing software package.

To enable a reliable comparison of the experimental results obtained with the two methods presented above, the distortion caused by the applied loads is also measured in five section selected along the wing span. This is realised using a three dimensional Co-ordinate Measuring Machine, in general used to determine the accuracy of aircraft models that are manufactured in the NLR workshop.

Also a theoretical prediction of the deformation was obtained using the Computer-Aided-Design (CAD) system.

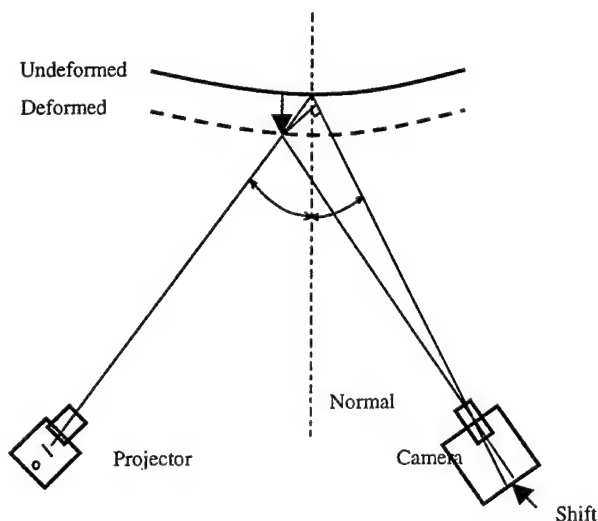


Figure 1: Optical set-up of the Projected Pattern Method

2. DESCRIPTION OF THE MEASUREMENT METHODS

2.1 The Projected Pattern Method (PrPM)

In this method, a random pattern is projected on the surface of a structural component, which is deformed out-of-plane.

Looking from a direction, which forms an angle with the projection direction, the deformation of the component can be read from the characteristics of the pattern image. When the surface of the component changes, the image of the pattern changes and in principle the out-of-plane deformation can be measured.

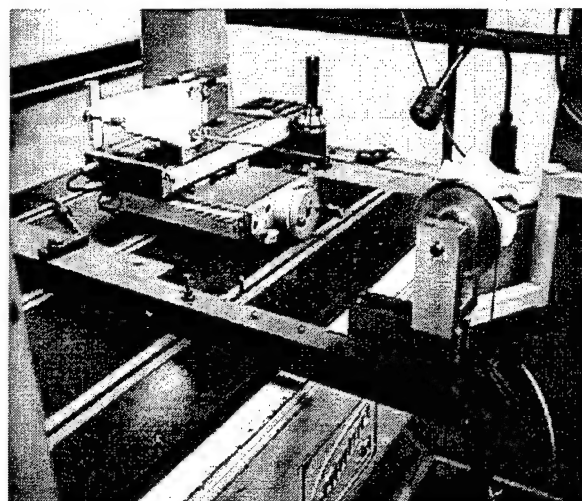
The basic optical set-up for the Projected Pattern Method consists of a projector and a camera. Both are pointed to the same location of the component surface: their optical axes form an angle with the local normal in the undeformed situation, selected by estimating the maximum deflection caused by the applied loads.

A schematic view of the basic optical set-up is showed in Figure 1.

2.1.1 Experimental set-up

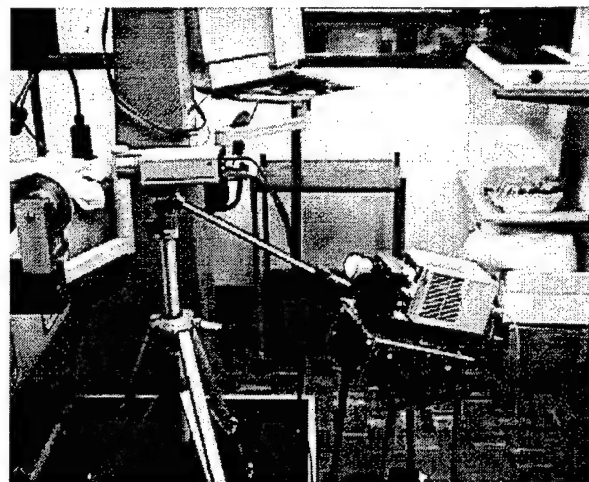
For all sets of measurements, the test object is a dull white painted wing with a span of 24.8cm and a thickness of about 4mm. The wing was mounted on a traversing stage, by which it could be accurately translated. In this way it was possible to simulate pure translations in a given direction and over a given distance, and use them as calibration images to calculate afterwards the out-of-plane deflections.

The loads are applied on the wing using a simple system of cables over pulleys and scales, as shown in Picture 2, which refers to the set-up for bending measurements using the Projected Pattern Method.



Picture 2: Actual set-up for bending test using the Projected Pattern Method.

Concerning the optical set-up used performing the Moire test with the Projected Pattern Method,



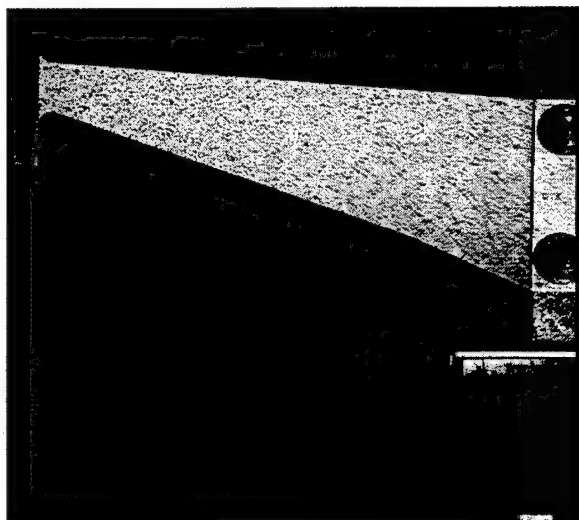
Picture 3: Optical set-up for the Projected Pattern Method.

the CCD video camera is positioned perpendicular to the wing at a distance of about 87cm, while the position of the projector with respect to the camera is clearly characterised in Picture 3.

The distance of the projector from the test object is 143cm forming an angle with the video camera of about 30 degrees in both vertical and horizontal directions. This angle was selected compatible with the lack of space in the workshop and the capacity to detect the maximum deflection expected from the test.

The CCD camera used is equipped with a 25mm focal length lens. This is the same video camera in use in HST performing both Moire and PIV experiments. Because of the small size of the wing model, there were no difficulties to cover the entire surface with the pattern projected, using a 90mm focal length lens.

Picture 4 is an example of the images recorded during the experiment.



Picture 4: Image recorded performing the Projected Pattern Method.

Looking carefully at this picture, it is possible to find that the projector lens used from the selected distance doesn't focus uniformly over the entire wing. This is revealed not to be a problem because the PIV processing software is capable to apply the correlation method accurately as long as there is a visible pattern. Moreover, the wing was mounted upside-down on the traversing stage just for practical reasons during this part of the experiment.

The results for these measurements with the Projected Pattern Method will be presented and discussed in Section 4.

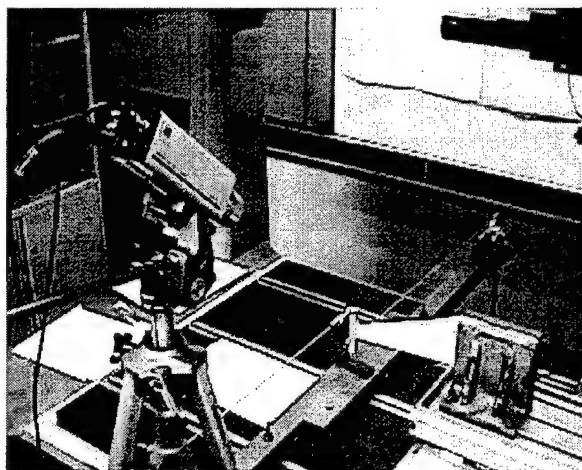
2.2 The Painted Pattern Method (PaPM)

In this method, a random pattern with black dots is directly painted over one side of the wing model. The basic principles are the same of the Projected Pattern

Method, the main differences are in the absence of the projector and the position considered for the video camera. In fact, in order to detect any shift of the pattern, it is necessary to look at the model under an angle, but this will cause a loss of resolution that will affect the final out-of-plane deformations determined with this method.

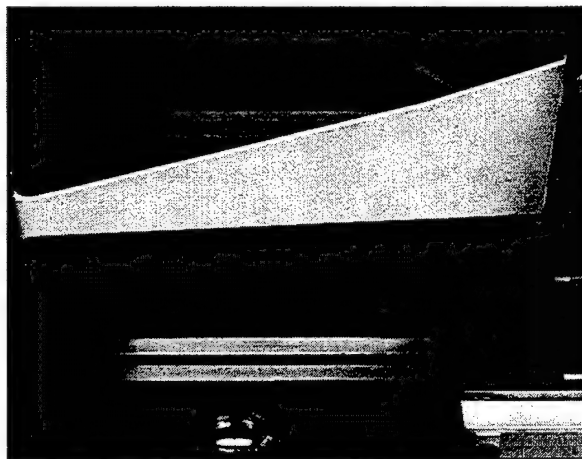
2.2.1 Experimental set-up

The set-up used in this set of measurements is clearly shown in Picture 5:



Picture 5: Actual set-up for torsion test using the Painted Pattern Method.

The size of the wing model and the way to apply loads is exactly the same as the previous method. The video camera is also in this case equipped with a 25mm focal length lens but positioned with an angle of approximately 45 degrees with respect to the model. An example of the images recorded with this configuration is presented in Picture 6:



Picture 6: Image recorded performing the Painted Pattern Method.

Another aspect to consider referring to the Painted Pattern Method is that because the black dots are painted on the wing, every undesired in-plane movement of the surface is detected as a shift of the pattern. That is not the case in the previous method described, because the pattern is projected over the wing surface and only an unexpected movement of the slide or of the projector can cause disturbing shift.

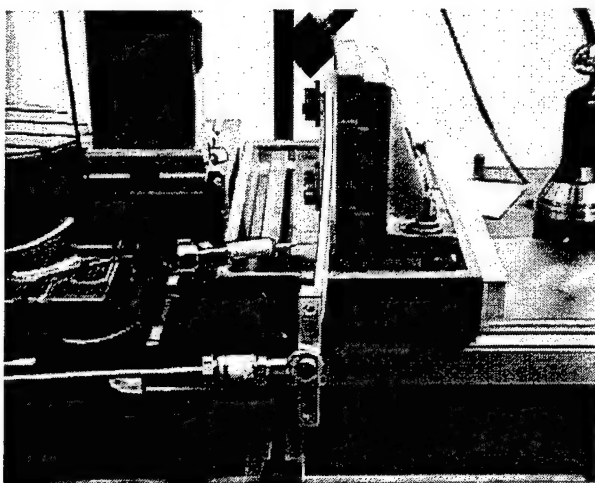
This aspect has to be taken into account when this method is applied to measure deformations of a model in a vibrating wind tunnel.

The results for these measurements with the Painted Pattern Method will be presented and discussed in Section 4.

The set-up described in this Section was also used for a series of torsion tests, as clearly seen in Picture 5. Loads of 20kg and 30kg were applied in order to produce consistent deformation of the wing. Unfortunately, the difficulties encountered to fix the loads properly were the cause of an unreliable series of measurements carried out under torsion. This is the main reason why it was decided not to present the data, with the intention to perform them in a more accurate way in a future experiment.

2.3 Deformation measurements using the 3D Co-ordinate Measuring Machine

The three-dimensional Co-ordinate Measuring Machine is used to measure the distortion at any required point on the model surface by touching the model with a special sensor, as shown in Picture 7.



Picture 7: Detailed view of the sensor of the 3D Co-ordinate Measuring Machine.

The three-dimensional coordinates are produced in 5 sections selected along the wing span while performing the measurements with the Painted Pattern Method.

These results will be used as a comparison with the previously described experimental methods in Section 4.

The accuracy obtained with this special machine is about $\pm .005\text{mm}$.

3. DATA ACQUISITION

3.1 Moire calibration

Before applying loads to the wing model, calibration images were acquired moving the model on the translation stage, simulating pure translations from a reference position (0mm) to 16mm with increments of 1mm until 10mm and increments of 2mm until 16mm. This operation was repeated for both the Projected and Painted Pattern Method.

For the final processing only calibration images, which refer to a translation of 5mm towards the video camera were selected.

3.2 Reference images

Before and after deformed images, undeformed images were acquired. The last ones were used as reference images for the deformed images, and they were also used to detect any undesired shift of the hardware (video camera, projector, slide, lenses etc.) due to external factors.

It was also necessary to take into account the weight of the scales used to apply loads on the model. In this sense, reference images were acquired with and without scales to detect any shift of the pattern.

In order to avoid this influence on the measured deformations, the reference images selected were those ones acquired without scales.

3.3 Deformed images

Deformed images were acquired under the following load conditions:

- Pure bending: 5kg ($\sim 49\text{ N}$) and 10kg ($\sim 98\text{ N}$) applied in both of directions, towards and away from the video camera

4. EXPERIMENTAL RESULTS

In Table 1, the experimental results obtained during our investigations are presented and compared with the deformation measurements performed with the 3D Co-ordinate Measuring Machine and the theoretical prediction from the CAD system.

Bending	CAD (mm)	3D (mm)	PaPM (mm)	PrPM (mm)
5kg towards camera	9.86	9.83	9.22	9.07
5kg away camera	8.85	8.90	8.31	8.15
10kg towards camera	13.52	13.48	12.80	14.68

Table 1: The out-of-plane deflection estimated for a wing section at $x \cong 199\text{mm}$ and $z \cong 97\text{mm}$ from the root.

The values showed in Table 1 are considered for a point of the wing section positioned at $x \cong 199\text{mm}$ and $z \cong 97\text{mm}$ from the wing root. The origin of the XYZ reference system is placed at the leading edge of the wing root section.

This section was selected near to the wing tip, where large distortions are expected. The point on the section was chosen approximately in the middle to be sure that the values calculated with the correlation method, used to detect the shift of the pattern, were reliable (being far from the wing edges).

The analysis of these data shows some interesting results. Looking at the values measured applying a load of 5kg in the center position of the wing tip (bending), the Painted Pattern Method provides better results than the Projected Pattern Method. This can be due to a better spatial resolution obtained with the set-up tuned for the Painted Pattern Method. In fact, the expected resolution with the optical system used during this test is about 0.2 pixel. This value was estimated after previous PIV experiments in the DNW-HST wind tunnel. Taking this into consideration, the spatial resolution obtained with the Painted Pattern Method is about 0.08mm, slightly higher than that calculated with the Projected Pattern Method which is about 0.1mm.

Another factor that can influence the accuracy of the data is the different number of spots per interrogation area between the two methods, as can be seen in Picture 4 and Picture 6 respectively. The accuracy can be improved by projecting a denser pattern.

Moreover, for all the experimental methods considered, there is a difference in the displacements measured when loads are applied towards or away from the CCD camera. This is caused by the different weight of the scales used to apply loads: 2.8kg for the scale on the side of the camera and 2.03kg for the scale on the opposite side of the camera.

The differences between the measured data are shown in detail in Table 2.

Bending	Difference 3D - PaPM (mm)	Difference 3D - PrPM (mm)	Difference PaPM - PrPM (mm)
5kg towards camera	0.61	0.76	0.15
5kg away camera	0.59	0.75	0.16
10kg towards camera	0.68	1.20	1.88

Table 2: Overview of the differences between the measured data.

The same behavior is found out applying a load of 10kg in the center position of the wing. The Painted Pattern Method shows more reliable results than the Projected Pattern Method.

Nevertheless, in this case as can be seen from Table 2, the difference between the data measured with the two Moire methods is considerably high, so not reliable to give other information about the accuracy of the Projected Pattern Method.

The explanation for that can be found in all the unknown factors that can cause an undesired shift of the pattern. In this case, an accidental movement of the camera or/and the projector, when the loads were applied on the scales or when the traversing table was translated to record the calibration images, are the most probable reasons.

A complete view of the out-of-plane deformations measured over the entire wing can be obtained using contour plots. A good example is given in Figure 8 and Figure 9, where the results for bending with a load of 5kg using the Painted Pattern Method and the Projected Pattern Method respectively, are presented.

The contour plots presented are produced using a commercially available plotting software package. With this software, it was possible to merge the two sets of data obtained by selecting two different areas of interests of the recorded images of the wing, during the data processing. In this way, it was possible to select different interrogation areas for the region near the wing tip, where large deflections were expected, and the region near the wing root, where the measure deflections were almost zero.

This is revealed to be a considerable improvement whether in terms of accuracy of the measured data or in terms of a better presentation of the final results provided to the customers.

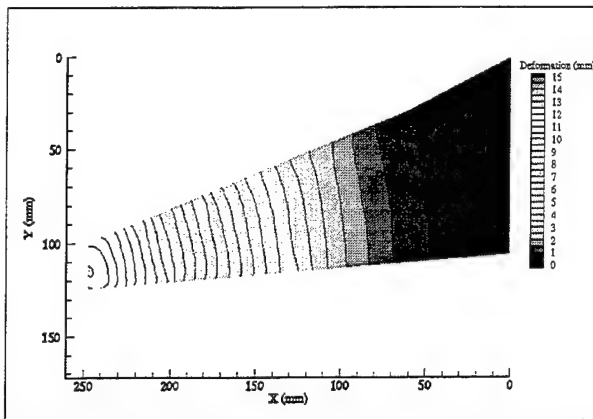


Figure 8: Contour plot of the deflections measured using the Painted Pattern Method (bending 5kg away camera).

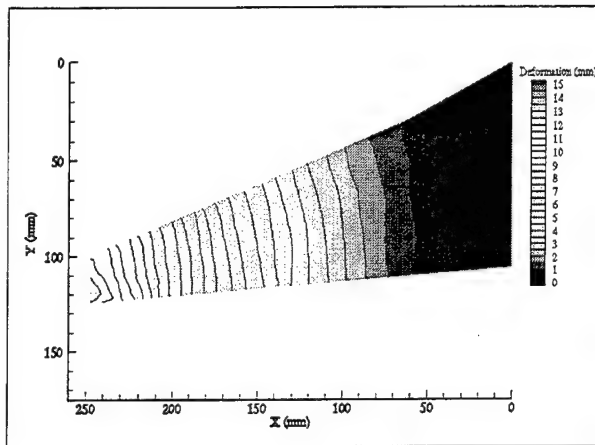


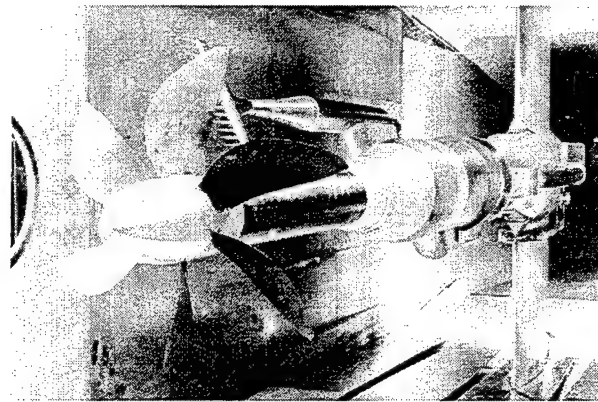
Figure 9: Contour plot of the deflections measured using the Projected Pattern Method (bending 5kg away camera).

5. EXAMPLES OF WIND TUNNEL EXPERIMENTS

As already mentioned before, the Projected Pattern Method has been used in the DNW-HST many times. Since most experiments are of industrial nature, only few examples are available.

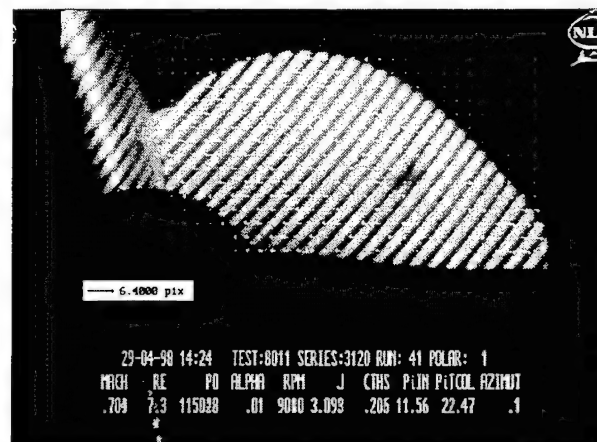
An example of the Projected Grid Method was performed on the APIAN propeller. This method is also in use in the Large Low Speed Facility of DNW. Picture 10 shows the propeller with one dull white blade.

The pattern was projected continuously on the blades. However, by triggering the camera, one of the blades



Picture 10: Deformation measurements using the Projected Grid Method performed on the APIAN propeller in the DNW-HST.

was always captured at the same position. Picture 11 shows the blade in a frozen position with the projector grid.



Picture 11: APIAN blade with the projector grid in frozen position.

The method was applied while varying many parameters of the propeller. In Figure 12 an example of the blade distortion is presented.

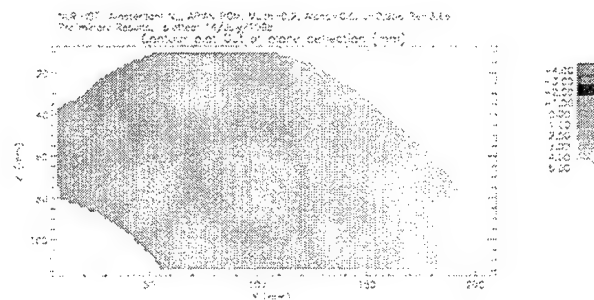
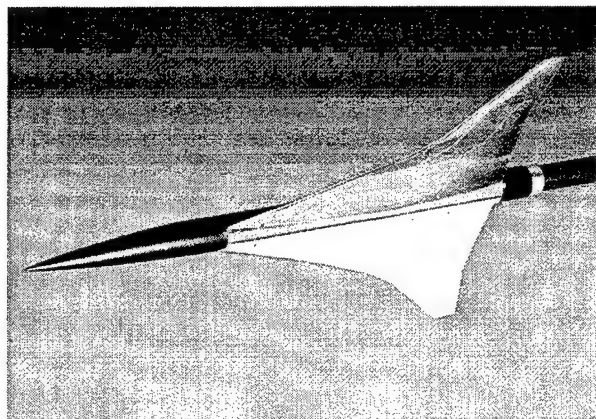


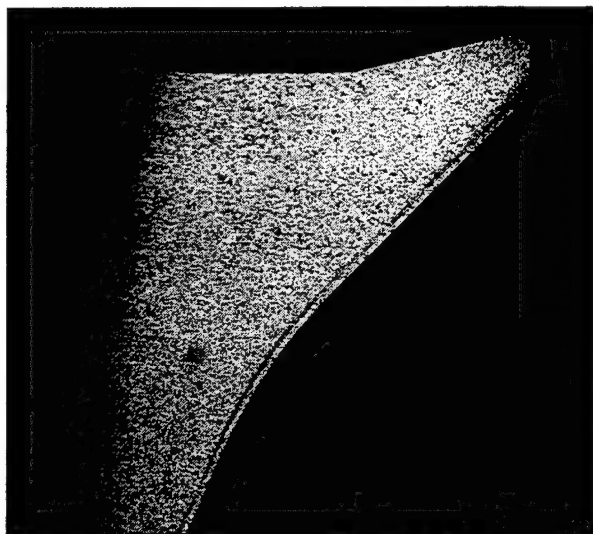
Figure 12: Projected Grid Method on the APIAN propeller.

Another example was performed with the Projected Pattern Method. This was used in the case of the EUROSUP wing. Picture 13 shows the model with one wing painted dull white.



Picture 13: EUROSUP model used to perform deformation measurements with the Projected Pattern Method.

Picture 14 shows an image of the wing as recorded by the CCD camera.



Picture 14: An image of the EUROSUP wing as recorded by the CCD camera.

Since the set-up in the wind tunnel is vibrating, the deformed pattern is measured many times and then averaged to give a final result. This is shown in Figure 15.

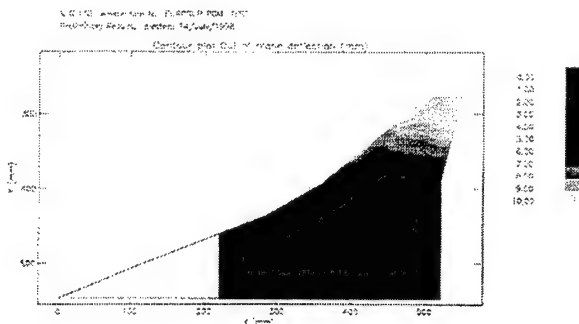


Figure 15: Projected Pattern Method on the EUROSUP wing.

6. DRAWBACKS

The Painted Pattern Method requires the right pattern to be painted on the object of interest. The paint however, is adding extra roughness, which is not always acceptable for the client.

The elements of the optical set-up of the Projected Pattern Method are more sensitive in comparison to the Painted Pattern Method. This implies the necessity to acquire more images and to average the results.

Both methods show the difficulties of measuring in-plane movements and calculating the out-of-plane displacements. Thus, in-plane shifts, which are not caused by an out-of-plane displacement, will be translated into out-of-plane displacements.

7. CONCLUSIONS

The Projected Pattern Method and the Painted Pattern Method are both very reliable and valuable to be performed in wind tunnel tests.

Up to now NLR never performed the Painted Pattern Method in a wind tunnel test because it produces extra roughness on the wing since the pattern is painted onto it. The results of the experiment described in this paper show that it is valuable to look for a way to paint the right pattern on a wing in a smooth layer. By projecting the grid onto the wing surface, rather than painting it, the problem of extra roughness can be avoided.

The Projected Pattern Method as performed by DNW-Amsterdam consists of PIV method elements with a wind tunnel proof projector and a proper pattern slide. This clearly shows how the capital costs involved are extremely low.

The accuracy to be expected is in the order of 0.1mm out-of-plane displacement. It should be mentioned that because of the vibrations of the wind tunnel, the model, the video camera and the projector, the measurements should be repeated several times and averaged to give reliable results.

FEASIBILITY OF AIRFOIL TESTS WITH A SMALL HIGH SUBSONIC CRYOGENIC WIND TUNNEL

Yutaka Yamaguchi, Masashi Kashitani, Kenji Kaibara and Teruo Saito
Department of Aerospace Engineering
National Defense Academy
1-10-20 Hashirimizu, Yokosuka Japan

ABSTRACT

A cryogenic wind tunnel has a capability to perform relatively high Reynolds number airfoil testing using a small airfoil model. However, it is desirable to use a model as large as possible to utilize the high Reynolds number flow capability of the cryogenic wind tunnel. The most serious problem on the airfoil testing is the tunnel sidewall interference. As the NDA cryogenic tunnel has a very narrow width, and the possible shortest chord length of model is 0.06 m with our present fabricating method, the aspect ratio of models for the present tunnel is only up to 1.0. The Barnwell-Sewall and the Murthy methods are the readily available corrections, and were applied to the experimental pressure distributions of airfoils which have aspect ratios less than unity in order to evaluate feasibility of airfoil tests with models of such low aspect ratios, and to contribute to the database on the wind tunnel testing techniques. From the experimental study, the simple global correction to the main stream conditions still works in some degree for the experimental data of low aspect ratio cases. This result may support the feasibility of airfoil tests with models of low aspect ratios as the first order tests.

INTRODUCTION

The cryogenic wind tunnel concept has been proven as the best way to obtain the full scale Reynolds number capability of wind tunnel used for developing advanced aircrafts. Even a small cryogenic wind tunnel has a capability to perform relatively high Reynolds number aerodynamic tests.

The National Defense Academy of Japan built a small high subsonic cryogenic wind tunnel for developing cryogenic wind tunnel testing techniques and basic aerodynamic research works in 1985. It has been used to develop basic airfoil testing and model fabricating techniques for a small cryogenic tunnel, and to

expand the operational capability of such a tunnel[1]-[10]. These efforts established a model fabricating technique, but also revealed a problem of two dimensionality on airfoil pressure distributions due to the wall interferences of the test section because the realized aspect ratios of airfoil models were less than 1.0 with our model fabricating technique.

Barnwell showed that the sidewall boundary layer effect should be considered for two-dimensional airfoil tests, and developed a technique correcting the effect[11]. Sewall extended the Barnwell's technique to transonic flows[12], and Murthy further extended the Barnwell-Sewall method to include the effect of the aspect ratio of an airfoil model[13]. As for the top and bottom wall interference effects, a correction to the freestream Mach number and angle of attack is sufficient for a large number of flows up to transonic speeds[14]. These correction techniques are considered to have worked well.

However, Ganzer and et al. reported that their experiments with models of aspect ratios below 2 showed fairly strong sidewall interferences, and that simple global corrections to the mainstream conditions do not adequately eliminate the sidewall boundary layer effects[15]. Sudani and et al. also conducted a two dimensional airfoil test with low aspect ratio models, and showed that the sidewall effects strongly influenced the spanwise width of the local separation at relatively high angles of attack[16],[17]. They suggested that an airfoil model should have an aspect ratio of 1.5 at least, even in relatively low Mach number flows. They also showed that their corrected experimental results with the Murthy technique were in good agreement with those measured in other wind tunnel, and that such a wall correction is very promising for eliminating the sidewall effects from experimental results.

According to the results of Ref.[16], our value of the model aspect ratio may be too low for airfoil tests. However, to the authors' knowledge, there are quite

few data on the correction for low aspect ratio model such as our models. So, it will contribute to the database of the tunnel wall corrections to evaluate the airfoil test results of models of low aspect ratio, and it is expected that such an evaluation will give some hints of feasibility of airfoil tests with a small wind tunnel. So, the present paper describes the established model fabricating techniques first, and gives the evaluation of cryogenic airfoil testing results of airfoil models with extremely low aspect ratios.

MODEL FABRICATION TECHNIQUES

It was important to develop an optimum model fabrication technique for relatively small 2-dimensional cryogenic wind tunnel as we had no experience to make any airfoil models used in the cryogenic transonic flows. Two techniques were developed for the present purpose.

Technique I

This technique is described as follows;

1. an airfoil contour is machined from a block of a stainless steel, or SUS304, and its span should be fit to the test section width.
2. pressure orifices of 0.3 mm diameter are drilled perpendicularly to the upper and lower surfaces.
3. a long hole of the 1.0 mm diameter is drilled from the left wing tip of the model to each pressure orifice.
4. the stainless steel pipes of the 1.0 mm diameter are inserted into the long holes and are brazed to lead the surface pressures to a pressure transducer.

This technique may be a modified one in some degree to one of methods developed by NASA, or "the channel and cover" method. However, it was difficult to provide many pressure taps for a model of chord length of 0.12 m with this technique, and only 21 pressure taps were provided for such a model. So, this technique were considered to be inadequate for more precise aerodynamic testing, and led to the development of the another technique.

Technique II

The second technique, the technique II, was developed to provide 43 pressure taps for an airfoil model of the chord length of 0.12 m, at least. This technique II is described as same as the technique I.

1. an airfoil contour is machined from a block of the stainless steel, SUS304, and divided into two parts, the upper surface part, and the lower one.
2. the inner surface of each part is hollowed to provide a space for pressure tubes.
3. the diameter of a pressure tap is of 0.3 mm.
4. each pressure tap is connected to a pressure tube of 0.3 mm and 0.5 mm inner and outer diameter, respectively with an epoxy adhesive agent.
5. the upper and lower surface assemblies are riveted together.

For a model having a chord length of 0.12 m, twenty four and seventeen pressure orifices can be provided with this technique on the upper and lower surfaces, respectively, and twenty one and seventeen orifices for one of 0.10 m chord. For the shortest chord length of 0.06 m, eleven orifices can be made on both upper and lower surfaces. These numbers of orifices provided with the technique II may be satisfactory for basic aerodynamic studies. So, the technique II has been used for the models tested in the NDA cryogenic wind tunnel.

EXPERIMENTAL APPARATUSES

NDA cryogenic wind tunnel

The cryogenic wind tunnel of the National Defense Academy (designated as the NDA Cryogenic Tunnel) is a centrifugal compressor-driven, high subsonic, two-dimensional tunnel. The nominal range of stagnation temperature, T_0 is ambient to 108 K. The total temperature is controlled by regulating the flow rate of liquid nitrogen (LN_2) injected through six injection nozzles which are located just in front of the compressor intake. The control accuracy of T_0 is about $\pm 0.5K$. The range of the total pressure, P_0 is up to 177 kPa. The nominal maximum freestream Mach and the unit Reynolds numbers are 0.83 and 9.3×10^7 , respectively.

The test section is of 0.06 m in width, and of 0.30 m in height. Each of the top and bottom walls has two slots of 0.36 mm wide, and also 19 pressure taps are distributed on each center member to measure the local Mach number near the wall. The sidewalls are solid ones. The turntable system is mounted on the test section sidewalls, and the axis center of the turntable is located at 0.50 m from the upstream end of the test section. An electric pulse motor drives this turntable. The angle of attack is changed up to ± 15 deg in steps of 0.1 deg. However, experiments were only performed at a low angle of attack range, -4° to $+4^\circ$ at most.

Airfoil models

Adopted models were two NACA0012 airfoil models and one supercritical airfoil.

One of the NACA0012 models has an aspect ratio of unity, and the other has one of 0.5. The blockage factors of the NACA0012 are 0.024 and 0.048, respectively.

One supercritical airfoil is of NASA SC(3)-0712(B). This airfoil (designated as the SC airfoil in the present paper) is about 12 % thick and has a design lift coefficient of 0.7[18]. The aspect ratio of the supercritical airfoil is of 0.6. The blockage factor of the airfoil model is 0.04.

WALL INTERFERENCE CORRECTIONS

The wall interferences of a two-dimensional test section are due to the sidewall boundary layers, and due to the top and bottom walls.

As mentioned in the previous section, Barnwell developed a technique accounting for the effect of the attached sidewall boundary layer thickness at subsonic conditions. Sewall also extended the Barnwell's technique to transonic conditions. Murthy developed another technique to account for the airfoil aspect ratio, which was neglected in both of the Barnwell and Sewall correction techniques.

To provide corrections for the ventilated wall interference effects, The techniques utilizing experimental wall pressure data have been published by Blackwell[20], Mockry and Ohman[21], and Sawada[22].

The adopted correction techniques will be briefly described in the following sections, and the details are given in Appendix.

Sidewall corrections

The Sewall correction technique[12], sometimes referred to as the Barnwell-Sewall type method, has been used as a baseline sidewall correction technique. This technique neglects the effect of the aspect ratio of a model, and gives the relationship between the measured M_∞ and an interference-free \overline{M}_∞ . The relationship between the measured pressure coefficient C_p and the interference-free coefficient \overline{C}_p is also given. The related equations are given in Appendix.

Murthy extended the Sewall method to take into account of the aspect ratio[13]. He assumed that the crossflow velocity variation along the airfoil span with sidewall boundary layer effects can be represented by the wavy wall flow model. As mentioned before, this

technique may be recommended to be used for the correction of wind tunnel experiments with airfoil models of which the aspect ratio is greater than unity. The relationships between M_∞ and \overline{M}_∞ , and between C_p and \overline{C}_p are given in Appendix.

The effect of the aspect ratio is contained in this wavelength, and it has arbitrariness in some degree. In Ref.[13], Murthy gave the wavelength, $l = 2c$ for an airfoil model of which the aspect ratio is 2.66. c is the chord length of the model. He also showed that $l = c$ gave better correction than $l = 2c$ for a model having the aspect ratio of 0.73. Though the present models have the aspect ratios of 0.5, 0.6 and 1.0, two cases of different wavelengths of the equivalent wavy wall were evaluated. One was assumed to be equal to the airfoil chord, and the other was twice of the chord. They were evaluated by comparing with the results of the Barnwell-Sewall method and the numerical computations.

Top and bottom wall correction

In low speed wind tunnel testing, the top and bottom wall interference is well defined, and corrected easily.[19] However, at high subsonic and transonic speeds, the analytical correction becomes more difficult, and semi-empirical techniques should be adopted. As in the previous works, the Blackwell's method[20] was again adopted for the present study. This technique only requires the pressure distributions between the leading and the trailing edge positions of an airfoil model at the top and bottom walls, and gives only the correction on the freestream Mach number. The Mach number correction ΔM_B is obtained by the equations given in Appendix.

Simplified four wall correction technique

In the previous preliminary work[8] it was shown that the sidewall interference dominates the wall interference effects in the present tunnel, but the top and the bottom walls also contribute substantially to the interference.

As for the simplified four wall interference correction, the ordinary sequential procedure was employed. At first, the mainstream conditions, airfoil surface pressures and those of the top and bottom walls are corrected with the Barnwell-Sewall (Eqs.(1), (2) and (3) in Appendix) or Murthy (Eqs.(4) and (5) in Appendix) techniques. Hence, the boundary-layer effect-free Mach number distributions on the walls can be calculated from the corrected wall pressures. Then, the Blackwell's correction, Eq.(6) in Appendix, is applied to the first corrected results. The final, corrected freestream Mach number denoted as M_c is obtained.

When the Barnwell-Sewall technique is used, this sequential correction will be denoted as the correction I. Also, the sequential corrections for using the Murthy technique with $l = c$, and for that with $l = 2c$ will be denoted as the correction II and the correction III, respectively.

CFD codes

Two computational methods for predicting transonic airfoil flow were employed to compare with the experimental data. One of them is based on a finite volume solution of the time dependent Euler equation with the O-grid, which was developed by Jameson and Schmidt. This code is known as FLO54[23]. It gives the inviscid solutions of transonic airfoil flow, and rather accurately captures a shock wave on an airfoil.

A 128×32 grid with 130 points on the airfoil surface was used for the computations. A typical computation time is about three minutes per iteration with an IBM PC compatible (OS:Linux kernel 2.0.0, CPU: Intel Pentium 166 MHz, RAM:64MB). The g77 FORTRAN compiler (the GNU Fortran 77 compiler) was used for the present computations.

The other is based on a finite difference solution of the full, inviscid, perturbation potential equation in a cartesian grid system, developed by Carlson[24], and designated as TRANDES. The effects of viscous interaction is included, and the boundary layer characteristics are determined by the Nash-Macdonald method. When the strong shock wave appears on an airfoil surface, this code does not converge, so it was used to calculating the flows with relatively weak shock waves.

A 97×49 grid with 101 points on an airfoil is used. The typical computation time is 6 seconds per iteration with the abovementioned PC and the compiler.

RESULTS AND DISCUSSION

The NACA0012 airfoil models were tested at the temperature range of $120 \sim 108K$, and at the nominal Mach number range of $0.4 \sim 0.8$. The ranges of the Reynolds number were 3 to 6 million for the chord length of 0.06 m, and 6 to 11 million for one of 0.12 m.

The test conditions of the SC airfoil model were almost same as the NACA0012 models. The range of the total temperature, and of the nominal Mach number were $120 \sim 108K$, and 0.5 to 0.78 , respectively. The resulted Reynolds number based on the chord length was 4 to 7 million.

No trip strips were placed on the surfaces of the models, and the all pressure distributions obtained were of the free transition.

The sidewall boundary layer of the present tunnel was measured at the cryogenic temperature range by

Sakaue[25]. He indicated that the displacement thickness δ^* was about 1 mm up to $M_\infty = 0.8$. Recently, the sidewall boundary layer of the present cryogenic tunnel was re-examined and evaluated by the co-author of the present paper[26]. He found that the the present sidewall boundary layer was well described by the $1/7$ th power law. So, in this study, this fact was adopted to calculate the sidewall boundary layer effects.

In the subcritical Mach number range, the corrected data of the tested airfoil models were in good agreement with the corresponding computational data. However, in the supercritical Mach number range, a fairly strong shock wave appears on the upper surface of a NACA0012 model at a positive angle of attack. Such a shock wave may cause the sidewall boundary layer to separate at the shock wave position[16]. However, we had no means to know if a sidewall boundary layer separation occurred or not in the present NDA cryogenic tunnel, such a separation was ignored in the present paper.

Figures 1, 2, and 3 show examples of the uncorrected experimental data. The symbols of \circ and \times , or of \diamond and \triangle indicate the experimental pressure coefficients of the upper and lower surfaces of the airfoil, respectively. The computational results are showed by the solid lines. The normal force coefficients were obtained by integrating the experimental pressure distributions. Figures 1 and 2 are of NACA0012 of the aspect ratio of 0.5 and of 1.0, respectively. Figure 3 is of the SC airfoil of the aspect ratio of 0.6.

In computations, the angle of attack was varied to produce the experimental value of c_n , while the Mach number was fixed. When a relatively strong shock wave was formed on an airfoil surface, the TRANDES did not converge, and the only FLO54 pressure distributions were plotted.

From Figs. 1 to 3, it is obvious that the uncorrected experimental data were quite different from the computed ones, qualitatively and quantitatively. As for the NACA0012 airfoils, the experimental shock waves stand between about 30 to 40 % chord position, but those of the computation are on about 50 to 65 %. As for the pressure recovery behind the shock wave, the experimental recovery seems to be much more gradual than that of the computation. These facts indicate that the real flow conditions differ far from the nominal ones, and it would be a serious question if the interference corrections should work well for data obtained in the present tunnel.

Figures 4, 5, and 6 show the sequentially corrected results by the correction I. The corrected experimental pressure coefficients \bar{c}_p are plotted as symbols of \circ or \diamond for the upper surface and \times or \triangle for the lower

surface. In Figs. 4, 5, and 6 the corresponding FLO54 pressure distributions are plotted in the same way of Fig. 1.

Comparing Figs. 1 to 3 with Figs. 4 to 6, it is clear that the simplified four wall correction, the correction I, produces the substantially improved agreement between the corrected data and the computed ones, and that the agreement may be better for a higher aspect ratio case than for a lower one. Figure 7 is an example comparing between the corrected NDA data of SC airfoil, NASA SC(3)-0712, and those of the NASA 0.3 m TCT[18]. The symbols of \diamond and \triangle are of the NDA data, and the solid lines are of the NASA's data. The magnitude for the wall correction of the NDA cryogenic tunnel is about three times as big as that of the NASA 0.3 m TCT. Those facts may encourage to expect aerodynamic data of low aspect ratio model less than 1.0 can be corrected by the simple four wall correction, including the flows in which a shock wave is formed on an airfoil surface.

The experimental data showed in Fig. 1 was also corrected with other sequential corrections. Figures 8 and 9 show the sequentially corrected results by the correction II and III, respectively. From these figures, it can be seen that the correction III gives better correction than the correction II though the difference is not large, and also that the result of the correction III is almost similar to that of the correction I. This may indicate that it is reasonable to assume $l = 2c$ even in a case such as the present model with a very low aspect ratio. Other data also seem to support this assumption.

Figure 10 shows the Mach number correction vs the nominal freestream Mach number for the models having various aspect ratios. The corrected Mach numbers differ due to the correction methods. The Mach number difference for the aspect ratio of 0.5 between the correction I and III varies from about 0.7 to 0.4 % respect to the M_∞ range of 0.6 ~ 0.75, and that between the correction I and II is in the range of about 1.8 ~ 1.2 %. This may show the effect of the aspect ratio.

As for the correction III, the Mach number correction decreases as the aspect ratio of a model increases. From Fig. 10, it is also known that the averaged Mach number correction for the aspect ratio of 1.0 is about 87 % of that for one of 0.5.

Figure 11 shows the correction factors for c_n and C_p , the ratio of \bar{C}_p and C_p in Eqs.(3) and (5) of Appendix. It indicates that the correction I and III give almost same results. The difference between the correction I and II is at most about 1 %. Those data may also support that assuming $l = 2c$ is acceptable even in a case such as a model with a very low aspect ratio.

The computed FLO54 distributions with the corrected freestream conditions become closer to the corrected experimental data. However, the quantitative discrepancy of the pressure distribution still exists between them. This discrepancy may be partly due to the insufficient number of top and bottom wall pressure taps for the blockage correction, and partly due to the FLO54 code which did not include the airfoil boundary layer effect.

Figures 12 and 13 show the comparison between an experiment and the FLO54 and that of the TRANDES, respectively. The same experimental data of the aspect ratio of 0.5 is used in both figures, and corrected with the correction I. Again, the symbols of \circ and \times are the corrected experimental C_p of the upper and lower surfaces, respectively. The TRANDES pressure distribution shows better agreement with the corrected experimental one than the FLO54. This indicates that a computational code which can treat the surface boundary layer is desirable for the qualitative comparison. Again, the similar results were obtained with models of other aspect ratio. Though some degree of uncertainty still exists in the top and bottom walls correction, these comparisons may indicate that the simple global corrections to the mainstream conditions adopted in the the present study give almost satisfactory pressure distributions for the first order evaluation, even for a model with a low aspect ratio, which is less than 1.0, and with a shock wave on the surface.

As mentioned before, the corrections of the pressure distribution and normal force coefficient are generally good, but the difference of the Mach number correction may be substantial. When a drag divergent Mach number is needed, this difference will not be neglected. However, the drag measurement was not performed in the present study, and this evaluation should be left for a future study. As described in the previous section, the present interference correction does not provide the correction for the angle of attack, and any measurement for the two-dimensional airfoil characteristics cannot be performed presently. Therefore, it will be highly desirable to include the angle of attack correction for utilizing the capability of the present tunnel as a cryogenic wind tunnel.

CONCLUDING REMARKS

The Murthy technique was evaluated as the sidewall boundary layer effect correction for the experimental results of airfoil models having the very low aspect ratios of 0.5, 0.6 and 1.0, and the two wavelength of the wavy wall, $l = c$ and $2c$ were examined.

The corrected experimental data by the Murthy and Blackwell techniques were compared with those of the Barnwell-Sewall and Blackwell, and with the corresponding numerical computations. The Murthy technique reduces to the Barnwell-Sewall technique in the limit of vanishing aspect ratio of the airfoil model. The comparison of the corrected data and the computed ones indicated that the Murthy technique of $l = 2c$ gave the same order of correction as the Barnwell-Sewall technique, and better correlation for the pressure distribution than that of $l = c$, and $l = 2c$ may be used in the sidewall correction for a model of which the aspect ratio is less than or equal to 1.0. Therefore, the simple global correction to the main stream conditions still seems to work in some degree for aerodynamic experiments with models of the low aspect ratio, and it may support the feasibility of airfoil tests using models of low aspect ratios as the first order tests.

However, the corrected Mach numbers of the Murthy technique were slightly higher than those of the Barnwell-Sewall technique. This will affect the determination of the drag divergent Mach number, and further experimental and numerical studies should be performed to evaluate the influence of the difference of the corrected Mach number between the two techniques, and the angle of attack correction should be included for more complete evaluation of such airfoil tests.

REFERENCES

- [1] Yamaguchi, Y., Kaba, H., Yoshida, S. and Kuribayashi, N., "Preliminary Test Results of NDA Cryogenic Wind Tunnel and Its System," Society of Automotive Engineers, SAE TP 881449, Oct. 1988.
- [2] Yamaguchi, Y., Kaba, H., Yoshida, S., Kuribayashi, N., Nakauchi, Y., and Saito, T., "Instrumentation and Operation of NDA Cryogenic Wind Tunnel," *Proceedings of ICIASF'89*, IEEE, 1989, pp.460-469.
- [3] Yamaguchi, Y., Kaba, H., Kuribayashi, N. and Nakauchi, Y., "Characteristics of a Cryogenic Wind Tunnel at National Defense Academy; Tunnel Characteristics at Ambient and Cryogenic Temperatures," *Journal of the Japan Society for Aeronautical and Space Sciences*, Vol.38, No.441, 1990, pp.339-565(in Japanese).
- [4] Yamaguchi, Y., Nakauchi, Y., Yorozu, M. and Saito, T., "Preliminary Airfoil Testing Experience in the NDA Cryogenic Wind Tunnel," *Proceedings of ICIASF'91*, IEEE, 1991, pp.223-230.
- [5] Yamaguchi, Y., Nakauchi, Y., Kuribayashi, N. and Saito, T., "Characteristics of NDA Cryogenic Wind Tunnel; Model Fabrication and Preliminary Airfoil Testing I," *Reports of Engineering and Science of National Defense Academy*, Vol.30, No.2, 1993, pp.125-131(in Japanese).
- [6] Yamaguchi, Y., Sakaue, T., Saito, T. and Wada, S., "An Improvement on Cooldown for the NDA Cryogenic Wind Tunnel," *Journal of the Japan Society for Aeronautical and Space Sciences*, Vol.41, No.476, 1993, pp.55-58(in Japanese).
- [7] Yamaguchi, Y., Sakaue, T., Yorozu, M. and Saito, T., "The Design and Operating Experience of the NDA Cryogenic Wind Tunnel," *Advances in Cryogenic Engineering*, Vol.39, 1994, pp.79-88.
- [8] Yamaguchi, Y., Yorozu, M. and Saito, T., "Preliminary Assessment of Tunnel Wall Interference in the NDA Cryogenic Wind Tunnel," *Journal of Aircraft*, Vol.31, No.5, Sept.-Oct. 1994, pp.1078-1083.
- [9] Sakaue, T. and Yamaguchi, Y., "A Thin Airfoil Experiment in a Cryogenic Wind Tunnel," *Theoretical and Applied Mechanics*, Vol.42, 1993, pp.277-285.
- [10] Yamaguchi, Y., Sakaue, T. and Saito, T., "On the Wall Interference and Corrections for A Small Cryogenic Tunnel," *AIAA-95-1781*, 1995.
- [11] Barnwell, R. W., "Similarity Rule for Sidewall Boundary-Layer Effect in Two-Dimensional Wind Tunnels," *AIAA Journal*, Vol.18, No.9, 1980, pp.1149-1151.
- [12] Sewall, W. G., "Effects of Sidewall Boundary Layers in Two-Dimensional Subsonic and Transonic Wind Tunnels," *AIAA Journal*, Vol.20, No.9, 1982, pp.1253-1256.
- [13] Murthy, A. V., "Effect of Aspect Ratio on Sidewall Boundary-Layer Influence in Two-Dimensional Airfoil Testing," *NASA CR-4008*, Sept. 1986.
- [14] Nixon, D., *Transonic Aerodynamics*, Vol.81, Progress in Astronautics and Aeronautics, AIAA, New York, 1981, pp.189-238.
- [15] Ganzer, U., Stanewsky, E. and Ziemann, J., "Sidewall Effects on Airfoil Tests," *AIAA Journal*, Vol.22, No.2, Feb., 1984, pp.297-299.

- [16] Sudani, N., Kanda, H., Sato, M., Miwa, H., Matsuno, K. and Takanashi, S., "Evaluation of NACA0012 Airfoil Test Results in the NAL Two-Dimensional Transonic Wind Tunnel," NAL TR-1109T, May 1991.
- [17] Sudani, N., Sato, M., Kanda, H. and Mastuno, K., "Flow Visualization Studies on Sidewall Effects in Two-Dimensional Transonic Airfoil Testing," AIAA paper 93-0090, Jan. 1993.
- [18] Johnson, Jr., G. W., Hill, S. A., and Eichmann, O., "High Reynolds Number Tests of a NASA SC(3)-0712(B) Airfoil in the Langley 0.3-Meter Transonic Cryogenic Tunnel," NASA TM 86371, June 1985.
- [19] Rae Jr., W. H. and Pope, A., "Low Speed Wind Tunnel Testing," 2nd edition, John Wiley & Sons, New York, 1984.
- [20] Blackwell Jr., J. A., "Wind-Tunnel Blockage Correction for Two-Dimensional Transonic Flow," *Journal of Aircraft*, Vol.16, No.4, April 1979, pp.256-263.
- [21] Mockry, M. and Ohman, L. H. "Application of the Fast Fourier Transform to Two-Dimensional Wind Tunnel Wall Interference," *Journal of Aircraft*, Vol.17, No.6, June 1980, pp.402-408.
- [22] Sawada, H., "A New Method of Calculating Corrections for Blockage Effects in Two-Dimensional Wind Tunnel with Ventilated Walls, Using Wall Pressure Measurements," *Transactions of Japan Society for Aeronautical and Space Sciences*, Vol.23, No.61, Nov. 1980, pp.155-168.
- [23] Sakata, T., "On FLO54 Program Usage (unpublished)," Bulletin for the 3rd Institute of Research and Development, Defense Agency, 1980 (in Japanese).
- [24] Carlson, L. A., "TRANDES: A Fortran Program for Transonic Airfoil Analysis and Design," NASA CR-2821, June 1977.
- [25] Sakaue, T., "Aerodynamic Study of Airfoil models of Low Aspect Ratio in A Cryogenic Wind Tunnel (unpublished)," a thesis for the graduate school of National Defense Academy, March 1993 (in Japanese).
- [26] Kaibara, K., "Evaluation of Airfoil Test of aspect ratio less than or equal to unity in the NDA Cryogenic Wind Tunnel (unpublished)," a thesis for the graduate school of National Defense Academy, March 1996 (in Japanese).

APPENDIX

The Barnwell-Sewall technique

M_∞ : the measured Mach number
 \overline{M}_∞ : interference-free Mach number

$$\Delta M_W = M_\infty - \overline{M}_\infty \quad (1)$$

and

$$\Delta M_W = \frac{3M_\infty}{2 + M_\infty^2} \left(2 + \frac{1}{H} - M_\infty^2 \right) \frac{\delta^*}{b} \quad (2)$$

where δ^* and H are the displacement thickness and the shape factor of the sidewall boundary layer, respectively, and b is the width of the test section.

$$\overline{C}_p = \left(\beta / \sqrt{1 - \overline{M}_\infty^2} \right) C_p \quad (3)$$

where

$$\beta = \{ 1 - M_\infty^2 + (2\delta^*/b) [2 + (1/H) - M_\infty^2] \}^{1/2}$$

The Murthy technique

M_∞ : the measured freestream Mach number
 \overline{M}_∞ : the corrected Mach number
 C_p : the measured pressure coefficient
 \overline{C}_p : the corrected pressure coefficient

$$\frac{1 - M_\infty^2 + k}{M_\infty^{4/3}} = \frac{1 - \overline{M}_\infty^2}{\overline{M}_\infty^{4/3}} \quad (4)$$

$$\overline{C}_p = \left(\frac{M_\infty^2}{\overline{M}_\infty^2} \right)^{1/3} C_p \quad (5)$$

where

$$k = \frac{2\delta^*}{b} \left(2 + \frac{1}{H} - M_\infty^2 \right) \left(\frac{k_1}{\sinh k_1} \right)$$

and

$$k_1 = \frac{\pi \beta b}{l}$$

l is the wavelength of the wavy wall, and $\beta = \sqrt{1 - M_\infty^2}$.

The Blackwell correction

ΔM_B : the Mach number correction

$$\Delta M_B = \overline{M}_E - \overline{M}_T \quad (6)$$

$$\overline{M}_E = \frac{1}{c} \int_0^c \frac{M_u + M_l}{2} dx$$

$$\overline{M}_T = \left\{ \frac{5 + M_\infty^2}{1 - 0.2 M_\infty^2 \left[\left(\frac{\overline{u}}{U_\infty} + 1 \right)^2 - 1 \right]} - 5 \right\}^{1/2}$$

and

$$\frac{\overline{u}}{U_\infty} = \frac{A}{2\pi\beta} \left\{ \left[\frac{0.75}{(0.75)^2 + \overline{Z}^2} \right] + \left[\frac{0.25}{(0.25)^2 + \overline{Z}^2} \right] \right\}$$

where, again, $\beta = \sqrt{1 - M_\infty^2}$. A is the nondimensional airfoil cross-sectional area, and \overline{M}_E and \overline{M}_T are the averaged experimental and theoretical Mach numbers at the walls over the airfoil model, respectively.

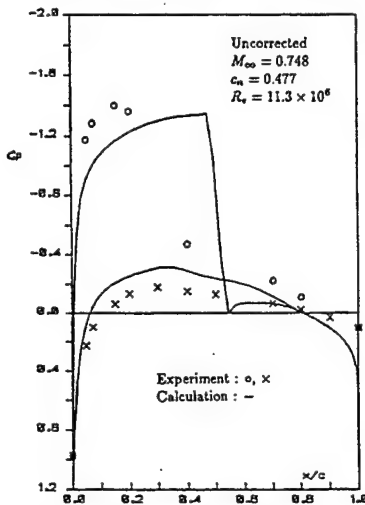


Figure 1: Uncorrected data compared with computed results, NACA0012, AR=0.5, FLO54.

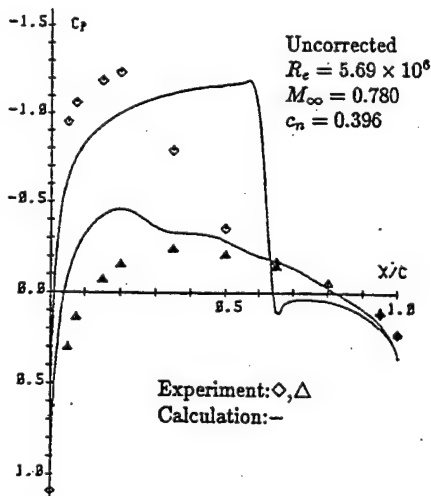


Figure 2: Uncorrected data compared with computed results, NACA0012, AR=1.0, FLO54.

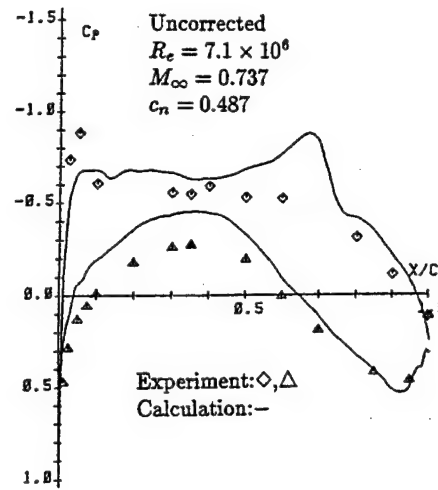


Figure 3: Uncorrected data compared with computed results, NASA SC(3)-0712(B), AR=0.6, FLO54.

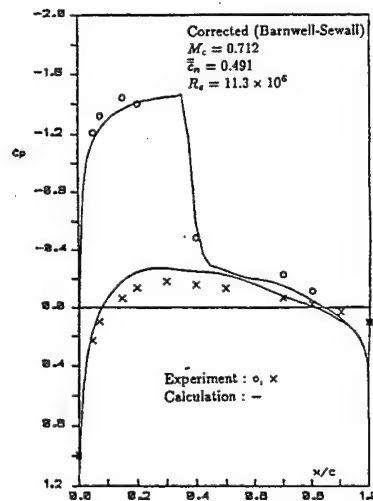


Figure 4: Corrected data with correction I compared with computed results, NACA0012, AR=0.5, FLO54, $M_c = 0.712$, $\overline{c}_n = 0.491$, $R_e = 11.3 \times 10^6$.

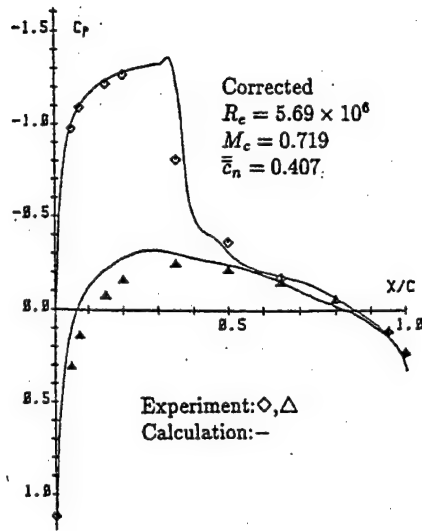


Figure 5: Corrected data with correction I compared with computed results, NACA0012, AR=1.0, FLO54, $M_c = 0.719$, $\bar{c}_n = 0.407$, $R_e = 5.69 \times 10^6$.

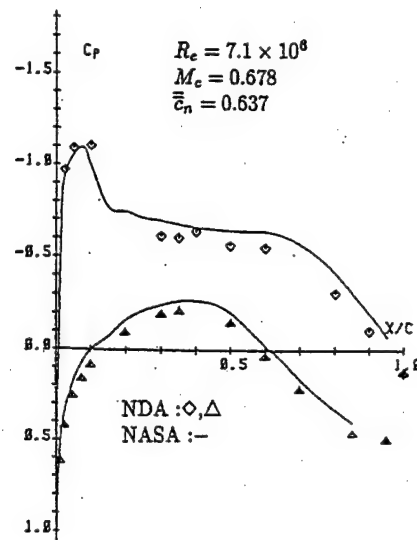


Figure 7: Comparison of corrected experimental results, NASA SC(3)-0712(B), \diamond, \triangle : NDA HSCT, $-$: NASA 0.3m TCT.

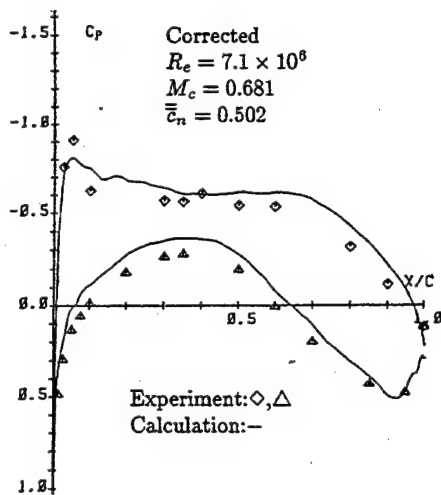


Figure 6: Corrected data with correction I compared with computed results, NASA SC(3)-0712(B), AR=0.6, FLO54, $M_c = 0.681$, $\bar{c}_n = 0.502$, $R_e = 7.1 \times 10^6$.

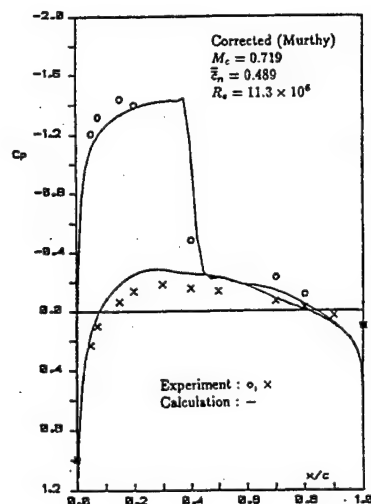


Figure 8: Corrected data with correction II compared with computed results, NACA0012, AR=0.5, FLO54, $l = c$, $M_c = 0.719$, $\bar{c}_n = 0.489$, $R_e = 11.3 \times 10^6$.

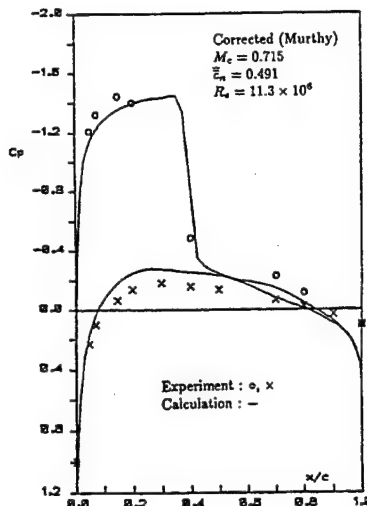


Figure 9: Corrected data with correction III compared with computed results, NACA0012, AR=0.5, FLO54, $M_c = 0.715$, $\bar{c}_n = 0.491$, $R_e = 11.3 \times 10^6$.

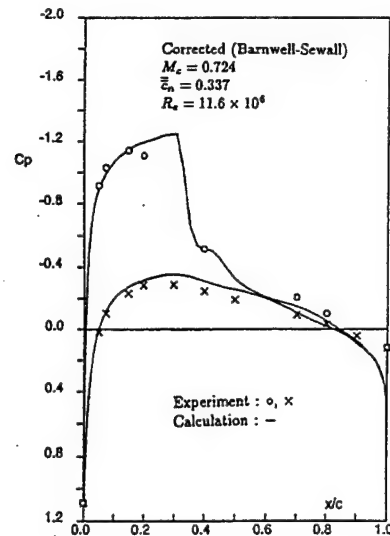


Figure 12: Corrected data with correction I compared with computed results, NACA0012, AR=0.5, FLO54, $M_c = 0.724$, $\bar{c}_n = 0.337$, $R_e = 11.6 \times 10^6$.

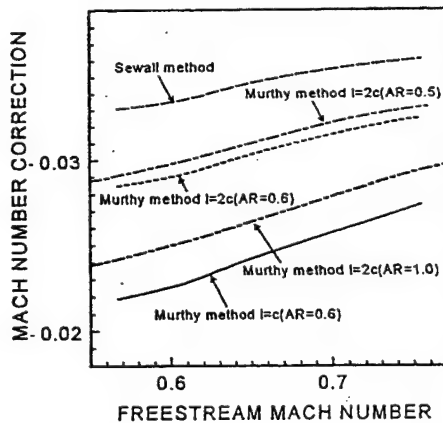


Figure 10: Mach number correction due to sidewall boundary layers.

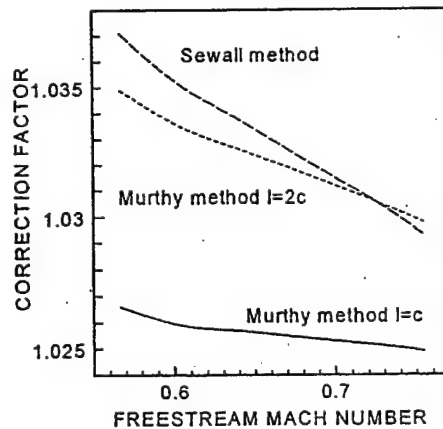


Figure 11: Correction factor due to sidewall boundary layers.

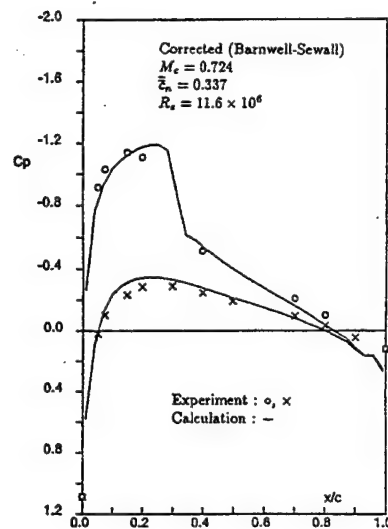


Figure 13: Corrected data with correction I compared with computed results, NACA0012, AR=0.5, TRANDES, $M_c = 0.724$, $\bar{c}_n = 0.337$, $R_e = 11.6 \times 10^6$.

DETERMINATION OF RESIDUAL WALL INTERFERENCES FOR MEASUREMENTS ON THE TWIG MODEL - COMPARISON OF DIFFERENT METHODS AND ANALYSIS

H. Holst¹, J.-P. Archambaud², A. Mignosi², M. Jacobs¹
¹DLR, Göttingen, Germany, ² ONERA, Toulouse, France

May 14, 1999

ABSTRACT

Measurements have been carried out in the two-dimensional adaptive test sections of the Transonic Windtunnel Göttingen TWG of DLR and the T2 wind tunnel of the ONERA Toulouse. The TWIG model (Transonic Wall Interference Generator) was available in two different scales, so that for the test sections of different sizes the relative model size was the same. The wall adaptation was performed using the fast Wedemeyer/Lamarche method for determining the wall shapes in both cases.

As a first step, different methods for the determination of residual wall interferences have been applied to data from the adaptive test section of the University of Southampton, U.o.S. These were regarded as very reliable and accurate, and wall contour data and very dense pressure distributions were available. Residual wall interferences computed by the U.o.S., DLR, ONERA and NLR show very good agreement.

The measurements on the two different TWIG models in the adaptive test sections of T2 and TWG show good agreement for the wall shapes and the measured pressure distribution. Data from TWG were taken for the determination of residual wall interferences by the different methods. The residual wall interferences do not agree so perfect as it had been before with the U.o.S. data. The reasons for this are/could possibly be:

- wall pressure data not so dense as before
- influence of the finite length of the test section
- model representation not "good" enough
- model not centrally placed
- support influences
- exit section not taken into account

LIST OF SYMBOLS

α	angle of attack
b	span of model
β	transonic parameter, $\beta = \sqrt{1 - M^2}$
B	width of test section
c	chord of profile
c_L	lift coefficient

C_p	pressure coefficient, $C_p = \frac{p - p_\infty}{q_\infty}$
$\Delta\alpha$	angle of attack correction
$\Delta n, DN$	wall displacements, upward positive
Λ	sweep angle of model
H	height of test section
L	length of test section
M	Mach number
q_∞	dynamic pressure of undisturbed flow
s	semispan of model
U_∞, U_{inf}	free stream velocity
u_i	longitudinal interference velocity
w_i	vertical interference velocity
x_M	position of model in the tunnel
x, y, z	cartesian co-ordinates

SUBSCRIPTS

c	corrected
$c/4$	quarter chord
i	interference
j	jack for wall adjustment
$l.e.$	leading edge
M, m	model
max	maximum
p	static pressure, pressure orifice
$strake$	strake
$t.e.$	trailing edge
$t.s.$	test section
u	uncorrected
$wing$	wing
∞, inf	undisturbed flow

INTRODUCTION

The flow about a model in the test section of a wind tunnel is different from free flight. If the walls of a test section were three-dimensionally deformable, they could form streamlines and all the wall interferences could be eliminated. The model in the tunnel would not feel the presence of the walls. Because a fully three-dimensional wall adaptation is extremely difficult to perform, the proposal was made, to adapt only top and bottom walls, so that the wall interferences for three-dimensional models are eliminated on a target

line. This is in most cases the centreline of the test section.

This kind of wall adaptation is known as the VKI-method [1], [2], [3] or the Wedemeyer/Lamarche method, and in its very fast form it needs computing times of less than 0.1 sec on a modern work station, so it can be applied realtime [4]. For the determination of the new wall shapes which have to be adjusted to achieve interference-free conditions on the test section centreline (where normally the model is located), the wall shapes, and the accompanying wall pressures on top and bottom wall centrelines have to be known.

As mentioned before, the wall interferences can be eliminated on the test section centreline by the two-dimensional wall adaptation. If it is desired to have a view on the residual wall interference, the knowledge of the wall pressure distribution on all four walls and the flow conditions in the entrance and the exit section of the wind tunnel is required, otherwise a model representation is needed. The computed residuals will give information, whether the goal of zero wall interference on the centreline has been achieved as the theory had predicted. And also the residual wall interferences - i.e. Mach number correction $\Delta M = M_u [1 + 0.2 M_u^2] \frac{u_i}{U_\infty}$ [5] and angle of attack correction $\Delta \alpha [^\circ] = -\frac{180}{\pi} \frac{w_i}{U_\infty}$ - can be taken e.g. as spanwise averages to apply corrections to the measured force data.

Measurements in the transonic wind tunnel of DLR Göttingen and in the T2 of ONERA Toulouse have been performed. Both tunnels are equipped with two-dimensional adaptive test sections. Two TWIG models of different scales

1. TWIG/D750 (Germany, 750 mm span)
 2. TWIG/NL300 (The Netherlands, 300 mm span)
- but otherwise identical, were available. The investigation of the residual wall interferences has been performed by ONERA, NLR, DLR and British Aerospace within the framework of the GARTEur AD AG18 working group.

THE TRANSONIC WIND TUNNEL TWG OF DLR GÖTTINGEN

The transonic wind tunnel of DLR Göttingen (<http://www.wk.go.dlr.de>) is a continuously driven wind tunnel of the Göttingen type [6]. It is equipped with three test sections of 1 m by 1 m cross section: supersonic test section (Laval nozzle) for Mach number from 1.33 to 2.21, transonic test section (6 percent open, the holes being 30° inclined) for $0.3 \leq M \leq 1.2$ and the 2-D adaptive test section. The stagnation pressure can be varied: $0.3 \text{ bar} \leq p_0 \leq 1.5 \text{ bar}$.

The two-dimensional adaptive test-section is equipped with 22 jacks for adjusting the desired wall shape on

the flexible top wall; on the bottom wall there are 20 jacks for wall adjustment. Details can be seen on Fig.1. The side walls can be removed, so that the jacks and the wall pressure orifices are accessible. There are two different testing positions, the position for two-dimensional models being upstream of the three-dimensional testing position. The test section is 4.51 m long, the 3-D testing position is at $x_M = 3.28 \text{ m}$, the dimensionless distance to the end of the test section is $[L_{t.s.} - x_M]/H = 1.23$. Top and bottom flexible walls are made from 3 mm thick steel, and they are equipped with three lines of pressure orifices each. The sidewalls are parallel, one being equipped with three, the other with four lines of pressure orifices, see Fig.2.

The wall pressure distribution is needed for the computation of wall adaptation and the residual wall interferences. For three-dimensional models a computer program utilizing Green's theorem [7] is available for the determination of the residuals. For the two-dimensional case this task is performed by a code based on the Cauchy integral formula also used for wall shape computations [8].

THE TRANSONIC WIND TUNNEL T2 OF ONERA TOULOUSE [9]

The T2 wind tunnel is a transonic and cryogenic facility. The circuit is closed, and it can be pressurized up to 3 bars. The flow is driven by an injector system, and the T2 tunnel operates by runs of 50 seconds to 2 minutes.

The test section dimensions are $B = 0.39 \text{ m}$, $H = 0.37 \text{ m}$ and $L = 1.45 \text{ m}$. The model position is at $x = 0.80 \text{ m}$, upstream end is $x = 0$. The dimensionless distance of the model from the end of the test section is $[L_{t.s.} - x_M]/H = 1.76$. Top and bottom walls are flexible 1.3 mm thick flexible steel plates. Each flexible wall can be adjusted by 16 hydraulic jacks. The wall displacement is performed by stepper motors, and one step is 0.2 mm. The maximum displacement of each single jack is 25 mm. The jacks are closer together near the model position. The wall shape is measured by potentiometric comparators. Each flexible wall is equipped with 104 pressure orifices (3 lines, orifice diameter 0.3 mm), which are used for the computation of wall adaptation and determination of residual wall interferences. The sidewalls are straight and parallel. They are insulated inside. The flexible top and bottom walls, and the moving mechanism are not insulated. In fact, during a cryogenic run, the walls behave quasi-adiabatic, whereas the temperature of the wall adaptation mechanism is close to the ambient value. So there are no problems with the movement of the flexible walls, even not at temperatures of 120 K. The turbulence level in the test section is about 0.15%. The

Mach number is automatically controlled by adjustment of a sonic throat located just downstream the test section.

The two-dimensional wall adaptation for 3-D models is performed by the so called VKI procedure, also known as the Wedemeyer/Lamarche method. The very fast form [4] proposed by Wedemeyer is also used at T2, and it allows several iterative wall adaptations during one single run of the tunnel. The computation time of one iterative step is about 0.1 seconds.

METHODS FOR RESIDUALS

University of Southampton

The method used for wall interference assessment at the University of Southampton is based on that developed by Ashhill and Weeks [10] for solid straight-walled test sections, modified to account for curvature in the top and the bottom walls [11]. The wall adaptation for three-dimensional models is performed by an influence coefficient method, along with the appropriate wall interference assessment. An important feature used at the adaptive wall wind tunnel of the University of Southampton is the rotation of the test section about a point just downstream of its entrance. Hereby misalignment of the downstream ends of the flexible walls with the first diffuser is avoided.

British Aerospace

The method for the determination of residual wall interference is the the original method developed by Mokry [12]. It is "an engineering type estimation of wall corrections". It is based upon the classical linear wall interference concept (cf. [5] [13]), representing the model by singularities, deduced from the model geometry and measured forces. This method gives interference information about the test section centreline only. The Mokry code was applied by British Aerospace to the TWG data only.

ONERA

The method for wall adaptation used in the T2 transonic facility is the fast Wedemeyer/Lamarche method for two-dimensional wall adaptation for three-dimensional models. It was provided by DLR within a mutual exchange of computer codes. The method for wall interference assessment at ONERA T2 is based on the top and bottom flexible wall pressures only (Y. Le Sant). It is based on the method of images and it does need a model representation.

NLR

The method used at NLR for the determination of residual wall interferences is based on Green's theo-

rem. This method was derived to compute wall induced velocities on the tunnel centreline from a sparse set of wall pressure distributions [14]. To achieve this, it heavily uses all available arguments about symmetry etc. This limits the applicability, however, for positions outside the centreline.

DLR

The method used for wall adaptation at the DLR transonic facility TWG is fast Wedemeyer/Lamarche code [4]. The method GREEN for wall interference determination for straight and adapted walls is based on the application of Green's theorem [7]. This method allows the computation of wall interferences or residuals everywhere in the test section, including the test section walls. It is therefore also suited for determination of wall shapes - then using appropriate average values for the wall displacements to be applied on top and bottom flexible walls only.

In comparison to the fast Wedemeyer/Lamarche procedure, which needs about one tenth of a second for wall shape computation on a modern workstation, the method GREEN needs a few seconds. This is so, because in the latter case, the wall interferences have to be computed on all the control points of the panels into which the test section walls are subdivided. For the case of determining the residuals *at the position of the model*, only about 20 values have to be determined. This would need about a tenth of a second.

For the application of this method, the wall pressure distribution on all four test section walls has to be known, but it does not need a model representation.

U.o.S. ARROWHEAD DATA

Arrowhead model

The arrowhead model is shown in Fig.3. The model data for the arrow-head model are given in Table 1. It is a half model, and it is mounted halfway up the sidewall.

Test section

The adaptive test section of the U.o.S. is of square cross section, $H = B = 152.4$ mm. The port sidewall, on which the model was mounted, had no pressure tapings. The other three walls are equipped with rows of pressure orifices, evenly spaced at 25.4 mm intervals, the middle rows being on the centrelines. A sketch of the arrangement is given in Fig. 4, the positions of the jacks for wall adaptation and the positions of the pressure orifices are given in Table 2.

Wall shapes and wall pressures, arrowhead data

There were three cases for the arrowhead model, all at a Mach number of $M = 0.700$:

1. *Aerodynamically straight walls* (compensation for growth of boundary layer displacement thickness), these walls give nominally zero pressure gradient in the empty test section.
2. Wall shapes eliminating the model induced upwash on the target line, the blockage interference remains - *upwash walls*. The upwash walls are rotated, so misalignment at the downstream end of the test section with the diffuser is avoided.
3. Wall shapes removing model induced blockage interference on the target line, but leaving the upwash interference - *blockage walls*.

Within the coordinate system chosen, see Fig. 2 and Fig. 4, the wall shapes on top and bottom walls are identical for the case *upwash walls*, and they are of same magnitude but opposite sign for the case *blockage walls*. There were 19 jacks for wall adjustment on the top wall and on the bottom wall. The pressure distribution was very dense (in comparison to other tunnels), 15 lines with 18 pressure tapings each. In total there were 270 pressure orifices.

The wall shapes for the upwash walls are shown in Fig. 5. A comparison was made between the "Southampton" wall shape, and a wall shape computed using the Wedemeyer/Lamarche method. This wall shape was derived from the straight wall pressure distribution in a single step, based only on the interpolated top and bottom wall centreline pressures of the double tunnel, see Fig. 4. Good agreement was achieved by rotating the walls by 0.43° , also demonstrating that one iterative step is sufficient. The rotation angle of 0.43° corresponds to a constant value of $\frac{w_i}{U_\infty} = \tan(0.43^\circ) = 0.0075$ along the centreline of the test section, which is the target line. It should be mentioned that the rotation of the walls has to be accounted for when determining the effective angle of attack of the model.

The wall shape for *blockage walls*, also derived from the top and bottom wall centreline pressures in straight walls - necessarily in one single step - using the Wedemeyer/Lamarche, method is shown in Fig. 6. The differences are in the order of 0.1 mm.

ARROWHEAD RESIDUALS

The residual wall interferences for the three cases mentioned above were computed by different methods from the University of Southampton, British Aerospace, ONERA, NLR, and DLR. Only the methods of U.o.S., ONERA and DLR allow residual determination at off-centreline positions. The other ones are restricted to the centreline of the test section.

Straight walls

Fig. 7 shows the variation of the longitudinal interference velocity in straight walls. the maximum value $\left[\frac{w_i}{U_\infty}\right]_{max} = 0.006$ corresponds to a Mach number correction of $\Delta M = 0.0046$. The different methods show good agreement. Some differences at the end of the test section can be attributed to the different kinds of extrapolation of wall pressure data. The vertical component of interference velocity along the centreline of the test section is given in Fig. 8. At the position of the model, (i.e. root chord, quarter chord line, $x_M = 0.438$ m), we find $\frac{w_i}{U_\infty} = 0.006$, the angle of attack correction $\Delta\alpha$ is then 0.34° , differing from the rotation angle of 0.43° found for best agreement with the Wedemeyer/Lamarche method.

Blockage walls

Fig.9 and Fig.10 show the interference velocities $\frac{w_i}{U_\infty}$ and $\frac{w_v}{U_\infty}$ on the centreline of the test section respectively. For blockage walls, the residuals for the longitudinal interference should be zero, while the upwash interference remains as it was before in straight walls. The different methods show that this is the case within about ± 0.001 .

Upwash walls

The case "upwash walls" is presented in Fig. 11 to Fig. 14. As expected, the upwash has been removed by wall adaptation, and the longitudinal interference remains. It should be noted that the value of the residual vertical component of interference velocity $\frac{w_v}{U_\infty} = 0.006$ corresponds to the value of 0.34° , by this amount the test section had been rotated to avoid misalignment at the end of the test section with the diffuser. The amazing result is in Fig. 13 and Fig. 14 that the off-centre results for the residual wall interferences is not so bad represented also by the methods not designed for this purpose.

Remarks

The wall pressure distributions evaluated here are available very dense. With sparse wall pressure data, the good agreement would probably be worse, depending on the procedures for interpolation. It is remarkable that the two different approaches Wedemeyer/Lamarche and U.o.S. give nearly the same wall shapes in the two cases upwash walls and blockage walls.

For the upwash walls there is a difference in the angle of rotation (0.34° and 0.43°), which is probably related to the kind of extrapolation of the wall contours at both

ends of the test section, and to the kind of extrapolation of the wall pressure distribution in the different computer codes. Also the wall shapes adjusted during the tests are not exactly the wall shapes required for upwash removal, because - with or without rotation - the top and bottom walls had to stay attached to the rest of the tunnel circuit.

MEASUREMENTS ON TWIG MODELS

Measurements were performed in the 2-D adaptive test section of the T2 transonic facility, and the 2-D adaptive test section of the transonic wind tunnel of DLR Göttingen TWG. The wall adaptation is performed by the Wedemeyer/Lamarche method in both cases. The wall pressures and wall shapes from TWG were taken to compare the methods for the determination of residual wall interference, because all four TWG walls are equipped with pressure orifices, whereas only the top and bottom walls of the T2 have wall pressure tapings.

Models of different scale

There were two TWIG models, see Fig.15 and Table 3, of different scale. The smaller model TWIG/NL300, having a span $b = 300$ mm, has been taken for the measurements in T2. Its relative span is $\frac{b}{B} = 0.77$. The other model TWIG/D750, which was taken for the TWG measurements has a span of $b = 750$ mm, the relative span is therefore 0.75. The conditions for the model were nearly the same in the two different tunnels. Only the relative distance from the downstream end of the test section differ. For the T2 $[L_{t.s.} - x_M]/H$ is 1.76, whereas this ratio for the TWG is only 1.23.

Wall pressure distributions and wall shapes

An example for the measured wall pressure distributions is given in Fig. 16. On the top wall, the pressure coefficients at the downstream end of the test section are negative (acceleration due to positive lift and acceleration due to blockage). On the bottom wall the pressure coefficients are positive, because the lift influence is dominant there.

The normalized wall shapes for comparable cases from T2 and TWG have been compared in Fig. 17. The agreement is nearly perfect. Differences to the end can be explained by the different model distances to the downstream end of the test sections in T2 and TWG. The flexible walls in TWG have to be bent back to horizontal to stay attached to the downstream continuation of the tunnel (chamber surrounding the support and the diffuser). In TWG and in T2, the walls have not been rotated.

RESIDUALS FOR TWIG RESULTS FROM TWG

The comparison of residual wall interference, determined by different methods, is presented for two different cases in Fig. 18 to Fig. 21.

Not adapted case, $M = 0.700$

First shown is the datapoint 38ap5, a not adapted case, the Mach number is $M = 0.700$ and the angle of attack is 7.28° . In Fig. 18, upper diagram, the variation of $\frac{u_i}{U_\infty}$ along the centreline is given. At the nominal position of the model, $x_M = 0$, the value is about 0.02, corresponding to a Mach number correction of $\Delta M = 0.015$. The agreement of the different methods is not satisfactory. The lower diagram shows the same case for the vertical interference velocity component $\frac{w^{int}}{U_\infty}$, the value at the model position is -0.015 corresponding to $\Delta \alpha = 0.86^\circ$. Here the agreement between the ONERA method with model representation and the DLR method without model representation is quite satisfactory, whereas the Mokry-method applied by BAe underpredicts the angle of attack correction.

Along the quarter chord line the agreement of computed results for residual wall interferences between the ONERA-method and the DLR-method is better, see Fig. 19 and Fig. 20. The method applied by BAe is not applicable for off-centre positions.

Adapted case, $M = 0.800$

Results for residuals in an adapted case are given in Fig. 21. At the position of the model, $x_M = 0$, the longitudinal interference is reduced to about one tenth of its original value, the vertical interference velocity is reduced to one fourth of its original value in straight walls. Here the DLR result was taken as a reference. Nevertheless, the residual wall interferences are not zero on the centreline, but they are increasing to the end of the test section. As before for the straight wall case, the agreement of the different methods is better for the vertical component of the interference velocities and not at all good for the longitudinal interference velocities.

CONCLUDING REMARKS

Different methods for the computation of wall interference (straight walls) and residual wall interference (adapted walls) have been compared using different sets of data. The data from the University of Southampton are very dense, and the model was centrally located in the test section. This led to good agreement of the wall interference computations by different methods.

The two TWIG models of different scales, which had been tested in T2 and TWG respectively, show good

agreement of results for forces, wall shapes and wall pressures. This could be expected, because the relative span is the same in both cases.

For the wall pressure and wall shapes of TWG the different methods for the computation of residual wall interferences show only good agreement for the angle of attack correction, but not for the Mach number correction. Also, the residuals are not zero on the centreline as they should, after the adaptation of the walls. The reasons for not satisfactory agreement are that the data are not so dense as before, so probably a better interpolation procedure for the wall pressures would help. Probably the model representation - where applicable - is not adequate. The fact that the wall interference is not zero on the centreline after wall adaptation is probably due to

- finite length of test section
- method of aligning the adapted test section with the downstream component of the tunnel circuit (rotation of test section)
- model not centrally placed in the test section due to necessity of rear sting
- model too close to the end of the test section, support influences

REFERENCES

- [1] Lamarche, L., Wedemeyer, E.: *Minimization of Wall Interference for Three-Dimensional Models with Two-Dimensional Wall Adaptation*. Technical Note 149, von Kármán Institute for Fluid Dynamics, Brussels, Belgium, 1984.
- [2] Wedemeyer, E.: *The Computer in Experimental Fluid Dynamics*. Lecture Series 1986-06, von Kármán Institute for Fluid Dynamics, Brussels, Belgium 1986.
- [3] Wedemeyer, E.: *Adaptive Wind Tunnel Walls: Technology and Applications*. (Section 4: Testing of 3-D Models in 2-D Adaptive Wall Test Sections.) AGARD-AR-269, April 1990.
- [4] Holst, H.: *Realtime Computation of Wall Shapes in a Two-Dimensional Adaptive Test Section*. ICAS'94, Anaheim, California, USA, 1994.
- [5] Garner, H.G., Rogers, E.W.E., Acum, W.E.A., Maskell, E.C.: *Subsonic Wind Tunnel Wall Corrections*. AGARDograph 109, 1966.
- [6] Binder, B., Riethmüller, L., Tusche, S., Wulf, R.: *Modernisierung des Transsonischen Windkanals in Göttingen*. (Modernization of the Transonic Wind Tunnel in Göttingen). Jahrbuch 1992 I der deutschen Gesellschaft für Luft- und Raumfahrt e.V. (DGLR, Bonn, 1992).
- [7] Holst, H.: *Procedure for Determination of Three-Dimensional Wind Tunnel Wall Interferences and Wall Adaptation in Compressible Subsonic Flow Using Measured Wall Pressures*. DLR-FB 91-09, Göttingen, Germany, 1991.
- [8] Amecke, J.: *Direkte Berechnung der Wandinterferenzen bei zweidimensionaler Strömung in Windkanälen mit geschlossenen Wänden*. DFVLR-FB 85-62, DFVLR Göttingen, Germany, 1985.
- [9] Archambaud, J.-P., Michonneau, J.F., Prudhomme, S.: *Use of Flexible Walls to Minimise Interferences at T2 Tunnel*. Wind Tunnels and Wind Tunnel Test Techniques, European Forum, paper 15, Sept. 14 - Sept. 17, 1992, Southampton UK.

- [10] Ashill, P.R. and Weeks, D.J.: *A Method for Determining Wall-Interference Corrections in Solid Walled Tunnels from Measurements of Static Pressure at the Wall*. AGARD CP335, 1982.
- [11] Goodyer, M.J. and Wolf, S.W.D.: *Development of a Self Streamlining Flexible Walled Transonic Test Section*. AIAA Journal, Vol.20, no.2, February 1982, pp.227-234.
- [12] Mokry, M.: *Subsonic Wall Interference Corrections for Finite-Length Test Sections Using Boundary Pressure Measurements*. AGARD-CP-335 (10), London 1982.
- [13] Ewald, B.F.R. (Editor): *Wind Tunnel Wall Correction*. AGARDograph 336, 1998.
- [14] Labrujère, T.E., Maarsingh, R.A., Smith, J.: *Evaluation of Measured-Boundary-Condition Methods for 3D Subsonic Wall Interference*. Report NLR TR 88072 U., 1988.

ILLUSTRATIONS, DIAGRAMS

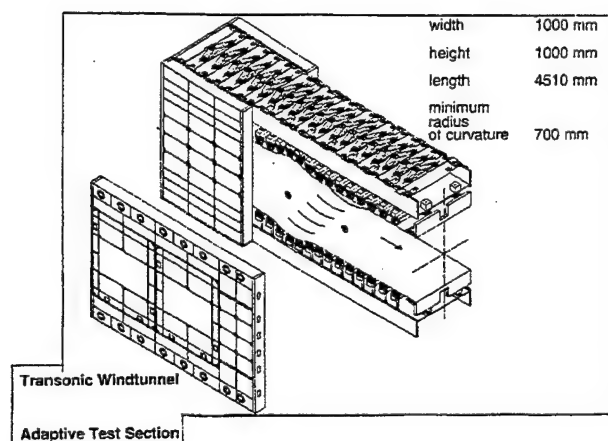


Figure 1: The two-dimensional adaptive test section of TWG.

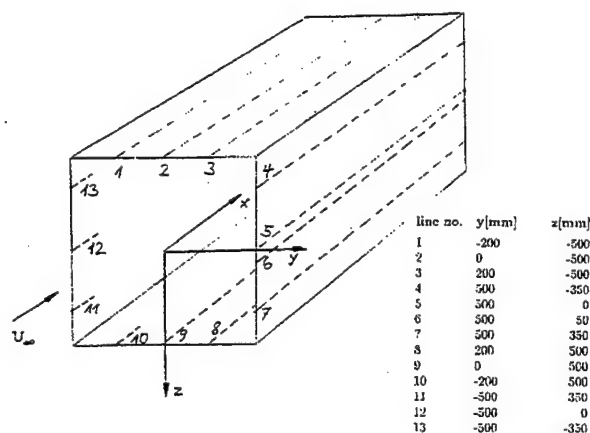


Figure 2: Co-ordinate system and position of the lines of pressure orifices at TWG.

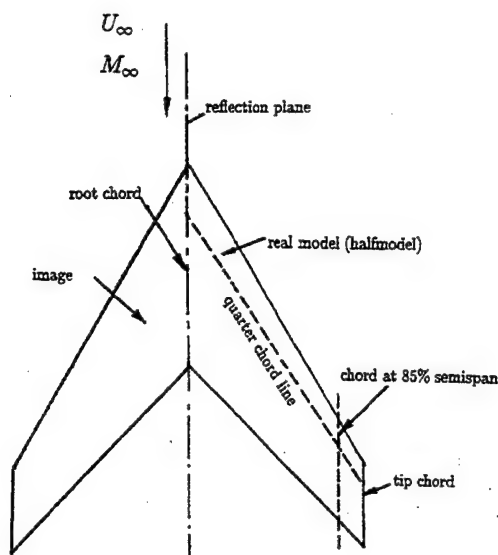


Figure 3: The arrowhead model of the University of Southampton.

semispan	$s = 93.14 \text{ mm}$
section	RAE 102
aspect ratio	2.67
taper ratio	0.389
thickness-to-chord ratio	0.06
root chord	$c_{\text{root}} = 10 \text{ mm}$
tip chord	$c_{\text{tip}} = 39.1 \text{ mm}$
mean chord	$c_{\text{mean}} = 69.8 \text{ mm}$
quarter chord sweep angle	$\Lambda_{c/4} = 56.3^\circ$
leading edge sweep angle	$\Lambda_{l.e.} = 59.03^\circ$
trailing edge sweep angle	$\Lambda_{t.e.} = 45.20^\circ$
apex angle	61.94°
position of root chord	$x=413.0\text{mm}$ to $x=513.6\text{mm}$
position of tip chord	$x=568.2\text{mm}$ to $x=607.4\text{mm}$
chord position at spanwise station $y=79.2\text{mm}$ (85% semispan)	$x=526.5\text{mm}$ to $x=584.8\text{mm}$

Table 1: Arrowhead model data.

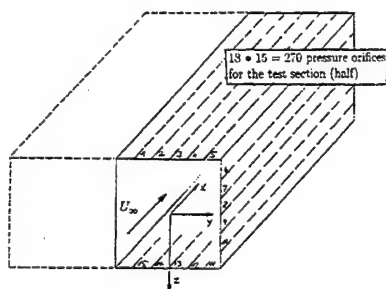


Figure 4: The adaptive wind tunnel of the University of Southampton. The tunnel is of square cross section, $H = B = 152.4 \text{ mm}$, and the halfmodel is mounted half way up the sidewall. The spacing of the pressure lines is 25.4 mm .

no.	x_j x-pos. of jack [mm]	x_p x-position of press. orifice [mm]
1	76.2	215.9
2	152.4	241.3
3	228.6	292.1
4	304.8	342.9
5	381.0	393.7
6	431.8	444.5
7	457.2	495.3
8	482.6	546.1
9	508.0	571.5
10	533.4	622.3
11	558.8	647.7
12	584.2	698.5
13	609.6	749.3
14	660.4	800.1
15	736.6	850.9
16	812.8	901.7
17	889.0	952.5
18	965.2	977.9
19	1041.4	—

Table 2: Coordinates the jacks for wall adaptation and of the wall pressure orifices at the adaptive test section of the University of Southampton.

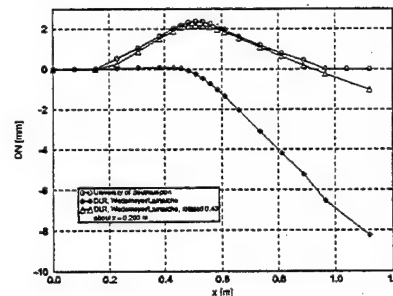


Figure 5: Wall shapes for "upwash" walls: the wall-induced upwash is removed by wall adaptation. The wall displacements are upward positive. Top and bottom wall displacements are identical.

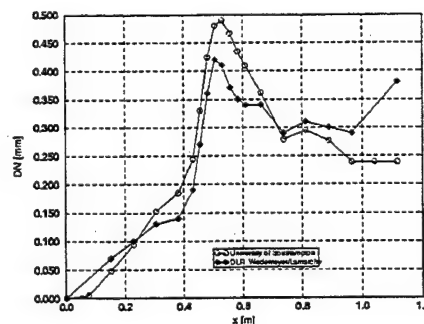


Figure 6: Wall shapes for "blockage" walls: the wall-induced blockage is removed by wall adaptation. The wall displacements are upward positive. Shown here is the top wall, wall displacements for the bottom wall are of the same magnitude but opposite sign.

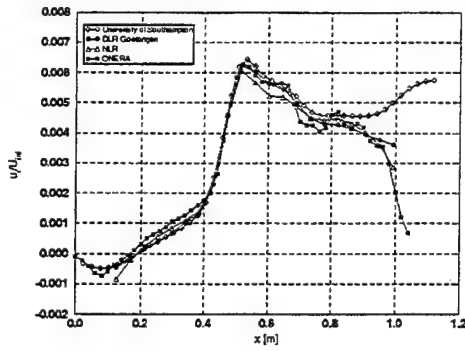


Figure 7: Variation of interference velocity u_i along the centerline for straight walls.

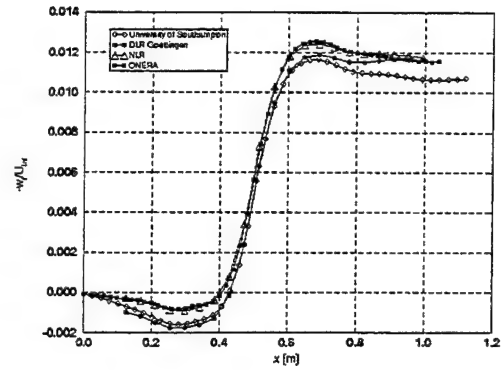


Figure 10: Variation of interference velocity w_i along the centerline for blockage walls.

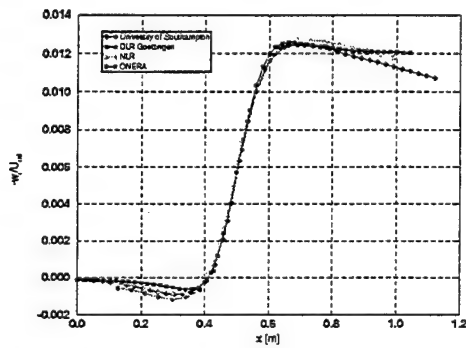


Figure 8: Variation of interference velocity w_i along the centerline for straight walls.

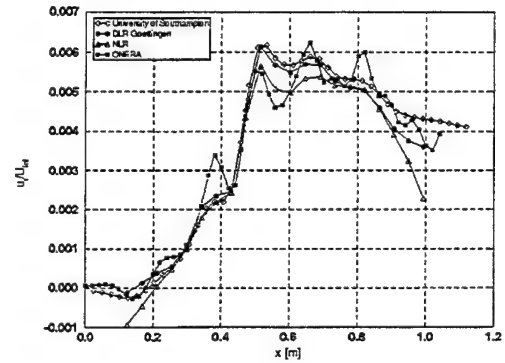


Figure 11: Variation of interference velocity u_i along the centerline for upwash walls.

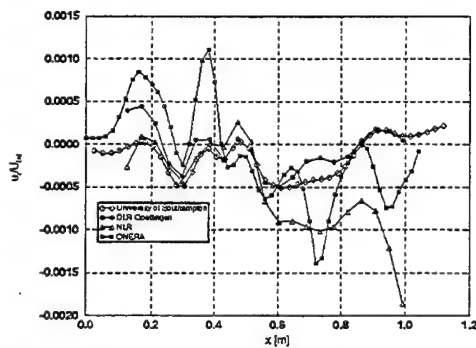


Figure 9: Variation of interference velocity u_i along the centerline for blockage walls.

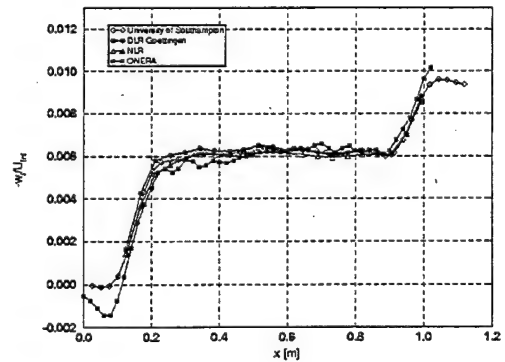


Figure 12: Variation of interference velocity w_i along the centerline for upwash walls.

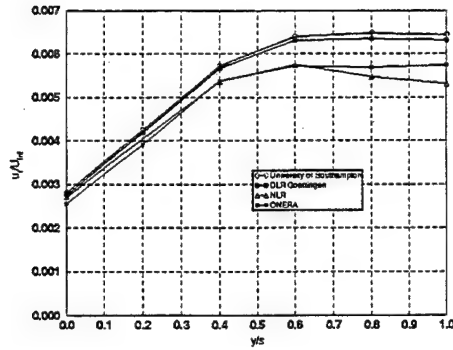


Figure 13: Variation of interference velocity u_i along the quarter chord line for upwash walls.

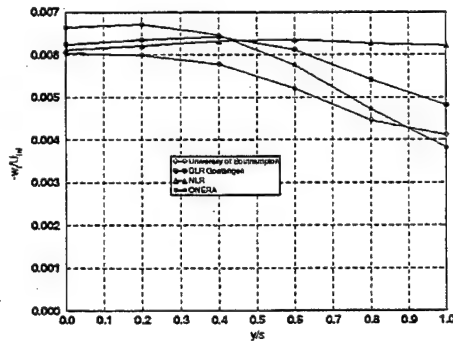


Figure 14: Variation of interference velocity w_i along the quarter chord line for upwash walls.

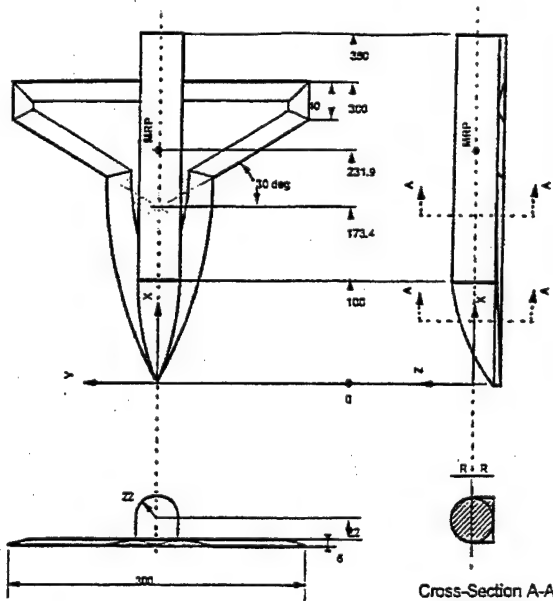


Figure 15: The model TWIG/NL300. The Model TWIG/D750 is larger by a factor of 2.5. (The span of TWIG/D750 is 750 mm.)

Strake contour:
Fuselage contour

Wing reference area
Wing bevel angle:
Cross-sectional area:
Strake area ratio
MRP
TWIG

$y_s = 25.85 \left[\frac{3x}{235} - \left(\frac{x}{235} \right)^3 \right] \text{ mm}$
 $R = 22 \text{ mm for } x \geq 100 \text{ mm}$
 $R = 11 \left[\frac{3x}{100} - \left(\frac{x}{100} \right)^3 \right] \text{ mm}$
for $0 \leq x \leq 100 \text{ mm}$
 $A_M = 0.025 \text{ m}^2$
 15°
 0.0028 m^2
 $A_{\text{strake}}/A_{\text{wing}} = 0.15$
reference point of model
is a low wing configuration

Table 3: Model data for TWIG/NL300.

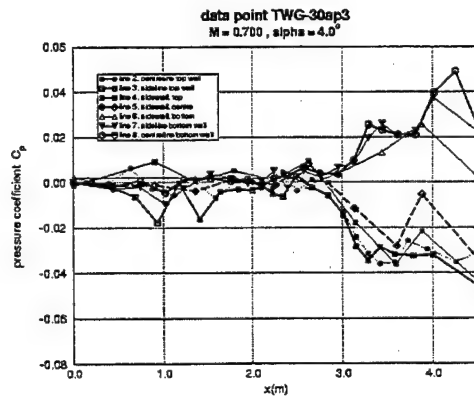


Figure 16: Pressure distribution for data point TWG-30ap3, $M = 0.700$, $\alpha = 4.0^\circ$, walls adapted.

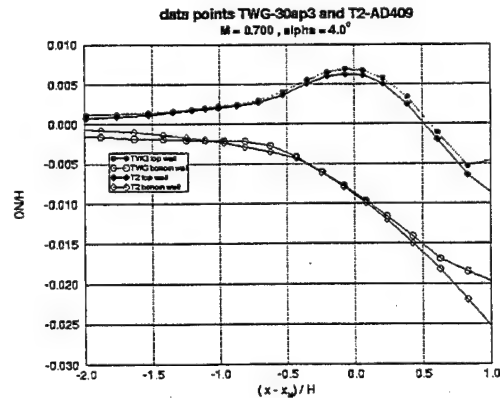


Figure 17: Comparison of wall shapes for data points TWG-30ap3, and T2-AD409 for $M = 0.700$ and $\alpha = 4.0^\circ$.

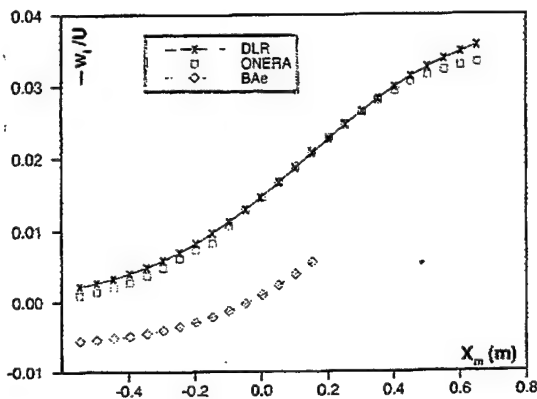
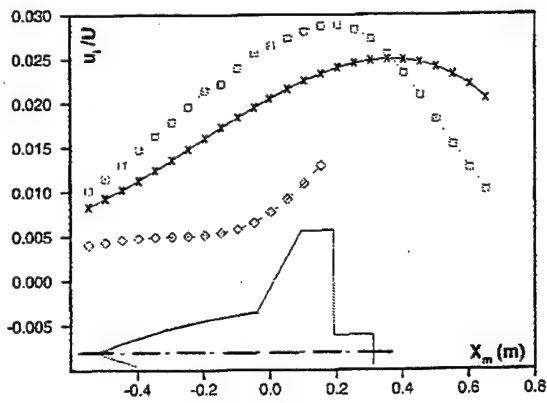


Figure 18: Comparison of different methods for wall interference determination in *aerodynamically straight* walls. Variation of interference velocities along centerline for data point 38ap5. $M = 0.700$ and $\alpha = 7.28^\circ$.
Upper diagram: longitudinal velocity, u_i .
Lower diagram: vertical velocity, w_i .

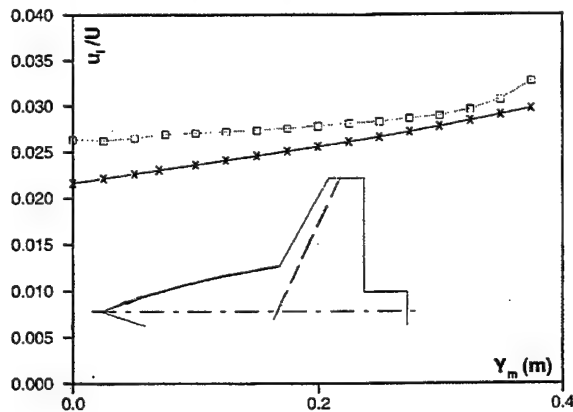


Figure 19: Comparison of different methods for wall interference determination in *aerodynamically straight* walls. Variation of u_i along quarter chord line for data point 38ap5. $M = 0.700$ and $\alpha = 7.28^\circ$.

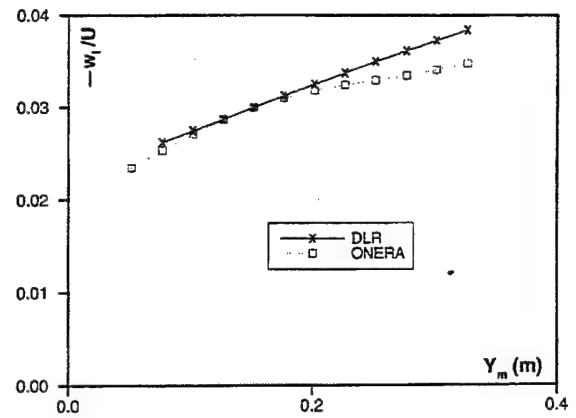


Figure 20: Comparison of different methods for wall interference determination in *aerodynamically straight* walls. Variation of w_i along quarter chord line for data point 38ap5. $M = 0.700$ and $\alpha = 7.28^\circ$.

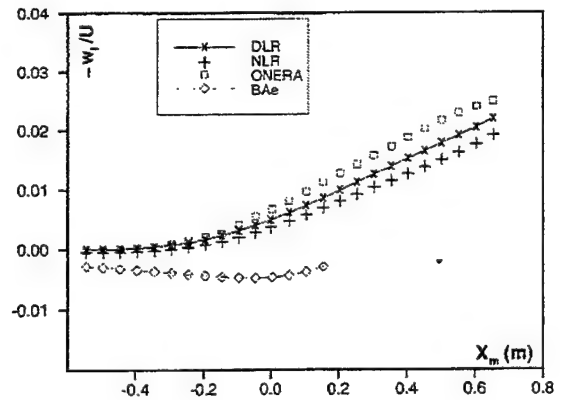
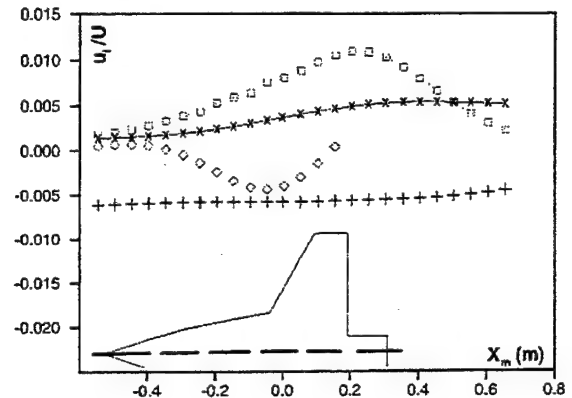


Figure 21: Comparison of different methods in adapted walls. Variation of residuals along centerline for data point 31ap5. $M = 0.800$ and $\alpha = 7.85^\circ$.
Upper diagram: longitudinal velocity, u_i .
Lower diagram: vertical velocity, w_i .

SESSION : 8

TEST TECHNIQUES

Electronically Scanned Pressure Measurement Scanner For Cryogenic Wind Tunnel Applications

Qamar A. Shams
NYMA Inc.
NASA\ Langley Research Center
M. S. 236
Hampton, VA 23681

Allan J. Zuckerwar
NASA\ Langley Research Center
M. S. 236
Hampton, VA 23681

ABSTRACT

Electronically scanned pressure (ESP) measurement modules are used in wind tunnels to measure surface pressures on models. Measurement channels are connected to pressure ports through small diameter tubing. Use of current state-of-the art ESP scanners in cryogenic wind tunnels has led to several practical problems which contribute to additional expense and loss of data quality. First current use of ESP scanners in cryogenic wind tunnels (at room temperature below - 25 C) dictates the need for protection against the thermal environment. The current solution is the use of a heater box which causes a number of operational problems. The installation of the heater box is time-consuming and labor-intensive. Its size reduces the amount of space available for scanner installation. Secondly, a wind tunnel test must be interrupted for on-line calibration which consumes as much as 15% of the total test time. Finally, the pressure and balance measurements are taken in separate runs because of an "apparent strain" problem. An electronically scanned pressure measurement module capable of operating directly in a cryogenic environment has been developed and tested over an extended temperature span. Total uncertainty, which is measured at less than 0.1% of FSO at 1 atmospheric reference pressure will be discussed.

accuracy. However, as with any other instrument, there are difficulties to use these devices at cryogenic temperature (NTF temperatures), because of charge carrier freeze-out [3,4]. Pressure dice and electronic components fail to work properly when temperature is lowered [3,4]. The traditional way to overcome this difficulty is to enclose each commercially available electronically-scanned pressure module in a heating box, shown in figure 1(b) before placing in a model to be tested in wind tunnels. This procedure is time consuming and expensive. Disadvantages of existing ESP technology are

1. Scanner needs heater box to maintain constant temperature.
2. Additional wiring across balance to power heater box are required.
3. Uncertain temperature distribution across pressure bridges.
4. Containing "Zero" shift or drift.
5. Pneumatic tubes crossing the balance to operate calibration valve.
6. Test interruptions for calibration.
7. "Apparent strain problem"
8. Separate runs for balance and pressure.

INTRODUCTION

Today, no aircraft, spacecraft, or space launch or reentry vehicle is built or committed to flight until after its design and components have been thoroughly tested in wind tunnels. The National Aeronautics and Space Administration (NASA) maintains 42 major wind tunnels. Out of these 42 major tunnels, 17 are cryogenic wind tunnels [1]. One of the desired parameters to be measured at different orifice locations on the model is static pressure. Electronically-scanned pressure systems [2], shown in figure 1(a) have become a mainstay of experimental testing because they provide a low-cost-per channel. These systems are small and computer controlled. They are easy to use and capable of high

There was need of an instrument which could work in the National Transonic Facility (NTF) operational environment. This paper is written to present results of langley developed cryo-ESP module which can be used to measure differential pressure over a wide range of temperature. A cross-section of the critical interfaces across the sensor to kovar base plate is shown in figure 2. This module was constructed using commercially available existing parts. Use of these existing parts have saved a considerable amount of design and construction costs of the cryo-temperature range multichannel ESP modules and also served the purpose of establishing basis for developing and fabricating 32-channel, 48-channel and 64-channel cryo-ESP modules.

Three most important areas of developing a wide-temperature range multichannel ESP modules are silicon pressure sensor dice, wide-temperature range compatible packaging of the modules, and signal conditioning circuits which are integrated within the ESP module housing.

DATA ACQUISITION SYSTEM:

The Calibration system consists of following five subsystems as shown in figure 3.

1. Cryo-High Pressure Chamber.
2. Measurement and Control of Chamber Temperature.
3. Pressure Supply Panel for Reference and Calibration.
4. System-8400 Data Acquisition System.
5. Liquid Nitrogen Supply System.

The Cryo-High pressure chamber simulates conditions in the National Transonic Facility (NTF) and is made of schedule 40 seamless steel. This system is 60.96 cm (24 inches) long with 20.32 cm (8 inches) diameter and has two 20.32 cm (8 inches) flanges at each end as shown in figure 4.

On the back flange, several feedthroughs were inserted with continuous wire feedthrough for thermocouples and low voltage instrumentation for measuring temperature and supplying power voltage for amplifier, multiplexers and constant current for RTD's on silicon chips.

Inside the chamber, there is another solid copper cylinder block for cooling and heating the cryo-ESP module. On this copper block, 6.25 mm (0.25 inches) copper tubing is wound through which liquid nitrogen flows by a solenoid valve. This copper tubing is wound over the whole block from one end to the other. On this copper tubing, pressure sensitive thermofoil heaters are pasted. On one circular end, a U-shaped piece is taken out to fit the Cryo-ESP module inside copper block.

Two solid state relays CS02410 and WEST 5010 temperature controller were used to regulate the temperature at cryo-ESP module site. The first solid state relay was used to control the ASCO solenoid valve for control of liquid nitrogen flow and the second solid state relay was used to control the Minco pressure heating thermofolios. From these both solid state relays, connections were made to the WEST 5010 temperature controller.

A commercially available analog to digital data acquisition system, the System 8400 PSI, Inc was used with a standard personal computer to scan the pressure

sensor output. As cryo-ESP modules have also RTD's to read temperature in real time for pressure measurements, an interface box was made to make System 8400 compatible to scan the temperature sensor outputs. The system 8400 consists of many components that operate together under the control of the System Processor (SP) which is the heart of the System 8400. All data acquired in the System 8400 must go through the SP to reach the host computer for processing. One of several units that operate under the control of SP is Scanner Digitizer Unit (SDU) which is a high-speed (50 KHz), 16-bit digital converter. The second unit is the Pressure Calibration Unit (PCU) which is a digitally controlled, pneumatic calibration source and/ or pressure generator.

MEASUREMENT UNCERTAINTY:

The objective of a measurement is to determine the value of the measurand, that is, in our case the value of the pressure. A measurement therefore begins with an appropriate specification of the method of measurement and measurement procedure.

In general, the result of a measurement is only an approximation or estimate of the value of the measurand and thus is complete only when accompanied by a statement of the uncertainty of that estimate.

Example - If the pressure on a model is to be measured, its specification should include the temperature and reference pressure at which pressure is defined.

SYSTEM 8400 ACCURACY:

Measurement	Accuracy
Air Pressure Scanning	+/-0.1% F.S.
High Pressure Accuracy	+/-0.02% F.S.
Pressure Calibration	+/-0.02% F.S.

EXPERIMENTAL RESULTS AND DISCUSSIONS:

The Langley developed Cryo-ESP module was calibrated using the calibration chamber as shown in figure 4. The NTF environment can be created by using liquid nitrogen flow, heating coils, different reference pressures and different calibration pressures. The following thirty (30) environmental conditions were used to calibrate cryo-ESP module.

CALIBRATION MATRIX:

Temperature © 50, 25, 0, -25, -50, -75, -100, -120, -140 and -160.

Reference pressure (atm.) 1, 3, and 8 atm.

Calibration Pressure -83 to 83 KPa (-12 to +12 psid) in 13.833 KPa (2 psid) steps.

A basic software was written to be used with system 8400 to scan the 16-channel Cryo-ESP module. This software scans 16-pressure ports and 16 RTD's in the module. This program applies differential pressure from -83 Kpa to 83 Kpa (-12 to +12 psid) in 13.833 Kpa (2 psi) steps on each port and scans output voltage (Vp) and temperature voltages (Vrtd) at each step. Raw data was taken for all reference pressures.

Figure 5 shows typical variations of offset voltages of the sensors with the amplifier gain of 100. Offset voltage, as expected changes with change in temperature. Comparing the profiles of the silicon pressure sensor offset voltages to those of the assembled ESP, the effects of difference in temperature coefficients of the ESP components are minimal or negligible.

Figure 6 shows the typical response of pressure sensor channel of the ESP module with increasing and decreasing pressure variation. Figures 7, 8, 9, and 10 show the components of the measurement uncertainty as well as the total uncertainty, expressed as a percentage of full scale output (%FSO), over the full temperature range. Noteworthy are the facts that (1) the total uncertainty does not exceed 0.1% FSO over the entire temperature range of the calibration, and (2) the contribution of the components (non-repeatability, hysteresis, and non-linearity) are all comparable in magnitude. The total uncertainty was computed as the sum of the absolute magnitudes of the three conditions, which is the worst possible case. Since each of the three contributions is independent of the others, it would be appropriate to value the root mean square uncertainty, in which case the total uncertainty could not exceed 0.07% FSO.

BENEFITS:

The benefits for this newly Langley developed scanner is fourfold.

1. The first utilizes one of the major differences between conventional and cryogenic scanners, namely the method of maintaining calibration during a test. The conventional scanner requires that a test be interrupted periodically so that a sliding valve can be activated to apply a known calibration pressure to the silicon pressure dice. The cryogenic scanner, on the other hand, contains a temperature sensor on each die, which together with a reference pressure measurement, permits continuously updated

calibration. The calibration coefficients, obtained from careful laboratory calibration, are preloaded into the data acquisition system. There is no need to interrupt a test for calibration.

2. Conventionally the pressure lines together with the heavy copper cables needed to power the heater box run from the model to the sting, crossing the force balance. These conduits shunt the force balance and cause an "apparent strain" problem, which corrupts the accuracy of the force balance. For this reason force balance and pressure measurements are conducted in two separate runs. The elimination of three pressure lines and the heater cable in the cryo-scanner will hopefully eliminate the apparent strain problem and permit force balance and pressure measurements to be taken in the same run.
3. The heater box needed for operation of the conventional scanner generates a variety of problems. It reduces available space for scanners, requires labor-intensive setup time, and consumes considerable electrical power. The cryogenic scanner eliminates the problems associated with the heater box.
4. Cryo scanner's calibration is extremely stable for months.

REFERENCES:

1. Cryo Newsletter, June 23, 1991, Current Cryogenic Wind Tunnels, P.10.
2. 16, 32-Channel Electronically Scanned Module, Pressure Systems, Inc. Hampton, VA 23666.
3. Kahng, Seun and Chapman, John J., "Piezoresistive Silicon Sensors in Cryogenic Environment, "Proceedings of the 35th International Instrumentation Symposium, May 1-4, 1989, Orlando, Florida.
4. Shams, Qamar A. Fox, Rober L., Adcock, Edward E., and Kahng Seun K. "A Cryogenic Multichannel Electronically Scanned Pressure Module" Proceedings of the 39th International Symposium, April 26-30, 1992.

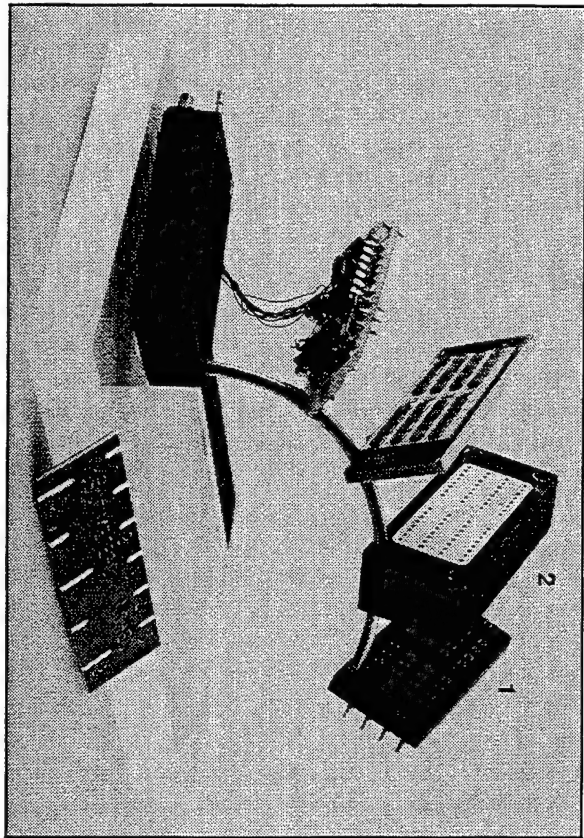


Figure 1 (a)

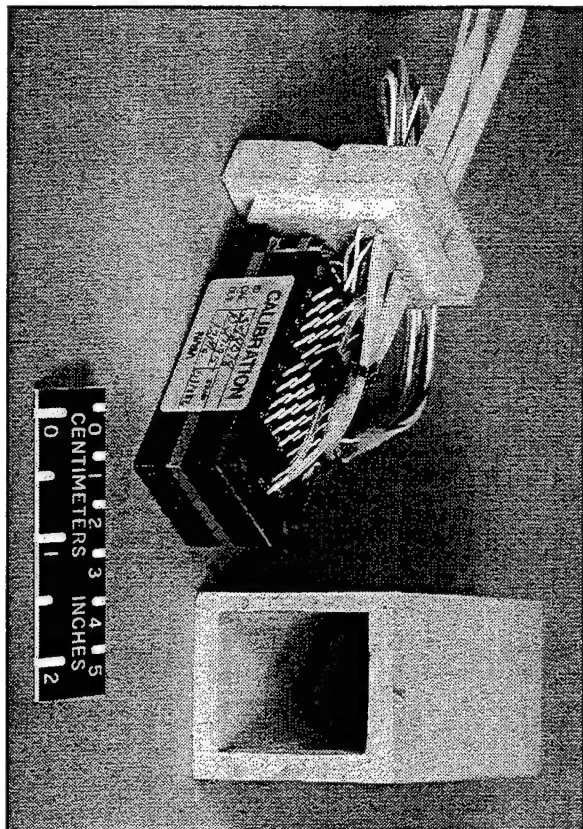


Figure 1 (b)

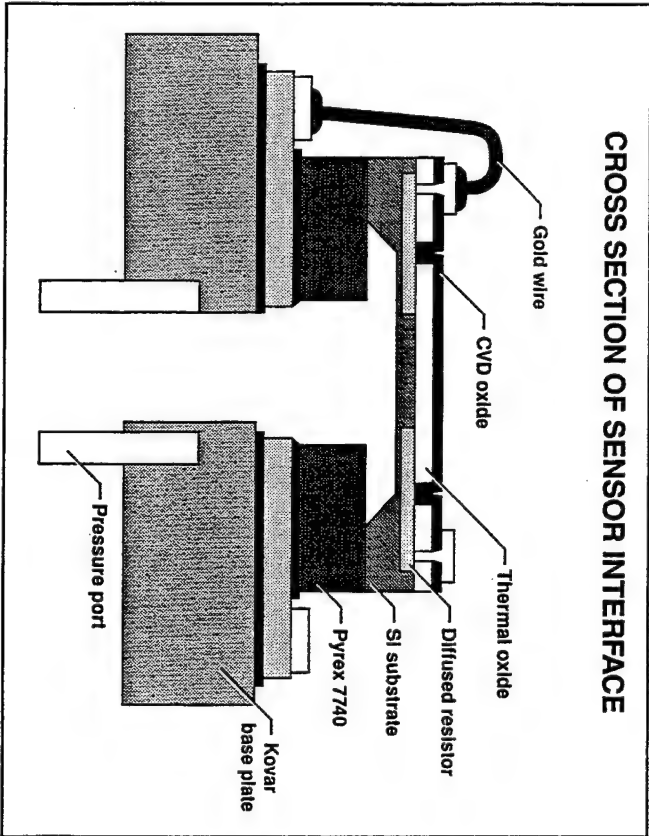


Figure 2

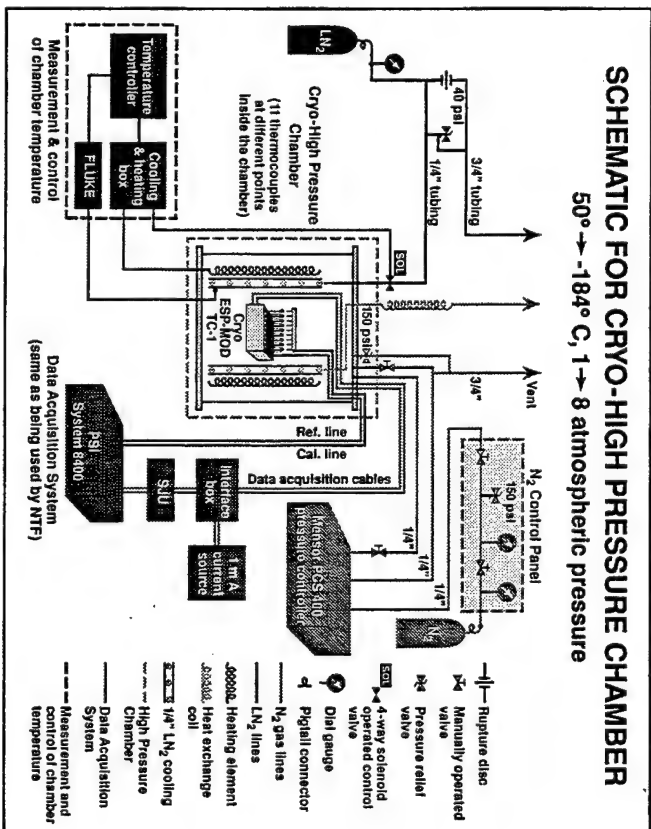


Figure 3

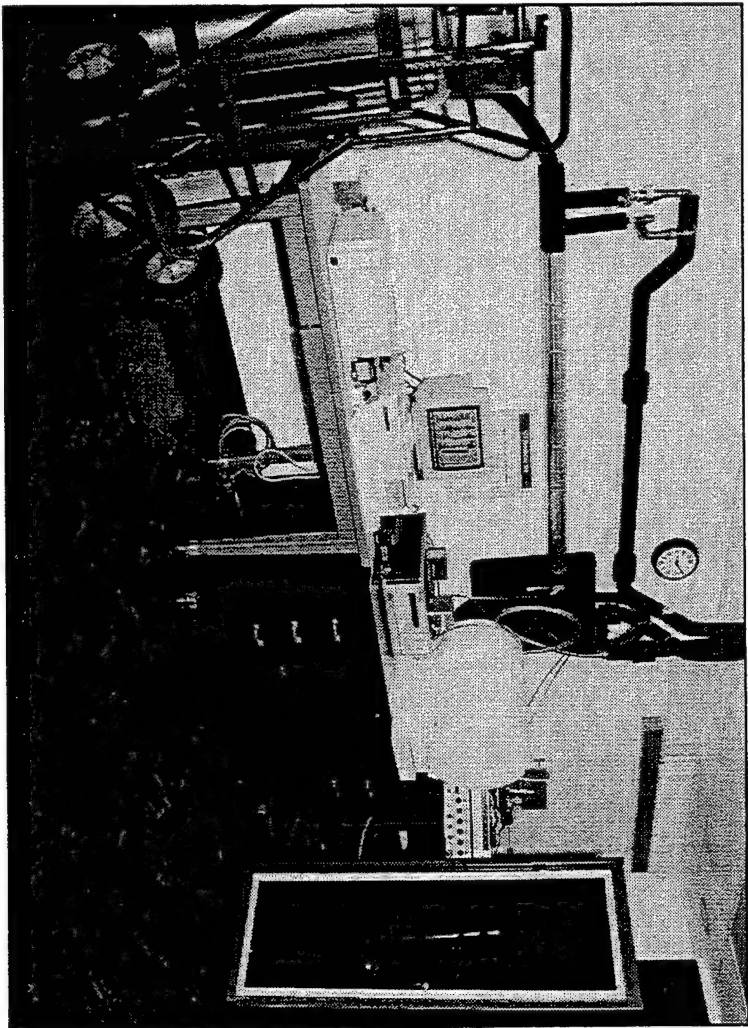


Figure 4

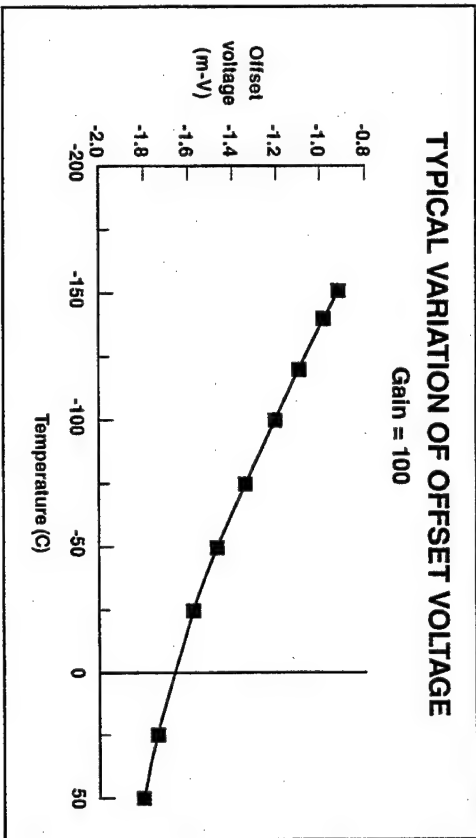


Figure 5

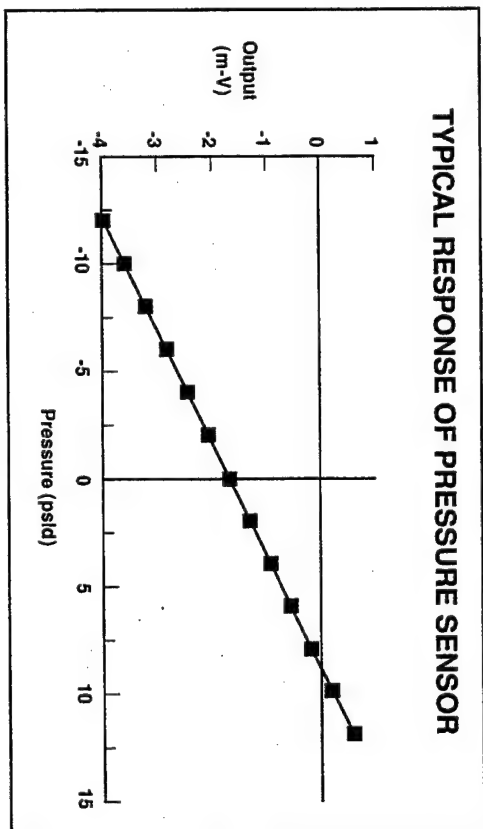


Figure 6

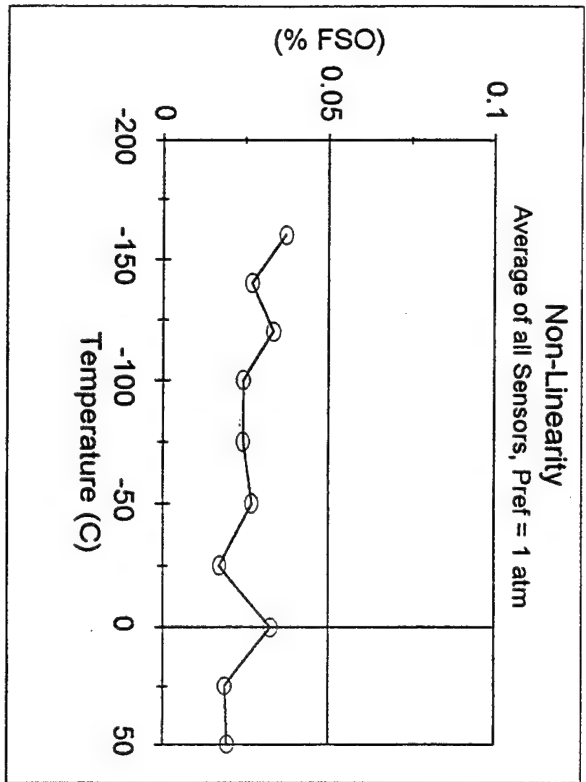


Figure 7

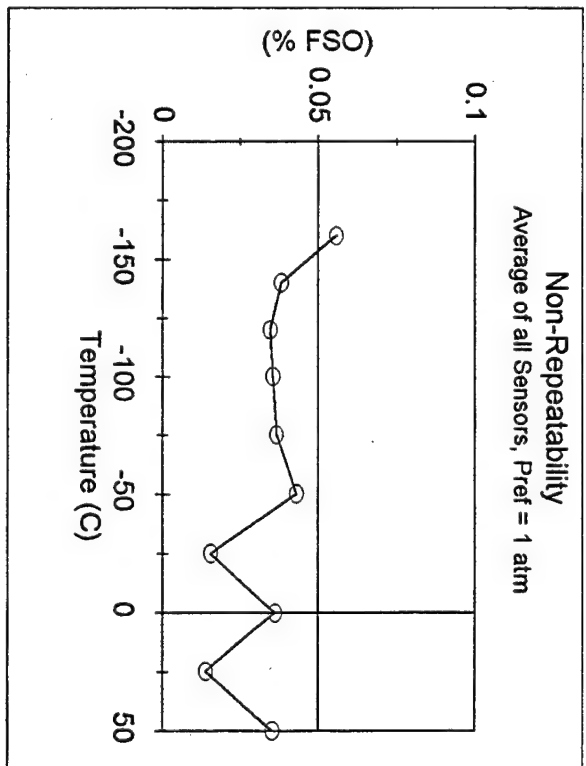


Figure 8

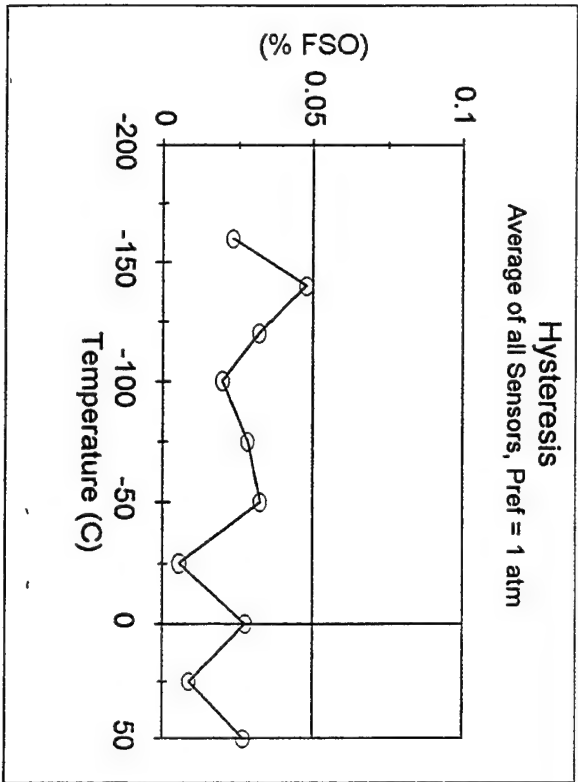


Figure 9

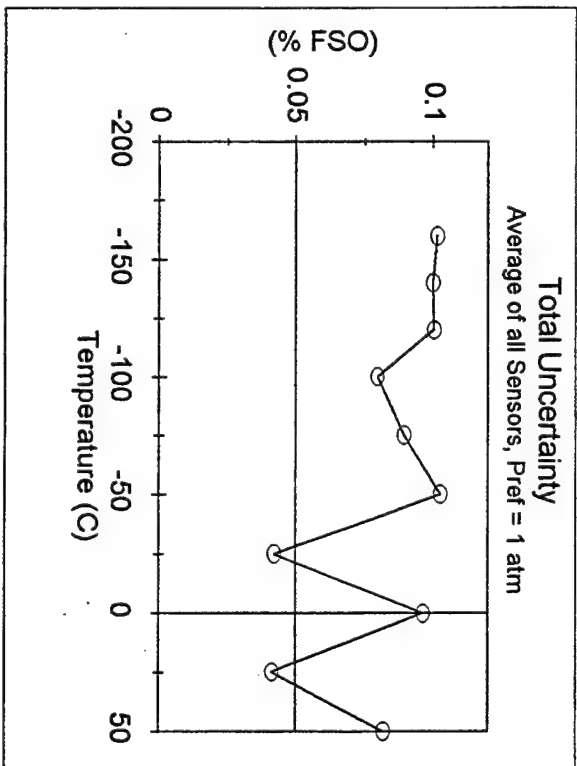


Figure 10

USING OF OSCILLATORY CONNING EXPERIMENTAL RIG FOR SEPARATION OF ROTARY AND UNSTEADY AERODYNAMIC DERIVATIVES

A. Khrabrov, K. Kolinko, O. Miatov, J. Vinogradov, A. Zhuk
Central aerohydrodynamics institute (TsAGI), Russia

Abstract

The TsAGI's oscillatory conning experimental rig is presented in the paper. The model motion kinematics is considered. The test procedure and data processing technique are described. The unsteady aerodynamic characteristics experimental results for 70 degree delta wing at high angles of attack are presented. The experimental technique to obtain the pure unsteady aerodynamic derivatives (derivatives with respect to $\dot{\alpha}$ and $\dot{\beta}$) with the use of this rig is considered. The results of small amplitude forced oscillations and oscillatory conning are compared.

1 Introduction

In the problems of flight dynamics the mathematical models of aerodynamics are developed with the use of experimental data obtained in wind tunnels in various static and dynamic tests. Various dynamic experimental rigs are used to investigate aerodynamic responses for different types of aircraft motion.

The following types of dynamic rigs are widely used:

- Experimental rigs of forced or free oscillations type. During the experiment in wind tunnel flow $\alpha, \beta, p, q, r = \text{var}, \Omega = 0$.
- Rotary balance experimental rigs. During the experiment $\alpha, \beta, \Omega = \text{const}, \vec{\Omega} \parallel \vec{V}$.

During the experiments at the rigs of the first type the angles of attack and sideslip are varied simultaneously with corresponding angular rates. The mean angular rate is equal to zero. These experimental results are very valuable to investigate stability of aircraft motion.

During the experiments at the rigs of the second type the angles of attack and sideslip are constant as long as corresponding angular rates. These experiments are important to investigate spin regimes of aircraft. It is important also to investigate the unsteady

derivatives in the presence of non zero angular rate. The oscillatory conning experimental rigs [1] enable to investigate unsteady aerodynamic loads during intensive rotation. Such experiments are valuable to investigate stability of spin motion, departure and oscillatory spin conditions.

The traditional approach used in rotary balance testing [2] involves aligning the angular velocity vector $\vec{\Omega}$ of the model with the wind tunnel free stream velocity vector \vec{V}_0 . This type of motion is known as "conning". Since the linear and angular velocity vectors are collinear in this arrangement, the angles of attack and sideslip are constant during the motion. For specified angles of attack and sideslip the aerodynamic forces and moments are determined by the motion non dimensional spin rate $\Omega b/2V$.

If the axis of rotation is intentionally given an angle of inclination relative to the free stream, the possibility exists for obtaining certain types of dynamic aerodynamic data which may prove to be of great value in the analysis of large amplitude high rate motions at high angles of attack.

Usually the forced oscillations rigs are used to investigate aerodynamic responses for perturbed rectilinear motion. Rotary balance experimental rigs are used to investigate the aerodynamic loads during aircraft intensive rotation. The so called oscillatory conning experimental rigs [1, 2] enable to investigate unsteady aerodynamic loads during perturbed rotation. The oscillatory conning experiments can help also to find the pure unsteady aerodynamic derivatives (derivatives with respect to $\dot{\alpha}$ and $\dot{\beta}$). The TsAGI's oscillatory conning experimental rig is presented in the paper. The experimental technique to obtain the pure unsteady aerodynamic derivatives with the use of this rig is described. The experimental results for 70 degree delta wing at high angles of attack are presented.

2 Experimental rig

At TsAGI the oscillatory conning experimental rig was obtained by the modernization of forced oscillations rig. The modernization consists of using chain drive for steady rotation of the sting with the model. The geometrical scheme of the oscillatory conning rig is shown in Fig. 1. With the use of the wind tunnel turn table it is possible to change the angle λ between axis of rotation and wind tunnel free stream velocity. Special unit is used to vary the inclination angle θ between the sting and the longitudinal axis of the model.

The draft of the oscillatory conning experimental rig in the TsAGI's low subsonic T-103 wind tunnel is shown in Fig. 2. In the Fig. 3 the corresponding photograph of the rig with delta wing aerodynamic model in the wind tunnel is shown.

The internal strain gage balance was used during the experimental investigations. Electrical signals from the rotating strain gage balance are transmitted to the stationary part of the rig with the use of current collector (36 channels of mercury slip rings).

3 Motion kinematics

To describe the kinematics of model motion the following systems of coordinate will be used:

- System of coordinate connected with the wind tunnel $0x_0y_0z_0$. Axis $0x_0$ coincides with the direction of free stream wind tunnel velocity as shown in Fig. 4. Vector of free stream velocity has the following components in this coordinate system $\vec{V}_0 = (-V_0, 0, 0)^T$.
- System of coordinate connected with the moving floor of wind tunnel (turn table) $0x_1y_1z_1$. Axis $0x_1$ is directed along the sting of the experimental setup. This coordinate system has turned with respect to the wind tunnel coordinate system $0x_0y_0z_0$ by angle λ around the $0y_0$ axis. Equations of transition from wind tunnel coordinate system to the current one are as follows

$$\begin{pmatrix} x_1 \\ y_1 \\ z_1 \end{pmatrix} = \begin{pmatrix} \cos \lambda & 0 & -\sin \lambda \\ 0 & 1 & 0 \\ \sin \lambda & 0 & \cos \lambda \end{pmatrix} \begin{pmatrix} x_0 \\ y_0 \\ z_0 \end{pmatrix}$$

where the transition matrix can be designated as A_1 .

- System of coordinate connected with the sting of the experimental rig $0x_2y_2z_2$. Axis $0x_2$ is directed along the sting and coincides with the axis $0x_1$.

This coordinate system is rotated with the angular rate Ω around this axis. If the instantaneous angle of rotation is designated by $\psi = \Omega t$ then the transition from previous coordinate system can be expressed as follows

$$\begin{pmatrix} x_2 \\ y_2 \\ z_2 \end{pmatrix} = \begin{pmatrix} 1 & 0 & 0 \\ 0 & \cos \psi & \sin \psi \\ 0 & -\sin \psi & \cos \psi \end{pmatrix} \begin{pmatrix} x_1 \\ y_1 \\ z_1 \end{pmatrix}$$

Where A_2 is the corresponding transition matrix. Vector of the model angular rate has the following representation in the current coordinate system $\vec{\Omega} = (\Omega, 0, 0)^T$.

- Body fixed coordinate system of the model $0x_3y_3z_3$. This coordinate system can be obtained by the rotation of previous coordinate system in the model hinge by the angle θ around the axis $0y_2$. The equations of transition has the following appearance

$$\begin{pmatrix} x_3 \\ y_3 \\ z_3 \end{pmatrix} = \begin{pmatrix} \cos \theta & 0 & \sin \theta \\ 0 & 1 & 0 \\ \sin \theta & 0 & \cos \theta \end{pmatrix} \begin{pmatrix} x_2 \\ y_2 \\ z_2 \end{pmatrix}$$

where the transition matrix can be designated as A_3 .

With account of the all transition matrices the components of wind tunnel free stream velocity in body fixed coordinate system can be obtained as follows

$$\begin{pmatrix} V_x \\ V_y \\ V_z \end{pmatrix} = A_3 A_2 A_1 \begin{pmatrix} -V_0 \\ 0 \\ 0 \end{pmatrix}$$

After some calculations one can have

$$\begin{aligned} V_x &= -V_0(\cos \lambda \cos \theta - \sin \lambda \cos \psi \sin \theta) \\ V_y &= -V_0 \sin \lambda \sin \psi \\ V_z &= -V_0(\cos \lambda \sin \theta + \sin \lambda \cos \psi \cos \theta) \end{aligned} \quad (1)$$

Taking into account kinematical relations for angles of attack and sideslip

$$\begin{aligned} \tan \alpha &= \frac{V_z}{V_x} \\ \sin \beta &= -\frac{V_y}{V_0} \end{aligned}$$

one can get the following expressions of instantaneous model incidence and sideslip

$$\tan \alpha = \frac{\cos \lambda \sin \theta + \sin \lambda \cos \psi \cos \theta}{\cos \lambda \cos \theta - \sin \lambda \cos \psi \sin \theta} \quad (2)$$

$$\sin \beta = \sin \lambda \sin \psi$$

In the above expressions the periodic functions $\sin \psi$ and $\cos \psi$ ($\psi = \Omega t$) are included. Hence the model angles of attack and sideslip are also periodic functions of time.

Geometrical approximation of angles of attack and sideslip during oscillatory conning motion is shown in Fig. 5. The scheme in the upper part of the Fig. 5 shows the α and β excursions during complete revolution $\psi = \Omega t$ for given values of λ and θ . The plots in the lower part of the Figure show corresponding time dependencies.

Model angular rate components in body fixed coordinate system can be expressed as follows

$$\begin{pmatrix} p \\ q \\ r \end{pmatrix} = A_3 \begin{pmatrix} \Omega \\ 0 \\ 0 \end{pmatrix} = \begin{pmatrix} \Omega \cos \theta \\ 0 \\ \Omega \sin \theta \end{pmatrix} \quad (3)$$

In the case of oscillatory conning (rotation around the axis inclined with respect to free stream velocity) rates of angles of attack and sideslip changing can be obtained either with differentiating of expressions (2) or with the use of standard equations for rate of change of α and β

$$\begin{aligned} \dot{\alpha} &= q - (p \cos \alpha + r \sin \alpha) \tan \beta \\ \dot{\beta} &= p \sin \alpha - r \cos \alpha \end{aligned} \quad (4)$$

In the case of steady conning motion ($\lambda = 0$) angles of attack and sideslip are constant and following relationships are valid for $\beta = 0$ case

$$\begin{aligned} r &= p \tan \alpha \\ q &= 0 \\ \dot{\alpha} &= 0 \\ \dot{\beta} &= 0 \end{aligned} \quad (5)$$

Thus with use of expressions (2), (3) and (4) one can find all kinematic parameters of the model motion α , β , p , q , r , $\dot{\alpha}$, $\dot{\beta}$ which are determining for aerodynamics at any time instant $\psi = \Omega t$. In these relations the intrinsic parameters of the experimental rig λ , θ and Ω are included.

4 Data processing technique

During the experiments the model angular positions (λ and ψ) were measured along with five components of the strain gage balance signals and dynamic pressure

of the free stream. Inclination angle θ was registered on a paper since the corresponding sensor is absent.

The signals were sampled at the frequencies depending upon the frequency of model rotation. Usually the sampling frequency was chosen to result in 360 readings for one period of model rotation. Thus for $\Omega = 0.5\text{Hz}$ the sampling frequency was 180 Hz, for $\Omega = 1.5\text{Hz}$ the sampling frequency was 540 Hz. The total number of reading for one run usually was 3600 (10 revolts).

The process of unsteady aerodynamic characteristics development due to the model oscillatory motion is rather complex phenomenon especially when flow separation and vortex breakdown take place. So it is necessary to perform some preliminary analysis of the strain gage balance signals before calculating the aerodynamic coefficients.

So the spectral analysis of the signals during model rotation at wind-off and wind-on conditions was performed. The experimental results for wind-off conditions are presented in Fig. 6. In wind-off conditions the strain gage balance measures mainly the gravitational and centripetal loads. The corresponding results for wind-on conditions are shown in Fig. 7. Both pictures corresponds to the angular rate of rotation $\Omega = 1.5\text{ Hz}$. The strain gage balance signals are measured in kg (forces) and kgm (moments). The registered signals in time domain are shown by the thin solid lines. By the thick solid lines the results after digital filtering [3] with cut-off frequency 5 Hz are shown. It is seen that signals are regular with good repetitions. These data confirm that the cut-off frequency 5 Hz is adequate approximation for strain gage signals processing.

For the wind-off conditions the mathematical model of strain gage balance loads can be described depending on model turning angle ψ and its time derivative ($\sin \psi$ and $\cos \psi$). Then with the use of linear regression technique [4, 5] the corresponding coefficients can be found. After that to obtain the pure aerodynamic loads the gravitational, centripetal and other wind-off constituents should be excluded using the current wind-on readings of the model turning angle ψ .

After the digital filtering the obtained pure aerodynamic signals for 10 period of oscillations (10 revolts) should be averaging in one period to exclude remainder random oscillations.

5 Delta wing model

The special light 70 degree delta wing was manufactured for current tests. The weight of model is about 2.5 kg. This was done to diminish centripetal loads on

the strain gage balance. The geometrical scheme of the wing with main sizes is shown in Fig. 8. The model was made from the plywood of 12 mm thickness. The root chord of the wing is 741mm and the wing span is 540mm. The leading edges of the wing was rounded. The trailing edge was beveled. The bevel angle is equal to 20° .

The strain gage balance can be attached to the model with the use of two types of support. In the first case the tail sting with strain gage balance is fastened directly to the wing. In the second case the special unit with the sector is used to fasten the upper sting to the strain gage balance and the wing. The relative position of the balance and its of conventional center of gravity in both cases is the same. The reference point of center of gravity position is equal to 0.5 of mean aerodynamic chord (2/3 of root chord or 247mm from the wing railing edge). The orifice in the model body upper surface enables to mount the sting at some inclination angle θ with respect to the wing surface. The size of current model orifice enables to vary this angle in the region $\theta = 21^\circ \div 90^\circ$. In Fig. 9 the photograph of the wing with upper sting having inclination angle $\theta = 60^\circ$ is shown.

6 Unsteady aerodynamics experimental results

During oscillatory conning experimental investigations the simultaneous variation of angles of attack and sideslip takes place in the presence of steady rotation. It is very important to take into account these data for development of adequate mathematical model of aerodynamics which should be valid for arbitrary type of aircraft motion.

During the experiment a number of parameters were varied. The mean angle of attack of oscillations α_0 was varied by the inclination of upper sting θ . In the case $\alpha_0 = 0$ the tail sting was used. The amplitude of angle of attack and sideslip variation was varied by the inclination of axis of rotation with respect to the wind tunnel free stream direction (angle λ). The frequency of rotation was varied in magnitude (0.5, 1.0 and 1.5 Hz) and in direction (clockwise and counter-clockwise rotation). The wind tunnel velocity was equal to 40 m/s. Obtained experimental data reveal the considerable dynamic properties of vortex breakdown processes for the delta wing aerodynamics during complex oscillatory conning motion.

The dependencies of aerodynamic coefficients upon angle of attack obtained for $\alpha_0 = 0$ and $\Omega = 1.5\text{Hz}$ are presented in Fig. 10. The steady state dependencies of aerodynamic coefficients for the case $\beta = 0$ are also

shown for comparison by lines with markers. The same dependencies upon angle of sideslip are presented in Fig. 12. Here also the steady state dependencies of aerodynamic coefficients upon sideslip angle obtained for the case $\alpha_0 = 0$ are shown by lines with markers. In these Figures the experimental results for amplitude of oscillations $\lambda = 30^\circ$ and 40° are presented.

It is seen that for unseparated flow regimes the obtained dynamic dependencies are very close to steady state ones. As the amplitude of oscillations is enlarged the nonlinear and dynamic effects are also enlarged. For example it is seen that for amplitude of oscillations $\lambda = 40^\circ$ the vortex flow has no time for full development at high angles of attack. It is very clear from α -dependencies of vertical force coefficient C_Z . Such dynamic effects are revealed in others coefficients too.

The dependencies of aerodynamic coefficients upon angle of attack and sideslip obtained for $\alpha_0 = 30^\circ$ and $\Omega = 1.5\text{Hz}$ are presented in Fig. 11 and Fig. 13. The steady state dependencies of aerodynamic coefficients for the case $\beta = 0$ are shown by lines with markers in the first of above figures. The steady state dependencies of aerodynamic coefficients upon sideslip angle obtained for the case $\alpha_0 = 30^\circ$ are shown by lines with markers in the second figure.

It is seen that the oscillatory conning experiment gives a fair amount of information on unsteady nonlinear aerodynamic characteristics dependencies. The quality of information is rather good. The development of dynamic effects with enlarging of the frequency of rotation is rather predictable. The repetition of all data is also good enough. The obtained experimental data are very regular. The influence of direction of rotation is very explicit. It is interesting to trace the symmetrical properties of longitudinal and lateral aerodynamic coefficients for clockwise and counter-clockwise rotation. For example α -dependencies of longitudinal aerodynamic coefficients (C_Z and C_m) are almost the same for clockwise and counter-clockwise rotation. The corresponding β -dependencies for clockwise and counter-clockwise rotation are symmetrical relatively vertical axis. The α -dependencies of lateral aerodynamic coefficients (C_Y , C_l and C_n) for two different rotation directions are symmetrical relatively horizontal axis. The β -dependencies of lateral coefficients for various directions of rotation can be obtained from each other by two reflections relatively vertical and horizontal axes (central symmetry).

7 Pure unsteady aerodynamic derivatives separation

In linear approximation for $\lambda \ll 1$ disturbances of angles of attack and sideslip are $\Delta\alpha = \lambda \cos \psi$ and $\Delta\beta = \lambda \sin \psi$. Then the corresponding rates of changing are $\dot{\alpha} = -\Omega \lambda \sin \psi$ and $\dot{\beta} = \Omega \lambda \cos \psi$. So $\dot{\beta}$ is changing in phase with $\Delta\alpha$ and $\dot{\alpha}$ is changing in phase with $\Delta\beta$. The expressions of aerodynamic loads during these experiments in linear approximation can be presented as follows

$$C_i = C_{i_0}(\alpha, \Omega) + \tilde{C}_{i_\alpha} \Delta\alpha + \tilde{C}_{i_\beta} \Delta\beta$$

where $i = Y, Z, l, m$ or n and

$$\begin{aligned} \tilde{C}_{i_\alpha} &= C_{i_\alpha} + C_{i_\beta} \Omega \\ \tilde{C}_{i_\beta} &= C_{i_\beta} - C_{i_\alpha} \Omega \end{aligned}$$

Coefficients \tilde{C}_{i_α} and \tilde{C}_{i_β} can be found with the use of linear regression technique during experimental data processing. If the experiments can be repeated for clockwise and counter-clockwise model rotation then the unsteady aerodynamic derivatives can be found with the use of following relations

$$\begin{aligned} C_{i_\alpha} &= -\frac{\tilde{C}_{i_\beta}^+ - \tilde{C}_{i_\beta}^-}{\Omega^+ + \Omega^-} \\ C_{i_\beta} &= \frac{\tilde{C}_{i_\alpha}^+ - \tilde{C}_{i_\alpha}^-}{\Omega^+ + \Omega^-} \end{aligned}$$

Here $\Omega = \Omega^+$ is the angular rate for clockwise rotation and $\Omega = -\Omega^-$ for counter-clockwise rotation.

In Fig. 14 the complex $C_{m_\alpha} + C_{m_\beta}$ obtained during pitch forced oscillations experiments with various frequencies is shown. In Fig. 16 the complex $C_{l_p} + C_{l_\beta} \sin \alpha$ obtained during roll forced oscillations is presented. Dimensionless frequencies of oscillations is designated as $\bar{\omega}$.

During oscillatory conning experiments with various mean angles of attack and various angular rates for clockwise and counter-clockwise rotation the following unsteady aerodynamic derivatives C_{m_α} (Fig. 15) and C_{l_β} (Fig. 17) were obtained for inclination angle $\lambda = 5^\circ$. Here $\bar{\omega}$ is the dimensionless angular rate.

It is seen that considerable nonlinearities and dependencies of rotary and unsteady aerodynamic derivatives complexes upon the frequencies of oscillations is mainly due to unsteady derivatives constituents. Thus the oscillatory conning rig can be used for estimation of various aerodynamic models pure unsteady derivatives.

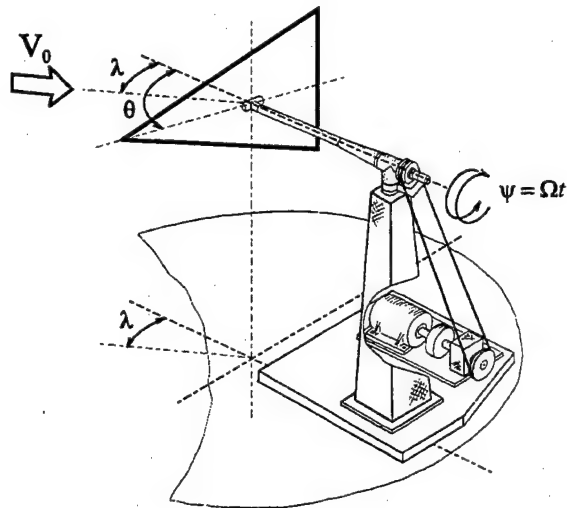


Figure 1: Geometrical scheme of oscillatory conning rig

References

- [1] D. Tristan, O. Renier. *Recents developments des techniques de simulation dynamique appliquees a l'identification des parametres de stabilite*, AGARD - CP -386, Paper 22, 1985.
- [2] *Rotary - Balance testing for aircraft dynamics*, AGARD Advisory Report No. 265, pp. 69 - 76, 1990.
- [3] A. Khrabrov, A. Zhuk *Using of large amplitude free oscillations in pitch and roll to investigate unsteady aerodynamic characteristics at separated flow regimes*, ICIASF'95 Records, pp. 24.1-24.7, July 1995.
- [4] Affi A.A., Azen S.P., *Statistical Analysis. A computer oriented Approach*, Academic press, 1979.
- [5] S. Kabin, K. Kolinko, A. Khrabrov, P. Nush-taev *Dynamic test rig and test technique for the aircraft models unsteady aerodynamic characteristics measurements in high subsonic and transonic wind tunnels*, ICIASF'95 Records, pp. 26.1-26.7, July 1995.

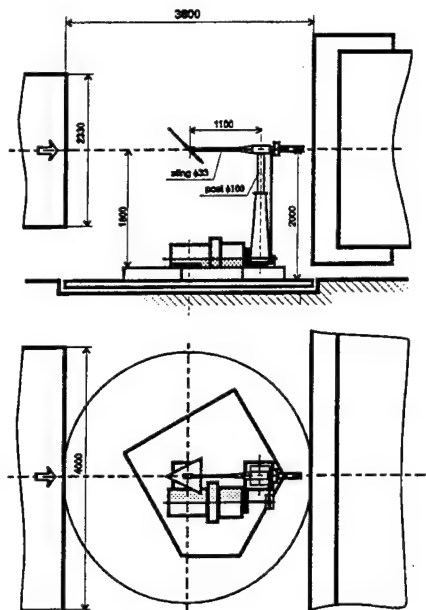


Figure 2: General view of oscillatory conning rig in T-103 wind tunnel

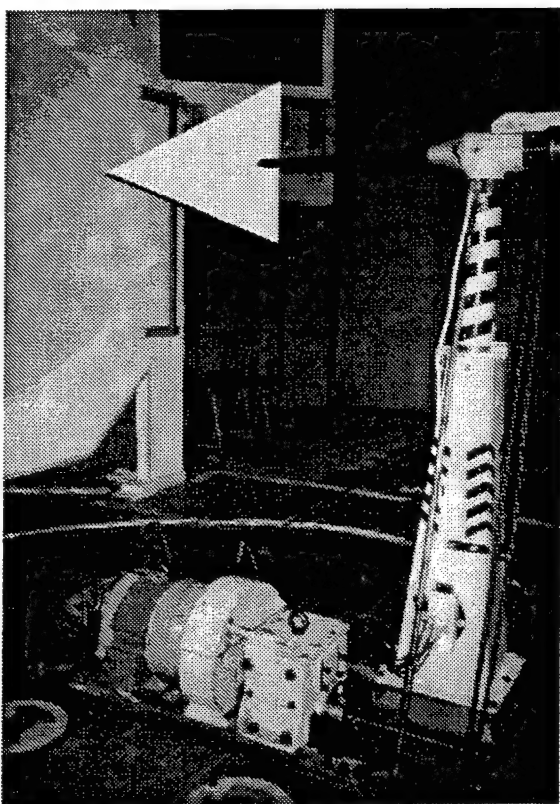


Figure 3: Oscillatory conning rig in T-103 wind tunnel(side view)

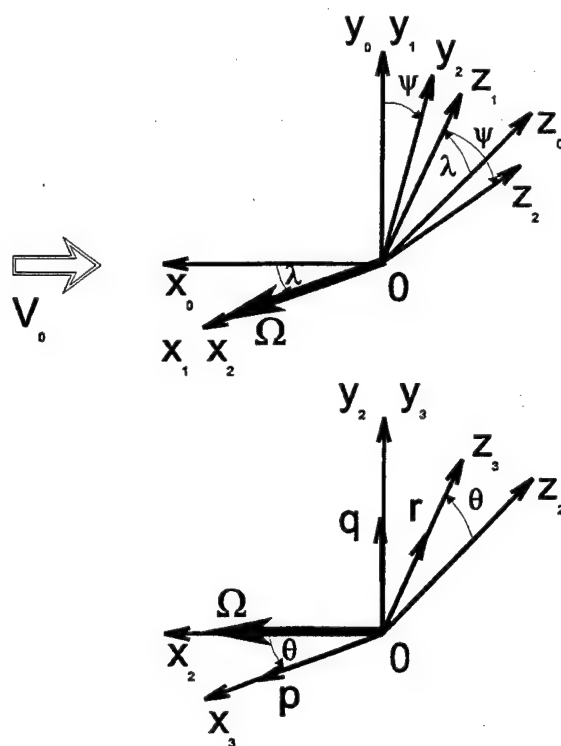


Figure 4: Axes of coordinate used in model motion kinematics consideration

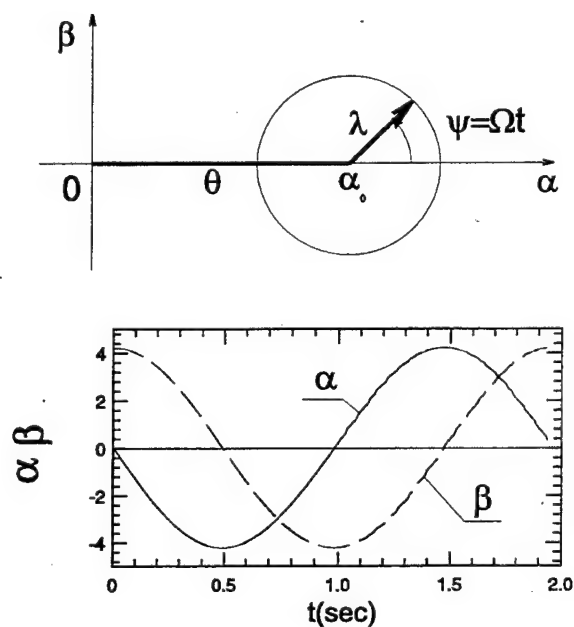


Figure 5: Geometrical representation of model motion kinematics

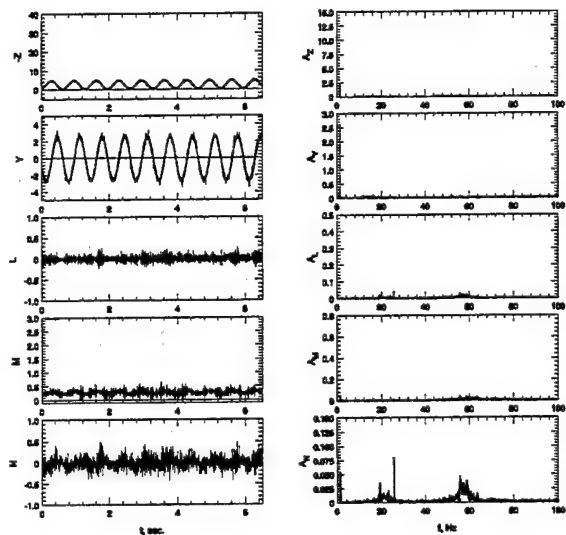


Figure 6: Time dependencies and corresponding spectral analysis of experimental signals for $\theta = 30^\circ$ at $V=0$ m/s

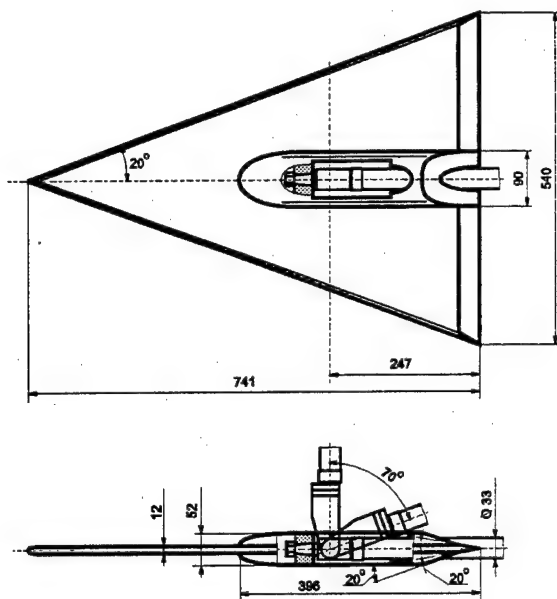


Figure 8: Geometrical scheme of delta wing model

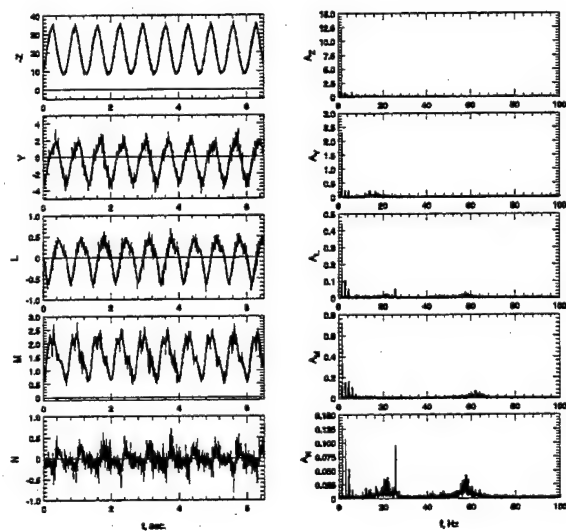


Figure 7: Time dependencies and corresponding spectral analysis of experimental signals for $\theta = 30^\circ$ at $V=40$ m/s

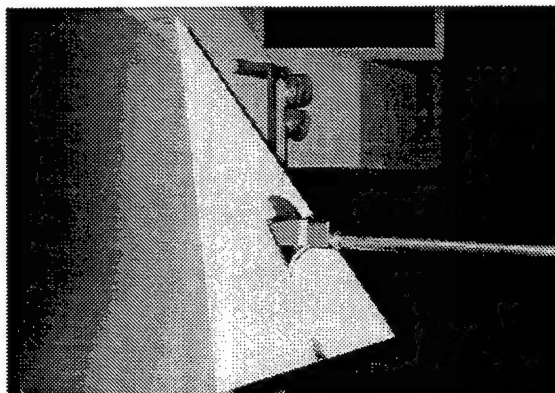


Figure 9: Delta wing model on upper sting $\theta = 60^\circ$

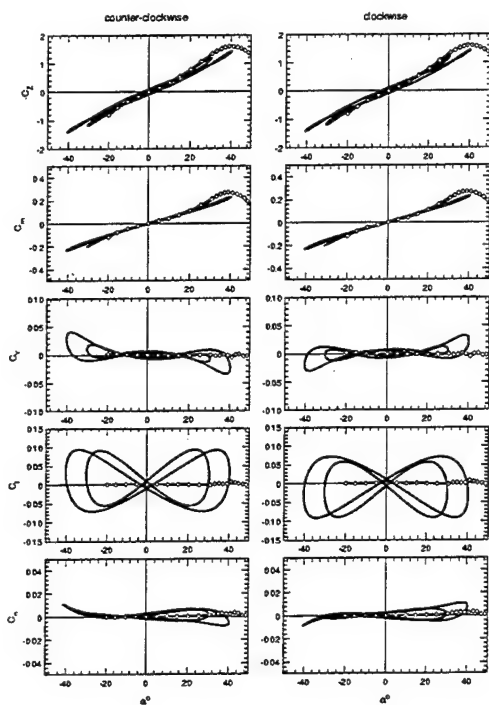


Figure 10: Experimental results for $\alpha_0 = 0^\circ$, $\Omega = 1.5\text{Hz}$

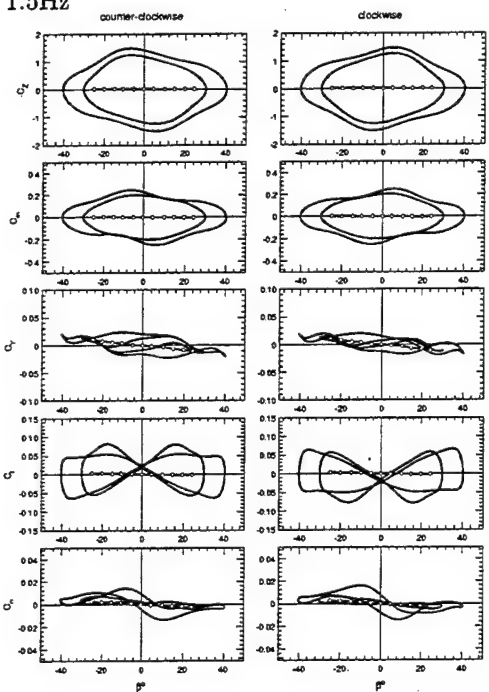


Figure 12: Experimental results for $\alpha_0 = 0^\circ$, $\Omega = 1.5\text{Hz}$

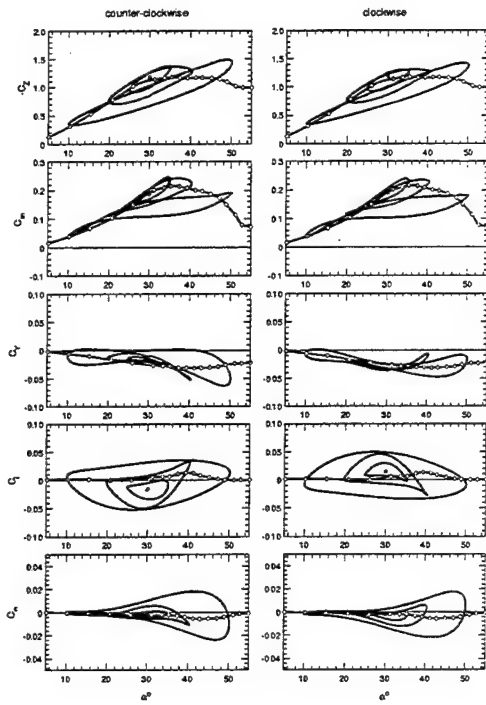


Figure 11: Experimental results for $\alpha_0 = 30^\circ$, $\Omega = 1.5\text{Hz}$

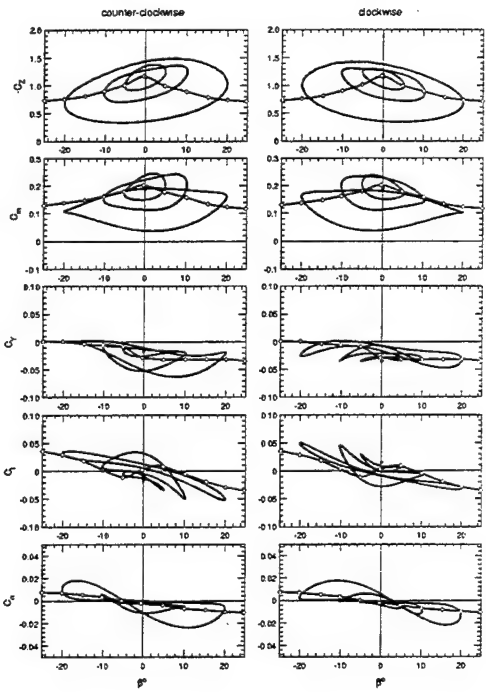


Figure 13: Experimental results for $\alpha_0 = 30^\circ$, $\Omega = 1.5\text{Hz}$

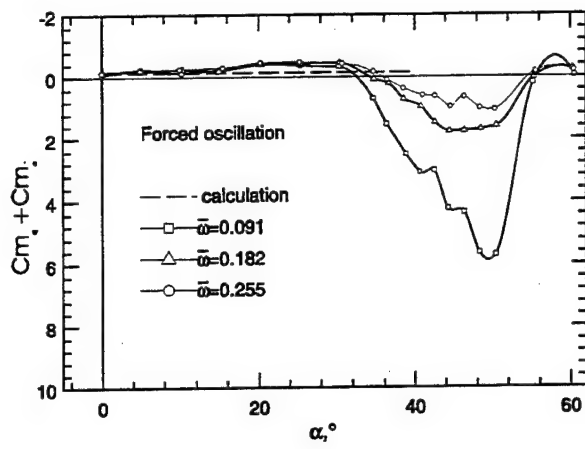


Figure 14: Longitudinal complex $C_{m_q} + C_{m_{\dot{\alpha}}}$

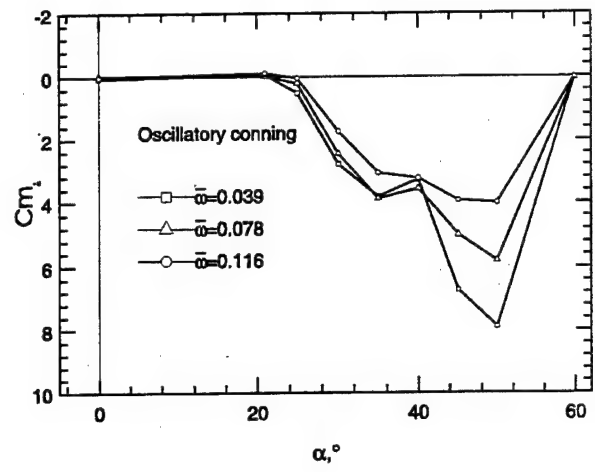


Figure 15: Unsteady derivative $C_{m_{\dot{\alpha}}}$

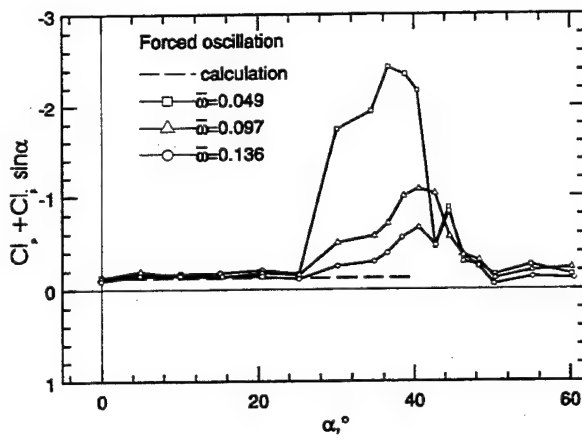


Figure 16: Lateral complex $C_{l_p} + C_{l_{\dot{\beta}}} \sin \alpha$

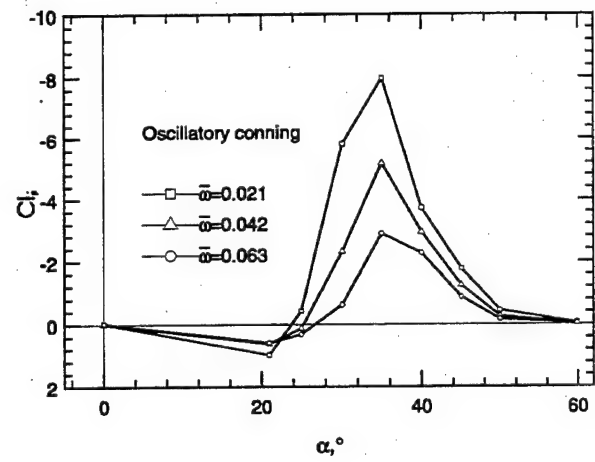


Figure 17: Unsteady derivative $C_{l_{\dot{\beta}}}$

DETERMINING THE TRANSFER FUNCTION FOR UNSTEADY PRESSURE MEASUREMENTS USING A METHOD OF CHARACTERISTICS SOLUTION*

Donald D. McBride and John F. Henfling, Sandia National Laboratories
and
Edward L. Clark, Consultant

ABSTRACT

An inverse Fourier transform method for removing lag from pressure measurements has been used by various researchers, given an experimentally derived transfer function to characterize the pressure plumbing. This paper presents a Method of Characteristics (MOC) solution technique for predicting the transfer function and thus easily determining its sensitivity to various plumbing parameters. The MOC solution has been used in the pipeline industry for some time for application to transient flow in pipelines, but it also lends itself well to this application. For highly nonsteady pressures frequency-dependent friction can cause significant distortion of the traveling waves. This is accounted for in the formulation. A simple bench experiment and proof-of-principle test provide evidence to establish the range of validity of the method.

INTRODUCTION

When possible, measurement of unsteady pressures is best accomplished with in-situ, high-frequency response, flush-diaphragm pressure transducers. However, in many situations, either the geometry of the experiment or the medium in which the experiment is conducted may preclude such an optimum solution^{1,2}. In the experiment which engendered the development of the method which this paper describes, both of these constraints were active. The differential pressures were being measured across thin, ribbon-like structures that had no space for in-situ transducers, and the experiment was conducted in a water tow tank. Were thin, surface-mounted transducers to have been used, it would have been necessary to coat them to protect them from the water. For the very low pressures being measured (~ 0.20 psi full-scale), the errors associated with the "bridging" of the diaphragm by the coating material would have been significant. Further, the heat transfer characteristics of the water (as compared to air) would have increased the transducers' temperature sensitivity and the subsequent errors associated with that sensitivity. Therefore, since it was necessary to locate the transducers

on the tow tank carriage, long capillary-like tubes were necessary to connect them to the pressure taps on the towed model. To avoid the errors associated with air-water interfaces, the tubes (and variable reluctance transducers) were filled with deaerated water and purged of any entrapped air bubbles. It should be admitted that prior to the test, the first author (who had spent his entire professional life working with air as a test medium) had naively assumed that measurement lag would not be a problem due both to water's "incompressibility" and to the very high acoustic speed in water coupled with the very low velocities (~ 4 ft/s) expected in the tow tank experiment. Subsequent examination of the test data proved this assumption not only wrong but *dreadfully* wrong. In a flurry of Monday-morning quarterbacking, it was found that the acoustic speed of water is significantly reduced (from ~ 4915 ft/s to ~ 200 ft/s) in the plastic tubing used for a majority of the capillary. Further, the high-sensitivity variable reluctance transducers required significant diaphragm movement as a function of pressure and, therefore, a significant flow of water to effect such movement. The very small diameter of the tubing coupled with its long length introduced large amounts of frictional resistance to that flow.

A method of characteristics (MOC) solution, outlined in *Fluid Transients in Systems*, a textbook³ on transient flow analysis, was adapted to the transducer plumbing system to derive the response at the transducer to an input signal at the measurement orifice. It was found that when a signal proportional to the dynamic pressure (obtained from the measured carriage velocity which experienced no lag) was input to the MOC method, the resulting response was in every way similar to the actual pressure traces obtained during the test. Concurrent with this observation exposure to a paper by Sims-Williams and Dominy⁴ suggested the possibility of deriving an inverse function that could be used to reconstruct the pressure at the orifice, given the measured pressure and the MOC-derived transfer function associated with the pressure tubing. They had used a method first described by Irwin, Cooper, and Girard⁵, in which an experimentally obtained transfer function was

* Sandia National Laboratories is a multiprogram laboratory operated by Sandia Corporation, a Lockheed Martin Company, for the United States Department of Energy under Contract DE-AC04-94AL85000.

used to correct signal distortion caused by pressure tubing. Another method used to correct the distortion effects of tubing systems on pressure measurements relies on an experimental determination of the transfer function to establish a natural frequency and damping ratio for use in a second-order linear filter approximation to the system response⁶.

This paper describes the application of the MOC solution to obtain the necessary transfer function and an experiment that was used to validate the method. The formulation accounts for the strong effects of elasticity of the tubing walls on the acoustic speed in water. *It must be emphasized that we do not claim the development of this methodology — merely the application of it to the pressure lag problem endemic to instrumentation in aerospace simulation facilities and particularly acute in water facilities.*

NOMENCLATURE

a	acoustic speed
A	internal cross-sectional area of tube
B	tubing characteristic impedance
C^+	refers to conditions along + characteristic line — i.e., $a = +dx/dt$
C^-	refers to conditions along — characteristic line — i.e., $a = -dx/dt$
D	inside diameter of tube
e	tubing wall thickness
E	modulus of elasticity of tube wall material
f	Darcy-Weisbach friction factor
K	bulk compression modulus of fluid medium
p	pressure
p^+	pressure immediately downstream of node point
p^-	pressure immediately upstream of node point
p_f	frictional pressure drop per unit length
Δp_i	pressure drop across node point i
Q	volumetric flow rate
R	tubing resistance coefficient
Re	Reynolds number
t	time
u	velocity
V	volume of transducer at pressure, p
W	weighting function
x	distance along tubing
η	Poisson's ratio for tube wall material
λ_1, λ_2	multipliers
ν	kinematic viscosity
ξ	non-dimensional time
ρ	density

Subscripts

i	index on location <i>along</i> tubing
-----	---------------------------------------

j	index on time
P	point at which velocity and pressure are being calculated
A	point upstream of P along + characteristic (see calculation grid)
B	point downstream of P along — characteristic (see calculation grid)

METHOD OF CHARACTERISTICS FORMULATION

In a pressure tubing system the flow can be reasonably assumed to be not only laminar but also basically one-dimensional in character. In the Method of Characteristics formulation, simplifying assumptions are made that transform the partial differential equations governing this flow into total differential equations. These equations may be integrated to yield finite difference algebraic equations which are then solved numerically.

For the pressure tubing system used in this analysis, the flow is governed by the continuity and momentum equations written in terms of two dependent variables, velocity and pressure, and two independent variables, distance along the tubing and time. Following the derivation outlined by Zielke⁷:

Continuity Equation

The continuity equation for one-dimensional unsteady flow may be written³

$$\frac{\partial u}{\partial x} + \frac{u}{\rho a^2} \frac{\partial p}{\partial x} + \frac{1}{\rho a^2} \frac{\partial p}{\partial t} = 0, \quad (1)$$

but for $(u/a^2) \ll 1$, the equation reduces to

$$\rho a^2 \frac{\partial u}{\partial x} + \frac{\partial p}{\partial t} = 0. \quad (2)$$

Momentum Equation

The one-dimensional, unsteady momentum equation can be written³

$$\frac{\partial p}{\partial x} + \rho u \frac{\partial u}{\partial x} + \rho \frac{\partial u}{\partial t} + p_f = 0, \quad (3)$$

in which p_f is the pressure drop per unit length due to fluid friction. The inertial term, $\rho u(\partial u/\partial x)$, can be considered negligible for the low-speed flows and the closed tubing system with which we are working, so we are left with

$$\frac{\partial p}{\partial x} + \rho \frac{\partial u}{\partial t} + p_f = 0. \quad (4)$$

Characteristics Equations

We can now form two new equations from Equations (2) and (4) by linearly combining them using multipliers, λ_1 and λ_2 .

$$\frac{\partial p}{\partial x} + \rho \frac{\partial u}{\partial t} + p_f + \lambda_1 \left[\rho a^2 \frac{\partial u}{\partial x} + \frac{\partial p}{\partial t} \right] = 0 \quad (5)$$

$$\frac{\partial p}{\partial x} + \rho \frac{\partial u}{\partial t} + p_f + \lambda_2 \left[\rho a^2 \frac{\partial u}{\partial x} + \frac{\partial p}{\partial t} \right] = 0 \quad (6)$$

Now by setting $\lambda_1 = 1/a$ and $\lambda_2 = -1/a$ and rearranging,

$$\left[a \frac{\partial p}{\partial x} + \frac{\partial p}{\partial t} \right] + \rho a \left[a \frac{\partial u}{\partial x} + \frac{\partial u}{\partial t} \right] + a p_f = 0 \quad (7)$$

$$\left[-a \frac{\partial p}{\partial x} + \frac{\partial p}{\partial t} \right] + \rho a \left[-a \frac{\partial u}{\partial x} + \frac{\partial u}{\partial t} \right] - a p_f = 0. \quad (8)$$

By setting $a = dx/dt$ and $-dx/dt$ in Equations (7) and (8), respectively, we obtain the following two pairs of equations which we have identified as the C^+ and C^- equations. The partial differential equations have been converted to total differential Equations (9) and (11), each of which is valid and can be integrated only along its appropriate characteristic line, Equation (10) or (12).

$$C^+: \begin{cases} \frac{dp}{dt} + \rho a \frac{du}{dt} + a p_f = 0 & (9) \\ \frac{dx}{dt} = +a & (10) \end{cases}$$

$$C^-: \begin{cases} \frac{dp}{dt} - \rho a \frac{du}{dt} - a p_f = 0 & (11) \\ \frac{dx}{dt} = -a & (12) \end{cases}$$

Finite Difference Formulation

We divide the pressure tubing into an even number of reaches N , separated by $N-1$ node points. The length of all reaches should be set such that the transit time of an acoustic wave over any reach is equal. The acoustic speed in a fluid contained in elastic tubing anchored at its upstream end is given by Wylie³:

$$a = \sqrt{\frac{K/\rho}{1 + [(K/E)(D/e)]c_1}}, \quad (13)$$

where for thick-walled ($D/e < 25$) tubing,

$$c_1 = \frac{2e}{D}(1+\eta) + \frac{D}{D+e}(1-\eta/2). \quad (14)$$

Figure 1 shows a typical grid for solving the pressure tubing problem.

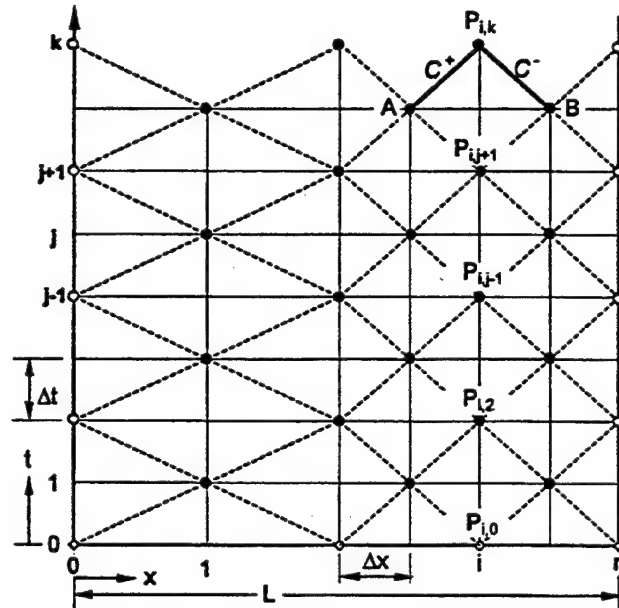


Figure 1. Characteristics grid

The characteristic equations are integrated along the appropriate characteristic lines, C^+ and C^- , to give the algebraic finite difference equations. Thus, the two dependent variables, u and p , are solved for at Point P using the two equations relating conditions at Point P to known conditions at points A and B . It should be noted that at this point, the pressure has been defined to have two possible values at any computation point, depending upon whether the point was approached from upstream along the C^+ characteristic (in which case it carries a - superscript) or from downstream along the C^- characteristic (in which case it carries a + superscript). An additional equation is added at each point to define the pressure drop across the point. This allows introduction of known pressure losses, Δp_P , associated with sudden expansions, contractions, orifices, etc. By introducing the tubing cross-sectional area, A , and writing the equations in terms of flow rate, Q , instead of velocity to assure conservation of mass at discontinuities in tubing size, we obtain the following difference equations:

$$p_P^- - p_A^+ + \frac{\rho a}{A}(Q_P - Q_A) + a\Delta t p_{fA} = 0 \quad (15)$$

$$p_P^+ - p_B^- - \frac{\rho a}{A}(Q_P - Q_B) - a\Delta t p_{fB} = 0 \quad (16)$$

$$p_P^- - p_P^+ = \Delta p_P \quad (17)$$

If the flow were steady, the pressure loss due to fluid friction would be modeled by the familiar

$$p_{f \text{ steady}} = \frac{f}{DA^2} \frac{\rho Q^2}{2}, \quad (18)$$

and since for laminar flow

$$f = \frac{64}{\text{Re}} = \frac{64A\nu}{QD} \quad (19)$$

$$p_{f \text{ steady}} = \frac{32\rho\nu}{AD^2} Q. \quad (20)$$

However, for the unsteady flow associated with the problem we are modeling, the fluid friction becomes frequency dependent. In such flows the fluid in the center of the tube is dominated by inertial effects, whereas that at the walls responds primarily to viscous forces. The velocity distribution is no longer parabolic, and in the extreme the fluid near the wall may even be moving in the opposite direction from the overall mass average. In 1966 Zielke studied this type of flow as the subject of a Ph.D. thesis working under Professor Wylie. His derivation of the effects of this unsteadiness on the MOC solution is outlined in Reference 7 and is too complex to duplicate here. The results, however, are not extremely complex and simply reduce to splitting the friction pressure loss into two components, steady and unsteady. The steady loss is equal to that given by Equation 20, and the unsteady loss is calculated with a convolution integral that factors in the past history of the flow.

$$p_{f \text{ unsteady}} = \frac{16\rho\nu}{AD^2} \int_0^t \frac{\partial Q}{\partial \tau}(\tau) W(t-\tau) d\tau, \quad (21)$$

where the weighting function is given by

$$W(\xi) = e^{-26.3744\xi} + e^{-70.8493\xi} + e^{-135.0193\xi} + e^{-218.9216\xi} + e^{-322.5544\xi} \quad \xi > 0.02 \quad (22a)$$

$$W(\xi) = 0.282095\xi^{-1/2} - 1.25 + 1.057855\xi^{1/2} + 0.9375\xi + 0.396696\xi^{3/2} - 0.351563\xi^2 \quad \xi < 0.02 \quad (22b)$$

where the dimensionless time, ξ , is defined by

$$\xi = \frac{4\nu t}{D^2}. \quad (23)$$

Algebraic Solution

After starting with known initial conditions at time zero, the solution proceeds by determining p and Q at alternate grid points at time Δt , proceeding to time $2\Delta t$, and solving for the interior intervening grid points from the previously determined p 's and Q 's and the boundary points directly from the known boundary conditions. This is continued until the desired time span has been calculated. Thus, by properly minding one's p 's and Q 's, a complete solution is obtained.

The simultaneous solution for p and Q at any interior point is obtained after defining two new parameters: the tubing's "characteristic impedance," B_i , and its "resistance coefficient," R_i , over reach, i .

$$B_i = \frac{\rho a_i}{A_i} \quad (24)$$

$$R_i = \frac{32\rho\nu a_i \Delta t}{A_i D_i^2} \quad (25)$$

After rearranging Equations 15 and 16, we obtain

$$C^+: \quad p_P^- = C_A - B_{i-1} Q_P \quad (26)$$

$$C^-: \quad p_P^+ = C_B + B_i Q_P, \quad (27)$$

where

$$C_A = p_A^+ + (B_{i-1} - R_{i-1}) Q_A - \frac{R_{i-1}}{2} \sum_{j=1,3,\dots}^{k-1} (Q_{i,k-j+1} - Q_{i,k-j-1}) W(j\Delta t) \quad (28)$$

$$C_B = p_B^- - (B_i - R_i) Q_B + \frac{R_i}{2} \sum_{j=1,3,\dots}^{k-1} (Q_{i,k-j+1} - Q_{i,k-j-1}) W(j\Delta t). \quad (29)$$

Equations 17, 26, and 27 can be solved to give:

$$p_P^- = \frac{C_A B_i + (C_B + \Delta p_P) B_{i-1}}{B_i + B_{i-1}} \quad (30)$$

$$p_P^+ = \frac{(C_A - \Delta p_P) B_i + C_B B_{i-1}}{B_i + B_{i-1}} \quad (31)$$

$$Q_P = \frac{C_A - C_B - \Delta p_P}{B_i + B_{i-1}} \quad (32)$$

Boundary Conditions

To solve the finite difference equations, boundary conditions need to be supplied at both ends of the tubing. For the pressure response problem, the pressure at the upstream boundary simply becomes the orifice pressure as a function of time, whereas the flow rate can be obtained directly from Equation 27. For a system terminating at the pressure transducer – i.e., a gage pressure or absolute pressure transducer – a zero flow rate boundary condition (with corresponding pressure obtained from Equation 26) would be appropriate at the downstream end of the tubing if the transducer diaphragm exhibited negligible movement over the pressure range of interest. However, if the transducer diaphragm deforms noticeably, a relationship between the volumetric displacement caused by this movement and the exhibited pressure must be obtained. A pressure boundary condition is then obtained as a time integral of the volumetric flow rate entering that boundary.

For the tow tank test since differential pressure transducers were used, the entire plumbing system stretched from the orifice supplying pressure to one side of the diaphragm to the orifice supplying pressure to the reference side. The tubing on both sides of the diaphragm were mirror images of each other. It was assumed that the differential pressure was obtained by all of the pressure acting on one orifice while the other was held at zero reference pressure. (This assumption was validated numerically by applying half of the pressure at one end and a negative half at the other end with identical results.) Thus the boundary condition supplying the transfer function was at a node point T in the center of the tubing. At this point Δp_P was obtained by integrating the flow rate at that point, T:

$$\begin{aligned} \Delta p_T &= \left(\frac{dp}{dV} \right) \int_0^t Q_T dt \\ &= \left(\frac{dp}{dV} \right) \sum_{j=1,3,\dots}^k Q_{T,j} (2\Delta t), \end{aligned} \quad (33)$$

where (dp/dV) is the experimentally derived slope of pressure versus transducer volumetric displacement.

CALCULATION OF TRANSFER FUNCTION

The transfer function was calculated by applying a sinusoidal pressure at the upstream end of the tubing; calculating the response, Δp_T , at the transducer, as

outlined above; and determining a least squares fit of the output data (constrained to be a sine wave with frequency equal to the input frequency). The gain and phase at that particular frequency were then determined by the relationship between the input and output sine waves. Figure 2 shows a typical plot of such a calculation.

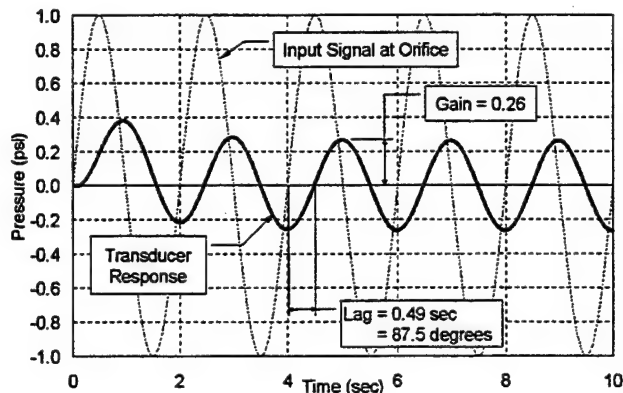


Figure 2. Transducer Response to 0.5 Hz Sine Wave at Orifice

EXPERIMENTAL VALIDATION OF TRANSFER FUNCTION

An experiment was conducted to validate the transfer function calculated by the MOC method (see Figure 3). In this experiment a reference pressure transducer was "short-coupled" to a tank of water whose pressure was also measured by a response transducer coupled to the tank through 6 ft. of 0.038 in. ID x 0.062 in. OD stainless steel tubing connected to 14 ft. of 0.050 in. ID x 0.090 in. OD Tygon tubing. This tubing connection was identical to that used in the calculation (and in the water tow tank experiment mentioned above). The pressure tubing on the reference side of the differential transducer was a mirror image and was connected to a reference tank kept at constant pressure. An audio loudspeaker pressurized the tank with a sinusoidal pressure of known frequency. The amplitude ratio and phase relationship between the response transducer output and the reference transducer output defined the system transfer function as a function of frequency. Figure 4 shows a comparison between the transfer function calculated using the method outlined above with that obtained experimentally. In the MOC calculation, 200 terms (adding more terms does not significantly affect the answer) were included to represent velocity history for determining the unsteady fluid friction term, $\Delta p_{f \text{ unsteady}}$. Error bars represent a two-sigma scatter in the experimental data (most of the error bars cannot be seen in the figure because they are hidden by the size of the data points.)

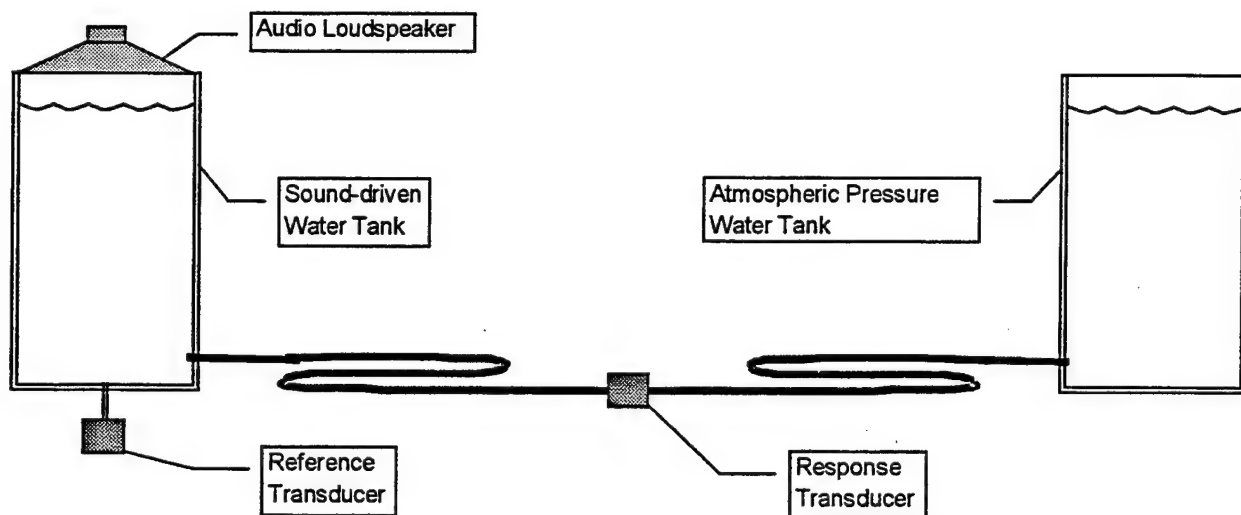
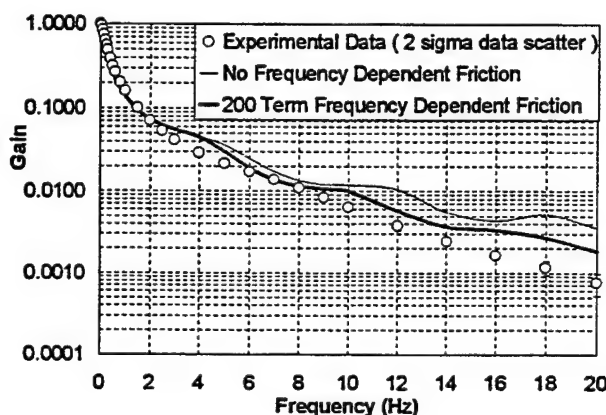
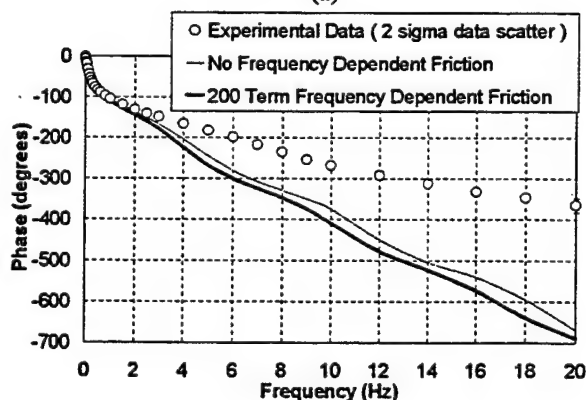


Figure 3. Apparatus for Experimental Validation of MOC-Calculated Transfer Function



(a)



(b)

Figure 4. Comparison of Experimentally Determined System Transfer Function with MOC Calculations

Relatively good agreement is obtained for the gain, whereas poor agreement is shown for the phase for frequencies above ~ 2 Hz. It is assumed that the gain shows better agreement since the factors influencing

pressure drop (tube diameter and laminar friction modeling) were relatively well known, whereas the primary influence on phase – namely the extensibility of the tubing walls – was not. The value used for Young's modulus for the Tygon tubing was obtained from the manufacturer but was certainly open to doubt. In fact, during the experimental phase it was found that the phase repeatability was strongly influenced by the temperature of the Tygon tubing. Fortunately the velocity profile for the tow tank was not dominated by "high" frequencies, so those errors were not critical to the use of the method in this case. Were time correlation of higher frequency data important, it would be required that the phase relationship be better determined. It should also be noted that the actual time lag does not increase with frequency to a large degree, since it is proportional to the phase divided by the frequency.

PROOF OF PRINCIPLE TEST

A second experiment was conducted in which the speaker was removed and the tank was used as a means of applying a time-varying pressure signal that was typical of the signals measured in the water tow tank. Water was poured into the tank, agitated at varying rates, and then evacuated. The pressure signal measured by the response transducer was then corrected using the calculated transfer function, and the result reproduced the signal measured by the reference transducer to a very high degree (see Figure 5). We have included an expanded plot of that comparison for the time span from 12 to 18 seconds when the agitation points out the inadequacy of the phase modeling in recapturing a time-accurate reconstructed pressure. (It should be noted that the phase lag problem was not evident when the experimentally-derived transfer function was used.)

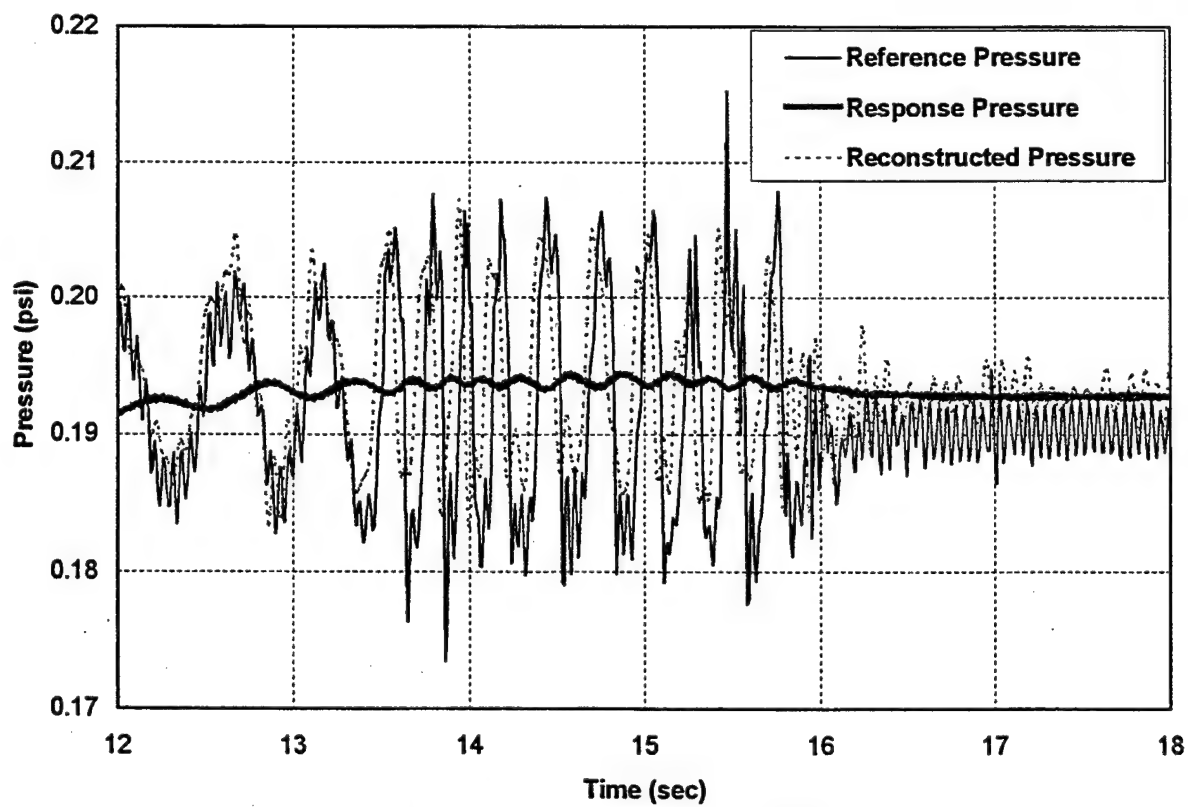
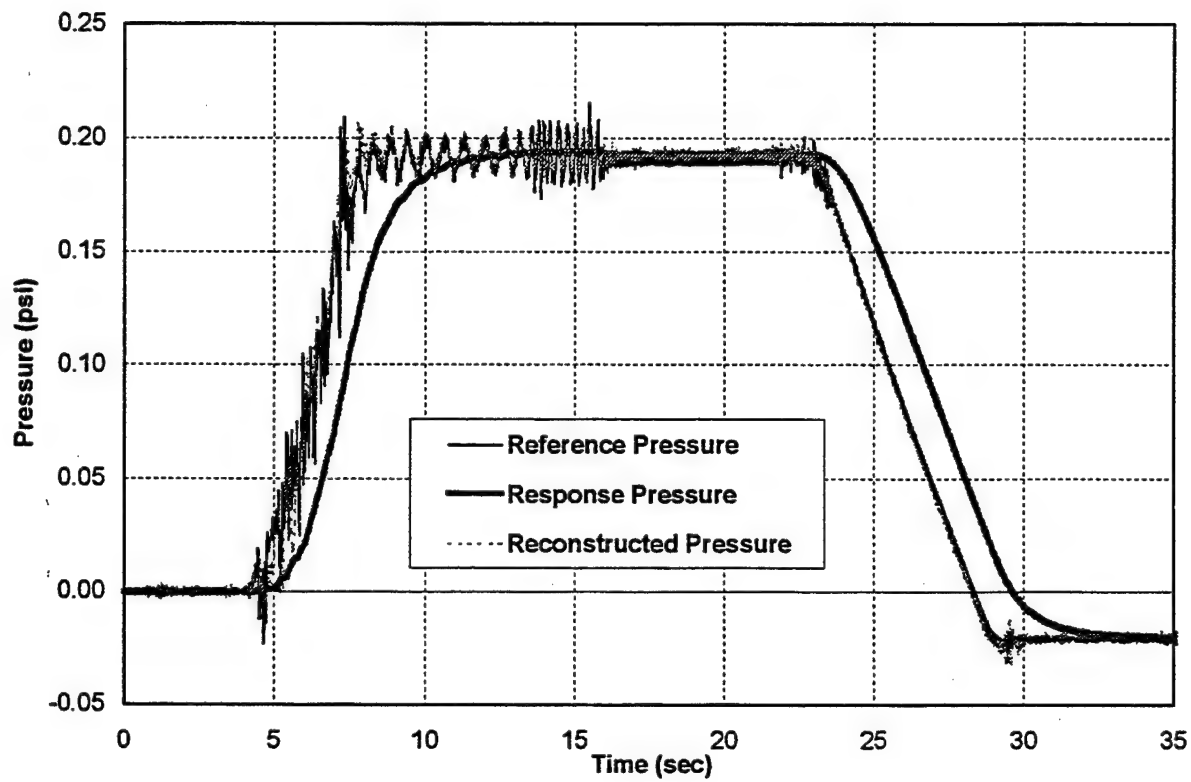


Figure 5. Proof of Principle Pressure Reconstruction

The inability to reconstruct a steady-state pressure of ~0.191 psi (the plot shows a reconstruction of ~0.193 psi) is not due to the reconstruction but rather to the experimental error in measurement – i.e., the response and reference transducers are not expected to agree to a precision greater than ±1%. A complete error analysis can be found in Reference 1.

A bit needs to be said here about the method used for correcting the response pressure signal by use of the transfer function. In a manner similar to that outlined in Reference 5, first, we represent the pressure at the upstream end of the tubing, p_{ref} , by a Fourier series,

$$p_{ref}(t) = \sum_{n=-\infty}^{\infty} A_n e^{in\omega t} \quad (34)$$

where A_n are complex Fourier coefficients. Similarly the response pressure, p_{resp} , can be represented as,

$$p_{resp}(t) = \sum_{n=-\infty}^{\infty} B_n e^{in\omega t} \quad (35)$$

The system transfer function relates these two in the following way:

$$B_n = T_n A_n \quad (36)$$

so the desired coefficients A_n can be calculated from

$$A_n = B_n / T_n \quad (37)$$

Finally, the desired corrected (or reconstructed) orifice pressure may be obtained by computing the inverse Fourier transform of $A_n(\omega)$. This is best achieved by the use of Fast Fourier Transform (FFT) techniques which require $(2)^n$ terms, where n is an integer. This was achieved in our case by taking exactly $(2)^n$ points of time data and calculating the FFT of that data to obtain $(2)^n$ B_n 's. We fit cubic splines to both the gain and phase terms of the transform, interpolated to obtain the gain and phase at the required n frequencies, recast them into complex form, performed the term-by-term complex divide and then took the inverse FFT of the result.

However, there was one intervening step that was necessary to obtain meaningful results. Since the gain dropped to such a low value (~0.001 @ 20 Hz), division results in amplification of the noise to the degree that it obscures the real data. As a result, the A_n coefficients of the reconstructed reference pressure Fourier transform were zeroed for frequencies greater than 15 Hz or less than -15 Hz prior to the inverse FFT process.

MOC METHOD APPLICATIONS

A Method of Characteristics solution similar to that used for calculating transient pipe flows has been successfully applied to the pressure tubing response problem. While the application derived here was specifically validated for very low speed flows with water as the pressure conduit medium, the method should be extensible to the wind tunnel problem so long as the assumptions made in simplifications leading to Equations (2) and (4) are not violated. While experimental determination of dp/dV (used in Equation 33) was a simple process with water, it is assumed that a simple equation of state argument could give reasonable values for large volume transducers being used with a medium such as air, which has a much lower bulk modulus than water.

Once derived and programmed, the method can give very accurate sensitivity coefficients for determining the effects of varying certain tubing parameters or installing restrictors in the tubing.

We feel that this general approach could also have applications to other instrumentation lag problems where the reasons for the lag are not only known but can be modeled. Solution of the model simulation (either analytically or numerically) could be used with an inverse Fourier transform technique to resolve at least part of the lag problem.

ACKNOWLEDGEMENTS

The authors would especially like to thank two individuals who were instrumental in the accomplishment of this project. Ron Dykhuizen of Sandia National Laboratories first informed us of the highly dependent nature of acoustic speed in water in a pipe on the elasticity of the pipe walls. Professor Ben Wylie of the University of Michigan, besides teaching a summer course in Transient Flow Analysis in which the first author originally became aware of using the method of characteristics for such analysis, further assisted him with proper application of the boundary conditions necessary for the transducer when used interior to the tubing.

REFERENCES

- ¹ McBride, D. D., Henfling, J. F., and Clark, E. L., "Pressure Data for the Experimental Validation of a Vortex-Based Parachute Inflation Code," AIAA Paper 99-1747, 15th CEAS/AIAA Aerodynamic Decelerator Systems Technology Conference and Seminar, Toulouse, France, June, 1999.
- ² Clark, E. L., "Pressure Measurements in High Speed Water Tunnels," *Instrument Society of America 38th International Instrumentation Symposium*, Las Vegas, NV, April, 1992.
- ³ Wylie, E. B., and Streeter, V. L., *Fluid Transients in Systems*, Prentice-Hall, New Jersey, 1993, pp. 37-79.
- ⁴ Sims-Williams, D. B. and Dominy, R. G., "Experimental Investigation in Unsteadiness and Instability in Passenger Car Aerodynamics," SAE Paper 980391, Detroit, MI, 1998.
- ⁵ Irwin, H. P. A. H., Cooper, K. R., and Girard, R., "Correction of Distortion Effects Caused by Tubing Systems in Measurements of Fluctuating Pressures," *Journal of Industrial Aerodynamics*, Vol. 5, 1979, pp. 93-107.
- ⁶ Whitmore, S. A., Lindsey, W. T., Curry, R. E., and Gilyard, G. B., *Experimental Characterization of the Effects of Pneumatic Tubing on Unsteady Pressure Measurements*, NASA TM-4171, 1990.
- ⁷ Zielke, W., "Frequency-Dependent Friction in Transient Pipe Flow," *Journal of Basic Engineering, Transactions of the ASME*, Series D, Vol. 90, No. 1, March, 1968, pp. 109-115.

A RE-EVALUATION OF A PULSED LASER TECHNIQUE FOR MEASURING SURFACE HEAT TRANSFER COEFFICIENTS

W.E. Carscallen

W.O. Turnbull

Institute for Aerospace Research, National Research Council Canada
1500 Montreal Road, Ottawa, Ont., K1A 0R6

ABSTRACT

Data from a previously reported experimental technique, for measuring wall shear stress using a pulsed laser, is re-evaluated using a new numerically based data reduction technique in order to determine surface heat transfer coefficients. This new technique was suggested by recent experimental studies into the use of uncalibrated liquid crystals and periodic heat fluxes to measure absolute values of the local heat transfer coefficient and wall shear stress. These studies, which were initially based upon a one-dimensional analytical conduction model, demonstrated that the shape of the temperature-time response, to an instantaneous deposition of energy on a surface, is a function of the thermophysical properties of the surface and the value of the local heat transfer coefficient. In order to account for situations where two-dimensional effects are important a new numerical model has been developed. It is possible, using this new model, to extend the previous phase delay technique to measure heat transfer coefficients to the case whereby a pulsed laser is used to initiate a temperature transient. The new results using the old data show reasonable agreement with those predicted by a standard correlation. Suggestions are made on how the technique can be significantly improved.

NOMENCLATURE

a, b, c	Euler coefficients
c	surface layer specific heat capacity, $\text{J kg}^{-1} \text{K}^{-1}$
h	local heat transfer coefficient, $\text{W m}^{-2} \text{K}^{-1}$
k	thermal conductivity, $\text{W m}^{-1} \text{K}^{-1}$
Q, q	local heat flux, W m^{-2}
T	measurement period, s
t	surface layer thickness, m
α	substrate thermal diffusivity, $\text{m}^2 \text{s}^{-1}$
$\varepsilon = \rho c t$	surface layer thermal capacity
ρ	surface layer density, kg m^{-3}
θ	surface temperature, above ambient, $^{\circ}\text{C}$
ϕ	phase delay angle, radians
τ	time, s
ω	heat flux angular frequency, Hz
erfc	complimentary error function
FC	Fresnel \cos integral
FS	Fresnel \sin integral

INTRODUCTION

The use of localized non-intrusive surface heating to determine wall shear stress distributions was first proposed by Carscallen [1]. The proposal suggested that an experimentally obtained cooling rate parameter, β , determined from the transient temperature history subsequent to the cessation of irradiation, could be used to ascertain the wall shear stress. In order to achieve this it was first necessary to obtain a correlation between the measurable cooling rate parameter and the local heat transfer coefficient using a transient axi-symmetric conduction model (Oosthuizen and Carscallen, [2]). A second turbulent, thermal three-dimensional boundary layer model was then used to determine a second correlation, that between the local heat transfer coefficient and the local wall shear stress. Combining the results of the two numerical models yielded a correlation between the cooling rate parameter and the local wall shear stress.

Experimentally obtained results, for the case of turbulent flow over a flat plate, were reported by Carscallen, Oosthuizen and Arthur [3]. They concluded that the new method is sufficiently sensitive to allow the changes in wall shear stress that occur in many situations to be determined with adequate accuracy. However, in absolute terms the experimentally measured cooling rate parameter, when plotted as a function of the wall shear stress, was approximately 20% less than that predicted using the numerical model.

In the present re-assessment an attempt is made to determine if it is possible to derive values for surface heat transfer coefficients using a combination of the old temperature data and a new data reduction process. This new procedure was suggested by a recently developed experimental technique (Turnbull and Oosthuizen, [4]) that uses periodic heat fluxes and uncalibrated thermochromic liquid crystals to measure values of the local heat transfer coefficient. The principle underpinning this new method is that a phase delay will develop between the heat flux and the subsequent surface temperature response that is a function of the thermophysical properties of the model and the local heat transfer coefficient. Even though the surface temperature response to a single laser strike is not in itself

periodic, it can be considered so by treating the captured data as a single period "window" in an infinite number of periods.

PREVIOUS STUDY

The temperature data used in the current study was obtained from a previous experiment, [3]. This earlier study attempted to determine local wall shear stress values from the surface temperature response to a high-powered laser strike. The experimental setup consisted of a flat plate mounted on the sidewall of a large low speed wind tunnel, see Fig. 1. Various points on the flat plate could be targeted by the laser through the use of wedge shaped prisms. Thermocouples were used to monitor the surface temperature response as a function of time.

The design of the plate and the flow through the wind tunnel were such that the boundary layer on the plate was turbulent. The flat plate was made from aluminium and was approximately 900mm wide by 1200mm long in the flow direction. A 305mm by 305mm hole was cut in this plate and a target element was mounted in this hole. The target element was composed of a phenolic resin substrate (green glass) with a thin copper sheet bonded to its surface. Thermocouples were mounted at various points on the underside of this copper sheet. The test plate assembly was mounted vertically on four streamlined struts on the wall of the National Research Council of Canada's Propulsion Wind Tunnel (3m by 6m working section). This tunnel is of the open circuit type and draws air directly from the atmosphere. It is fully described by Williamson [5].

The laser used in the earlier study was a Candela SLL-5000 tuneable, coaxial flashlamp pulsed dye laser equipped with a Schotland Triax Dye Cell. It was capable of delivering a 30J output pulse with a duration of $2.5 \mu\text{s}$. The laser beam with an initial diameter of 25mm was focused down to 12.5mm diameter on the target surface located 3.65m away. This focused beam diameter was the minimum diameter achievable with a simple focusing lens. The laser beam was steered to within .025 mm of any selected point on the target surface by two circular wedge prisms. In a given test with known free stream velocity the laser beam was steered to lie symmetrically over a chosen thermocouple junction. The laser was then fired and the temporal variation of the output of the thermocouple was then measured at 20 samples/second for up to 10 seconds after the firing of the laser. Tests were carried out at air velocities from 5 to 35 m/s. Reynolds numbers based on the distance from the leading edge of the plate to the centre of the test element varied between 200,000 to 1,500,000.

CURRENT TECHNIQUE

Background

In an effort to obviate the need to calibrate temperature sensing devices when they are used in the determination of local heat transfer coefficients, such as on turbine blade

models in wind tunnels, a new periodic experimental technique was recently developed by Turnbull and Oosthuizen [4]. The technique was suggested by earlier experiments, undertaken by Turnbull [5], using thermochromic liquid crystals, square wave surface heat fluxes and Fourier analysis, and it is based upon the premise that a phase delay will develop between the fundamental harmonic of the imposed periodic surface heat flux and the fundamental harmonic of the subsequent surface temperature response. This phase delay is a function of the thermophysical properties of the surface and substrate, the local heat transfer coefficient and the heat flux frequency. It was shown that because a phase delay is being used there is no requirement to calibrate the temperature-sensing device. Furthermore, the analytical solution suggests, and the experimental results confirm, that the phase delay is not a function of the magnitude of the local heat flux.

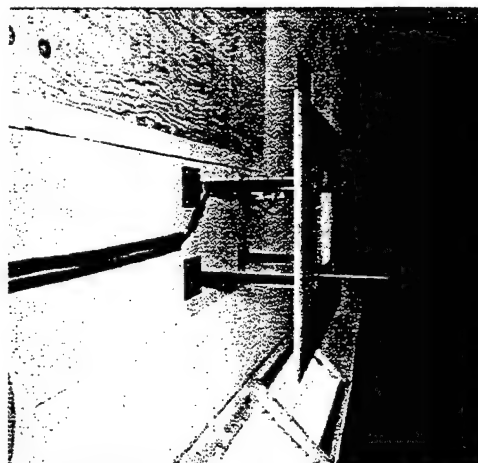


Figure 1. Experimental Set-up: Flat plate model mounted on wind tunnel sidewall

For the case of impulse heating on a one-dimensional surface Turnbull, [6], has shown that the surface temperature response, in absolute terms, is a function of the amount of energy deposited. However, depositing different amounts of energy results in temperature-time plots that have similar *shapes*. Therefore, if a way can be found to relate the shape of the temperature response to the local heat transfer coefficient no correction needs to be made for the energy deposited. Furthermore, the use of shapes also implies that it may be possible to use an uncalibrated temperature sensor, as is the case for a periodic surface flux, and in fact such a relationship can be derived.

Analytical Model

Consider the case of a thermally thin layer attached to a substrate of low thermal conductivity. For the one-dimensional case it can be shown that, see Appendix A, the surface temperature response (above ambient) to an impulse heating function will be given by:

$$\theta(\tau) = C_1 e^{\Phi_1^2 \tau} \operatorname{erfc}(-\Phi_1 \sqrt{\tau}) + C_2 e^{\Phi_2^2 \tau} \operatorname{erfc}(-\Phi_2 \sqrt{\tau}) \quad (1)$$

where

$$C_1 = BQ\Phi_1, \quad C_2 = -BQ\Phi_2, \quad B = 1/\sqrt{k\rho c - 4h\varepsilon},$$

$$\Phi_1 = -k/\varepsilon\sqrt{\alpha} + \frac{1}{2}\sqrt{k^2/\varepsilon^2\alpha - 4h/\varepsilon}, \text{ and}$$

$$\Phi_2 = -k/\varepsilon\sqrt{\alpha} - \frac{1}{2}\sqrt{k^2/\varepsilon^2\alpha - 4h/\varepsilon}.$$

Q is the energy deposited, per unit area, by the heating function, ε the surface layer thermal capacity, k and α the substrate thermal conductivity and diffusivity respectively.

Assume Eq. (1) is a windowed function with period T , such that $\theta(\tau+T) = \theta(\tau)$. (In practical terms T will be the length of the temperature versus time record). The Fourier series expansion of a periodic function, with period T , is given by, assuming Dirichlet's conditions are met,

$$\theta(\tau) = \frac{a_0}{2} + \sum_{n=1}^{\infty} c_n \sin(n\omega\tau + \phi_n) \quad (2)$$

where

$$c_n = \sqrt{a_n^2 + b_n^2}, \quad \phi_n = \arctan\left(-\frac{b_n}{a_n}\right),$$

$$a_n = \frac{2}{T} \int_0^T \theta(\tau) \cos(n\omega\tau) d\tau$$

$$\text{and } b_n = \frac{2}{T} \int_0^T \theta(\tau) \sin(n\omega\tau) d\tau.$$

For the purposes of this derivation we are interested in the phase delay angle of the fundamental harmonic only, i.e.

$$\phi_1 = \tan^{-1}\left(\frac{-b_1}{a_1}\right) = \tan^{-1}\left[-\frac{\int_0^T \theta(\tau) \cos(\omega\tau) d\tau}{\int_0^T \theta(\tau) \sin(\omega\tau) d\tau}\right] \quad (3)$$

where $\theta(\tau)$ is given by Eq. (1). Note that ϕ_1 is not a function of the energy deposited, because the Q term will cancel. It can be shown, Turnbull [8], that the fundamental harmonic phase delay angle, ϕ_1 , evaluates to:

$$\phi_1 = \arctan\left[-\frac{F-G}{H-I}\right] \quad (4)$$

where

$$\begin{aligned} F &= \frac{\Phi_1}{d_1\omega} \left[1 - e^{\Phi_1^2 T} \operatorname{erfc}(-\Phi_1 \sqrt{T}) \right] - \sqrt{\frac{2}{\omega}} \left[\frac{\Phi_1^4}{d_1\omega^2} FS(2) + \frac{\Phi_1^2}{d_1\omega} FC(2) \right] \\ G &= \frac{\Phi_2}{d_2\omega} \left[1 - e^{\Phi_2^2 T} \operatorname{erfc}(-\Phi_2 \sqrt{T}) \right] - \sqrt{\frac{2}{\omega}} \left[\frac{\Phi_2^4}{d_2\omega^2} FS(2) + \frac{\Phi_2^2}{d_2\omega} FC(2) \right] \\ H &= \frac{\Phi_1^3}{d_1\omega^2} \left[e^{\Phi_1^2 T} \operatorname{erfc}(-\Phi_1 \sqrt{T}) - 1 \right] + \sqrt{\frac{2}{\omega}} \left[\frac{\Phi_1^4}{d_1\omega^2} FC(2) - \frac{\Phi_1^2}{d_1\omega} FS(2) \right] \\ I &= \frac{\Phi_2^3}{d_2\omega^2} \left[e^{\Phi_2^2 T} \operatorname{erfc}(-\Phi_2 \sqrt{T}) - 1 \right] + \sqrt{\frac{2}{\omega}} \left[\frac{\Phi_2^4}{d_2\omega^2} FC(2) - \frac{\Phi_2^2}{d_2\omega} FS(2) \right] \end{aligned}$$

$$\text{and } d_x = 1 + \Phi_x^4/\omega^2.$$

FS and FC are the *Fresnel* integrals and *erfc* the complimentary error function,

$$FC(z) = \int_0^z \cos\left(\frac{\pi}{2} t^2\right) dt \quad FS(z) = \int_0^z \sin\left(\frac{\pi}{2} t^2\right) dt$$

$$\operatorname{erfc}(z) = 1 - \frac{2}{\sqrt{\pi}} \int_z^{\infty} e^{-t^2} dt$$

and ω is the pseudo heat flux frequency, based on the measurement period T .

Equation (4) is significant; it implies, for the one-dimensional case, that the phase delay is a function of the thermophysical properties of the model, the local heat transfer coefficient and the pseudo heat flux frequency. It is not a function of the energy deposited. Furthermore, as is the case for the earlier phase delay techniques, there is no requirement for the calibration of the temperature-sensing device.

The pulsed laser technique approximates an axi-symmetric case and may not be well approximated by the one-dimensional model used above. In order to determine if this is the case an axi-symmetric transient model has been developed.

Numerical Models and Results

The axi-symmetric model used during the current investigation is a modified version of that used by Arthur, [7]. The original code was written using a finite difference approach that was implicit in the depth direction (j -coordinate) and explicit in the radial direction (i -coordinate). The resulting nodal equations were solved using a simple tri-diagonal matrix solver (Thomas Algorithm). The thin surface layer was modeled using a single j node, assuming that there would be no temperature gradients through the very thin copper sheet. However, modifications were found to be necessary to account for the presence of thermocouples and their wires. This is primarily due to two reasons. The first is the fact that the thermocouple itself is an integral part of the surface layer at the measurement locations, see [7]. The second

reason centres on the fact the constantin thermocouple wires have a much higher thermal conductivity than the substrate, and thus represent additional paths for conduction away from the surface (stem conduction).

In order to achieve grid and time independent solutions it was necessary to use nodal spacing of 1.5×10^{-4} m in the radial direction, 1.0×10^{-4} m in the axial direction, and time steps of 10^{-6} seconds. A total of 200 nodes are used radially and 150 nodes axially. To model a two-second transient typically requires 30 hours on a PII 450 MHz processor.

Figure 2 compares the numerically computed two-dimensional surface temperature response to that obtained using the one-dimensional analytical model, Eq. (1). In both instances the local heat transfer co-efficient is $90 \text{ W m}^{-2} \text{ K}^{-1}$, the thin surface sheet is assumed to be made of copper and the substrate of phenolic resin (green glass). Clearly, there are considerable differences between the results of the two models. Consequently the use of the one-dimensional analytical model would not appear to be justified.

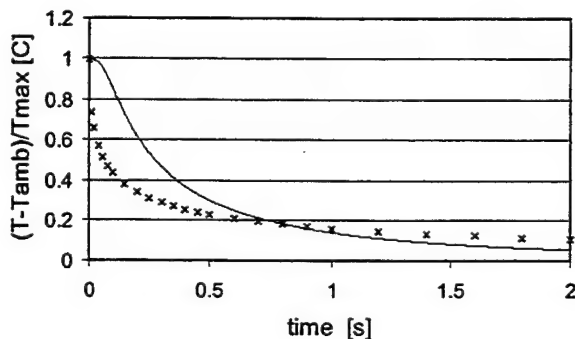


Figure 2. Comparison of temperature predictions from one-dimensional analytical model (x) and axis-symmetric numerical model (-) for the case of $h = 90 \text{ W m}^{-2} \text{ K}^{-1}$.

Although the one-dimensional analytical solution has been shown to be an inaccurate predictor of the axis-symmetric case it is possible, using numerical results, to obtain an explicit relationship between the local heat transfer coefficient and the fundamental harmonic of the predicted surface temperature response. This has been carried out for values of h ranging from 30 to $90 \text{ W m}^{-2} \text{ K}^{-1}$ using the same thermophysical properties as described earlier. Determination of the fundamental phase delay angle of the calculated temperature response is achieved through the application of a Fast Fourier Transform (FFT) to the numerically produced temperature-time data set. This is followed by a linear least squares approximation to the resulting plot of h versus phase delay angle, see Fig. 3. As before, the thin surface sheet is assumed to be made of copper and the substrate of phenolic resin (green glass). Using only the first two seconds of the temperature

response event record the resulting heat transfer coefficient, h , as a function of the fundamental harmonic phase delay angle, can be approximated by

$$h = z_1 \phi_1^3 + z_2 \phi_1^2 + z_3 \phi_1 + z_4 \quad (5)$$

with

$$z_1 = 16592.20979$$

$$z_2 = -13132.42992$$

$$z_3 = -57236.77637$$

$$z_4 = -28860.07150$$

and where ϕ_1 is the fundamental harmonic phase delay angle. The error in h associated with the least squares approximation, Eq. (5), is less than 1% over the range $30 - 90 \text{ W m}^{-2} \text{ K}^{-1}$.

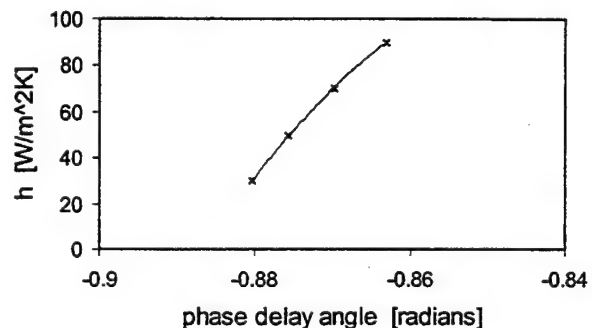


Figure 3. Plot of numerically produced phase delay angles. Also included is a least squares approximation.

Equation (5) is the numerically derived explicit equivalent of the analytically derived implicit relationship represented by Eq. (4). Figure 4 plots heat transfer coefficient as a function of phase delay angle using Eqs. (4) and (5). Again, it can be seen that the two models predict phase angle behaviour that is significantly different.

Equation (4) suggests that the phase delay angle will not be a function of the energy deposited on the surface for the one-dimensional case. This prediction can be shown to apply to the axis-symmetric case, albeit for a limited range of Q . Virtually identical phase delay angles were given by the two-dimensional numerical model for Q values that varied in the range $\pm 10\%$ of those used for Fig. 2. The reason for this limited range was postulated to be because of the presence of the thermocouple. This was confirmed after repeating the previous series of numerical approximations with the thermocouple removed from the model. The resulting dimensionless surface temperature responses were identical, as were the fundamental phase delay angles. This suggests that in order for the proposed

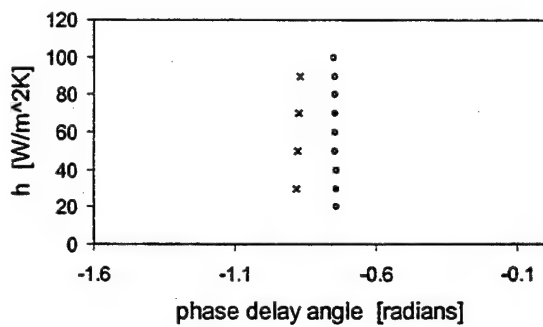


Figure 4. Comparison of phase delay angles predictions from one-dimensional analytical model (x) and axis-symmetric numerical model (o) for the case of copper on green glass. Based on two second event record.

experimental technique to be insensitive to the energy deposited by the heat source the surface temperature sensor should be of the non-intrusive variety, such as IR cameras or thermochromic liquid crystals. This not only simplifies the numerical model but also allows for easier estimation of the surface layer thermal capacity.

A review of Eq. (5) highlights the fact that the fundamental phase delay angle does not appear to be a strong function of the local heat transfer coefficient for the given experimental set-up. The reason for this is apparent in Fig. 5, which plots the dimensionless surface temperature responses for two different surface heat transfer coefficients: $30 \text{ W m}^{-2} \text{ K}^{-1}$ and $90 \text{ W m}^{-2} \text{ K}^{-1}$. (This range was chosen as it brackets the predicted values for turbulent flow over a flat plate that can be expected for the given experimental conditions). Immediately apparent from Fig. 5 is the fact that the change in heat transfer coefficient has had only a small effect upon the surface temperature response. This in turn suggests that convection may not be the dominant mode of heat transfer away from the point where the energy was initially deposited.

There are four possible heat transfer paths from the strike zone, they are as follows: convection to the free stream boundary layer, lateral conduction in the thin copper sheet, conduction into the green glass substrate, and stem conduction through the thermocouple wires. In order to make a quantitative estimate of the magnitude of the energy transferred by the various heat transfer paths the axis-symmetric model was modified to determine these ratios at each of the time steps. The results show that for the initial two-second transient the two dominant heat transfer paths are lateral conduction along the thin surface sheet and convection. Conduction into the substrate and along the wire is insignificant by comparison. This latter result was anticipated; the substrate has a very low thermal conductivity and the wire is very thin.

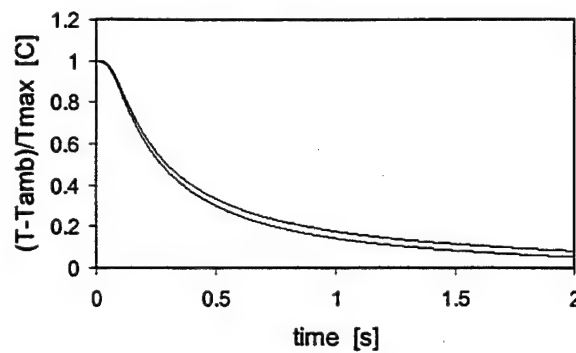


Figure 5. Comparison of predicted surface temperatures for two different values of surface heat transfer coefficient, $90 \text{ W m}^{-2} \text{ K}^{-1}$ (lower) and $30 \text{ W m}^{-2} \text{ K}^{-1}$ (upper).

Although convection is one of the two dominant modes of heat transfer overall, Fig. 6 shows that its importance during the early stages of the transient is relatively small compared to lateral conduction along the copper sheet. In this instance the heat transfer coefficient has a value of $90 \text{ W m}^{-2} \text{ K}^{-1}$. This implies that changing the value of the heat transfer coefficient will have only a small effect on the overall surface temperature response during this period, resulting in poor sensitivity. Fig. 7 plots convection as a percentage of overall heat transfer for the case where h is $30 \text{ W m}^{-2} \text{ K}^{-1}$. Also included are the percentage values from Fig. 6 ($h = 90 \text{ W m}^{-2} \text{ K}^{-1}$). In this instance it can be seen that the effect of convection is even smaller, which will result in an even lower sensitivity. This is the same conclusion as that reached by Carscallen, Oosthuizen, and Arthur [3], when determining wall shear stress using a pulsed laser.

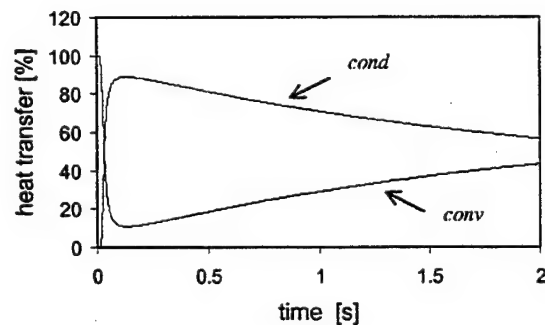


Figure 6. Convection/Conduction as a percentage of overall heat transfer away from the laser strike zone for $h = 90 \text{ W m}^{-2} \text{ K}^{-1}$.

In order to permit the effect of convection to play a significant role in the overall heat transfer process two approaches were considered: allowing the event record to exceed two seconds, and replacing the thin surface sheet

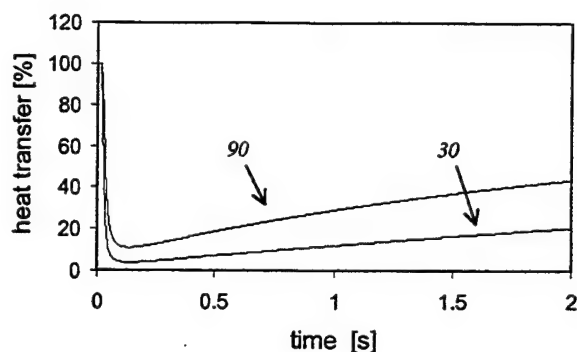


Figure 7. Convection as a percentage of overall heat transfer away from the laser strike zone for $h = 30 \text{ W m}^{-2} \text{ K}^{-1}$. Also included are the results from Fig.6.

with one of lower thermal conductivity. The former is not considered viable due to the fact that by the time $\tau = 2$ seconds the surface temperatures are only a little above ambient, resulting in variations that are a significant percentage of the mean value. However, the second approach, replacing the thin surface layer, does show promise. Figure 8 plots convective heat transfer as a percentage of the overall heat loss for two cases: a copper sheet ($k = \sim 396 \text{ W m}^{-1} \text{ K}^{-1}$) and an Inconel sheet ($k = \sim 12 \text{ W m}^{-1} \text{ K}^{-1}$). The local value of h was assumed to be $30 \text{ W m}^{-2} \text{ K}^{-1}$ and the substrate made of green glass. It is readily apparent that by changing the surface material thermal conductivity there is a significant change in the importance that convection plays in overall heat transfer. This in turn should result in a significant increase in sensitivity.

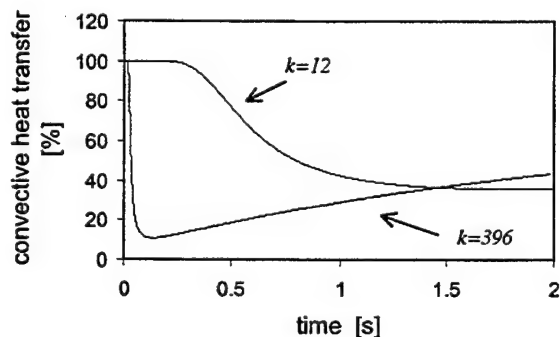


Figure 8. Convection as a percentage of overall heat transfer away from the laser strike zone for two different values of surface layer thermal conductivity.

Experimental Results

The purpose of the experimental stage of the investigation was to determine local values for h from the experimental data using the numerically generated relationship between h and the fundamental phase delay angle, Eq. (5). Figure 9 plots these values as a function of the local Reynolds number, Re_x , for a total of seven measurement points on the

test surface. Also included, for comparison purposes are the predicted values using the equation of Whitaker, [9],

$$Nu_x = 0.029 Re_x^{0.8} Pr^{0.43} \quad (6)$$

where $Nu_x = hx/k$. x is the distance of the measurement point downstream of the plate leading edge, k the thermal conductivity of the free stream air and Pr the Prandtl number. Equation (6), which is valid for

$$0.7 < Pr < 400 \quad \text{and} \quad 5 \times 10^5 < Re_x < 3 \times 10^7,$$

is for an isothermal surface with a turbulent boundary layer. For the case of a constant heat flux boundary condition the heat transfer coefficients may be up to 5% lower. It is considered that the current technique, that of using a pulsed laser, approximates a surface boundary condition somewhere between these two alternatives.

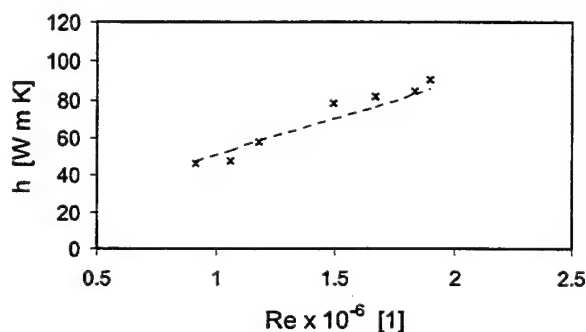


Figure 9. Measured heat transfer coefficients (x) as a function of the local Reynolds number. Also included for comparison is a standard correlation for turbulent flow over a flat plate, Eq. (6).

The reported fundamental phase delay angles were obtained using the first two seconds worth of the temperature versus time event record of each of the seven embedded thermocouples. Due to the limited data capture rates, approximately 20 readings per second, it was necessary to use a spline fitting routine to increase the number of data points so that sufficient accuracy could be achieved when using the Fast Fourier Transforms.

Two aspects of Fig. 9 are important. The first is the fact that the proposed technique of using phase delay angles is capable of producing values for the local heat transfer coefficient from experimentally obtained temperature data. Secondly, the observed qualitative behaviour, over the reported Reynolds number range, is consistent with that predicted using a standard correlation from the literature.

Although there appears to be reasonable agreement between the measured and predicted values it must be remembered that in order to approximate the experimental setup numerically it was necessary to use a surface layer thermal conductivity that was a combination of copper, constantin,

and tin. This parameter could vary significantly from that used, which was simply a best estimate based upon relative volumes. Consequently the results in Fig. 9, insofar as absolute values are concerned, must be treated with caution at this stage.

The uncertainty in the reported measurements, due to the necessity to estimate a thermal conductivity for the copper/thermocouple combination, could be eliminated by not using thermocouples as the temperature sensor. Under the experimental conditions described an IR camera would be more suitable. In this instance the surface emissivity of the thin sheet would not be required, as it is the shape of the temperature time profile that is important, not its absolute value. Thus the combination of an IR camera and a phase delay data reduction technique would permit determination of absolute values of the local heat transfer coefficients on a surface without the need to know the heat flux that was deposited or the absolute temperatures on the surface.

CONCLUSIONS

The principle aim of this investigation was to demonstrate that it was possible to determine absolute values for the local heat transfer coefficient on a surface using a pulsed laser to initiate a temperature difference between the surface and the free stream. It was based upon a new phase delay data reduction technique. This technique is an extension of a previously reported method that uses periodic surface heat fluxes where it was shown that a phase delay will develop between the imposed heat flux and the subsequent surface temperature response.

In order to develop a relationship between the surface heat transfer coefficient and the fundamental phase delay angle for the case of a pulsed surface heat flux both a one dimensional analytical and a two-dimensional axisymmetric numerical model have been developed. An investigation of these models indicated that the numerical model is best suited for describing the experimental conditions.

Using a numerically generated equation it has been possible to obtain absolute values of the surface heat transfer coefficient using the previously reported experimental data. The results are in reasonable agreement with those predicted using a standard correlation from the literature. In order to improve the sensitivity and reduce the uncertainty of the technique it is suggested that an IR camera be used as the surface temperature sensor, rather than thermocouples.

ACKNOWLEDGMENTS

The authors wish to acknowledge the support of Dr P.H. Oosthuizen, of Queen's University at Kingston, and the National Research Council Canada, for their support during this investigation.

REFERENCES

1. Carscallen, W.E., "A Proposal in Response to the President's Request", internal National Research Council of Canada document dated 30 July 1987.
2. Oosthuizen, P.H. and Carscallen, W.E., "A Numerical Investigation of a Method of Using Measurements of the Heat Transfer from a Laser Heated Spot to Determine Wall Shear Stress", *Experimental Heat Transfer, Fluid Mechanics, and Thermodynamics*, J.F. Keffer, R.K. Shah, and E.N. Ganic' Eds., Elsevier Science Publishing Co. Inc., 1991.
3. Carscallen, W.E., Oosthuizen, P.H. and Arthur, F.J., "An Experimental Evaluation of a Novel Method of Using Localized Laser Heating in the Determination of Wall Shear Stress", *Proceedings of the Fifth International Symposium on Applications of Laser Techniques to Fluid Mechanics*, Lisbon, 1990.
4. Turnbull W.O. and Oosthuizen, P.H., "A New Experimental Technique for Measuring Surface Heat Transfer Coefficients Using Uncalibrated Liquid Crystals", accepted for presentation at the ASME International Congress and Exposition, Nashville, USA, 1999.
5. Williamson, R.G., "Further Flow Calibration Tests in the VISTOL Propulsion Tunnel", National Research Council of Canada, Div. Mech. Eng. Lab. Memorandum GD-200, 1972
6. Turnbull W.O., "An Evaluation of Periodic Heat Fluxes and Uncalibrated Liquid Crystals to Measure Local Heat Transfer Coefficients", Ph.D. Thesis, Dept. of Mechanical Engineering, Queen's University at Kingston, Canada, 1998.
7. Arthur, F.J., "Determination of Local Skin Friction Coefficients by Transient Surface Heating with a High Energy Laser Beam", M.Sc. Thesis, Dept. of Mechanical Engineering, Queen's University at Kingston, Canada, 1990.
8. Turnbull, W.O., "Analytical Solution for a Single Pulse Heat Flux - Composite Structure", internal National Research Council document TAD-102/99, dated January 1999.
9. Mills, A.F., "Heat and Mass Transfer", Richard D. Irwin, Inc., Chicago, 1995.

APPENDIX A

This appendix contains a partial derivation of a solution to the one dimensional, transient, heat conduction equation whereby a single pulse surface heat flux is applied to a semi-infinite substrate. The heat flux can be generated within a thermally thin, isothermal, surface layer, or through the use of a non intrusive device heat source impinging on the surface. For the purposes of this investigation it is assumed that there is no contact resistance between the surface layer and the substrate. The substrate is of low thermal conductivity, and it's thermophysical properties are considered constant. Thermal radiation effects are not included. The temperature variation within the substrate is given by:

$$\frac{\partial^2 \theta}{\partial x^2} - \frac{1}{\alpha} \frac{\partial \theta}{\partial \tau} = 0 \quad (A1)$$

Let the surface heat flux be approximated using the *Dirac* delta function such that,

$$q(\tau) = \tilde{q} \delta(\tau) \quad (A2)$$

with the following boundary conditions:

$$\varepsilon \frac{\partial \theta}{\partial \tau} \bigg|_{x=0} = -h(\theta_{x=0} - \theta_{\infty}) + \tilde{q} \delta(\tau) + k \frac{\partial \theta}{\partial x} \bigg|_{x=0}, \quad \tau > 0$$

$$\theta \rightarrow 0 \text{ as } x \rightarrow \infty, \text{ and } \theta = 0 \text{ when } \tau = 0, x \geq 0$$

where $\varepsilon = \rho c t$.

A solution to Eq. (A1) is found by transforming the pde, Eq. (A1) to an ode using Laplace Transforms. Thus the governing equation and the boundary/initial conditions become:

$$\frac{d^2 \bar{\theta}}{dx^2} - l^2 \bar{\theta} = 0, \quad (A3)$$

$$G \bar{\theta}_{x=0} = -h \bar{\theta}_{x=0} + \frac{A}{P} + Q + k \frac{d \bar{\theta}}{dx} \bigg|_{x=0}, \quad (A4)$$

and

$$\bar{\theta} \rightarrow 0 \text{ as } x \rightarrow \infty, \text{ and } \bar{\theta} = 0 \text{ when } \tau = 0, x \geq 0 \quad (A5)$$

$$\text{where } G = P\varepsilon, \quad A = h\theta_{\infty}, \quad Q = \tilde{q}, \quad l^2 = P/\alpha.$$

An initial guess as to a solution for the subsidiary governing differential equation, Eq. (A3) is:

$$\bar{\theta} = D e^{lx} + E e^{-lx} \quad (A6)$$

Initial conditions require that coefficient $D = 0$ (otherwise there will be no convergence), and Eq.(A6) then becomes:

$$\bar{\theta} = E e^{-lx} \quad (A7)$$

Substituting Eq. (A7) into Eq.(A4) yields, after some arranging,

$$\bar{\theta}_{x=0} = \left[\frac{k}{G+h} \right] [-lE] + \frac{A}{P(G+h)} + \frac{Q}{(G+h)} \quad (A8)$$

Initial conditions require that the substrate temperature and the thin film temperature be equal at $x = 0$. Therefore

$$E e^{-l(0)} = \left[\frac{k}{G+h} \right] [-lE] + \frac{A}{P(G+h)} + \frac{Q}{(G+h)} \quad (A9)$$

Solving for E yields:

$$E = \left[\frac{A/P + Q}{(G+h) + lk} \right] \quad (A10)$$

Substituting Eq.(A10) back into Eq.(A7) gives:

$$\bar{\theta} = \left[e^{-lx} \right] \left[\frac{A/P + Q}{(G+h) + lk} \right] \quad (A11)$$

Finally, substituting in the values for l gives:

$$\bar{\theta} = \left[e^{-\frac{x}{\sqrt{\alpha}} \sqrt{P}} \right] \left[\frac{A}{P \left(GP + \frac{k}{\sqrt{\alpha}} \sqrt{P} + h \right)} + \frac{Q}{\left(GP + \frac{k}{\sqrt{\alpha}} \sqrt{P} + h \right)} \right] \quad (A12)$$

Using the identities $\delta = h/\varepsilon$ and $\psi = k/\varepsilon \sqrt{\alpha}$ Eq.(A12) becomes, where $\varepsilon = \rho c t$,

$$\bar{\theta} = \left[\frac{e^{-\frac{x}{\sqrt{\alpha}} \sqrt{P}}}{\varepsilon} \right] \left[\frac{A}{P(P + \psi \sqrt{P} + \delta)} + \frac{Q}{(P + \psi \sqrt{P} + \delta)} \right] \quad (A13)$$

Using the normal procedure for finding the roots of a quadratic equation

$$(P + \psi \sqrt{P} + \delta) = (\sqrt{P} - \Phi_1)(\sqrt{P} - \Phi_2)$$

where

$$\Phi_1 = -\frac{\psi}{2} + \frac{1}{2} \sqrt{\psi^2 - 4\delta} \text{ and } \Phi_2 = -\frac{\psi}{2} - \frac{1}{2} \sqrt{\psi^2 - 4\delta}$$

Equation (A13) may now be written as:

$$\bar{\theta} = \left[\frac{e^{-\frac{x}{\sqrt{\alpha}}\sqrt{P}}}{\varepsilon} \right] \left[\frac{A}{P(\sqrt{P}-\Phi_1)(\sqrt{P}-\Phi_2)} + \frac{Q}{(\sqrt{P}-\Phi_1)(\sqrt{P}-\Phi_2)} \right] \quad (\text{A14})$$

Setting

$$\frac{1}{(\sqrt{P}-\Phi_1)(\sqrt{P}-\Phi_2)} = \frac{H}{(\sqrt{P}-\Phi_1)} + \frac{L}{(\sqrt{P}-\Phi_2)}$$

and solving for H and L yields:

$$H = -L = 1/(\Phi_1 - \Phi_2).$$

Thus Eq.(15) may be written as:

$$\bar{\theta} = \left[\frac{e^{-\frac{x}{\sqrt{\alpha}}\sqrt{P}}}{\varepsilon(\Phi_1 - \Phi_2)} \right] \left[\frac{A}{P(\sqrt{P}-\Phi_1)} - \frac{A}{P(\sqrt{P}-\Phi_2)} + \frac{Q}{(\sqrt{P}-\Phi_1)} - \frac{Q}{(\sqrt{P}-\Phi_2)} \right] \quad (\text{A15})$$

Equation (A15) must first be transformed back into the time domain by rearranging Eq. (A15) into sums and products with known inverse Laplace Transforms using Convolution Theorem. Thus a time domain solution to Eq. (A1), for the thin surface layer is given by:

$$\theta_{x=0} = BA[f(\Phi_1) - f(\Phi_2)] + BQ[g(\Phi_1) - g(\Phi_2)] \quad (\text{A16})$$

where

$$g(\Phi) = \frac{1}{\sqrt{\pi\tau}} + \Phi e^{\Phi^2\tau} \operatorname{erfc}(-\Phi\sqrt{\tau})$$

and

$$f(\Phi) = -\frac{1}{\Phi} + \frac{1}{\Phi} e^{\Phi^2\tau} \operatorname{erfc}(-\Phi\sqrt{\tau}).$$

Eq. (A16) further reduces to

$$\theta_{x=0} = C + C_1 e^{\Phi_1^2\tau} \operatorname{erfc}(-\Phi_1\sqrt{\tau}) + C_2 e^{\Phi_2^2\tau} \operatorname{erfc}(-\Phi_2\sqrt{\tau}) \quad (\text{A17})$$

where

$$\begin{aligned} C &= \frac{A}{\varepsilon\Phi_1\Phi_2} \\ C_1 &= \left(BQ\Phi_1 + \frac{BA}{\Phi_1} \right) \\ C_2 &= -\left(\frac{BA}{\Phi_2} + BQ\Phi_2 \right). \end{aligned}$$

For the case where the initial ambient temperature, θ_∞ , is equal to 0 the coefficients in Eq. (A17) become:

$$C = 0 \quad C_1 = BQ\Phi_1 \quad C_2 = -BQ\Phi_2.$$

Hence

$$\theta_{x=0} = C_1 e^{\Phi_1^2\tau} \operatorname{erfc}(-\Phi_1\sqrt{\tau}) + C_2 e^{\Phi_2^2\tau} \operatorname{erfc}(-\Phi_2\sqrt{\tau}). \quad (\text{A18})$$

PERFORMANCE STUDIES OF THE CONSTANT VOLTAGE ANEMOMETER IN A MACH 2.3 BOUNDARY LAYER

Geneviève Comte-Bellot, ECL, Lyon
Garimella R. Sarma, Tao Systems, Inc., Williamsburg, VA, USA
Thierry M. Faure, LEMFI, Paris-Orsay
Jean-Paul Dussauge, Pierre Dupont and Jean-François Debiève, IRPHE, Marseille

ABSTRACT

The operational features of the Constant Voltage Anemometer (CVA) are shown to be well adapted for measurements in supersonic flows. The time constant of hot-wire under constant voltage operation is verified to be much smaller than that under constant current operation. Good noise immunity feature of the constant voltage operation with large bandwidth of the CVA circuit were also noticed from the experiments. An extensive investigation has been conducted in a Mach 2.3 boundary layer. The software compensation approach described in an earlier study is again applied to the data in the present experiments. The approach of compensating the CVA for the hot-wire time constant partially with hardware during the experiment and later correcting the CVA output with the actual *in-situ* measured time constant has produced consistently good results with an increased bandwidth. The turbulence levels estimates deduced from CVA data collected at different wire overheats agree well with earlier published results. Comparisons with the Constant Current Anemometer (CCA) and the Constant Temperature Anemometer (CTA) were conducted in the same experimental conditions.

INTRODUCTION

The Constant Voltage Anemometer (CVA) and the associated circuits were patented by Sarma [1] and it has been under active development since 1991. The present work focuses on supersonic boundary layer measurements where large bandwidths and low noise are needed from the anemometers. Sarma et. al. [2] have reported results of experiments performed in a Mach 2 supersonic boundary layer at the CEAT-Poitiers. The software correction of the hot-wire thermal lag was applied for the first time in those experiments.

Further improvements in the CVA were incorporated recently which resulted larger bandwidth, an automatic *in situ* measurement of the hot-wire time constant, and finer settings of the hardware compensation. This article presents the results of the experiments conducted using the improved CVA at the IRPHE Laboratory in Marseille.

WIND TUNNEL AND HOT-WIRE

A basic zero pressure gradient boundary layer at Mach 2.3 has been selected for the investigation, and the tunnel was run at three pressures: 0.163, 0.492 and 0.746×10^5 Pa. The boundary layer is investigated at 0.75 m downstream from the nozzle. Its thickness, δ , is 15 mm, the free stream velocity is 555 m/s, so that according to Kistler [3] turbulent energy up to 150 kHz can be expected.

The hot-wire was tungsten-platinum plated with a diameter d of $2.5 \mu\text{m}$. Its length, $2l$, was around 0.5 mm. The wire Reynolds numbers (Re), were 2.5, 7.4, and 11.2 respectively in the external flow for the three pressures considered. $Re = 6.0$ in the boundary layer at a wall distance $y=4.1$ mm and for the intermediate pressure of 0.492×10^5 Pa. The cold wire resistance, R_c , of the hot-wire was obtained in every case by plotting the hot-wire

resistance, R_w , versus the electric power injected into the wire and extrapolating the curve towards a zero power. The wire overheat is defined by $a_w = (R_w - R_c)/R_c$. All the turbulence signals were acquired at a sampling rate of 1 MHz, by a LeCroy 8007, module 8901A. For the CVA 127 segments of 4096 samples each were processed and averaged.

CONSTANT VOLTAGE ANEMOMETER

A sketch of the CVA system is given in Figure 1 and its principle is available in Comte-Bellot [4]. The CVA transfer function is fully described in Sarma [5].

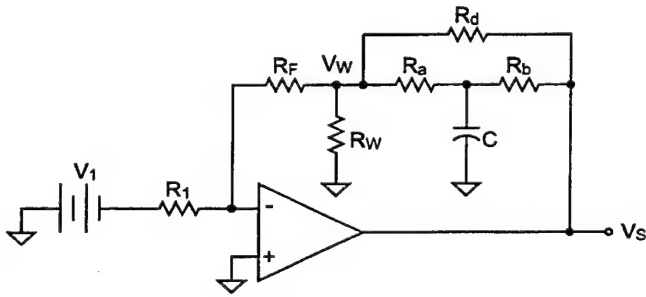


Figure 1. Compensated CVA Circuit, R_w is wire resistance, V_w wire voltage.

Any change in wire resistance, R_w , due to fluid flow produces a current change in the hot-wire, the path for which is only through the resistance $(R_a + R_b) \equiv R_2$ of the circuit. The output signals, $E \equiv V_s$ and e' , for the mean and fluctuating parts are therefore large. They can be directly recorded without any further amplification.

The voltage V_w across the wire, which is fixed by the resistances R_f and R_1 , and the DC source V_1 , can be continuously adjusted from 0.005 to 2 Volts. The value of the wire resistance R_w in series with the cable leads and prongs resistances r_L , is obtained from measured V_w and the CVA circuit output DC voltage E by the relation established from Sarma [5]

$$R_w + r_L = \frac{R_2}{\frac{E}{V_w} - \left[1 + \frac{R_2}{R_f}\right]} \quad (1)$$

This value is used for overheat calculations.

CVA TIME CONSTANTS

Measurement of the wire time constant M_w^{CVA} is made *in situ* by injection of a 20 Hz square wave at the junction of R_1 and R_f . A differential procedure has been developed by Sarma [5] to retrieve only the dynamic change in resistance of the wire due to the step voltage change.

The results of the measured time constants are shown in Figure 2. M_w^{CVA} decreases significantly with the wire overheat a_w , and it is always less than M_w^{CCA} in the same operating conditions. The results agree well with the approximate relation

$$M_w^{CVA} = \frac{M_w^{CCA}}{1 + 2a_w} \quad (2)$$

shown in Comte-Bellot [4]. For $a_w > 0.25$, the measured M_w^{CVA} values are even a little smaller than predicted.

These small M_w^{CVA} values have the advantage of making the thermal lag correction easier for the CVA with low noise and larger bandwidths from the circuit.

Moreover, the M_w^{CVA} values obtained at 4.1 mm in the boundary layer, where $Re \approx 6$, are in perfect agreement with those obtained in the free stream, at a value of $Re = 7.4$, hence demonstrating that the *in situ* measured M_w^{CVA} values are accurate even in the presence of turbulence, because of the averaging process used in the computation.

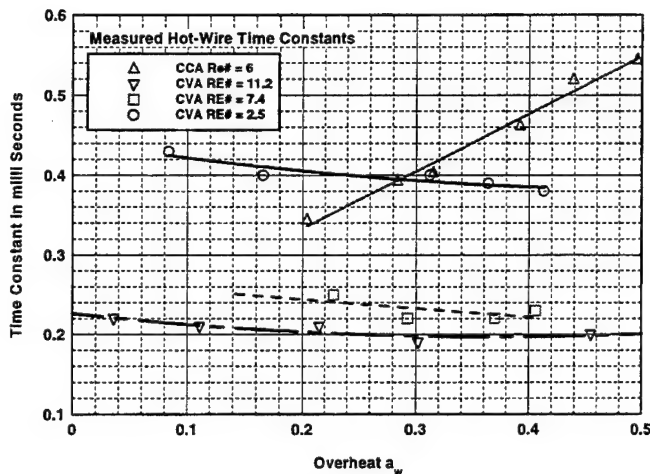


Figure 2. Measured hot-wire time constants, wire diameter $2.5 \mu\text{m}$

CVA THERMAL LAG COMPENSATION AND BANDWIDTHS

Two methods are possible to compensate the wire time constant: (i) a full hardware compensation built into the CVA circuit and (ii) a partial fixed hardware compensation in the CVA circuit followed by a software correction with the actual measured M_w^{CVA} value. Full software compensation is not a good approach due to its low signal levels.

Hardware Compensation

The hardware thermal compensation is done by a resistance-capacitance combination (R_a, R_b, R_d, C) within the op-amp feedback path as shown in Figure 1. The time constant of the zero (henceforth referred as TC) introduced by this combination cancels the measured hot-wire time constant M_w^{CVA} . A hardware TC range of 0.10 ms to 0.50 ms is covered in the CVA in 0.01 ms steps.

Software Correction

In the method adapted here for applying the software correction procedure, the CVA hardware during the test provides a fixed compensation ($TC = 0.1 \text{ ms}$) irrespective of the actual measured hot-wire time constant M_w^{CVA} . The latter was typically around 0.25 ms in most of the cases. This procedure increases the productivity by eliminating all adjustments of the anemometer during the blow-down.

During the blow-down, M_w^{CVA} , E , V_w , and turbulence signals are routinely acquired for post processing.

The software correction makes use of the relation

$$e_{corr} + TC \frac{de_{corr}}{dt} = e_{raw} + M_w^{CVA} \frac{de_{raw}}{dt} \quad (3)$$

obtained from the software correction formula given in Sarma *et al.* [2] where the software correction approach was also described. In (3), e_{raw} denotes the partially hardware corrected output, and e_{corr} the software corrected output.

The high fidelity of the software correction is illustrated for sine wave signals at 100 kHz in Figure 3, where the raw CVA output along with the software corrected output and the associated input to the hot-wire are given.

Therefore, the software correction retains the bandwidth associated with the fixed TC setting used.

Moreover, it can be established that as soon as the frequency is high enough, around 10 kHz in the present case, relation (3) simplifies into

$$TC \frac{de_{corr}}{dt} = M_w^{CVA} \frac{de_{raw}}{dt} \quad (4)$$

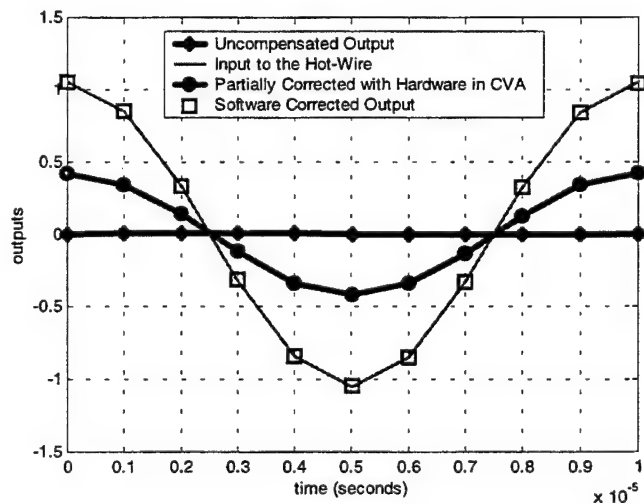


Figure 3. Validity of the software CVA correction, illustration for $f=100 \text{ kHz}$. The sampling rate is 1 MHz as in the experiments

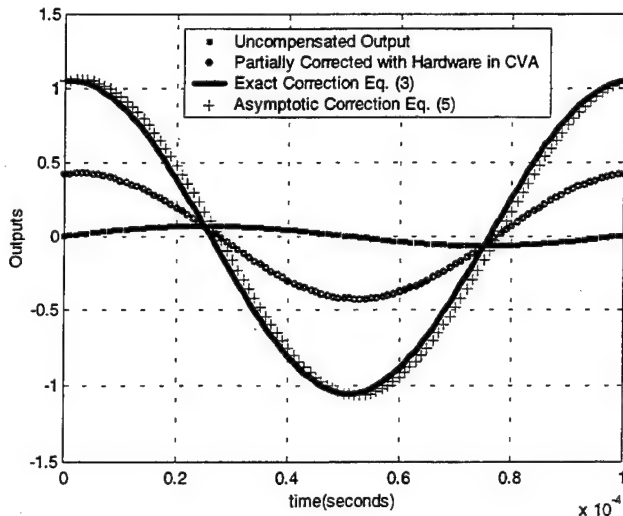


Figure 4. Importance of the asymptotic relation (5) at $f=10$ kHz.

so that asymptotically we have:

$$e_{corr} = \frac{M_w^{CVA}}{TC} e_{raw} \quad (5)$$

Figure 4 illustrates how the asymptotic signal given by relation (5) is close to the exactly corrected signal given by (3), even at $f = 10$ kHz. The amplitude is already recovered and the small phase advance which is noted, as expected, is also small. Thus the simple relation (5) applies to almost the whole frequency range concerned by the present supersonic flow investigation. This result is very useful when comparing the $fE(f)$ spectral plateau heights in a later section.

BANDWIDTHS

The bandwidth of the CVA was determined from the normalized gain plots of the CVA response to sine wave input described by Sarma [5]. Plots of this normalized gain at two TC settings are shown in Figure 5. It shows CVA bandwidth (-3 dB) of 470 kHz for $TC = 0.10$ ms, and 270 kHz for $TC = 0.25$ ms.

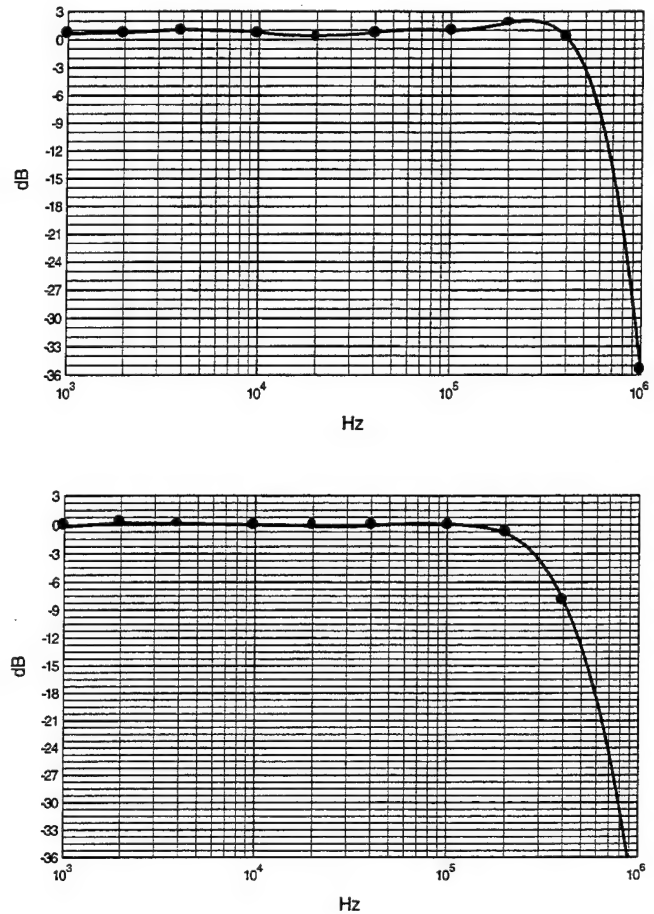


Figure 5. Measured normalized gain of the CVA at $TC = 0.10$ ms (upper plot) and $TC = 0.25$ ms (lower plot).

CVA NOISE AT $TC=0.10$ ms AND $TC = 0.25$ ms

The CVA noise was investigated with the hot-wire in still air in the wind tunnel, so that all the wire connections were kept unchanged. For different V_w values and cable lengths data was acquired. Figure 6 shows spectral plots for $TC=0.10$ ms and 0.25 ms.

The spikes from spurious signals in the noise spectra are very small due to insignificant cable capacitance effects in the CVA. The noise psd is almost flat for $TC=0.10$ ms. There is just a slight f^{+1} increase associated with the gain frequency increase for the thermal lag compensation. At $TC=0.25$ ms, the increase is more pronounced, as expected.

The spurious noise rise as f^{+2} was not observed anywhere. This constitutes a very interesting behavior in comparison with the Constant Temperature Anemometer (CTA) for which Saddoughi & Veeravalli [6] have reported dramatic noise rise at high frequencies for four different CTA products.

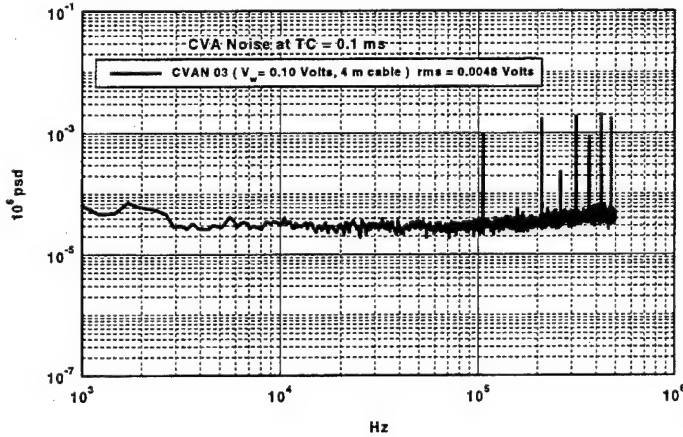
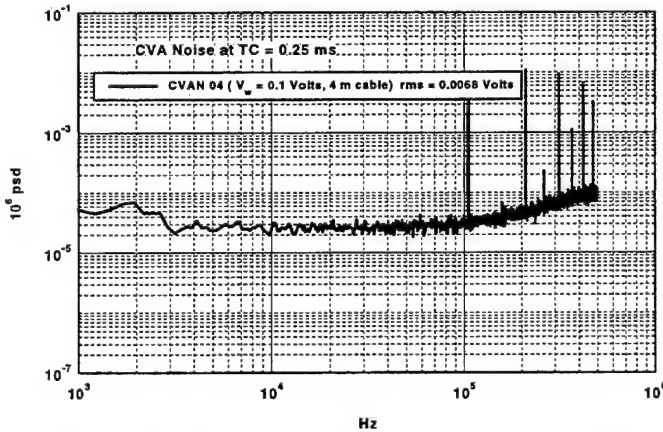


Figure 6. CVA noise at $TC = 0.10$ ms, and $TC = 0.25$ ms,



for $V_w = 100$ mV. The Dantec connecting cable is 4 m long.

The output rms noise level at $TC=0.10$ ms - used in most of the present data acquisition - is 4.8 mV from Figure 6.

This gives an estimated input noise of $0.8 \text{ nV}/\sqrt{\text{Hz}}$ using the frequency bandwidth given figure 5 (top), a compensation gain of the order of 700 and the value of the ratio R_2/R_w which is around 12.

It has also been observed that there was no significant change in the rms noise level either, with the time constant TC or V_w . The reason is that an increase in TC is always associated with a decrease in the CVA bandwidth from the circuit and a variation in V_w does not alter the gain or TC of the circuit. By far this noise feature is significantly different from the other anemometers.

TURBULENCE SPECTRA

In the following presentation of the signal spectra only the frequency weighted spectra in the form $fE(f)$ will be considered because of the linearity of the $\ln f$ scale for the associated x axis:

$$\overline{e'^2} = \int_0^\infty E(f) df = \int_0^\infty fE(f) d \ln f \quad (6)$$

By simple visual inspection we can deduce from the highest part of $fE(f)$, or even its plateau, the frequency range which contributes the most to the mean square of e' . This property subsists even with the log y-scale used in the subsequent figures. Of course, it is only a linear y-scale, as already used in [2], which would permit to obtain the kinetic energy by direct visual integration of $fE(f)$ vs $\ln f$.

At this point it is also important to recall that wall turbulence spectra possess a large region with a f^{-1} slope for wall distances belonging to the logarithmic zone, for either sub or supersonic boundary layers as explained by Dussauge *et al.* [7]. The wall distance $y = 4.1$ mm we selected for the measurements is a little outside that region, but we can still expect an approximate f^{-1} region. Further, $fE(f)$ was multiplied by 10^6 to enable the graphics program to handle the numbers, and $\ln f$ divided by 2.3 to ease the correspondence with decimal logarithms and frequencies.

CVA Hardware Compensated Output Spectra

The spectra of turbulent signals at $y = 4.1$ mm obtained with full hardware compensation in the CVA are presented in Figure 7 for both a small overhear, $a_w \approx 0.15$, and a large overhear $a_w \approx 0.60$. That means for this data hardware TC has been set to be equal to *in situ* measured M_w^{CVA} .

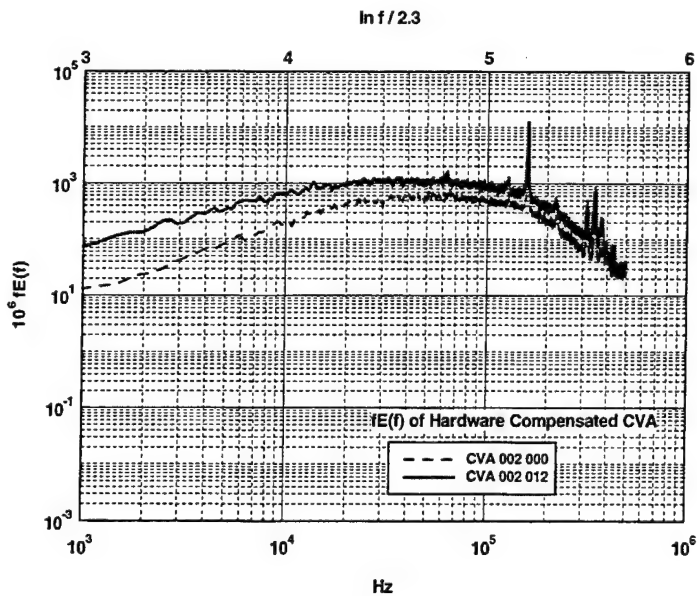


Figure 7. Full hardware CVA response with $fE(f)$ vs $\ln f$ representation, at two overheat values, ... $a_w = 0.15$ and -- $a_w = 0.59$.

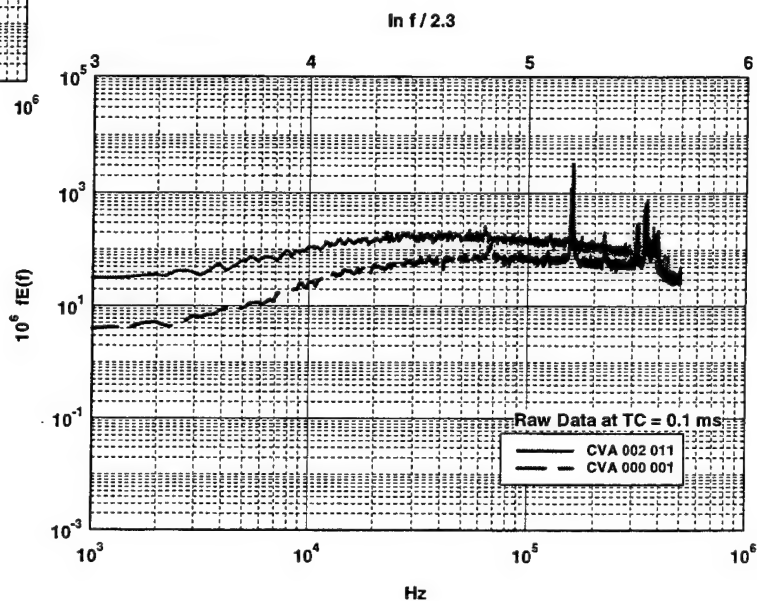


Figure 8. Raw CVA spectra with $fE(f)$ vs $\ln f$ representation, at two overheat values, ... $a_w = 0.15$ and -- $a_w = 0.59$.

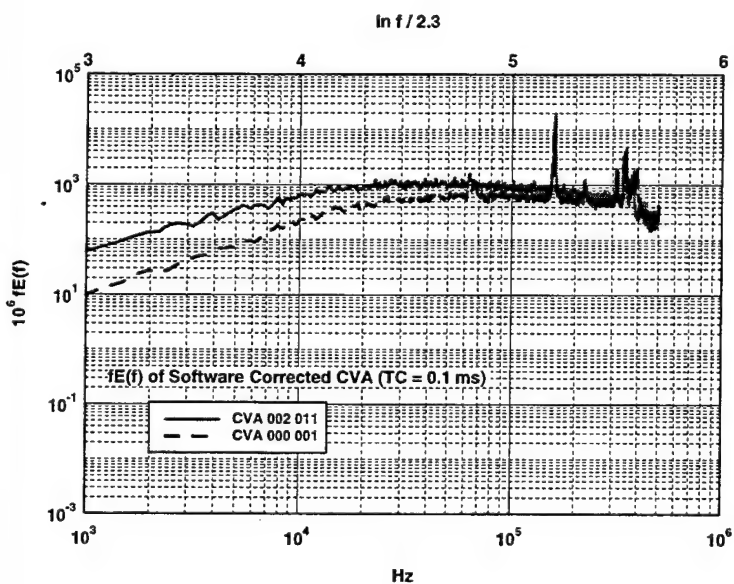


Figure 9. Software corrected CVA spectra with $fE(f)$ vs $\ln f$ representation, for two overheat values, $a_w = 0.15$ and --- $a_w = 0.59$.

A plateau readily appears in these turbulent energy spectra, particularly noticeable at the highest overheat. Its spectral extent is however limited, up to about 100 kHz, because of the reduced CVA bandwidth in the hardware compensated operational mode.

Strain gage peaks are visible around 150 kHz and 250 kHz. Such peaks are generally common in many supersonic experiments, depending on the details of the soldering conditions of hot-wires, as reported by Dussauge et al. [7].

Raw CVA Spectra

The raw CVA spectra obtained with $TC=0.10$ ms are given in Figure 8, at the two same overheat values as before, $a_w \approx 0.15$, and $a_w \approx 0.60$. These intermediate data are of the greatest importance because they permit to assess the quality of the signals prior to any transformation.

In particular, a long plateau exists for the turbulent kinetic energy at higher overheat. Of course its level is too low, because of the absence of thermal lag compensation, but the high frequency extent, which is quite large, is correct because of the asymptotic relation (5) discussed earlier.

Software Corrected CVA Spectra

When applying the software compensation, each turbulence data is of course corrected for its *in situ* measured M_w^{CVA} value, thus 0.25 ms for $a_w = 0.15$ and 0.20 ms for $a_w = 0.60$. The rms values and the spectra are calculated after applying this correction.

The spectra with the software correction are presented in Figure 9. The first result is that the plateau height is the same for the software corrected spectra and for the full hardware corrected spectra.

The second result is that a low roll-off rate beyond the plateau, up to around 300 kHz, is now observable with the software correction. This is a clear illustration of the larger bandwidth offered by the software compensation.

COMPARISON BETWEEN CVA, CCA AND CTA SPECTRA

The same wire was kept for all the turbulence measurements, thus reinforcing the validity of the different comparisons.

The Constant Current Anemometer (CCA) DISA 56C02 available at IRPHE is an improved version of the circuit described by Gaviglio [8]. In particular the amplifier ceiling-to-floor ratio of the compensating amplifier has been boosted up to 1000. The thermal lag compensation is done by hardware in two steps: at first, 50 μ s in a preamplifier, then the main compensation, up to 0.50 ms by the conditioner which consists of three stages.

Typical bandwidth (-3db) for the CCA is 800 kHz for $M_w^{CCA} = 0.15$ ms and 600 kHz for $M_w^{CCA} = 0.50$. A low pass filter (lpf) with a -3dB cutoff at 400 kHz was introduced before the final power stage. A data acquisition system connected to a PC processes the compensation automatically in the conditioner. Typical equivalent input noise figures of the amplifier are 1.2 to 1.6 nV/\sqrt{Hz} for a time constant of 0.05 to 1.5 ms, and 0.8 nV/\sqrt{Hz} per volt of probe voltage on the current generator.

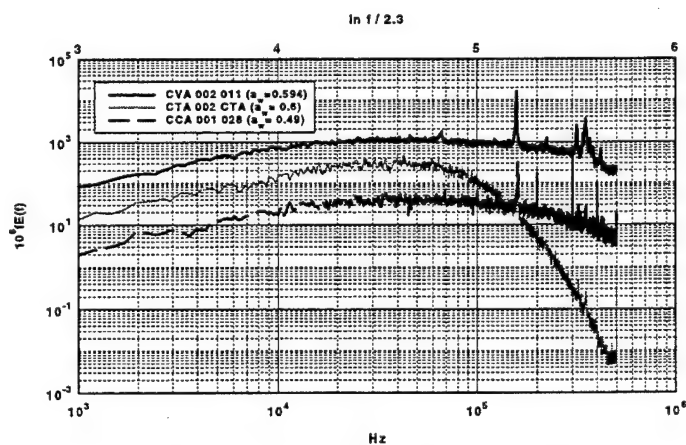


Figure 10. Comparison of Software Corrected CVA, CCA and CTA at high overheat with the $fE(f)$ vs $\ln f$ representation.

The Constant Temperature Anemometer (CTA) is a Dantec Streamline 90C10 module. It uses a symmetric (left:right) bridge with a top resistance of 20 ohms. The wire was operated at a fixed overheat, $a_w=0.60$. The feedback adjustment of gain and filter was monitored by a PC, the wire being placed in the free stream. This leads to the following positions : Filter 10, Gain 14, Tune -5. Afterwards, the wire was placed at the same position where the CVA was tested with the wire.

For the CCA and CTA data acquisition, only 31 blocks were used, compared to the 127 blocks used for the CVA, so CCA and CTA plots are more jagged.

Figure 10 compares the spectra obtained with the software corrected CVA, CCA and CTA anemometers for a moderate overheat ratio, $a_w= 0.50 - 0.60$. No noise correction has been made.

It is very clear that only the CVA, when used with its software correction of thermal lag is able to reproduce a long smooth region up to 300 kHz.

The CCA response was slightly limited by the large time lag which has to be taken into account and moreover by the 400 kHz low pass filter presently integrated in the circuit. In particular, a slight drop appears in the CCA spectrum around 300 kHz at the highest overheat and it could be directly attributed to the lpf cutoff. Up to 200 kHz the CCA and CVA responses agree very well.

Finally, the CTA underestimates the high frequencies due to low pass filter which has to be incorporated in the feedback loop for stability. In addition, the overheat value $a_w=0.60$ is not the optimal one for the feedback loop, a value around $a_w=0.80$ is usually advised by the manufacturer.

TURBULENCE ESTIMATES USING CVA DATA

Mean (E) and fluctuating CVA outputs (e') are easily collected at different wire overheats, so that sets of equations can be solved for the turbulence characteristics involving the mass flux and total temperature fluctuations. The values of the sensitivity coefficients have been established by Comte-Bellot [4], and details of the procedure are available in Sarma et al [2]. Using this procedure, at $y=4.1$ mm from the wall, $y/\delta = 0.27$, the calculated value for $\sqrt{\rho u'^2}/\tau_w \approx 1.7$, a value which agrees

well with the data already available for supersonic turbulent boundary layers, cf. Smits et al [9].

CONCLUSIONS

Software correction of the thermal lag is possible with the CVA because of its well defined transfer function [5] which is independent of the cable capacitance effects. This overcomes certain hardware limitations imposed by the circuits and retains the bandwidth obtained with the lower time constant (TC) setting in the CVA even when the software correction is applied. Also, studies with the algorithm show that the software correction is accurate up to half the sampling frequency.

The hardware design of the CVA is under continuous improvements over the last 4 years. The prototype used in the present experiments at IRPHE had a 470 kHz bandwidth at a TC = 0.1 ms. With a further recent improvement in the CVA hardware design, the bandwidth had been improved to 520 kHz at the same TC. The new prototype had been tested to have 700 kHz bandwidth at a TC of 0.056 ms. It was shown by Sarma *et al.*[2] that the software correction can be applied irrespective of the hardware TC setting. To obtain even larger bandwidths when needed, this new TC setting can be readily used.

CVA can be used over wide overheat ratios, a feature that is very useful in the turbulence investigation of hypersonic and supersonic flows.

Finally, the CVA was found to be highly portable. It was possible to place the CVA next to the wind tunnel at IRPHE without any optimization of position or cable lengths and to start the experiment right away.

REFERENCES

- [1] G.R. Sarma, U.S. Patent Nos. 5074147 (1991) and 5854425 (1998)
- [2] G.R. Sarma, G. Comte-Bellot & T.M. Faure, 1998, Software corrected hot-wire thermal lag for the constant voltage anemometer featuring a constant bandwidth at the selected compensation setting, Rev. Sci. Instrum., 69, 3223-3231.
- [3] A.L. Kistler, 1959, Fluctuation measurements in a supersonic turbulent boundary layer, Phys. Fluids, 2, 29-269.

[4] G. Comte-Bellot, 1998, Hot-Wire Anemometry, Chap. 34, in *Handbook of Fluid Dynamics*, edited by R.W. Johnson, CRC Press.

[5] G.R. Sarma, 1998, Transfer function analysis of the constant voltage anemometer, *Rev. Sci. Instrum.*, 69, 2385-2391.

[6] S.G. Saddoughi & S.V. Veeravalli, 1996, Hot-wire anemometry behaviour at very high frequencies, *Meas. Sci. Technol.*, 7, 1297-1300.

[7] J.P. Dussauge, R.W. Smith, A.J. Smits, H. Fernholz, P.J. Finley & E.F. Spina, edited by W.S. Saric, 1996, *Turbulent boundary layers in subsonic and supersonic flows*, AGARDograph 335.

[8] J. Gaviglio, 1978, Sur les méthodes de l'anémométrie par fil chaud des écoulements turbulents compressibles de gaz, *J. Mécanique Appliquée*, 2, 449-498.

[9] A.J. Smits, K. Hayakawa & K.C. Muck, 1983, Constant Temperature Hot-Wire Anemometer Practice in Supersonic Flows, *Exp. in Fluids*, 1, 83-92.

SESSION : 9

HIGH SPEED FLOW DIAGNOSTICS

NON-INTRUSIVE DIAGNOSTICS FOR THE AEDC IMPULSE FACILITY: APPLICATIONS AND RESULTS

W. D. Williams, M. S. Smith, F. L. Heltsley, C. W. Brasier, P. M. Sherrouse,
W. M. Ruyten, L. L. Price, E. J. Felderman, K. M. Stephens
Sverdrup Technology, Inc./AEDC Group
Arnold AFB, TN 37389-4300

Abstract—As part of a modernization of the AEDC hypersonic test capability, a free-piston shock tunnel, known as the Impulse Facility, was constructed. Initial shakedown and calibration tests were completed in 1994. The facility remained dormant until the recent resurgence in interest in hypersonics at AEDC. A cooperative project was established between AEDC and the DLR/HEG with the objectives of accelerating and improving the development cycle for both the Impulse Facility and the HEG. An integral part of this project was an ambitious plan for the use of non-intrusive diagnostics to provide key information about the flow field. This paper is essentially a status report of the efforts to date.

INTRODUCTION

The AEDC Impulse Facility [1] is a free-piston shock tunnel (see Fig. 1), which uses gunpowder to drive an expendable or re-useable piston to potentially achieve nozzle stagnation pressures of several thousand bar at total enthalpies greater than 20 MJ/kg. The conditions used for this project have stagnation pressures ranging from 225-1725 bar and total enthalpies of 9-17 MJ/kg. The current nozzle is an 8-deg half-angle conical nozzle with a replaceable throat section, which has a diameter of 1.9 cm for the current project. The nozzle exit diameter is 45.7 cm, and the test section diameter is 107 cm with excellent optical access. Windows at the 90° positions have two 30-cm diameter viewing ports, and the four windows at the 45° positions have single 13-cm diameter viewing ports. A cruciform rake of 11 pitot probes and 2 coaxial thermocouple probes is used for facility calibrations. Test articles have consisted of a variety of blunt cone models, and all are instrumented with pressure and coaxial thermocouple gages. Standard facility instrumentation is listed in Fig. 2. The most important standard instrumentation relative to non-intrusive diagnostics (NID) is designated ST6 which is the shock tube gage nearest the nozzle throat. It provides the conical nozzle reservoir pressure and is the trigger mechanism for all NID systems.

The potential Impulse Facility free stream conditions in terms of total number density (molecules/cm³) and temperature (K) are shown in Fig. 3. The conditions of the 35 shots to date are shown as the blue and black data points in Fig. 3. These shot conditions were determined from measured nozzle stagnation pressure and an assumed isentropic process from reflected shock to measured pressure and nozzle exit. The red data points are the predictions of flow conditions for shots 26-35 provided by the GASP code, which has chemistry and thermal non-equilibrium capability. The difference in free stream temperature values is substantial. Also shown for reference in Fig. 3 are the operating envelopes for the major relevant NID calibration and validation laboratory devices—a laboratory shock tube/tunnel, a flat flame burner, and a heated, quasi-static cell.

The requirements for NID are to provide multiple, independent measurements to yield information about run time, thermal non-equilibrium, spatial variations of flow properties, flow temporal evolution, and particulate contamination. A suite of NID was chosen to meet these requirements. Planar Mie scattering (PMIE) and non-absorptive Laser Beam Transmission (LBT) were used to provide information about particulate contamination and its distribution within the flow. Emission Spectroscopy (ES) was also used to identify the atomic content of particulate species in the flow as well as to monitor rubidium (Rb) seed emission as an indicator of helium arrival. Laser Diode Absorption (LDA) was used with Rb seeding of the driver gas to indicate helium arrival with a potential measurement of flow velocity. High Speed Flow Visualization (HSFV) was obtained using a Cu-vapor laser system and high-speed camera/recorder systems to provide shadowgraph, schlieren, and holographic interferogram visualizations of the flow around the test articles. Planar Laser-Induced Fluorescence (PLIF) of nitric oxide (NO) was used for rotational temperature and NO concentration measurements. A crude

version of Filtered Rayleigh scattering (FILRAY) was used as another indicator of helium arrival. A Pulsed Electron Beam Fluorescence (PEBF) system was also developed but has not been applied to date.

PMIE

The physical setup for the application of PMIE at the Impulse Facility is shown in Fig. 4. A copper vapor laser system and beam shaping optics were used to provide a 3 cm wide sheet of radiation at a wavelength of 510 nm across the flow. In Fig. 4 the laser sheet is shown traversing the nozzle boundary layer into the free-stream. Images of the Mie scattered radiation were obtained with an ICCD camera with a gate width of 100 ns. Similar images to that shown in Fig. 4 were obtained with the beam traversing the other direction. It is believed that these images indicate a concentration of particulates in the boundary layer. In the cross-section plot of Fig. 4 where the predicted variation of density across the flow is also shown, it is clear that molecular scattering cannot explain the large scattering signal in the boundary layer.

LBT

A chopped, 10 mw, 632.8 nm (He-Ne) laser beam was passed across the exit plane of the facility nozzle just upstream of the test article. The transmitted beam passed through a 10 nm laser line filter before impinging on a photodiode operated in the photoconductive mode. The detected signal was processed in real time by a lock-in amplifier to compensate for flow induced background light levels and detector bias. The recorded data was normalized post event to produce flow field percent transmission vs. time. Fig. 5 shows the LBT setup as well as a typical data trace overlaid with the ST6 trace, which is the nozzle reservoir pressure and provides the trigger mechanism for all NID systems. The time delay between the peak of the reservoir pressure and the minimum in beam transmission caused by debris from the flow starting process is due to the nozzle transit time.

When a plot of average beam transmission during the estimated run time of the facility vs. nozzle stagnation pressure is constructed, as shown in Fig. 6, it appears that a nozzle stagnation pressure of 1000 atm. is almost like a barrier. That is, if the pressure is less than 1000 atm, the beam transmission is excellent; if the

pressure is greater than 1000 atm, then the flow is optically thick. The data shown here are only for runs where the nozzle throat material was the same, specifically, a tantalum-tungsten steel alloy that has proved to be the most durable throat material used to date.

Assuming a geometric extinction cross section, a 50 μm diameter monodisperse particulate size distribution based on witness plate sample analysis, and a uniform spatial distribution, a particle number density of 57.2 particles/cm³ can be estimated for the flow during the predicted run time. Assuming a 5 ms erosion/ablation period and predominantly iron for the material, then approximately 15 g are eroded.

Based on the PMIE results, a two-layer model that has a different particle density in the flow core than in the shear layer can be invoked. Using this model, the core particle number density is 8.1 particles/cm³, and the shear layer density is 339.6 particles/cm³.

PLIF

Dual Nd:YAG/dye/WEX laser systems and beam shaping optics are used to generate two overlapping sheets of laser radiation at nominal 226 nm wavelengths exciting transitions in the NO gamma bands (see Fig. 7). Temperature is obtained from the fluorescence intensity ratio and NO number density can be obtained from the least temperature sensitive fluorescence signal [2-3] providing a proper calibration has been obtained. The two laser pulses are temporally separated by approximately 300 ns. The observed PLIF sheet dimensions are typically 3 cm wide and 17.5 cm in length with the sheet thickness maintained at approximately 0.5 mm to prevent saturation of the excitation transition. The fluorescence images are obtained with a pair of ICCD cameras with intensifier gatewidths of 300 ns. The PLIF images are obtained at a nominal 1.6 ms from the ST6 pulse. The PLIF freestream rotational temperature data that have been reduced to date are shown in Fig. 8. It can be seen that, as the data is reduced taking into account the effects of absorption [4-6] and vibrational non-equilibrium, the measured values approach predictions. As an indication of the uniformity of the flow, Fig. 9 shows the variation of normalized intensity ratio across the flow, and the location of the shock at the model is clearly observed.

FILRAY

The copper vapor laser system has an additional output at 578.2 nm, and this second beam was brought into the Impulse Facility in a direction almost directly opposed to the general flow velocity vector as shown in Fig. 10. The Rayleigh scattered light from a point along the laser beam in the flow core was collected and imaged through a gaseous iodine filter onto a PMT. The spectral line shape of the copper laser overlaps a number of molecular iodine transitions, and the use of the filter serves to prevent laser radiation scattered from test cell surfaces from reaching the PMT. When facility flow is established, the Doppler-shifted Rayleigh scattered light is passed by the iodine filter. Because the Rayleigh scattering cross section for the helium driver gas is approximately 80 times smaller than for the test gas, the signal begins to drop steadily as the helium driver gas arrives. As shown for Run No. 26 in Fig. 10, the helium driver gas begins to arrive at approximately 2.6 ms past ST6. The data shown are raw data, and the signal trace has not been normalized to account for laser beam transmission variations.

LDA

Non-naturally occurring Rubidium (Rb) was seeded into the driver gas, and the presence of the Rb was detected with absorption spectroscopy using a tunable laser diode operating at a nominal 780.2 nm. Potentially, flow temperature and gas velocity can also be determined from the absorption spectral profile. This technique had been previously demonstrated at the DLR/HEG [6].

The LDA system is shown in Fig. 11 and primarily consists of a GaAlAs single mode laser diode operating at approximately 5-mw continuous laser power. The laser is wavelength tuned across the Rb absorption line at 780.2 nm at a 15 kHz rate by varying the laser diode current. The laser wavelength is monitored by directing a portion of the laser beam through a Rb reference cell. Absorption in both the reference cell and the test facility is monitored by silicon photodiodes, and the output is recorded on a high-speed digital oscilloscope. In the laboratory shock tunnel the laser beam path was through the shock region just in front of the model.

In the laboratory shock tube, experiments were performed with either the driver gas or test gas seeded with RbNO_3 . Shown in Figure 12 is a reduced data set for a laboratory shock tunnel run with seeding in the driver gas. LDA transmission data is obtained as a function of time from the beginning of the run and as a function of laser wavelength or frequency. The data is presented three dimensionally in Fig. 12. An integrated absorption history clearly indicates the arrival of the helium driver gas. By picking the point in time where the driver gas has arrived, a Rb spectral absorption profile can also be obtained.

The LDA apparatus was set up at the Impulse Facility as it was for the laboratory shock tunnel. However, in this case the laser beam was directed through the test cell free stream approximately 4.5 inches (11.4 cm) below the model tip. The Impulse Facility was seeded with RbNO_3 on the driver gas diaphragm or on the wall just upstream of the diaphragm. Shown in Fig. 13 is a reduced data set for Run 33. The arrival of the helium driver gas is clearly indicated at ~2.6 ms from ST6.

ES

Emission spectroscopy was used to monitor the self-radiation from the Impulse Facility flow. Radiation from the flow was imaged onto the entrance slit of a small spectrometer, and an ICCD was used for detection. Through pixel binning, eight 6.1-mm vertical regions near the nose of a calibration rake's hemispherical probe or nose of the test article were observed. This provided spectra from the bow shock region out into the free stream. For the early Impulse Facility runs the spectra obtained near 256 nm were dominated by iron and copper lines. For later runs the spectra near 780 nm showed rubidium, potassium, copper, iron, and aluminum. The rubidium was observed as a consequence of seeding the driver gas. No species were found to interfere with the Rb transition being probed by the LDA system.

HSFV

The HSFV system for obtaining temporally-resolved shadowgraph and schlieren images of the flow over the test article is shown in Fig. 14. The heart of the system is the high pulse rate copper vapor laser system and its companion rotating drum streak camera. The optical setup

uses a 12-inch (600 mm) Z-path Schlieren layout with spherical mirrors having a 90-inch (2.29 m) focal length. Because the window clear aperture was 11 inches (280 mm), the system f-number was approximately 8. The copper vapor laser's green line (533 nm) was used for visualization purposes and the yellow line (578 nm) was split off and used for other diagnostics. A correction optic was used on the receiver side to reduce the astigmatism induced by the optical system. The image aperture and drum speed were selected depending on the number of frames and the frame rate desired for a given facility run. While the drum camera is actually a streak camera, the narrow pulse width of the laser performs a pseudo-framing function. Imaging was performed in either the shadowgraph or schlieren mode depending on the test situation.

Figure 15 is a partial image of an actual camera filmstrip and shows the initiation of Impulse Facility Run 31. The frames were recorded with the laser operating at 15 kHz (one pulse every 66.7 μ s) and triggered by the shock tube gage pulse, ST6. Emission from the starting process upstream appears to add illumination in the first four frames. The delayed establishment of flow over the model between the fourth and fifth frames is consistent with the model nose temperature and pressure traces. The arrival of the starting shock at the model nose can also be seen superimposed on the filmstrip as the bright flash in the fourth and fifth frames. The hot nose continued to emit through frame eight, as indicated by the bright streak along the film centerline. Impingement of a particle from the starting process can be observed as a small flash and deformation of the bow shock in frame nine.

Analysis of the shock shape data as a function of time from ST6 provided a clear determination of useful run time as shown in Fig. 16. Indeed, the run time agreed well with facility code predictions of helium driver gas arrival.

SUMMARY AND CONCLUSIONS

An ambitious, but successful, NID program has been executed at the AEDC Impulse Facility. No facility-related operational problems were encountered with the possible exceptions of boundary layer and recirculation effects on LDA measurements and potential copper absorption effects on HSFV. Further measurement emphasis will be on LDA for flow velocity and PEBF for vibrational temperature.

Facility flow is established within 0.67 ms from the shock tube gage (ST6) trigger pulse, and a nominal run time of 2.5 ms free from driver gas effects is available for nozzle stagnation pressures less than 1000 atmospheres. Facility flow appears optically thick as a result of particulate scattering for nozzle stagnation pressures greater than 1000 atmospheres. Measured NO rotational temperatures are in agreement with calculated values only under the assumption of vibrational non-equilibrium.

REFERENCES

1. Blanks, J. R. and DeWitt, J. R. "Calibration Test of AEDC Free-Piston Shock Tunnel," AIAA-94-2526, presented at the 18th AIAA Aerospace Ground Testing Conference, June 20-23, 1994, Colorado Springs, CO.
2. Smith, M. S., Price, L. L., and Williams, W. D. "Laser induced fluorescence diagnostics using a two-line excitation method," AIAA J 31, 478-482 (1993).
3. Ruyten, W. M., Williams, W. D., and Heltsley, F. L. "Computational Flow Imaging for Planar Laser-Induced Fluorescence Applications," AIAA-94-2621, presented at the 18th AIAA Aerospace Ground Testing Conference, June 20-23, 1994, Colorado Springs, CO.
4. Ruyten, W. M., Smith, M. S., and Williams, W. D. "On the role of laser absorption in planar laser-induced fluorescence imaging of high-enthalpy flows," Shock Waves, Vol. 2, Proceeding of the 20th International Symposium of Shock Waves, Pasadena, CA, July 23-28, 1995, pp. 1639-1644.
5. Ruyten, W. M. "Comparison of Calculated and Measured Temperature Fields in the AEDC Impulse Facility," AIAA-96-2237, presented at the 19th Advanced Measurements and Ground Testing Technology Conference, New Orleans, LA, June 17-20, 1996.
6. Ruyten, W. M., Smith, M. S., Price, L. L., and Williams, W. D., "Three-Line Fluorescence Thermometry of Optically Thick Shock-Tunnel Flow," Applied Optics, Vol. 37, No. 12, April 20, 1998, pp. 2334-2339.
7. Trinks, Ole, "Diode laser-Atomic absorption spectroscopy of atomic Rubidium in the high enthalpy tunnel HEG for determining flow velocities and gas temperatures," DLR-IB 223-97 A31, September 1997.

ILLUSTRATIONS

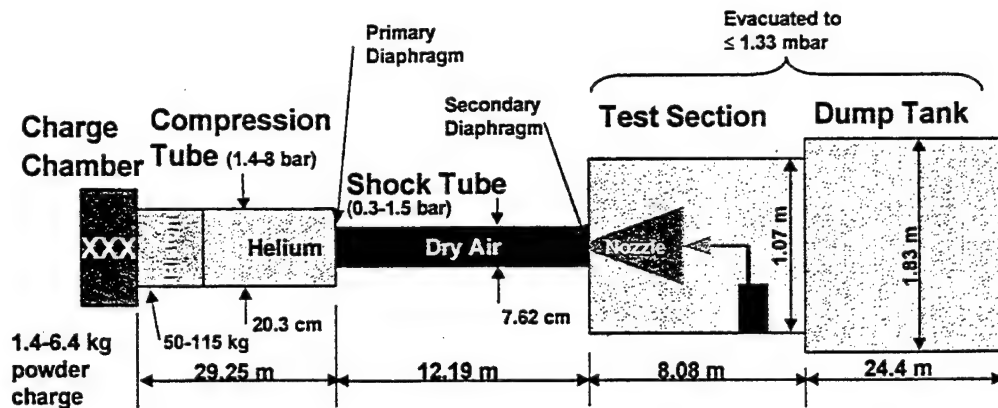


Fig. 1 AEDC Impulse Facility

POWDER CHAMBER	2 PRESSURE TRANSDUCERS
COMPRESSION TUBE	6 PISTON PROBES
HIGH PRESSURE SECTION	2 PRESSURE TRANSDUCERS
SHOCK TUBE	6 PRESSURE TRANSDUCERS
FACILITY RECOIL	1 LVDT
NOZZLE	12 PRESSURE TRANSDUCERS
DATA RECORDERS	48 CHANNELS LECROY 6810
TEST SECTION FLOW	Flow Field Rake: 13 Pressure Transducers Cal. Model: 4 Pressure Transducers 5 Coaxial Thermocouples Probe: 5 Coaxial Thermocouples

Fig. 2 Standard Facility Instrumentation

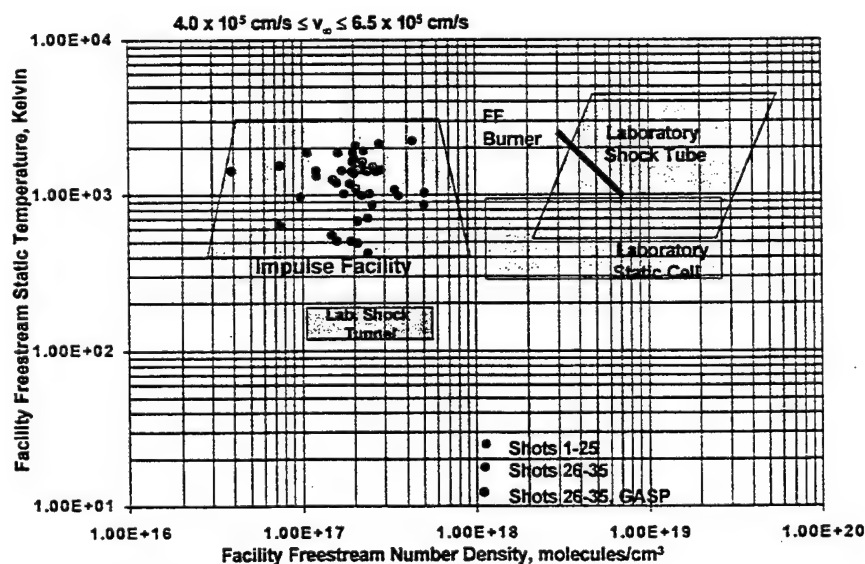


Fig. 3 Impulse Facility Free Stream Conditions

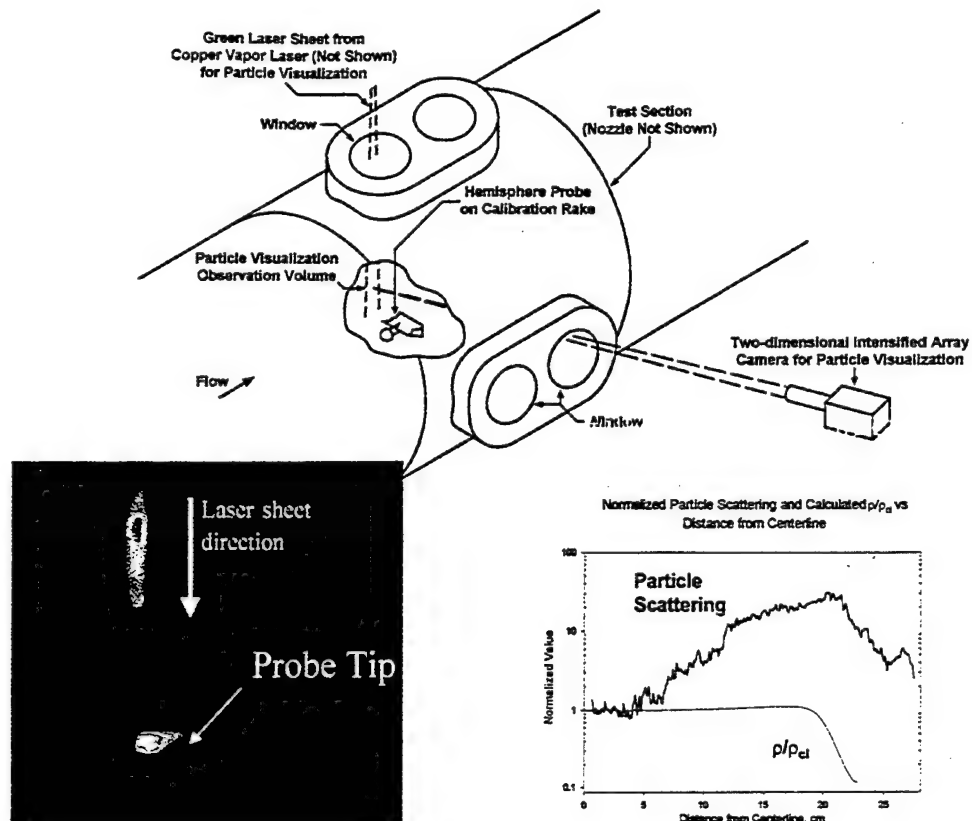


Fig. 4 Filtered Rayleigh Scattering at the Impulse Facility

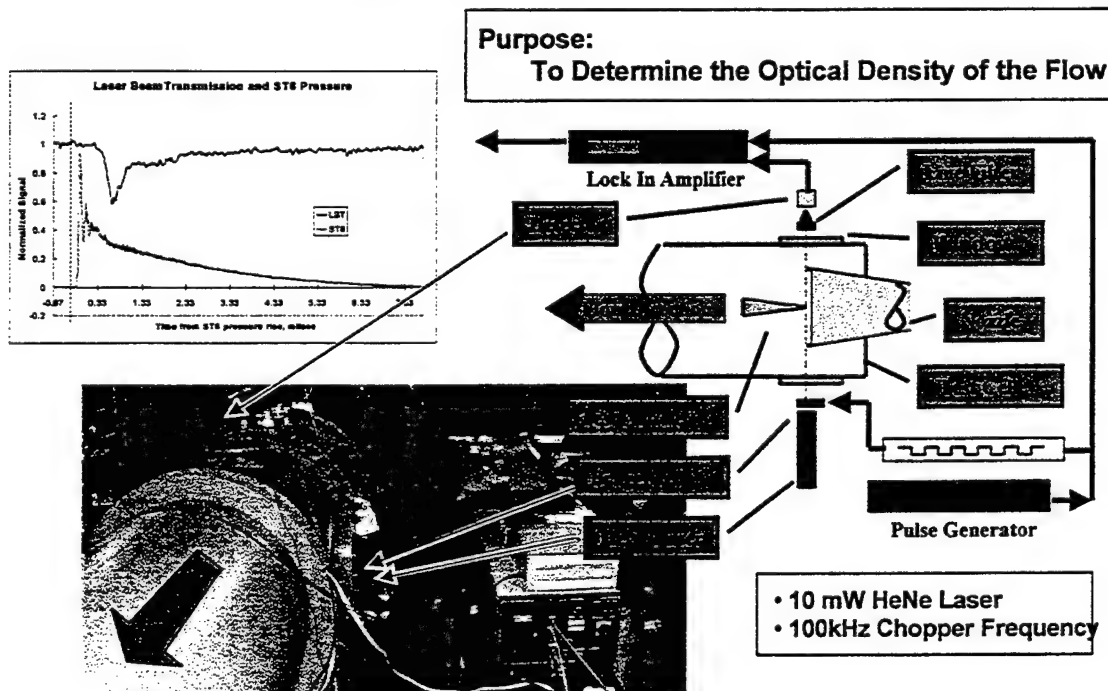


Fig. 5 Laser Beam Transmission (Non-Absorbing) at the Impulse Facility

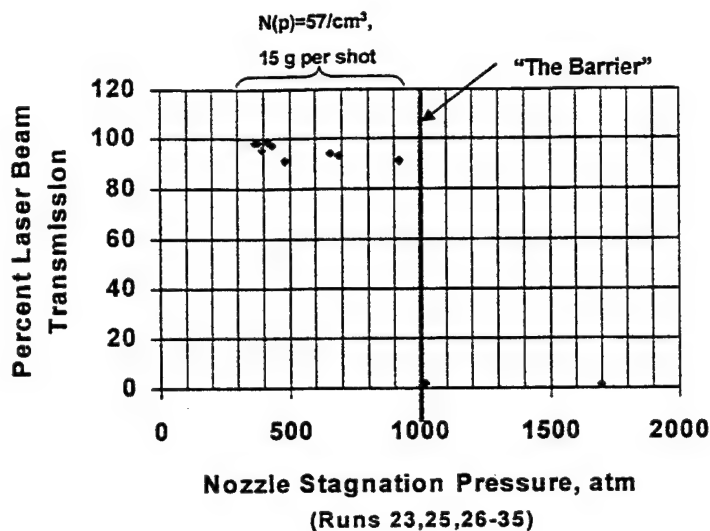


Fig. 6 LBT Data vs. Nozzle Stagnation Pressure

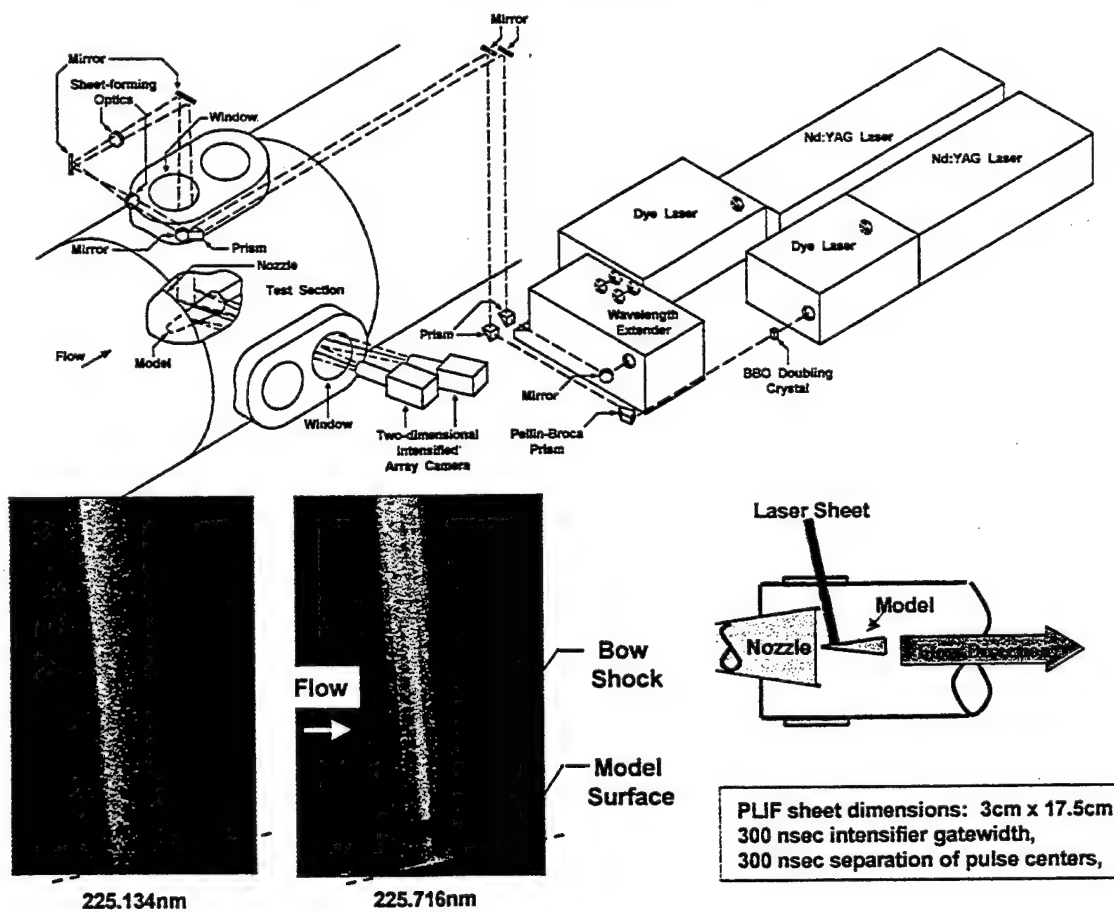


Fig. 7 Planar Laser-Induced Fluorescence at the Impulse Facility

Run No.	Time after ST6 (ms)	T_{∞} (K) (Isentropic Estimate)	T_r (K) ($T_v = T_r$)	T_r (K) ($T_v =$ 3000K)	T_r (K) (GASP, $T_v = 2900$ K)
21*	1.6	1382	350	750	661
23*	1.6	1356	400**	575	608
24*	1.6	1923	340	700	641

* Measurement point is 18.5
cm from outer edge of flow.

** Different excitation
transition used.

Fig. 8 Free Stream Rotational Temperatures Deduced from PLIF Data

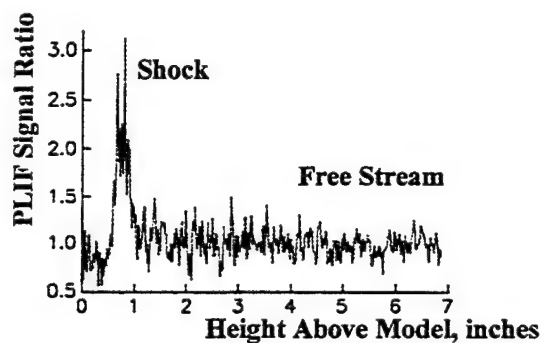
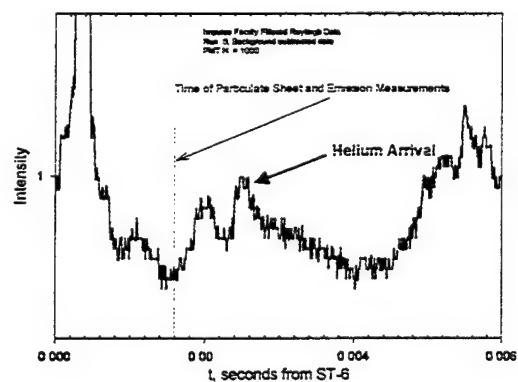
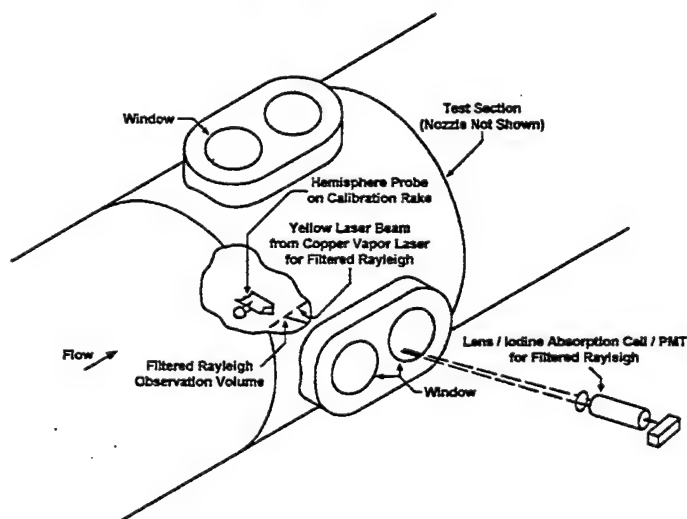


Fig. 9 Spatial Uniformity of Rotational Temperature (Run 35)



Filtered Rayleigh Data

Fig. 10 Filtered Rayleigh Scattering at the Impulse Facility

General Characteristics of LDA System:

- Sharp LT027MD laser diode
- 780.2 nm wavelength
- 5 mw output
- 30 GHz scan width
- 15 KHz scan rate
- ILX Lightwave Model LDC 3714 controller
- Silicon photodiode detectors
- Rubidium Nitrate ($RbNO_3$)

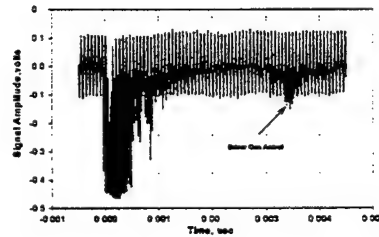
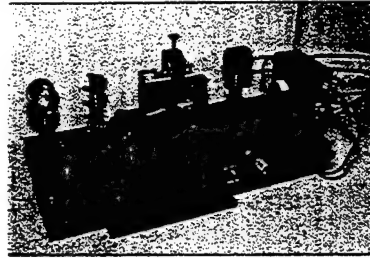
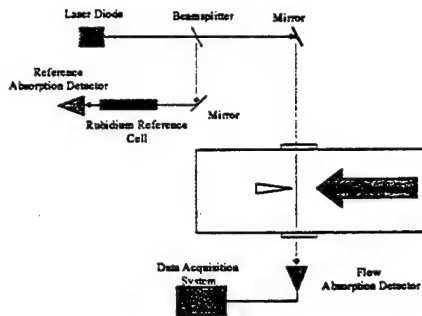


Figure 11 Laser Diode Absorption at the Laboratory Shock Tunnel

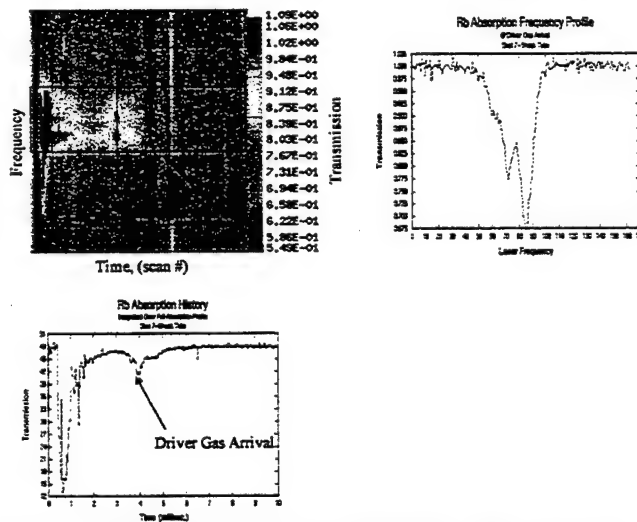


Figure 12 LDA Data from the Laboratory Shock Tunnel

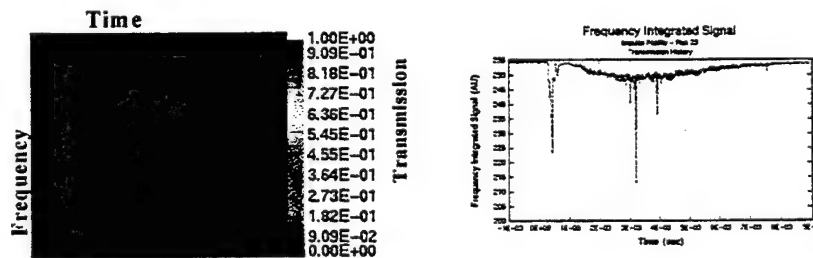


Figure 13 LDA Data from Impulse Facility Run 33

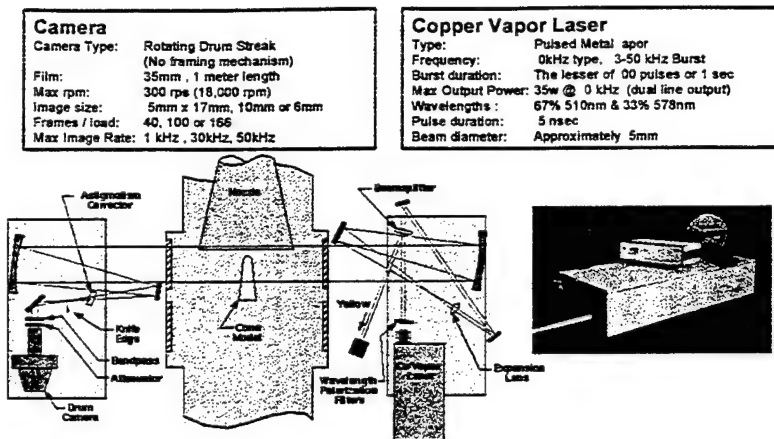


Figure 14 High Speed Flow Visualization System at the Impulse Facility

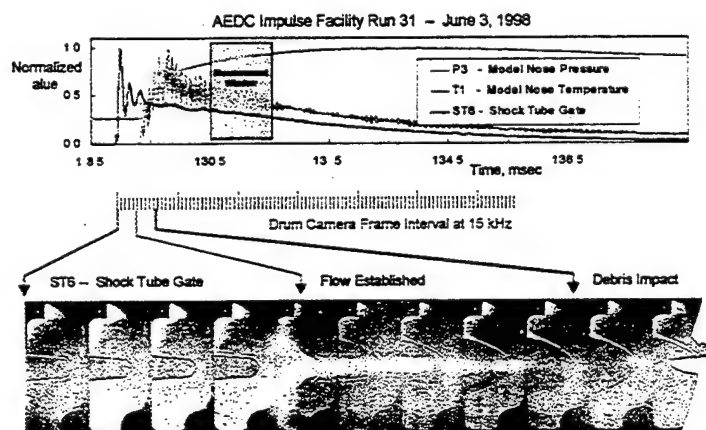


Figure 15 HSFV Images from the Impulse Facility

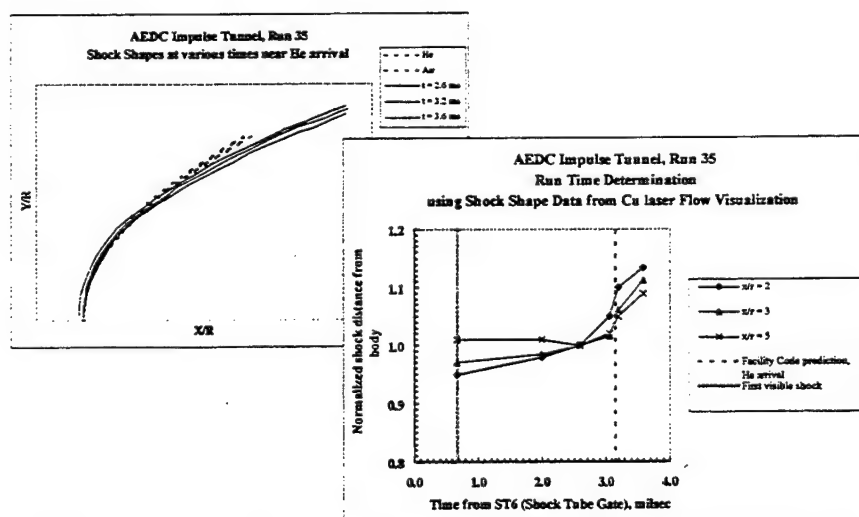


Figure 16 Analysis of HSFV Images for Facility for Run Time Determination

A Comparative Study of Planar Mie and Rayleigh Scattering for Supersonic Flowfield Diagnostics

Uwe Brummund, Bérangère Mesnier[#]
DLR Lampoldshausen, Germany
Langer Grund
D-74239 Hardthausen a.K.
[#]Université d'Orléans

Abstract

Planar Mie and Rayleigh Scattering has been applied in a supersonic ramjet model combustion chamber (Scramjet chamber) which allow for the direct visualization of the fluid shear/mixing layer zone along the central axis of the combustion chamber. Hydrogen was injected parallel to the center line of the combustion chamber through holes at the base of an injector plate into a Mach 2.0 air flow. The evolution of shear/mixing layer downstream of the injector part has been visualized by laser light sheet scattering directly from the gas molecules (Rayleigh scattering) or from TiO₂ seed particles (Mie scattering). The laser-based optical techniques reveal details of the turbulent structure of the supersonic mixing process by single shot measurements and allow for the direct determination of the absolute visual shear/mixing layer thickness by averaged image processing. Compared to former experimental investigations applying the optical schlieren method significant smaller values of the absolute shear/mixing layer thickness have been measured by planar Rayleigh scattering and even smaller ones by planar Mie scattering. This difference is partly due to the different measurement techniques used and the different definitions of the shear/mixing layer thickness. Nevertheless the measured shear/mixing layer growth rates agree with previous results by other experimenters, confirming the

compressibility effect of decreasing shear/mixing layer growth rates with increasing compressibility. Furthermore a slight but significant shear/mixing layer growth rate enhancement has been measured by shock/shear layer interactions.

Introduction

There has been considerable experimental activity in the field of compressible turbulent shear layers in recent years. These activities have been inspired by the effort to develop scramjet engine technology and to understand compressible turbulent shear flows. Progress has been made in understanding compressible free shear/mixing layers by the availability of improved computational resources for numerical investigations and also by the development of non-intrusive laser-based optical diagnostic techniques for detailed experimental studies of this fundamental flow.

The most common methods of flow visualization for compressible shear/mixing flows are the optical schlieren and shadowgraph methods [1]. These methods, however, integrate spatially and temporally through the flow and can give a misleading picture if the flow is inherently three-dimensional. Furthermore, the details of the

mixing process are usually not revealed in such integrated methods. The need for instantaneous planar cuts has long been recognized and several laser light sheet methods have been demonstrated in supersonic flows [2-6]. It has been shown that the planar Rayleigh scattering technique is well suited to measure the concentration field of turbulent gas jets and to obtain qualitative as well as quantitative information about the turbulent nature of the flow [7-8]. The advantage of Rayleigh scattering is that no seed material is needed, it is directly proportional to the molecular density, so that shock waves and turbulent structures are observable. The lower Rayleigh scattering intensity in comparison to the Mie scattering intensity can be much enhanced using ultraviolet laser sources due to the ω^4 frequency scaling of the Rayleigh scattering cross section. Background scattering from optical surfaces as well as from particles in the flow can be significantly reduced due to the poor reflectivity in the far ultraviolet. Using the Mie scattering method it is necessary to seed the flow eventually leading to misinterpretation of the flowfield due to multiple scattering, laser sheet attenuation and difficulties in uniformly seeding high-speed flows. On the other hand Mie scattering delivers very high signal intensities (much higher than Rayleigh scattering intensities) even far downstream the hydrogen injection. This advantage opens up the possibility to measure the shear/mixing layer thickness of the highly turbulent flow at far downstream positions where it is no longer possible to measure with the Rayleigh scattering technique due to the very low contrast ratio between the air and hydrogen streams. One task of this work is to describe the capabilities and limitations of both techniques for compressible shear/mixing layer analysis in supersonic flows. The other task of the work is to present a technique for rapid and efficient mixing of fuel and oxidizer which is crucial for supersonic ramjet (scramjet) propulsion.

Background

Compressible free shear / mixing layer

In order to clarify the notion shear layer and mixing layer we assume the following: two uniform parallel streams (i.e. air and H_2) with different velocities $u_1 > u_2$ are flowing from an injector plate in a constant area duct. A so called shear layer will be generated at the interface between the two streams, in which momentum and vorticity is transported laterally from the faster to the slower stream. If thermal and mechanical energy as well as mass (molecules) are transported laterally and the two streams have different molecular identities (as is the case for air and H_2), the shear layer is also a mixing layer, as denoted by the dashed curve in figure 2. The mixing layer thickness δ_m is defined as the region within which the mole fractions of air and fuel differ by one percent or more from their respective values in the unmixed streams. The distance downstream of the injector plate at which a significant amount of mixed fluid is first present is called the mixing transition point [11]. Following this mixing transition, it is known that the time-averaged mixing layer is observed to grow approximately as a constant fraction of the shear layer in the fully developed region of the shear layer [12]. It has to keep in mind that there are many different ways the shear layer thickness has been defined in literature, i.e. the visual shear layer thickness δ , the $10\%\Delta U$ thickness, the pitot thickness, the momentum layer thickness θ , and the vorticity thickness δ_ω [13]. In our study we use the visual shear layer thickness δ_{vis} defined as the full width at half maximum (FWHM) of the cross sections of the Rayleigh and Mie scattering images. The most well-known effect of compressibility on shear layers is the reduction of the growth rate $d\delta/dx$ that occurs as compared to that of

incompressible layers at the same velocity and density ratios. The reduced growth rate was thought to be due to the density difference between the streams that occur under compressible flow conditions. It was shown that the density effect was small and that the growth rate reduction must be due to a separate and stronger compressibility effect [14]. This compressibility effect is quantified by the convective Mach number M_c which is the Mach number of the two freestreams relative to the large scale structures in the mixing layer

$$M_c = \frac{U_1 - U_2}{a_1 + a_2}, \quad (1)$$

where u_i ($i = 1, 2$) is the freestream velocity of air and H_2 and a_j ($j = 1, 2$) is the speed of sound of air and H_2 , respectively.

For comparison with data from literature the growth rate $(d\delta/dx)_{com}$ of the compressible shear/mixing layer has been normalized using the incompressible growth rate

$$\left(\frac{d\delta}{dx}\right)_{inc} = C_\delta \cdot \frac{(1-r) \cdot (1+r)}{1+r \cdot \sqrt{s}}, \quad (2)$$

with $s = \rho_2/\rho_1$ and $r = U_2/U_1$ and $C_\delta = 0.17$ as a constant for pitot and schlieren flow visualization. This constant is not exactly known for Rayleigh and Mie scattering visualization. The decreasing mixing layer growth rate is in contradiction to the aim of a fast and effective mixing in supersonic flows. One possibility to enhance this growth rate is the interaction of a shock wave with the mixing layer. This study has been done by varying important parameters like the shock strength (by variation of the upper wall angle) and the convective Mach number M_c by varying the temperature of H_2 and air, respectively in order to perform a parametric study of the influence of these parameters on the growth rate enhancement.

Laser Rayleigh and Mie Scattering Technique

A brief overview of the advantages and limitations of the used laser based optical techniques (planar Rayleigh and Mie scattering) will be given.

Rayleigh scattering is the elastic (i.e. unshifted) scattering of light quanta from molecules and is not specific to the molecules causing the scattering. Thus, the technique cannot be used for individual species concentration measurements, but only for total number density. Nevertheless, due to the fact that the Rayleigh scattering cross section σ_i is different for different gases it is possible to detect a two component gas flow (like H_2 and air in this case) as long as the gas components are not totally mixed. Generally the Rayleigh technique suffers from low signal intensities due to the very low Rayleigh scattering cross sections ($\sigma \approx 10^{-27} \text{ cm}^2/\text{sr}$). As the Rayleigh signal is proportional to the fourth power of the laser frequency, the scattering efficiency can be enhanced by the use of uv laser excitation. Due to the very low intensity of Rayleigh scattering dust filters must be interposed in the coflow to avoid Mie scattering. Rejection of ambient light was achieved with high efficiency (up to 10^6) by using gated intensified detectors synchronized with the pulsed laser excitation. Great care must also be taken to eliminate the parasitic laser reflections that cannot be excluded by time or wavelength filtering since Rayleigh radiation is scattered with neither delay nor specific frequency shift. In spite of the severe precautions that have to be taken, the detected signal has been corrected for the residual stray light contributions. In order to correct for stray light problems test images are taken before and after each test run. Furthermore the background level was measured before each test run and subtracted from the detected images. In clean environments (like in H_2 /air flows) planar Rayleigh scattering is very advantageous

because no seeding is required, preventing misinterpretation due to dispersion of seed particles [14].

An alternative to Rayleigh scattering is to take advantage of the large scattering cross sections of particles. Mie scattering cross sections are ten to twenty orders of magnitude stronger than Rayleigh processes, leading to very strong signal intensities, even if the two gas streams mix very far downstream the injector plate. The Mie scattering cross section for a given laser radiation depends on specific properties of the particles (size, shape, index of refraction...) and on the optical configuration (polarization, scattering angle, collection aperture...) through the very complex Mie scattering theories and calculations [11], that are beyond the scope here. The flow must be properly seeded with particles (TiO_2 , $\varnothing=0.3\text{ }\mu\text{m}$, Kronos Titan). The seeding process has to be performed very carefully. Multiple scattering and extinction has to be negligible. The optical extinction depth must be lower than 0.1, which corresponds to a number density lower than 10^{13} m^{-3} for $1\text{ }\mu\text{m}$ size particles uniformly distributed over 10 cm [12]. This low extinction regime as well as the particle mass flow rate is very difficult to preliminarily controlled and has not been done in this study. Furthermore, the seeded particles must have small inertia to accurately track the fluid motion and density fluctuations. The incoming flow must be uniformly seeded with dry particles (to prevent agglomeration) at a constant rate. The particles were seeded through a cyclone seeder upstream the hydrogen injection and were dried before each test run. During the experiments it was observed that the injection rate varied, which was not corrected by reference measurements.

Experimental Setup

Test Facility

The details of the supersonic test facility has been described elsewhere [15] - therefore only a brief summary will be given here. The test facility is a modular setup, consisting of a separate air heater, a hydrogen support line equipped with an H_2/O_2 burner for heating up the hydrogen.

The air can be heated by a H_2/O_2 precombustion. The maximum total temperature is $T_t=1500\text{K}$ at a maximum mass flow rate of 3 kg/s. The H_2 can also be heated up by a fuel rich precombustion. The maximum total temperature is $T_t=1100\text{K}$ with a maximum mass flow rate of 50g/s. The estimated mass fraction of steam in the air supply was less than 2%. Typical test run times were 15-20 s.

Supersonic model combustion chamber

The scramjet model combustion chamber has a rectangular cross-section of 40 mm x 50 mm and a length of 300 mm. The measured test section has a length (x direction) of $x=240\text{ mm}$ and a height of $y=40\text{ mm}$.

Hydrogen is injected parallel by a 6 mm thick plate located in the center of the chamber. At the base of this injection plate six bores in a row are manufactured as laval nozzles with a Mach number of $M_{\text{H}_2}=2.0$. The leading edge of this injection plate is located upstream the laval nozzle of the air supply (Mach number $M_{\text{air}}=2.0$), so that no shock train can be initiated at this plate.

The shocks itself were generated by a wedge plate located at the upper wall of the combustion chamber, acting as a shock generator. The shock strength has been varied by changing the inclination angle of the shock generator ($\theta=7^\circ$ and 15°). The

position of the shock-mixing layer interaction was fixed to $x=40\text{mm}$ in this study, whereas in former experiments applying the schlieren and pitot probe technique we choose locations at $x = 40\text{mm}$, 60mm and 100mm [10]. The Reynolds numbers $Re = U \cdot l / \nu$ ($l=6\text{mm}$) calculated for air vary between $Re = 7.0 \cdot 10^5$ to $4.1 \cdot 10^6$ and from $Re = 6.4 \cdot 10^5$ to $8.0 \cdot 10^5$ for H_2 , respectively. Due to condensation effects it was not possible to cover the whole convective Mach number range ($Mc=0.7-1.2$), so that we had to limit this range to $Mc=0.8-1.0$. The combustion chamber was equipped with uv transmittive suprasil quartz windows from all four side in order to allow full optical access.

Laser System

An commercial excimer laser system (Lambda Physik LPX 150T) was employed for the Rayleigh and Mie scattering experiments. The KrF laser works in the deep uv at 248 nm . The laser energy was typically 250 mJ per pulse with a pulse duration of $\sim 15\text{ ns}$ which is essentially instantaneous to freeze the flow. Spherical and cylindrical lenses were used to form the rectangular laser band into a thin sheet (0.3 mm thickness, $40 - 60\text{ mm}$ width) which was then directed into the centerline of the combustion chamber initiating the scattering process. The emitted light (from Rayleigh or Mie scattering) was detected under 90° by an intensified charge-coupled device (CCD) camera via a uv-light-sensitive lens (UV-Nikkor 105mm , $f/4.5$). The CCD chip has a resolution of 384×286 pixels, 12 bit per pixel. A personal computer with special acquisition software controls the laser and the imaging system. The evaluation of the acquired CCD images was also possible with this software.

Results and Discussion

Figure 3 shows an over 20 laser shots averaged Mie scattering image of the supersonic H_2 /air mixing layer without any shock-mixing layer interaction for a convective Mach number $Mc=1.0$. This picture is a composite image consisting of five images taken at different axial locations of the chamber for five different test runs. The flow direction is from left to right. The image corrections have been made as described previously. As can be seen the mixing layer is spreading along the combustion chamber. Furthermore it can be recognized that it was possible to image the whole mixing layer along the combustion chamber. The reduced signal at $x = 160 - 180\text{ mm}$ is probably due to insufficient seeding of the TiO_2 particles at that location and test run conditions.

From these images the absolute shear/mixing layer thickness (visual thickness) has been estimated in the following way: at a selected location of the combustion chamber (x axis) a cross section of the image has been taken resulting in a one dimensional profile. The full width at half maximum (FWHM) of such a profile has been defined as the visual shear/mixing layer thickness δ . By measuring the so defined shear/mixing layer thickness at different locations along the combustion chamber the shear/mixing layer growth rate $d\delta_{vis}/dx$ can be calculated.

The corresponding Rayleigh scattering image has been measured between $x=0-180\text{ mm}$ (not seen here). The Rayleigh scattering cross section ratio between air and H_2 is approximately $\sigma_{air}/\sigma_{H_2} \approx 4$, so that pure hydrogen appears as dark region at the centerline of the combustion chamber due to the four times lower Rayleigh signal strength. In the vicinity of the H_2 injector the shear/mixing layer can be measured with reasonable contrast ratio. Further downstream this contrast ratio is much reduced due the enhanced mixing leading to

much higher errors in estimating the mixing layer thickness. It was not possible to take high quality images along the whole combustion chamber length as was the case for Mie scattering. Comparing the absolute visual layer thickness measured with the two laser based techniques the mixing layer thickness is an increasing function with increasing distance x downstream the injector as was expected. An unexpected result was that the shear/mixing layer thickness measured by Mie scattering is in any case smaller than measured by Rayleigh scattering. In order to analyse this result we have also made a comparison between former visual layer thickness measurements performed by optical schlieren measurements and that performed by the laser techniques. In any case the visual shear/mixing layer thickness are highest measured by the schlieren method. Differences of measured absolute shear/mixing layer thicknesses have also been observed by Samimy et. al [13]. These differences can be explained by the different definitions of the shear/mixing layer thickness made by the different authors. In our case this difference can be explained as follows (see also figure 2): for the schlieren method the absolute visual shear/mixing layer thickness has been estimated „by eye“ measuring the border line between the air and H_2 flow. Of course this is a somewhat subjective method. (This was one reason for applying laser based methods in order to get an objective measurement method for determining the shear/mixing layer thickness). As can be seen from figure 2 this line exactly defines the edge of the shear layer resulting in the highest values for the visual thickness. On the other hand Mie scattering only detects the edge of the H_2 flow because only this part is seeded by the TiO_2 particles, leading to the smallest values for the thickness. With Rayleigh scattering we finally measure values lying in between the ones measured by schlieren and Mie scattering.

The growth rate of the compressible mixing layer $\delta'_{com} = (d\delta_{vis}/dx)_{com}$ has been determined by fitting the slope of the curve of δ_{vis} along the x axis for each measurement technique. In order to compare the experimental results with known data from literature, it is necessary to define the normalized mixing layer growth rate, which is the ratio of the compressible mixing layer growth rate to that of the incompressible one $\delta'_{com}/\delta'_{inc} = (d\delta_{vis}/dx)_{com} / (d\delta_{vis}/dx)_{inc}$ at the same velocity and density ratios.

From our former pitot and schlieren measurements we have measured a lot of data spanning a much broader range of convective Mach numbers ($M_c = 0.7 - 1.2$). A fit to these measured experimental data is given by the following relation:

$$\delta'_{com} / \delta'_{inc} = 0.7 \cdot e^{-2.5 \cdot M_c^2} + 0.3 \quad (3)$$

This relation is used as a reference for the compressibility effect of the mixing layer studies and also as a reference for the shock/shear layer interaction studies. These data along with known data from literature are represented in figure 4. (The fitted curve is represented by the solid line in figure 4). This Figure shows the normalized mixing layer growth rate $\delta'_{com} / \delta'_{inc}$ in dependence of the convective Mach number M_c , which is a measure of the compressibility. As can be seen the mixing layer growth rate is reduced as the compressibility of the layer increases. This result is in good agreement with results from literature [13]. The Rayleigh and Mie scattering results have been compared with our former experiments [10] using pitot probe and optical schlieren measurements. All values of the normalized mixing layer growth rates measured by laser optical diagnostics are all a little bit lower than the pitot and schlieren measurements as can be expected from the determination of the shear/mixng layer thickness as described above. Nevertheless the trend of reduced

shear/mixing layer growth rates with increasing compressibility is well reproduced. In order to analyze the effect of the shock interaction with the shear/mixing layer a shock wave was generated at the upper chamber wall which was inclined by 7° and 15° , respectively. Rayleigh and Mie scattering experiments have been performed for the same convective Mach number range as for the compressibility studies. The performed images reveal the influence of the shock wave on the mixing layer. It can be recognized that the mixing layer is deflected downstream due to the shock impingement. Furthermore the mixing layer seems to be spread a little bit more after the shock impingement. In order to resolve the shock/mixing layer interaction process we have also performed single shot Rayleigh scattering. These images give good insight into the details of the shock mixing layer interaction process, showing that the reflected shock wave initiates vortices, rolling up the mixing layer and thereby enhancing the spreading of the mixing layer. The visual mixing layer thickness has been measured for the three different test cases ($M_c=0.8, 0.9$ and 1.0) by variation of the wedge angle of the shock generator (7° and 15°) and a fixed shock-mixing layer interaction region located at $x=40\text{mm}$. The comparison of the normalized mixing layer growth rate with shock interaction (for 7° and 15° wedge angle) together with the fitted curve of equation (2) show that all data points with shock interaction lay above this fitted curve, confirming that there is growth rate enhancement due to the shock impingement. For a wedge angle of 15° the data scatter is a little bit higher than for the 7° case. Nevertheless for the 15° wedge angle the shear/mixing layer values are higher than for the 7° case, showing that stronger shock/shear layer interaction leads also to enhanced growth rates.

Conclusions

An experimental investigation in a non-reacting $M=2.0$ supersonic combustion chamber has been performed in order to study the behavior of compressible mixing layers in high speed flows. The visual shear/mixing layer thickness has been measured by means of laser-based optical diagnostics, (Rayleigh and Mie scattering). The highly turbulent flow has been visualized and the structures have been resolved by single shot images. From averaged images the evolution of the shear/mixing layer has been revealed with Rayleigh scattering showing that a reduced contrast ratio between hydrogen and air far downstream the injector complicates a unambiguous estimation of the shear/mixing layer. In order to remove this unambiguousness Mie scattering has been applied which gives much higher signal strength. Due to this fact it was possible to image the shear/mixing layer along the whole combustion chamber length. The laser based measurements deliver lower absolute shear/mixing layer thicknesses compared to former schlieren measurements due to the definition of the visual shear/mixing layer thickness (FWHM). Nevertheless the mixing layer growth rate of the compressible shear/mixing layer determined by Rayleigh/Mie scattering show the same as the schlieren measurements, confirming the fact that there is a reduction of shear/mixing layer growth rate in dependence of compressibility. Furthermore this study shows that shear/mixing layer growth rate enhancement is possible by shock/mixing layer interaction. Slight but significant enhancement of the shear/mixing layer growth rate has been measured in dependence of the shock strength.

References

- [1] Chinzei, N., Masuya, G., Komuro, T., Murakami, A., and Kudou, K., "Spreading of Two-Stream Supersonic Turbulent Mixing Layers", *Physic of Fluids*, Vol. 29, May 1986, pp. 1345-1347.
- [2] Clemens, N. T., Mungal, M. G. Berger, T. E. and Vandsburger, U.; "Visualization of the structure of the turbulent mixing layer under compressible conditions", AIAA Paper 90-1978, 1990.
- [3] Smith, D.R., Poggie, J., Konrad, W., Smits, A. J.; "Visualization of the structure of shock wave turbulent boundary layer interactions using Rayleigh scattering", AIAA Paper 91-0460, 1991.
- [4] Clemens, N.T. and Mungal, M.G., "A planar Mie Scattering technique for visualizing supersonic mixing flows", *Exp. Fluids* 11, 175-185, 1991.
- [5] Gross, K.P., McKenzie, R.L., Logan, P. "Simultaneous Measurements of Temperature, Density, and Pressure in supersonic Turbulence Using Laser-Induced Fluorescence". *Exp. Fluids* 5, 1987.
- [6] Fletcher D.G., McDaniel, J.C. "Laser Induced Iodine Fluorescence Technique for Quantitative Measurement in a Nonreacting Supersonic Combustor," *AIAA Journal*, Vol. 27, No.5 May 1989.
- [7] Escoda, M.C., and Long, M.B., "Rayleigh Scattering Measurements of the Gas Concentration Field in turbulent Jets", *AIAA Journal*, Vol. 21, No.1, 81-84, 1983.
- [8] Miles, R., and Lempert, W., "Two-Dimensional Measurements of Density, Velocity and Temperature in Turbulent High-Speed Air Flows by UV Rayleigh Scattering", *Applied Physics B*, Vol. 51, 1-7, 1990.
- [9] Papamoschou, D., Roshko, A., "The Compressible Turbulent Shear Layer: An Experimental Study", *Journal of Fluid Mechanics*, Vol. 197, Dec. 1988, pp 453-477.
- [10] Menon, S. "Shock-Wave induced Mixing-Enhancement in Scramjet Combustors," AIAA Paper No. 89-0104, 1989.
- [11] Murthy, S.N.B., and Curran, E.T., (eds.), "High-Speed Flight Propulsion Systems", AIAA Progress in Astronautics and Aeronautics Series, Vol. 137, Washington, DC, 1991.
- [12] Heiser, W.H., and Pratt, D.T., "Hypersonic Airbreathing Propulsion", AIAA Education Series, American Institute of Aeronautics and Astronautics, Washington, DC, 1994.
- [13] Samimy, M., and Elliot, G.S., "Effects of Compressibility on the Characteristics of Free Shear Layers", *AIAA Journal*, Vol.28, No. 3, March 1990.
- [14] Brown, G.L., and Roshko, A., "On Density Effects and Large Structure in turbulent Mixing Layers", *Journal of Fluid Mechanics*, Vol.64, pp.775-816, 1974.
- [15] Waidmann, W., Alff, F., Böhm, M., Brummund, U., Clauss, W., and Oswald, M., "Supersonic Combustion of Hydrogen/Air in a Scramjet Combustion Chamber", *Space Technol.*, Vol.15, No.6, pp 421-429, 1995.

Figures

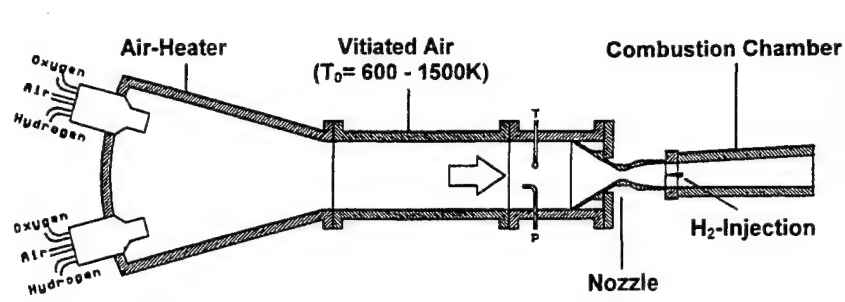


Fig. 1: Experimental setup of the supersonic test facility.

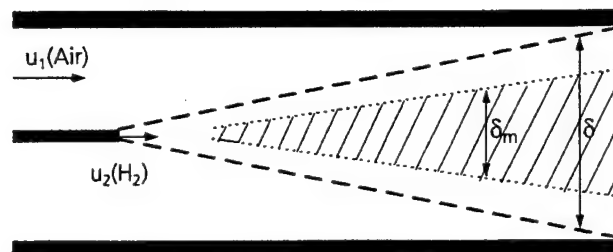


Fig. 2: Definition of the shear layer and mixing layer. The dashed area indicates the mixing layer.

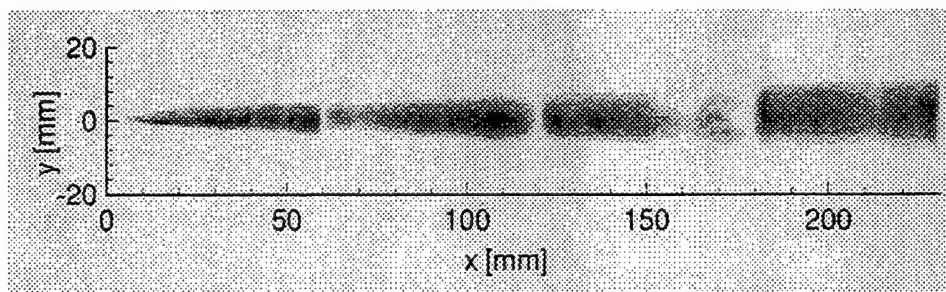


Fig.3: Mie scattering image of the mixing layer zone without shock interaction (over 20 laser shots averaged).

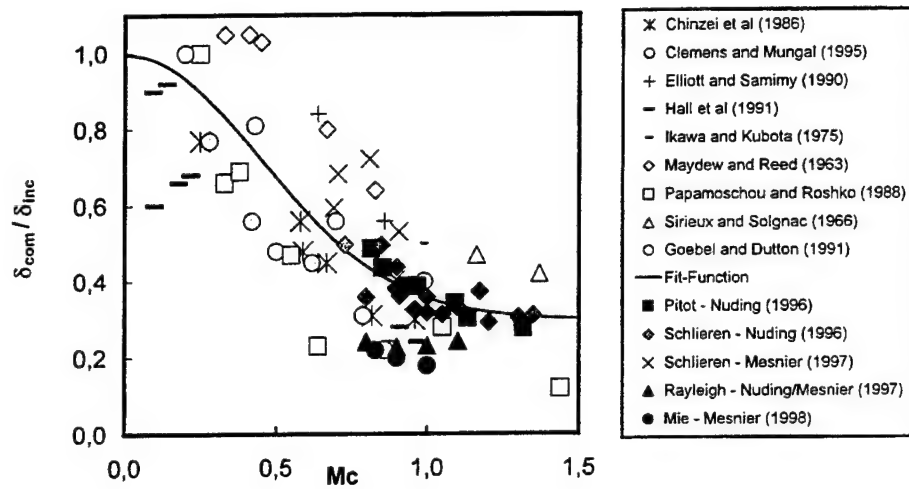


Fig. 4: Comparison of the normalized growth rate with data from literature.

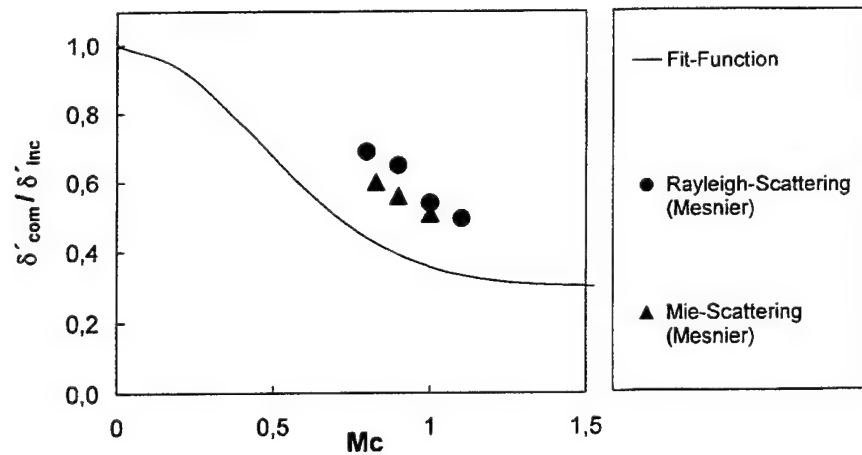


Fig. 5: Normalized growth rate with shock/shear layer interaction (wedge angle 15°).

AUTHORS BIOGRAPHIES



ARCHAMBAUD, Jean-Pierre, graduated from the Ecole Nationale Supérieure de Mécanique et d'Aérotechnique de Poitiers, France, in 1970. He joined the Aerodynamics Research Department of ONERA in Toulouse, France, in 1974. He worked in the field of Wall Adaptation and Passive Shock Control at the T2 Wind Tunnel.

Since a few years, he is involved in activities about Boundary Layer Stability and Transition Phenomenon at the ONERA/DMAE in Toulouse, France. *Page 35.1*



BANASZAK, David : graduated from the University of Wisconsin with a BS degree in Electrical Engineering. He received a MS degree in Applied Statistics from Wright State University. Since 1971, he has worked for the Air Vehicle Directorate of the Air Force Research Laboratory as a project and instrumentation engineer. He is responsible for marking acoustic, vibration and loads measurements for numerous Air Force test programs in the laboratory and the field.

Dave is a member of the AIAA, IEST and ASA.

Page 27.1



BARRICAU, Philippe worked at the ONERA (Office National d'Etudes et de Recherches Aérospatiales, French Aeronautics and Space Research Center) / DMAE T2 Wind Tunnel, from 1991 to 1994, in Toulouse, France. In 1997, he graduated from Institut National des Sciences Appliquées, where he made a special study of Applied Physics. Since 1998, he has worked in the field of instrumentation applied to aerodynamics. He is in charge of developing the optical arrangement of Doppler Global Velocimetry system.

Page 9.1



BAUST, Henry D. : holds a Bachelor of Science Degree in Electrical Engineering and a Master of Science Degree in Computer Science. His 28 years working for the Air Force has evolved around wind tunnel testing. He has been involved with the design and installation of specialized measurement instrumentation, data systems, and control systems.

Most recently he has been involved with optical flow field diagnostics systems.

Page 20.1



BECKER, S. received his diploma in Fluid Mechanics at the Technical University Dresden in 1986 and his doctor degree in 1996 for an investigation on the flow behind rectangular obstacles.

Since 1991 he is working at the Institute of Fluid Mechanics, University Erlangen-Neremberg. His interest was focussed on laser sensors to wind tunnel applications and in-flight measurements for studies of boundary layer transition. *Page 20.1*



BOUVIER, Florence, graduated from Ecole Nationale d'Ingenieurs en Mecanique Energetique of Valenciennes, France and received her Master's Degree in Fluid Mechanics from Valenciennes University, in 1989.

She joined ONERA Experimental Aerodynamics Department, France, in 1989 and currently working with Pressure Sensitive Paint (PSP). *Page 19.1*

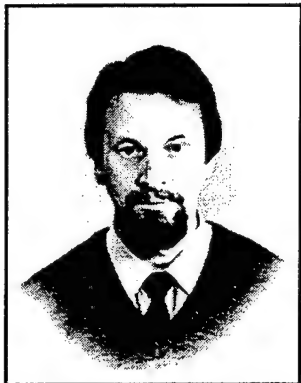


BRUMMUND, Uwe, 1978/79 : Practical course of mechanical engineering at compagny Brötje (Household Burner Development). 1979/82 : Engineer of Technical Physics, University of Applied Science Lübeck. 1982/85 : Physics (Scientific Course)-Physicist, University Göttingen. 1985/87 : Diploma-Thesis at Max-Planck-Institute Göttingen. 1988/92 : Ph. D. Thesis at Institute of Physical Chemistry University Göttingen. 1992/96 : German Aerospace Center, DLR - Optical Diagnostic Group, Application of laser based techniques to combustion systems, Laser Induced Fluorescence - Spontaneous Raman Scattering - Rayleigh Scattering - Mie Scattering. 1997 : Head of the Supersonic Combustion Group - Mixing & Combustion, Studies in supersonic model chambers, Studies of the behaviour of compressible mixing layers Ignition and flame stabilization studies for supersonic flows fuel injector studies and development. *Page 42.1*



BÜTEFISH, K. A. received his degree of Dipl.-Phys. (1965) in nuclear physics from the University of Göttingen. He joined the AVA today DLR and became responsible for measuring techniques in rarefied gas flows. In 1969 he obtained the degree of Dr. rer. nat. for his work on electron beam technique.

Since 1981 he has responsibility for a group concerned with measuring physics in the field of fluid mechanics. *Pages 10.1 - 14.1*



BYKOV, Anatolii was born June 18, 1950 in Arhangelskaja reg. (Russia, North), nationality-Russian. Since 1968 to 1974, he studied in Moscow Institute of Physics and Technology (MPhTI). After graduation of MPhTI in 1974, he had entered by Junior Researcher to Central Aerohydrodynamic Institute (TsAGI). Doctor of Science is from 1985. Now, he is Senior Scientist in TsAGI's Measurement Technics Department.

His professional interest consists methods and means in experimental aerodynamic. The total list of the publications of Anatolii Bykov includes more then 30 titles and more 20 patents.

Page 17.1



CARRERE, Alain born in 1947, is graduated of ENSICA (Ecole Nationale Supérieure d'Ingénieurs de Constructions Aéronautiques), Toulouse, France, in 1971.

Engineer in the Aeronautical Center of Toulouse, France, from 1971 to 1977. Then in charge of the Propulsion Laboratory of SUPAERO, Toulouse, France. Since 1981, he is Professor and Head of the Energetics and Propulsion Department. He is in the same time part time Research Engineer at ONERA, Toulouse, France, in charge of the Research Laboratory LAMEP.

Page 8.1



CARSCALLLEN, Bill received his undergraduate degree in Mechanical Engineering i, 1973, a Masters degree in 1974 and a PhD in 1990 from Queen's University at Kingston, Ontario. In 1976, he received an Honours Diploma from the Von Kerman Institute for Fluid Dynamics. Presently, he is Head of the Gas Turbine Aerodynamics and Combustion Group within the Aerodynamics Laboratory of Institute for Aerospace Research at the National Research Council of Canada.

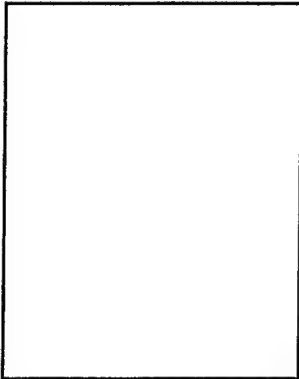
Page 39.1



CHARBONNIER Jean-Marc was born in 1963 in Jonzac, Charente-Maritime, France. He graduated from the ENSMA Poitiers (France) in 1986 as mechanical engineer specialized in fluid dynamics. He worked as mechanical engineer in a test center of the ministry of defense (CEL), Biscarosse (France) and as research engineer in detonics at SNPE-CRB, Le Bouchet (France). Then he joined the aerodynamic laboratory of the research center (CEAT) of the University of Poitiers for a PhD research on the interaction of a jet with a transverse cross flow which was presented in 1992. Since 1991, he joined the Aeronautics / Aerospace Department of the von Karman institute for fluid dynamics in (Belgium) as assistant and then associate professor.

His area of research involves high speed aerodynamics in particular in hypersonic regime and low speed unsteady flows.

Page 30.1



CLARK, Edward L. : received a BSME from the University of Missouri-Rolla and a MAE from Cornell University. From 1957 to 1966 he was a project engineer with ARO, Inc., at the USAF Arnold Engineering Development Center, responsible for testing in the 50-Inch Hypersonic Tunnels B and C. From 1966 through 1994 he was a staff member at Sandia National Laboratories with responsibility for experimental aerodynamics measurements on research vehicles and weapons. He conducted over 50 tests in ground test facilities, covering subsonic through hypersonic velocities in air and low velocities in water. He has published numerous reports and papers on testing techniques, time series analysis, and uncertainty analysis.

Since 1994, he has been a consultant with Sandia providing advice on experimental programs in aerodynamic and hydrodynamic facilities. *Page 38.1*



COTON, Patricia : Engineer working in the Department for System Control and Flight Dynamics (DCSD) of ONERA (Office National d'Etudes et de Recherches Aérospatiales, French Aeronautics and Space Research Center) in Lille, France, responsible for the theme "Flight-Environment".

In charge of studies relative to modelling of aircraft behaviour in adverse environmental conditions, and involved in research relative to the characterisation of aircraft wake vortices by means of scaled model flight tests. *Page 1.1*



DALE, Gary A. : received his BS in Systems Engineering from Wright State University in 1979 and his MS in Aerospace Engineering from the University of Dayton in 1984. He has worked for the U.S. Air Force Research Laboratory for 20 years. His work has spanned a wide variety of responsibilities in instrumentation, and test article design and development for the wind tunnel facilities operated by the Air Vehicles Directorate. These include a trisonic facility, vertical wind tunnel, water tunnel, 7 x 10 ft subsonic, and 3 hypersonic facilities. His most recent work has focused in the area of luminescent paints for pressure and temperature measurements.

He has been a member of the IEEE Instrumentation in Aerospace Simulation Facilities (IASF) Panel since 1993 and is currently Vice-Chairman. He is also a member of the American Society of Mechanical Engineers. *Pages 20.1-21.1- 27.1*



DEOM, Alain was born in 1948. He is graduated from the Conservatoire National des Arts et Métiers, in Electronics in 1977. He is worked at ONERA (Office National d'Etudes et de Recherches Aérospatiales, French Aeronautics and Space Research Center), France, since 1970 and is currently head of the Experiment Mechanics and Instrumentation Unit of the Structures and Damage Mechanics Department. His main fields of activity are rain erosion testing, flight sensors development for reentry vehicles, ultrasounds and photothermal measurements. *Page 29.1*



DIETERLE, Lutz : studied mineral processing at the Technical University of Clausthal-Zellerfeld, Germany, and made his Diploma in mining December 1992.

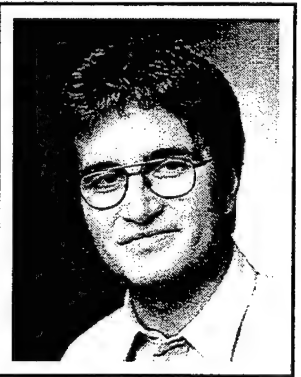
He worked first as a Dechema-scholar and afterwards as a scientific employee at the Institut für Mechanische Verfahrenstechnik und Umweltverfahrenstechnik of the TU Clausthal. November 1996 he got his Ph.D. in mechanical process engineering with a thesis on the development of a Particle Image Velocimetry (PIV) system for microscopic turbulent flows.

Since March 1997 he has worked at the Institut für Strömungsmechanik of the DLR, in Göttingen, Germany. He is responsible for the planning and implementation of PIV measurements in industrial wind tunnels. *Page 1.1*



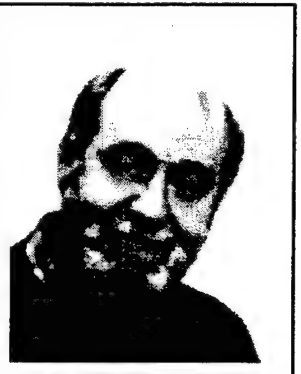
DURST, F. received his diploma degree in aerospace engineering at University Stuttgart in 1967, and his Ph.D. in 1972 at Imperial College of London for the thesis "Development and Application of Optical Anemometers".

In 1982 he was appointed Professor at the University of Erlangen-Nuremberg and is the head of the Institute of Fluid Mechanics. *Page 25.1*



EHRENFRIED, Klaus : study of physics at the University of Göttingen, Germany. Diploma in physics February 1988. Title of the Diploma thesis : "Dynamic of Laval-nozzle flow at different boundary conditions". Ph.D. thesis at the University of Göttingen. Ph.D. degree in physics June 1991. Title of the Ph.D. thesis : "Numerical investigation of vortex-airfoil interactions in transonic flows".

From 1991 to 1993 researcher at the Max-Planck-Institut für Strömungsforschung in Göttingen. Worked in the field of numerical simulations of transonic flows with vortices. From 1993 to 1998 researcher at the Institut für Strömungsmechanik of the DLR. Numerical and experimental work in the field of sound generation in flows with vortices. Since 1998 scientific assistant at the Technical University of Berlin. Teaching and research in the field of aeroacoustics. *Page 1.1*



ENGLER, Rolf was born in Bad Essen, Germany, in 1944. In 1969, he received his Dipl. Ing. degree at the Ing.-Academy of Wolfenbüttel in the field of air conditioning. After three years in industry, he started a study at the University of Göttingen. He received his Dipl.-Physiker degree in 1979 for vortex investigation using Ultrasonic pulses. In 1986, he received the Dr. rer. nat. degree for experimental investigations of vortex breakdown using a newly developed non intrusive technique - the Ultrasonic-Laser-Method. He was still engaged to develop nonintrusive methods for flow field and surface investigations and temperature measurements. Since 1991, he works on pressure sensitive paint techniques PSP in different wind tunnels of DLR and Europe. Since 1995, he is the project leader of the PSP team at DLR Göttingen and created with his team an DLR-PSP-Intensity system for various speed ranges as well as the PSP-Lifetime technique. *Pages 22.1-23.1-24.1*



ESCURE, Cyril : Ph. D. Student

Education : Ing., 1997, ENSIL (Engineering School of Limoges), department of surface treatment and materials. "Diplôme d'Etudes Approfondies" : Ceramics Materials and Surface Treatment.

Research in the field of plasma spraying. Particular interest in the particles impacts phenomena : experimental study of the interaction of plasma sprayed particles on a solid or liquid surface, particle diagnostic (PDA, Pyrometry, Imaging technics).

Page 12.1



FAUCHAIS, Pierre : Professor, Director of P2LM, In charge of the "Diplôme d'Etudes Approfondies : Matériaux Céramiques et Traitements de Surface".

Education : Dr. Ing., 1962, ENSMA (Aeronautic) Engineering School in Poitiers, D. Sc., 1968, University of Poitiers.

Research : actively involved in research work in the areas of plasma diagnostics, chemical synthesis, plasma furnaces, and thermal spray-coatings. He has authored numerous papers, directed more than 50 Ph.D.'s, given numerous invited lectures.

Honors : ASM-TSS Hall of Fame 1998.

Page 12.1



FEIST, J. P. : graduated from the Gerhard-Mercator University Duisburg, Germany, in Physics in 1996. His final year (Diplomarbeit) was carried out at the Joint European Torus (JET), Oxfordshire, UK. There he worked in the 'Visible and Charge Exchange Spectroscopy Group' on quantitative spectroscopy measurements. Since 1997 he has been registered for a Ph.D. in the Mechanical Engineering department of Imperial College London, UK, as a research assistant.

His work involves the assessment of thermographic phosphors for high temperature gas turbine applications.

Page 6.1



FONOV, Sergey was born in Ufa, Russian Federation, in 1951. In 1973, he received his Dipl. Ing. Degree at the Moscow Institute of Physics and Technology in the field of Experimental Aerodynamics. From 1973 to 1998, he worked in TsAGI (Central Aerodynamics Institute, Zhukowsky, Russia) in the Division of Measurement Technique. The main fields of interest were optical methods for flow field visualization ; model deformations and position measurements. In 1982, he received the Dr. Degree for development of methodology of rotor blade deformation measurements. Since 1988, he works on pressure and temperature sensitive paint techniques as well as other optical methods for wind tunnel measurements. Currently, Sergey Fonov continues this work in German Aerospace Center (DLR, Göttingen). Dr. S. Fonov is author of more then 50 scientific papers and patents.

Pages 22.1-23.1-24.1



FÖRSTERMANN, M. received his degree in Physics in 1998 from the University of Göttingen. In 1996 he joined the Institute of Fluid Mechanics at the German Aerospace Center (DLR) in Göttingen.

He works on Doppler Global Velocimetry with emphasis on the development of time resolved 3 Dimensional DGV and its application to wind tunnel testing.

Page 10.1



GEORGE, A. was born in Rielasingen, Germany, in 1947. In 1967, he received a technical degree of the Lyceum in Saint-Louis, France. The same year he joined the Franco-German Research Institute ISL in Saint-Louis, France. He has been involved in several optical measuring problems applied to high-speed gasdynamics.

He still works in this field with emphasis now in developing several special optical flow diagnostic techniques.

Page 11.1



GRIMAUD, Alain : Engineer at the University of Limoges.

Education : Ph. D., 1973, University of Limoges

Activities: In charge of design , improvment and use of all processes involving arc plasma (APS,VPS ,PTA,...).

Page 12.1



GUILLE, Marianne was born in Tours, france, in 1975. In june 1998, she received her engineering diploma from EPF, engineering school (Paris, France), option aerospace engineering. She enrolled in August 1997 as a Master's student in the School of Aeronautics and Astronautics at Purdue University with a specialization in aerodynamics and in January 1998, started working as a research assistant at the Purdue Aerospace Sciences Laboratory, in the field of luminescent pressure and temperature sensitive paint. She is expected to receive her degree in December 1999.

Page 16.1



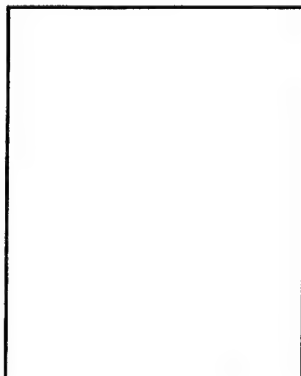
HANFF, Ernest obtained his B.A.Sc. at the University of Toronto and M.E.Sc. as well as Ph.D. from the University of Western Ontario. He has worked in the field of dynamic testing, maneuvering aerodynamics and aerodynamic modeling at the Institute for Aerospace Research, National Research Council of Canada, where he holds the position of Head of the Aircraft Dynamics Group. He is a member of the IASF Panel and received the TTCP Award for Excellence in Research on Combat Aerodynamics in 1996.

Page 28.1



HELTSLEY, Fred : was born in 1943 in Greenville, Kentucky, USA. He received a Bachelor of Science in Aerospace Engineering (BS AsE) in 1966 from the University of Cincinnati in Ohio. From 1967 to 1980 he did graduate work at the University of Tennessee Space Institute. He has worked from 1962 to present at the Arnold Engineering Development Center (AEDC), during which time, he has been employed by ARO, Inc, Calspan Corp., and Microcraft. He is currently an Engineering Specialist in Applied Technology for Sverdrup Technology, Inc., AEDC Group. His interests include non-intrusive off-body flow diagnostics, wind tunnel test techniques, and flow visualization. Previous experience includes the application of laser Doppler velocimetry, planar laser-induced fluorescence, and laser Raman spectroscopy for the investigation of plume-induced flow separation and supersonic jet plume flow diagnostics.

Page 41.1



HENFLING, John F. : earned his associate degree in electronics engineering technology from Oklahoma State University in 1977. After graduating, he worked for 5 years as a field engineer for a major computer firm in Oklahoma City, Oklahoma. In 1983, he joined the Aerodynamics Department at Sandia National Laboratories.

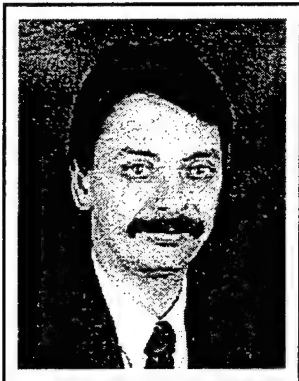
Currently, as a Distinguished Technologist, he writes data acquisition and reduction software, develops instrumentation, interfaces computers, and is in charge of operation of all of Sandia's wind tunnels. John is married, has a son and daughter, and resides in Albuquerque, New Mexico.

Page 38.1



HOLST, Hartmut : 1965-1972, study of Aerodynamics and Aerospace at University Carolo-Wilhelmina at Braunschweig, Germany. 1975-1976, Diploma Course at the Von-Kàrmàn-Institute for Fluid Dynamics in Brussels, Belgium. 1990, PhD at the University of Clausthal, Germany. 1973-Present, Research Scientist at DLR (German Aerospace Research Center), Wind Tunnel Department, and since 1994 at the DLR Institute for Fluid Dynamics at Göttingen. Research fields : 1973-1974, aeroacoustics, 1975-1976, wind tunnel wall interference, 1976-1985, low speed aerodynamics, wind tunnel corrections, 1986-1990, two-dimensional wall adaptation for 3D flows, 1991-1994, transonic flows, wall interference an wall adaptation, modernization of transonic facility TWIG of DLR Göttingen, 1994-Present, wall adaptation, residual wall interference, productivity, ventilated walls, wall corrections. Project DNW, member of GARTEUR Group.

Page 35.1



HUFNAGER, Klaus was born June 24, 1955. He is Dr.-Ing.
 1982 : Dipl.-Ing. from Darmstadt University of Technology (TUD)
 1982-1984 : Design engineer in power plant piping construction
 1984 : Research engineer on cryogenic balances at TUD
 1995 : Doctor's thesis on cryogenic balance development
 1995 : Head of wind tunnel facilities of TUD.

Page 32.1



JORDAN, Jeffrey D. : received his Ph.D. in Analytical Chemistry from the State University of New York at Buffalo in May of 1997 and joined the Optical Diagnostics Group at ISSI in June of 1997. Dr Jordan's doctoral work encompassed the development and application of sol-gel-based chemical and biological sensors. Under sponsorship of the Air Force Office of Scientific Research, Dr. Jordan has worked extensively on the development of pressure and temperature paints for turbomachinery and low-speed-flow applications. He is currently the program manager for the pressure-sensitive paint group at ISSI.

Pages 21.1-27.1



KAIBARA, Kenji : received Bachelor of Engineering in Mechanical Engineering from Tokyo Denki University, and Master of Engineering from National Defense Academy.

He currently works as a research engineer at The 3rd Research and Development Center of Defense Agency.

Page 34.1



KARATEKIN, Özgür was born in Ankara Turkey in 1971. He received his B.Sc. in 1993 and Ms.c in 1995 from the Aeronautical Engineering Department of Middle East Technical University, Ankara, Turkey. He graduated from the Diploma Course program of the von Karman institute for fluid dynamics, Belgium in 1996. Since 1996 he is a member of doctoral program at the same institute in the Aeronautics / Aerospace Department.

His current research interests are low speed unsteady flows and hypersonic boundary layer transition.

Page 30.1



KASHITANI, Masashi : received Bachelor of Engineering in Energy Mechanical Engineering from University of Ryukyu, and Master of Engineering and Doctor of Engineering in Energy Conversion Engineering from Kyushu University. He joined the Department of Aerospace Engineering at the National Defense Academy in 1998 as a Research Associate.

His research interests include airfoil characteristics in supersonic and transonic aerodynamics and flow visualization using a sharp focusing schlieren system.

Page 34.1



KHRABROV, Alexander received his Master of Science (Aerodynamics and Flight Dynamics) in 1980 from Moscow Physics and Technology Institute (MPTI), Department of Aeromechanics and Flying Vehicles. He received his Ph.D. degree from the same Institute in 1984.

Currently, he is head of unsteady aerodynamics subdivision of Central Aerohydrodynamics Institute (TsAGI). His scientific interests include development of experimental rig for unsteady aerodynamics investigation, mathematical modeling of unsteady aerodynamics in the problems of flight dynamics. *Page 37.1*



KIND, R.J. (Dick) obtained a Ph. D. in aerodynamics from the University of Cambridge in 1967. He has been with the Department of Mechanical and Aerospace Engineering of Carleton for most of his career and served as chair of the department from 1986 to 1992. He has authored numerous papers in the area of incompressible aerodynamics, with applications to wind engineering, turbomachinery and aircraft.

Page 28.1



KLEIN, Christian : He studied physics at the University of Göttingen and joined for his diploma work the Max-Planck Institute for Fluid Mechanics in Göttingen. The diploma work was an experimental investigation of turbulent channel flow using LVD. He received his diploma degree in 1994. For his following Ph. D. thesis, he investigated the application of Pressure Sensitive Paint (PSP) for transonic flows at the German Aerospace Center in Göttingen. He received his doctoral degree in 1997 from the University of Göttingen. Currently, he works as a researcher in the field of PSP applications for low-speed flows.

Pages 22.1-23.1-24.1



KULESH, Vladimir was born April 19, 1948 in Stavropol town (Russia, North Caucasus), nationality-Russian. Since 1966 to 1972, he studied in Moscow Institute of Physics and Technology (MPhTI). After graduation of MPhTI in 1974, he had entered by Junior Researcher to Central Aerohydrodynamic Institute (TsAGI). Since 1984 to present, Vladimir Kulesh is a Head of TsAGI's Optical Methods Investigations Department. Since 1990 to present, he is the Professor of Moscow Institute of Physics and Technology, Faculty of Aerohydromechanics and Flying Techniques (simultaneously with work at TsAGI).

His professional interest consists on laser, optics and electronics. Doctor of Physics is from 1979. The total list of the publications of Vladimir Kulesh includes more the 50 titles, 30 in USSR author's right Certificates and Russian Patents, 5 US Patents and 14 Patents of other lands.

Page 17.1



LEE, Richard is graduate student at Department of Mechanical and Aerospace Engineering at Carleton University, Ottawa, Canada. For his Ph. D. thesis, he has been researching the technique of dynamic manipulation of forebody vortices as a means of obtaining proportional control of side forces and yawing moments at high angles of attack. He has been employed by Canadair in Montreal and is also a graduate of the Ryerson Polytechnical Institute (currently Ryerson Polytechnical University) in Toronto.

Page 28.1



LEMPEREUR, Christine : graduated from Ecole Nationale d'Ingénieurs de Constructions Aéronautiques in 1981. Since then, she has worked in ONERA (Office National d'Etudes et de Recherches Aérospatiales, French Aeronautics and Space Research Center) Toulouse, as a research engineer. Her work focuses on the development of imaging systems for real-time 3D measurements, applied to various fields such as ship model tracking, plane model deformations in wind tunnels, quantitative flow visualization. She is now in charge of the BADGE project in ONERA, which consists in the design of a Doppler Global Velocimetry system.

Page 9.1



LEOPOLD, F. was born in Freudenstadt, Germany, on April 27, 1963. He received his Dipl.-Ing. degree in aeronautical engineering from the University Stuttgart, in 1989. In 1993, he received his Doctorate degree from the University Braunschweig. Since 1989, he works in the aerodynamic department of French-German Research Institute (ISL).

Page 11.1



LIENHART, H. graduated in aerospace engineering at University of Stuttgart in 1981. After some years of research on aerodynamics of buildings and structures, he joined the Institute of Fluid Mechanics at University of Erlangen where he is responsible for the aerodynamics group.

Since then he is mainly involved in development of test facilities and measurement techniques for wind tunnels especially based on LDA.

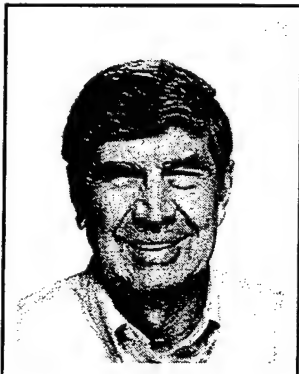
Page 25.1



LOZIER, Jean-François : Engineer working in the Department for System Control and Flight Dynamics of ONERA (Office National d'Etudes et de Recherches Aéronautiques, French Aeronautics and Space Research Center), in Lille, France, responsible for Scaled Model Flight Test Laboratory of ONERA/Lille.

In charge of tests relative to interaction of flight and environment and in particular to tests aiming at characterisation of aircraft wake vortices by means of scaled model flight tests.

Page 1.1



McBRIDE, Donald D. : received a BME from General Motors Institute, and an MSE and PhD. In Aeronautical Engineering from the University of Michigan. He went to Sandia National Laboratories in 1969 and was an analyst in reentry vehicle thermal protection until 1977. He managed the wind tunnels from 1977 until 1987 when he became manager of the Parachute Systems Division. In 1993 he felt he could no longer tolerate the managerial duties and stepped down to again become a worker bee.

Since that time he has been enjoying himself working primarily as an experimentalist in the field of high performance parachute systems.

Page 38.1



MERIENNE, Marie-Claude, began to work at ONERA, France, in 1980. She received her Engineering Diploma in Physical Measurements and Instrumentation, from the Conservatoire National des Arts et Metiers, Paris, France, in 1989.

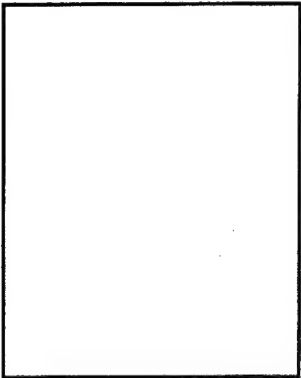
She joined the Experimental Aerodynamics Department at ONERA, France, in 1990. Since 1994, she involved in the study of the Pressure Sensitive Paint (PSP) technique.

Page 19.1



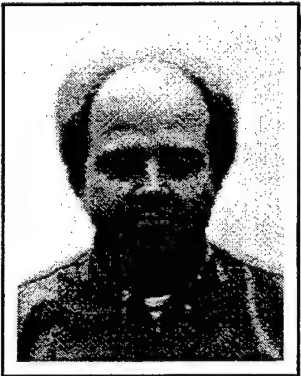
MESNIER, Bérangère : Engineer, option Aerodynamics, in 1997, University of Orleans, France.

1995 : Automobiles Citroën, Caen, France. 1996 E.D.F.-G.D.F., Orleans, France : investigation of the needs in environmental techniques of the industrial clients. 1997-1998 : DLR, Germany, 1st year of Ph.D. thesis in experimental study of the interaction between an oblique shock wave and a supersonic mixing layer, Rayleigh scattering, schlieren visualization, analysis of the layer growth and of the flowfield structure, application of a technique not used in this test facility : Mie scattering (seeding with TiO₂ solid particles). 1998 : 2nd year of Ph.D. thesis in experimental survey of turbulent variable density ratio in the near-field zone, laser tomography, Particle Image Velocimetry, determination of the 3D topological structure of flowfield, of the velocity field, estimation of the turbulence scales. *Page 42.1*



MICHELI, F. reaches his doctoral degree in Poitiers University, France, in 1985. The first studies were on the flow around the trailing edge on a pitching airfoil, both in wind tunnel and on a remote piloted vehicle equipped with a data acquisition system.

In 1990 he joined ONERA, France, in the Experimental Department, called today DAFE. The first work was to evaluate the use of LDV in a Mach 10 wind tunnel. Now, he is in charge of the improvement of LDV and works within the laser velocimetry team of DAFE. *Page 14.1*



MÖLLER, Thorsten Jens, received his degree in Physics (1993) from the University of Göttingen. Till the end of 1993, he was with the Max-Planck-Institute of Strömungsmechanik working on Sprays and Atomisation.

He joined the DLR in 1994. In 1996, he obtained the degree of Dr. rer. nat. from the University of Göttingen for his experimental and numerical work on particle laden flows. Since 1997 he is working on Doppler Velocimetry and its application to industrial simulation facilities. *Page 14.1*



MONNIER, Jean-Claude : received his doctorate in mechanics in 1990 from the University of Lille, France.

Since 1990, he is employed as a scientist by ONERA (Office National d'Etudes et de Recherches Aérospatiales, French Aeronautics and Space Research Center). He started with experimental work on problems of fundamental fluid mechanics.

Now he works mainly on the development of Particle Image Velocimetry (PIV) and its using in aerodynamic applications and in large industrial scale wind tunnels. Since 1998, he manages the PIV team of the Applied Aerodynamics Department. *Page 1.1*



ORLOV, Anatolii was born April 29, 1939 in Perm town. Since 1960 to 1965, he studies in the University of Tomsk. After graduation of the University from 1967, he had entered by Junior Researcher to Central Aerohydrodynamic Institute (TsAGI). Doctor of Science is from 1976. Now, he is Chief of Group in TsAGI's Measurement Technics Department.

His professional interest consists on the development optical measurement methods in aerodynamic. He is one of authors PSP Technology. The total list of the publications of Anatolii Orlov includes more 100 titles. *Page 17.1*



PESETSKY, Wladimir was born August 2, 1952, in Minsk, nationality-Russian. Since 1969 to 1975, he studied in Moscow Aviation Institute (MAI). After graduation of MAI in 1975, he had entered by Junior Researcher to Central Aerohydrodynamic Institute (TsAGI). Doctor of Science is from 1984. Now, he is Head of Division Maneuverable Aircraft Aerodynamics in TsAGI's Aerodynamic Department.

His professional interest consists on aerodynamic and application different methods of visualization, LVD and PSP Technology to investigation aircraft different configurations. The total list of the publications of Vladimir Pesetsky includes more the 50 titles. *Page 17.1*



ROEHLE, Ingo : Dipl.-Phys., Institute for Propulsion Technology, German Aerospace Centre (DLR), Cologne.

Studied Physics at the University in Bonn (1987-1993). Stated charier as Scientist in the field of Laser Fluid Diagnostics in 1993 at the German Aerospace Establishment (DLR) in Cologne.

Scientific activities : Doppler Global Velocimetry (DGV) - Laser-Two-Focus Anemometry (L2F) - Tracer based Shock Visualisation (TSV)

Research project at the ONERA (Office National d'Etudes et de Recherches Aéropatiales, French Aeronautics and Space Research Center) in Palaiseau in 1997.

Invitation to Lecture Series : VKI 1998, AGARD 1999, Uni-Darmstadt 1999.

Page 13.1

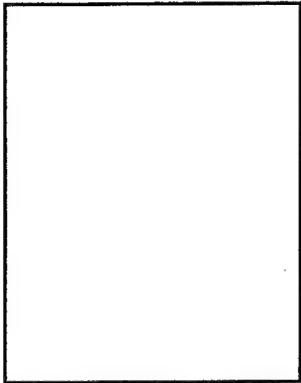


ROMICKI, Zbigniew Maciej, M.Sc. (Eng.), Institute of Aviation, Warsaw, Poland : member of Scientific Council, Head of Helicopter Group, Chief Designer of IS-2 light helicopter.

He graduated from Faculty of Aeronautics, Warsaw University of Technology (1959). In the Aerodynamic Department of IoA, he designed testing equipment for low velocity wind tunnels. Extensive expirience in R&D and manufacturing of stands for measurements of dynamic stability components of aeroplanes. In Max Planck Institute for Fluid Mechanic in Göttingen (1974-75), he studied generation and decay of turbulence and boundary layer with hot wire and ultrasound technique.

Author of 62 papers. Member of American Helicopter Society.

Page 5.1



SAITO, Teruo was engineer at Japan National Railways.

He is currently charged with the operation and maintenance of the NDA Cryogenic Wind Tunnel. *Page 34.1*



SCHEUERPFLUG, W. received his diploma degree in 1986 in aerospace engineering at the Technical University Munich. In 1992 he finished his PhD thesis at the Institute of Aeroengines at the TU Munich with a study on the measurement of fuel droplets laser techniques. After entering BMW-Rolls-Royce AeroEngines GmbH in 1991 he helped founding the advanced measurement capabilities to support compressor and engine testing.

He has some patents on imaging systems for determining temperature distributions on components by thermal paints. His special interests are pressure and temperature sensitive coatings, laser velocity measurements and the respective applications in challenging environments such as gas turbines for validation purposes. *Page 3.1*



SCHNEIDER, Gert : received his Diploma in Physics from the University of Mainz, Germany, in 1968 (experimental and theoretical work on electron scattering of 300 MeV on a C^{12} target) and he started his work at the DLR in Göttingen, Germany. From 1972 to 1973, he joined the "One Year Post Graduate Diploma Course" at the von-Karman-Institut for Fluid Dynamics in Brussels, Belgium. He returned to the DLR to join J.C. Rotta's group and to work on modelling of 3D boundary layers. In 1978, he gained his doctorate in physics from the University of Göttingen, for his theoretical investigations on turbulent boundary layers on an infinite swept wing using a 3D mixing length model. After 15 years, he moved to the experimental department of DLR-Institut für Strömungsmechanik. There he worked on detection of airframe noise sources with an acoustic mirror system. Since 1998 he works in the PIV group of the DLR in Göttingen. *Page 1.1*



SCHOLZ, D. received his degree in Physical Engineering (1980) from the TU Berlin. From 1977 till 1986 he was with the Herman Föttingen Institut für Strömungsmechanik. In 1985 he received his PhD. for his work on Vortex Induced Vibration.

Since 1986 he is working at INTA and he is responsible for a low speed wind tunnel. He is working on Laser Velocimetry since 1992. *Page 14.1*



SEILER, F. was born in Karlsruhe, Germany, in 1946. He received his Dipl.-Phys. degree in physics from the University of Karlsruhe, in 1975. He obtained his Dr.-Ing. degree at the same University in 1980. Since then, he works at the French-German Research Institute of Saint-Louis (ISL), France, where he is working with shock tubes in the field of gasdynamics. In 1992, he became the lecturer degree Privatdozent Dr.-Ing. habil. also the University of Karlsruhe in fluid mechanics and in 1998, the same University upgraded him to be Apl. Professor.

His student courses are dealing with the behavior of gases and with optical measuring techniques.

Since 1998, he is head of the Aerothermodynamics and Shock Tube Department at ISL.

Page 11.1



SEUNG, Taehun was born Feb. 9th. 1960 in Seoul, Korea. He studied Precision Mechanical Engineering at the Hanyang University in Seoul and Aeronautical Engineering at the Aachen University of Technology (RWTH Aachen), Germany, graduated as Dipl.-Ing.. He joined the scientific staff of the Experimental Aerodynamics at the Darmstadt University of Technology Germany, 1994. He works at the Wind Tunnel facility and has developed among other things a traversing rig for the low speed wind tunnel. His research interests include experimental drag analyses, aerodynamics of three surface aircraft, high lift configurations and CAD constructions.

Page 31.1



SHAMS, Qamar received the MS degree in Physics from West Virginia University and Ph.D. in Electrical Engineering from the University of Arkansas.

Since 1990 he has been engaged in cryogenic pressure sensor, smart sensing, and instrumentation research and development at the NASA Langley Research Center.

Page 36.2



SJÖRS, K. is a Master of Engineering (1980) from Lund Institute of Technology, Sweden. She works with Laser Doppler Velocimetry and Particle Image Velocimetry at the Aeronautical Research Institute in Sweden.

Page 14.1

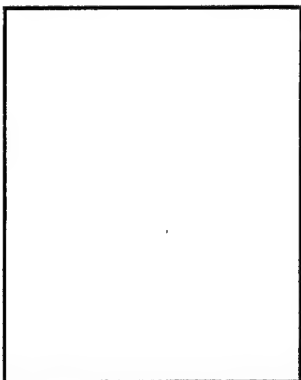


SMEETS, G. was born in Rheydt, Germany on May 28, 1935. He received the Physics Diploma and Doctorate degree from the University of Freiburg, Germany, in 1962 and 1964, respectively.

In 1964, he began working in the French-German Research Institute (ISL), being specially engaged in developing optical flow diagnostics for shock tube research.

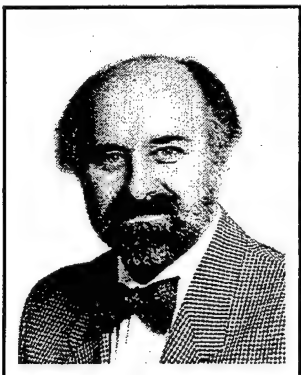
Since 1983, he is leading the Department of Gas Dynamics.

Page 11.1



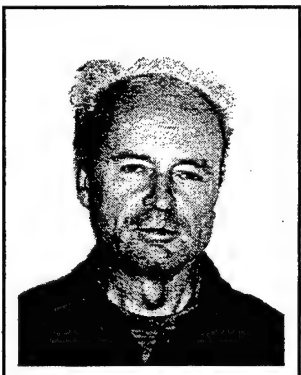
SMITH Cheryl : PhD in Control Systems applied to Industrial Systems followed by period of research in Signal Processing methods in Medical Application. Current position as Systems Engineer in Gas Turbine Products and Systems department at Rotadata Ltd.

Page 4.1



SRULIJES, J. was born in Argentina on July 5, 1947. He received his degree in Mechanical Engineering from the Technological University, Buenos Aires, Argentina, in 1972. He worked in the industry and in 1975 took up Ph. D. work at the Institute of Fluid Mechanics of the University of Karlsruhe, Germany. He obtained his Dr.-Ing. degree in 1979 with his work on cellular convection in containers with horizontal temperature gradients. From 1980 to 1983 Chief Engineer at the Institute for Theoretical Mechanics of the University of Essen. There he was mainly involved in planning a space experiment of thermocapillary migration of bubbles and drops flow in the D-1 Space Shuttle mission. Since 1984 Scientist at the French-German Research Institute in Saint-Louis, France, where he works on gasdynamics of high enthalpy flows. He has applied and participate in the development of several optical measuring techniques.

Page 11.1



STUFF Roland : he graduated from the Technical University of Aachen (Aix-la-Chapelle), Germany, in 1962 as an aeronautical engineer. The Diploma thesis was a magnetohydrodynamics.

In 1968 he obtained the Ph.D. with a thesis on the sonic boom. From 1962 to 1973 he worked at the DLR-Institut für Theoretische Gasdynamik, which was directed by Prof. Oswatitsch, and from 1973 to 1978 at the AVA Göttingen, Germany. In 1978 he became a DLR-visiting professor at the von-Karman-Institut for Fluid Dynamics in Brussels, Belgium, until 1980. From 1980 to 1983 he was back at Göttingen with AVA. Then, from 1984 to 1989 he was a professor for mechanical engineering at the King Fahad University for Petroleum and Minerals in Dhahran, Saudia Arabia. He is back to the AVA, now DLR-Institut für Strömungsmechanik, at Göttingen since 1989.

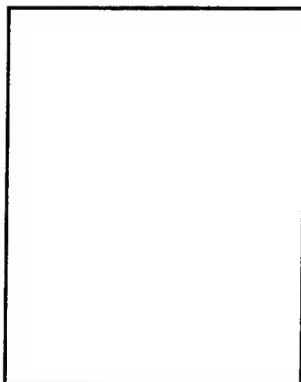
Page 1.1



SULLIVAN, John received his B.S. in mechanical and aerospace sciences with honors from University of Rochester in 1967, MS in 1969 and ScD in 1973 in aeronautical engineering from Massachusetts Institute of Technology.

Professor Sullivan has been a faculty member in the School of Aeronautics and Astronautics at Purdue University since 1975, served as Director of the Aerospace Sciences Laboratory from 1983 to 1995, and Head of the School from 1993 to 1998. His main area of expertise is in experimental aerodynamics. He is currently developing luminescent paints for pressure and temperature measurements in wind tunnels, gas turbine and flight vehicles.

Page 16.1



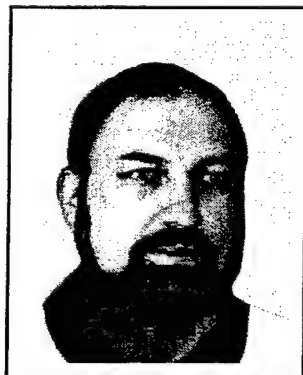
TAYLOR, Simon : DOB February 14, 1970. Degree in Manufacturing Engineering at Warwick University. Worked to date at Rolls Royce, MLH engineering, joined Rotadata 1994 as Sales Engineer, 1998 Product Development Manager.

Page 4.1



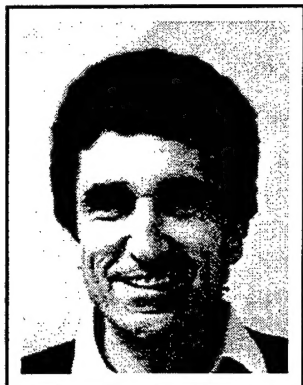
TRINKS, Ole was born in Lörrach, Germany, in 1972. After studying physics at the University of Bonn, University of Reykjavik (Iceland) and University of Göttingen, he joined for his diploma work the German Aerospace Center DLR in Göttingen. The diploma work was the development and application of non-intrusive, diode-laser based measurement technique to investigate high-enthalpy flows. He received his diploma degree in 1997. Since 1997, he works as a Ph.D.-Student in the field of Pressure Sensitive Paint. The main field of scientific interest is applied optics.

Pages 22.1-23.1



TURNBULL, Wayne, received his undergraduate degree in Physics from the Royal Military College of Canada in 1978. In 1988 he obtained a post graduate diploma in Nuclear Engineering from the Royal Naval College, Greenwich. In 1995 he received a MSc in Mechanical Engineering from Queen's University at Kingston, Ontario. He was subsequently awarded a PhD in 1998 by the same department. Presently he is a Research Officer with the Gas Turbine Aerodynamics and Combustion Group within the Aerodynamics Laboratory of the Institute for Aerospace Research at the National Research Council of Canada.

Page 39.1

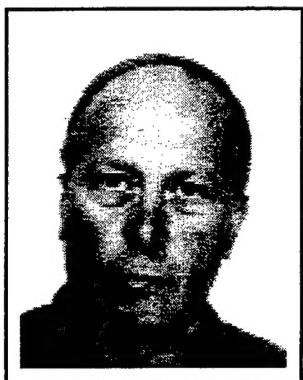


VARDELLE, Michel : Professor, in charge of the Master degree of Physics and Applications

Education : M.S., 1979, Ph. D., 1981, D. Sc., 1987, University of Limoges

Research interests include thermal spray technologies, diagnostics for high temperature processes, experimental investigation of thermal plasma-particles and interactions and particle impact on liquid or solid surfaces.

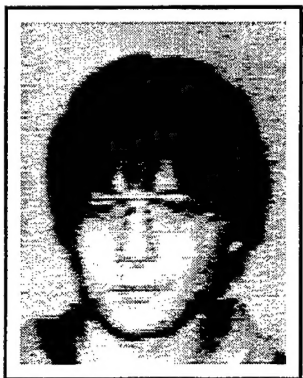
Page 12.1



VOETS, Robert was born in 1950 in Uccle (Belgium). He joined the Aeronautics / Aerospace Department of the von Karman institute for fluid dynamics in (Belgium) in 1976.

He is in charge of the experiments performed in the department in aerodynamic wind tunnels and of the de- and anti-icing test bench.

Page 30.1



WANG Frank Y. received his doctoral degree in aeronautics and astronautics from Polytechnic University (formerly "Brooklyn Poly") in New York, USA, in 1994. His thesis research involved in the characterization of vortices in supersonic streams. Subsequently, he participated in a range of activities at Polytechnic University, Flow Powers Inc., and the European Space Agency.

Since 1996, he has been at the von Karman Institute for Fluid Dynamics, Belgium conducting experimental researches in the vortex wakes of both blunt and slender bodies.

Page 30.1



WATKINS, A. Neal : received his Ph.D. in Analytical Chemistry from the University of Arkansas in 1996 and joined the Optical Diagnostics Group at ISSI in August of 1998. Dr Watkins doctoral work focused on constructing sensors and biosensors using quartz crystal microbalance technology. After completing his graduate work, Dr. Watkins took a postdoctoral position at the State University of New York at Buffalo, creating fluorescence-based sensors and biosensors, and utilizing advanced fluorescence techniques to study protein dynamics in solution and immobilized in sol-gel matrices.

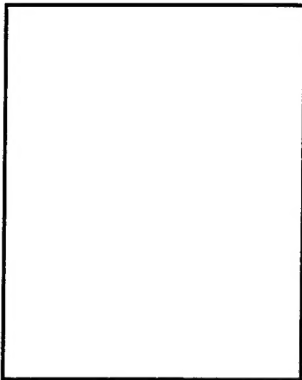
He is currently an analytical chemist in the pressure-sensitive paint group at ISSI.

Pages 21.1-27.1



WERNET, Mark has been employed at the NASA Glenn Research Center's Optical Instrumentation Technology Branch since 1985. He develops and applies optical instrumentation to aerospace applications, with a particular emphasis on turbomachinery applications.

His areas of interest are Time-of-Flight anemometry and Particle Image Velocimetry. *Page 2.1*



WIEDEMANN, Andreas received his degree in Physics (1997) from the University of Göttingen.

He joined the DLR in 1994. First he was working on boundary layers instabilities.

Since 1997, he is working on Laser Doppler Velocimetry. *Page 14.1*



YAMAGUCHI, Yutaka : received Bachelor of Engineering, Master of Engineering, and Doctor of Engineering in Aeronautical Engineering from Kyushu University. He joined the Department of Aeronautical Engineering at the National Defense Academy in 1975 as an Assistant Professor. He teaches Fluid Dynamics and Aerodynamics in Aerospace Engineering. His research includes unsteady aerodynamics, shock tube and transonic aerodynamics.

He is currently working in cryogenic wind tunnel research and wind tunnel testing techniques. *Page 34.1*



ZUCKERWAR, Allan received the BS and MS degree in Electrical Engineering from Carnegie Mellon University and the Dr. Sci. in Physics from the University of Stuttgart.

Since 1973, he has been engaged in acoustical and pressure sensor research and development at the NASA Langley Research Center. He is a fellow of the Acoustical Society of America. *Page 36.1*



ZURKOWSKI, Stanislaw, Ph.D., Eur. Ing. Adjunct Professor and chairman of Board of Aeroengines Department, Institute of Aviation, Warsaw, Poland. R&D works in combustion chambers ; 4 patents, 1 registred pattern, 39 papers, 1 book. M.Sc.M.E. of Technology (1979), Ph.D. (Applied Mechanics) from this University (1989). Fulbright Foundation grantee in University of California, Berkeley, U.S.A. (1991/92) and British Council grantee in Rolls-Royce, Derby, Great Britain (1993). Deputy Chairman of Polish Astronautical Society and Secretary of Astronautical Commission in Space Research Committee of Polish Academy of Sciences. Member of New York Academy of Sciences.

Page 5.1

